Internal-Tide Generation along Continental Margins

Joseph Andrew Elmes

Submitted in accordance with the requirements for the degree of

Doctor of Philosophy

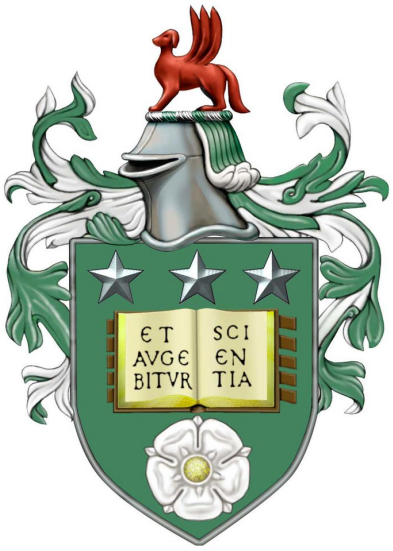

University of Leeds

Department of Applied Mathematics

July 2022

Le savant n'étudie pas la nature parce que cela est utile ; il l'étudie parce qu'il y prend plaisir et il y prend plaisir parce qu'elle est belle. Si la nature n'était pas belle, elle ne vaudrait pas la peine d'être vécue. Je ne parle pas ici, bien entendu, de cette beauté qui frappe les sens, de la beauté des qualités et des apparences ; non que j'en fasse fi, loin de là, mais elle n'a rien à faire avec la science ; je veux parler de cette beauté plus intime qui vient de l'ordre harmonieux des parties, et qu'une intelligence pure peut saisir.

Henri Poincaré

Intellectual Property Statement

The candidate confirms that the work submitted is their own, except where work which has formed part of jointly authored publications has been included. The contribution of the candidate and the other authors to this work has been explicitly indicated below. The candidate confirms that appropriate credit has been given within the thesis where reference has been made to the work of others.

Acknowledgements

This work was supported by the Leeds-York NERC SPHERES Doctoral Training Partnership (NE/L002574/1). This work was undertaken on ARC4, part of the High Performance Computing facilities at the University of Leeds, UK.

I would like to take this opportunity to express my sincere gratitude to both Stephen Griffiths and Onno Bokhove. In particular, I would like to thank Stephen for giving me the opportunity to pursue this project. Over the past six years, you have taught me so much, and for that I am grateful. I will always admire your ability to re-formulate and deconstruct complex mathematical expressions and expose their beauty. To Onno, thank you for being patient with me. Your work ethic and determination, as well as your love for communicating science to the general public, will always be a great source of inspiration.

For my colleagues, it is difficult to begin to acknowledge the many individuals who have accompanied me on this long journey. Particular individuals I would like to name include Oscar Brauer, Luke Gostelow, Alexander Kimbley, Patrick Lewis, Janet Peifer, Christina Pontin, Lucy Recchia, Matt Threadgold, and Nils de Vries. I have enjoyed our nonsense conversations and the many coffee breaks (especially when with biscuits!).

To those at Hyde Park Harriers running club, thank you for helping me stay healthy, both mentally and physically, over what has been a challenging four years.

Finally, I would like to express heartfelt gratitude to my fellow colleague and partner, Muyang Zhang. No matter what the future brings, I will always treasure the moments we shared together at home and in the office. Through good and through bad, your love and support have always provided me with a sense of stability and balance.

Abstract

Surface tides are the periodic motions of our world's ocean due to the gravitational attraction of the Sun and Moon. When these deep tidal flows encounter variable bottom topography, the stratified ocean interior is forced to move up and down periodically, leading to the generation of internal waves of tidal frequency - the internal tide. These internal tides radiate away from the topography and can break in the ocean interior, leading to vertical mixing that plays a role in the ocean potential energy budget. The energy conversion to internal tides is thus of great interest. While global satellite observations estimate a tidal conversion rate of $\sim 1\,\mathrm{TW}$, there remains considerable uncertainty in this estimate, and its split between open-ocean generation (seamounts, mid-ocean ridges, etc.) and coastal generation (continental slopes).

In this thesis, we perform mathematical and numerical modelling of internal-tide generation at continental slopes, which is less well-studied than for open-ocean topographic features. We use a two-layer linear shallow-water model to study the forcing of internal tides by a barotropic Kelvin wave, which is typical of many semi-diurnal coastal tides. Using a modal decomposition of the barotropic and internal modes above variable topography, we focus on two main problems.

The first problem is internal-tide generation along a uniform continental slope. Here, the internal tides are forced by a weak cross-shore flow that is induced in the barotropic Kelvin wave as it moves over variable bottom topography, the strength of which can be estimated asymptotically. This is a three-dimensional internal-tide generation problem, which we solve analytically when the continental slope is a step, and numerically for more realistic slopes of finite width.

The second problem is internal-tide generation along a continental slope that is incised by submarine canyons, which are a ubiquitous feature of continental slopes. Whilst there have been modelling studies of internal-tide generation at particular canyons, our emphasis is on understanding how the amplitude and direction of the radiating internal tides depend upon the canyon geometry more generally, given the diversity of canyons that exist across the globe. To do this, we study idealised canyon configurations incising idealised continental slopes, enabling us to define and then explore a wide parameter space. This is possible due to the development of a high-accuracy discontinuous Galerkin finite element numerical scheme, which enables us to focus the numerical reso-

lution on the narrow canyons and continental slope while still permitting wave radiation in the far field. We conclude that, despite the larger topographic gradients, canyons decrease the strength of internal-tide generation, because the canyons strongly modify the local form of the barotropic tide.

Contents

List of Figures

List of Tables

Chapter 1

Introduction

1.1 Waves and Tides in the Ocean

1.1.1 Waves in the Ocean

The world's ocean and atmosphere are in constant motion. One way this motion typically manifests itself is through wave dynamics. Perhaps the most familiar example is that of surface waves: the waves which form at the interface between the ocean surface and the atmosphere. The most common of these is the wave which forms at the ocean surface, which is a type of gravity wave. From the perspective of a fluid particle, if a fluid particle is perturbed vertically from its equilibrium position, it will acquire an oscillatory motion, much like a pendulum or spring. In this case, it is gravity that tries to return the fluid particle to its equilibrium position.

Besides surface waves, there are also internal waves. Internal waves exist within a fluid medium whose density profile varies with depth. This variation is more commonly referred to as the stratification—from the root Latin word *stratum*, meaning horizontal layer—of a fluid. In the world's ocean, the change in density occurs due to the variability in salt concentration and temperature. Towards the surface of the ocean, the fluid tends to be warmer and less saline. As one descends beyond the upper well-mixed layer, the water becomes colder and more saline as solar heating is no longer able to penetrate the deeper depths. The configuration where lighter fluid sits on top of heavier fluid is referred to as stable stratification. Internal waves are typically much greater in amplitude than surface waves. In some places, the amplitude of internal waves can reach up to several hundred metres in the deeper ocean and can leave small signatures on the surface of the ocean, as shown in Figure 1.1. While the theory of internal waves first began with the work of Stokes (1847), it took a further 60 years for the first modern scientific account for their observation in nature to be recorded by Helland-Hansen and Nansen (1909).

The generation of ocean waves, both surface and internal, typically occurs due to atmospheric (mainly wind) or tidal forcing. These waves, once forced, propagate energy through the ocean, where they will typically interact with other waves, eddies and bottom

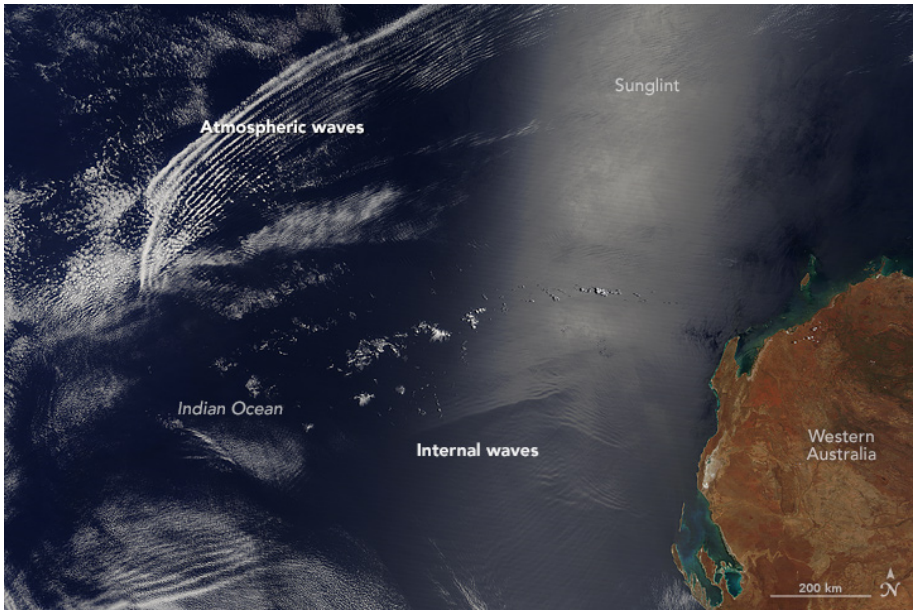

Figure 1.1: Atmospheric and oceanic internal gravity waves off the coast of Western Australia (from Schmaltz, 2016). The atmospheric waves appear as lines of clouds. The ocean waves are shown by the reflected sunlight.

topography. Internal waves travel at a fraction of the speed of surface waves; internal wave speeds of 3–4 m/s, dependent on the stratification, are common in the deep ocean, while wave speeds of 200 m/s are common for surface waves. Eventually, the propagating waves may break and induce vertical mixing. This vertical mixing is important for supplying the nutrients to the upper ocean where primary biological production occurs (see Garrett, 2001; Melet et al., 2022). Current climate projections suggest that the productivity of the open ocean will likely decrease by between 4% and 11% by the end of the current century, mostly because of the effects of enhanced upper ocean stratification in reducing the turbulent mixing supply of nutrients (see Intergovernmental Panel on Climate Change (IPCC), 2022).

1.1.2 Surface Tides

Surface tides are surface waves forced by the gravitational and rotational systems of the Sun and Moon with the Earth. These waves involve motion of the entire fluid column; this is referred to as barotropic motion. Consequently, surface tides are responsible for the periodic rise and fall of sea levels, and are of great importance for navigation, coastal safety, and coastal ecology (see Gerkema, 2019). The motions are typically forced at periods associated with the rotation rate of the Earth, i.e. diurnal (daily) and semi-diurnal (twice-daily) frequencies. While we speak largely of the Sun and Moon, there are in fact almost 400 constituents from various astronomical bodies within our solar system (see Godin, 1972). For each astronomical body, there may be several components due to eccentricity, obliquity, and precession. However, as Table 1.1 indicates, the most energetic are due to the Sun and Moon.

The amplitudes of surface tides depend greatly on resonance; particular tidal motions are

Darwinian Symbol	Period (Hours)	Origin	Kinetic Energy (PJ)	Tidal Dissipation (TW)	Contribution (%)
M2	12.42	Moon	177.86	2.435	63.4
S2	12.0	Sun	28.76	0.376	10.2
N2	12.66	Elliptical orbit of Moon	8.14	0.110	3.0
K2	11.97	Declinational Sun & Moon	2.34	0.030	0.8
K1	23.93	Declinational Sun & Moon	31.41	0.343	9.3
O1	25.82	Moon	16.03	0.173	4.7

Table 1.1: Kinetic energy and tidal dissipation of principal tidal constituents using tidal data from Egbert and Ray (2003), and tidal periods from Pond and Pickard (1983). The number in the mode symbol indicates typically the frequency of the constituent, i.e. diurnal (1) or semi-diurnal (2).

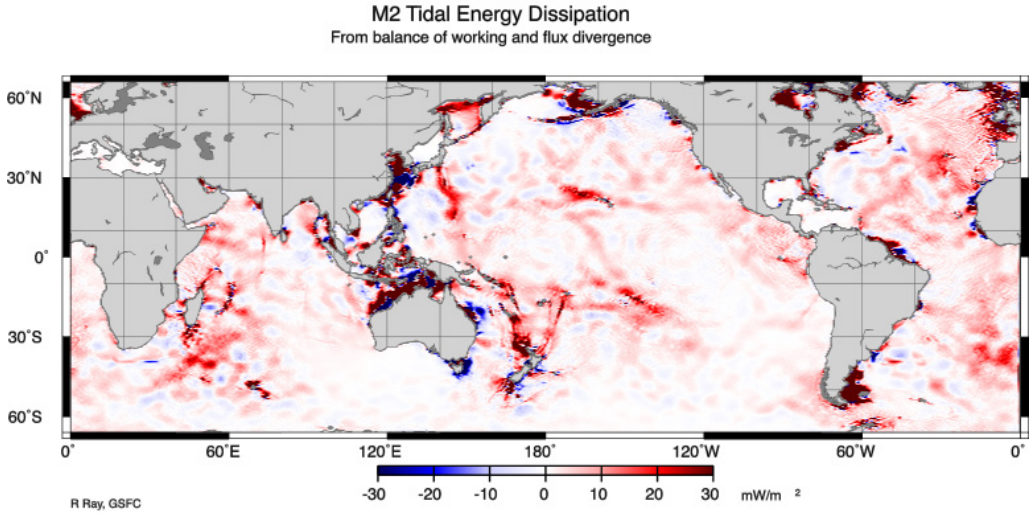

Figure 1.2: Principal lunar semi-diurnal (M2) tidal dissipation from Egbert and Ray (2001).

strongly excited if the mode's fundamental frequency is close to the forcing frequency. For example, in the North Atlantic and Pacific oceans, semi-diurnal motions are amplified (see Heath, 1981). However, tidal amplitudes can also depend on the effects of shoaling and funnelling as continuity in tidal energy flux leads to an increase in energetic density as a wave encounters a region of reduced depth or width, e.g. the Bristol channel of the UK, the Bay of Fundy of Canada, and the Baie du Mont Saint Michel of France. In general, tidal amplitudes observed on the surface of our oceans are 1 m near the coast, and around 0.5 m in the open ocean (e.g. Garrett, 1972; Arbic et al., 2007).

Despite a constant input of energy due to tidal forcing, the amplitudes of surface tides do not grow since there is an equilibrium between the work done by continual astronomical forcing and the dissipation of tidal energy. This loss of energy manifests itself in the form of tidal recession (e.g. lunar recession). Using lunar-laser ranging, for example, a lunar recession of 3.8 cm/year can be calculated (see Chapront et al., 2002). From this rate of orbital recession, it is possible to infer a dissipation rate of 2.5 ± 0.05 TW for the M2 tide

(e.g. Lambeck, 1980; Munk & Wunsch, 1998). The total tidal dissipation in our oceans can also be estimated using sea-surface height (SSH) measurements collected by satellite altimetry (see §14 of Cartwright, 1999). The data are then assimilated into numerical models (e.g. Egbert & Ray, 2000, 2001, 2003). An example of the latter is shown in Figure 1.2 for the M2 tide and implies a total dissipation rate of 2.536 ± 0.016 TW. Using the same process, the total tidal dissipation rate of all constituents is estimated to be 3.7 TW (Egbert & Ray, 2003). The tidal constituents shown in Table 1.1 account for 91.4% of the total dissipation rate.

The nature of the dissipation has been a central question in geophysics for over 100 years. Since the very beginning of this endeavour, it was largely acknowledged that very little dissipation took place in the solid Earth. In fact, Egbert and Ray (2001) estimates that ~ 0.2 TW of this power is lost in the atmosphere or solid Earth. Most early dissipation theories appealed to the existence of a turbulent bottom-boundary layer (BBL), which would be greatest in coastal waters where tidal flows are strongest. Jeffreys (1921) gave an initial estimation of ~ 1.1 TW, which has since been revised up to ~ 2.6 TW. Over the past 70 years, the geophysical community has identified the potential missing key to resolve the global energy budget of our ocean: the generation of internal tides. These are internal waves generated in our stably stratified ocean and are forced by the barotropic motions of tidal frequencies flowing over variable bottom topography. These waves transport energy over large length scales (see Munk & Wunsch, 1998; Wunsch, 2000), which subsequently break and produce vertical mixing. The associated mixing not only affects ocean structure and circulation (Garrett & Kunze, 2007), but also provides a "key mechanism for transferring heat from the upper ocean to the depth" (Chandler, 2014).

1.1.3 Internal Tides

The initial recognition of internal tides is credited to Swedish oceanographer Otto Petterson (see Petterson, 1908). These internal motions are typically referred to as baroclinic and have no net horizontal volume transport. According to Hendershott (1981) and Vlasenko et al. (2005), early investigations were motivated by Nansen (1902) which observed that during the Norwegian expedition to the North pole aboard the *Fram*, the ship was retarded when sailing over a thin layer of fresh water overlying saltier water along the Barents Sea.[1] Ekman (1904) later confirmed that this phenomenon was a result of the generation of interfacial waves between the two layers. On the subject of internal tides though, it was experiments conducted by Zeilon (1912, 1934) which produced the first theoretical account. As told in Hendershott (1981), these experiments seem to have been the precursor to the now widely accepted theory that energy is transferred from the surface wave to the internal wave by the flow over variable bottom topography. During the 1970s, the first sets of observational data started to appear (e.g. Wunsch, 1975; Schott, 1977). At the time however, energy dissipation for internal wave generation was thought to be around 10% of the total tidal dissipation. Nonetheless, Wunsch (1975), Garrett (1979) and Hendershott

[1] The melting ice produces fresh, less saline water. An exception is under ice shelves, perhaps, where ice solidifying can leave salt behind.

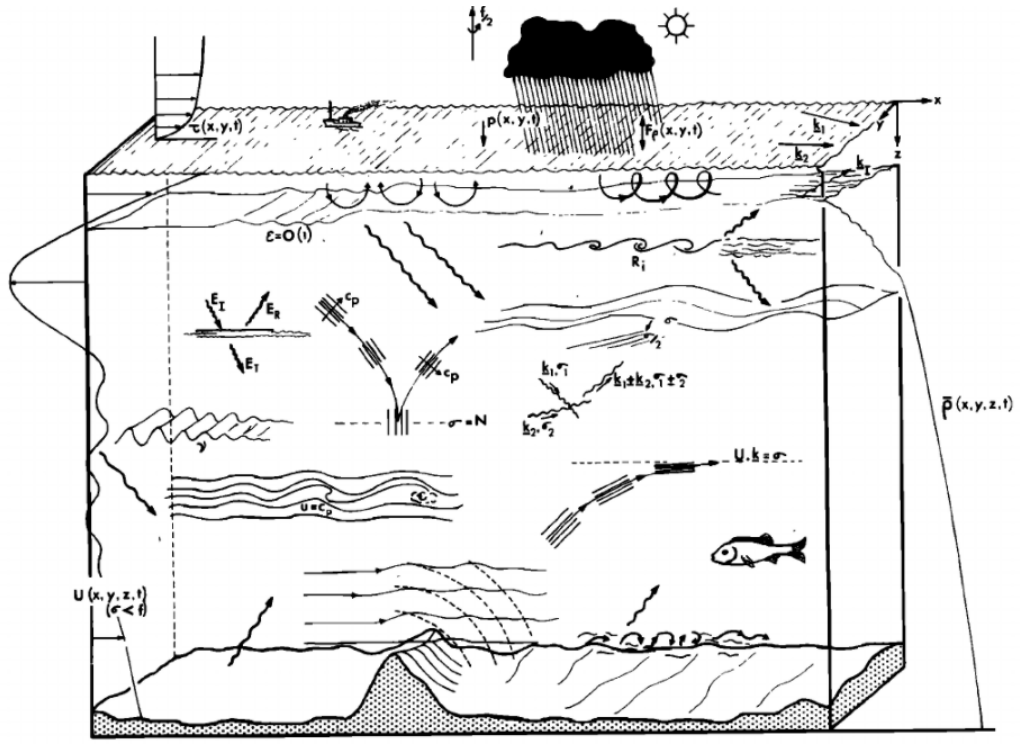

Figure 1.3: Representation of processes which affect internal waves within the ocean (from Thorpe, 1975), including internal wave breaking, shear instabilities and resonant interactions.

(1981) still argued that this figure could still play a significant role in deep-ocean mixing.

In the past two decades, research on internal-tide generation has attracted renewed interest largely due to a greater significance placed on mid-ocean topographic features such as the Mariana Trench and the Mid-Atlantic Ridge (see Munk & Wunsch, 1998). Kantha and Tierney (1997) and Ray and Mitchum (1997) explain the significance of satellite altimetry in mapping SSH and how the process had shown for the first time the generation of internal waves propagating away from mid-ocean ridges. The latter observation is corroborated by Morozov (1995), whereby measurements were made on clusters and arrays of moored buoys in more than 30 areas of the ocean. Using both numerical models and observations to investigate the cascade from tides to turbulence (Rudnick et al., 2003), the HOME mission carried out along the Hawaiian Ridge was able to account for 2% of the global deep-water tidal loss, showing that "tidal conversion at ridges is an important source of energy for mixing." With the turn of the new millennium, the joint Topex/Poseiden satellite mission between France and America revised previous figures for total tidal dissipation in internal wave generation to 30% (Egbert & Ray, 2000, 2001) which is equivalent to $\sim 1.2\,\mathrm{TW}$, a rate which accounts for over half of the power needed to drive abyssal mixing and sustain the overturning circulation (Munk & Wunsch, 1998). A summary of the processes which affect internal waves in the ocean, including the generation of internal waves over variable topography, is shown in Figure 1.3, along with other rich phenomena such as wave-breaking, shear instabilities, resonant interactions, and wave scattering (see Munk, 1981).

In essence, however, there are three key processes of internal tides: generation, propagation, and dissipation. For each aspect, the modelling can vary quite substantially. For example, it has long been known that the generation of internal tides is largely a linear phenomenon (e.g. Rattray, 1960; Cox & Sandstrom, 1962; Bell, 1975a, 1975b; Baines, 1982). On the other hand, oceanic observations consistently show the existence of internal solitary waves (e.g. R. D. Pingree et al., 1986; New & Pingree, 1992; Small et al., 1999) propagating away from generation sites, such as ridges or continental slopes, and even breaking on distant continental slopes (see Nash et al., 2004). Figure 1.4, taken from Bourgault et al. (2016), illustrates the large-amplitude hump-shaped nature of internal solitary waves. Mathematically, these solitary waves are often associated with the travelling-wave solution

$$u\,(x,t) = a\,\mathrm{sech}\,[\beta\,(x - c\,t)] \qquad \text{with} \qquad \mathrm{sech}\,(y) = \frac{1}{\cosh\,(y)} \tag{1.1}$$

of the Korteweg–de Vries (KdV) equation

$$\partial_t u + 6u\,\partial_x u + \partial_{xxx} u = 0, \tag{1.2}$$

first derived in Korteweg and de Vries (1895). This equation, as Pelinovsky et al. (2007) shows, is constructed using a multi-scale asymptotic procedure of the governing equations. Further information on solitary waves and the KdV equation can be found in Dodd et al. (1982) and Drazin (1988). Yuan, Grimshaw, and Johnson (2018), for example, considers the propagation of an internal wave in a three-layer system described by a variable-coefficient form of (1.2) (see Grimshaw, 2007, for more context on the variable-coefficient KdV equation).

Along with the internal tide mechanism, there is also the aspect of location: coastal or open ocean. For example, internal tides in the open ocean tend to be generated within the weakly stratified interior over ridges, sea mounts and trenches (e.g. Holloway & Merrifield, 1999; Rudnick et al., 2003; Pétrélis et al., 2006). Conversely, internal tides in coastal waters are typically trapped in the pycnocline and are generated along the continental slope (e.g. Baines, 1982; Subeesh et al., 2021). In fact, the introduction of Huthnance (1989) includes a detailed list of literature documenting observations of internal tides along continental margins.

Given the large-scale nature of internal tides, the use of experiments to understand internal-tide generation and propagation is a challenging feat. Nonetheless, Mercier et al. (2013) considered a large-scale experiment using the Coriolis Platform of LEGI (Grenoble, France) to model internal-tide generation in the Luzon Straight. The Luzon Straight is a complex double-ridge system in the South China Sea and sees some of the strongest sources of internal tides in the world's ocean. The experiment considered many key factors of internal-tide generation, including three-dimensional bathymetry, non-linear stratification, semi-diurnal (M2) tidal forcing, and background rotation. The experiment concluded that the Luzon Straight appears to radiate a weakly non-linear M2 internal tide shaped

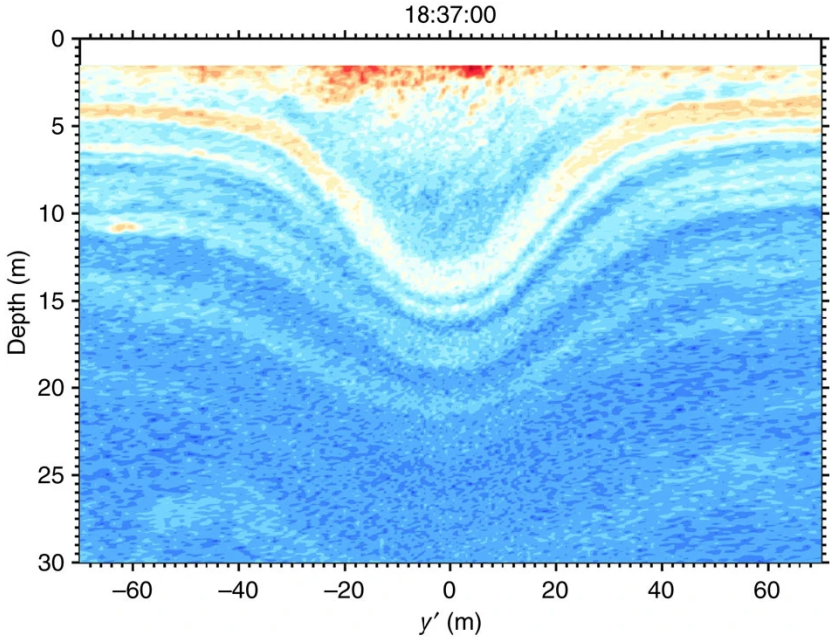

Figure 1.4: Echogram of a large internal solitary wave in nature, taken from Bourgault et al. (2016).

by the geometry. To put it another way, the generation mechanism of the internal tide is linear, and that the radiating wave steepens to become an internal solitary wave.

Basic mathematical models on internal-tide generation and propagation were first established in Rattray (1960) with the modelling of an internal wave generated along the interface of a two-layer fluid medium under the Boussinesq approximation forced by a 1D Poincaré wave over step topography. Using Fourier transforms and a Green's function, Cox and Sandstrom (1962) then looked at coupling linear internal waves with the surface mode over limited-sloping topography and considered the barotropic conversion by a Gaussian seamount. Using ray theory, a single integral equation was used by Baines (1973) to consider rotating two-dimensional linear flow under the Boussinesq approximation with a rigid lid in the sub-critical sloping regime. In this regime, the topographic slope is much smaller than the slope of the internal wave. The critical and supercritical regimes were then investigated by Baines (1974) using the same formulation but allowing the wave characteristic to intersect slopes. For the first time three-dimensional topography was considered in Bell (1975b) where, under linear theory, "solutions are linear transformations of the bottom topography." The latter meant that in phase space they were also proportional to the Fourier transform of the topography. This work however had two limitations: linear theory on topography, and the constraint of a rigid lid. In essence, these assumptions neglect the free surface, and apply the bottom boundary condition at some flat surface $z = -H$, as opposed to the true sea floor positioned at $z = -H + b(\mathbf{x})$.

More recently, Llewellyn Smith and Young (2002) analysed a finite-depth system with arbitrary stratification expressed in terms of the Brunt–Väisälä frequency, $N(z)$, under both the hydrostatic and Boussinesq approximations. A weak-topography assumption was

also made whereby variations in topography are much smaller than the vertical scale of the waves, which in itself is much smaller than the slope of the tidal beam. The latter work is carried out using a WKB approximation[1] to solve for arbitrary $N(z)$ and considered idealised ridge shapes. Concerning 3D topography, Holloway and Merrifield (1999) and Munroe and Lamb (2005) have shown using the Princeton Ocean Model (POM) (see Blumberg & Mellor, 1987) that large seamounts are ineffective at internal-tide generation, unless elongated perpendicular to barotropic motion. Linear theory for small slopes and small variations in 2D topography compared to deep-ocean depth have also been developed. St. Laurent and Garrett (2002), for example, identified that choosing a coordinate axis parallel to the major and minor axis of the basic tidal current means that the internal tides generated by the two current components are out of phase and may be treated independently.

The work of Griffiths and Grimshaw (2007a) was pioneering in that modal equations modelling topographic coupling were developed without any restriction on topography or stratification. Its mathematical formulation used a three-dimensional modal decomposition and permitted the governing equations to reduce to a linear coupled system of equations for modal horizontal velocities $U_n(x, y, t)$ and $V_n(x, y, t)$ for $n = 0, 1, 2, \ldots$, with $n = 0$ denoting the barotropic component, and $n = 1, 2, 3, \ldots$ the baroclinic ones. The theory for modes is well-known in the case of uniform topography (e.g. LeBlond & Mysak, 1978; Gill, 1982; Vlasenko et al., 2005). The modal equations developed by Griffiths and Grimshaw (2007a) were then applied to internal-tide generation along continental margins, albeit in a two-dimensional setting (no variations along-shore). They derived an analytical solution for the case of a two-layer fluid and solved the case of uniform stratification numerically. This modal decomposition was reformulated in Griffiths (2010), which used it to produce estimates of global tidal dissipation using the first few baroclinic modes. A specialisation to multi-layer stratification was given by Shimizu (2011). Essentially the same ideas are present in the modal decompositions of Kelly (2016) and Lahaye and Llewellyn Smith (2020), which again focus on continuous stratification.

1.2 Research Scope

There is great interest in the energy conversion of the surface tides to the internal tides in a bid to resolve the global energy budget of the ocean. This is crucial since tidal dissipation and resultant mixing plays a significant role in the overall ocean circulation (Wunsch, 2000). However, much uncertainty exists in ocean circulation models over the continental margin due to the computational cost to resolve small-scale features of coastal topography over which internal-tide generation occurs. These small-scale features are important to resolve the global energy budget (Polzin et al., 1997). Current models do a reasonable job of parameterising mixing and dissipation in the open ocean, but tend to underestimate enhanced dissipation around coastal regions with small-scale topographic features, such

[1] A method for finding approximate solutions to linear differential equations with spatially varying coefficients.

as canyons or gullies (Jachec, 2012).

In almost all models of the Earth's climate, the sinking of cold dense water at high latitudes drives the meridional overturning circulation (Wunsch, 2000). This circulation leads to flows along the bottom of the ocean, where they are eventually brought back toward the surface by upwelling.[1] A steady state is reached when making the elementary assumption of balance between uniform upwelling of cold water and downward mixing of warm water (see page 284 of Wunsch & Ferrari, 2004, for more details). However, such assumptions on uniform mixing do not produce the strong flows observed along the ocean bottom. Instead, observations show that there is strong spatio-temporal variability in the processes which drive both dissipation and mixing, particularly around complex topographies (Vic et al., 2019).

Examples of coastal topography are shown in Figure 1.5. Note that the continental shelf, indicated by the light blue, and how the shelf break mirrors the coastline. To leading order, the width of the continental shelf can be considered uniform in the along-shore direction. However, a closer inspection reveals a myriad of small-scale topographic features.

Often, the form of the surface tide in coastal regions is that of a Kelvin wave. Kelvin waves have some of the largest horizontal length scales (around $2,000\,\text{km}$) amongst all gravity waves which exist under the effects of planetary rotation (more commonly referred to as inertia-gravity waves). In addition, these waves are trapped by the coastline. While it is more commonly described as a gravity wave which balances the effect of rotation (the Coriolis force) with the coastal lateral boundary, Huthnance (1981) gives a more illustrative interpretation: "trapping occurs because the Coriolis force piles up the forward-moving water at the crest against the coast." A result of this trapping is that the surface tide's wave energy is confined to the shelf and decreases off-shore. However, small-scale topographic features, such as submarine canyons, banks, and promontories, can intercept the along-shore propagation of the surface tide along the shelf where energy fluxes remain significant (Yankovsky & Zhang, 2017).

Indeed, there is much scope to develop mathematical models which parameterise the internal wave drag of the surface tide along the continental margin, particularly due to small-scale features. Of interest to the ocean sciences community, is how the dissipation rate of the surface tide and the direction of energy propagation depend upon the geometries of the continental margin. From the latter, regions of strong mixing may be inferred. For example, observations of large-scale internal tides indicate that they are able to propagate thousands of kilometres from the generation site before dissipating, while small-scale internal tides tend to break almost immediately and generate mixing in close proximity to the generation site. Such parameterisation can then be used in ocean circulation models without the need to numerically resolve the resulting flows around each small-scale feature.

[1] Upwelling is a process by which cold, dense water is brought up from the ocean depths to replace the warmer water at the surface being displaced by wind (NOAA, 2017).

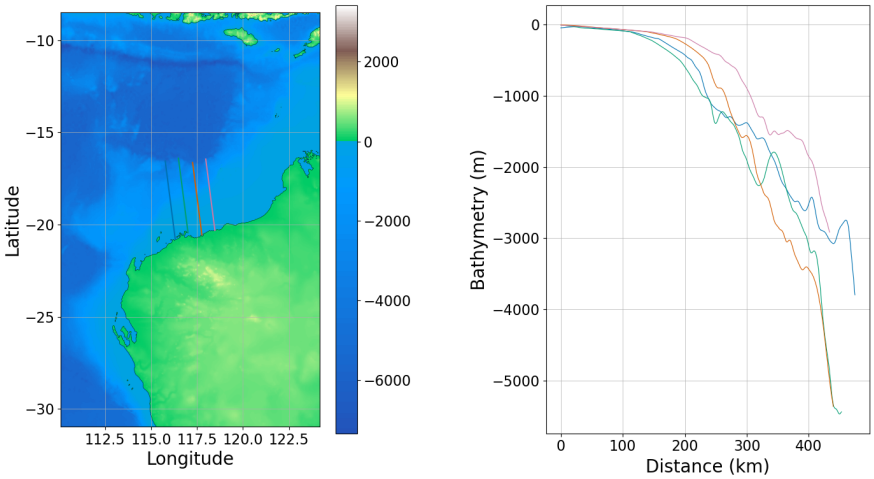

(a) North-West Australia

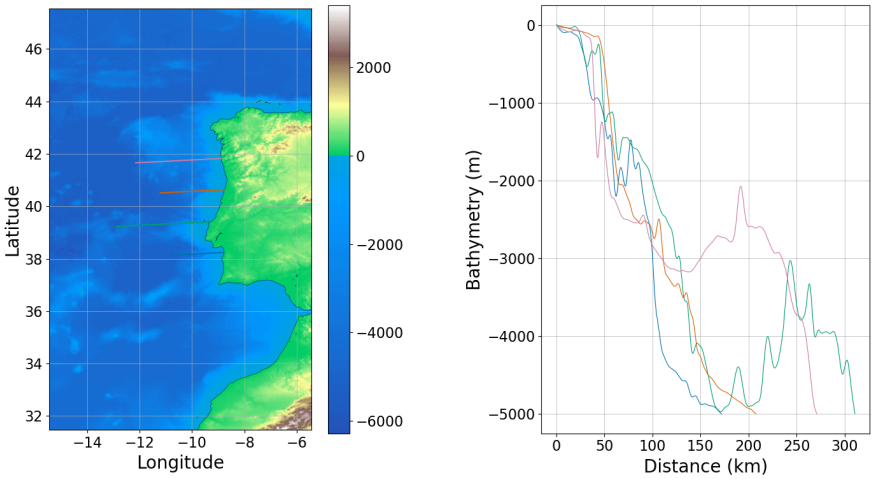

(b) Portugal

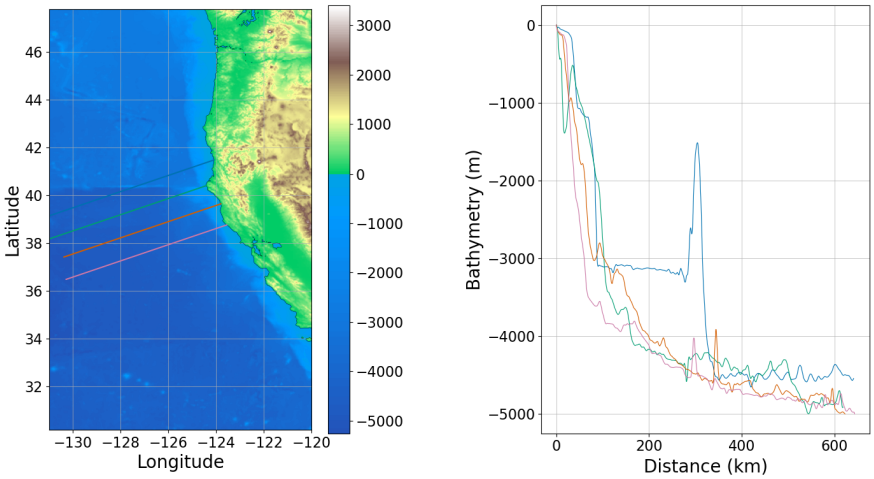

(c) West Coast of US

Figure 1.5: Bathymetry of continental margins using data from NOAA National Geophysical Data Center (2006). Here, the coastal bathymetry runs perpendicular to the coastline of: (a) North-West Australia; (b) Portugal; (c) West Coast of US. On the left, we show a contour plot of the fluid depth, while on the right, 1D cross-sections of bathymetry are plotted corresponding to those overlaid on the right.

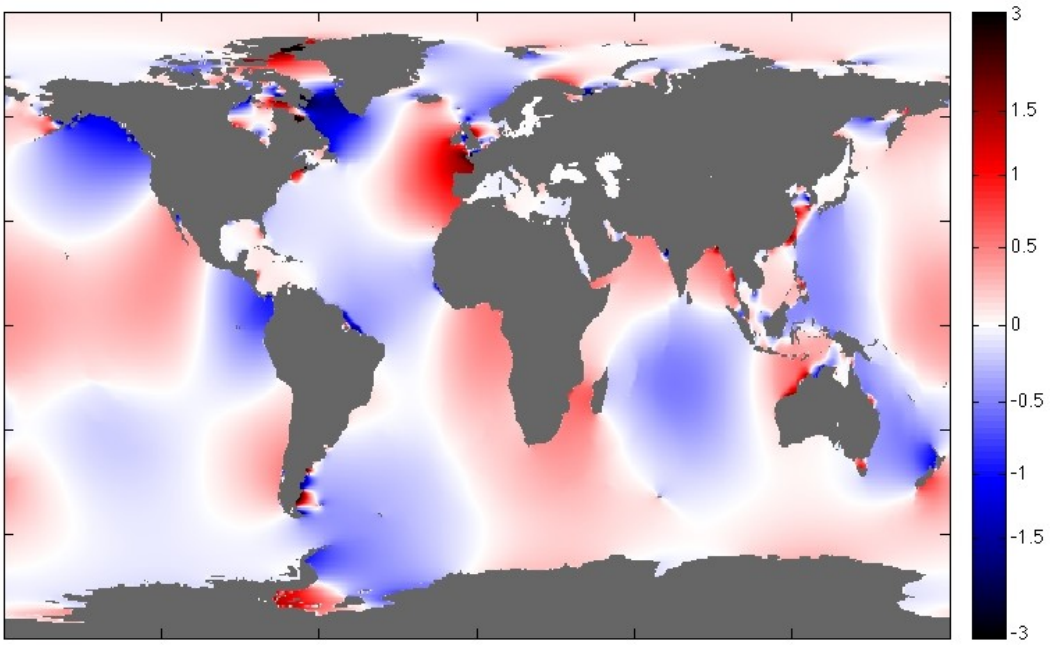

Figure 1.6: Principal lunar semi-diurnal (M2) tidal elevation (m) (composed using data from Egbert & Erofeeva, 2002). Kelvin waves are seen propagating at semi-diurnal frequency along the Patagonian shelf, along the Californian coastline and around the UK on the European continental shelf.

1.2.1 Kelvin Waves

The Kelvin wave is the dominant form of the surface tide in many coastal areas, as shown in Figure 1.6. One reason is that Kelvin waves can exist at all wave frequencies ω, independent of Coriolis parameter f and according to along-shore wavenumber k: $\omega = \omega(k)$ (see §7 of Huthnance, 1975). The latter is contrary to Rossby waves (which are sub-inertial such that $\omega^2 < f^2$) and inertia-gravity/Poincaré waves (which are super-inertial such that $\omega^2 > f^2$). Studies have also successfully fitted observational data to the Kelvin wave form, e.g. Munk et al. (1970) along the Californian coast and Cartwright et al. (1980) along the Scottish coast. In the trivial case of uniform topography in a semi-infinite ocean (see Thomson, 1879; Lamb, 1895), the cross-shore volume transport of the pure Kelvin wave is identically zero. The introduction of a continental slope introduces a cross-shore volume transport of around 10–30 m^2/s at the shelf break and can be of the same order of magnitude as along-shore volume transport along the shoreline. It is expected therefore that a significant proportion of internal-tide generation along continental margins can be attributed to the coastal Kelvin wave, making implied energy transfers significant on a global scale.

Previous analytical models of internal-tide generation along continental margins typically involve an incident surface wave which then transfers energy to an interfacial mode as the wave encounters a step-like shelf break (e.g. Rattray, 1960; Rattray et al., 1969; Barthélemy et al., 2000). This interfacial mode is used to model waves trapped along the pycnocline where the change in density gradient is greatest due to a well-mixed upper

layer heated by solar radiation overlaying a cold weakly stratified interior. The benefit to simple analytical models is that they provide tractable solutions which can easily be interpreted. These results can then be used to understand key scaling laws between system parameters (e.g. upper-layer depth, shelf width, density profile, wave frequency) and the implied radiating energy fluxes.

However, despite the surface tide along continental margins often taking the form of a Kelvin wave (e.g. Huthnance & Baines, 1982), there has been no corresponding analysis of the generation of a pycnocline mode by a Kelvin wave. In particular, how the resulting tidal dissipation depends upon coastal geometry (shelf width, slope width, etc.) remains unknown.

1.2.2 Canyons

One ubiquitous feature of continental margins are canyons. The definition of a canyon, coined by Shepard (1963), is a "steep-walled, sinuous valleys with V-shaped cross sections." Figure 1.7 from Harris and Whiteway (2011) shows a global map of around 5,000 different canyons which feature along the world's continental margins. The figure also shows that canyons can be categorised into three types: (1) those which incise the shelf and connect to rivers; (2) those which incise the shelf; (3) those which are confined to the slope. Figure 1.8 shows the key features of canyons (e.g. the head, the meandering nature, the composition of multiple tributaries), and how they incise the continental slope and reach onto the shelf. Examples of canyon systems, along with their key characteristics, are also shown in Table 1.2, including Congo, Monterey and Whittard. These characteristics, such as length and depth, are important length scales which should be considered in idealised modelling. Table 1.3, constructed using data provided by Harris and Whiteway (2011), also shows mean values of geomorphic attributes and how they differ among the three different canyon types. It should be noted that the absence of canyon width data in Harris and Whiteway (2011) is possibly due to the uncertainty in both measurement and definition. However, additional data from Harris et al. (2014) (accessed via Blue Habitats) gives a mean canyon width of 14.6 km with a standard deviation of 15.7 km.[1] Data from Harris et al. (2014) also updates the previous number of canyons to $\sim 9,450$. Here, it is suggested that canyons cover $\sim 11\%$ of the Earth's continental slopes, while Hickey (1995) estimated $\sim 20\%$ of north-west America.

Of interest to those studying internal-tide generation along continental margins, including Petruncio et al. (2002), Jachec et al. (2006) and Zhang et al. (2014), is that canyons can be efficient generators of internal tides through the dissipation of the barotropic tide (Bell, 1975b; Baines, 1983). For others, including Nazarian and Legg (2017a), Nazarian and Legg (2017b), Nazarian et al. (2021), Hall and Carter (2011) and Vlasenko et al. (2016), is that canyons are thought to trap remotely generated internal waves through reflection, and then channel the energy toward the canyon head (Gordon & Marshall, 1976; Hotchkiss

[1] It can only be assumed that the widths provided are averaged over the meandering tributary of the canyon.

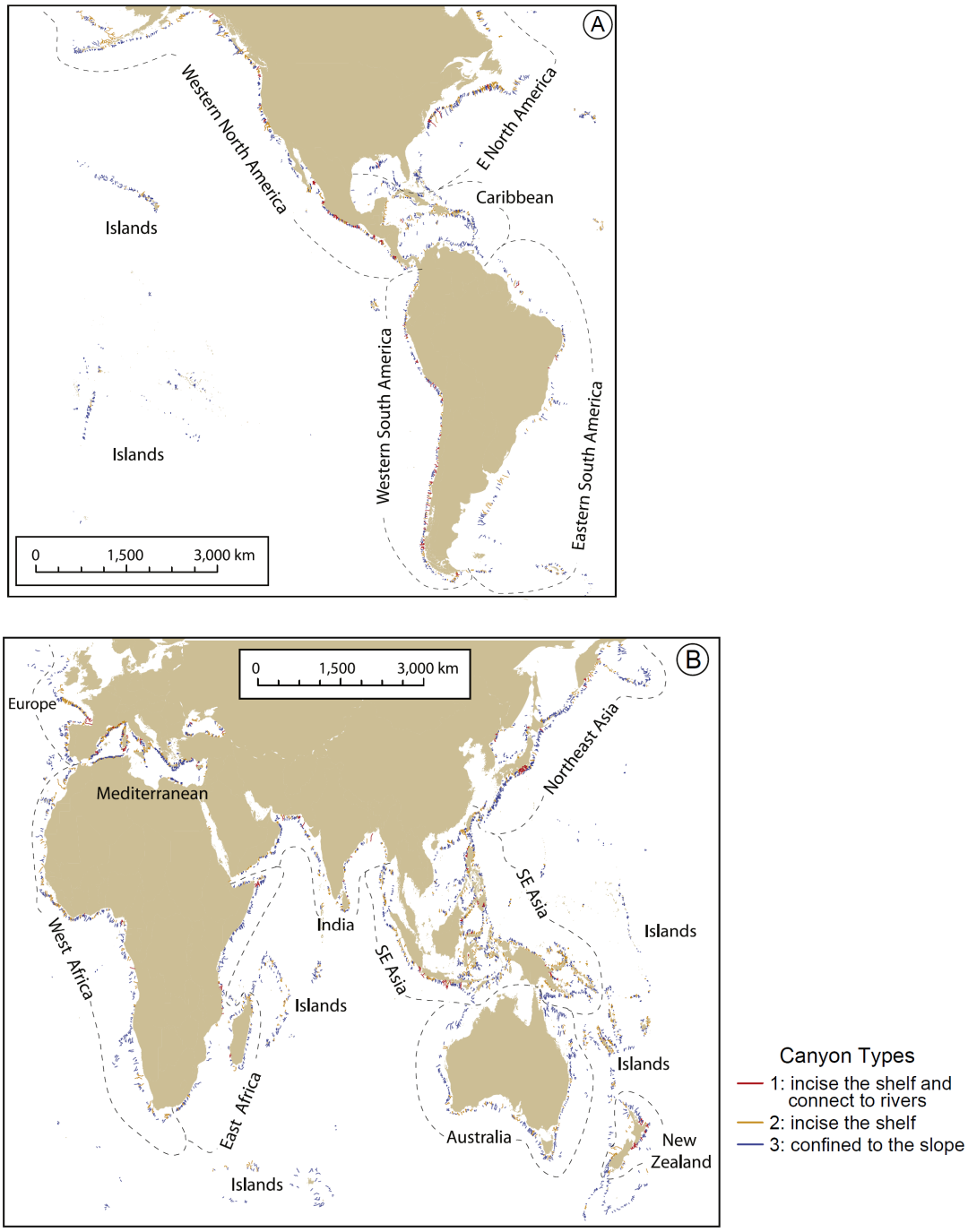

Figure 1.7: From Harris and Whiteway (2011), positions of around 5,000 canyons across America and Afro-Eurasia are shown to be a ubiquitous feature of continental slopes. The Figure also illustrates canyon type, as indicated by the legend. Most canyons are observed to be confined to the slope (type 3).

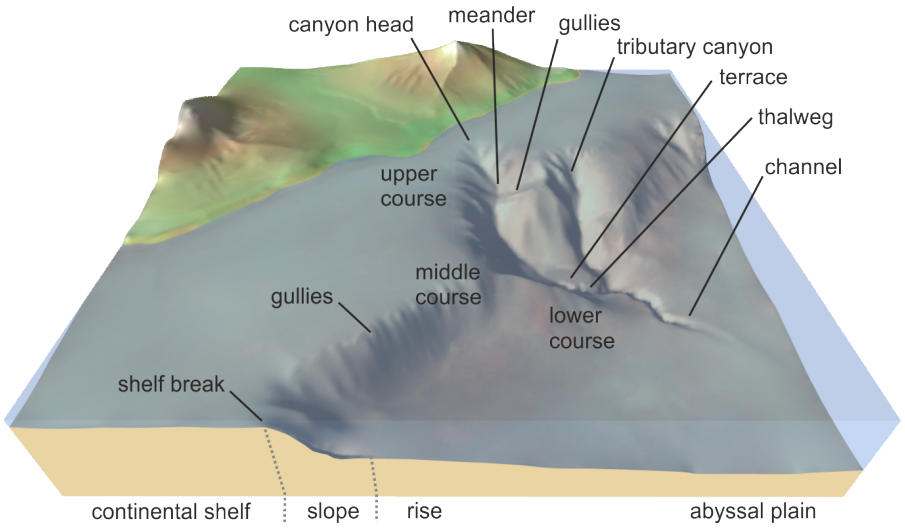

Figure 1.8: Geomorphology of shelf-incising canyons (Figure 3 of Amblas et al., 2018).

Name (Active/Passive)	Length (km)	Head Depth (m)	Termination Depth (m)	Slope °	Sinuosity	Spacing (km)
Amazon (P)	211	96	2631	1.40	1.28	45.2
Bering (A)	412	199	3338	1.20	1.35	108.1
Congo (P)	100	14	1852	3.55	1.03	103.6
Ganges (P)	183	85	1537	2.05	1.04	110.9
Hydrographer (P)	40	191	2025	4.43	1.08	33.6
Monterey (A)	93	123	3661	3.82	1.22	33.2
Nazaré (P)	91	55	4458	5.39	1.27	36.0
Whittard (P)	184	166	4033	2.89	1.19	46.5

Table 1.2: Examples of submarine canyons and their geomorphic attributes (extracted from Supplementary materials 2 of Harris & Whiteway, 2011). Here, the nature of the continental margin is also indicated as being active or passive.

& Wunsch, 1982). Indeed, observations have supported this notion. For example, Hallock and Field (2005) reports observations on the New Jersey shelf showing vertical profiles of time-averaged energy fluxes. It is observed that the highest energy fluxes occur 18 km southwest of the Hudson Canyon and are dominated by the pycnocline mode.

Understanding the dependence of internal-tide generation upon canyon geometry would be challenging and extremely time-consuming with traditional ocean circulation models, because of the small length scales of both the canyons and the internal tides. The closest we have to this is the study of Zhang et al. (2014), using the Regional Ocean Modelling System (ROMS) (see Shchepetkin & McWilliams, 2005), which gave 13 simulations covering seven different canyon widths (5 km–70 km) and five different canyon lengths (5 km–20 km) in various combinations. Although their results are interesting and illuminating (e.g. with regard to asymmetrical beams of internal tides propagating onto the shelf), they do not give a comprehensive parameter sweep showing the dependence of tidal dissipation upon canyon geometry.

	Type 1	Type 2	Type 3	Combined
Number	153	1,671	4,025	4,380
Length (km)	80.9	50.4	39.1	43.4
Depth Range (m)	2,767	2,265	1,849	1,992
Slope (degrees)	3.8	5.2	5.2	5.1
Spacing (km)	33.8	33.5	32.7	33.0
Sinuosity	1.187	1.121	1.111	1.111

Table 1.3: Mean values of geomorphic attributes extracted from data provided by Harris and Whiteway (2011) for 4,380 recorded submarine canyons of type: (1) those which incise the shelf and connect to rivers; (2) those which incise the shelf; (3) those which are confined to the slope.

1.3 Aims of Thesis

This thesis develops simplified mathematical models of internal-tide generation and propagation in idealised three-dimensional geometries, building on previous two-dimensional cases. This will involve the combination of simplifying assumptions around the fluid motion, density stratification and sea-floor topography so that the governing system of non-linear partial differential equations may be reduced to a more tractable system. Consequently, both analytical and numerical solutions shall be sought, allowing a wide range of parameter space to be investigated. This will in turn give a better understanding of the energy transfer from surface tides to internal tides under varying forcing scenarios, which are known to have a non-trivial dependence upon topographic length scales.

Motivated by the research scope presented in the previous section, the main goals of the thesis are to:

- Understand internal tides generated by a three-dimensional surface tide (in the form of a Kelvin wave) about a two-dimensional topography (representing a continental margin).
- Understand the role of topographic variations in the along-shore direction, i.e. for a three-dimensional tide above a fully three-dimensional topography in the form of a canyon incising a continental margin. It is known from observations (e.g. Hallock & Field, 2005) that canyons can lead to enhanced internal-tide generation (and dissipation) since they intercept the along-shore propagation of the tide.

To achieve these goals, the thesis considers the modelling of a semi-diurnal barotropic tide in the form of a Kelvin wave propagating along an idealised continental margin. This surface tide is then used to force a baroclinic response, from which time-averaged radiating energy fluxes are implied to calculate the dissipation of the surface tide. The ubiquitous nature of submarine canyons which incise the continental margins of the world's ocean basins are a potential source of enhanced barotropic dissipation, which, on a global scale could be significant in resolving the ocean's energy budget. Being able to parameterise the effect of canyons on the tide, both surface and internal, brings an additional level of complexity which cannot be approached without the use of sophisticated numerical

methods.

For efficiency, the multi-modal linear modelling strategy of Griffiths and Grimshaw (2007a) and Griffiths (2010) (see also Shimizu, 2011; Kelly, 2016; Lahaye & Llewellyn Smith, 2020), which accounted for arbitrarily large topographic variations to couple the surface and internal tide, can be considered. For flow around submarine canyons, we solve the governing equations with cutting-edge numerics in the form of discontinuous Galerkin finite element methodology (DG-FEM).

Compared to more familiar grid-based computational methods, there are many properties of DG-FEM which render the method ideal for tidal flows around continental margins. In particular, DG-FEM allows one to resolve tidal dynamics over discontinuous topographies in complex geometries with high-order adaptive accuracy, all while satisfying conservation laws. In addition, the localised nature of DG-FEM means that operators are often incredibly sparse, making the method much more efficient than regular finite element methods. Coupled with high-quality variable-resolution meshes, the method has a lot of potential in allowing parameter space to be explored.

1.4 Thesis Outline

The proposed aims of the thesis, also given, sought to address some of these research questions directly. Having stated the means of achieving the research goals, the outline of the thesis is as follows.

Chapter 2 introduces the theoretical framework necessary to study tides, both surface and internal, in a localised region along the coast. Here, the governing equations are derived under a range of simplifying assumptions, along with the implied laws for energy conservation. This required developing the theory of modal decomposition proposed by Griffiths and Grimshaw (2007a) for multi-layer stratification as in Shimizu (2011). From the governing equations, key quantities of interest in our study are derived: the barotropic dissipation rate and the baroclinic energy flux. For time-periodic flows, the dissipation of the surface tide is found to equal the total energy flux of radiating internal waves.

Chapter 3 deals with the notion of normal modes of ocean basins. It is shown that for tidal frequencies, the dominant form of the tide along continental margins is the Kelvin wave. The latter motivates the derivation of the analytical form of the mode, reproducing known results of Miles (1972) and Smith (1972). This will allow us to consider above all the dependence of volume transport across the continental margin on the form of the slope, the forcing frequency, the form of the equilibrium tide and the geometric length scales of the continental margin.

Chapter 4 focuses on the internal-tide response by a surface tide in the form of a Kelvin wave along a continental margin that is uniform in the along-shore direction. Here, we compare the internal-tide response of a tidally forced surface tide with that of a decoupled Kelvin mode. An extension to the analytical solution for non-trivial topography derived

in Griffiths and Grimshaw (2007a) is pursued, but with a free wave. The aforementioned result will then allow greater understanding of the implied energy fluxes of the internal-tide response by developing key scaling laws.

Chapter 5 deals with the methodology of discontinuous Galerkin finite elements, and how it can be used to solve the governing equations of motion. The implementation of the numerical method, which includes a range of numerical fluxes and orders, is then verified for barotropic motion under different means of convergence. This process of verification has two steps. The first is to consider known eigenvalue problems for which there are analytical solutions (including with rotation). The second is to consider the boundary-value problem associated with the non-trivial coastal Kelvin wave.

Chapter 6 focuses on the effect of canyon geometry on the tide. For the first time in the thesis, along-shore variations in topography are considered. A model for canyons is conceived, offering a novel means of parameterising the geometry of shelf-incising canyons. A parameter sweep is conducted to determine the effect of canyon geometry on a free Kelvin wave. In a decoupled model, it is necessary to solve for the surface tide to force a baroclinic response. From this analysis, we try to understand possible implications on the baroclinic response and its implied radiating energy fluxes.

In Chapter 7, we use the form of the barotropic tide, or Kelvin wave—as calculated in Chapter 6—to force a baroclinic response around canyon topography. Having configured the means by which radiating conditions are applied, around 10,000 simulations are carried out to create a robust understanding of the effects of canyon topography on internal-tide generation. From this study, made possible only by using DG-FEM and high-quality mesh generation, it is possible to investigate the effect of canyon topography on the magnitude and direction of baroclinic energy fluxes. Furthermore, we are able to conclude to what extent, if any, canyon topography enhances tidal dissipation.

Finally, Chapter 8 summarises the main results of the thesis and compares them with the research aims. Looking to the future and the legacy of this work, further research questions beyond the thesis are considered.

Chapter 2

Mathematical Background

2.1 Introduction

In this chapter, we introduce the framework in which internal-tide generation is modelled throughout the thesis. As part of this, we consider the derivation of the governing equations. The result is the linearised shallow-water equations (SWEs) and are a further simplification of Laplace's tidal equations (see Laplace, 1775). Here, one considers the 2D motion of a fluid medium whose vertical scale is much smaller than its horizontal. Waves of this nature are typically referred to in the literature as "long-waves". Despite their relative simplicity, the equations can be used to describe a wide range of geophysical phenomena within oceanic and atmospheric dynamics (see Vallis, 2006).

Over uniform topography, the linearised SWEs suggest that the horizontal and vertical dynamics can be decoupled, implying normal modes of vertical structure $Z(z)$ travelling at wave speed c. To understand what this means, we consider the motion of oscillatory waves of the form

$$\eta\left(x,z,t\right)=\mathrm{Re}\left\{A\left(z\right)\,\exp\left[i\left(k\,x-\omega\,t\right)\right]\right\} \tag{2.1}$$

propagating along the interface of two stably stratified fluids, as in Stokes (1847). This permits a relationship between wave frequency ω and horizontal wavenumber k to be obtained (for full details, see §2.3 of Sutherland, 2010). It should be noted that the above plane-wave solution can be extended to two horizontal dimensions by considering a coordinate transformation, aligning the horizontal spatial coordinate to that of the horizontal wavenumber vector.

To obtain the aforementioned relation, let us consider the two-dimensional flow of two stably superimposed fluids of different densities in a rigid box of uniform depth h. Here, the fluid of the upper layer has density ρ_1 and thickness h_1, while the fluid of the lower layer has density $\rho_2>\rho_1$ and thickness h_2, such that $h=h_1+h_2$. The Poisson equations governing the potential flow in each fluid, upon imposition of all relevant boundary conditions[1],

[1]These boundary conditions are the linearised kinematic and dynamic boundary conditions at the interface, as well as impermeability along the walls.

imply a dispersion relation

$$\omega = \pm\sqrt{\frac{\rho_2\, g'\, k}{\rho_1\, \coth\left(k\, h_1\right) + \rho_2\, \coth\left(k\, h_2\right)}}, \tag{2.2}$$

where $g' = g\left(\rho_2 - \rho_1\right)/\rho_2$ for gravitational acceleration g, which represents the reduced gravity at the interface of the two fluids. Moreover, the sign of ω indicates the direction of propagation in the horizontal.

Note that equation (2.2) reduces to the dispersion relation of a surface wave in the limit $\rho_1 \to 0$,

$$\omega = \pm\sqrt{g\, k\, \tanh\left(k\, h_2\right)}. \tag{2.3}$$

In the long-wave limit whereby $k\, h_2 \ll 1$ is considered, one obtains

$$\omega = \pm c\, k, \tag{2.4}$$

where $c = \sqrt{g\, h_2}$ denotes the phase speed of a surface wave in a fluid of depth h_2. The phase speed is the speed of individual wave crests (see §5.4 of Gill, 1982).

Alternatively, if one considers the Boussinesq approximation with $\rho_1 \approx \rho_2$, then equation (2.2) reduces to a more simplified dispersion relation of an internal wave,

$$\omega = \pm\sqrt{\frac{g'\, k}{\coth\left(k\, h_1\right) + \coth\left(k\, h_2\right)}}. \tag{2.5}$$

In the long-wave limit, where $k\, h_1, k\, h_2 \ll 1$, we re-observe the dispersion relation

$$\omega = \pm c\, k. \tag{2.6}$$

This time however, $c = \sqrt{g'\, h_1\, h_2/h}$ denotes the phase speed of an internal wave in a rigid box, recalling that $h = h_1 + h_2$. Hence, we have shown that in the long-wave limit, the dispersion relations of an internal wave of a two-layer fluid and a surface wave of uniform density have a similar structure, but with a different wave speed, c.

These calculations, whilst describing the fundamentals of internal wave dynamics, have obvious shortcomings: there is a rigid lid, the stratification is the simplest possible, there is no background rotation, there is no bottom topography, and the dynamics are linear. This chapter is devoted to presenting the relevant extensions of internal wave theory to overcome most of these problems.

In Section 2.2, we derive the linearised SWEs on a tangent plane. Here, we cover the main assumptions used, including the tangent-plane approximation, linearisation, and the hydrostatic approximation. In each case, justification of each assumption is made in the context of internal-tide generation over continental margins.

Having defined the equations of motion governing shallow-water flow, Section 2.3 considers

separable linear solutions for wave motion in a continuously stratified fluid with a free surface. The associated eigenvalue problem for vertical structure is solved for separation constants; these correspond to modal wave speeds. This provides a combined theory of surface and internal waves. The eigenvalue problem is solved analytically in the case of constant stratification, and numerically in the case of observational data.

Additional simplifications arise, however, by discretising the stratification profile, wherein layers of uniform density are assumed. To show these simplifications, a multi-layer framework of the SWEs—first considered by Lighthill (1969)—is developed in Section 2.4.[1] This allows the primitive set of equations to be reformulated into equations which govern individual barotropic and baroclinic motions coupled over variable bottom topography. As a result, these motions evolve independently over uniform topography. The framework we present builds on more recent work of Shimizu (2011) and Griffiths and Grimshaw (2007a). In particular, the framework re-formulates the work of Shimizu (2011) by exploiting the linear algebra of the associated eigenvalue problem; parts of this closely follow unpublished notes by Griffiths (2020; personal communication).

Typically, as Baines (1982) remarks, the stratification profile over continental margins consists of a shallow pycnocline surmounting a weakly stratified interior. It suffices to consider, as in Rattray (1960), to model the pycnocline mode using a two-layer model. This comes at the expense of neglecting internal wave motion in the weakly stratified interior, which we understand to be important for critical and super-critical wave generation. The governing equations of motion are simply those derived in the generalised multi-layer framework, but for two layers. These equations, along with implied modal energy relations prevalent to our study, are shown to follow immediately in Section 2.4.8. We conclude in Section 2.5.

2.2 Derivation of SWEs on a Tangent Plane

To derive the shallow-water equations (SWEs), we begin with the incompressible stratified equations under the influence of rotation:[2]

$$\rho\left(\mathbf{x},t\right)\left(\frac{\mathrm{D}}{\mathrm{D}t}\mathbf{u}\left(\mathbf{x},t\right)+2\boldsymbol{\Omega}\times\mathbf{u}\left(\mathbf{x},t\right)\right)=-\boldsymbol{\nabla}p\left(\mathbf{x},t\right)+\rho\left(\mathbf{x},t\right)\,\mathbf{g}+\mathbf{F}\left(\mathbf{x},t\right),\tag{2.7}$$

$$\frac{\mathrm{D}}{\mathrm{D}t}\rho\left(\mathbf{x},t\right)=0,\tag{2.8}$$

$$\boldsymbol{\nabla}\cdot\mathbf{u}\left(\mathbf{x},t\right)=0.\tag{2.9}$$

Here, an Eulerian description is used to consider the motion of a fluid particle whose velocity $\mathbf{u}\left(\mathbf{x},t\right)=\begin{pmatrix}u\left(\mathbf{x},t\right) & v\left(\mathbf{x},t\right) & w\left(\mathbf{x},t\right)\end{pmatrix}$, pressure $p\left(\mathbf{x},t\right)$, and density $\rho\left(\mathbf{x},t\right)$. We suppose that the fluid particle is subject to the effects of gravitational acceleration ($\mathbf{g}=$

[1] The work of Lighthill (1969) was presented in the context of mode characteristics over uniform topography for parts of the Indian Ocean near the equator whose stratification profile can be modelled by well-mixed layers.

[2] E.g. see equations (3.9)–(3.11) of LeBlond and Mysak (1978), or equations (1.29), (1.30) and (1.35) (neglecting viscous damping) of Sutherland (2010).

$-g\,\hat{\mathbf{e}}_z$ with $\hat{\mathbf{e}}_z$ denoting the vertical unit vector and where $g = 9.81\,\mathrm{m/s^2}$) and further external forces, denoted $\mathbf{F}(\mathbf{x},t) = \begin{pmatrix} F_x(\mathbf{x},t) & F_y(\mathbf{x},t) & 0 \end{pmatrix}$. We shall also consider the effects of rotation through Coriolis acceleration $2\boldsymbol{\Omega}\times\mathbf{u}(\mathbf{x},t)$. For the Earth, the magnitude of the vector aligned with the rotation axis is $\Omega = |\boldsymbol{\Omega}| = 7.29\times10^{-5}\,\mathrm{rad/s}$ (see §4.10 of Goldstein et al., 2001).

Equations (2.7) represent the momentum equations for an inviscid fluid in a rotating frame subject to gravitational acceleration aligned with the vertical axis. The use of the Lagrangian derivative, $\mathrm{D}/\mathrm{D}t = \partial_t + \mathbf{u}(\mathbf{x},t)\cdot\boldsymbol{\nabla}$, describes the time-evolution of a quantity following a fluid particle. For example, the term $\mathrm{D}\mathbf{u}(\mathbf{x},t)/\mathrm{D}t$ in (2.7) denotes the acceleration of a fluid particle being followed in space, while $\mathrm{D}\rho(\mathbf{x},t)/\mathrm{D}t = 0$ of (2.8) implies that the density of the fluid medium remains constant in time as we follow a fluid particle. The set of equations are completed with the addition of the continuity condition given by (2.9). Equations (2.7)–(2.9) describe the time-evolution of quantities $\mathbf{u}(\mathbf{x},t)$, $\rho(\mathbf{x},t)$ and $p(\mathbf{x},t)$ in terms of their spatial variation.

2.2.1 Localised Approximations

For large scales whereby the horizontal length scale of the fluid motion is comparable to the radius of the Earth $R = 6,371\,\mathrm{km}$, equations (2.7)–(2.9) can be framed in the context of planetary waves using spherical coordinates - these are Laplace's tidal equations (see Laplace, 1775). Laplace's tidal equations are particularly useful if one is interested in the large-scale motions of the ocean, such as planetary tides. The solutions have been studied extensively for standard cases (e.g. by Hough, 1898; Longuet–Higgins, 1968), with various distinct classes of wave motion known to exist. However, the issue of internal-tide generation over continental margins (as opposed to propagation) is a local phenomenon, and not a planetary-scale one. This allows the consideration of a much simpler Cartesian coordinate system where locally, a tangent-plane approximation can be made.

One approach used to model localised fluid motion on an intermediate scale is the β-plane approximation. The β-plane approximation was first proposed in Rossby et al. (1939) as a conceptual model for fluid motion in a localised region of a sphere. This would be ideal if one was considering the propagation of internal waves across many latitudinal degrees over which the variation in Coriolis force varies considerably. An example of such a study is Hazewinkel and Winters (2011).[1] For some reference mid-latitude $\theta_0 \approx \pm45°$, we may consider the orthogonal right-handed coordinate system (x,y,z) with x eastwards, y northwards and z upwards anti-parallel to the local gravitational acceleration (see Dellar, 2010). In a sufficiently small region around reference latitude θ_0, equations (2.7)–(2.9) become

[1] Hazewinkel and Winters (2011) considered low-mode oceanic internal tides propagating pole-ward.

$$\rho\left(\mathbf{x},t\right)\left(\frac{\mathrm{D}}{\mathrm{D}t}\mathbf{u}\left(\mathbf{x},t\right)+f\,\hat{\mathbf{e}}_z\times\mathbf{u}\left(\mathbf{x},t\right)\right)=-\boldsymbol{\nabla}p\left(\mathbf{x},t\right)-\rho\left(\mathbf{x},t\right)\,g\,\hat{\mathbf{e}}_z+\mathbf{F}\left(\mathbf{x},t\right), \tag{2.10}$$

$$\frac{\mathrm{D}}{\mathrm{D}t}\rho\left(\mathbf{x},t\right)=0, \tag{2.11}$$

$$\boldsymbol{\nabla}\cdot\mathbf{u}\left(\mathbf{x},t\right)=0, \tag{2.12}$$

where Coriolis parameter

$$f=f_0+\beta\,y, \tag{2.13}$$

with

$$f_0=2\Omega\,\sin\left(\theta_0\right)\qquad\text{and}\qquad\beta=\frac{2\Omega}{R}\cos\left(\theta_0\right). \tag{2.14}$$

At mid-latitudes, $f_0=10^{-4}\,\mathrm{rad/s}$ and $\beta=1.6\times10^{-11}\,\mathrm{m^{-1}rad/s}$. For more details regarding the derivation of equations (2.10)–(2.14), including why the horizontal component of $\mathbf{f}$ is neglected, see pages 17–22 of LeBlond and Mysak (1978).

An additional term in the vertical component of (2.10) has also been neglected under the thin-layer approximation. The term

$$-\frac{u^2\left(\mathbf{x},t\right)+v^2\left(\mathbf{x},t\right)}{R} \tag{2.15}$$

characterises the vertical translation of the horizontal velocities due to the Earth's curvature, and is negligible when small compared to the vertical acceleration term. For vertical and horizontal length scales H and L, this assumption requires $\xi=H/L\ll1$. Indeed, for internal-tide generation $H=O\left(1,000\,\mathrm{m}\right)$ and $L=O\left(100\,\mathrm{km}\right)$, giving $\xi=O\left(10^{-2}\right)$.

For ever smaller horizontal length scales, a more localised tangent plane can be considered where the local vertical component of the Coriolis force, f, can be approximated by just the leading-order term $f_0=2\Omega\sin\left(\theta_0\right)$. This simplification first used by Thomson (1879), known as the f-plane approximation, is perfectly reasonable in the study of internal-tide generation where the horizontal length scales are $O\left(10\,\mathrm{km}\right)$, and suggests that the effects of sphericity are entirely negligible. Note that equations (2.10)–(2.12) remain unchanged, and that Coriolis force $\mathbf{f}=f_0\,\hat{\mathbf{e}}_z$ is constant and aligned with the vertical irrespective of reference latitude.

2.2.2 Boundary Conditions

In a basin of finite dimensions, we use the impermeability condition to prevent fluid motion passing through the lateral boundaries. It is necessary to impose therefore

$$\hat{\mathbf{n}}\cdot\mathbf{u}\left(\mathbf{x},t\right)=0, \tag{2.16}$$

where $\hat{\mathbf{n}}$ is a unit normal vector along the boundary. For variable fluid depth $h\left(x,y\right)$, the sea-floor is at $z=-h\left(x,y\right)$. It follows that at the bottom boundary, along the sea floor,

the normal vector $\hat{\mathbf{n}} = \boldsymbol{\nabla}\left(z + h\left(x, y\right)\right)$, and that (2.16) gives vertical velocity

$$w\left(\mathbf{x}, t\right) = -\left(u\left(\mathbf{x}, t\right)\, \partial_x + v\left(\mathbf{x}, t\right)\, \partial_y\right) h\left(x, y\right), \qquad z = -h\left(x, y\right). \tag{2.17}$$

At the perturbed free-surface $z = \eta\left(x, y, t\right)$, neglecting both turbulent viscosity and surface tension, we require continuity of pressure and surface displacement:

$$p_A = p_O \qquad \text{and} \qquad \frac{\mathrm{D}}{\mathrm{D}t}\left(z - \eta\left(x, y, t\right)\right) = 0, \tag{2.18}$$

where p_A and p_O denote respectively the pressures of the atmosphere and ocean. Since $\mathrm{D}z/\mathrm{D}t = w\left(\mathbf{x}, t\right)$, the continuity of fluid motion at the surface can also be written as

$$w\left(\mathbf{x}, t\right) = \frac{\mathrm{D}}{\mathrm{D}t}\eta\left(x, y, t\right), \qquad z = \eta\left(x, y, t\right). \tag{2.19}$$

2.2.3 Oceanic Approximations

Equations (2.10)–(2.12) and free-surface condition (2.19) contain non-linear terms. We now ask ourselves, are non-linear terms essential in the study of internal tides?

Non-linearities are certainly important for propagation and dissipation. For example, when considering wave–wave interactions (e.g. Müller et al., 1986; MacKinnon & Winters, 2005; Alford & Zhao, 2007b), large-amplitude internal waves (e.g. Buijsman et al., 2010; Yuan, Grimshaw, & Johnson, 2018; Yuan, Grimshaw, Johnson, & Chen, 2018), tide–topography interactions with long tidal excursions (e.g. Bell, 1975a; Yuan et al., 2020), high Froude number (e.g. Legg & Klymak, 2008), and turbulent boundary layers along critical slopes (e.g. Gayen & Sarkar, 2010).

To generate internal waves, however, all that is required is fluid flow up and down variable topography. We know from Stokes (1847) that small-amplitude oscillations can be described using linear theory. While linear theory may not be used to accurately model internal-tide propagation or dissipation, as discussed in the preceding paragraph, linearisation does isolate the core mechanism of internal-tide generation.

Of course, there are additional benefits to linearisation. The omission of non-linear terms permits tractable solutions which can be more-easily analysed. Analytical solutions allow for parameter space to be explored in ways ocean models, which typically include non-linearities and are computationally expensive, cannot. To run a single simulation can take days or even weeks. The omission of non-linear terms can also facilitate the construction of scaling laws. Scaling laws permit greater understanding of parameter dependence. They can help identify what parameters are most important in a problem, as well as what happens if a parameter's value is changed, all without having to use a computer.

To linearise equations (2.10)–(2.12), we ask ourselves under what regime does linearisation produce viable results? We noted in Section 1.1.1, for example, that the amplitude of internal waves can reach up to several hundred metres in the deeper ocean. Can such

waves really be described as small-amplitude oscillatory waves?

To answer this question, let us consider the tidal-excursion parameter

$$\tau = k\, u_0/\omega. \tag{2.20}$$

Here, u_0, ω and $1/k$ characterise respectively the flow speed, tidal frequency and horizontal length scale. The parameter is found by considering the ratio of advective term $\mathbf{u}\cdot\boldsymbol{\nabla}\mathbf{u}$ in (2.10) with the acceleration term $\partial_t\mathbf{u}$. If $\tau \ll 1$, the non-linear advection term is negligible.

To see if $\tau \ll 1$, we recall that in equations (2.4)–(2.6), phase speed $c = |\omega/k|$ in the absence of rotation. For simplicity, we shall neglect the effects of rotation. Using (2.6), we find that $c = \sqrt{g'\, h_1\, h_2/(h_1+h_2)} = 1.9$–$3.8\,\mathrm{m/s}$ for ocean parameters.[1] In other words, a small-amplitude wave permitting linearisation of equations (2.10)–(2.12) requires $u_0 \ll c$. For tidal flows, one might expect $u_0 = O\left(10^{-2}\,\mathrm{m/s}\right)$ along continental margins, and therefore $u_0 \ll c$ would be satisfied. We argue therefore that the non-linear advection term could be neglected in the study of internal-tide generation provided that $u_0 \ll c$. For a more detailed discussion, we refer the reader to §3.2 of Garrett and Kunze (2007).

Having justified a linearised approach, we consider now in equations (2.10)–(2.12) small perturbations to the state of rest. To achieve this, we write fluid velocity, pressure and density as

$$\mathbf{u} = \mathbf{0} + \mathbf{u}'\left(\mathbf{x},t\right), \qquad p = p_0\left(z\right) + \tilde{p}\left(\mathbf{x},t\right), \qquad \rho = \rho_0\left(z\right) + \tilde{\rho}\left(\mathbf{x},t\right), \tag{2.21}$$

where at rest, $p_0\left(z\right)$ and $\rho_0\left(z\right)$ satisfy hydrostatic balance,

$$\frac{\mathrm{d}p_0\left(z\right)}{\mathrm{d}z} = -g\,\rho_0\left(z\right). \tag{2.22}$$

Here, $\mathbf{u}'$, $\tilde{p}$ and $\tilde{\rho}$ are small deviations from the hydrostatic state. A schematic is shown in Figure 2.1, where on the left the fluid is shown at rest, while on the right the fluid is shown in motion.

As a result of (2.21), equations (2.10)–(2.11) are linearised to give

$$\rho_0\left(z\right)\left(\partial_t u'\left(\mathbf{x},t\right) - f\, v'\left(\mathbf{x},t\right)\right) = -\partial_x\tilde{p}\left(\mathbf{x},t\right) + F_x\left(\mathbf{x},t\right), \tag{2.24}$$

$$\rho_0\left(z\right)\left(\partial_t v'\left(\mathbf{x},t\right) + f\, u'\left(\mathbf{x},t\right)\right) = -\partial_y\tilde{p}\left(\mathbf{x},t\right) + F_y\left(\mathbf{x},t\right), \tag{2.25}$$

$$\rho_0\left(z\right)\,\partial_t w'\left(\mathbf{x},t\right) = -\partial_z\tilde{p}\left(\mathbf{x},t\right) - g\,\tilde{\rho}\left(\mathbf{x},t\right), \tag{2.26}$$

$$\partial_x u'\left(\mathbf{x},t\right) + \partial_y v'\left(\mathbf{x},t\right) + \partial_z w'\left(\mathbf{x},t\right) = 0, \tag{2.27}$$

$$\partial_t\tilde{\rho}\left(\mathbf{x},t\right) - \frac{\rho_0\left(z\right)}{g}\,N^2\left(z\right)\,w'\left(\mathbf{x},t\right) = 0, \tag{2.28}$$

[1] Here, we use upper-layer depth $h_1 = 150\,\mathrm{m}$, lower-layer depth $h_2 = 50$–$3850\,\mathrm{m}$ and reduced gravity $g' \approx 10^{-1}\,\mathrm{m/s^2}$.

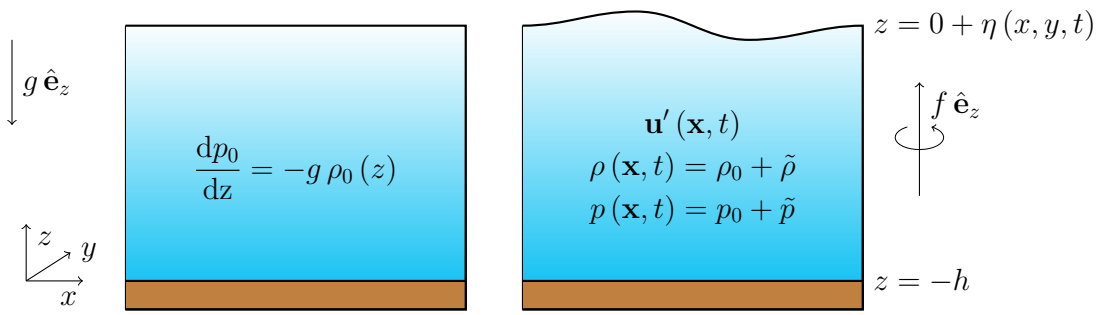

Figure 2.1: Schematic of a hydrostatic continuously stratified fluid medium over uniform topography. Here, both the rotation axis and the gravitational acceleration are aligned at the vertical. At rest, the fluid is in hydrostatic balance, while in motion, fluid pressure and density can be expressed in terms of a perturbation of the background state.

where Brunt–Väisälä frequency

$$N\,(z) = \sqrt{-\frac{g}{\rho_0\,(z)}\frac{\mathrm{d}\rho_0\,(z)}{\mathrm{d}z}} \tag{2.29}$$

is the natural oscillation frequency associated with small-amplitude, simple-harmonic motion of a neutrally buoyant element of displaced fluid. The period associated to this frequency, $2\pi/N$, can vary from a few minutes in the thermocline to several hours in the deep ocean (LeBlond & Mysak, 1978).

For horizontal velocity $\mathbf{u}' = \begin{pmatrix} u' & v' \end{pmatrix}$, equations (2.24)–(2.28) are subject to the linearisation of equation (2.17) and (2.19):

$$w'\,(\mathbf{x}, t) = -\mathbf{u}'\,(\mathbf{x}, t) \cdot \boldsymbol{\nabla} h\,(x, y) \qquad \text{at } z = -h\,(x, y)\,, \tag{2.30}$$

$$w'\,(\mathbf{x}, t) = \partial_t \eta\,(\mathbf{x}, t) \quad \text{and} \quad \tilde{p}\,(\mathbf{x}, t) = \rho_0\,(z)\; g\,\eta\,(x, y, t) \qquad \text{at } z = 0. \tag{2.31}$$

To obtain the pressure perturbation condition in (2.31), we follow the methodology presented on page 57 of LeBlond and Mysak (1978) and take the Taylor series of pressure around $z = 0$, such that

$$p_0\,(z) + p_0'\,(z)\;\eta\,(\mathbf{x}, t) + \cdots + \tilde{p}\,(\mathbf{x}, t) + \partial_z \tilde{p}\,(\mathbf{x}, t)\;\eta\,(\mathbf{x}, t) + \cdots = p_A, \qquad \text{at } z = 0. \tag{2.32}$$

Considering only leading-order terms of (2.32), which excludes the term $\partial_z \tilde{p}\,(\mathbf{x}, t)\;\eta\,(\mathbf{x}, t)$, we use (2.22) on $p_0'\,(z)$ and remark that $p_0\,(z = 0) = p_A$.

One further approximation that can easily be applied is the hydrostatic balance approximation associated with long waves. Hydrostatic balance assumes the vertical acceleration on the left-hand side of (2.26) is negligible, leaving the upward-directed pressure gradient force to balance with the downward-directed force of gravity on the right-hand side of (2.26).

To justify the hydrostatic equilibrium, we combine the methodologies presented in Lecture 4 of Bretherton (2014) and Lecture 4 of Chomaz (2019). Denoting non-dimensional

quantities with asterisks, we consider the scaling

$$(x, y) = L\,(x^*, y^*)\,, \qquad \left(u', v'\right) = U\,(u^*, v^*)\,, \qquad z = H\,z^*, \qquad t = T\,t^*, \qquad \rho = \rho_{00}\,\rho^{'*}$$

where L, U, H, T and ρ_{00} denote respectively the horizontal length scale, horizontal velocity scale, vertical length scale, temporal scale and density scale. We note that for internal-tide generation along continental margins, one may anticipate $L = 100\,\mathrm{km}$, $U = O\left(10^{-2}\,\mathrm{m/s}\right)$, $H = O\left(10^{3}\,\mathrm{m}\right)$, $T = O\left(10^{-4}\,\mathrm{s}\right)$ and $\rho_{00} = O\left(10^{3}\,\mathrm{kg/m^3}\right)$, recalling from Section 2.2.1 that $\xi = H/L = O\left(10^{-2}\right)$. We shall also consider the scaling

$$w' = W\,w^*, \qquad\qquad \tilde{p} = \Pi\,p^*, \tag{2.33}$$

using W and Π as gauges for vertical velocity and pressure perturbation.

From the incompressibility condition (2.27), we deduce that

$$W/H = \left[\partial_z w'\,(\mathbf{x}, t)\right] = \left[-\partial_x u'\,(\mathbf{x}, t) - \partial_y v'\,(\mathbf{x}, t)\right] = U/L, \tag{2.34}$$

implying that

$$W = U\,H/L = U\,\xi = O\left(10^{-4}\,\mathrm{m/s}\right). \tag{2.35}$$

From the horizontal momentum equations (2.24)–(2.25),

$$\rho_{00}\,U/T = \left[\rho_0\,(z)\left(\partial_t \mathbf{u}'\,(\mathbf{x}, t) + f\,\hat{\mathbf{e}}_z \times \mathbf{u}'\,(\mathbf{x}, t)\right)\right] = \left[-\boldsymbol{\nabla}\tilde{p}\,(\mathbf{x}, t)\right] = \Pi/L, \tag{2.36}$$

from which we observe that

$$\Pi = \rho_{00}\,U\,L/T = O\left(10^{2}\,\mathrm{Pa}\right). \tag{2.37}$$

Lastly, from the vertical momentum equation (2.26), we determine that

$$\rho_{00}\,W/T = \left[\rho_0\,(z)\;\partial_t w'\,(\mathbf{x}, t)\right] = \left[-\partial_z\tilde{p}\,(\mathbf{x}, t) - g\,\tilde{\rho}\,(\mathbf{x}, t)\right] = \Pi/H. \tag{2.38}$$

Taking the ratio between the vertical acceleration on the left-hand side and the pressure gradient balanced by buoyancy on the right-hand side, it follows that

$$\frac{\left[\rho_0\,(z)\;\partial_t w'\,(\mathbf{x}, t)\right]}{\left[-\partial_z\tilde{p}\,(\mathbf{x}, t) - g\,\tilde{\rho}\,(\mathbf{x}, t)\right]} = \frac{\rho_{00}\,W/T}{\Pi/H}. \tag{2.39}$$

Using the gauges for vertical velocity and pressure perturbation given in equations (2.35) and (2.37), we conclude that

$$\frac{\left[\rho_0\,(z)\;\partial_t w'\,(\mathbf{x}, t)\right]}{\left[-\partial_z\tilde{p}\,(\mathbf{x}, t) - g\,\tilde{\rho}\,(\mathbf{x}, t)\right]} = \frac{\rho_{00}\,U\,\xi/T}{\rho_{00}\,U/T\,\xi} = \xi^2 = O\left(10^{-4}\right). \tag{2.40}$$

That is to say, the hydrostatic approximation is valid so long as the horizontal length scale is small compared to that of the vertical. The latter is not the case when the horizontal

and vertical length scales are of the same magnitude, which may, for example, arise in the case of supercritical internal-tide generation.

To see the effect of enacting the hydrostatic approximation, $-g\cdot(2.46)/\rho_0\,(z) + \partial_t\cdot(2.44)$ gives

$$\left(\cancel{\partial_{tt}} + N^2\,(z)\right) w'\,(\mathbf{x},t) = -\frac{1}{\rho_0\,(z)}\partial_{zt}\tilde{p}\,(\mathbf{x},t)\,, \tag{2.41}$$

where the red-striken term is absent under the hydrostatic balance approximation. We observe that for time-periodic flow of wave frequency ω, equation (2.41) illustrates that the hydrostatic approximation assumes that $\omega^2 \ll N^2\,(z)$. Consequently, waves governed by equations (2.24)–(2.28) have both "long" periods as well as long wavelengths (see LeBlond & Mysak, 1978). For semi-diurnal (twice daily) and diurnal (daily) forcing associated with the tides, the wave period is much longer than the period associated to the buoyancy frequency at the pycnocline, which we have previously stated is several minutes.

The governing equations for hydrostatic motion linearised about the state of rest on an f-plane are therefore

$$\rho_0\,(z)\left(\partial_t u'\,(\mathbf{x},t) - f\,v'\,(\mathbf{x},t)\right) = -\partial_x\tilde{p}\,(\mathbf{x},t) + F_x\,(\mathbf{x},t)\,, \tag{2.42}$$

$$\rho_0\,(z)\left(\partial_t v'\,(\mathbf{x},t) + f\,u'\,(\mathbf{x},t)\right) = -\partial_y\tilde{p}\,(\mathbf{x},t) + F_y\,(\mathbf{x},t)\,, \tag{2.43}$$

$$\tilde{\rho}\,(\mathbf{x},t) = -\frac{1}{g}\partial_z\tilde{p}\,(\mathbf{x},t)\ , \tag{2.44}$$

$$\partial_x u'\,(\mathbf{x},t) + \partial_y v'\,(\mathbf{x},t) + \partial_z w'\,(\mathbf{x},t) = 0, \tag{2.45}$$

$$\partial_t\tilde{\rho}\,(\mathbf{x},t) - \frac{\rho_0\,(z)}{g}\,N^2\,(z)\ w'\,(\mathbf{x},t) = 0, \tag{2.46}$$

and are subject to boundary conditions (2.30)–(2.31).

Following the methodology of §2.3 in Bokhove and Pegler (2018), the last approximation we consider is the Boussinesq approximation (first used in Boussinesq, 1901). For reference density ρ_{00}, consider the background density profile $\rho_0\,(z)$ written in the form

$$\rho_0\,(z) = \rho_{00}\,(1+\varepsilon\,(z))\,, \qquad \text{where} \qquad \varepsilon\,(z) = (\rho_0\,(z) - \rho_{00})\,/\rho_{00}, \qquad |\varepsilon\,(z)| \ll 1. \tag{2.47}$$

Note that the reference density is typically a depth average of the background density, $\rho_0\,(z)$, but that need not be the case (e.g. the background density at the surface). Substitution of (2.47) into equations (2.42)–(2.44) and considering leading-order equations in

$\varepsilon(z)$, we have the equations governing the motion of hydrostatic Boussinesq flows:

$$\rho_{00}\left(\partial_t u'(\mathbf{x},t) - f\,v'(\mathbf{x},t)\right) = -\partial_x\tilde{p}(\mathbf{x},t) + F_x(\mathbf{x},t), \tag{2.49}$$

$$\rho_{00}\left(\partial_t v'(\mathbf{x},t) + f\,u'(\mathbf{x},t)\right) = -\partial_y\tilde{p}(\mathbf{x},t) + F_y(\mathbf{x},t), \tag{2.50}$$

$$\tilde{\rho}(\mathbf{x},t) = -\frac{1}{g}\partial_z\tilde{p}(\mathbf{x},t), \tag{2.51}$$

$$\partial_x u'(\mathbf{x},t) + \partial_y v'(\mathbf{x},t) + \partial_z w'(\mathbf{x},t) = 0, \tag{2.52}$$

$$\partial_t\tilde{\rho}(\mathbf{x},t) - \frac{\rho_{00}}{g}N^2(z)\,w'(\mathbf{x},t) = 0, \tag{2.53}$$

where now the Brunt–Väisälä frequency is defined as

$$N(z) = \sqrt{-\frac{g}{\rho_{00}}\frac{\mathrm{d}\rho_0(z)}{\mathrm{d}z}}, \tag{2.54}$$

and with boundary conditions

$$w'(\mathbf{x},t) = -\mathbf{u}'(\mathbf{x},t)\cdot\boldsymbol{\nabla}h(x,y) \qquad \text{at } z = -h(x,y), \tag{2.55}$$

$$w'(\mathbf{x},t) = \partial_t\eta(x,y,t) \quad \text{and} \quad \tilde{p}(\mathbf{x},t) = \rho_{00}\,g\,\eta(x,y,t) \qquad \text{at } z = 0. \tag{2.56}$$

It is worth adding that a similar such approximation is not made to the perturbation to background density $\tilde{\rho}(\mathbf{x},t)$, since it is this which provides the restoring force of internal waves that is buoyancy.

The Boussinesq approximation is a perfectly reasonable assumption to be made since the density field typically varies by no more than 2% from the average density (Baines, 1973). Indeed, Figure 2.2 shows an observational stratification profile using data from National Oceanographic Data Center (U.S.) (2013) in the middle of the North-Atlantic ocean at 39°N, 125°W. Along with the stratification profile, various means by which the stratification can be modelled are also shown. These means are a uniform-density profile (depth-averaged, much like the Boussinesq approximation for the background density field), a two-layer profile (used to model the thermocline/pycnocline mode, and is layer-averaged), and a constant-stratification profile. Here, we can see the pycnocline occurs at a depth of around 150 m and is indicated by the sharp change in density gradient.

2.2.4 Conservation of Energy

Consider now the energy conservation in a fluid column of small-amplitude motions in a continuously stratified fluid medium governed by equations (2.42)–(2.46). Here, we do not employ the Boussinesq approximation, but this would mostly entail the use of reference density ρ_{00} in lieu of background density profile $\rho_0(z)$ apart from in the definition of the Brunt–Väisälä frequency $N(z)$.

Taking the scalar product of the linearised momentum equations (2.42) with horizontal

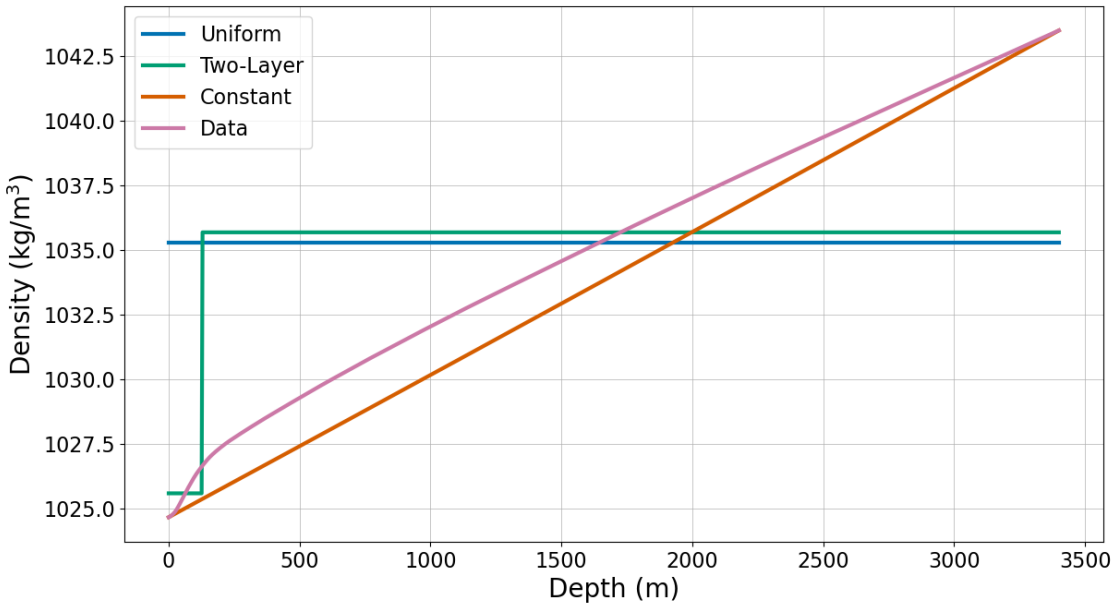

Figure 2.2: Ocean stratification profiles modelling observational data taken from National Oceanographic Data Center (U.S.) (2013) at 39°N, 125°W, where here the pycnocline is located at a depth of $\sim 150\,\mathrm{m}$. There are three common means of modelling ocean stratification shown: uniform density, two-layer and constant stratification.

velocity vector $\mathbf{u}'(\mathbf{x},t) = \begin{pmatrix} u'(\mathbf{x},t) & v'(\mathbf{x},t) \end{pmatrix}$ and integrating over the fluid depth yields

$$\int_{z=-h(x,y)}^{0} \left(\frac{\rho_0(z)}{2} \partial_t |\mathbf{u}'(\mathbf{x},t)|^2 + \mathbf{u}'(\mathbf{x},t) \cdot \boldsymbol{\nabla} \tilde{p}(\mathbf{x},t) \right) \mathrm{d}z = \int_{-h(x,y)}^{0} \mathbf{u}'(\mathbf{x},t) \cdot \mathbf{F}(\mathbf{x},t)\, \mathrm{d}z, \tag{2.57}$$

where $\boldsymbol{\nabla}$ is the horizontal gradient operator, and recalling that the external force vector reads

$$\mathbf{F}(\mathbf{x},t) = \begin{pmatrix} F_x(\mathbf{x},t) & F_y(\mathbf{x},t) \end{pmatrix}. \tag{2.58}$$

Next, take the product of $\tilde{p}(\mathbf{x},t)$ with equation (2.45) and integrate once more over fluid depth:

$$\int_{-h(x,y)}^{0} \left(\tilde{p}(\mathbf{x},t)\ \boldsymbol{\nabla} \cdot \mathbf{u}'(\mathbf{x},t) + \tilde{p}(\mathbf{x},t)\ \partial_z w'(\mathbf{x},t) \right) \mathrm{d}z = \left[\tilde{p}(\mathbf{x},t)\ w'(\mathbf{x},t) \right]_{-h(x,y)}^{0} + \int_{-h(x,y)}^{0} \left\{ \tilde{p}(\mathbf{x},t)\ \boldsymbol{\nabla} \cdot \mathbf{u}'(\mathbf{x},t) - w'(\mathbf{x},t)\ \partial_z \tilde{p}(\mathbf{x},t) \right\} \mathrm{d}z. \tag{2.59}$$

Substituting in for $w'(\mathbf{x},t)$ from (2.52) and $\partial_z \tilde{p}(\mathbf{x},t)$ from (2.44), and then applying the boundary conditions

$$\tilde{p}(\mathbf{x},t) = \rho_0(z)\ g\,\eta(x,y,t) \quad \text{and} \quad w'(\mathbf{x},t) = \partial_t \eta(x,y,t) \qquad \text{at } z = 0, \tag{2.60}$$

$$w'(\mathbf{x},t) = -\mathbf{u}'(\mathbf{x},t) \cdot \boldsymbol{\nabla} h(x,y) \qquad \text{at } z = -h(x,y), \tag{2.61}$$

on the rightmost term, equation (2.59) simplifies to give

$$\int_{-h(x,y)}^{0}\left(\tilde{p}\left(\mathbf{x},t\right)\,\boldsymbol{\nabla}\cdot\mathbf{u}'\left(\mathbf{x},t\right)+\frac{\rho_0\left(z\right)}{2}\partial_t\left(\frac{g\,\tilde{\rho}\left(\mathbf{x},t\right)}{\rho_0\left(z\right)\,N\left(z\right)}\right)^2\right)\mathrm{d}z \tag{2.62}$$
$$+\frac{\rho_0\left(z\right)\,g}{2}\partial_t\eta^2\left(x,y,t\right)\mid_{z=0}+\boldsymbol{\nabla}h\left(x,y\right)\cdot\mathbf{u}'\left(\mathbf{x},t\right)\,\tilde{p}\left(\mathbf{x},t\right)\mid_{z=-h(x,y)}.$$

Adding together (2.57) and (2.62), one obtains the conservation relation for energy in a column of hydrostatic fluid:

$$\partial_t E\left(\mathbf{x},t\right)+\boldsymbol{\nabla}\cdot\mathbf{J}\left(\mathbf{x},t\right)=W\left(\mathbf{x},t\right), \tag{2.63}$$

where depth-integrated energy density and energy flux are defined respectively as

$$E\left(\mathbf{x},t\right)\equiv\frac{1}{2}\left\{\int_{-h(x,y)}^{0}\rho_0\left(z\right)\left(\left|\mathbf{u}'\left(\mathbf{x},t\right)\right|^2+\left(\frac{g\,\tilde{\rho}\left(\mathbf{x},t\right)}{\rho_0\left(z\right)\,N\left(z\right)}\right)^2\right)\mathrm{d}z+\right.$$
$$\left.g\,\rho_0\left(z\right)\,\eta^2\left(x,y,t\right)\mid_{z=0}\right\} \tag{2.64}$$

and

$$\mathbf{J}\left(\mathbf{x},t\right)\equiv\int_{-h(x,y)}^{0}\tilde{p}\left(\mathbf{x},t\right)\,\mathbf{u}'\left(\mathbf{x},t\right)\,\mathrm{d}z, \tag{2.65}$$

where, using the Leibniz integration rule,

$$\int_{-h(x,y)}^{0}\boldsymbol{\nabla}\cdot\left(\tilde{p}\left(\mathbf{x},t\right)\,\mathbf{u}'\left(\mathbf{x},t\right)\right)\,\mathrm{d}z=\boldsymbol{\nabla}\cdot\mathbf{J}\left(\mathbf{x},t\right)- \tag{2.66}$$
$$\boldsymbol{\nabla}h\left(x,y\right)\cdot\mathbf{u}'\left(\mathbf{x},t\right)\,\tilde{p}\left(\mathbf{x},t\right)\mid_{z=-h(x,y)}.$$

The second term in (2.66) then cancels with the last term in (2.62). We have also

$$W\left(\mathbf{x},t\right)=\int_{-h(x,y)}^{0}\mathbf{u}'\left(\mathbf{x},t\right)\cdot\mathbf{F}\left(\mathbf{x},t\right)\,\mathrm{d}z, \tag{2.67}$$

which represents the work input from external forces. Energy E is the sum of depth-integrated kinetic and potential energies, i.e.

$$E_K\left(\mathbf{x},t\right)=\frac{1}{2}\int_{-h(x,y)}^{0}\rho_0\left(z\right)\,\left|\mathbf{u}'\left(\mathbf{x},t\right)\right|^2\mathrm{d}z \tag{2.68}$$

and

$$E_P\left(\mathbf{x},t\right)=\frac{1}{2}\left\{\int_{-h(x,y)}^{0}\rho_0\left(z\right)\left(\frac{g\,\tilde{\rho}\left(\mathbf{x},t\right)}{\rho_0\left(z\right)\,N\left(z\right)}\right)^2\mathrm{d}z+g\,\rho_0\left(z\right)\,\eta^2\left(x,y,t\right)\mid_{z=0}\right\}. \tag{2.69}$$

2.3 Continuously Stratified SWEs

In this section, we solve for wave motion in a continuously stratified ocean over uniform topography with a free surface. Using separation of variables, we show that equations

(2.42)–(2.46) can be separated into one which governs vertical structure, and another which governs horizontal wave propagation. The separation constant here corresponds to modal wave speed.

The equation governing vertical structure is a regular Sturm–Liouville problem, meaning that an infinite discrete set of positive eigenvalues corresponding to inverse-squared wave speeds exist, and whose corresponding vertical structures are orthogonal with respect to some weight function when integrated over fluid depth. Both analytical and numerical solutions to the aforementioned eigenvalue problem are briefly explored.

2.3.1 Pressure Equation

To understand the type of waves governed by equations (2.42)–(2.46) subject to equations (2.30)–(2.31), we first obtain a single equation for the pressure perturbation, $\tilde{p}$. To derive the pressure equation, we follow the methodology given on page 124 of LeBlond and Mysak (1978). One notable difference, however, is the use of the f-plane approximation as opposed to the β-plane approximation. To begin, expressions for u' and v' in terms of $\tilde{p}$ are found from equations (2.42) with $F_x = F_y = 0$:

$$\mathcal{L}_t u' = -\frac{1}{\rho_0}\left(\partial_{tx} + f\,\partial_y\right)\tilde{p}, \tag{2.70}$$

$$\mathcal{L}_t v' = -\frac{1}{\rho_0}\left(\partial_{ty} - f\,\partial_x\right)\tilde{p}, \tag{2.71}$$

where $\mathcal{L}_t = \partial_{tt} + f^2$. Substitution of $\partial_x\cdot$(2.70) and $\partial_y\cdot$(2.71) into $\mathcal{L}_t\cdot$(2.45) gives

$$\mathcal{L}_t \partial_z w' = \frac{1}{\rho_0}\partial_t \nabla^2 \tilde{p}. \tag{2.72}$$

We then substitute in for $\tilde{\rho}$ from (2.51) into (2.53) to obtain

$$\partial_{zt}\tilde{p} + \rho_0 N^2(z)\, w' = 0 \qquad \Longrightarrow \qquad w' = -\frac{1}{\rho_0} N^{-2}(z)\, \partial_{zt}\tilde{p}. \tag{2.73}$$

The expression for w' in (2.73) can be used in (2.72) to yield a partial differential equation for the pressure perturbation:

$$\partial_t\left(\frac{1}{\rho_0}\nabla^2 + \mathcal{L}_t\partial_z\left(\frac{1}{\rho_0} N^{-2}(z)\,\partial_z\right)\right)\tilde{p} = 0, \tag{2.74}$$

where $N(z)$ is as defined in (2.29), and is assumed non-zero for all z.

To derive the impermeability condition at $z = -h$ on pressure perturbation $\tilde{p}$, we may use equation (2.41). Since $w' = 0$ at $z = -h$, it follows that

$$\partial_{tz}\tilde{p} = 0 \qquad \text{at} \qquad z = -h. \tag{2.75}$$

As for the free-surface condition expressed in (2.31), we may substitute in for w' from

(2.41) to obtain

$$\partial_t \left(\partial_z + \frac{N^2(z)}{g} \right) \tilde{p} = 0 \qquad \text{at} \qquad z = 0. \tag{2.76}$$

Equation (2.74) for $\tilde{p}$, subject to boundary conditions (2.75) and (2.76), govern wave propagation in a stratified shallow-water system on an f-plane.

2.3.2 Separation of Pressure Equation

To study propagating-wave solutions to (2.74) in an ocean of uniform depth, it is customary at this point to use the method of separation of variables to obtain one equation for the vertical structure, and another for the time-evolution of the wave's propagation in space. This method was first done for handling problems in rotating fluids by Taylor (1936) for the case of continuous stratification, and then by Charney (1955) and Veronis and Stommel (1956) for the case of a two-layer fluid.

Provided that $N^2(z)$ is non-zero everywhere, consider pressure perturbation, using separation of variables, of the form

$$\tilde{p}(\mathbf{x}, t) = P_n(x, y, t)\, Z_n(z), \tag{2.77}$$

where $n \in \mathbb{N}$. By substituting equation (2.77) into (2.74), we observe the existence of infinitely many modes whose vertical structure is governed by an equation dependent only on stratification profile:

$$\left(\frac{\mathrm{d}}{\mathrm{d}z} \left(\frac{1}{\rho_0 N^2} \frac{\mathrm{d}}{\mathrm{d}z} \right) + \frac{1}{\rho_0 c_n^2} \right) Z_n(z) = 0. \tag{2.78}$$

Equation (2.78) is subject to the boundary conditions

$$\frac{\mathrm{d}}{\mathrm{d}z} Z_n(z = -h) = 0 \qquad \text{and} \qquad \left(\frac{\mathrm{d}}{\mathrm{d}z} + \frac{N^2(z)}{g} \right) Z_n(z = 0) = 0. \tag{2.79}$$

In addition, horizontal wave propagation is governed by the linear Klein–Gordon equation

$$\partial_t \left(\mathcal{L}_t - c_n^2 \nabla^2 \right) P_n(x, y, t) = 0. \tag{2.80}$$

Here, $1/c_n^2 = 1/g\,h_n$ is the separation constant. LeBlond and Mysak (1978) uses the factor g so that h_n has the dimensions of length. This is typically referred to as the equivalent depth. I.e. waves of mode n will propagate with wave speed equivalent to that of a surface wave in a fluid of depth h_n.

The domain of (2.78) is given by $-h \leq z \leq 0$, and is subject to the relevant boundary conditions prescribed in equation (2.79). The vertical eigenfunctions $Z_n(z)$ and the corresponding eigenvalues $\lambda_n = c_n^{-2}$ can then be determined for any given stratification $N(z)$

subject to the physical boundary conditions of the problem; kinematic on the free-surface and impermeability on the bottom boundary.

Equation (2.78) is a regular Sturm–Liouville eigenvalue problem, where in standard notation

$$-\left(P\,Z'\right)' + Q\,Z = \lambda\,R\,Z,$$

we have $P = \left(\rho_0\,N^2\right)^{-1} > 0$, $Q = 0$, weight function $R = 1/\rho_0 > 0$ and eigenvalues $\lambda = 1/c^2$. We may conclude therefore that there exists an infinite discrete set of positive real eigenvalues corresponding to real eigenfunctions orthogonal with respect to R, such that

$$\int_{-h}^{0} \frac{Z_m\left(z\right)\,Z_n\left(z\right)\,\mathrm{d}z}{\rho_0\left(z\right)} \propto \delta_{mn}, \tag{2.81}$$

where δ_{mn} is the Kronecker delta function (see Boyce et al., 2017). Here, we identify the gravest mode ($n = 0$) as the barotropic mode, and the modes $n = 1, 2, 3, \ldots$ are the sequence of baroclinic modes. Although strictly speaking, a barotropic flow is one where pressure is constant on surfaces of constant density, this is only approximately true (see Gill, 1982). The substitution of a plane-wave form into equation (2.80) then yields the dispersion relation corresponding to the eigenfunction $Z_n\left(z\right)$, or more simply, the vertical mode number n. Since (2.80) is third-order in time, it follows that such a substitution yields a cubic in wave frequency ω:

$$\omega\left(\omega^2 - f^2 - c_n^2\left(k^2 + l^2\right)\right) = 0, \tag{2.82}$$

Therefore, corresponding to each mode n, there are three branches of the dispersion relation corresponding to the three roots of the cubic polynomial in ω; two of which correspond to inertia-gravity modes dominated by gravity and modified only by Coriolis parameter f, and the other the geostrophic with steady currents. When including variation in rotation (or even topography), through say, a β-plane approximation, the latter becomes instead low-frequency quasi-geostrophic Rossby modes.

2.3.3 Analytical Solutions for Constant Stratification

For typical stratification profiles of $N^2\left(z\right)$, the boundary-value problem (2.78) and (2.79) can be solved using standard numerical methods. More conveniently, for certain analytical forms of background density ρ_0 (and hence $N^2\left(z\right)$), (2.78) can be reformulated into an ODE with known solutions. Here, we follow pages 125–126 of LeBlond and Mysak (1978), and consider the Boussinesq approximation with $N^2 =$ constant. The steps shown yield a second-order constant coefficient ODE which can be solved analytically subject to the boundary conditions expressed in (2.79). From here, it is easy to see the significance of the free-surface which would otherwise be neglected had we been solving for the case of a rigid lid.

With both $N^2(z)$ and ρ_0 taken constant, equation (2.78) becomes

$$\left(\frac{\mathrm{d}^2}{\mathrm{d}z^2} + \frac{N^2}{c_n^2}\right) Z_n(z) = 0, \qquad -h \le z \le 0.$$

From here, it is practical to consider the non-dimensional vertical coordinate $z^* = z/h$; then $Z_n(z) = Z_n(h\,z^*)$ and

$$\left(\frac{\mathrm{d}^2}{\mathrm{d}z^{*2}} + \lambda_n^2\right) Z_n(h\,z^*) = 0, \qquad 0 \le z^* \le 1, \tag{2.83}$$

where

$$\lambda_n = N\,h/c_n. \tag{2.84}$$

The corresponding boundary conditions are then given as

$$\frac{\mathrm{d}}{\mathrm{d}z^*} Z_n = 0 \qquad \text{at} \qquad z^* = -1, \tag{2.85}$$

$$\left(\frac{\mathrm{d}}{\mathrm{d}z^*} + \varepsilon\right) Z_n = 0 \qquad \text{at} \qquad z^* = 0, \tag{2.86}$$

where for typical ocean parameters, $\varepsilon \equiv N^2\,h/g = O\left(10^{-3}\right)$.[1] It should also be noted that $\varepsilon = 0$ corresponds to the case of a rigid lid, where instead of a free-surface condition, we have instead impermeability. Equations (2.83)–(2.86) for $\varepsilon \ll 1$ admit solutions of two distinct classes (Wunsch, 1975; Hendershott, 1981; Pedlosky, 2003), as we shall now go on to discuss.

General solutions to (2.83) are easily found to be

$$Z_n(z^*) = \alpha_n \cos(\lambda_n\,z^*) + \beta_n \sin(\lambda_n\,z^*) \tag{2.87}$$

for unknown constant coefficients α_n and β_n. Applying boundary conditions (2.85) and (2.86) on (2.87) gives the following system of equations to resolve for α_n and β_n:

$$\begin{pmatrix} \sin(\lambda_n) & \cos(\lambda_n) \\ \varepsilon & \lambda_n \end{pmatrix} \begin{pmatrix} \alpha_n \\ \beta_n \end{pmatrix} = \begin{pmatrix} 0 \\ 0 \end{pmatrix}. \tag{2.88}$$

For a non-trivial solution, we then consider the case for which the determinant of coefficients in (2.88) is zero. This gives the characteristic equation for λ_n:

$$\lambda_n \sin(\lambda_n) - \varepsilon \cos(\lambda_n) = 0 \qquad \Longrightarrow \qquad \tan(\lambda_n) = \varepsilon/\lambda_n. \tag{2.89}$$

As explained in LeBlond and Mysak (1978), the roots of (2.89) are best seen graphically when plotting the individual functions $f_1(\lambda) = \tan(\lambda)$ and $f_2(\lambda) = \varepsilon/\lambda$, and identifying values at which the two curves intersect, as illustrated in Figure 2.3. For small vales of λ,

[1] We consider here a deep-ocean depth of 4000 m and Brunt–Väisälä frequency of $5 \times 10^{-3}\,\mathrm{s}^{-1}$.

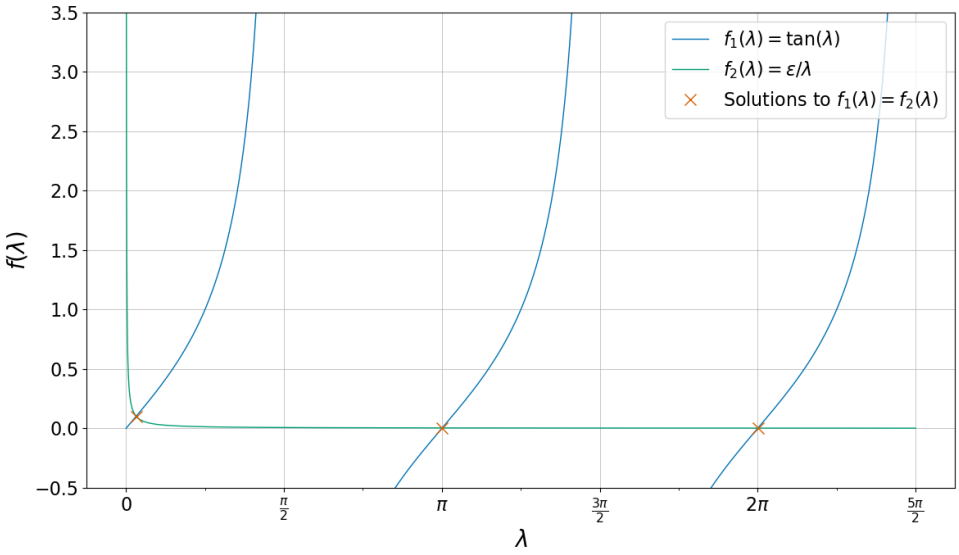

Figure 2.3: Equivalent to Figure 15.2 of LeBlond and Mysak (1978), graphical solutions to the eigenvalue equation $\tan(\lambda) = \varepsilon/\lambda$ for $\varepsilon = 10^{-3}$ and constant stratification are shown. Eigenvalues are indicated by the crosses marking the intersections of the two functions f_1 and f_2, solved using Newton–Raphson (with a tolerance of 10^{-14}).

note that $\tan(\lambda) \approx \lambda$, and therefore the lowest (barotropic) eigenvalue λ_0 is given by

$$\lambda_0 = \sqrt{\varepsilon}\left(1 + O\left(\sqrt{\varepsilon}\right)\right). \tag{2.90}$$

We see from (2.90) that the barotropic mode is zero in the case of a rigid lid whereby $\varepsilon = 0$. In the case of the higher (baroclinic) eigenvalues, we consider large λ relative to $\varepsilon \ll 1$ such that $f_2(\lambda) \approx 0$, so the roots to $f_1(\lambda) = f_2(\lambda)$ are given by

$$\lambda_n = n\,\pi\left(1 + O\left(\sqrt{\varepsilon}\right)\right), \qquad n = 1, 2, 3, \ldots. \tag{2.91}$$

It follows from (2.87) and (2.88) that

$$Z_0(z^*) = \alpha_0\left(1 + (z^*\,\varepsilon)\right) \tag{2.92}$$

for the barotropic vertical eigenfunction, and

$$Z_n(z^*) = \alpha_n\left(\cos(n\,\pi\,z^*) + O(\varepsilon)\right), \qquad n = 1, 2, 3, \ldots \tag{2.93}$$

for the baroclinic. For small ε, we observe that the baroclinic eigenfunctions may simply be approximated by $\cos(n\,\pi\,z/h)$. Consequently, it follows from equations (2.70)–(2.71) that both u' and v' also have the same structural dependence on $\cos(n\,\pi\,z/h)$, while equations (2.26) and (2.41) on the other hand indicate that $\tilde{\rho}$ and w' depend on $\sin(n\,\pi\,z/h)$. By similar approach for the barotropic mode, we identify that both u' and v' are proportional to $1 + O(\varepsilon\,z^*)$, while $\tilde{\rho}$ and w' are $O(\varepsilon)$ quantities.

It is now useful to regard the corresponding equivalent depths substituting eigenmodes

(2.90) and (2.91) into (2.84):

$$h_0 = h\,(1 + O\,(\varepsilon)) \qquad \text{and} \qquad h_n = \frac{N^2\,h^2}{g\,n^2\,\pi^2}\,(1 + O\,(\varepsilon))\,, \quad n = 1, 2, 3, \ldots. \tag{2.94}$$

For the barotropic mode, the equivalent depth h_0 is approximately equal to the true depth, h, with some small correction term proportional to the relative density difference throughout the fluid medium. Since $N^2\,h/g = \varepsilon \ll 1$, (2.94) shows that the baroclinic equivalent depths h_n are always much less than the fluid depth:

$$h_0 (\simeq h) \gg h_1 > h_2 > \ldots.$$

2.3.4 Numerical Solutions

The continuously stratified eigenvalue problem defined by equations (2.78) and (2.79) can be solved numerically with the help of numerical approximations of the derivatives using finite-differences. Here, we propose a stable numerical method involving second-order central finite-differences which uses ghost points on the boundaries which are then solved subject to the boundary conditions. Initial attempts at solving the eigenvalue problem involved using forward and backward finite-differences along the boundaries without the use of ghost points but would frequently obtain noisy solutions. The latter can be overcome by using high-accuracy pseudo-spectral methods. The problem however is that the discrete differential operators of such methods are typically dense (and can be computationally expensive for many nodes), e.g. Chebyshev differential matrices (see Fornberg, 1996).

To begin, let us discretise equation (2.78) at some location $z = z_m$ whereby $Z_m = Z\,(z_m)$. With $M + 1$ grid-points, we may use central finite-differences with uniform grid-spacing $\Delta = -h/M$ such that $z_m = m\,\Delta$ to arrive at

$$\frac{\rho_m}{\Delta^2}\left(\frac{Z_{m+1} - Z_m}{\rho_{m+\frac{1}{2}}\,{N^2}_{m+\frac{1}{2}}} - \frac{Z_m - Z_{m-1}}{\rho_{m-\frac{1}{2}}\,{N^2}_{m-\frac{1}{2}}}\right) + \frac{Z_m}{{c_n}^2} + O\left(\Delta^2\right) = 0, \tag{2.95}$$

using the fact that

$$\begin{aligned}\left.\frac{\mathrm{d}}{\mathrm{d}z}\left(a\frac{\mathrm{d}b}{\mathrm{d}z}\right)\right|_m &= \frac{\left.a\frac{\mathrm{d}b}{\mathrm{d}z}\right|_{m+\frac{1}{2}} - \left.a\frac{\mathrm{d}b}{\mathrm{d}z}\right|_{m-\frac{1}{2}}}{\Delta} + O\left(\Delta^2\right) \\ &= \frac{a_{m+\frac{1}{2}}\,(b_{m+1} - b_m) - a_{m-\frac{1}{2}}\,(b_m - b_{m-1})}{\Delta^2} + O\left(\Delta^2\right).\end{aligned}$$

We may then simplify equation (2.95) through the second-order approximation of the squared Brunt–Väisälä frequency:

$${N^2}_m = -\frac{g}{\rho_m}\frac{\rho_{m+\frac{1}{2}} - \rho_{m-\frac{1}{2}}}{\Delta} + O\left(\Delta^2\right), \qquad m = 1, 2, \ldots, M-1.$$

Upon substitution of the latter into equation (2.95), we obtain

$$\frac{-\rho_m}{g\,\Delta}\left(\frac{Z_{m+1}-Z_m}{\rho_{m+1}-\rho_m}-\frac{Z_m-Z_{m-1}}{\rho_m-\rho_{m-1}}\right)+\frac{Z_m}{c_n^2}+O\left(\Delta^2\right)=0, \tag{2.96}$$

subject to the relevant discretisation of the boundary conditions. Note that since ρ_{-1} and ρ_{M+1} are undefined, we are unable to simply use (2.96) alone.

At the free-surface, $z=z_0$, we are required to use second-order forward finite-differences:

$$-\frac{\rho_0}{4\Delta^2}\left(-3\frac{Z_1-Z_{-1}}{\rho_0\,{N^2}_0}+4\frac{Z_2-Z_0}{\rho_1\,{N^2}_1}-\frac{Z_3-Z_1}{\rho_2\,{N^2}_2}\right)+\frac{Z_0}{c_n^2}+O\left(\Delta^2\right)=0, \tag{2.97}$$

subject to the free-surface condition

$$\left(\frac{\mathrm{d}}{\mathrm{d}z}+\frac{N^2\left(z\right)}{g}\right)Z\left(z=z_0\right)=0.$$

The latter is numerically approximated using second-order central finite-differences:

$$\frac{Z_1-Z_{-1}}{2\Delta}+\frac{{N^2}_0}{g}Z_0+O\left(\Delta^2\right)=0,\qquad\Longrightarrow\qquad Z_{-1}\approx Z_1+\frac{2\Delta\,{N^2}_0}{g}Z_0.$$

Upon substitution of the latter into equation (2.97), we have

$$-\frac{\rho_0}{4\Delta^2}\left(\frac{6\Delta}{g\,\rho_0}Z_0+4\frac{Z_2-Z_0}{\rho_1\,{N^2}_1}-\frac{Z_3-Z_1}{\rho_2\,{N^2}_2}\right)+\frac{Z_0}{c_n^2}+O\left(\Delta^2\right)=0.$$

The latter may be simplified further using the second-order approximation of ${N^2}_m$,

$${N^2}_m=\frac{-g}{\rho_m}\frac{\rho_{m+1}-\rho_{m-1}}{2\Delta}+O\left(\Delta^2\right), \tag{2.98}$$

giving

$$-\frac{\rho_0}{2g\,\Delta}\left(\frac{3}{\rho_0}Z_0-4\frac{Z_2-Z_0}{\rho_2-\rho_0}+\frac{Z_3-Z_1}{\rho_3-\rho_1}\right)+\frac{Z_0}{c_n^2}+O\left(\Delta^2\right)=0. \tag{2.99}$$

At the rigid-bottom of the fluid medium, $z=-z_M$, we are required to use second-order backward finite-differences:

$$-\frac{\rho_M}{4\Delta^2}\left(\frac{Z_{M-3}-Z_{M-1}}{\rho_{M-2}\,{N^2}_{M-2}}-4\frac{Z_{M-2}-Z_M}{\rho_{M-1}\,{N^2}_{M-1}}+3\frac{Z_{M-1}-Z_{M+1}}{\rho_M\,{N^2}_M}\right)+\frac{Z_M}{c_n^2}+O\left(\Delta^2\right)=0, \tag{2.100}$$

subject to the impermeability condition

$$\frac{\mathrm{d}}{\mathrm{d}z}Z\left(z=-z_M\right)=0.$$

The latter may also be numerically approximated using second-order forward finite differ-

ences:

$$\frac{Z_{M-1} - Z_{M+1}}{2\Delta} + O\left(\Delta^2\right) = 0 \qquad \Longrightarrow \qquad Z_{M+1} \approx Z_{M-1}.$$

Upon substitution of the latter into equation (2.100), we have

$$-\frac{\rho_M}{2\Delta}\left(-\frac{Z_{M-3} - Z_{M-1}}{\rho_{M-3} - \rho_{M-1}} + 4\frac{Z_{M-2} - Z_M}{\rho_{M-2} - \rho_M}\right) + \frac{Z_M}{c_n^2} + O\left(\Delta^2\right) = 0, \tag{2.101}$$

having already substituted in for ${N^2}_{M-1}$ and ${N^2}_{M-2}$ using equation (2.98).

Equations (2.95), (2.99) and (2.101) complete the discretised eigenvalue problem as defined in equations (2.78) and (2.79).

To understand the effectiveness of the method proposed, we compare it with the pseudo-spectral Chebyshev method using the observational stratification data from National Oceanographic Data Center (U.S.) (2013) at 39°N, 125°W (shown in Figure 2.2). The results are shown in Figure 2.4 for increasing number of grid points: (a) 64; (b) 128; (c) 256. Here, the non-dimensionalised modal wave speed is shown to three decimal places, along with the modes corresponding vertical structure. Wave speeds have been non-dimensionalised with respect to $c = \sqrt{g\,H}$ such that $\tilde{c}_0 \approx 1$ corresponds to the barotropic mode, while eigenmodes have been normalised such that $Z\left(z/H = -1\right) = 1$.

The most striking difference between the two methods is the rate of convergence, particularly for the barotropic mode. For the Chebyshev method, the barotropic wave speed remains approximately unchanged despite increasing the number of grid points. From this, we can assume that the mode has been resolved up to three decimal places with just 64 grid points. On the other hand, the finite-differences method proposed in equations (2.95), (2.99) and (2.101) sees the relative error of the barotropic wave speed reduce from $\sim 2.2\%$ to $\sim 0.6\%$ after quadrupling the number of grid points.

We deduce therefore that it is easier and more accurate to implement the Chebyshev method to perform the modal decomposition than the aforementioned finite-differences scheme. Along with being of spectral accuracy, a further benefit to the Chebyshev method is that nodes are disproportionately positioned towards the boundary, allowing much greater resolution over the pycnocline. To achieve a similar level of accuracy for the finite-differences method would require significantly more grid points and would therefore be computationally more expensive. Of course, iterative methods do exist (e.g. Arnoldi iteration), but these are typically better adapted to solving for large dominant eigenvalues. The latter is not the case for (2.78) and (2.79), where eigenvalues $\lambda = c^{-2}$ of interest are small. It is thus more advantageous to consider a small but dense matrix involving Chebyshev differential matrices than a large but sparse matrix using a second-order finite-difference scheme when performing modal decomposition of a continuously stratified fluid.

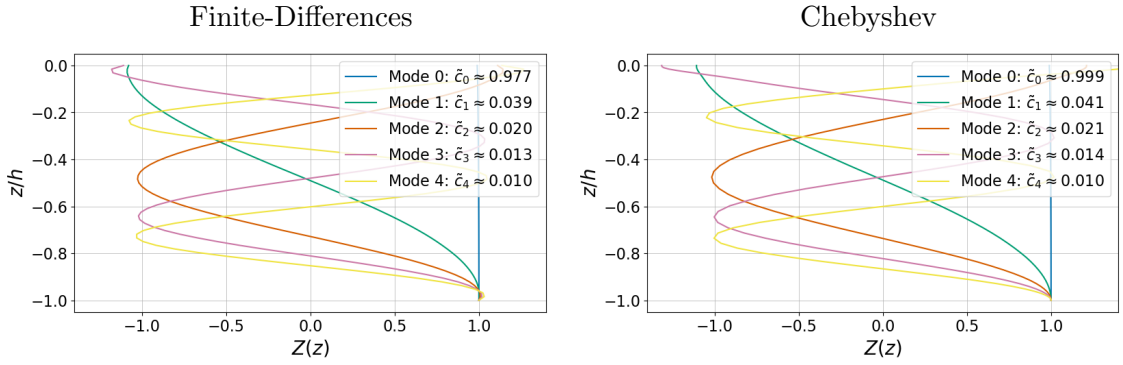

(a) 64 Grid points

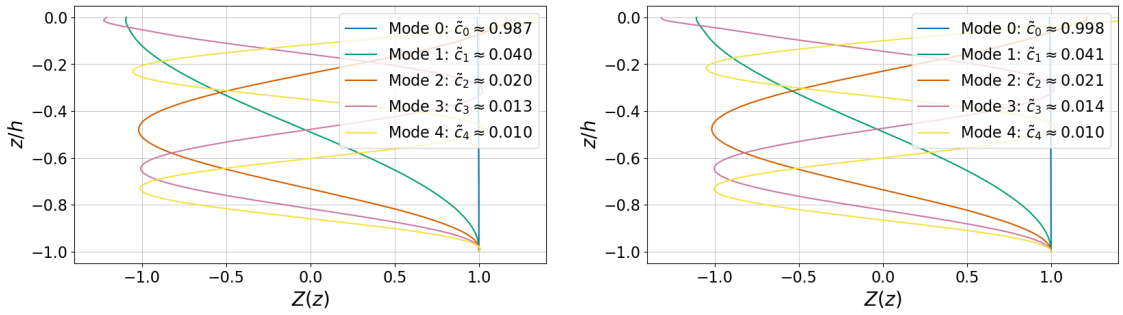

(b) 128 Grid points

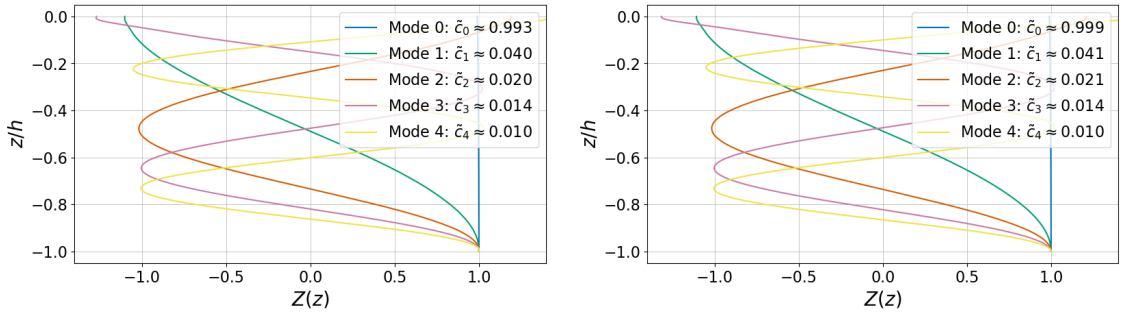

(c) 256 Grid points

Figure 2.4: Eigenvalue problem: modal decomposition of observational stratification data from National Oceanographic Data Center (U.S.) (2013) at 39°N, 125°W (shown in Figure 2.2). In each plot the five largest modal wave speeds to three decimal places are given and are accompanied with their vertical structure. Modal wave speeds are non-dimensionalised with respect to $c = \sqrt{g\,H}$, such that $\tilde{c}_0 \approx 1$ corresponds to the barotropic mode, while eigenmodes have been normalised such that $Z(z/H = -1) = 1$. Here, we compare the finite-differences method proposed in equations (2.95), (2.99) and (2.101) (left) with the Chebyshev method (right). Moreover, we compare the accuracy of modal wave speeds and vertical modal structure while varying the number of grid points: (a) 64; (b) 128; (c) 256.

2.3.5 Intermediate Summary

To summarise, the work in this section solved for modes of a continuously stratified fluid medium. An analytical solution for constant stratification with the Boussinesq approximation was also shown, where the leading-order solution corresponded with the case of a rigid lid. Lastly, the eigenvalue problem associated with continuously stratified hydrostatic flow was discretised using second-order finite-differences. The resulting vertical structures and modal wave speeds were then briefly compared to those using pseudo-spectral Chebyshev method. It was concluded that the modal decomposition of the continuously stratified SWEs was more efficient and accurate using Chebyshev differential matrices since far fewer grid points were required to achieve similar accuracy.

While we have only considered the subject of modes of hydrostatic flow over uniform topography, the equations involving modal coupling as a result of topographic variations are the subject of Griffiths and Grimshaw (2007a, 2007b). For modal wave speed $c_m\,(h)$ for fluid depth h, these equations, presented on page 16 of Griffiths and Grimshaw (2007b), are

$$\partial_t \mathbf{U}_m + \mathbf{f} \times \mathbf{U}_m + \boldsymbol{\nabla} P_m = -\boldsymbol{\nabla} h \cdot \sum_{m=0}^{\infty} \mathcal{T}_{mn}\, P_n, \tag{2.102}$$

$$\partial_t P_m + \boldsymbol{\nabla} \cdot \left(c_m^2\, \mathbf{U}_m\right) = -\boldsymbol{\nabla} h \cdot \sum_{m=0}^{\infty} \mathcal{T}_{mn}\, c_n^2\, \mathbf{U}_n, \tag{2.103}$$

and require modal-interaction coefficients

$$\mathcal{T}_{mn} = \begin{cases} \dfrac{\partial_h c_m^2}{c_n^2 - c_m^2}, & m \neq n, \\ -\dfrac{\partial_{hh} c_m^2}{2\partial_h c_m^2}, & m = n. \end{cases} \tag{2.104}$$

The topographic coupling is crucial since it is the flow over variable topography which generates internal waves within the ocean, providing the all-important mechanism for barotropic dissipation. It is worth noting that 2D modal equations allowing for topographic coupling have also been derived for weakly non-linear non-hydrostatic flow.[1]

The problem with the modal decomposition of continuously stratified flow is that the formulation leads to an infinite set of coupled equations, and that to obtain a numerical solution, truncation is required. For time-periodic solutions of wave frequency ω, truncation is considered by Griffiths and Grimshaw (2007a) for regimes of slope criticality

$$s = \frac{\max\left(|\boldsymbol{\nabla} h|\right)}{\alpha}, \qquad \alpha = \frac{\sqrt{\omega^2 - f^2}}{\sqrt{N^2\,(z) - \omega^2}}. \tag{2.105}$$

Here, s denotes the ratio between the bathymetric gradient and the magnitude of the characteristic slope, α. The effect of non-hydrostatic flow is shown in red and is reminiscent to what is shown in equation (2.41), where $\omega^2 \ll N^2$ is implied from the hydrostatic approximation. The case of critical topography ($s = 1$) leads to resonant forcing, produc-

[1] See equations (36)–(39) of Maugé and Gerkema (2008).

ing large vertical displacements within beam-like structures. In the supercritical regime ($s \gtrsim 1$), Griffiths and Grimshaw (2007a) notes that the fine vertical scales of the beams can require several hundred modes to achieve sufficient resolution; the change in modal flow is no more than 5% when doubling the number of modes.

For internal-tide generation over continental margins, however, the modal conversion is confined to the shelf break where the stratification profile typically consists of a shallow pycnocline surmounting a weakly stratified interior (see Baines, 1982). As such, any internal-tide response will be dominated by the pycnocline mode and can be modelled as an interface between two stably stratified immiscible fluids (a two-layer fluid). Garrett and Munk (1979) remark that these interfacial waves along the pycnocline are often observed in summer when solar heating produces a light surface layer over the shelf. Of course, the benefit of using a two-layer model is that instead of an infinite set of modes seen in the previous section, we have but two: a barotropic mode and a baroclinic mode. For this, we proceed to the equivalent theory for vertical modes of a layer-stratified fluid.

2.4 Multi-Layer SWEs

In this section, the framework for modal decomposition of the shallow-water equations (SWEs) in the case of discrete layers of uniform density is developed. The consideration of the latter will enable us to employ the modal equations in lieu of the primitive equations where the imposition of boundary conditions and external forcing on specific modes is convoluted. On top of this, post-processing is required of the modal solutions to obtain quantities of interest, such as the barotropic-to-baroclinic energy transfer. With all this in mind, we seek to develop the theory required to treat the modal equations of a two-layer hydrostatic fluid.

One of the first instances of modal decomposition beyond two layers was reviewed by Longuet-Higgins (1952). Here, the case of a three-layer fluid in a rectangular basin of uniform depth—a crude model to assist a study of Lake Windermere conducted by Mortimer (1952)—is considered. Wave equations implied from the primitive shallow-water equations are combined to seek oscillatory motion of a single wave speed, and results in the dispersion relationship seen in (A8). The work by Lighthill (1969), as discussed previously, goes further by considering the generalised decomposition of the multi-layer primitive equations, but stops short of deriving the modal equations over variable topography.

For multi-layer flow over variable topography, the theory of Griffiths and Grimshaw (2007a) was implicit; the infinite set of modes are replaced with a finite number. That is to say, equations (2.102)–(2.103) are what we seek to derive, but with a finite number of modes in the summation. We will derive these using multi-layers and remaining within this framework; this corresponds to the work of Shimizu (2011). The work of Shimizu (2011) is achieved by introducing a matrix framework. However, certain exploits of the matrix framework are omitted, such as those which result in the strict inequality on squared wave speed for stably stratified flow. These are results of Griffiths (2020; personal

communication).

To be clear, Sections 2.4.1, 2.4.2 and 2.4.4 are minor variations of unpublished work by Griffiths (2020; personal communication). These are themselves a reformulation of the matrix theory used by Shimizu (2011) for multi-layer flow over variable topography. The work presented in Section 2.4.3 is original work and illustrates the ease at which the theory presented in Section 2.4.2 can be implemented, and how the modes compare with the continuously stratified analogue using Chebyshev matrices. Section 2.4.5 is analogous to Appendix B of Shimizu (2011) to obtain the governing equations but made in the context of the revised formulation of Griffiths (2020; personal communication).

To achieve the aims of this section, the theory for M-layer shallow-water modal equations is developed. From the generalised theory, the modal decomposition for a two-layer fluid follows immediately, reproducing well-known results of modal wave speed and vertical structure (e.g. LeBlond & Mysak, 1978; Gill, 1982; Vallis, 2006; Sutherland, 2010) first considered by Stokes (1847). These equations though, upon derivation, will allow modal interaction over variable topography.

2.4.1 Derivation of Primitive Equations

Griffiths (2020; personal communication) considers the case a fluid medium composed of M-layers of constant density ρ_j, as illustrated in Figure 2.5. At rest, each layer j occupies $z_{j+1} < z < z_j$ with constant depth $h_j = z_j - z_{j+1}$. Variable topography is accompanied for by letting the bottom-layer depth $h_M = h_M(x, y)$ vary. Since density ρ_j is constant within each layer, it follows that Brunt–Väisälä frequency $N(z) = 0$ within each layer also. However, continuity requires that

$$\int_{z_j^-}^{z_j^+} \rho_0 N^2(z)\,\mathrm{d}z = \left[-g\,\rho_0\right]_{z_j^-}^{z_j^+} = g\,(\rho_j - \rho_{j-1}), \qquad 2 \le j \le M. \tag{2.106}$$

Within layer j, the horizontal flow is written as (u_j, v_j) and the hydrostatic pressure perturbation as p_j (both independent of z in the shallow-water limit). The upper interface of layer j is displaced to η_j (so that η_1 is the surface displacement). Then, the forced linearised momentum equations are

$$\rho_j\,(\partial_t u_j - f\,v_j) = -\partial_x p_j + F_{x_i}, \qquad \rho_j\,(\partial_t v_j + f\,u_j) = -\partial_y p_j + F_{y_i}, \tag{2.107}$$

where for interfacial displacement η_j, hydrostatic pressure

$$p_j = \sum_{k=1}^{j} g\,(\rho_k - \rho_{k-1})\,\eta_k, \qquad \rho_0 = 0. \tag{2.108}$$

We have also mass conservation

$$\partial_t\,(\eta_j - \eta_{j+1}) + \partial_x\,(h_j\,u_j) + \partial_y\,(h_j\,v_j) = 0, \qquad \eta_{M+1} = 0. \tag{2.109}$$

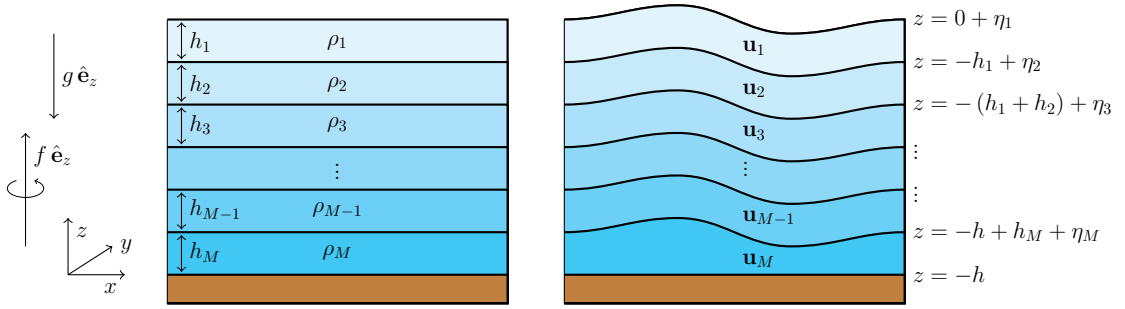

Figure 2.5: Schematic of a hydrostatic stably stratified M-layer fluid medium, assuming that densities $\rho_1 < \rho_2 < \ldots < \rho_M$. Here, we consider the f-plane approximation, where both gravity and Coriolis force are aligned with the vertical unit vector. At rest, we assume all layer depths are constant.

Together, equations (2.107)–(2.109) form the governing equations of motion.

This can be written in matrix form by introducing M-component column vectors of the form $\mathbf{u} = (u_1, u_2, \ldots, u_M)^{\mathsf{T}}$, and likewise for $\mathbf{v}$, $\mathbf{p}$, $\boldsymbol{\eta}$, $\boldsymbol{F}_x$ and $\boldsymbol{F}_y$. In which case, the horizontal momentum equations are

$$\mathsf{R}\,(\partial_t \mathbf{u} - f\,\mathbf{v}) = -\partial_x \mathbf{p} + \boldsymbol{F}_x, \qquad \mathsf{R}\,(\partial_t \mathbf{v} + f\,\mathbf{u}) = -\partial_y \mathbf{p} + \boldsymbol{F}_y, \tag{2.110}$$

while equations (2.108)–(2.109) are given as

$$\mathbf{p} = \mathsf{L}\,\Delta\,\boldsymbol{\eta}, \qquad \mathsf{D}^{\mathsf{T}}\,\partial_t \boldsymbol{\eta} + \partial_x\,(\mathsf{H}\,\mathbf{u}) + \partial_y\,(\mathsf{H}\,\mathbf{v}) = \mathbf{0}. \tag{2.111}$$

This construction is facilitated by $M \times M$ matrices

$$\Delta = g\,\mathrm{diag}\,(\rho_1, \rho_2 - \rho_1, \ldots, \rho_M - \rho_{M-1})\,, \qquad \mathsf{H} = \mathrm{diag}\,(h_1, h_2, \ldots, h_M)\,,$$

$$\mathsf{R} = \mathrm{diag}\,(\rho_1, \rho_2, \ldots, \rho_M)\,, \tag{2.112}$$

$$\mathsf{D}_{ij} = \begin{Bmatrix} +1 & i = j, \\ -1 & i = j+1, \\ 0 & \text{otherwise} \end{Bmatrix} = \begin{pmatrix} +1 & & & \\ -1 & \ddots & & \\ & \ddots & \ddots & \\ & & -1 & +1 \end{pmatrix}, \tag{2.113}$$

$$\mathsf{L}_{ij} = \begin{Bmatrix} 1 & i \geq j, \\ 0 & \text{otherwise} \end{Bmatrix} = \begin{pmatrix} 1 & & & \\ 1 & \ddots & & \\ \vdots & \ddots & \ddots & \\ 1 & \cdots & 1 & 1 \end{pmatrix}, \tag{2.114}$$

and are predominantly sparse.

2.4.2 Eigenvalue Problem

Although the vertical structure of the resulting flow is commonly analysed using M-layer shallow-water equations (e.g. Lighthill, 1969; Müller, 2006; Shimizu, 2011), the analysis of Griffiths (2020; personal communication) begins with the integration of (2.78) over vertical depth:

$$\frac{\mathrm{d}Z\left(z\right)}{\mathrm{d}z} + \frac{\rho_0\, N^2}{c^2} \int_{-h}^{z} \frac{Z\left(\zeta\right)}{\rho_0\left(\zeta\right)}\, \mathrm{d}\zeta = 0. \tag{2.115}$$

Griffiths (2020; personal communication) notes that eigenmode $Z\left(z\right)$ can be written as a column vector since within each layer, $N^2 = 0$. Equation (2.115) implies therefore that eigenmode $Z\left(z\right)$ is constant therein. Writing $Z\left(z\right) = Z_{(j)}$ for $z_{j+1} < z < z_j$, $Z\left(z\right)$, this gives vector $\mathbf{Z} = \left(Z_{(1)}, Z_{(2)}, \ldots, Z_{(M)}\right)^{\mathsf{T}}$. Equation (2.115) is then integrated across interface $z = z_j$, using (2.106), to arrive at

$$c^2\left(Z_j - Z_{j-1}\right) - g\left(\rho_j - \rho_{j-1}\right) \sum_{k=1}^{j} \frac{h_k\, Z_k}{\rho_k} = 0, \qquad 0 \leq j \leq M. \tag{2.116}$$

Equation (2.116) is subjected to the free-surface condition

$$c^2\, Z_1 - g\,\rho_1 \sum_{k=1}^{M} \frac{h_k\, Z_k}{\rho_k} = 0 \tag{2.117}$$

as given in (2.79) since the background density at the ocean surface $\rho_0\left(0\right) = \rho_1$. Equations (2.116) and (2.117) are written in matrix form

$$\left(c^2\,\mathsf{D} - \mathsf{\Delta}\,\mathsf{L}^{\mathsf{T}}\,\mathsf{H}\,\mathsf{R}^{-1}\right)\mathbf{Z} = \mathbf{0}. \tag{2.118}$$

In (2.118), the first row corresponds to equation (2.117), whilst the j-th row corresponds to equation (2.116) with $j = 2, 3, \ldots, M$. Note also that L^{T} is simply an upper-triangular matrix of ones, and that

$$\mathsf{L}\,\mathsf{D} = \mathsf{D}\,\mathsf{L} = \mathsf{I} \tag{2.119}$$

for $M \times M$ identity matrix I. This means that multiplying (2.118) by L,

$$\left(\mathsf{S} - c^2\,\mathsf{I}\right)\mathbf{Z} = \mathbf{0}, \qquad \text{where} \qquad \mathsf{S} = \mathsf{L}\,\mathsf{\Delta}\,\mathsf{L}^{\mathsf{T}}\,\mathsf{H}\,\mathsf{R}^{-1}. \tag{2.120}$$

Equation (2.120) is an $M \times M$ eigenvalue problem for the squared wave speeds c^2 and corresponding eigenvectors $\mathbf{Z}$. Additionally, equation (2.120) is equivalent to equation (10b) of Shimizu (2011). Shimizu (2011) worked from the multi-layer shallow-water equations and posed the problem in terms of vertical structure $\hat{\boldsymbol{\alpha}}$; these corresponded to layer-integrated volume transports (so $\hat{\boldsymbol{\alpha}} = \mathsf{H}\,\mathsf{R}^{-1}\,\mathbf{Z}$).

Multiplying (2.120) by $\mathsf{R}^{-1/2}\,\mathsf{H}^{1/2}$, the eigenvalue problem can be re-posed in the form

$$\left(\mathsf{T} - c^2\,\mathsf{I}\right)\mathbf{Y} = \mathbf{0}, \tag{2.121}$$

where matrix

$$\mathsf{T} = \mathsf{A}\,\mathsf{A}^{\mathsf{T}} \qquad \text{for} \qquad \mathsf{A} = \mathsf{R}^{-1/2}\,\mathsf{H}^{1/2}\,\mathsf{L}\,\Delta^{1/2} \tag{2.122}$$

and eigenvector

$$\mathbf{Y} = \mathsf{R}^{-1/2}\,\mathsf{H}^{1/2}\,\mathbf{Z}. \tag{2.123}$$

For stable stratification, all non-zero entries of Δ are positive. Consequently, matrix $\Delta^{1/2}$ is real, as is matrix A. By multiplying (2.121) by $\mathbf{Y}^{\mathsf{T}}$, it follows that $|\mathsf{A}^{\mathsf{T}}\,\mathbf{Y}|^2 = c^2\,|\mathbf{Y}|^2$, and therefore $c^2 \geq 0$. Since $\mathbf{Y}$ is an eigenvector of real-symmetric matrix T, and therefore non-trivial, this inequality on wave speed is strict. This is identical to the case of continuous stratification where vertical structure and wave speed is determined by a regular Sturm–Liouville eigenvalue problem.

The construction of matrices S and T given in (2.120) and (2.122) requires a fair amount of matrix construction and multiplication. Fortunately however, Griffiths (2020; personal communication) shows that the form of matrices S and T can be simplified. First, it is remarked that

$$\Delta\,\mathsf{L}^{\mathsf{T}} = g\begin{pmatrix} \rho_1 & \rho_1 & \cdots & \rho_1 \\ & \rho_2 - \rho_1 & \cdots & \rho_2 - \rho_1 \\ & & \ddots & \vdots \\ & & & \rho_M - \rho_{M-1} \end{pmatrix}, \tag{2.124}$$

such that

$$\mathsf{L}\,\Delta\,\mathsf{L}^{\mathsf{T}} = g\begin{pmatrix} \rho_1 & \rho_1 & \cdots & \rho_1 \\ \rho_1 & \rho_2 & \cdots & \rho_2 \\ \vdots & \vdots & \ddots & \vdots \\ \rho_1 & \rho_2 & \cdots & \rho_M \end{pmatrix}. \tag{2.125}$$

Griffiths, (2020; personal communication) observes that equation (2.125) can be formulated as

$$\left(\mathsf{L}\,\Delta\,\mathsf{L}^{\mathsf{T}}\right)_{ij} = g\min\left(\rho_i, \rho_j\right). \tag{2.126}$$

The latter is incredibly useful when considering the structure of matrix S:

$$\mathsf{S}_{ij} = \frac{g\,h_j}{\rho_j}\min\left(\rho_i, \rho_j\right). \tag{2.127}$$

Likewise, we may matrix T can be written as:

$$\mathsf{T}_{ij} = \left(\frac{h_i}{\rho_i}\right)^{1/2} g\min\left(\rho_i, \rho_j\right)\left(\frac{h_j}{\rho_j}\right)^{1/2} = g\left(\frac{h_i\,h_j}{\rho_i\,\rho_j}\right)^{1/2}\min\left(\rho_i, \rho_j\right). \tag{2.128}$$

Equation (2.128), in which the symmetry of T is evident, is also given on page 86 of Lighthill (1969).

2.4.3 Numerical Implementation

The Python code for the construction of matrices S and T associated with the modal decomposition of the multi-layer SWEs, defined in (2.127) and (2.128) respectively, is shown in Listing 2.1. Here, we consider the observational stratification data from National Oceanographic Data Center (U.S.) (2013) at 39°N, 125°W (shown in Figure 2.2) in the case of 16 layers of uniform thickness. Having defined the physical parameters, the construction of either matrix is no more than two lines of code each.

Listing 2.1: Python code for construction of matrices S and T, defined in (2.127) and (2.128) respectively.

```
import numpy as np

## gravity ##
g = 9.81

## density within each layer ##
r0 = np.array([1026.360, 1028.193, 1029.473, 1030.679,
               1031.818, 1032.919, 1033.983, 1035.036,
               1036.080, 1037.103, 1038.113, 1039.102,
               1040.074, 1041.056, 1042.035, 1043.002])

## thickness of each layer ##
h_max = 3400
h = (h_max/16) * np.ones(16)

## Construction of matrix S ##
S = g * (h/r0)[None,:] * np.fmin(r0[:, None], r0[None, :])

## Construction of matrix T ##
T = g * np.sqrt(h/r0)[None, :] * np.sqrt(h/r0)[:, None] * \
    np.fmin(r0[:, None], r0[None, :])
```

Having discussed how to construct matrix S associated with (2.120), we now consider comparing the resulting modal wave speeds and vertical structures with the case of the continuously stratified eigenvalue problem defined in (2.78)–(2.79). In the previous section, we found that using Chebyshev differential matrices is much more efficient than using a proposed second-order finite-differences scheme. Consequently, it is these numerical results against which the multi-layer eigenvalue problem will be compared. The modal wave speeds and vertical structures were also found to be sufficiently resolved for the Chebyshev method when using 64 grid points, providing a benchmark against which the multi-layer eigenvalue problem can be compared.

In Figure 2.6, we show the non-dimensional modal wave speeds and vertical structure for the multi-layer eigenvalue problem (left) with those for the continuously stratified eigenvalue problem discretised using the Chebyshev method (right) while increasing the number of uniform layers/grid points: (a) 16; (b) 32; (c) 64. Here, the non-dimensionalised modal wave speed is shown to three decimal places, along with their corresponding vertical structure. Wave speeds have been non-dimensionalised with respect to $c = \sqrt{g\,H}$ such that $\tilde{c}_0 \approx 1$ corresponds to the barotropic mode, while vertical structures have been normalised such that $Z\,(z/H = -1) = Z_{(M)} = 1$.

Indeed, Figure 2.6 shows that the multi-layer eigenvalue problem given in (2.120) does well to approximate both the vertical structure and the modal wave speed. As to be expected, the vertical structures of the multi-layer eigenvalue problem converge towards those of the continuously stratified as the number of layers increases. It can quite easily be concluded that the multi-layer eigenvalue problem, in terms of matrix construction and accuracy of low-order modes, far exceeds the finite-difference approach previously considered. Moreover, in terms of complexity and efficiency, the continuously stratified problem using high-accuracy Chebyshev differential matrices almost becomes obsolete, especially if one were to consider locally refined layer thicknesses which the formulation permits.

2.4.4 Orthogonality of Modes

Orthogonality properties of the multi-layer eigenvalue problem are made clear in the formulation of (2.121). We know that c^2 is an eigenvalue of the real-symmetric matrix $\mathsf{T} = \mathsf{A}\,\mathsf{A}^{\mathsf{T}}$, and that both eigenvalues c^2 and eigenvectors $\mathbf{Y}$ are real for stable stratification. From the Spectral Theorem (see Proposition 5.15 of Meckes & Meckes, 2018), eigenvectors $\mathbf{Y}$ of symmetric matrix T are orthogonal:

$$\mathbf{Y}_m \cdot \mathbf{Y}_n \propto \delta_{mn}, \tag{2.129}$$

where δ_{mn} is the Kronecker delta function. Using equation (2.123), (2.129) implies the orthogonality relation

$$\left(\mathsf{R}^{-1/2}\,\mathsf{H}^{1/2}\,\mathbf{Z}_m\right)^{\mathsf{T}}\left(\mathsf{R}^{-1/2}\,\mathsf{H}^{1/2}\,\mathbf{Z}_n\right) = \mathbf{Z}_m^{\mathsf{T}}\,\mathsf{H}\,\mathsf{R}^{-1}\,\mathbf{Z}_n \propto \delta_{mn}, \tag{2.130}$$

As Griffiths (2020; personal communication) observes, this is a direct analogue of the continuous eigenvalue problem posed in (2.78). It is also equivalent to equations (A13) of Lighthill (1969) and (11) of Shimizu (2011).

2.4.5 Derivation of Modal Equations

Having constructed the framework for modal decomposition for multi-layered stratified fluids, we seek now to derive equations which govern the modal variables. The resulting equations enables us to solve directly for a given mode without the need to apply awkward manipulations to apply conditions on the barotropic or baroclinic motion within the

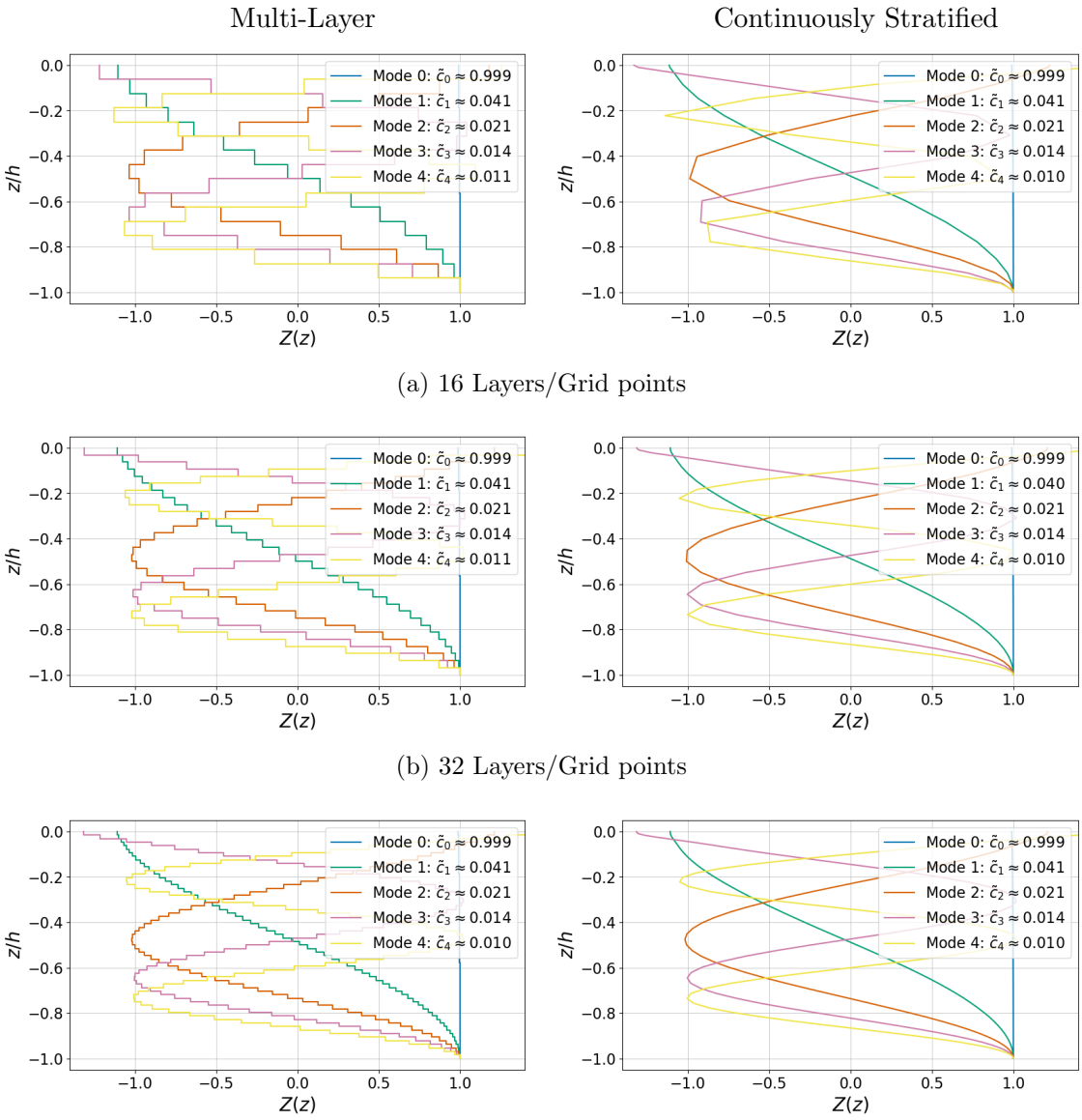

(a) 16 Layers/Grid points

(b) 32 Layers/Grid points

(c) 64 Layers/Grid points

Figure 2.6: Eigenvalue problem: modal decomposition of observational stratification data from National Oceanographic Data Center (U.S.) (2013) at 39°N, 125°W (shown in Figure 2.2) while varying the number of layers/grid points: (a) 16; (b) 32; (c) 64. On the left, we solve the multi-layer eigenvalue problem associated with (2.120) with uniform layers, while on the right the continuously stratified eigenvalue problem in (2.80)–(2.79) using Chebyshev differential matrices. In each plot the five largest modal wave speeds to three decimal places are given and are accompanied with their vertical structure. Modal wave speeds are non-dimensionalised with respect to $c = \sqrt{g\,H}$, such that $\tilde{c}_0 \approx 1$ corresponds to the barotropic mode, while eigenmodes have been normalised such that $Z_{(M)} = 1$.

primitive framework. As in Griffiths (2020; personal communication), primitive variables can be expressed in the form

$$(\mathbf{u}(x,y,t),\mathbf{v}(x,y,t)) = \mathsf{R}^{-1}\,\rho_{00}\sum_{n=0}^{M-1}(U_n(x,y,t),V_n(x,y,t))\,\mathbf{Z}_n(x,y) \tag{2.131}$$

and

$$\mathbf{p}(x,y,t) = \rho_{00}\sum_{n=0}^{M-1}P_n(x,y,t)\;\mathbf{Z}_n(x,y), \tag{2.132}$$

where ρ_{00} is some reference density. The addition of the density term is purely arbitrary, Griffiths (2020; personal communication) adds, and made so that

$$(U_n(x,y,t),V_n(x,y,t))\,\mathbf{Z}_n(x,y)$$

have dimensions of speed. It follows that equations (2.110)–(2.111) become

$$\sum_{n=0}^{M-1}\{\partial_t U_n - f\,V_n\}\,\mathbf{Z}_n = -\sum_{n=0}^{M-1}\partial_x(P_n\,\mathbf{Z}_n) + \boldsymbol{F}_x, \tag{2.133}$$

$$\sum_{n=0}^{M-1}\{\partial_t V_n + f\,U_n\}\,\mathbf{Z}_n = -\sum_{n=0}^{M-1}\partial_y(P_n\,\mathbf{Z}_n) + \boldsymbol{F}_y, \tag{2.134}$$

$$\sum_{n=0}^{M-1}\mathbf{Z}_n\,\partial_t P_n = -\mathsf{L}\,\Delta\,\mathsf{L}^{\mathsf{T}}\sum_{n=0}^{M-1}\left[\partial_x\left(\mathsf{H}\,\mathsf{R}^{-1}\,\mathbf{Z}_n\,U_n\right) + \partial_y\left(\mathsf{H}\,\mathsf{R}^{-1}\,\mathbf{Z}_n\,V_n\right)\right]. \tag{2.135}$$

Multiplying the governing equations of motion by $\mathbf{Z}_m^{\mathsf{T}}\,\mathsf{H}\,\mathsf{R}^{-1}$, we may use the orthogonality result in (2.130) to arrive at the M-modal equation

$$\partial_t U_m - f\,V_m = -\frac{1}{\mathcal{I}_m}\sum_{n=0}^{M-1}\mathbf{Z}_m^{\mathsf{T}}\,\mathsf{H}\,\mathsf{R}^{-1}\partial_x(P_n\,\mathbf{Z}_n) + F_{xm}, \tag{2.136}$$

$$\partial_t V_m + f\,U_m = -\frac{1}{\mathcal{I}_m}\sum_{n=0}^{M-1}\mathbf{Z}_m^{\mathsf{T}}\,\mathsf{H}\mathsf{R}^{-1}\,\partial_y(P_n\,\mathbf{Z}_n) + F_{ym}, \tag{2.137}$$

$$\partial_t P_m = -\frac{1}{\mathcal{I}_m}\sum_{n=0}^{M-1}\mathbf{Z}_m^{\mathsf{T}}\,\mathsf{S}^{\mathsf{T}}\left[\partial_x\left(\mathsf{H}\,\mathsf{R}^{-1}\,\mathbf{Z}_n\,U_n\right) + \partial_y\left(\mathsf{H}\,\mathsf{R}^{-1}\,\mathbf{Z}_n\,V_n\right)\right], \tag{2.138}$$

where

$$\mathcal{I}_m = \mathbf{Z}_m^{\mathsf{T}}\,\mathsf{H}\,\mathsf{R}^{-1}\,\mathbf{Z}_m \tag{2.139}$$

is the normalisation coefficient and

$$\mathsf{S}^{\mathsf{T}} = \mathsf{H}\,\mathsf{R}^{-1}\,\mathsf{L}\,\Delta\,\mathsf{L}^{\mathsf{T}}. \tag{2.140}$$

We have now also decomposed the primitive forcing into modal forcing, giving

$$\mathbf{F}_m = \begin{pmatrix} F_{xm} & F_{ym} \end{pmatrix} = \frac{\mathbf{Z}_m^{\mathsf{T}} \, \mathsf{H} \, \mathsf{R}^{-1}}{\mathcal{I}_m} \begin{pmatrix} \boldsymbol{F}_x & \mathbf{F}_y \end{pmatrix}. \tag{2.141}$$

Remarking that the transpose of (2.120) implies that

$$\mathbf{Z}_m^{\mathsf{T}} \, \mathsf{S}^{\mathsf{T}} = c_m^2 \, \mathbf{Z}_m^{\mathsf{T}}, \tag{2.142}$$

we may apply both the product rule and the orthogonality relationship to obtain

$$\partial_t \mathbf{U}_m + \mathbf{f} \times \mathbf{U}_m + \boldsymbol{\nabla} P_m = -\boldsymbol{\nabla} h \sum_{n=0}^{M-1} \mathcal{T}_{mn} \, P_n + \boldsymbol{F}_m, \tag{2.143}$$

$$\partial_t P_m + \boldsymbol{\nabla} \cdot \left(c_m^2 \, \mathbf{U}_m \right) = -\boldsymbol{\nabla} h \cdot \sum_{n=0}^{M-1} \mathcal{T}_{mn} \, c_n^2 \, \mathbf{U}_n, \tag{2.144}$$

where

$$\mathcal{T}_{mn} = \frac{1}{\mathcal{I}_m} \mathbf{Z}_m^{\mathsf{T}} \, \mathsf{H} \, \mathsf{R}^{-1} \, \partial_h \left(\mathbf{Z}_n \right) \tag{2.145}$$

is the normalised modal-interaction coefficient. Note that here, we have also used the chain rule whereby

$$\boldsymbol{\nabla} h \, \partial_h \left(\mathbf{Z}_n \right) = \boldsymbol{\nabla} \mathbf{Z}_n. \tag{2.146}$$

To simplify the governing equations, the modal interaction term in (2.145) can be simplified as in Griffiths and Grimshaw (2007a). However, we adapt the methodology provided in Appendix B of Shimizu (2011). It is observed that

$$\mathsf{S} \, \mathbf{Z}_n = \mathsf{L} \, \Delta \, \mathsf{L}^{\mathsf{T}} \, \mathsf{H} \, \mathsf{R}^{-1} \, \mathbf{Z}_n = c_n^2 \, \mathbf{Z}_n \qquad \Longrightarrow \qquad \mathsf{H} \, \mathsf{R}^{-1} \, \mathbf{Z}_n = c_n^2 \, \mathsf{D}^{\mathsf{T}} \, \Delta^{-1} \, \mathsf{D} \, \mathbf{Z}_n, \tag{2.147}$$

such that by multiplying on the left by $\mathbf{Z}_m^{\mathsf{T}}$ and taking the derivative with respect to fluid depth h, it follows that

$$\partial_h \left(\mathbf{Z}_m^{\mathsf{T}} \, \mathsf{H} \, \mathsf{R}^{-1} \, \mathbf{Z}_n \right) = \partial_h \left(\mathcal{I}_m \right) \delta_{mn} \tag{2.148}$$

$$= \partial_h \left[c_n^2 \left(\mathsf{D}^{\mathsf{T}} \, \Delta^{-1} \, \mathsf{D} \, \mathbf{Z}_m \right)^{\mathsf{T}} \, \mathbf{Z}_n \right]. \tag{2.149}$$

Equations (2.148) and (2.149) are equivalent to (B1) of Shimizu (2011). Using the product rule on both sides of (2.149), we have that

$$\partial_h \left(\mathbf{Z}_m^{\mathsf{T}} \, \mathsf{H} \, \mathsf{R}^{-1} \right) \mathbf{Z}_n + \mathbf{Z}_m^{\mathsf{T}} \, \mathsf{H} \, \mathsf{R}^{-1} \partial_h \left(\mathbf{Z}_n \right) = \partial_h \left(c_n^2 \right) \, \mathbf{Z}_m^{\mathsf{T}} \, \mathsf{D}^{\mathsf{T}} \, \Delta^{-1} \, \mathsf{D} \, \mathbf{Z}_n + c_n^2 \, \partial_h \left(\mathbf{Z}_m^{\mathsf{T}} \, \mathsf{D}^{\mathsf{T}} \, \Delta^{-1} \, \mathsf{D} \, \mathbf{Z}_n \right), \tag{2.150}$$

which, when rearranged, gives

$$\begin{aligned}\mathbf{Z}_m^{\mathsf{T}}\,\mathsf{H}\,\mathsf{R}^{-1}\partial_h\left(\mathbf{Z}_n\right) &= \partial_h\left(c_n^2\right)\,\mathbf{Z}_m^{\mathsf{T}}\,\mathsf{D}^{\mathsf{T}}\,\mathsf{\Delta}^{-1}\,\mathsf{D}\,\mathbf{Z}_n + \\ &\quad c_n^2\,\partial_h\left(\mathbf{Z}_m^{\mathsf{T}}\,\mathsf{D}^{\mathsf{T}}\,\mathsf{\Delta}^{-1}\,\mathsf{D}\,\mathbf{Z}_n\right) - \partial_h\left(\mathbf{Z}_m^{\mathsf{T}}\,\mathsf{H}\,\mathsf{R}^{-1}\right)\mathbf{Z}_n \\ &= \partial_h\left(c_n^2\right)\,\mathbf{Z}_m^{\mathsf{T}}\,\mathsf{D}^{\mathsf{T}}\,\mathsf{\Delta}^{-1}\,\mathsf{D}\,\mathbf{Z}_n + \\ &\quad c_n^2\,\mathbf{Z}_m^{\mathsf{T}}\,\mathsf{D}^{\mathsf{T}}\,\mathsf{\Delta}^{-1}\,\mathsf{D}\,\partial_h\left(\mathbf{Z}_n\right) - \mathbf{Z}_m^{\mathsf{T}}\,\partial_h\left(\mathsf{H}\,\mathsf{R}^{-1}\right)\mathbf{Z}_n,\end{aligned} \tag{2.151}$$

implying that

$$\begin{aligned}\mathbf{Z}_m^{\mathsf{T}}\,\mathsf{H}\,\mathsf{R}^{-1}\left(1 - c_n^2\,\mathsf{R}\,\mathsf{H}^{-1}\,\mathsf{D}^{\mathsf{T}}\,\mathsf{\Delta}^{-1}\,\mathsf{D}\right)\partial_h\left(\mathbf{Z}_n\right) &= \partial_h\left(c_n^2\right)\,\mathbf{Z}_m^{\mathsf{T}}\,\mathsf{D}^{\mathsf{T}}\,\mathsf{\Delta}^{-1}\,\mathsf{D}\,\mathbf{Z}_n - \\ &\quad \mathbf{Z}_m^{\mathsf{T}}\,\partial_h\left(\mathsf{H}\,\mathsf{R}^{-1}\right)\mathbf{Z}_n.\end{aligned} \tag{2.152}$$

Since $\mathsf{S}^{\mathsf{T}} = \left(\mathsf{R}\,\mathsf{H}^{-1}\,\mathsf{D}^{\mathsf{T}}\,\mathsf{\Delta}^{-1}\,\mathsf{D}\right)^{-1}$, we have that

$$\left(\frac{c_m^2 - c_n^2}{c_m^2}\right)\mathbf{Z}_m^{\mathsf{T}}\,\mathsf{H}\,\mathsf{R}^{-1}\,\partial_h\left(\mathbf{Z}_n\right) = \frac{1}{c_m^2}\partial_h\left(c_n^2\right)\,\mathcal{I}_m\,\delta_{mn} - \mathbf{Z}_m^{\mathsf{T}}\,\partial_h\left(\mathsf{H}\,\mathsf{R}^{-1}\right)\mathbf{Z}_n. \tag{2.153}$$

With $m = n$, the first term in equation (2.153) is zero, from which we deduce that the normalisation coefficient, as introduced in (2.139), is

$$\mathcal{I}_m = \frac{c_m^2\,\mathbf{Z}_m^{\mathsf{T}}\,\partial_h\left(\mathsf{H}\,\mathsf{R}^{-1}\right)\mathbf{Z}_m}{\partial_h\left(c_m^2\right)}. \tag{2.154}$$

Equation (2.154) is equivalent to (B4) of Shimizu (2011). Taking $m \neq n$ results in

$$\mathbf{Z}_m^{\mathsf{T}}\,\mathsf{H}\,\mathsf{R}^{-1}\,\partial_h\left(\mathbf{Z}_n\right) = \frac{c_m^2\,\mathbf{Z}_m^{\mathsf{T}}\,\partial_h\left(\mathsf{H}\,\mathsf{R}^{-1}\right)\mathbf{Z}_n}{c_n^2 - c_m^2}, \tag{2.155}$$

implying

$$\mathcal{T}_{mn} = \frac{\partial_h\left(c_m^2\right)}{c_n^2 - c_m^2}\cdot\frac{\mathbf{Z}_m^{\mathsf{T}}\,\partial_h\left(\mathsf{H}\,\mathsf{R}^{-1}\right)\mathbf{Z}_n}{\mathbf{Z}_m^{\mathsf{T}}\,\partial_h\left(\mathsf{H}\,\mathsf{R}^{-1}\right)\mathbf{Z}_m}. \tag{2.156}$$

To obtain the self-interaction coefficient $\mathcal{T}_{mm}$, we rearrange (2.148) to give

$$\begin{aligned}\mathbf{Z}_m^{\mathsf{T}}\,\mathsf{H}\,\mathsf{R}^{-1}\,\partial_h\left(\mathbf{Z}_m\right) &= \partial_h\left(\mathcal{I}_m\right) - \partial_h\left(\mathbf{Z}_m^{\mathsf{T}}\,\mathsf{H}\,\mathsf{R}^{-1}\right)\mathbf{Z}_m \\ &= \partial_h\left(\mathcal{I}_m\right) - \mathbf{Z}_m^{\mathsf{T}}\,\partial_h\left(\mathsf{H}\,\mathsf{R}^{-1}\right)\mathbf{Z}_m^{\mathsf{T}} - \partial_h\left(\mathbf{Z}_m^{\mathsf{T}}\right)\mathsf{H}\,\mathsf{R}^{-1}\,\mathbf{Z}_m.\end{aligned} \tag{2.157}$$

Since the last term on the right-hand side is just the transpose of the left-hand side, and is in fact a scalar, it follows using (2.154) that for $m = n$,

$$2\mathbf{Z}_m^{\mathsf{T}}\,\mathsf{H}\,\mathsf{R}^{-1}\,\partial_h\left(\mathbf{Z}_m\right) = \partial_h\left(\mathcal{I}_m\right) - \frac{\partial_h\left(c_m^2\right)}{c_m^2}\,\mathcal{I}_m, \tag{2.158}$$

which can be rearranged to give

$$\mathcal{T}_{mm} = \frac{1}{2}\left[\frac{\partial_h\left(\mathcal{I}_m\right)}{\mathcal{I}_m} - \frac{\partial_h\left(c_m^2\right)}{c_m^2}\right]. \tag{2.159}$$

Equation (2.159) is equivalent to (B7) of Shimizu (2011), which observes that the self-interaction coefficient $\mathcal{T}_{mm}$ is exactly zero if $\mathcal{I}_m \propto c_m^2$.

In the case of internal-tide generation, Shimizu (2011) adds that it useful to consider the case for which only the bottom layer varies in thickness. Along with the hydrostatic approximation, modal-interaction coefficients are simplified under the normalisation condition with $Z_m(z=-h) = \mathbf{Z}_{mM}\left(h\right) = \hat{Z}_m\left(h\right)$ specified, such that

$$\frac{\mathbf{Z}_m^{\mathsf{T}}\,\partial_h\left(\mathsf{H}\,\mathsf{R}^{-1}\right)\mathbf{Z}_n}{\mathbf{Z}_m^{\mathsf{T}}\,\partial_h\left(\mathsf{H}\,\mathsf{R}^{-1}\right)\mathbf{Z}_m} = \frac{\partial_h\left(h_M\,\rho_M^{-1}\right)\hat{Z}_m\,\hat{Z}_n}{\partial_h\left(h_M\,\rho_M^{-1}\right)\hat{Z}_m^2} = \frac{\hat{Z}_n}{\hat{Z}_m}, \tag{2.160}$$

implying that

$$\mathcal{T}_{mn} = \frac{\partial_h c_m^2}{c_n^2 - c_m^2}\,\frac{\hat{Z}_n}{\hat{Z}_m}. \tag{2.161}$$

As for the self-interaction term, Griffiths (2020; personal communication) makes clear that simplifications arise by using the hydrostatic approximation:

$$\partial_h\left(h_M\,\rho_M^{-1}\right) = \rho_M^{-1} \qquad \Longrightarrow \qquad \mathcal{I}_m = \frac{c_m^2\,\hat{Z}_m^2}{\rho_M\,\partial_h\left(c_m^2\right)}. \tag{2.162}$$

It follows therefore that

$$\begin{aligned}\frac{\partial_h\left(\mathcal{I}_m\right)}{\mathcal{I}_m} &= \frac{\partial_h\left(c_m^2\right)}{\rho_M\,c_m^2\,\hat{Z}_m^2}\,\frac{\rho_M}{\left(\partial_h\left(c_m^2\right)\right)^2}\Big(\hat{Z}^2\left[\left(\partial_h\left(c_m^2\right)\right)^2 - c_m^2\,\partial_{hh}\left(c_m^2\right)\right] + \\ &\qquad c_m^2\,\partial_h\left(c_m^2\right)\,\partial_h\left(\hat{Z}_m^2\right)\Big) \\ &= \frac{\partial_h\left(c_m^2\right)}{c_m^2} - \frac{\partial_{hh}\left(c_m^2\right)}{\partial_h\left(c_m^2\right)} + \frac{\partial_h\left(\hat{Z}_m^2\right)}{\hat{Z}_m^2},\end{aligned} \tag{2.163}$$

and that the self-interaction term simplifies to give

$$\mathcal{T}_{mm} = -\frac{\partial_{hh}c_m^2}{2\partial_h c_m^2} + \frac{\partial_h\left(\hat{Z}_m^2\right)}{2\hat{Z}_m^2} = -\frac{\partial_{hh}c_m^2}{2\partial_h c_m^2} + \frac{\partial_h\left(\hat{Z}_m\right)}{\hat{Z}_m}. \tag{2.164}$$

We have therefore for forced hydrostatic multi-layer flows with variation in layer thickness

occurring only in the bottom layer, the modal SWEs:

$$\partial_t \mathbf{U}_m + \mathbf{f} \times \mathbf{U}_m + \boldsymbol{\nabla} P_m = -\boldsymbol{\nabla} h \sum_{n=0}^{M-1} \mathcal{T}_{mn}\, P_n + \mathbf{F}_m, \tag{2.165}$$

$$\partial_t P_m + \boldsymbol{\nabla} \cdot \left(c_m^2\, \mathbf{U}_m\right) = -\boldsymbol{\nabla} h \cdot \sum_{n=0}^{M-1} \mathcal{T}_{mn}\, c_n^2\, \mathbf{U}_n, \tag{2.166}$$

where under relevant conditions, we have shown that the interaction coefficients may be expressed in the general form

$$\mathcal{T}_{mn} = \begin{cases} \dfrac{\partial_h c_m^2}{c_n^2 - c_m^2}\, \dfrac{\hat{Z}_n}{\hat{Z}_m}, & m \neq n, \\ \dfrac{\partial_h \left(\hat{Z}_m\right)}{\hat{Z}_m} - \dfrac{\partial_{hh} c_m^2}{2 \partial_h c_m^2}, & m = n. \end{cases} \tag{2.167}$$

Equations (2.165)–(2.166) are identical to those in Griffiths (2010), but with a finite number of modes. From equations (2.165)–(2.166), it is evident that modes do not interact over topography in which $\boldsymbol{\nabla} h = \mathbf{0}$, i.e. over uniform topography. A discussion on the connection of the discrete-layer case to its continuous counterpart as the number of layers is increased is provided in §5 of Shimizu (2011).

Griffiths (2020; personal communication) suggests two convenient choices of normalisation which simplify the form of (2.167). The first is $\hat{Z}_m = \hat{Z}_n$, independent of fluid depth h. This normalisation leads to modal-interaction coefficients given in (2.104):

$$\mathcal{T}_{mn} = \begin{cases} \dfrac{\partial_h c_m^2}{c_n^2 - c_m^2}, & m \neq n, \\ -\dfrac{\partial_{hh} c_m^2}{2 \partial_h c_m^2}, & m = n. \end{cases} \tag{2.168}$$

This choice of normalisation is used in Griffiths and Grimshaw (2007b) and Griffiths (2010, 2012) to model tidal dissipation using modal decomposition.

The second convenient choice of normalisation, also suggested in (23) of Shimizu (2011), supposes that $\hat{Z}_m = \sqrt{\partial_h \left(c_m^2\right)}$, and leads to modal-interaction coefficients of the form

$$\mathcal{T}_{mn} = \begin{cases} \dfrac{\sqrt{\partial_h \left(c_m^2\right)\, \partial_h \left(c_n^2\right)}}{c_n^2 - c_m^2} = \dfrac{\hat{Z}_m\, \hat{Z}_n}{c_n^2 - c_m^2}, & m \neq n, \\ 0, & m = n. \end{cases} \tag{2.169}$$

In this form, $\mathcal{T}_{mn}$ is anti-symmetric such that $\mathcal{T}_{mn} = -\mathcal{T}_{nm}$ and $\mathcal{T}_{mm} = 0$.

An alternative form of (2.166), as given in Griffiths (2020; personal communication), is

$$\frac{1}{c_m^2} \partial_t P_m + \frac{1}{\mathcal{I}_m} \boldsymbol{\nabla} \cdot \left(\mathcal{I}_m\, \mathbf{U}_m\right) = \frac{\mathcal{I}_n}{\mathcal{I}_m}\, \boldsymbol{\nabla} h \cdot \sum_{n=0}^{M-1} \mathcal{T}_{nm}\, \mathbf{U}_n, \tag{2.170}$$

and is particularly useful when considering the modal energetics, as we shall see in the following section.

To derive equation (2.170), we begin with (2.138) using the fact that $\mathbf{Z}_m^{\mathsf{T}}\,\mathsf{S}^{\mathsf{T}} = c_m^2\,\mathbf{Z}_m^{\mathsf{T}}$ from (2.142):

$$\frac{1}{c_m^2}\partial_t P_m = -\frac{1}{\mathcal{I}_m}\sum_{n=0}^{M-1}\mathbf{Z}_m^{\mathsf{T}}\,\boldsymbol{\nabla}\cdot\left(\mathsf{H}\,\mathsf{R}^{-1}\,\mathbf{Z}_n\,\mathbf{U}_n\right). \tag{2.171}$$

Using the chain rule, it follows that

$$\begin{aligned}\frac{1}{c_m^2}\partial_t P_m &= -\frac{1}{\mathcal{I}_m}\sum_{n=0}^{M-1}\left(\boldsymbol{\nabla}\cdot\left(\mathbf{Z}_m^{\mathsf{T}}\mathsf{H}\,\mathsf{R}^{-1}\,\mathbf{Z}_n\,\mathbf{U}_n\right) - \boldsymbol{\nabla}\left(\mathbf{Z}_m^{\mathsf{T}}\right)\cdot\left(\mathsf{H}\,\mathsf{R}^{-1}\,\mathbf{Z}_n\,\mathbf{U}_n\right)\right)\\ &= -\frac{1}{\mathcal{I}_m}\left(\boldsymbol{\nabla}\,\left(\mathcal{I}_m\,\mathbf{U}_m\right) - \sum_{n=0}^{M-1}\boldsymbol{\nabla}\left(\mathbf{Z}_m^{\mathsf{T}}\right)\cdot\left(\mathsf{H}\,\mathsf{R}^{-1}\,\mathbf{Z}_n\,\mathbf{U}_n\right)\right)\\ &= -\frac{1}{\mathcal{I}_m}\left(\boldsymbol{\nabla}\cdot\left(\mathcal{I}_m\,\mathbf{U}_m\right) - \boldsymbol{\nabla}h\cdot\sum_{n=0}^{M-1}\left(\mathbf{Z}_n^{\mathsf{T}}\,\mathsf{H}\,\mathsf{R}^{-1}\,\partial_h\left(\mathbf{Z}_m\right)\right)^{\mathsf{T}}\mathbf{U}_n\right).\end{aligned} \tag{2.172}$$

The last term on the right-hand side can then be simplified by using (2.145), which implies that $\left(\mathbf{Z}_n^{\mathsf{T}}\,\mathsf{H}\,\mathsf{R}^{-1}\,\partial_h\left(\mathbf{Z}_m\right)\right)^{\mathsf{T}} = \left(\mathcal{I}_n\,\mathcal{T}_{nm}\right)^{\mathsf{T}} = \mathcal{I}_n\,\mathcal{T}_{nm}$. The resulting equation,

$$\frac{1}{c_m^2}\partial_t P_m = -\frac{1}{\mathcal{I}_m}\boldsymbol{\nabla}\cdot\left(\mathcal{I}_m\,\mathbf{U}_m\right) + \frac{\mathcal{I}_n}{\mathcal{I}_m}\,\boldsymbol{\nabla}h\cdot\sum_{n=0}^{M-1}\mathcal{T}_{nm}\,\mathbf{U}_n,, \tag{2.173}$$

is then rearranged to give (2.170).

2.4.6 Conservation of Energy

To obtain the governing equation for modal energy conservation, we consider the addition of ${\rho_{00}}^2\,\mathcal{I}_m\,\mathbf{U}_m\cdot$(2.165) with ${\rho_{00}}^2\,\mathcal{I}_m\,P_m$ (2.170), which gives

$$\partial_t E_m + \boldsymbol{\nabla}\cdot\mathbf{J}_m = \sum_{n=0}^{M-1} S_{mn} + W_m. \tag{2.174}$$

Here, we have

$$E_m = \frac{{\rho_{00}}^2}{2}\,\mathcal{I}_m\left(|\mathbf{U}_m|^2 + \frac{1}{c_m^2}\,P_m^2\right) \qquad \text{and} \qquad \mathbf{J}_m = {\rho_{00}}^2\,\mathcal{I}_m\,\mathbf{U}_m\,P_m \tag{2.175}$$

which denote respectively the depth-integrated modal energy density and the depth-integrated modal energy flux,

$$W_m = {\rho_{00}}^2\,\mathcal{I}_m\,\mathbf{U}_m\cdot\boldsymbol{F}_m, \tag{2.176}$$

which denotes the work input from external forces, and

$$S_{mn} = {\rho_{00}}^2\,\boldsymbol{\nabla}h\cdot\left(\mathcal{I}_n\,\mathcal{T}_{nm}\,P_m\,\mathbf{U}_n - \mathcal{I}_m\,\mathcal{T}_{mn}\,P_n\,\mathbf{U}_m\right), \tag{2.177}$$

which denotes the rate of energy transfer from mode n to mode m. Equation (2.177) is equivalent to (28) of Shimizu (2011), which makes explicit that $S_{mn} = -S_{nm}$ and $S_{mm} = 0$, such that when all modes are summed over, energy is indeed conserved.

A further simplification can be made to modal energy transfer term S_{mn} of equation (2.177) when considering the internal-tide generation problem, i.e. the barotropic-to-baroclinic energy transfer. We begin by applying the Boussinesq approximation whereby $\rho_{00}\,\mathsf{R}^{-1} = \mathsf{I}$, such that primitive horizontal velocity

$$(\mathbf{u}\,(x,y,t)\,,\mathbf{v}\,(x,y,t)) = \sum_{n=0}^{M-1} (U_n\,(x,y,t)\,,V_n\,(x,y,t))\,\mathbf{Z}_n\,(x,y)\,. \tag{2.178}$$

With the latter in mind, we remark that by using the Boussinesq approximation,

$$\rho_{00}{}^2\,\mathcal{I}_m\,\mathcal{T}_{mn}\,P_n\,\mathbf{U}_m = \frac{c_m^2}{c_n^2 - c_m^2}\,\hat{P}_n\,\hat{\mathbf{U}}_m, \tag{2.179}$$

where $\hat{P}_m = \rho_{00}\,\hat{Z}_m\,P_m$ and $\hat{\mathbf{U}}_m = \hat{Z}_m\,\mathbf{U}_m$ denote respectively the mode-m pressure and horizontal velocities in the bottom layer, and with $\rho_{00}/\rho_M \approx 1$. By considering the barotropic-to-baroclinic energy transfer with $m = 0$ and $c_0^2 \gg c_n^2$ for baroclinic mode n, it is found that the total rate of tidal energy conversion can be expressed as

$$D = \sum_{n=1}^{M-1} S_{0n}, \qquad\qquad S_{0n} \approx \hat{W}_0\,\hat{P}_n, \tag{2.180}$$

where

$$\hat{W}_0 = -\boldsymbol{\nabla} h \cdot \hat{\mathbf{U}}_0 \tag{2.181}$$

is the barotropic vertical velocity along the sea floor (see equation (2.30)). Simply put, the tidal dissipation due to internal-tide generation D is approximately given by the product of the baroclinic pressure with the barotropic vertical velocity along the sea floor (see Llewellyn Smith & Young, 2002; Shimizu, 2011). This approximation is easy to implement numerically and gives an error proportional to $c_n^2/c_0^2 = O\,(\varepsilon)$. For typical pycnocline settings, this error is around 10^{-4}.

Another way to look at the result in (2.180) is in terms of power: power is force times velocity (much like in (2.67)). Consequently, equation (2.180) can be written instead as

$$D = -\hat{\mathbf{U}}_0 \cdot \sum_{n=1}^{M-1} \hat{P}_n\,\boldsymbol{\nabla} h, \tag{2.182}$$

where $-\hat{P}_n\,\boldsymbol{\nabla} h$ is the baroclinic drag.

For completeness, we remark that the depth-integrated modal energy flux can also be

written in terms of the modal quantities in the bottom layer:

$$\mathbf{J}_m = {\rho_{00}}^2 \frac{\hat{\mathbf{U}}_m \hat{P}_m}{\rho_{00} \hat{Z}_m^2} \mathcal{I}_m = \frac{c_m^2}{\partial_h c_m^2} \hat{\mathbf{U}}_m \hat{P}_m, \tag{2.183}$$

again, using the hat notation to indicate the modal variable in the bottom layer.

Lastly, for time-periodic flows, equation (2.174) can be time-averaged. With $\dot{W}_m = 0$ (no external work input), it follows that

$$\boldsymbol{\nabla} \cdot \langle \mathbf{J}_m \rangle = \sum_{n=0}^{M-1} \langle S_{mn} \rangle, \tag{2.184}$$

where $\langle \cdot \rangle$ denotes the time-averaging operator.

A particular result is found by integrating (2.184) over arbitrary domain Ω with boundary $\partial\Omega$ (and therefore volume and surface respectively, since the quantities have already been depth-integrated):

$$\int_\Omega \boldsymbol{\nabla} \cdot \langle \mathbf{J}_m \rangle \, \mathrm{d}A = \sum_{n=0}^{M-1} \int_\Omega \langle S_{mn} \rangle \, \mathrm{d}A. \tag{2.185}$$

Applying the divergence theorem, the latter becomes

$$\int_{\partial\Omega} \hat{\mathbf{n}} \cdot \langle \mathbf{J}_m \rangle \, \mathrm{d}l = \sum_{n=0}^{M-1} \int_\Omega \langle S_{mn} \rangle \, \mathrm{d}A, \tag{2.186}$$

where $\hat{\mathbf{n}}$ is the outward-pointing unit normal to the domain boundary. From equation (2.186), it follows that over each wave period, the total barotropic dissipation in some domain Ω is equal to the total energy flux across its boundary $\partial\Omega$. Consequently, the baroclinic energy flux alone can be used to quantify the rate of barotropic-to-baroclinic energy transfer.

2.4.7 Two-Layer Example

Let us consider the example of a two-layer fluid medium ($M = 2$) in which

$$\mathsf{S} = g \begin{pmatrix} h_1 & \rho_1 h_2/\rho_2 \\ h_1 & h_2 \end{pmatrix} \qquad \text{and} \qquad \mathsf{T} = g \begin{pmatrix} h_1 & \sqrt{h_1 h_2 \rho_1/\rho_2} \\ \sqrt{h_1 h_2 \rho_1/\rho_2} & h_2 \end{pmatrix}. \tag{2.187}$$

Here, both S and T have characteristic equation in c^2:

$$c^4 - g h c^2 + g g' h_1 h_2 = 0, \tag{2.188}$$

where $h = h_1 + h_2$ and $g' = g(\rho_2 - \rho_1)/\rho_2$ are respectively the total fluid depth and the reduced gravity at the interface and is equivalent to the penultimate equation in Stokes

(1847). We may of course find exact solutions for c^2:

$$c^2 = \frac{g\,h}{2}\left(1 \pm \sqrt{1 - \frac{4g'\,h_1\,h_2}{g\,h^2}}\right). \tag{2.189}$$

In the case where $\varepsilon = g'/g = (\rho_2 - \rho_1)/\rho_2 \ll 1$, typical of pycnocline regimes, it is possible to pose the squared wave speeds as a power-series of ε:

$$c^2 = \frac{g\,h}{2}\left(1 \pm \left(1 - 2\frac{h_1\,h_2}{h^2}\,\varepsilon - 2\left(\frac{h_1\,h_2}{h^2}\right)^2\varepsilon^2 + O\left(\varepsilon^3\right)\right)\right), \tag{2.190}$$

giving barotropic squared wave speed

$$c_0^2 = g\,h\left(1 - \frac{h_1\,h_2}{h^2}\,\varepsilon + O\left(\varepsilon^2\right)\right), \tag{2.191}$$

as well as baroclinic squared wave speed

$$c_1^2 = \frac{g'\,h_1\,h_2}{h}\left(1 + \frac{h_1\,h_2}{h^2}\,\varepsilon + O\left(\varepsilon^2\right)\right). \tag{2.192}$$

To leading order, we obtain the approximate squared wave speeds

$$c_0^2 \approx g\,h \qquad \text{and} \qquad c_1^2 \approx \frac{g'\,h_1\,h_2}{h} \tag{2.193}$$

which were encountered in the introduction of this chapter when considering a two-layer immiscible fluid in a rigid-box.

From equation (2.187), we may also obtain the eigenvector for S,

$$\mathbf{Z} = \begin{pmatrix} \dfrac{\rho_1\,g\,h_2}{\rho_2\,(c^2 - g\,h_1)} & 1 \end{pmatrix}^{\mathsf{T}} = \begin{pmatrix} \dfrac{(1-\varepsilon)\,g\,h_2}{c^2 - g\,h_1} & 1 \end{pmatrix}^{\mathsf{T}}. \tag{2.194}$$

In the case whereby $\varepsilon = (\rho_2 - \rho_1)/\rho_2 \ll 1$, we may use equations (2.191)–(2.192) to obtain the eigenvectors as a power series in $\varepsilon = g'/g$:

$$\mathbf{Z}_0 = \begin{pmatrix} 1 - \dfrac{h_2}{h}\,\varepsilon \\ 1 \end{pmatrix} + O\left(\varepsilon^2\right) \qquad \text{and} \qquad \mathbf{Z}_1 = \begin{pmatrix} -\dfrac{h_2}{h_1}\left(1 + \dfrac{h_2}{h}\,\varepsilon\right) \\ 1 \end{pmatrix} + O\left(\varepsilon^2\right). \tag{2.195}$$

Again, the latter are well-known results, between which, we may verify the orthogonality

relationship:

$$\begin{aligned}\mathbf{Z}_0^{\mathsf{T}}\,\mathsf{H}\,\mathsf{R}^{-1}\,\mathbf{Z}_1 &= \frac{1}{\rho_2}\begin{pmatrix}1-\dfrac{h_2}{h}\,\varepsilon & 1\end{pmatrix}\begin{pmatrix}h_1 & 0\\ 0 & h_2\end{pmatrix}\begin{pmatrix}1-\varepsilon & 0\\ 0 & 1\end{pmatrix}^{-1}\begin{pmatrix}-\dfrac{h_2}{h_1}\left(1+\dfrac{h_2}{h}\,\varepsilon\right)\\ 1\end{pmatrix}\\ &\quad + O\left(\varepsilon^2\right)\\ &= -\frac{h_2}{\rho_2}\begin{pmatrix}1-\dfrac{h_2}{h}\,\varepsilon & 1\end{pmatrix}\begin{pmatrix}1+\left(1+\dfrac{h_2}{h}\right)\varepsilon\\ -1\end{pmatrix}+O\left(\varepsilon^2\right).\end{aligned} \tag{2.196}$$

Upon further evaluation of the latter, one arrives at the result

$$\mathbf{Z}_0^{\mathsf{T}}\,\mathsf{H}\,\mathsf{R}^{-1}\,\mathbf{Z}_1 = 0 + O\left(\varepsilon^2\right). \tag{2.197}$$

This orthogonality result was also given in Griffiths (2020; personal communication), but to $O(\varepsilon)$. We have shown that the modal vectors in the two-layer case are orthogonal up to second-order in $\varepsilon = (\rho_2 - \rho_1)/\rho_2 \ll 1$, as expected.

As for modal energetics in the case of two layers, we begin by recalling that for reference density $\rho_{00} = \rho_2$,

$$(\mathbf{u},\mathbf{v}) = \sum_{m=0}^{M-1}\mathsf{R}^{-1}\,\rho_{00}\,(U_m,V_m)\,\mathbf{Z}_m \qquad \Longrightarrow \qquad (U_m,V_m) = \frac{\mathbf{Z}_m^{\mathsf{T}}\,\mathsf{H}}{\rho_{00}\,\mathcal{I}_m}\,(\mathbf{u},\mathbf{v}) \tag{2.198}$$

and

$$\mathbf{p} = \sum_{m=0}^{M-1}\rho_{00}\,P_m\,\mathbf{Z}_m \qquad \Longrightarrow \qquad P_m = \frac{\mathbf{Z}_m^{\mathsf{T}}\,\mathsf{H}\,\mathsf{R}^{-1}\,\mathbf{p}}{\rho_{00}\,\mathcal{I}_m}. \tag{2.199}$$

Substituting the modal variables into equation (2.175), the modal depth-integrated energy densities in terms of the primitive variables to leading order in $\varepsilon = (\rho_2 - \rho_1)/\rho_2$ are

$$E_0 = \frac{\rho_{00}}{2}\left(\left[\frac{|h_1\,\mathbf{u}_1 + h_2\,\mathbf{u}_2|^2}{h}\right] + \left[\frac{(h_1\,p_1 + h_2\,p_2)^2}{g\,{\rho_{00}}^2\,h^2}\right]\right) \tag{2.200}$$

and

$$E_1 = \frac{\rho_{00}}{2}\left(\left[\frac{h_1\,h_2}{h}|\mathbf{u}_2 - \mathbf{u}_1|^2\right] + \left[\frac{(p_2 - p_1)^2}{g\,{\rho_{00}}^2\,\varepsilon}\right]\right), \tag{2.201}$$

where the first square-bracket term indicates the kinetic energy and the second the potential energy. Moreover, the total depth-integrated energy densities are

$$E = E_0 + E_1 = \frac{\rho_{00}}{2}\left(\left[h_1\,|\mathbf{u}_1|^2 + h_2\,|\mathbf{u}_2|^2\right] + \left[\frac{(p_1 - p_2)^2}{2g\,{\rho_{00}}^2\,\varepsilon} + \frac{p_1^2}{g\,{\rho_{00}}^2}\right]\right). \tag{2.202}$$

Again, the first square-bracket term represents the kinetic energy, while the second represents the potential energy in the system. In the potential energy term, the first term is due

to the interfacial displacement, while the second corresponds with the displacement of the upper free surface. In the limit as $\rho_1 \to \rho_2$, and therefore $\varepsilon \to 0$, pressure perturbations $p_1 \to p_2$, meaning that the potential energy from the displacement of the interface is zero. Moreover, the baroclinic (mode $m = 1$) depth-integrated energy density, E_1, is zero.

Similarly, the modal depth-integrated energy densities in terms of the primitive variables to leading order in ε are

$$\mathbf{J}_0 = \frac{(h_1\, p_1 + h_2\, p_2)\,(h_1\, \mathbf{u}_1 + h_2\, \mathbf{u}_2)}{h} \qquad \text{and} \qquad \mathbf{J}_1 = \frac{h_1\, h_2\,(p_2 - p_1)\,(\mathbf{u}_2 - \mathbf{u}_1)}{h}, \tag{2.203}$$

such that the total depth-integrated energy flux

$$\mathbf{J} = \mathbf{J}_0 + \mathbf{J}_1 = h_1\, p_1\, \mathbf{u}_1 + h_2\, p_2\, \mathbf{u}_2. \tag{2.204}$$

The most important remark to be made is that in the limit as $\rho_1 \to \rho_2$, and therefore $\varepsilon \to 0$, horizontal velocity $\mathbf{u}_1 \to \mathbf{u}_2$ and pressure perturbation $p_1 \to p_2$, meaning that the baroclinic depth-integrated energy flux, $\mathbf{J}_1$, becomes zero.

2.4.8 Modal Equations for Two-Layer Fluid

From the work carried out in this section so far, it has been concluded that the equations governing the motion of a stably stratified two-layer hydrostatic fluid of fixed upper-layer depth, a model for pycnocline-dominated flow over continental margins, can be represented in modal form: motions which travel at a given wave speed and vertical structure as determined by equations (2.191)–(2.192) and (2.195) respectively. Using the anti-symmetric normalisation with modal-interaction coefficients given by equation (2.169), these equations are

$$\partial_t \mathbf{U}_0 + f\, \hat{\mathbf{e}}_z \times \mathbf{U}_0 + \boldsymbol{\nabla} P_0 = +\mathcal{T}_{10}\, \boldsymbol{\nabla} h\, P_1 + \boldsymbol{F}_0, \tag{2.205}$$

$$\partial_t P_0 + \boldsymbol{\nabla} \cdot \left(c_0^2\,(\mathbf{x})\ \mathbf{U}_0\right) = +\mathcal{T}_{10}\, \boldsymbol{\nabla} h \cdot \left(c_1^2\,(\mathbf{x})\ \mathbf{U}_1\right), \tag{2.206}$$

and

$$\partial_t \mathbf{U}_1 + f\, \hat{\mathbf{e}}_z \times \mathbf{U}_1 + \boldsymbol{\nabla} P_1 = -\mathcal{T}_{10}\, \boldsymbol{\nabla} h\, P_0 + \boldsymbol{F}_1, \tag{2.207}$$

$$\partial_t P_1 + \boldsymbol{\nabla} \cdot \left(c_1^2\,(\mathbf{x})\ \mathbf{U}_1\right) = -\mathcal{T}_{10}\, \boldsymbol{\nabla} h \cdot \left(c_0^2\,(\mathbf{x})\ \mathbf{U}_0\right), \tag{2.208}$$

with the former governing barotropic flow, and the latter governing baroclinic flow. These equations include external modal forces $\boldsymbol{F}_0$ and $\boldsymbol{F}_1$. Moreover, the two sets of equations are coupled through variable topography comprising the product of bathymetric gradient and modal-interaction coefficient

$$\mathcal{T}_{10} = \frac{\sqrt{\partial_h\left(c_0^2\right)\ \partial_h\left(c_1^2\right)}}{c_0^2 - c_1^2} = \frac{h_1}{h^2}\sqrt{\varepsilon}\left(1 + O\left(\sqrt{\varepsilon}\right)\right), \qquad \varepsilon \equiv (\rho_2 - \rho_1)/\rho_2 \ll 1. \tag{2.209}$$

Equations (2.205)–(2.208) satisfy the energy conservation law given in equations (2.174)–

(2.177) with normalisation coefficient

$$\mathcal{I}_m = c_m^2/\rho_2. \tag{2.210}$$

In addition, we have using equation (2.186) that for time-periodic flows, the barotropic dissipation due to the generation of internal waves along the pycnocline over some region Ω with boundary $\partial\Omega$ is approximately

$$\int_{\partial\Omega} \hat{\mathbf{n}} \cdot \frac{h\,(h-h_1)}{h_1} \langle \hat{P}_1\, \hat{\mathbf{U}}_1 \rangle \,\mathrm{d}l = -\int_{\Omega} \langle \hat{W}_0\, \hat{P}_1 \rangle \,\mathrm{d}A. \tag{2.211}$$

We recall that $\hat{W}_0$, $\hat{\mathbf{U}}_1$, $\hat{P}_1$ denote respectively the bottom-layer variables of barotropic vertical velocity, baroclinic horizontal velocity and baroclinic pressure.

2.5 Summary

In this chapter, we have provided the framework we use in this thesis to model internal-tide generation along continental margins. The work of this chapter began, in Section 2.2, with the derivation of the equations which govern linearised hydrostatic flow on an f-plane.

In Section 2.3, modes of a continuously stratified fluid over uniform topography were investigated. Using separation of variables, it was shown that the governing equations for vertical structure and horizontal wave propagation are decoupled over uniform topography. The equation for vertical structure was dependent only on stratification profile. The equation for vertical structure and wave speed is a regular Sturm–Liouville eigenvalue problem. Analytical solutions were sought following the methodology of LeBlond and Mysak (1978) for constant stratification under the Boussinesq approximation. Here, it is made explicit that the barotropic mode relies on the free-surface boundary condition; that is, for a rigid-lid approximation the barotropic mode disappears. Lastly, numerical solutions for wave speed and vertical structure were computed. Here, we compared the results using a second-order finite differences method and the pseudo-spectral Chebyshev method. Our results concluded that the finite differences method, while sparse, required a significant number of grid points to accurately resolve vertical structures and modal wave speeds. Consequently, it was more efficient to solve the eigenvalue problem using the Chebyshev method.

In the most basic form, internal waves generated along a continental margin can be modelled using a two-layer system. In Section 2.4, however, we provide the generalised theory for the modal decomposition of the shallow-water equations in the case of discrete layers of uniform density. This required developing the theory of modal decomposition introduced by Griffiths and Grimshaw (2007a) for multi-layer stratification, as in Shimizu (2011) and Griffiths (2020; personal communication). Here, it was observed that the resultant eigenvalue problem is a direct analogue of the continuously stratified case. By exploiting the linear algebra of the problem further, relationships on modal wave speed and orthogonality are inherent. Moreover, the structure of the matrix means that vertical modes and

wave speeds are computed fast, accurately and with minimal effort. Having constructed the framework for modal decomposition for multi-layered stratified fluids, the equations governing barotropic and baroclinic motion are derived in Section 2.4.5. Coupling the modes over variable topography is a modal-interaction coefficient; this considers the spatial variability of wave speed and vertical structure. These coefficients are much simpler when restricting variability of layer thickness to the bottom layer since only the bottom layer may influence a normalisation. For certain choices of normalisation, the form of the modal-interaction coefficients $\mathcal{T}_{mn}$ can be expressed neatly. For example, an anti-symmetric normalisation proposed by Shimizu (2011) gives $\mathcal{T}_{mn} = -\mathcal{T}_{nm}$ and $\mathcal{T}_{mm} = 0$.

From the modal equations for multi-layer stratification, equations governing modal energetics are derived; this includes a term to account for energy transfer between modes across variable bottom topography. For barotropic flow, the total rate of energy transfer can be simplified, and shows that the rate of tidal energy conversion can be approximated as the product between the bottom pressure induced by baroclinic motion and the bottom barotropic-induced vertical motion. A relation between modal energy flux and modal energy transfer is confirmed in the case of time-periodic flow. This indicates that the total energy of a mode leaving an enclosed domain is the total energy conversion across the domain. This provides two means of calculating tidal dissipation. In general, we are most interested in the baroclinic energy flux. While the modal energy conversion allows you to identify regions of energy sources and sinks (e.g. along continental slopes), it does not indicate the direction of energy propagation. These more generalised M-layer equations could be of particular interest to those studying incident tidal motions, both barotropic and baroclinic, in the deep ocean (e.g. over seamounts or ridges (see Bell, 1975b; Llewellyn Smith & Young, 2002), where many layers may be required to sufficiently model the generation of internal tides within the weakly stratified interior (see Garrett & Kunze, 2007).

In Section 2.4.7, it is shown that relations on modal structure and wave speed in the case of two-layer stratification follows immediately from the generalised M-layer case. Lastly, in Section 2.4.8, the governing equations for two-layer flow in modal form are provided and are accompanied by the expressions used to calculate tidal dissipation. These equations, modelling internal-tide generation at the pycnocline along continental margins, provide the necessary means to estimate the implied energy fluxes, with implications for the global ocean energy budget (see Section 1.2).

Chapter 3

Surface Tides along Continental Margins

3.1 Introduction

Surface tides are surface waves forced by the gravitational and rotational systems of the Earth with the Sun and Moon. Consequently, surface tides are responsible for the periodic rise and fall of sea levels (most observable at the coast when at high or low tide). As the tide rises, water from the deep ocean is transported over the continental margin, and onto the shelf. For the stratified ocean, this energetic motion leads to the generation of internal waves of tidal frequency: the internal tide. To investigate the internal-tide generation problem over the continental margin, it is important to first analyse the form of the barotropic motion excited by tidal forcing.

For many regions of the world's coast, as discussed in Section 1.2.1, the Kelvin wave is the dominant form of the surface tide. However, it is well-understood that the classical Kelvin wave over uniform topography exhibits no flow cross-shore. However, the introduction of coastal topography leads to cross-shore flows over the continental slope. Dependent on the form of the continental margin, the resultant flows cross-shore can be significant at the shelf break, comparable even to the Kelvin wave's energetic flows along-shore (where they are strongest at the shoreline). In this chapter, we seek to gain a greater understanding of the Kelvin wave in the presence of coastal topography. This will permit the use of a representative three-dimensional surface tide to generate internal waves along a continental margin, whether two-dimensional (see Chapter 4) or three-dimensional (see Chapter 7), as per the aims listed in Section 1.3.

We start, in Section 3.2, by stating the equations of motion used to model decoupled tidally forced barotropic motion. In Section 3.3, we consider forced surface tides in a basin. In the first instance, as per Section 3.3.1, we consider forced motions in an arbitrary basin. In the second, in Section 3.3.2, we take a uniform channel of fixed depth. In particular, we argue here that the surface tide is likely to resemble the Kelvin wave. In Section 3.4, we

reproduce analytical solutions of the free Kelvin wave over arbitrary coastal topography, first derived independently by Smith (1972) and Miles (1972). Having obtained analytical expressions for the form of the free Kelvin wave, we also consider any modifications which arise due to potential forcing, and to what extent incidental flows at the shelf break are characteristic of the full response.

3.2 Decoupled Barotropic Equations of Motion

In this chapter, we will consider uniquely the barotropic modal equations given in (2.205)–(2.206) and will neglect the baroclinic drag of the barotropic tide. Clarke (1991) explains that the baroclinic drag on barotropic tides can be neglected because despite the baroclinic horizontal motions being the same order of magnitude as the barotropic, variations of the baroclinic horizontal motion occur over much smaller horizontal length scales and vertical depths than those of the barotropic (see Section 4.3 for scaling argument). The governing equations (2.205)–(2.206), having multiplied through by anti-symmetric normalisation $\hat{Z}_0 = \sqrt{g}$, are therefore

$$\partial_t \hat{\mathbf{U}}_0 + \mathbf{f} \times \hat{\mathbf{U}}_0 + \boldsymbol{\nabla} \hat{P}_0 = \cancel{\hat{Z}_0 \mathcal{T}_{10} \boldsymbol{\nabla} h P_1} + \hat{Z}_0 \mathbf{F}_0, \tag{3.1}$$

$$\partial_t \hat{P}_0 + \boldsymbol{\nabla} \cdot \left(c_0^2 \hat{\mathbf{U}}_0 \right) = \cancel{\hat{Z}_0 \mathcal{T}_{10} \boldsymbol{\nabla} h \cdot \left(c_1^2 \mathbf{U}_1 \right)}, \tag{3.2}$$

recalling that $\hat{\mathbf{U}}_0 = \hat{Z}_0 \begin{pmatrix} U_0 & V_0 \end{pmatrix}^{\mathsf{T}}$ and $\hat{P}_0$ denote respectively the barotropic horizontal velocity vector and pressure (normalised with reference density along the sea floor, ρ), and that $c_0^2 \approx g\,h$ denotes the squared barotropic wave speed with gravitational acceleration $g = 9.81\,\mathrm{m/s^2}$ and fluid depth h. Moreover, $\boldsymbol{\nabla}$ denotes the horizontal Del operator $\partial_x \hat{\mathbf{e}}_x + \partial_y \hat{\mathbf{e}}_y$, while $\mathbf{f}$ is the rotation vector $f\,\hat{\mathbf{e}}_z$ with $f \equiv 2\Omega_E \sin(\theta)$ being the Coriolis parameter at latitude θ for planetary rotation rate Ω_E using the f-plane approximation. Since in this chapter, we shall consider uniquely the barotropic mode, we shall drop the index notation used to identify the barotropic mode.

3.3 Forced Surface Tides in a Basin

One approach of understanding the tides along continental margins is by taking a large-scale approach and considering modes of an entire ocean basin. Considering that the Earth's radius is $6,370\,\mathrm{km}$, it is fair to assume that the accuracy of such a model would break down beyond the confines of the Cartesian geometry on which we assume the effects of rotation are uniform. Notwithstanding, our interest here lies in the local effects around the coastline, and therefore any variations in Coriolis force can be assumed negligible. One consequence of the f-plane approximation is the lack of sub-inertial Rossby modes (although the modes do arise with variations in topography). Since these modes are sub-inertial, they do have the potential to become excited by diurnal forcing. We will discuss this matter later.

Starting from equations (3.1)–(3.2), we shall consider both a scalar potential forcing, along with a linear dissipation term, meaning that the governing equations of our system become

$$(\partial_t + r)\,\mathbf{U} + f\,\hat{\mathbf{e}}_z \times \mathbf{U} + \boldsymbol{\nabla} P = g\,\boldsymbol{\nabla}\eta_{eq}, \tag{3.3}$$

$$\partial_t P + \boldsymbol{\nabla}\cdot\left(c^2\,\mathbf{U}\right) = 0, \tag{3.4}$$

where η_{eq} represents the depth of the equilibrium tide, $r = O\left(10^{-6}\,\mathrm{s}^{-1}\right)$ the Rayleigh friction coefficient (also known as resistance coefficient).

The Rayleigh friction term can be seen, for example, as a linear approximation of quadratic friction. For example, in the deep ocean whereby fluid depth $h = O\,(4,000\,\mathrm{m})$ and with drag coefficient $C_d \approx 2 \times 10^{-3}$ (see §9.4.1 of Gurvan et al., 2022), Rayleigh friction $r \approx 2C_d\,\mathbf{U}/h = O\left(10^{-7}\,\mathrm{s}^{-1}\right)$ for barotropic flows $|\mathbf{U}| = O\,(0.1\,\mathrm{m/s})$ (see equation (9.6.6) of Gill, 1982). The Rayleigh friction term here corresponds to a decay scale of $r^{-1} = O\,(100\,\mathrm{days})$. On the other hand, over the shallow shelves whereby fluid depth $h = O\,(200\,\mathrm{m})$, Rayleigh friction $r = O\left(10^{-6}\,\mathrm{s}^{-1}\right)$ and corresponds to a decay scale of $O\,(5\,\mathrm{days})$. To simplify our work, we take r constant.

As for the equilibrium tide, this is the hypothetical form of the surface displacement that would be produced by tidal forces in the absence of ocean constraints and dynamics, such as landmass and dissipation. On a localised plane, the large horizontal length scales of the equilibrium tide, typically in the form of low-order spherical harmonics (see §8 of Abramowitz & Stegun, 1964), mean that the equilibrium tide could be approximated taking

$$\eta_{eq}\,(x, y, t) = \mathrm{Re}\left\{\hat{\eta}_{eq}\,(y)\,\exp\left(i\,[k\,x - \omega\,t]\right)\right\}, \tag{3.5}$$

where the cross-shore form of the equilibrium tide across the shelf could be considered approximately linear. The form, however, is not immediately obvious across whole basin length scales, and will depend on various features, including the tidal constituent and the basin dimensions.

First, we shall obtain partial-differential equations for horizontal velocities in terms of pressure perturbation P. To achieve the latter, we remark that $(\partial_t + r)\cdot(3.3) - \mathbf{f}\times(3.3)$ yields

$$\mathcal{L}_D\mathbf{U} = -\boldsymbol{\Delta}\,(P - g\,\eta_{eq}) \qquad \text{for} \qquad \boldsymbol{\Delta} = (\partial_t + r)\,\boldsymbol{\nabla} - \mathbf{f}\times\boldsymbol{\nabla}, \tag{3.6}$$

defining $\mathcal{L}_D \equiv (\partial_t + r)^2 + f^2$. In the case of no damping, $\mathcal{L}_D$ becomes $\mathcal{L}_t \equiv \partial_{tt} + f^2$. Note however, that (3.6) does not hold in the case where $r = 0$ and $\omega = \pm f$, as we are unable to solve for the horizontal velocities in terms of pressure.

It follows from equation (3.6) that at any horizontal boundary with normal vector $\hat{\mathbf{n}}$, the impermeability condition $\mathbf{U}\cdot\hat{\mathbf{n}} = 0$ implies the condition on pressure

$$\hat{\mathbf{n}}\cdot\left(\boldsymbol{\Delta}\,(P - g\,\eta_{eq})\right) = 0. \tag{3.7}$$

An equation for pressure in terms of the scalar potential forcing is obtained by taking $\mathcal{L}_D\cdot$(3.2) and substituting in both $\boldsymbol{\nabla}\cdot(h\cdot$(3.6)) to give

$$\left(\frac{1}{g}\partial_t\mathcal{L}_D - \mathcal{N}\right) P = -\mathcal{N}\eta_{eq}, \tag{3.8}$$

where

$$\mathcal{N} \equiv \boldsymbol{\nabla}\cdot\left(c^2\,\boldsymbol{\Delta}\right). \tag{3.9}$$

In the case of uniform topography with c^2 constant,

$$\mathcal{N} = c^2\left(\partial_t + r\right)\nabla^2, \tag{3.10}$$

giving

$$\frac{1}{g}\left(\partial_t\mathcal{L}_D - c^2\left(\partial_t + r\right)\nabla^2\right) P = -c^2\left(\partial_t + r\right)\nabla^2\eta_{eq} \tag{3.11}$$

with

$$c \equiv \sqrt{g\,h} \qquad \text{and} \qquad \nabla^2 \equiv \boldsymbol{\nabla}\cdot\boldsymbol{\nabla}.$$

If there is no damping, then equation (3.11) reduces further still to give the inhomogeneous Klein–Gordon equation

$$\frac{1}{g}\partial_t\left(\mathcal{L}_t - c^2\,\nabla^2\right) P = -c^2\,\partial_t\nabla^2\eta_{eq}. \tag{3.12}$$

3.3.1 Orthogonal Modes in Arbitrary Basins

One fundamental property of tides, at least within the remits of linear theory (i.e. small-amplitude perturbations to the state of rest), is its linear composition of orthogonal modes. Each with their own fundamental frequency and spatial structure, the modes may be excited by forcing of a given spatial and temporal structure. These forcings are typically of astronomical (tidal) or meteorological timescales, varying from 24 hours (diurnal tidal forcing) to mere seconds (wind stress). The mode's fundamental frequency depends on the ocean basin geometry. For example, if one considers a crude model of a lake of width 10 km and depth 50 m without considering the effects of rotation, surface gravity waves, whose periods are of the order of seconds as opposed to hours, are more likely to be excited by wind forcing. As we shall go onto discover, for typical ocean basins the time periods associated with large-scale wave motions are considerably longer and are therefore more prone to excitation by tidal forcing.

In this section, we introduce the boundary-value problem associated with surface waves in an arbitrary basin, as well as the form of the response for a given potential forcing, forcing frequency, and prescribed Rayleigh friction. In the context of localised surface tide dynamics, the problem of two-dimensional free oscillations of an arbitrary ocean basin was first considered by Platzman (1972), and is developed further in Platzman (1984, 1991). For example, Platzman (1991) investigates tidal evidence for normal modes,

investigating three cases whereby calculations of world-ocean normal modes by previous studies are consistent with those derived from tidal harmonic constants. To aid reader comprehension, the presentation of the problem follows the structure of §11.3 of Boyce et al. (2017) regarding non-homogeneous Sturm–Liouville problems.

Boundary-Value Problem

Consider the boundary-value problem associated to the forced linearised shallow-water equations,

$$i\,\mathcal{L}\,[\mathbf{a}] = \partial_t \mathbf{a} + i\,\mathbf{F}, \tag{3.13}$$

where

$$\mathcal{L} \equiv i \begin{pmatrix} 0 & -f & \partial_x \\ +f & 0 & \partial_y \\ \partial_x c^2 & \partial_y c^2 & 0 \end{pmatrix} \qquad \text{and} \qquad \mathbf{a} = \begin{pmatrix} U \\ V \\ P \end{pmatrix}, \tag{3.14}$$

with operator $\mathcal{L}$ assumed to be continuous. Equations (3.13) and (3.14) are valid on the domain $(x, y) \in \Omega$, and subject to the boundary condition

$$\hat{\mathbf{n}} \cdot \left(c^2\,\mathbf{U}\right) = 0 \qquad \text{on} \qquad \partial\Omega, \tag{3.15}$$

where $\hat{\mathbf{n}}$ is the outward pointing unit normal at each point on the piece-wise smooth boundary $\partial\Omega$ such that energy flux in and out of Ω is prohibited. We will solve the problem (3.13), (3.15) by making use of the eigenfunctions, of which there are infinitely many, of the corresponding homogeneous problem defined by

$$\mathcal{L}\,[\hat{\mathbf{a}}_m] = -\omega_m\,\hat{\mathbf{a}}_m, \tag{3.16}$$

where $\mathbf{a}\,(x, y, t) = \mathrm{Re}\,\{\hat{\mathbf{a}}\,(x, y)\,\exp\,(-i\,\omega\,t)\}$ is time-periodic with wave frequency ω.

Inner Product

Following Platzman (1972), we define the energy-like inner product

$$\langle \hat{\mathbf{a}}_m,\ \hat{\mathbf{a}}_n \rangle \equiv \int_\Omega \left(\hat{P}_m\,\hat{P}_n^* + c^2\,\hat{\mathbf{U}}_m \cdot \hat{\mathbf{U}}_n^*\right)\,\mathrm{d}A, \tag{3.17}$$

with b^* denoting the complex conjugate of $b \in \mathbb{C}$, and where $\mathrm{d}A$ is an element of area. The integration is over the region enclosed by $\partial\Omega$ on which (3.15) applies. From the latter definition and that of purely imaginary operator $\mathcal{L}$ whereby $\mathcal{L}^* = -\mathcal{L}$, we are able to

derive Green's identity

$$\begin{aligned}\langle \hat{\mathbf{a}}_m,\ \mathcal{L}[\hat{\mathbf{a}}_n]\rangle - \langle \mathcal{L}[\hat{\mathbf{a}}_m],\ \hat{\mathbf{a}}_n\rangle &= -i \int_\Omega \Big(\hat{P}_m \boldsymbol{\nabla}\cdot\left(c^2\,\hat{\mathbf{U}}_n^*\right) \\ &\qquad + c^2\,\hat{\mathbf{U}}_m\cdot(\mathbf{f}\times\hat{\mathbf{U}}_n^* + \boldsymbol{\nabla}P_n^*)\Big)\,\mathrm{d}A \\ &= -i\int_\Omega \left(\hat{P}_n^*\,\boldsymbol{\nabla}\cdot\left(c^2\,\hat{\mathbf{U}}_m\right) + c^2\,\hat{\mathbf{U}}_n^*\cdot\boldsymbol{\nabla}\hat{P}_m\right)\mathrm{d}A \\ &= -i\int_\Omega \boldsymbol{\nabla}\cdot\left(c^2\left(\hat{P}_m\,\hat{\mathbf{U}}_n^* + \hat{P}_n^*\,\hat{\mathbf{U}}_m\right)\right)\,\mathrm{d}A. \end{aligned} \tag{3.18}$$

Applying the divergence theorem on (3.18) where $c^2\left(\hat{P}_m\,\hat{\mathbf{U}}_n^* + \hat{P}_n^*\,\hat{\mathbf{U}}_m\right)$ is a continuously differentiable vector field defined on a neighbourhood of Ω, then

$$\langle \hat{\mathbf{a}}_m,\ \mathcal{L}[\hat{\mathbf{a}}_n]\rangle - \langle \mathcal{L}[\hat{\mathbf{a}}_m],\ \hat{\mathbf{a}}_n\rangle = -i\int_{\partial\Omega} c^2\left(\hat{P}_m\,\hat{\mathbf{U}}_n^* + \hat{P}_n^*\,\hat{\mathbf{U}}_m\right)\cdot\hat{\mathbf{n}}\,\mathrm{d}l, \tag{3.19}$$

where $\mathrm{d}l$ is an element of line along the boundary $\partial\Omega$. If both $\mathbf{a}_m$ and $\mathbf{a}_n$ satisfy the boundary conditions expressed in (3.15), the right-hand side of (3.19) is zero, giving

$$\langle \hat{\mathbf{a}}_m,\ \mathcal{L}[\hat{\mathbf{a}}_n]\rangle = \langle \mathcal{L}[\hat{\mathbf{a}}_m],\ \hat{\mathbf{a}}_n\rangle, \tag{3.20}$$

such that the complete system (3.13), (3.15) is self-adjoint and operator $\mathcal{L}$ is Hermitian.

Orthogonality

Since we know from (3.16) that $\mathcal{L}[\hat{\mathbf{a}}_m] = -\omega_m\,\hat{\mathbf{a}}_m$, equation (3.20) can be rewritten as

$$\langle \hat{\mathbf{a}}_m,\ -\omega_n\,\hat{\mathbf{a}}_n\rangle = \langle -\omega_m\,\hat{\mathbf{a}}_m,\ \hat{\mathbf{a}}_n\rangle. \tag{3.21}$$

Writing out equation (3.21) in full using (3.17), we obtain

$$-\omega_n^*\int_\Omega\left(\hat{P}_m\,\hat{P}_n^* + c^2\,\hat{\mathbf{U}}_m\cdot\hat{\mathbf{U}}_n^*\right)\mathrm{d}A = -\omega_m\int_\Omega\left(\hat{P}_m\,\hat{P}_n^* + c^2\,\hat{\mathbf{U}}_m\cdot\hat{\mathbf{U}}_n^*\right)\mathrm{d}A, \tag{3.22}$$

which, when $n = m$, reduces to

$$(\omega_m - \omega_m^*)\int_\Omega\left(|\hat{P}_m|^2 + c^2\left(|\hat{U}_m|^2 + |\hat{V}_m|^2\right)\right)\mathrm{d}A = 0. \tag{3.23}$$

The integrand in (3.23) is non-negative and not identically zero. Since the integrand is also continuous, it follows that the integrand is positive. Therefore the factor $\omega_m - \omega_m^*$ must be zero, and hence ω_m must be real.

Supposing instead that $n \neq m$, equation (3.22) becomes

$$(\omega_m - \omega_n)\int_\Omega\left(\hat{P}_m\,\hat{P}_n^* + c^2\,\hat{\mathbf{U}}_m\cdot\hat{\mathbf{U}}_n^*\right)\mathrm{d}A = 0. \tag{3.24}$$

Since $\omega_m \neq \omega_n$, it follows that $\hat{\mathbf{a}}_m$ and $\hat{\mathbf{a}}_n$ must satisfy the identity

$$\langle \hat{\mathbf{a}}_m,\ \hat{\mathbf{a}}_n \rangle = 0. \tag{3.25}$$

Normalising our eigenfunctions allows us to define the orthogonality condition

$$\frac{\langle \hat{\mathbf{a}}_m,\ \hat{\mathbf{a}}_n \rangle}{\sqrt{\langle \hat{\mathbf{a}}_m,\ \hat{\mathbf{a}}_m \rangle}\sqrt{\langle \hat{\mathbf{a}}_n,\ \hat{\mathbf{a}}_n \rangle}} = \delta_{mn}, \tag{3.26}$$

making use of the Kronecker delta defined by

$$\delta_{mn} \equiv \begin{cases} 0, & \text{if } m \neq n, \\ 1, & \text{if } m = n. \end{cases}$$

Forced Modal Solutions

We now consider a forced problem with

$$\mathbf{F} = \mathrm{Re}\left(\hat{\mathbf{F}}\,(x,y)\,\exp\left(-i\,\omega\,t\right)\right) \tag{3.27}$$

and

$$\mathbf{a} = \mathrm{Re}\left(\hat{\mathbf{a}}\,(x,y)\,\exp\left(-i\,\omega\,t\right)\right) \tag{3.28}$$

with arbitrary forcing frequency ω. It follows from (3.13) that

$$i\,\mathcal{L}\left[\hat{\mathbf{a}}\right] = -i\,\omega\,\hat{\mathbf{a}} + i\,\hat{\mathbf{F}}, \tag{3.29}$$

of which we may take the inner product of each term with $\hat{\mathbf{a}}_m$ which we know satisfies already the homogeneous problem along with the boundary conditions expressed in (3.15), giving

$$\langle \mathcal{L}\left[\hat{\mathbf{a}}\right], \hat{\mathbf{a}}_m \rangle = -\omega\,\langle \hat{\mathbf{a}}, \hat{\mathbf{a}}_m \rangle + \langle \hat{\mathbf{F}}, \hat{\mathbf{a}}_m \rangle, \tag{3.30}$$

where we consider both $\hat{\mathbf{a}}$ and $\hat{\mathbf{F}}$ as a series composed of orthogonal functions satisfying (3.26), such that

$$\hat{\mathbf{a}}\,(x,y) = \sum_{n=1}^{\infty} \alpha_n\,\hat{\mathbf{a}}_n \qquad \text{and} \qquad \hat{\mathbf{F}}\,(x,y) = \sum_{n=1}^{\infty} \beta_n\,\hat{\mathbf{a}}_n. \tag{3.31}$$

In the inhomogeneous problem, the response α_n will depend on β_n through equation (3.30) since only $\hat{\mathbf{F}}$ is prescribed. To find β_n, we simply take the inner product (defined in (3.17) of the eigenfunction series definition expressed in (3.31) with eigenfunction $\hat{\mathbf{a}}_n$ satisfying (3.26). It follows that

$$\langle \hat{\mathbf{F}}, \hat{\mathbf{a}}_m \rangle = \sum_{n=1}^{\infty} \langle \beta_n\,\hat{\mathbf{a}}_n, \hat{\mathbf{a}}_m \rangle = \sum_{n=1}^{\infty} \beta_n\,\langle \hat{\mathbf{a}}_n, \hat{\mathbf{a}}_m \rangle \tag{3.32}$$

from linearity in the first argument of an inner product. Normalising eigenfunctions $\hat{\mathbf{a}}_m$ and $\hat{\mathbf{a}}_n$, equation (3.32) becomes

$$\frac{\langle \hat{\mathbf{F}}, \hat{\mathbf{a}}_m \rangle}{\sqrt{\langle \hat{\mathbf{a}}_m,\ \hat{\mathbf{a}}_m \rangle}\,\sqrt{\langle \hat{\mathbf{a}}_n,\ \hat{\mathbf{a}}_n \rangle}} = \sum_{n=1}^{\infty} \beta_n \frac{\langle \hat{\mathbf{a}}_n, \hat{\mathbf{a}}_m \rangle}{\sqrt{\langle \hat{\mathbf{a}}_m,\ \hat{\mathbf{a}}_m \rangle}\,\sqrt{\langle \hat{\mathbf{a}}_n,\ \hat{\mathbf{a}}_n \rangle}} = \sum_{n=1}^{\infty} \beta_n\, \delta_{mn}, \tag{3.33}$$

from which it is deduced that

$$\beta_n = \frac{\langle \hat{\mathbf{F}}, \hat{\mathbf{a}}_n \rangle}{\langle \hat{\mathbf{a}}_n, \hat{\mathbf{a}}_n \rangle}. \tag{3.34}$$

By the same logic, it can be found that for known response $\hat{\mathbf{a}}$, coefficient

$$\alpha_n = \frac{\langle \hat{\mathbf{a}}, \hat{\mathbf{a}}_n \rangle}{\langle \hat{\mathbf{a}}_n, \hat{\mathbf{a}}_n \rangle}. \tag{3.35}$$

In the case where $\hat{\mathbf{F}}$ represents the net external force of both potential forcing with equilibrium tide $\hat{\eta}_{eq}$ and Rayleigh friction,

$$\hat{\mathbf{F}} = i \left(g\, \boldsymbol{\nabla} \hat{\eta}_{eq} - r\, \hat{\mathbf{U}} \right), \tag{3.36}$$

we may obtain a neat expression for response coefficient β_n. Substituting (3.36) into the numerator of (3.34), and writing the inner product explicitly,

$$\begin{aligned} \langle \hat{\mathbf{F}}, \hat{\mathbf{a}}_n \rangle &= i \int_\Omega c^2 \left(g\, \boldsymbol{\nabla} \hat{\eta}_{eq} - r\, \hat{\mathbf{U}} \right) \cdot \hat{\mathbf{U}}_n^* \, \mathrm{d}A \\ &= i\, g \left(\int_{\partial\Omega} \hat{\mathbf{n}} \cdot \left(c^2\, \hat{\eta}_{eq}\, \hat{\mathbf{U}}_n^* \right) \mathrm{d}l - \int_\Omega \hat{\eta}_{eq}\, \boldsymbol{\nabla} \cdot \left(c^2\, \hat{\mathbf{U}}_n^* \right) \mathrm{d}A \right) - \\ &\qquad i\, r \left(\langle \hat{\mathbf{a}}, \hat{\mathbf{a}}_n \rangle - g \int_\Omega \eta_{eq}\, \hat{P}_n^* \, \mathrm{d}A \right) \end{aligned} \tag{3.37}$$

using the divergence theorem. From (3.15), $\hat{\mathbf{n}} \cdot \left(c^2\, \hat{\mathbf{U}}_n \right) = 0$ on $\partial\Omega$ so the first integral disappears, leaving

$$\langle \hat{\mathbf{F}}, \hat{\mathbf{a}}_n \rangle = -i\, g \int_\Omega \hat{\eta}_{eq}\, \boldsymbol{\nabla} \cdot \left(c^2\, \hat{\mathbf{U}}_n^* \right) \mathrm{d}A - i\, r\, \alpha_n \left(\langle \hat{\mathbf{a}}_n, \hat{\mathbf{a}}_n \rangle - \int_\Omega |\hat{P}_n|^2 \, \mathrm{d}A \right). \tag{3.38}$$

Furthermore from (3.16), since $\boldsymbol{\nabla} \cdot \left(c^2\, \hat{\mathbf{U}}_m \right) = i\, \omega_m\, \hat{P}_m$, then

$$\langle \hat{\mathbf{F}}, \hat{\mathbf{a}}_n \rangle = g\, \omega_n \int_\Omega \hat{\eta}_{eq}\, \hat{P}_n^* \, \mathrm{d}A - i\, r\, \alpha_n \left(\langle \hat{\mathbf{a}}_n, \hat{\mathbf{a}}_n \rangle - \int_\Omega |\hat{P}_n|^2 \, \mathrm{d}A \right). \tag{3.39}$$

It follows therefore that in the case where external force $\hat{\mathbf{F}}$ represents the act of both Rayleigh friction and potential forcing with equilibrium tide $\hat{\eta}_{eq}$,

$$\beta_n = \omega_n\, \gamma_n - i\, r\, \alpha_n\, (1 - \delta_n) \tag{3.40}$$

for

$$\gamma_n = \frac{g}{\langle \hat{\mathbf{a}}_n, \hat{\mathbf{a}}_n \rangle} \int_\Omega \hat{\eta}_{eq}\, \hat{P}_n^*\, \mathrm{d}A \qquad \text{and} \qquad \delta_n = \frac{1}{\langle \hat{\mathbf{a}}_n, \hat{\mathbf{a}}_n \rangle} \int_\Omega |\hat{P}_n|^2\, \mathrm{d}A.$$

Having already defined coefficients α_n and β_n in (3.34) and (3.40) respectively, we may use (3.16) in (3.30) to determine that

$$-\omega_n\, \alpha_n = -\omega\, \alpha_n + \beta_n \qquad \Longrightarrow \qquad \alpha_n = \frac{\omega_n\, \gamma_n}{\omega - \omega_n + i\, r\, (1 - \delta_n)}. \tag{3.41}$$

In the case whereby Rayleigh coefficient $r = 0$ (no damping), equation (3.41) for response coefficient reduces to

$$\alpha_n = \frac{\omega_n}{\omega - \omega_n} \gamma_n, \qquad \gamma_n = \frac{g}{\langle \hat{\mathbf{a}}_n, \hat{\mathbf{a}}_n \rangle} \int_\Omega \hat{\eta}_{eq}\, \hat{P}_n^*\, \mathrm{d}A. \tag{3.42}$$

Here, α_n is a product of two terms: the frequency factor $\omega_n/(\omega - \omega_n)$ and the shape factor γ_n. We must now distinguish between two main cases, one of which has two sub-cases.

First suppose that $\omega \neq \omega_n$ for $n = 1, 2, 3, \ldots$; that is, ω is not equal to any eigenvalue of the corresponding homogeneous eigenvalue problem. Then

$$\mathbf{a}\,(x, y, t) = \exp\,(-i\, \omega\, t) \sum_{n=1}^{\infty} \frac{\omega_n}{\omega - \omega_n + i\, r\, (1 - \delta_n)}\, \gamma_n\, \hat{\mathbf{a}}_n\,(x, y)\,. \tag{3.43}$$

equation (3.43), with β_n given by (3.34), is a formal solution of the nonhomogeneous boundary value problem (3.13), (3.15). Our argument does not prove that the series (3.43) converges. However, any solution of the boundary value problem (3.13), (3.15) converges so long as both $\mathbf{F}\,(x, y, t)$ and $\boldsymbol{\nabla} \cdot \mathbf{F}\,(x, y, t)$ are piece-wise continuous on the domain Ω.

Now suppose that ω is equal to one of the eigenvalues of the corresponding homogeneous problem, say. $\omega = \omega_n$, then the situation is quite different. In this event, for $n = m$ equation (3.41) becomes $0 \cdot \alpha_n = \beta_n$. Again we must consider two cases:

- If $\omega = \omega_n$ and $\beta_n \neq 0$, then the nonhomogeneous problem (3.13), (3.15) has no solution. This is because of resonance; in a time-harmonic forced setting, the amplitude would become unbounded.

- If $\omega = \omega_n$ and $\beta_n = 0$, then equation (3.41) is satisfied regardless of the value of α_n; in other words, α_n remains arbitrary. In this case the boundary value problem (3.13), (3.15) does have a solution, but it is not unique, since it contains an arbitrary multiple of the eigenfunction $\hat{\mathbf{a}}_n\,(x, y)$. Since β_n is given by equation (3.34), the condition $\beta_n = 0$ means that

  $$\langle \hat{\mathbf{F}}, \hat{\mathbf{a}}_n \rangle = 0. \tag{3.44}$$

  Thus, if $\omega = \omega_n$, the nonhomogeneous boundary value problem (3.13), (3.15) can be solved only if $\mathbf{F}$ is orthogonal with respect to (3.17) to the eigenfunction corresponding to eigenvalue ω_n.

3.3.2 Orthogonal Modes in a Channel of Uniform Depth

The theory of forced modes in some arbitrary basin expands also to channels for modes periodic in the along-shore direction. This can be used as a crude model for large ocean basins, such as the Atlantic. In which case, we have that for along-shore wavenumber k and channel width L, the inner product to be considered instead is

$$\langle \hat{\mathbf{a}}_m,\ \hat{\mathbf{a}}_n \rangle \equiv \int_\Omega \left(\hat{P}_m\, \hat{P}_n^* + c^2\, \hat{\mathbf{U}}_m \cdot \hat{\mathbf{U}}_n^* \right) \mathrm{d}A, \tag{3.45}$$

where domain $\Omega = [x_0, x_0 + L_x] \times [0, L_y]$, where x_0 is some reference position along-shore and $L_x = 2\pi/k$ is the along-shore wavelength. If wave speed squared c^2, proportional to fluid depth h, depends only upon cross-shore variable y, then the aforementioned inner product can be reduced to

$$\langle \hat{\mathbf{a}}_m,\ \hat{\mathbf{a}}_n \rangle \equiv \int_0^{L_y} \left(\hat{P}_m\, \hat{P}_n^* + c^2\, \hat{\mathbf{U}}_m \cdot \hat{\mathbf{U}}_n^* \right) \mathrm{d}y. \tag{3.46}$$

Supposing some forcing over uniform fluid depth h, and therefore uniform squared wave speed c^2, with along-shore wavenumber k (periodic with wavelength $L_x = 2\pi/k$) and wave frequency ω, the original boundary-value problem (3.13) becomes

$$i\, \mathcal{L}\, [\mathbf{a}] = -i\, \omega\, \mathbf{a} + i\, \mathbf{F}, \tag{3.47}$$

with

$$\mathcal{L} \equiv i \begin{pmatrix} 0 & -f & i\,k \\ +f & 0 & \dfrac{\mathrm{d}}{\mathrm{d}y} \\ i\,c^2\,k & c^2\,\dfrac{\mathrm{d}}{\mathrm{d}y} & 0 \end{pmatrix}, \qquad \mathbf{a} = \begin{pmatrix} U \\ V \\ P \end{pmatrix}, \qquad \mathbf{F} = g \begin{pmatrix} i\,k \\ \dfrac{\mathrm{d}}{\mathrm{d}y} \\ 0 \end{pmatrix} \eta_{eq}, \tag{3.48}$$

valid on the domain $y \in [0, L_y]$ defining a channel of width L_y, and subject to impermeability boundary conditions,

$$V\,(x, y, t) = 0 \qquad \text{at} \qquad y = 0, L_y. \tag{3.49}$$

We can deduce from equation (3.12), that system (3.47)–(3.49) is governed by the second-order inhomogeneous ODE,

$$\frac{-i\,\omega}{g} \left(\omega_f^2 - c^2 \left(k^2 + \frac{\mathrm{d}^2}{\mathrm{d}y^2} \right) \right) P = i\, c^2\, \omega \left(k^2 + \frac{\mathrm{d}^2}{\mathrm{d}y^2} \right) \eta_{eq}. \tag{3.50}$$

where $\omega_f^2 = \omega^2 - f^2$ and $c^2 = g\,h$.

Seeking the fundamental modes to the periodic channel of uniform depth, we solve first

the homogeneous problem governed by the second-order ODE

$$\left(\frac{\mathrm{d}^2}{\mathrm{d}y^2} + \left\{\frac{\omega_f^2}{c^2} - k^2\right\}\right) P = 0, \tag{3.51}$$

and subject to the boundary condition on pressure:

$$\left(\frac{\mathrm{d}}{\mathrm{d}y} + k\,\frac{f}{\omega}\right) P = 0 \qquad \text{at} \qquad y = 0, L_y. \tag{3.52}$$

As Pedlosky (2003) notes, if there were no rotation, $f = 0$, there would exist a solution of P independent of cross-shore spatial variable, y, whereby $\omega = \pm c\,k$. The latter would be the lowest cross-stream mode and have the lowest possible non-geostrophic frequency. Gravity modes of the form $\cos(n\,\pi\,y/L_y)$ would also exist, and have wave frequency

$$\omega = \pm c\sqrt{k^2 + \frac{n^2\,\pi^2}{L_y^2}}, \qquad n = 1, 2, \ldots. \tag{3.53}$$

Of course however, in planetary settings, typically $f \neq 0$, and so it is of interest to examine how rotation alters the previously simple structure of the problem (see also Gill, 1982; Pedlosky, 1987). Quite evidently, the major change will lead to a mixed boundary condition, seen in equation (3.52), involving the solution and its derivative.

Let us define the cross-shore wavenumber

$$l = +\sqrt{\frac{\omega_f^2}{c^2} - k^2}, \tag{3.54}$$

allowing us to write down solutions to equation (3.51) of the form

$$P(y) = \alpha\,\sin(l\,y) + \beta\,\cos(l\,y), \tag{3.55}$$

where constants α and β become fixed via the application of (3.52). As such, substitution of the latter into (3.52) returns the following matrix system:

$$\begin{pmatrix} l & k\,\dfrac{f}{\omega} \\ l\,\cos(l\,L_y) + k\,\dfrac{f}{\omega}\,\sin(l\,L_y) & k\,\dfrac{f}{\omega}\,\cos(l\,L_y) - l\,\sin(l\,L_y) \end{pmatrix} \begin{pmatrix} \alpha \\ \beta \end{pmatrix} = \begin{pmatrix} 0 \\ 0 \end{pmatrix}. \tag{3.56}$$

Not only does it follow from equation (3.56) that

$$\alpha = -\frac{k\,f}{l\,\omega}\,\beta \qquad \text{with} \qquad l, \omega \neq 0, \tag{3.57}$$

but by considering the case for which the determinant of coefficients in (3.56) must be

zero, we obtain non-trivial solutions satisfying the dispersion relation

$$\omega_f^2 \left(\omega^2 - c^2\, k^2\right) \sin\left(l\, L_y\right) = 0. \tag{3.58}$$

It is observed from equation (3.58) that there are three possible solutions:

1. $\omega = \pm f$
2. $\sin\left(l\, L_y\right) = 0$
3. $\omega = \pm c\, k$

We have, however, already indicated in (3.6) that the inertial mode, $\omega = \pm f$, needs to be treated separately, so here, we consider the root spurious. Furthermore, it is interesting that in the non-rotating case, we concluded that the pressure solution corresponding to $\omega = \pm c\, k$ is independent of the cross-shore spatial variable, and yet, the mode appears once more despite the boundary condition (3.52) now prohibiting the trivial solution. What follows, is standard textbook material, and can be found in Gill (1982), Pedlosky (1987) and Vallis (2006), amongst others.

Inertia-Gravity Modes

Let us begin by considering modal solutions corresponding to inertia-gravity waves. These are waves whose wavelength is large enough to be affected by the Earth's rotation. As a consequence, the waves, unlike gravity waves, are also restored by the Coriolis force which arises in an inertial frame. We shall observe that under differing parameter regimes, either one of the forces may dominate the other (or contribute equally).

The solution to $\sin\left(l\, L_y\right) = 0$ is satisfied when

$$l = \frac{n\,\pi}{L_y}, \qquad\qquad n = 1, 2, \ldots, \tag{3.59}$$

since the solution corresponding to $n = 0$ yields the trivial solution.

Using our definition of the cross-shore wavenumber in (3.54), we may substitute it into (3.59) to yield the dispersion relation

$$\omega_n^2 = f^2 + c^2 \left(k^2 + \frac{n^2 \pi^2}{L_y^2}\right) \qquad\qquad n = 1, 2, \ldots. \tag{3.60}$$

Note that (3.60) is identical to the gravity mode but with the inclusion of the Coriolis term which leads to waves of shorter periods.

Using the relation between α and β, as carried out by Pedlosky (2003), we choose $\alpha = \eta_0$ to prescribe the pressure at $y = 0$:

$$P\left(x, y, t\right) = g\, \eta_0 \left[\cos\left(\frac{n\,\pi\, y}{L_y}\right) - \frac{k\, f\, L_y}{\omega_n\, n\, \pi} \sin\left(\frac{n\,\pi\, y}{L_y}\right)\right] \cos\left(k\, x - \omega_n\, t\right). \tag{3.61}$$

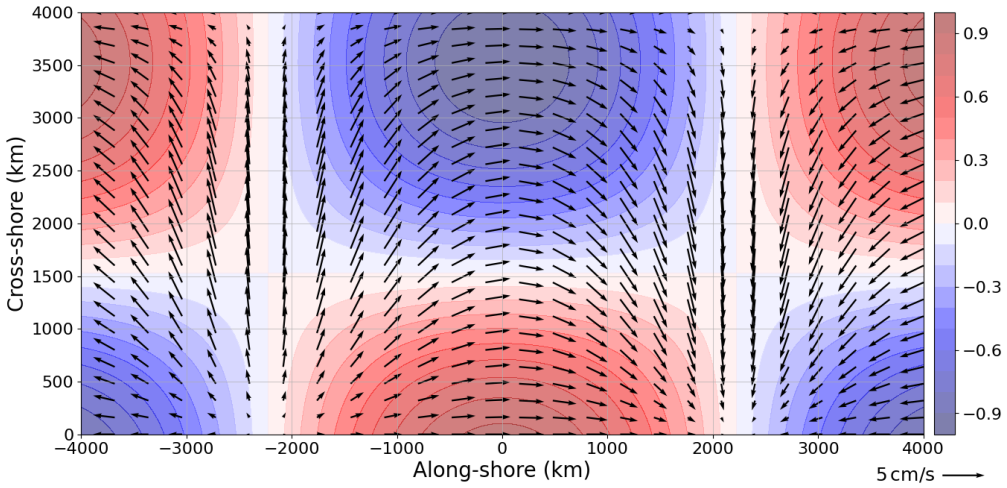

(a) Mode 1

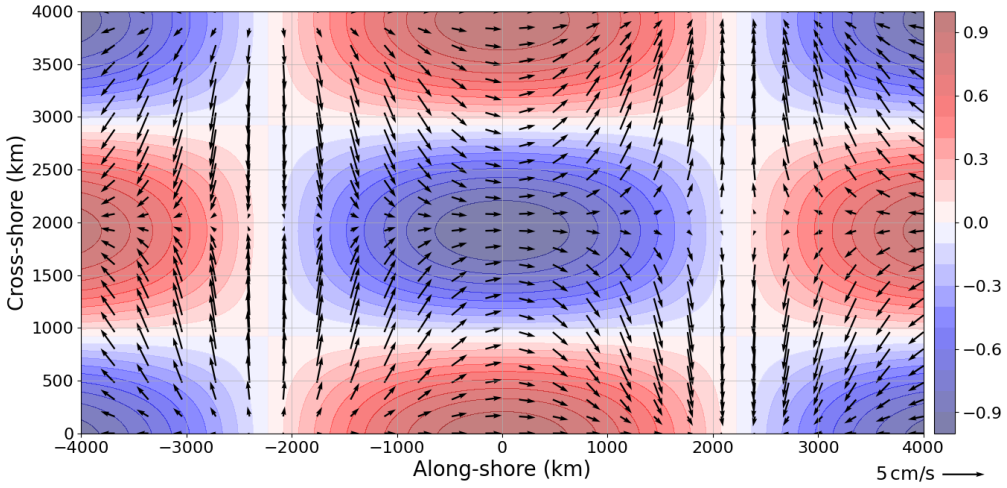

(b) Mode 2

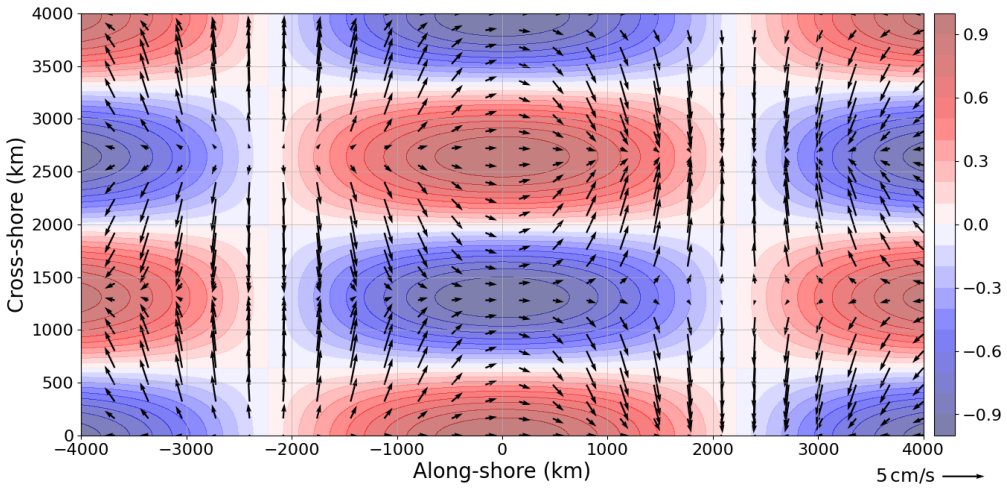

(c) Mode 3

Figure 3.1: Free wave solutions of rightward-propagating inertia-gravity modes 1–3 at mid-latitude with Coriolis parameter $f = 10^{-4}\,\mathrm{s}^{-1}$ in a uniform channel of width $4,000\,\mathrm{km}$ and a depth of $4,000\,\mathrm{m}$. Shown is a contour plot of surface displacement (maximum amplitude $1\,\mathrm{m}$) accompanied by the associated horizontal velocity field (see $5\,\mathrm{cm/s}$ key).

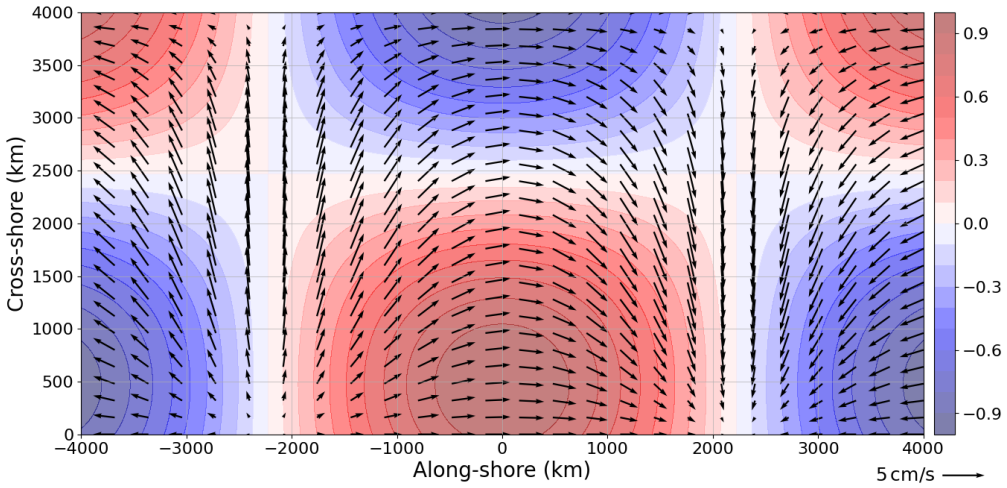

(a) Mode 1

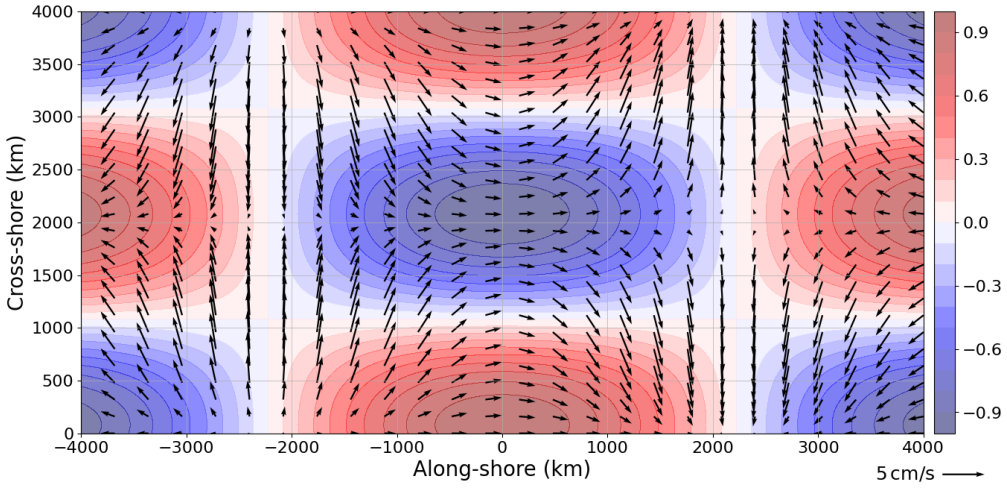

(b) Mode 2

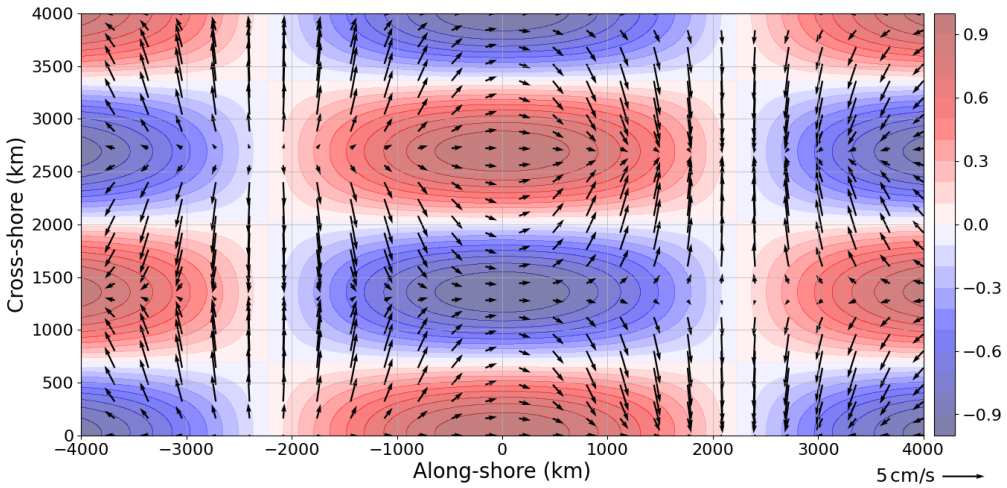

(c) Mode 3

Figure 3.2: Free wave solutions of leftward-propagating inertia-gravity modes 1–3 at mid-latitude with Coriolis parameter $f = 10^{-4}\,\mathrm{s}^{-1}$ in a uniform channel of width $4,000\,\mathrm{km}$ and a depth of $4,000\,\mathrm{m}$. Shown is a contour plot of surface displacement (maximum amplitude $1\,\mathrm{m}$) accompanied by the associated horizontal velocity field (see $5\,\mathrm{cm/s}$ key).

It is interesting to note that as $n \to \infty$, the effect of the Coriolis force becomes negligible in (3.60), and that the waves appear ever-more like high-frequency gravity waves. We also remark that for each k, there exists two roots of ω_n. It follows therefore that the structure of the inertia-gravity modes, for f non-zero, will differ for waves propagating to the right and for waves propagating to the left.

To obtain the corresponding velocity solutions, we deduce from (3.6) that

$$\omega_f^2\, U = \left(f\,\frac{\mathrm{d}}{\mathrm{d}y} + \omega\, k\right) P, \qquad\qquad \omega_f^2\, V = i\left(\omega\,\frac{\mathrm{d}}{\mathrm{d}y} + f\, k\right) P. \tag{3.62}$$

It follows therefore that along-shore velocity is

$$U\,(x,y,t) = \frac{g\,\eta_0}{c^2}\left[\frac{c^2\,k}{\omega_n}\cos\left(\frac{n\,\pi\,y}{L_y}\right) - \frac{f\,L_y}{n\,\pi}\sin\left(\frac{n\,\pi\,y}{L_y}\right)\right]\cos\left(k\,x - \omega_n\,t\right), \tag{3.63}$$

and that cross-shore velocity is

$$V\,(x,y,t) = \frac{-g\,\eta_0}{c^2}\,\frac{L_y\left(\omega_n^2 - c^2\,k^2\right)}{\omega_n\,n\,\pi}\,\sin\left(\frac{n\,\pi\,y}{L_y}\right)\sin\left(k\,x - \omega_n\,t\right). \tag{3.64}$$

Figures 3.1–3.2 show rightward- and leftward-propagating inertia-gravity wave solutions to equations (3.47)–(3.48) at mid-latitude for a uniform basin of depth $4,000\,\mathrm{m}$ and width $4,000\,\mathrm{km}$, and correspond with an along-shore wavenumber $7.07\times10^{-7}\,\mathrm{m}^{-1}$. Contour plots show the corresponding surface displacement and quiver plots show the horizontal velocity vector field (see key). More specifically, Figure 3.1 illustrates rightward-propagating inertia-gravity waves of modes 1–3. The latter is made evident through the undulations of the cross-shore velocity. Similarly, Figure 3.2 shows leftward-propagating inertia-gravity waves of mode 1–3. The most significant difference between the two is that the along-shore velocity and free-surface displacement are in phase for rightward-propagating modes, while out of phase for leftward-propagating modes.

Kelvin Modes

In 1879, Lord Kelvin published his findings of the existence of a new type of gravity wave, trapped in the vicinity of a lateral boundary. Thomson (1879) shows that with the presence of rotation, the amplitude of a Kelvin wave decays exponentially away from the lateral boundary with decay scale L_R, as defined later.

To analyse the Kelvin wave, consider now the solution of the dispersion relation of equation (3.58),

$$\omega = \pm c\,k. \tag{3.65}$$

What is most interesting about this dispersion relation, unlike that of the inertia-gravity waves, is that the wave solutions are non-dispersive. That is, the group speed and phase speed are identical, meaning that all waves, regardless of their wavelength, propagate at the same velocity.

We discussed previously that in the non-rotating case, the solution of this modal frequency is independent of the cross-shore spatial variable, y. However, equation (3.52) dictates that the latter solution is no longer possible in a periodic channel of uniform depth since the boundary condition is a linear combination of the variable and its derivative. We begin by considering the cross-shore wave number

$$l = +\sqrt{\frac{\omega_f^2}{c^2} - k^2},$$

such that using equation (3.65), it follows that

$$l = \pm \frac{i}{L_R}, \tag{3.66}$$

where $L_R \equiv c/|f| = O\,(2,000\,\mathrm{km})$ is the Rossby radius of deformation.[1] Observe that for this mode, the cross-shore wavenumber is purely imaginary, i.e. decaying from the shore. Again, using the relationship between constant coefficients α and β seen in (3.56), we may substitute both (3.65) and (3.66) into (3.55), and simplify to give the cross-shore structure of pressure,

$$P\,(y) = \frac{g\,\eta_0}{2}\left(\left\{1 + \frac{\omega}{c\,k}\right\}\exp\left(\frac{-y}{L_R}\right) - \left\{1 - \frac{\omega}{c\,k}\right\}\exp\left(\frac{+y}{L_R}\right)\right), \tag{3.67}$$

redefining $\alpha = i\,\eta_0$. The solution presented in (3.67) is a superposition of two exponential terms decaying from either boundary whose decay scale corresponds to the Rossby radius of deformation.

Consider now the wave frequency of the Kelvin wave, $\omega = \pm c\,k$. We remark that for $\omega = c\,k$, the second term in (3.67) disappears, while $\omega = -c\,k$ makes the first term disappear. We have therefore the pressure profile of the Kelvin wave,

$$P\,(x,y,t) = g\,\eta_0\,\exp\left(\frac{\mp y}{L_R}\right)\cos\left(k\,x - \omega\,t\right), \qquad \omega = \pm c\,k. \tag{3.68}$$

Here, η_0 is the amplitude of free-surface displacement along the shoreline at $y = 0$. In the example of the rightward-propagating Kelvin wave, free-surface displacement (3.68) is valid uniquely in the domain $y > 0$ when only the lateral boundary at $y = 0$ is present, such that the decay condition $|U|, |V|, |P| \to 0$ as $y \to +\infty$ is satisfied and the solution remains bounded. By the same argument, the leftward-propagating solution is valid uniquely in the domain $y < L_y$ if only the boundary at $y = L_y$ were present.

Let us now consider the flow field of the rightward- and leftward-propagating Kelvin wave

[1] Here, we consider fluid depth $h = 4,000\,\mathrm{m}$ and Coriolis parameter $f = 10^{-4}\,\mathrm{s}^{-1}$.

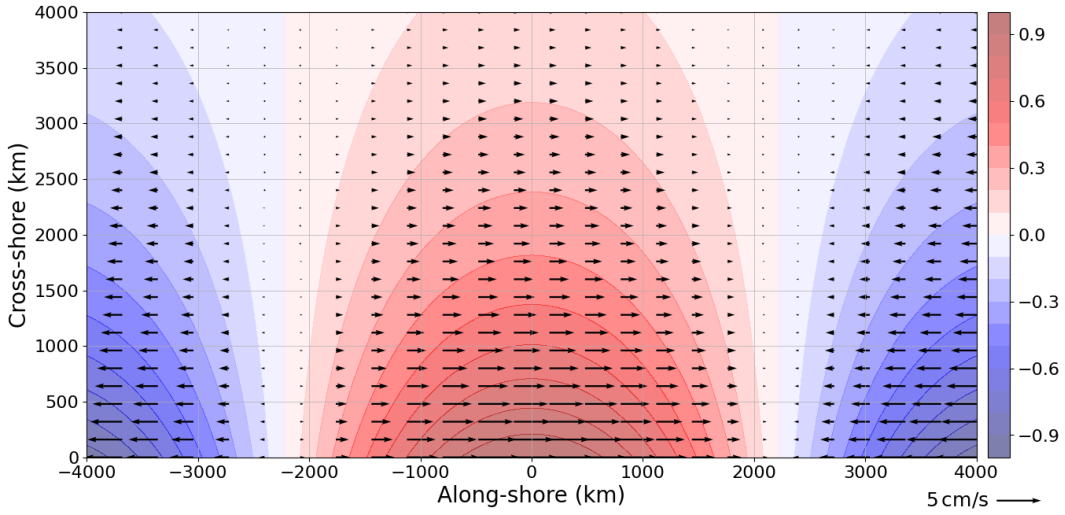

(a) Rightward-propagating solution

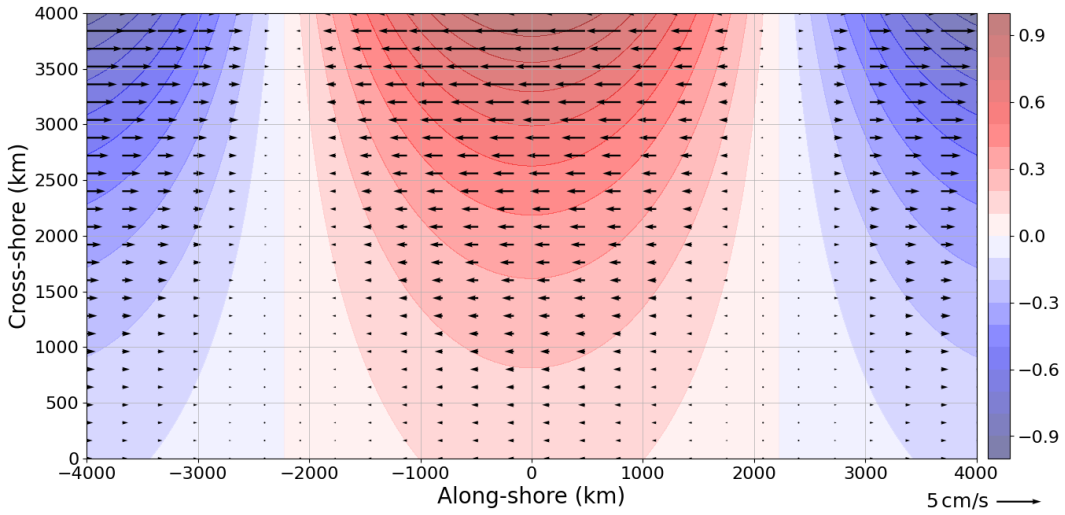

(b) Leftward-propagating solution

Figure 3.3: Free wave solutions of rightward- (top) and leftward- (bottom) propagating Kelvin wave at mid-latitude with Coriolis parameter $f = 10^{-4}\,\mathrm{s}^{-1}$ in a uniform channel of width $L_y = 4,000\,\mathrm{km}$ and a depth of $4,000\,\mathrm{m}$. Shown is a contour plot of surface displacement (maximum amplitude 1 m) accompanied by the associated horizontal velocity field (see 5 cm/s key). The amplitude of the wave decays exponentially.

using (3.62): the along-shore velocity is

$$\begin{aligned} U(x,y,t) &= \frac{1}{\omega_f^2}\left(f\,\frac{\mathrm{d}}{\mathrm{d}y} + \omega\,k\right)P \\ &= \frac{g\,\eta_0}{2c^2\,k\,\omega_f^2}\left((\omega + c\,k)\left(\omega\,c\,k - f^2\right)\exp\left(\frac{-y}{L_R}\right) + \right. \\ &\qquad \left. (\omega - c\,k)\left(\omega\,c\,k + f^2\right)\exp\left(\frac{+y}{L_R}\right)\right)\cos\left(k\,x - \omega\,t\right), \end{aligned} \tag{3.69}$$

while the cross-shore velocity is given by

$$\begin{aligned} V(x,y,t) &= \frac{i}{\omega_f^2}\left(\omega\,\frac{\mathrm{d}}{\mathrm{d}y} + f\,k\right)P \\ &= \frac{f\,g\left(\omega^2 - c^2\,k^2\right)\eta_0}{c^2\,k\,\omega_f^2}\sinh\left(\frac{f\,y}{c}\right)\sin\left(k\,x - \omega\,t\right). \end{aligned} \tag{3.70}$$

Solutions (3.69)–(3.70) simplify to give velocity profiles

$$U(x,y,t) = \frac{\eta_0}{h}c\,\exp\left(\frac{\mp y}{L_R}\right)\cos\left(k\,x - \omega\,t\right), \qquad V(x,y,t) = 0, \qquad \omega = \pm c\,k, \tag{3.71}$$

meaning that not only is $V = 0$ satisfied at the boundaries, but throughout the entire spatial domain. We remark that along-shore velocity can also be written in the form

$$U = -\frac{1}{f}\partial_y P,$$

such that Coriolis force is balanced by the pressure gradient perpendicular to the coastal boundaries (see LeBlond & Mysak, 1978; Pedlosky, 2003).

Considering the limit $f \to 0$, the complete solution (3.68) and (3.71) become independent of cross-shore spatial variable y. As Pedlosky (2003) explains, this becomes the mode 0 surface wave which also has zero cross-shore velocity in the domain, and in the presence of rotation, introduces a sloping pressure field to balance the Coriolis acceleration of the along-shore velocity.

Figure 3.3 shows both leftward- and rightward-propagating Kelvin wave solutions at mid-latitude for a uniform channel of depth $4,000\,\mathrm{m}$ and width $4,000\,\mathrm{km}$, and with along-shore wavenumber $k = 7.07 \times 10^{-7}\,\mathrm{m}^{-1}$.[1] In both cases, the solution amplitude decays from the respected coastal boundary, while the cross-shore velocity is uniformly zero. Since in this example the decay scale is approximately half the domain width, we would anticipate the amplitudes having decreased by a factor of $\sim \exp(-2) \approx 0.14$.

[1] An along-shore wavenumber $k = 7.07 \times 10^{-7}\,\mathrm{m}^{-1}$ corresponds to an along-shore wavelength of $2\pi/k \approx 8,900\,\mathrm{km}$.

Forced Modal Solutions

In this section, we would like to show that for some given potential forcing of equilibrium tide η_{eq} at semi-diurnal frequency, that the dominant mode is often the Kelvin wave. While we consider uniquely the case of uniform topography, the assumption is that the coastal shelf is small compared to the dominant length scale of the Kelvin wave, the Rossby radius of deformation L_R, that the modal frequency and the form of the wave will be some perturbation of the trivial case.

Figure 3.4 shows non-dimensional modal wave frequencies with respect to non-dimensional along-shore wavenumber. Figure 3.4a shows the analytical dispersion relations for both rightward- and leftward-propagating surface gravity waves. Figure 3.4b considers ocean basin topography, shown in Figure 3.5, modelled using a Gaussian curve. At each end of the channel, a coastal shelf of depth 200 m and width 150 km is positioned. The dispersion relations for the case of variable topography were obtained from the eigenvalue problem using Chebyshev differential matrices with 128 nodes. Alongside the dispersion relationships, the diurnal and semi-diurnal wave frequencies at mid latitude (with Coriolis parameter $f = 10^{-4}\,\mathrm{s}^{-1}$) are shown.

It is observed from Figure 3.4 that for along-shore wavelengths of the same order of magnitude as the Rossby radius of deformation, the closest modal wave frequencies correspond to the Kelvin wave. Moreover, the presence of variable topography over some small coastal length scale (with respect to Rossby radius of deformation) leads to a retardation of all wave frequencies ω_n, and is more telling for larger values of $k\,L_R$ values (smaller along-shore wavelengths). Consequently, the modal frequency of the Kelvin wave is no longer proportional to along-shore wavenumber k. A further consequence of this is that the group speed $c_g = \mathrm{d}\omega_n/\mathrm{d}k$ is no longer equal to the phase speed $c_p = \omega_n/k$. However, the presence of variable topography—along with the addition of sub-inertial continental shelf waves (topographic Rossby modes) for which we do not consider (see §10.12 of Gill (1982), or Teeluck (2013) for a more in-depth analysis on the subject)—leads to dispersion relations which are indeed just some small perturbation of those in the case of uniform topography. Indeed, at first glance, the two figures might even appear identical. We conclude that in the case whereby the coastal shelf is small compared to the Rossby radius of deformation, it suffices to consider a channel of uniform topography for the excitation of surface modes in a basin.

From the previous sub-section, we learnt that the response of a given mode is proportional to two terms: the frequency factor and the shape factor. The frequency factor, $\omega_n/(\omega - \omega_n)$, would therefore suggest that the dominant response corresponds to the Kelvin wave. However, it is our aim now to briefly consider the effect of potential forcing of a given wavenumber and wave frequency, and determine whether for typical tidal ranges, the dominant factor remains the Kelvin wave. I.e. does the shape factor play an equally important role at determining the response as the frequency factor?

To investigate the role in the form of the equilibrium tide, we consider in Figures 3.6–3.8

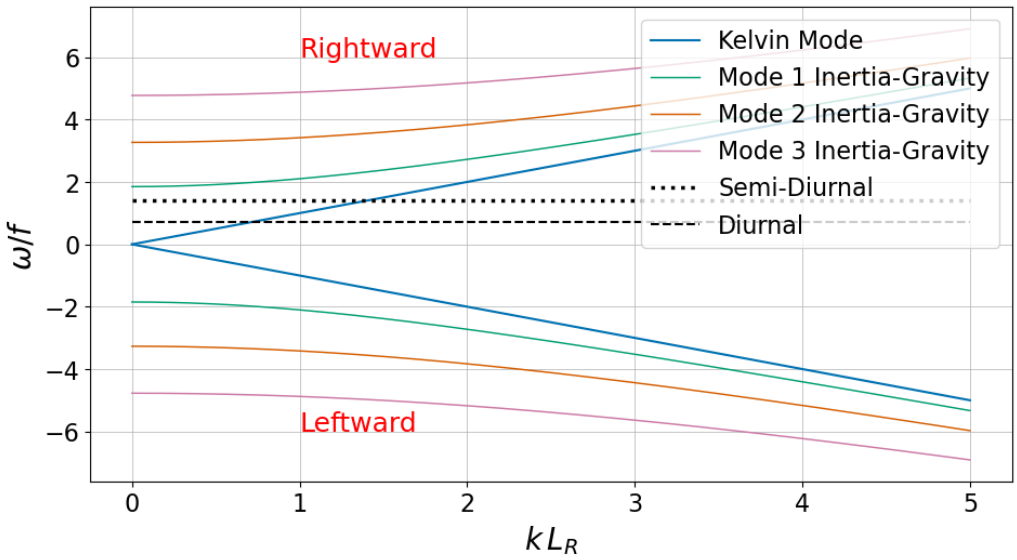

(a) Uniform channel

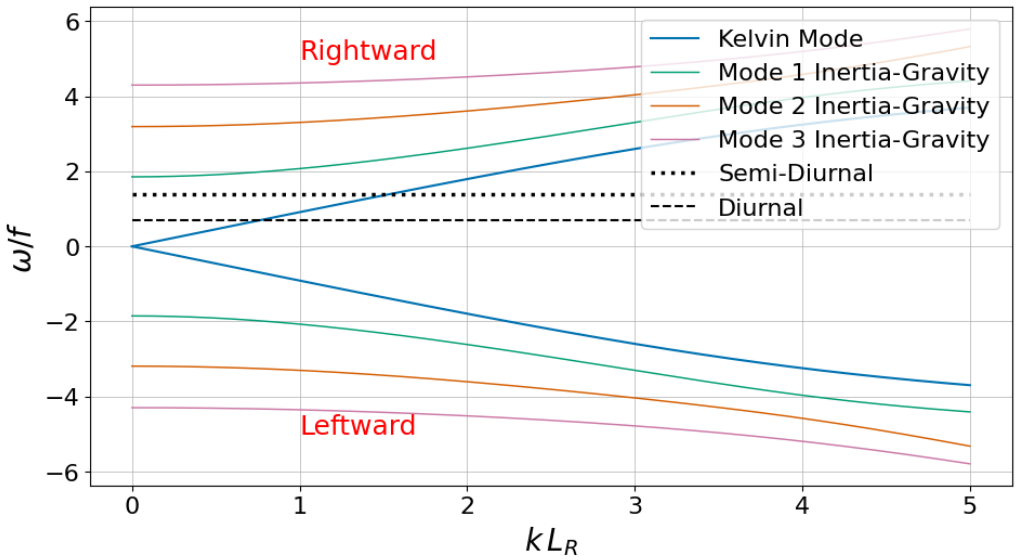

(b) Ocean basin

Figure 3.4: Dispersion relations for a channel of: (a) uniform depth; (b) basin topography modelled using a Gaussian profile to model coastal shelves at both shorelines with coastal length scale 150 km. In both cases, a channel width $L_y = 4,000\,\text{km} \approx 2L_R$ at mid-latitude ($f = 10^{-4}\,\text{s}^{-1}$) is considered, where Rossby radius of deformation $L_R \equiv c/|f| = 1,980\,\text{km}$. In the top half of each figure, the waves are rightward-propagating, while in the bottom half they are leftward-propagating. For $k\,L_R = O\,(1)$, the fundamental frequency of the rightward-propagating Kelvin wave will be closest to both the diurnal and semi-diurnal tidal frequencies (indicated with dashed black lines). Shelf modes are omitted in (b).

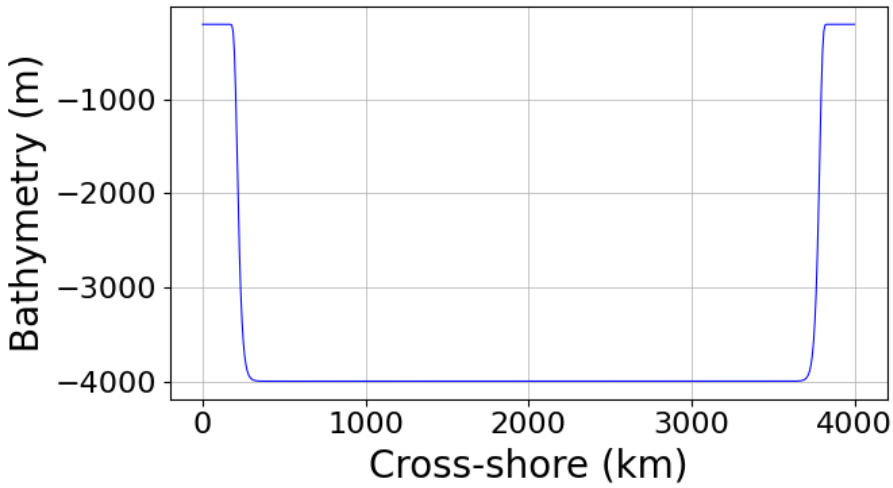

Figure 3.5: Ocean basin modelled using a Gaussian curve.

the modal contribution of low-order surface waves in a uniform channel of width $4,000\,\mathrm{km}$ and depth $4,000\,\mathrm{m}$ at mid-latitude ($f = 10^{-4}\,\mathrm{s}^{-1}$) in the tidal response of a given alongshore wavenumber k and forcing frequency ω. Since we are considering the response of semi-diurnal forcing, we pay particular attention to values $\omega/f \approx 1.4$.

The first tidal forcing considered, although artificial, is shown in Figure 3.6, and regards an equilibrium tide proportional to $\exp(-y/L_R)$. The reason for this consideration is that the shape factor is a measure of correlation, and if a Kelvin-like response is sought, then a Kelvin-like forcing is required. Although not possible with the use of potential forcing, if the forcing corresponded to a particular mode, say mode m, then the shape factor $\gamma_n \propto \delta_{mn}$, and therefore only mode m would be excited, irrespective of forcing frequency. In a bid to excite a predominantly Kelvin-like response, we consider a potential forcing whose cross-shore spatial structure is similar to the Kelvin wave.

Figure 3.6, much like Figures 3.7 and 3.8, is composed of a series of contour plots indicating modal contribution (%) of low-order surface gravity modes. This modal contribution looks at all modal coefficients α_n, and considers the magnitude with respect to the sum of all modal coefficients for which $|\omega_n/f| < 50$. On the left of each Figure, the modal contributions of rightward-propagating surface gravity modes are shown, while on the right, those of leftward-propagating modes.

Figure 3.6 shows that for $\omega/f > 0$ and $k\,L_R > 0$, leftward-propagating modes are barely excited at all (less than 30%), with the mode 1 inertia-gravity mode excited the strongest amongst them. In addition, the leftward-propagating mode 1 inertia-gravity wave is excited more strongly than the leftward-propagating Kelvin wave with $\sim 30\%$ modal contribution versus $\sim 20\%$. As for rightward-propagating modes, when both $\omega/f = O(1)$ and $k\,L_R = O(1)$ an equilibrium tide proportional to $\exp(-y/L_R)$ sees a modal contribution of around 50% for the Kelvin mode. When close to resonance, this figure reaches 100%, as one might expect. Similarly, rightward-propagating inertia-gravity modes are excited (shown by the bright bands) close to resonance, and reflects the dispersion relations

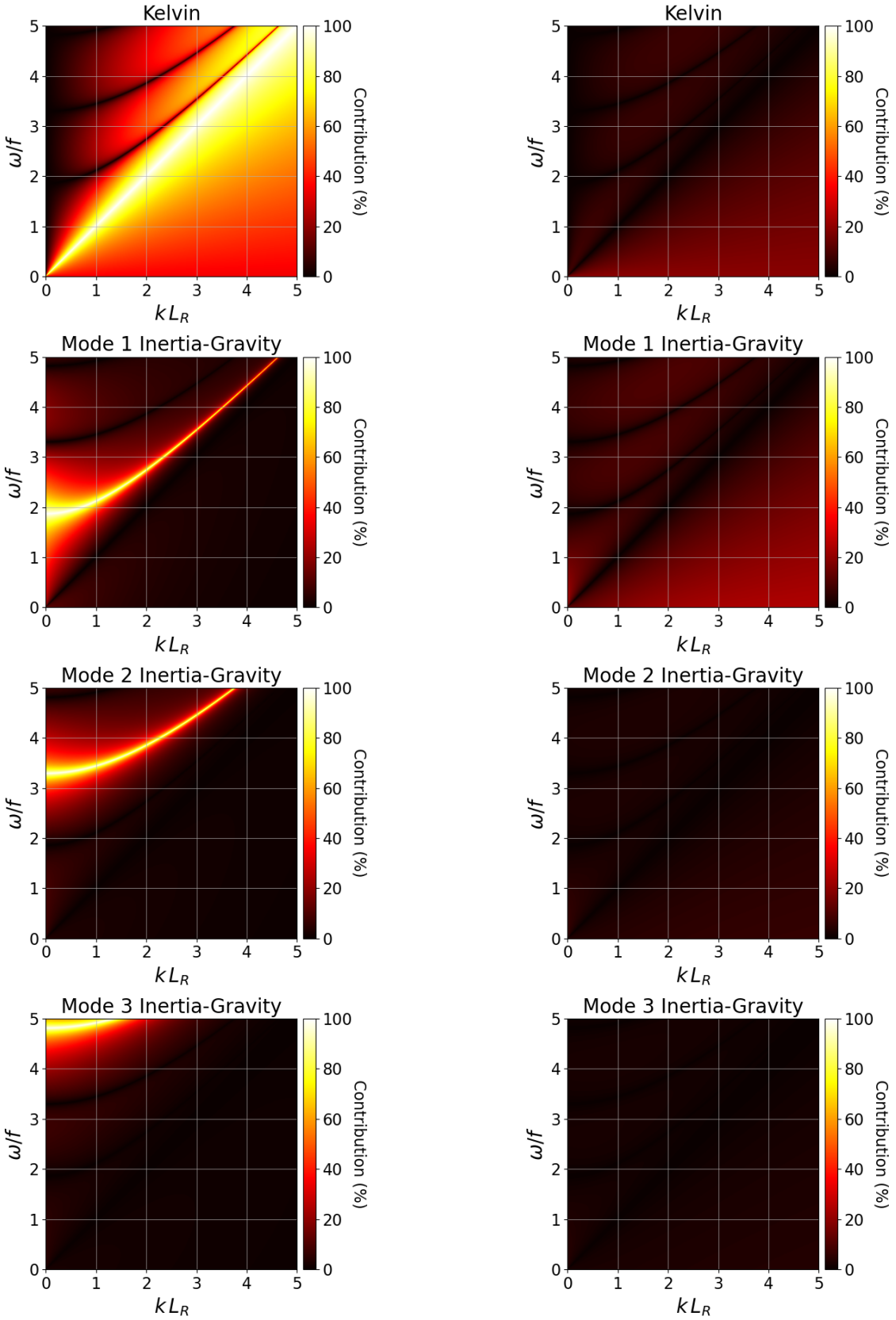

(a) Rightward-propagating modes

(b) Leftward-propagating modes

Figure 3.6: Modal contributions (%) of low-order surface gravity waves propagating: (a) rightwards; (b) leftwards. Modal contributions represent the response of a potential forcing proportional to $\exp(-y/L_R)$ with along-shore wavenumber k and forcing frequency ω.

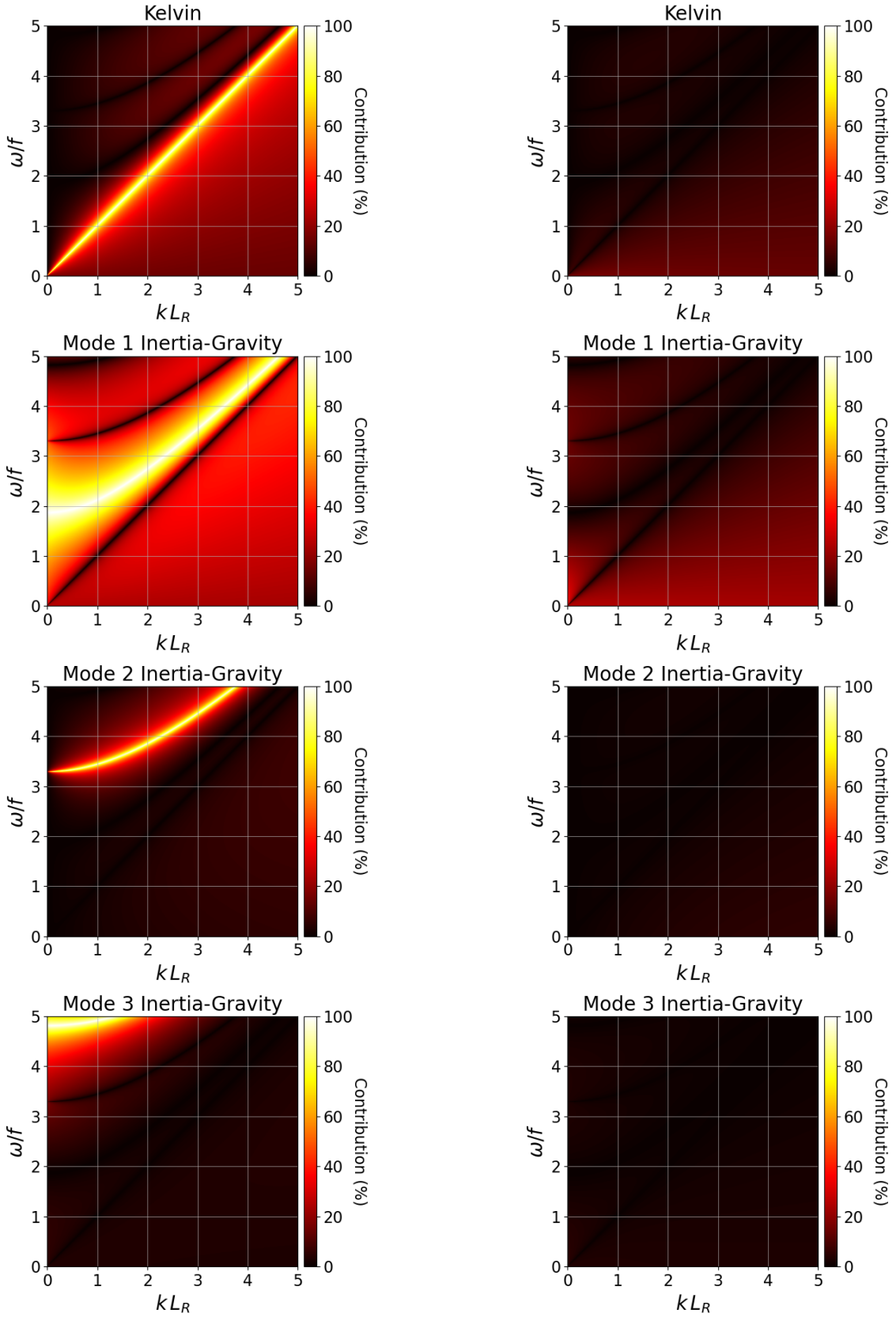

(a) Rightward-propagating modes

(b) Leftward-propagating modes

Figure 3.7: Modal contributions (%) of low-order surface gravity waves propagating: (a) rightwards; (b) leftwards. Modal contributions represent the response of a potential forcing proportional to $1 - y/L_R$ with along-shore wavenumber k and forcing frequency ω.

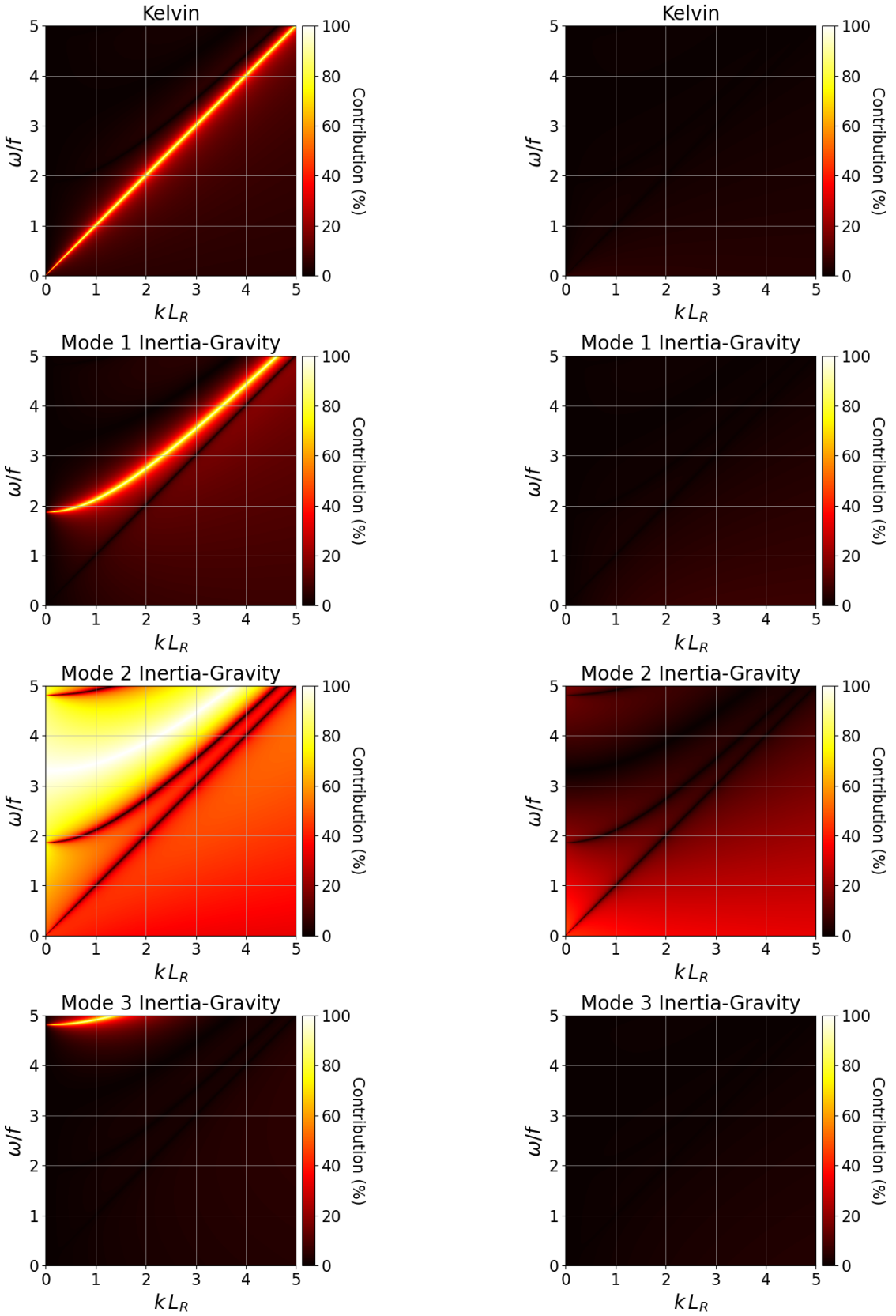

(a) Rightward-propagating modes

(b) Leftward-propagating modes

Figure 3.8: Modal contributions (%) of low-order surface gravity waves propagating: (a) rightwards; (b) leftwards. Modal contributions represent the response of a potential forcing proportional to $\cos(2\pi\, y/L_y)$ with along-shore wavenumber k and forcing frequency ω.

shown in Figure 3.4. In conclusion, the rightward-propagating Kelvin mode is excited the strongest. For tidal frequencies at mid-latitude, the Kelvin wave is expected to be the principal component (at least 40%) of the surface tide.

The second form of the potential forcing we consider, shown in Figure 3.7, is for an equilibrium tide proportional to $1 - y/L_R$. The idea behind this forcing is twofold: the forcing is almost spatially uniform, particularly for the cross-shore momentum component; the equilibrium tide should be almost identical to the previous equilibrium tide proportional to $\exp(-y/L_R)$ along the continental margin. This is because for $y/L_R \ll 1$,

$$\exp\left(-y/L_R\right) = 1 - y/L_R + O\left(\left(y/L_R\right)^2\right).$$

While the leftward-propagating modes continue to play little role in the constitution of the surface tide, the composition for rightward-propagating modes is remarkably different to the previous case for which the equilibrium tide was proportional to $\exp\left(-y/L_R\right)$. To begin, the Kelvin mode is less excited, but remains significantly close to resonance whereby $\omega/f \approx 1.4$ and $k\,L_R \approx 1.4$. Instead, odd rightward-propagating inertia-gravity modes have a greater contribution to the form of the surface tide and are typically no less than $\sim 30\%$. The latter is shown by the thick bright resonant bands for modes 1 and 3 in Figure 3.7a, while the Kelvin mode and the mode 2 inertia-gravity mode see much thinner bright bands around their fundamental frequencies.

So far, we have seen two different forcing scenarios: one which excites primarily the rightward-propagating Kelvin mode, and one which excites primarily the odd rightward-propagating inertia-gravity modes. The last forcing scenario we consider, shown in Figure 3.8, excites primarily the mode 2 rightward-propagating inertia-gravity wave. The modal contribution of the mode-2 inertia-gravity mode is typically around 40%, but much greater close to resonance. Here, the equilibrium tide is proportional to $\cos\left(2\pi\, y/L_y\right)$. Again, while the leftward-propagating modes are weakly excited, the mode 2 leftward-propagating inertia-gravity mode constitutes around 30% for typical tidal forcing parameters. All other rightward-propagating modes are only excited close to their fundamental frequencies.

In all three scenarios, even if the Kelvin wave is unlikely to have the greatest shape factor, the fact that the along-shore wavenumber and semi-diurnal forcing frequencies correspond well with the Kelvin tide, the frequency factor is likely to be large, and result in a strong excitation of the Kelvin mode. We conclude from this investigation that a truncation of the surface tide to include solely the Kelvin wave is reasonable when considering $\omega/f \approx k\,L_R = O\left(1.4\right)$ at mid-latitude whereby $f \approx 10^{-4}\,\mathrm{s}^{-1}$.

3.3.3 Intermediate Summary

In this section, forced time-periodic modes of the surface tide of an arbitrary basin were considered using normal-mode theory of the linearised decoupled barotropic shallow-water

equations. Following the methodology of both Platzman (1972) and Boyce et al. (2017) to construct the Sturm–Liouville problem, analytical expressions for modal coefficients were derived, showing that for arbitrary potential forcing and a parameterisation of bottom friction, the coefficients were the product of two factors. The first of which was the frequency factor and was responsible for a resonant response when the forcing frequency was close to a mode's fundamental frequency. The second of which was the shape factor and considered how well the potential forcing correlated with a mode's spatial structure.

To obtain tractable solutions, a channel of uniform depth was considered to derive the analytical free-wave solutions for modes periodic in both time and the along-shore. This was used as a crude model of an ocean basin, such as the Atlantic ocean. In this set-up, two types of non-trivial modes were found: Kelvin waves and inertia-gravity waves. These are large-scale waves, and typically super-inertial. However, this is not the case for the Kelvin wave for small along-shore wavenumbers. Notwithstanding, for diurnal and semi-diurnal forcing frequencies, the fundamental frequency of the rightward-propagating Kelvin wave (for sufficiently large along-shore wavenumbers) was typically closest. Since the frequency factor is inversely proportional to the difference in forcing frequency and fundamental frequency, the closer these two frequencies are, the greater the excitation.

However, it is not just a matter of how close a mode's fundamental frequency is to the forcing frequency. It is almost of equal importance to consider the spatial structure of the equilibrium tide. Through three different forcing scenarios, it was shown that different modes can be excited. For example, an equilibrium tide proportional to $\exp(-y/L_R)$ results in a strong excitation of the rightward-propagating Kelvin mode in ω/f–$k\,L_R$ parameter space because of the correlation between cross-shore spatial structures.

In summary, we conclude that since the forcing frequency correlates well with that of the fundamental frequency of the Kelvin wave for tidal length scales, it suffices to model the surface tide by considering uniquely the Kelvin wave. Neglecting the excitation of other modes allows the tide to be modelled in two manners: a potentially forced tide with bottom friction parameterisation (the modal coefficient is readily available to us through equation (3.43)), or as a free wave where for a given forcing frequency, an associated along-shore wavenumber is given. The amplitude of the free-wave solution is then given by some prescription of the solution at a particular cross-shore position. Useful prescriptions of the Kelvin wave solution include the surface displacement at the shoreline (used in Chapters 6 and 7) or the volume transport at the shelf break (used in Section 4.3.3).

For now, we have limited the form of the surface tide to that over uniform topography. This simplification allowed well-known analytical solutions to be obtained. However, to consider internal-tide generation over continental margins, it is necessary to consider variable bottom topography in the form of a continental slope. Not only will the latter lead to non-zero cross-shore volume transports over the shelf break but will also allow coupling between the surface and internal tide. Since the internal-tide generation problem is linear, the contribution from inertia-gravity waves can be added to that of the Kelvin wave. We

argue that given the Kelvin wave is the dominant contribution to internal-tide forcing, it is therefore the case that the wave is the dominant contribution to the internal-tide response. These factors are key in our aim of understanding internal tides generated along continental margins, as well as their implied time-averaged radiating energy fluxes.

3.4 Coastal Kelvin Wave

Motivated by the data shown in Figure 1.5 of Section 1.2, we consider a model for the continental shelf whereby fluid depth

$$h(y) = \begin{cases} H_C, & 0 \leq y \leq L_C, \\ H_C + (H_D - H_C)\,\varphi\left(\dfrac{y - L_C}{L_S}\right), & L_C \leq y \leq L_C + L_S, \\ H_D, & y > L_C + L_S. \end{cases} \tag{3.72}$$

Here, $H_C = O(200\,\mathrm{m})$, $H_D = O(4,000\,\mathrm{m})$, $L_C = O(100\,\mathrm{km})$ and $L_S = O(50\,\mathrm{km})$ represent the coastal shelf depth, the deep ocean depth, the shelf width, and the slope width, while the shoreline is positioned at $y = 0$. The function $\varphi : [0,1] \to [0,1]$ with $\varphi(0) = 0$ and $\varphi(1) = 1$ is any monotonically increasing function, such as $\varphi(Y) = Y$ or $\varphi(Y) = \sin^2(\pi Y/2)$. A schematic of the slope-topography is shown in Figure 3.9.

To isolate the Kelvin wave, we consider solutions once more of the form

$$\mathbf{a}(x,y,t) = \mathrm{Re}\left\{\hat{\mathbf{a}}(y)\,\exp\left(i\left(k\,x - \omega\,t\right)\right)\right\}$$

to (3.13). These are solutions which are periodic in time and along-shore spatial direction. To enable future scaling arguments in developing an explicit solution to the coastal Kelvin wave, we non-dimensionalise as follows:

$$\mathbf{U} = \tilde{c}\,\mathbf{U}^*, \qquad P = \tilde{c}^2\,P^*, \qquad \mathbf{x} = L_R\,\mathbf{x}^*, \qquad t = t^*/|f|, \qquad \mathbf{F} = L_R\,\mathbf{F}^*, \tag{3.73}$$

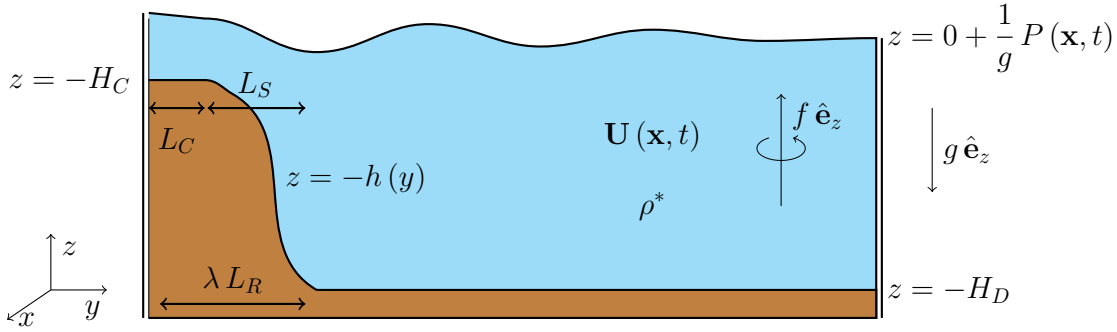

Figure 3.9: System schematic of surface tide flowing along some arbitrary coastal topography $z = -h(y)$ defined over coastal length scale $L_R\,\lambda = L_C + L_S$. We recall that Rossby radius of deformation $L_R = \sqrt{g\,H_D}/|f|$, while L_C and L_S represent respectively the shelf width and slope width. Over the coastal shelf, fluid depth $h(y) = H_C$, and transitions to the deep ocean depth $h(y) = H_D$ over the slope width.

where $\tilde{c} = \sqrt{g\,H_D} = O\,(200\,\mathrm{m/s})$ and $L_R = \tilde{c}/|f| = O\,(2,000\,\mathrm{km})$ at mid-latitude whereby Coriolis parameter $f = O\left(10^{-4}\,\mathrm{s}^{-1}\right)$. We also recall that barotropic wave speed squared $c^2\,(y) = g\,h\,(y)$ for fluid depth $h(y)$ as given in (3.72). As a result, $c^2/\tilde{c}^2 = h\,(y)\,/H_D = \tilde{h}\,(y)$ with $\tilde{h}\,(y^*) = 1$ for $y^* \geq \lambda$, where $\lambda = (L_C + L_S)\,/L_R = O\left(10^{-2}\right) \ll 1$ represents the non-dimensional coastal length scale.

Applying the latter to (3.13), we obtain the non-dimensional Sturm–Liouville problem

$$i\,\tilde{\mathcal{L}}\,[\hat{\mathbf{a}}] = -i\,\tilde{\omega}\,\tilde{I}\,\hat{\mathbf{a}} + i\,\tilde{\mathbf{F}}, \tag{3.74}$$

where

$$\tilde{\mathcal{L}} \equiv i \begin{pmatrix} 0 & -1 & i\,\tilde{k} \\ +1 & 0 & \dfrac{\mathrm{d}}{\mathrm{d}y^*} \\ i\,\tilde{k}\,\tilde{h} & \dfrac{\mathrm{d}}{\mathrm{d}y^*}\tilde{h} & 0 \end{pmatrix} \tag{3.75}$$

and $\tilde{I}$ is the 3×3 identity matrix, while

$$\tilde{k} = L_R\,k, \qquad\qquad \tilde{\omega} = \omega/f \tag{3.76}$$

are non-dimensional parameters which consider respectively the ratio of the along-shore wavelength with the dominant horizontal length scale that is the Rossby radius of deformation, and the forcing frequency with the Coriolis parameter. For typical coastal parameters at mid-latitude forced at tidal frequency, we have already established that $\tilde{k} = O\,(1)$ and $\tilde{\omega} = O\,(1)$.

3.4.1 Orthogonal Modes

Dropping all tildes, let us consider the homogeneous problem to (3.74)–(3.75),

$$(\mathcal{L} - i\,\omega\,I)\,\mathbf{a} = \mathbf{0}, \tag{3.77}$$

which can be reduced to the second-order variable-coefficient ODE in surface displacement,

$$\left(h\,(y)\;P'\,(y)\right)' - K\,(y)\;P\,(y) = 0, \qquad K\,(y) = 1 + k^2\,h\,(y) - \omega^2 - k\,\omega^{-1}\,h'\,(y)\,, \tag{3.78}$$

where the prime denotes the derivative with respect to cross-shore spatial variable y.

As indicated by our choice of non-dimensionalisation along the vertical, we shall consider a semi-infinite domain in the cross-shore direction. The supposition here is that the waves are trapped at the coastal boundary. Here, we require an impermeability condition at the coastal boundary,

$$V\,(y = 0) = 0 \qquad\qquad \Longrightarrow \qquad\qquad \left(\frac{\mathrm{d}}{\mathrm{d}y} + k\,\omega^{-1}\right) P\,(y = 0) = 0. \tag{3.79}$$

Additionally, we require bounded solutions in space, implying the use of the decaying

condition:

$$|U(y)|, |V(y)|, |P(y)| \to 0 \qquad \text{as} \qquad y \to +\infty. \tag{3.80}$$

Equations (3.77), (3.79) and (3.80) form a boundary-value problem which can be solved on a finite domain, so long as there exists a point beyond which fluid depth is constant such that surface displacement satisfies the constant coefficient second-order ODE

$$\left(\frac{\mathrm{d}^2}{\mathrm{d}y^2} - l_D^2\right) P(y) = 0 \qquad \text{with} \qquad l_D = +\sqrt{k^2 + 1 - \omega^2} \tag{3.81}$$

denoting the non-dimensional cross-shore wavenumber in this region. Provided that

$$l_D^2 = k^2 + 1 - \omega^2 > 0, \tag{3.82}$$

the decaying condition

$$P(y) \propto \exp(-l_D\, y) \tag{3.83}$$

for $y \geq \lambda = (L_C + L_S)/L_R \ll 1$ can be imposed, which through (3.77), satisfies (3.80).

3.4.2 Analytical Solution to Kelvin Wave with Coastal Topography

In this section, we provide an analytical solution to the coastal Kelvin wave over arbitrary coastal topography defined over length scale $L_C + L_S$ much smaller than Rossby radius of deformation, L_R. The latter assumption allows us to introduce non-dimensional parameter $0 < \lambda \equiv (L_C + L_S)/L_R \ll 1$. The introduction of non-dimensional parameter λ permits an analytical solution to the perturbed Kelvin Wave (PKW) using asymptotic matching.

To obtain an analytical solution, much like that carried out in both Miles (1972) and Smith (1972), we consider an inner and an outer region over which the solution can be obtained as a power series in $\lambda = (L_C + L_S)/L_R$. These solutions, subject to continuity in volume transport and pressure, allow the solutions to be matched over some intermediate length scale. A composite solution, as well as an explicit dispersion relation, for arbitrary coastal topography is obtained, provided that $\lambda \ll 1$.

Outer Asymptotic Solutions

We know in the outer region where non-dimensional fluid depth $h = 1$, equation (3.78) becomes

$$\left(\frac{\mathrm{d}^2}{\mathrm{d}y^2} - l_D^2\right) P(y) = 0, \qquad l_D = +\sqrt{k^2 + 1 - \omega^2}, \tag{3.84}$$

and holds for all orders of λ. In particular, if we seek coastally trapped waves, we require $l_D^2 > 0$, implying the condition on wave frequency

$$\omega^2 < 1 + k^2, \tag{3.85}$$

and that pressure takes the form

$$P(y) = A \exp(-l_D\, y), \tag{3.86}$$

where A is the non-dimensional wave amplitude at $y = 0$. In the case of an unperturbed coastal Kelvin wave in a channel of uniform depth, we have the known result

$$\omega = \pm k, \qquad\qquad l_D = 1. \tag{3.87}$$

With the existence of a relatively small coastal feature of non-dimensional width $\lambda \ll 1$, let us consider a perturbation to the coastally trapped mode given in (3.87), such that for ω_1, ω_2 unknown,

$$\omega = k\left(1 + \omega_1\,\lambda + \omega_2\,\lambda^2 + O\left(\lambda^3\right)\right), \tag{3.88}$$

implying

$$\omega^2 = k^2\left(1 + 2\omega_1\,\lambda + \left(2\omega_2 + \omega_1^2\right)\lambda^2 + O\left(\lambda^3\right)\right), \tag{3.89}$$

meaning that from (3.86), we deduce that the cross-shore wavenumber

$$\begin{aligned} l &= \sqrt{k^2 + 1 - k^2\left(1 + 2\omega_1\,\lambda + \left(2\omega_2 + \omega_1^2\right)\lambda^2 + O\left(\lambda^3\right)\right)} \\ &= 1 - \omega_1\,k^2\,\lambda - \frac{1}{2}\left(\omega_1^2\,k^2\left(1 + k^2\right) + 2\omega_2\right)\lambda^2 + O\left(\lambda^3\right). \end{aligned} \tag{3.90}$$

Substituting (3.90) into (3.86), it is found to second order that the outer pressure field is

$$\begin{aligned} P_{\text{outer}}(y) = A\Bigg(1 + \omega_1\,k^2\,y\,\lambda + \frac{1}{2}k^2\,y\left(\left(1 + \ k^2\,(1+y)\right)\omega_1^2 + 2\omega_2\right)\lambda^2 \\ + O\left(\lambda^3\right)\Bigg)\exp(-y). \end{aligned} \tag{3.91}$$

Note that we could have alternatively used (3.84), and have solved in various orders of λ.

To find the outer solutions of the horizontal velocities, we substitute (3.91) into (3.6), giving along-shore velocity

$$\begin{aligned} U_{\text{outer}}(y) &= \left(1 + \frac{1}{2}\omega_1^2\,k^2\,\lambda^2 + O\left(\lambda^3\right)\right)P_{\text{out}}(y) \\ &= A\Bigg(1 + \omega_1\,k^2\,y\,\lambda + \frac{1}{2}k^2\left((1+y)\left(1 + k^2\,y\right)\omega_1^2 + 2y\,\omega_2\right)\lambda^2 \\ &\quad + O\left(\lambda^3\right)\Bigg)\exp(-y), \end{aligned} \tag{3.92}$$

and cross-shore velocity

$$V_{\text{outer}}(y) = -A\,i\,k\,\omega_1\,\lambda\left(1+\frac{1}{2\omega_1}\left(\omega_1^2\,k^2+2\omega_2\right)\lambda+O\left(\lambda^2\right)\right)\left(1+\omega_1\,k^2\,y\,\lambda\right.$$
$$\left.+\,O\left(\lambda^2\right)\right)\exp(-y)$$
$$= -A\,i\,k\,\omega_1\,\lambda\left(1+\frac{1}{2\omega_1}\left(2\omega_2+\omega_1^2\,k^2\,(2\,y+1)\right)\lambda+O\left(\lambda^2\right)\right)\exp(-y). \quad (3.93)$$

Inner Asymptotic Solutions

Along the continental shelf, we anticipate a spatially constant leading-order set of solutions, such that

$$U_{\text{inner}}(Y) = U_0 + U_1(Y)\;\lambda + O\left(\lambda^2\right), \quad (3.94)$$
$$V_{\text{inner}}(Y) = V_0 + V_1(Y)\;\lambda + V_2(Y)\;\lambda^2 + O\left(\lambda^3\right), \quad (3.95)$$
$$P_{\text{inner}}(Y) = P_0 + P_1(Y)\;\lambda + P_2(Y)\;\lambda^2 + O\left(\lambda^3\right) \quad (3.96)$$

for coordinate transformation

$$Y = y/\lambda = O(1) \qquad \Longrightarrow \qquad \partial_y = \frac{1}{\lambda}\partial_Y,$$

where constants U_0, V_0 and P_0, and functions $U_1(Y)$, $V_1(Y)$, $V_2(Y)$, $P_1(Y)$ and $P_2(Y)$ are yet to be determined.

Substitution of inner solutions (3.94)–(3.96) into system (3.77), using the fact that $V_0 = 0$ to maintain geostrophic balance in the cross-shore, allows us to consider terms of equal order in λ to obtain the following two sets of equations, where at $O(1)$:

$$-i\,k\,U_0 = -i\,k\,P_0, \quad (3.97)$$
$$U_0 = -\frac{\mathrm{d}}{\mathrm{d}Y}P_1, \quad (3.98)$$
$$i\,k\,h\,U_0 + \frac{\mathrm{d}}{\mathrm{d}Y}\left(h(y)\;V_1(y)\right) = i\,k\,P_0, \quad (3.99)$$

while at $O(\lambda)$:

$$-i\,k\left(\omega_1\,U_0+U_1\right) - V_1 = -i\,k\,P_1, \quad (3.100)$$
$$U_1 - i\,k\,V_1 = -\frac{\mathrm{d}}{\mathrm{d}Y}P_2, \quad (3.101)$$
$$i\,k\,h\,U_1 + \frac{\mathrm{d}}{\mathrm{d}Y}\left(h\,V_2\right) = i\,k\left(\omega_1\,P_0+P_1\right). \quad (3.102)$$

Equations (3.97)–(3.98) indicate that to leading order geostrophic balance is obtained in the cross-shore spatial direction, balancing the cross-shore Coriolis force with the pressure gradient induced at the coastal boundary.

Equations (3.97)–(3.99) indicate that

$$U_0 = P_0, \qquad P_1(Y) = -\int_0^Y U_0 \,\mathrm{d}Y + C_1,$$
$$V_1(Y) = \frac{i\,k}{h(Y)} \int_0^Y \left(P_0 - h(\tilde{Y})U_0\right) \mathrm{d}\tilde{Y}, \tag{3.103}$$

allowing us to deduce that

$$U_0 = P_0, \qquad P_1(Y) = -P_0\,(Y + C_1) \qquad V_1(Y) = \frac{i\,k\,P_0}{h(Y)} \int_0^Y \left(1 - h(\tilde{Y})\right) \mathrm{d}\tilde{Y}. \tag{3.104}$$

Indeed, we remark that $V_1(0) = 0$, satisfying the impermeability condition at the coastal boundary. Here, the factorised constant of integration C_1 will be determined through matching.

Using equation (3.100), it follows that the first-order correction to the inner solution of along-shore velocity is

$$\begin{aligned} U_1(Y) &= P_1(Y) - U_0\,\omega_1 + \frac{i}{k} V_1(Y) \\ &= -P_0 \left(Y + C_1 + \omega_1 + \frac{1}{h(Y)} \int_0^Y \left(1 - h(\tilde{Y})\right) \mathrm{d}\tilde{Y}\right). \end{aligned} \tag{3.105}$$

Further corrections to cross-shore velocity and pressure are possible. For example, substituting (3.105) into (3.102) gives the second-order correction to cross-shore velocity,

$$\begin{aligned} V_2(Y) &= \frac{i\,k}{h(Y)} \int_0^Y \left(P_0\,\omega_1 + P_1(\tilde{Y}) - h(\tilde{Y})\,U_1(\tilde{Y})\right) \mathrm{d}\tilde{Y} \\ &= \frac{i\,P_0\,k}{h(Y)} \int_0^Y \left(\omega_1 - Y - C_1 + h(\tilde{Y}) \left(\tilde{Y} + C_1 + \omega_1 + \right.\right. \\ &\qquad \left.\left. \frac{1}{h(\tilde{Y})} \int_0^{\tilde{Y}} \left(1 - h(\hat{Y})\right) \mathrm{d}\hat{Y}\right)\right) \mathrm{d}\tilde{Y} \\ &= \frac{i\,P_0\,k}{h(Y)} \int_0^Y \left(\omega_1 \left(1 + h(\tilde{Y})\right) - \left(\tilde{Y} + C_1\right) \left(1 - h(\tilde{Y})\right) + \right. \\ &\qquad \left. \int_0^{\tilde{Y}} \left(1 - h(\hat{Y})\right) \mathrm{d}\hat{Y}\right) \mathrm{d}\tilde{Y}. \end{aligned} \tag{3.106}$$

Likewise, to find the second-order correction to pressure, we combine equations (3.100) and (3.101):

$$\begin{aligned} \frac{\mathrm{d}}{\mathrm{d}Y} P_2 &= \frac{i}{k} \left(k^2 - 1\right) V_1(Y) - P_1(Y) + \omega_1\,U_0 \\ &= P_0 \left(Y + C_1 + \omega_1 - \frac{k^2 - 1}{h(Y)} \int_0^Y \left(1 - h(\tilde{Y})\right) \mathrm{d}\tilde{Y}\right), \end{aligned} \tag{3.107}$$

implying that

$$P_2(Y) = \frac{P_0}{2}\left(Y\left(Y + 2\left(\omega_1 + C_1\right)\right)\right. \\ \left. -2\left(k^2-1\right)\int_0^Y \frac{1}{h(\tilde{Y})}\left(\int_0^{\tilde{Y}}\left(1-h(\hat{Y})\right)\mathrm{d}\hat{Y}\right)\mathrm{d}\tilde{Y} + C_2\right) \tag{3.108}$$

for undetermined constant of integration, C_2.

It is through asymptotic matching over an intermediate length scale, that we can determine the unknowns in inner and outer solutions. Ultimately, this allows us to construct a uniform composite set of solutions describing a perturbed Kelvin wave over arbitrary coastal topography in a semi-infinite domain.

First-Order Asymptotic Matching

To consider constructing a uniform composite solution valid throughout the domain, let us consider van Dyke matching through the use of an intermediate interval. By considering the intermediate variable $\hat{y}$ such that

$$y = \hat{y}\,\lambda^{\alpha} \qquad \Longrightarrow \qquad Y = \hat{y}\,\lambda^{\alpha-1}, \tag{3.109}$$

where $0 < \alpha < 1$, we may find the matching solutions over the intermediate scale where our inner and outer solutions match, allowing us to define $\mathbf{a}_{\text{match}}$. This matching solution is then used to construct the uniform composite solution,

$$\mathbf{a}_{\text{composite}}(y) = \mathbf{a}_{\text{inner}}(y) + \mathbf{a}_{\text{outer}}(y) - \mathbf{a}_{\text{match}}(y). \tag{3.110}$$

To begin, let us consider inner and outer solutions of pressure, P, up to first order in λ, as given in equations (3.96) and (3.91):

$$P_{\text{inner}}(Y) = P_0\left(1 - (Y + C_1)\,\lambda + O\left(\lambda^2\right)\right), \tag{3.111}$$

$$P_{\text{outer}}(y) = A\left(1 + \omega_1 k^2\, y\,\lambda + O\left(\lambda^2\right)\right)\exp(-y). \tag{3.112}$$

To construct the composite solution, we must first obtain the matching solution over the intermediate interval. Upon substitution of (3.109) into (3.111)–(3.112), it follows that

$$A = P_0, \qquad C_1 = 0, \tag{3.113}$$

giving

$$P_{\text{match}} = P_0\left(1 - \hat{y}\,\lambda^{\alpha} + O\left(\lambda^2, \lambda^{2\alpha}\right)\right) = P_0\,(1-y). \tag{3.114}$$

Likewise, we can match the cross-shore volume transport over the intermediate scale. Beginning with inner and outer solutions of cross-shore volume transport, $Q = h\,V$, with

cross-shore velocities V as given by equations (3.95) and (3.93) respectively, we have that

$$Q_{inner}(y) = i\,k\,P_0\,\lambda \int_0^{y/\lambda} (1 - h(Y\,\lambda))\,\mathrm{d}Y\,(1 + O(\lambda))\,, \tag{3.115}$$

$$Q_{outer}(y) = -i\,k\,P_0\,\omega_1\,\exp(-y)\,\lambda\,(1 + O(\lambda))\,, \tag{3.116}$$

which, upon substitution of intermediate variable $\hat{y} = y\,\lambda^{-\alpha}$ for $0 < \alpha < 1$, we conclude that

$$\omega_1 = -\int_0^1 (1 - h(y\,\lambda))\,\mathrm{d}y, \qquad\qquad Q_{match} = -i\,k\,P_0\,\omega_1\,\lambda, \tag{3.117}$$

recalling that non-dimensional fluid depth $h(y) = 1$ for $y \geq \lambda$. Moreover, since $0 < h(y) < 1$, it is remarked that coastal topography induces a retardation effect upon the wave frequency of the coastal Kelvin wave.

Defining $\delta = H_C/H_D = O\left(10^{-2}\right)$, the form of (3.72) allows a neat simplification of the first-order correction to wave frequency given in (3.117):

$$\begin{aligned}\omega_1 &= -(1-\delta)\left[\int_0^{1-\nu}\mathrm{d}y + \int_{1-\nu}^{1}\left(1 - \varphi\left(\frac{Y-(1-\nu)}{\nu}\right)\right)\mathrm{d}y\right] \\ &= -(1-\delta)\left[(1-\nu) + \int_{1-\nu}^{1}\left(1 - \varphi\left(\frac{Y-(1-\nu)}{\nu}\right)\right)\mathrm{d}y\right],\end{aligned} \tag{3.118}$$

defining $\nu = L_S/(L_C + L_S)$.

From equation (3.118), the case of step topography follows immediately in the limit $L_S \to 0$, and therefore $\nu \to 0$, giving

$$\omega_1 = -(1 - \delta)\,. \tag{3.119}$$

This correction is equivalent to results derived in §4.4 of Munk et al. (1970), and indicates that the greatest perturbation in the case of step topography to wave frequency occurs with a shallow shelf (such that $\delta = H_C/H_D \ll 1$, giving $\omega_1 \approx 1$) and a large shelf width (so long as $\lambda \ll 1$).

Having obtained the matching terms of both the pressure and cross-shore volume transport up to first order in $\lambda \equiv (L_C + L_S)/L_R$ over some intermediate scale, we determine that the perturbed coastal Kelvin wave—which accounts for arbitrary coastal topography in the cross-shore direction—has analytical non-dimensional pressure (analogous to surface displacement)

$$P_{PKW}(y) = P_0\,\exp(-y)\left(1 - |\omega_1|\,k^2\,y\,\lambda + O\left(\lambda^2\right)\right) \tag{3.120}$$

and non-dimensional cross-shore velocity

$$\begin{aligned}V_{PKW}(y) = \frac{i\,k\,P_0\,\lambda}{h(y)}\{&|\omega_1|\,(\exp(-y) - 1) + \\ &\int_0^{y/\lambda}(1 - h(Y\,\lambda))\,\mathrm{d}Y\Big\}\Big(1 + O(\lambda)\Big),\end{aligned} \tag{3.121}$$

along with non-dimensional wave frequency

$$\omega = k\left(1 - |\omega_1|\,\lambda + O\left(\lambda^2\right)\right), \qquad |\omega_1| = \int_0^1 \left(1 - h\left(Y\,\lambda\right)\right)\,\mathrm{d}Y. \tag{3.122}$$

As expected, the trivial Kelvin wave is obtained from equations (3.120)–(3.122) when $\lambda \to 0$. I.e. the cross-shore velocity vanishes as the pressure decays purely exponentially from the shoreline in the absence of coastal topography.

To understand the structure of cross-shore volume transport, we consider constructing a Taylor expansion of cross-shore volume transport $Q_{PKW}\left(y\right) = h\left(y\right)\cdot$(3.121) at the shoreline. Since

$$Q'_{PKW}\left(y\right) = -i\,k\,P_0\,\lambda\left\{|\omega_1|\exp\left(-y\right) + \left[1 - h\left(y\right)\right]/\lambda\right\}\Big(1 + O\left(\lambda\right)\Big) \tag{3.123}$$

and

$$Q''_{PKW}\left(y\right) = i\,k\,P_0\,\lambda\left\{|\omega_1|\exp\left(-y\right) + h'\left(y\right)/\lambda\right\}\Big(1 + O\left(\lambda\right)\Big), \tag{3.124}$$

which at the shelf break where $h(y) = \delta$, provided that and $h'\left(y\right)$ is differentiable, it follows that

$$Q'_{PKW}\left(y\right) = -i\,k\,P_0\left(1 - \delta\right)\Big(1 + O\left(\lambda\right)\Big) \tag{3.125}$$

$$Q''_{PKW}\left(y\right) = i\,k\,P_0\,h'\left(y\right)\Big(1 + O\left(\lambda\right)\Big). \tag{3.126}$$

Constructing the Taylor series at $y = 0$ with $Q_{PKW}\left(y\right) = 0$, cross-shore volume transport along the continental margin, to leading order in λ, is

$$Q_{PKW}\left(y\right) \approx -i\,k\,P_0\,y\left(\left(1 - \delta\right) - h'\left(y\right)\,y\right), \qquad y, \lambda \ll 1. \tag{3.127}$$

Moreover, if $h'\left(y\right)\,y \ll 1$ at the shelf break, it follows that the volume transport at the shelf break can be approximated further to give

$$Q_{PKW}\left(y\right) \approx -i\,k\,P_0\,y\left(1 - \delta\right), \qquad y, \lambda \ll 1. \tag{3.128}$$

For completeness, substitution of equations (3.120) and (3.121) into the along-shore component of (3.77), it follows that

$$\begin{aligned} U_{PKW}\left(y\right) &= \frac{i\,V + k\,P}{\omega} \\ &= P_0\,\exp\left(-y\right)\Bigg(1 + \frac{\omega_1}{h\left(y\right)}\Big\{h\left(y\right)\left(k^2\,y - 1\right) + 1 \\ &\qquad - \exp\left(+y\right)\Bigg(1 + \frac{1}{\omega_1}\int_0^{y/\lambda}\left(1 - h\left(Y\,\lambda\right)\right)\,\mathrm{d}Y\Bigg)\Big\}\,\lambda + O\left(\lambda^2\right)\Bigg). \end{aligned} \tag{3.129}$$

In Figures 3.10–3.11, we show the first-order free-wave composite solutions to the perturbed Kelvin wave, and compare the analytical solutions to numerical solutions found

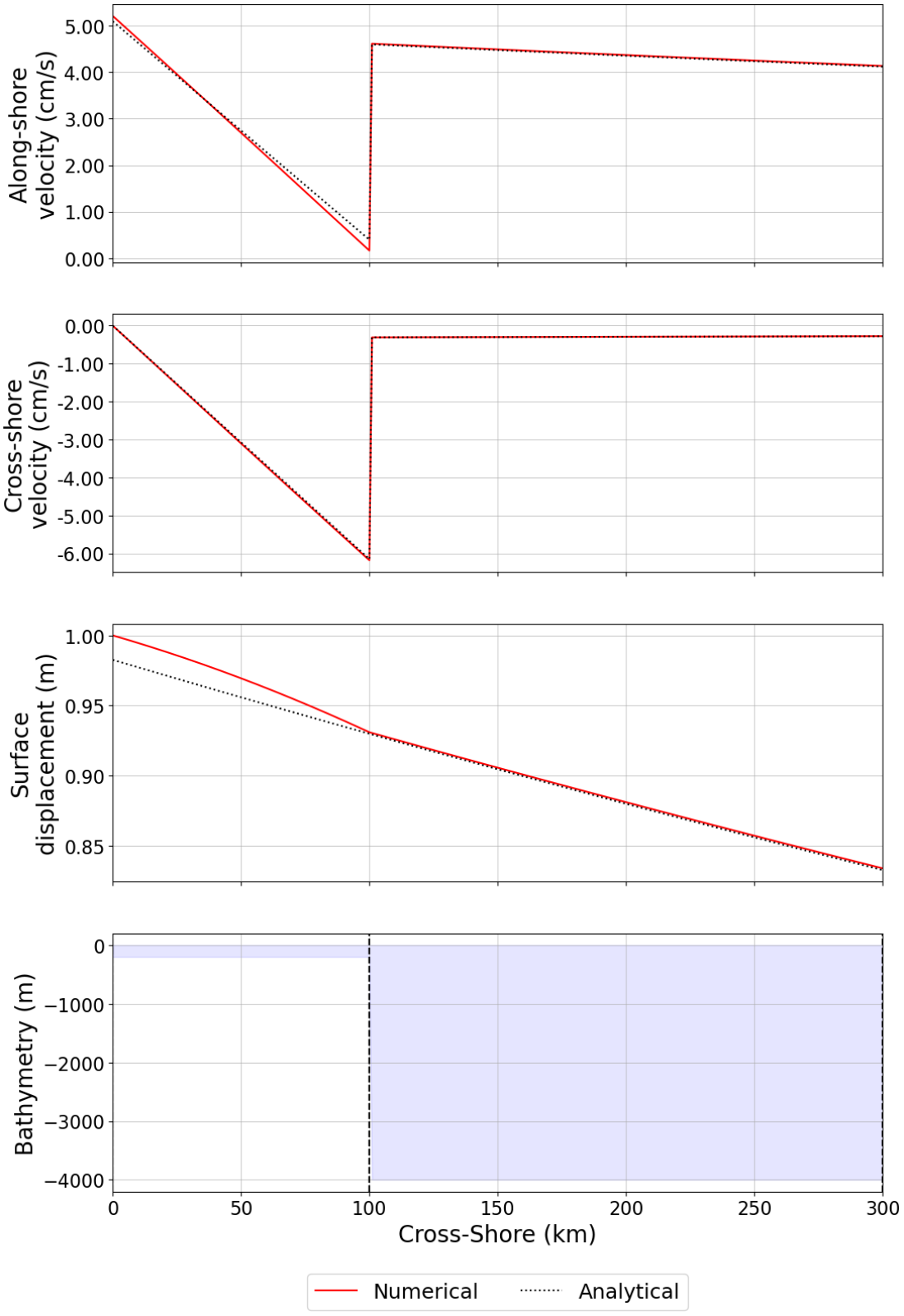

(a) Shelf profile ($L_S \to 0$)

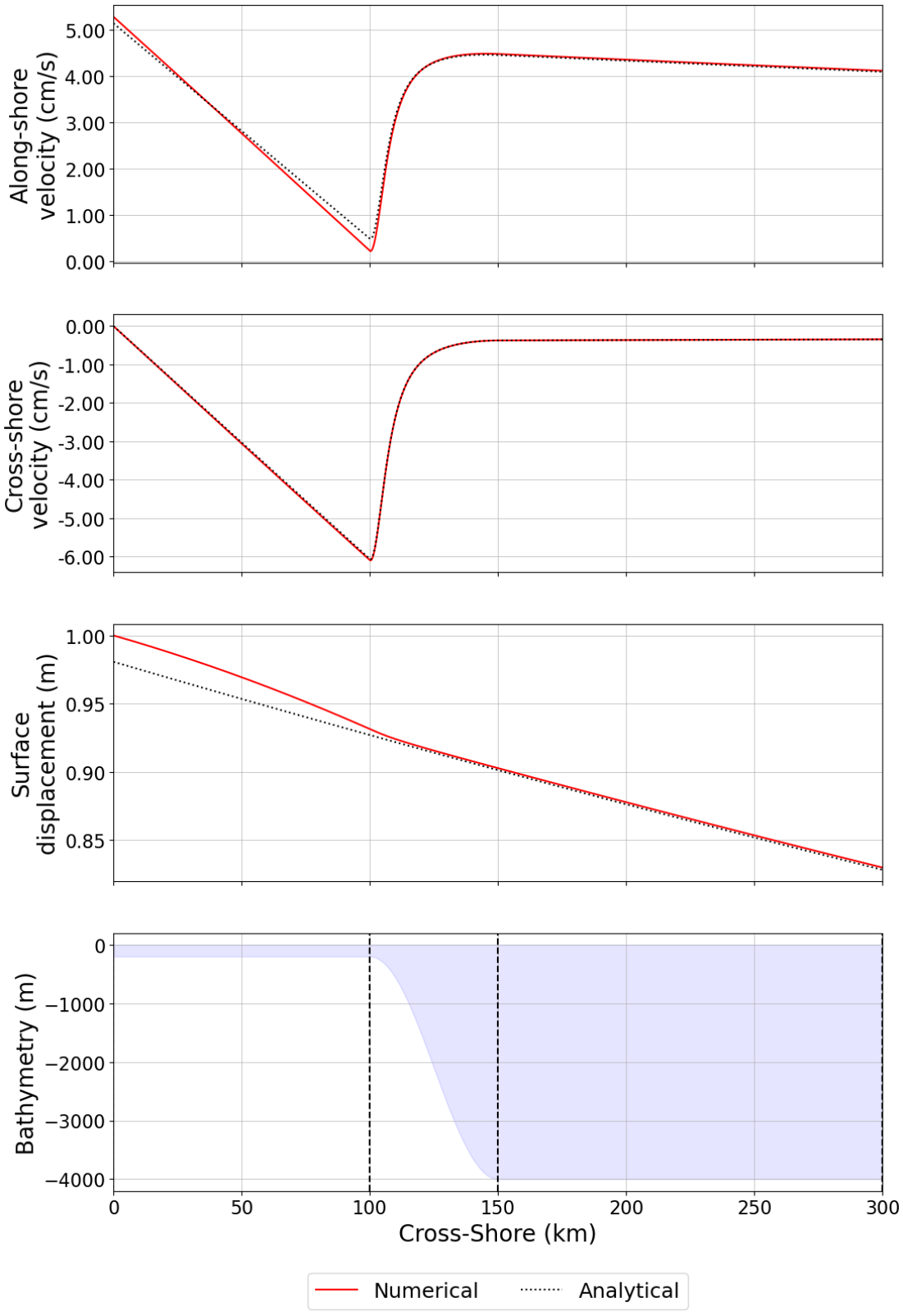

(b) Shelf-slope profile

Figure 3.10: First-order composite solution of perturbed Kelvin wave for when shelf width $L_C = 100\,\text{km}$ and slope width $L_S = 50\,\text{km}$ in the case of a: (a) shelf profile ($\lambda = 5 \times 10^{-2}$); (b) shelf-slope profile ($\lambda = 7.5 \times 10^{-2}$). Cross-shore velocity is out of phase by $\pi/2$, and surface displacement is shown in lieu of pressure. Slope topography is modelled using $\varphi(Y) = \sin^2(\pi Y/2)$ in (3.72).

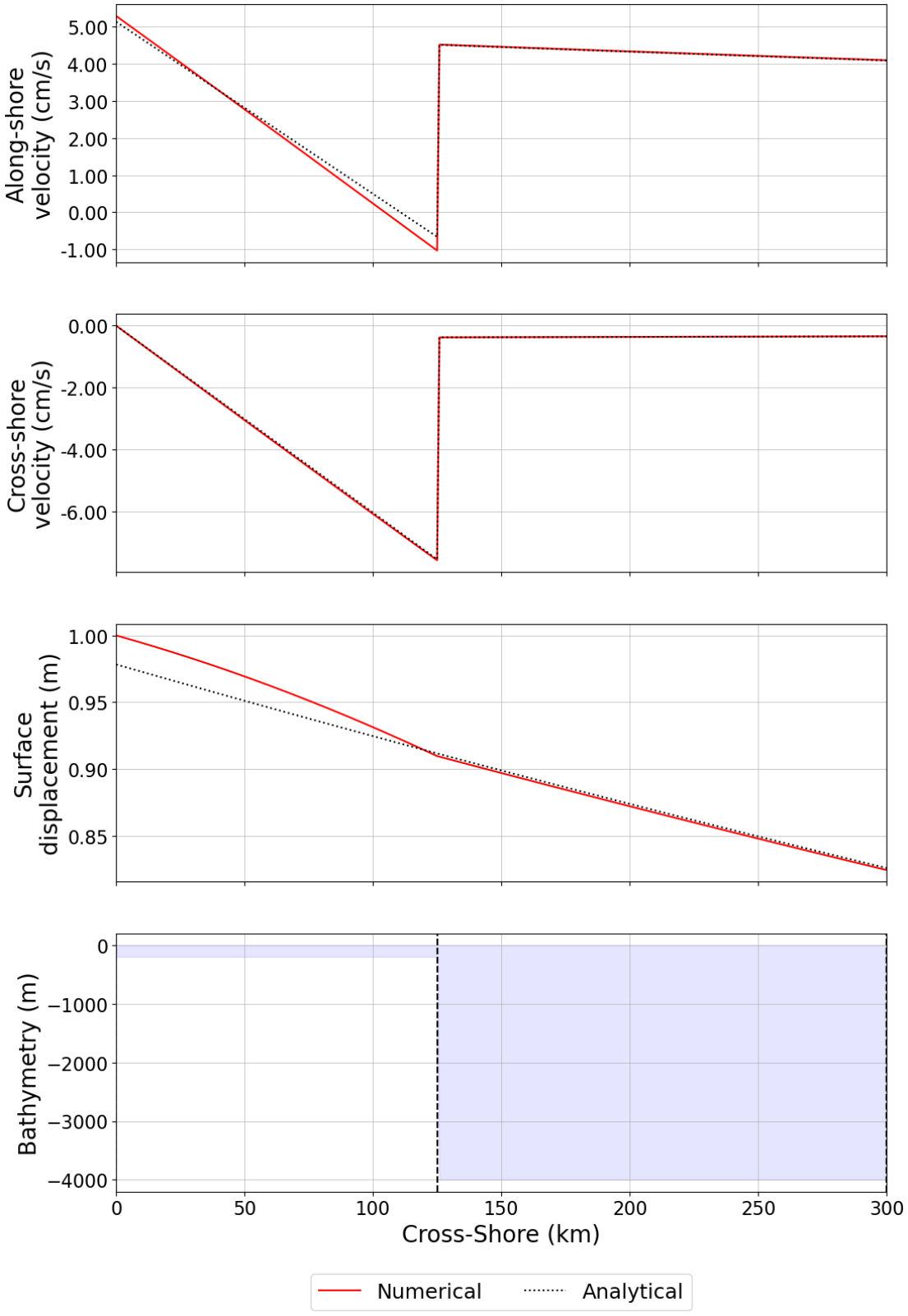

(a) Shelf profile ($L_S \to 0$)

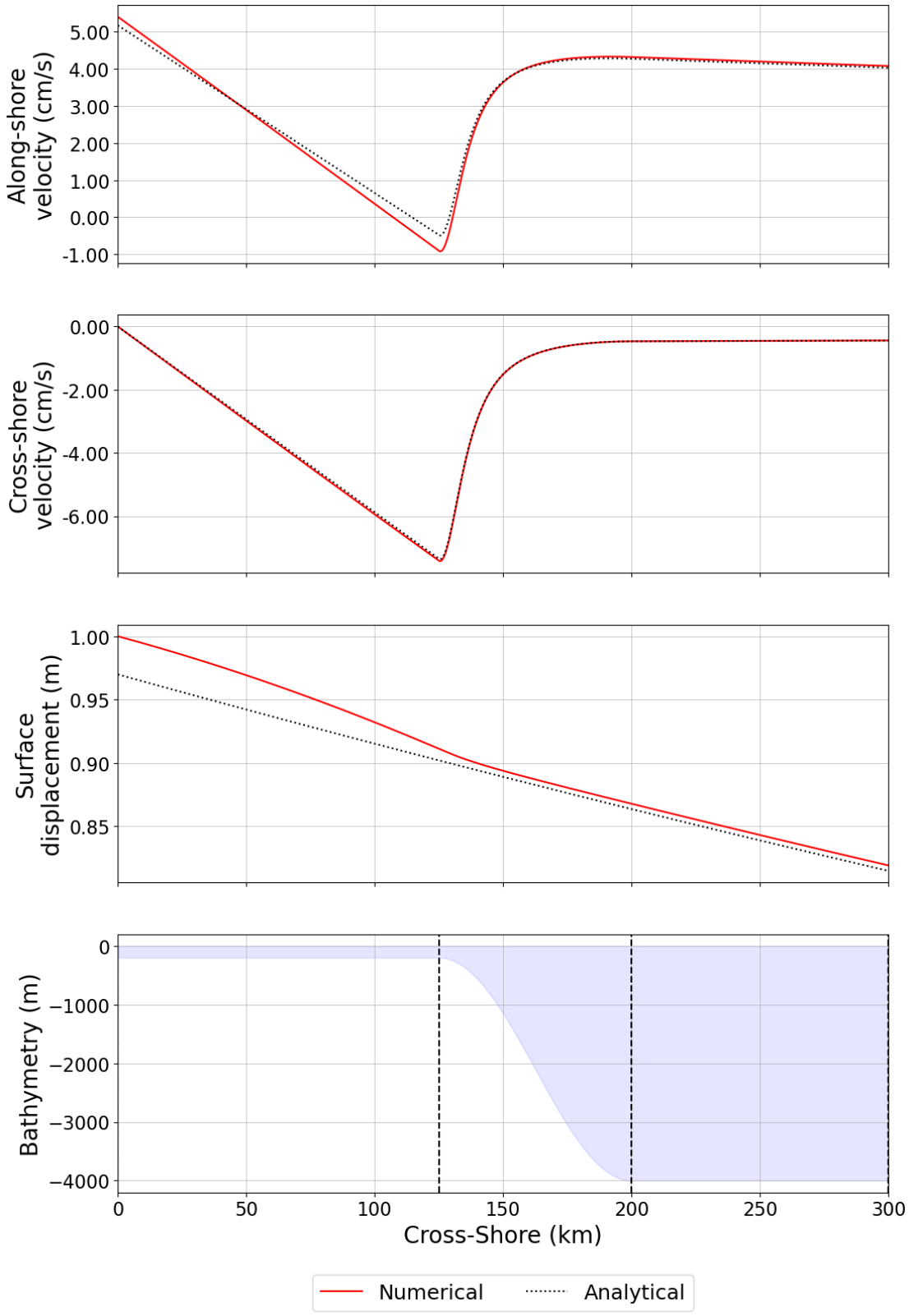

(b) Shelf-slope profile

Figure 3.11: First-order composite solution of perturbed Kelvin wave for when shelf width $L_C = 125\,\text{km}$ and slope width $L_S = 75\,\text{km}$ in the case of a: (a) shelf profile ($\lambda = 6.3\times10^{-2}$); (b) shelf-slope profile ($\lambda = 10^{-1}$). Cross-shore velocity is out of phase by $\pi/2$, and surface displacement is shown in lieu of pressure. Slope topography is modelled using $\varphi(Y) = \sin^2(\pi\, Y/2)$ in (3.72).

using the shooting method (see §18.1 of Press et al., 2007). We remark that the numerical solutions were obtained solving the SWEs using the shooting method with adaptive time-stepping (using the Cash–Karp method), having specified impermeability at $y = 0$ and decaying (equation (3.83)) at $y = 2\lambda$, and then matching at $y = \lambda$ as to ensure continuity in cross-shore volume transport and pressure. Furthermore, the shooting method is initialised using (3.122), the first-order analytical solution for wave frequency.

In both cases, the composite solutions are shown in the case of a: (a) shelf profile ($L_S \to 0$); (b) shelf-slope profile. Figure 3.10 uses a shelf width of 100 km and a slope width of 50 km, resulting in $\lambda = 5 \times 10^{-2}$ with the shelf profile, and $\lambda = 7.5 \times 10^{-2}$ when including the slope. Similarly, Figure 3.11 uses a shelf width of 125 km and a slope width of 75 km, resulting in $\lambda = 6.3 \times 10^{-2}$ with the shelf profile, and $\lambda = 10^{-1}$ when including the slope. Furthermore, Figures 3.10–3.11 highlight that the accuracy of the analytical solutions appears visibly to deteriorate with increasing λ, as per perturbation theory.

As for the solutions, we see for the first time the effect of coastal topography on the Kelvin wave. First, and perhaps most importantly, we observe that the cross-shore velocity at the shelf break can be of the same order of magnitude as the along-shore velocity at the shoreline ($y = 0$ km). While at the shelf break, the cross-shore velocity sees a maximum amplitude, the along-shore sees a minimum. The latter will mean that over coastal topography, internal-tide generation should be maximal at the shelf break, since the baroclinic drag (see equation (2.180)) is proportional to the bottom vertical velocity, which over the slope topography, consists entirely of the cross-shore component. Moreover, the cross-shore velocity profile in the limit of step topography is linear, increasing steadily before reach a maximum at the shelf break. This would suggest that even in the limit $L_S \to 0$ at which $h'(y)$ may be large, the volume transport profile could be modelled using the first-order approximation in (3.128). When including a slope profile, the cross-shore velocity is continuous as topography is continuous. Over the slope, the horizontal velocity profiles transition smoothly to amplitudes observed toward the shoreline, which then decay to zero, as per equation (3.83).

3.4.3 Kelvin Wave Response of Body Force

We seek to formulate the barotropic response of the coastal Kelvin wave in a channel with arbitrary coastal topography over some small length scale with respect to the Rossby radius of deformation. Fortunately, we have already the first-order analytical free-wave solutions to the Kelvin mode expressed in equations (3.120)–(3.129). Given external forcing composed of a non-dimensional potential forcing $\phi^*(y)$ dependent on non-dimensional cross-shore spatial variable y, and non-dimensional Rayleigh coefficient

$$\tilde{r} = r/f, \tag{3.130}$$

we deduce from equation (3.41) that non-dimensional response coefficient in a periodic channel of non-dimensional width $L = L_y/L_R$ is

$$\alpha_n = \frac{\omega_n}{\omega - \omega_n + i\,\tilde{r}\,(1-\delta_n)}\,\gamma_n,$$

where

$$\gamma_n = \frac{1}{\langle \mathbf{a}_n, \mathbf{a}_n \rangle}\int_0^L \phi^*(y)\; P_n(y)\; \mathrm{d}y, \qquad \delta_n = \frac{1}{\langle \mathbf{a}_n, \mathbf{a}_n \rangle}\int_0^L |P_n(y)|^2\,\mathrm{d}y \tag{3.131}$$

and non-dimensional inner product

$$\langle \mathbf{a}_m, \mathbf{a}_n \rangle = \int_0^L \left(h(y)\,\mathbf{U}_m(y)\cdot\mathbf{U}_n^*(y) + P_m(y)\; P_n^*(y) \right) \mathrm{d}y. \tag{3.132}$$

While we have previously obtained the analytical form of the Kelvin mode in a semi-infinite domain, the error of the decaying mode, whose form is considerably easier to obtain, scales to $\exp(-L)$. Figure 3.12, which compares the two Kelvin modes obtained numerically (again using a fixed-point shooting method), illustrates that the modes become indistinguishable as domain width increases. If the barotropic Kelvin mode in a channel is therefore approximated by that of a semi-infinite domain, the response of a perturbed Kelvin wave from a prescribed body force is therefore

$$\alpha_{PKW} = \frac{\omega_{PKW}}{\omega - \omega_{PKW} + i\,\tilde{r}\,(1-\delta_{PKW})}\,P_0\int_0^L \exp(-y)\,\phi^*(y)\,(1+ \omega_1\,k^2\,y\,\lambda + O\left(\lambda^2\right))\,\mathrm{d}y, \tag{3.133}$$

where P_0 is such that $\langle \mathbf{a}_{PKW}, \mathbf{a}_{PKW} \rangle = 1$, implying that

$$\begin{aligned}
1 &= \left[\langle \mathbf{a}_{PKW}, \mathbf{a}_{PKW} \rangle\right]^{-1} \\
&= \left[\int_0^L \left(|P_{PKW}|^2 + h(y)\left(|U_{PKW}|^2 + |V_{PKW}|^2\right)\right)\,\mathrm{d}y\right]^{-1} \\
&= \left[|P_0|^2\int_0^L \exp(-2y)\,(1+h(y))\left(1 + .\frac{2}{1+h(y)}\left(\omega_1\left[k^2\,y\,(1+h(y)) - h(y)\right] + \right.\right.\right. \\
&\qquad \left.\left.\left. \exp(+y)\left\{\omega_1\left[\exp(-y)-1\right] - \int_0^{y/\lambda}(1-h(\lambda\,Y))\,\mathrm{d}Y\right\}\right)\lambda + O\left(\lambda^2\right)\right)\,\mathrm{d}y\right]^{-1}
\end{aligned}$$

since for $k \in \mathbb{R}$,

$$|P_{PKW}|^2 = |P_0|^2\exp(-2y)\left(1 + 2\omega_1\,k^2\,y\,\lambda + O\left(\lambda^2\right)\right), \qquad |V_{PKW}|^2 = O\left(\lambda^2\right), \tag{3.134}$$

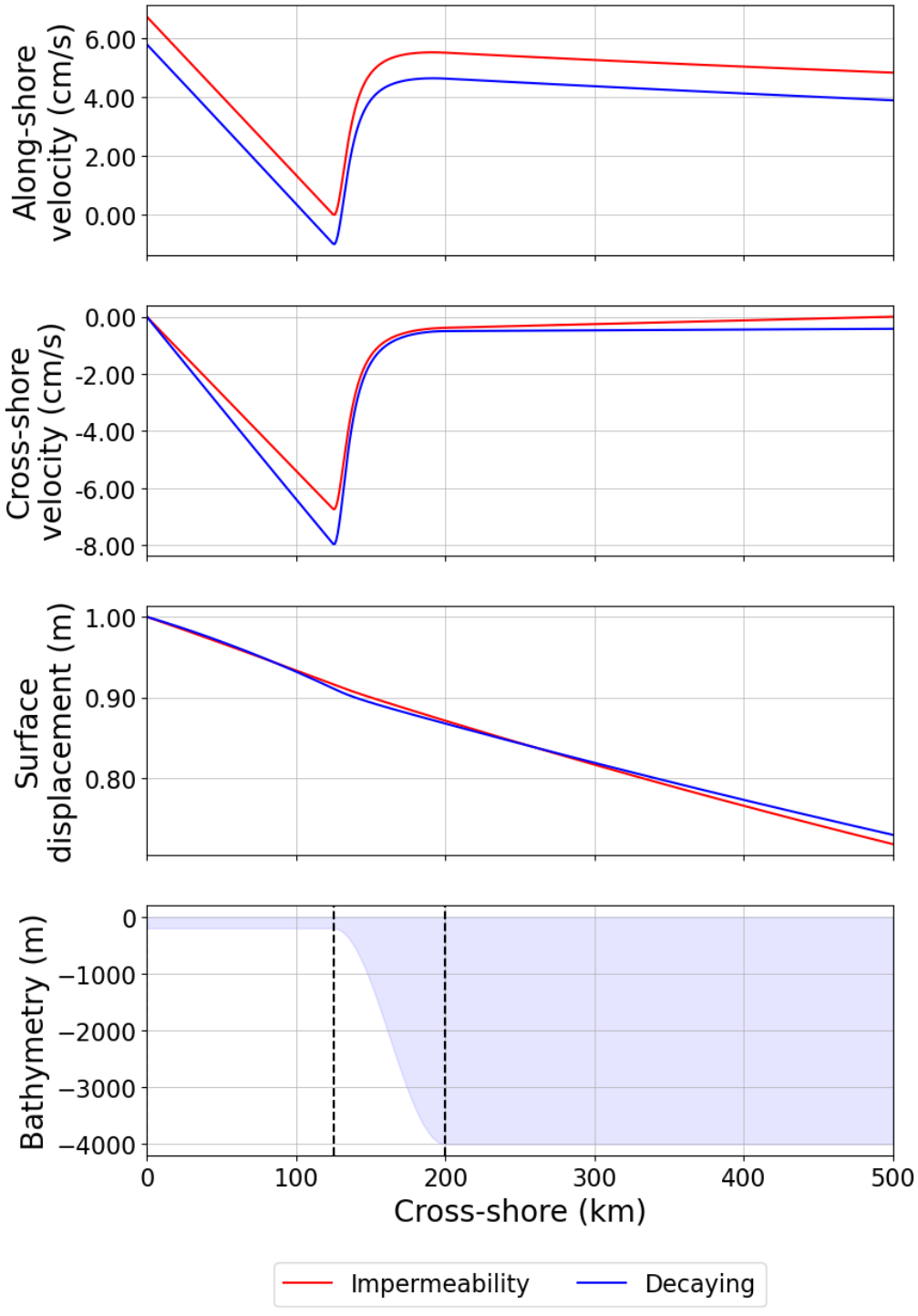

(a) $L_y = 500\,\mathrm{km}$

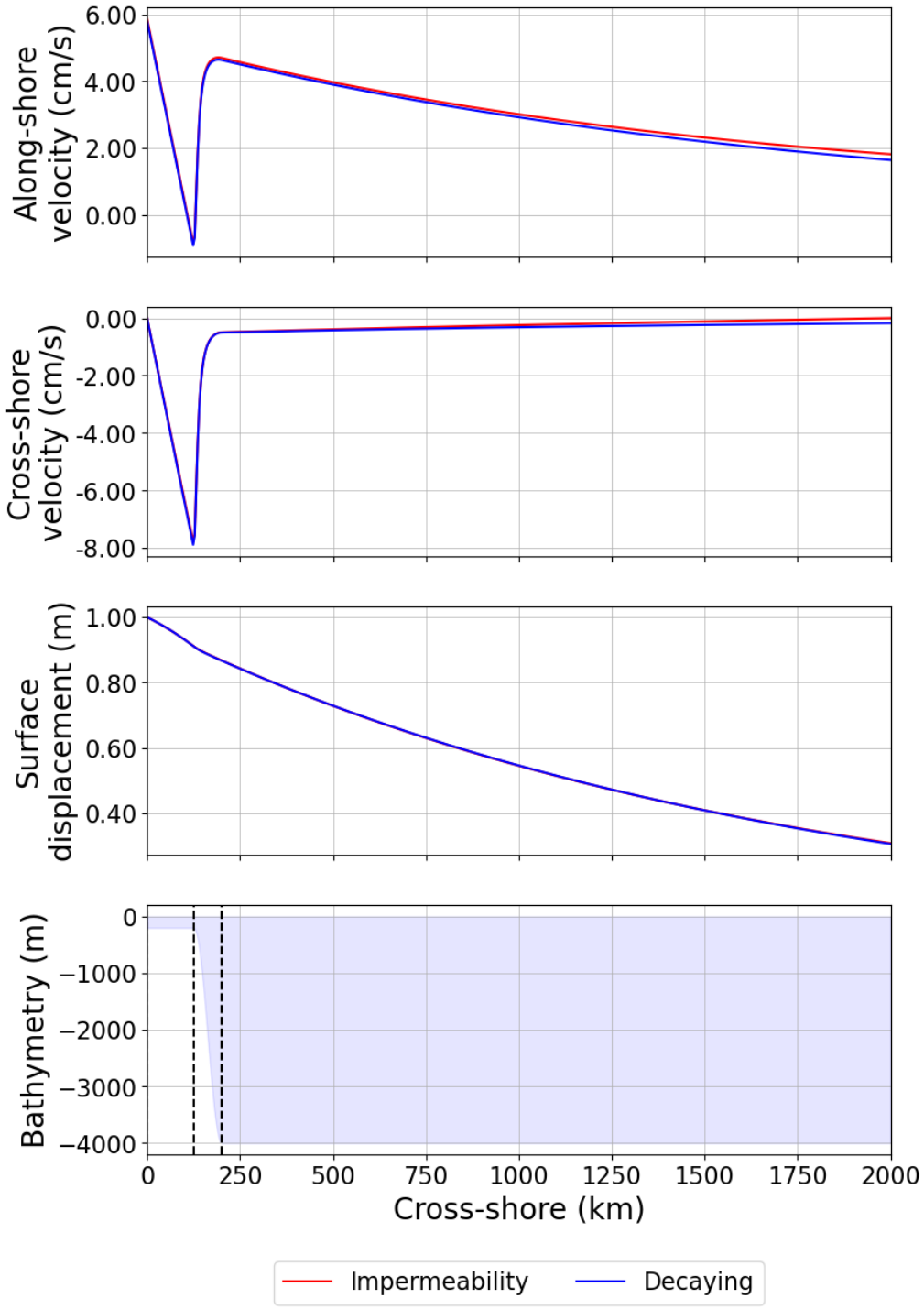

(b) $L_y = 2,000\,\text{km}$

Figure 3.12: Comparison of free Kelvin modes of a finite channel and a semi-infinite domain for domains of width: (a) 500 km; (b) 2,000 km. These modes correspond respectively to the imposition of impermeability and radiating boundary conditions. The figures show that the channel solution approaches the decaying solution as domain width increases.

meaning that from (3.129),

$$\begin{aligned}|U_{PKW}|^2 &= \frac{|V_{PKW}|^2+k^2\,|P_{PKW}|^2+i\,k\,(P^*_{PKW}\,V_{PKW}-P_{PKW}\,V^*_{PKW})}{\omega^2}\\ &= |P_0|^2\exp(-2y)\left(1+\frac{2}{h(y)}\left(\omega_1\,h(y)\left(k^2\,y-1\right)+\right.\right.\\ &\quad \left.\left.\exp(+y)\left\{\omega_1\left(\exp(-y)-1\right)-\int_0^{y/\lambda}(1-h(y))\,\mathrm{d}y\right\}\right)\lambda\\ &\quad +O\left(\lambda^2\right)\Big).\end{aligned} \tag{3.135}$$

We may then split the domain into the inner and outer regions, which upon manipulation, gives

$$\begin{aligned}|P_0|^2 &= \left[\int_0^{\lambda}\exp(-2y)\,(1+h(y))\,(1+O(\lambda))\,\mathrm{d}y+\right.\\ &\quad \left.2\int_{\lambda}^{L}\exp(-2y)\left(1+2k^2\,\omega_1\,y\,\lambda+O\left(\lambda^2\right)\right)\,\mathrm{d}y\right]^{-1}\\ &= \left[\int_0^{1}\exp(-2Y)\,(1+h(Y\,\lambda))\,\mathrm{d}Y\,\lambda+\right.\\ &\quad \left.2\int_{\lambda}^{L}\exp(-2y)\left(1+2k^2\,\omega_1\,y\,\lambda\right)\,\mathrm{d}y+O\left(\lambda^2\right)\right]^{-1},\end{aligned}$$

using a change of variable, $Y=y/\lambda$, on the inner integral. Evaluating the leading-order term in the outer region, we obtain

$$\begin{aligned}|P_0|^2 &= \left[\int_0^{1}\exp(-2Y)\,(1+h(Y\,\lambda))\,\mathrm{d}Y\,\lambda+\right.\\ &\quad \left.\{\exp(-2\lambda)-\exp(-2L)\}+2\omega_1\,k^2\,\lambda\int_{\lambda}^{L}y\,\exp(-2y)\,\mathrm{d}y+O\left(\lambda^2\right)\right]^{-1}\\ &= \left[\left\{1-\exp(-2L)\right\}\left(1-\frac{1}{2}\left(\coth(L)-1\right)\cdot\right.\right.\\ &\quad \left.\left.+\,O\left(\lambda^2\right)\right)\right]^{-1}\end{aligned} \tag{3.136}$$

which gives at last the analytical normalisation for the PKW mode,

$$\begin{aligned}|P_0|^2 &= \frac{1}{2}\left(1+\coth(L)\right)\left(1+\frac{1}{2}\left(\coth(L)-1\right)\cdot\right.\\ &\quad \left[\omega_1\,k^2\,(1+2L)+\exp(2L)\left(2-\omega_1\,k^2-\right.\right.\\ &\quad \left.\left.\left.\int_0^{1}\exp(-2Y)\,(1+h(Y\,\lambda))\,\mathrm{d}Y\right)\right]\lambda\\ &\quad \left.+\,O\left(\lambda^2\right)\right).\end{aligned} \tag{3.137}$$

Furthermore, since the mode in question is on a semi-infinite domain, we can simplify

(3.137) by taking the limit $L \to \infty$, giving

$$\begin{aligned} |P_0|^2 &= 1 + \left\{ 2 - \omega_1 \, k^2 - \int_0^1 \exp\left(-2Y\right) \left(1 + h\left(Y\,\lambda\right)\right) \, \mathrm{d}Y \right\} \lambda + O\left(\lambda^2\right) \\ &= 1 + \frac{1}{2} \left\{ 3 + \exp\left(-2\right) - 2 \left(\omega_1 \, k^2 + \right. \right. \\ &\qquad \left. \left. \int_0^1 \exp\left(-2Y\right) h\left(Y\,\lambda\right) \, \mathrm{d}Y \right) \right\} \lambda + O\left(\lambda^2\right). \end{aligned} \tag{3.138}$$

As for potential energy coefficient δ_{PKW} as given in (3.131),

$$\begin{aligned} \delta_{PKW} &= |P_0|^2 \int_0^{+\infty} \exp\left(-2y\right) \left(1 + 2\omega_1 \, k^2 \, y \, \lambda + O\left(\lambda^2\right)\right) \, \mathrm{d}y \\ &= \frac{1}{2} \, |P_0|^2 \left(1 + \omega_1 \, k^2 \, \lambda + O\left(\lambda^2\right)\right). \end{aligned} \tag{3.139}$$

equation (3.139) indicates that for a wave of amplitude $|P_0|$, the introduction of coastal topography reduces the Kelvin mode's potential energy (since $\omega_1 \leq 0$ and $0 \leq \lambda \ll 1$).

Upon substitution of (3.138), (3.139) reduces to

$$\delta_{PKW} = \frac{1}{2} \left(1 + \frac{1}{2} \left\{ 3 + \exp\left(-2\right) - 2 \int_0^1 \exp\left(-2Y\right) h\left(Y\,\lambda\right) \, \mathrm{d}Y \right\} \lambda + O\left(\lambda^2\right) \right). \tag{3.140}$$

For simplicity, we shall take the leading order components of $|P_0|^2$ and δ_n in equations (3.138) and (3.139) respectively, such that we now consider the response of the perturbed Kelvin mode

$$\alpha_{PKW} = \alpha_0 \left(1 + \alpha_1 \, \lambda + O\left(\lambda^2\right)\right), \tag{3.141}$$

where

$$\alpha_0 = \frac{2 \int_0^L \exp\left(-Y\right) \phi^*\left(Y\right) \, \mathrm{d}Y}{2\left(\omega - \omega_{PKW}\right) + i\,\tilde{r}} \tag{3.142}$$

and

$$\alpha_1 = \omega_1 \left\{ 1 + \frac{k^2 \int_0^L Y \, \exp\left(-Y\right) \phi^*\left(Y\right) \, \mathrm{d}Y}{\int_0^L \exp\left(-Y\right) \phi^*\left(Y\right) \, \mathrm{d}Y} \right\}. \tag{3.143}$$

Combining composite modal solutions of the perturbed Kelvin wave (see equations (3.120), (3.121), (3.129)) with normalisation condition (3.138) and response coefficient (3.141), we have that for a prescribed body forcing, $\phi^*\left(y\right) \exp\left\{i\left(k\,x - \omega\,t\right)\right\}$, the forced perturbed

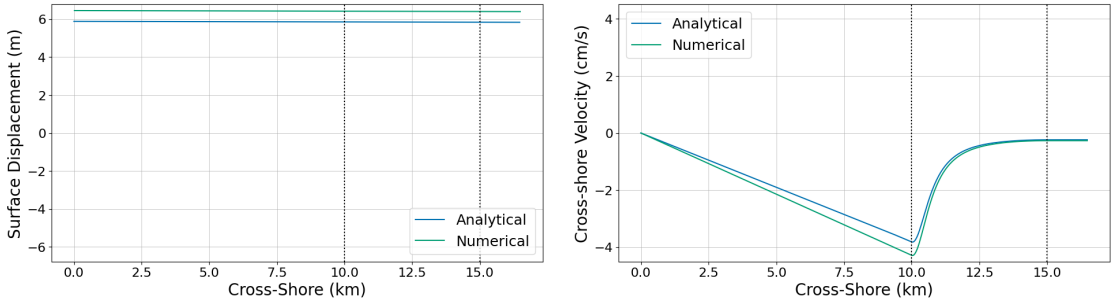

(a) $L_C = 10\,\text{km}$, $L_S = 5\,\text{km}$, $\lambda \approx 7.6 \times 10^{-3}$

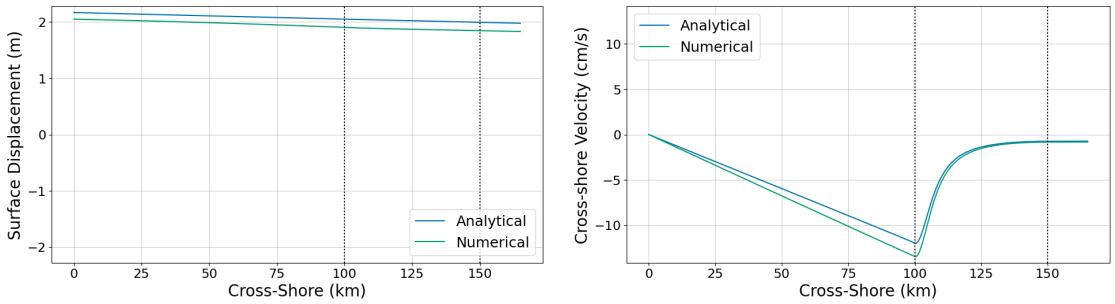

(b) $L_C = 100\,\text{km}$, $L_S = 50\,\text{km}$, $\lambda \approx 7.6 \times 10^{-2}$

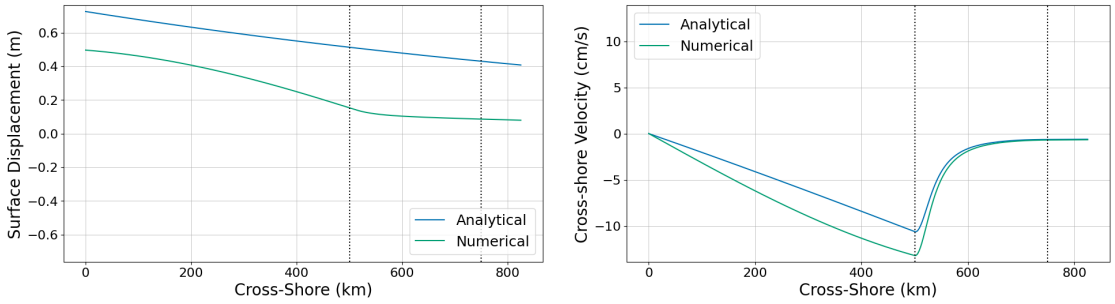

(c) $L_C = 500\,\text{km}$, $L_S = 250,\text{km}$, $\lambda \approx 3.8 \times 10^{-1}$

Figure 3.13: Comparison of forced solutions between analytical forced Kelvin wave and numerically determined forced solution in a $4,000\,\text{km}$ wide channel of uniform depth while increasing coastal topography length scales: (a) $L_C = 10\,\text{km}$, $L_S = 5\,\text{km}$, $\lambda \approx 7.6 \times 10^{-3}$; (b) $L_C = 100\,\text{km}$, $L_S = 50\,\text{km}$, $\lambda \approx 7.6 \times 10^{-2}$; (c) $L_C = 500\,\text{km}$, $L_S = 250,\text{km}$, $\lambda \approx 3.8 \times 10^{-1}$. Surface displacement is shown on the left, and cross-shore velocity is shown on the right ($\pi/2$ out of phase). Here, we use non-dimensional forcing frequency $\omega/f = 1.4$, non-dimensional along-shore wavenumber $k\,L_R \approx 1.39$ and non-dimensional Rayleigh friction $r/f = 5 \times 10^{-2}$. Dashed lines represent the position of the shelf break L_C and the foot of the slope $L_C + L_S$.

Kelvin wave modal solutions can be approximated to first order in λ as

$$\hat{U}_{PKW}(y) = \alpha_0 \exp(-y) \left(1+ \left[\omega_1 \left\{k^2 \left(y - 1 + \frac{\int_0^L Y \exp(-Y)\,\phi^*(Y)\,\mathrm{d}Y}{\int_0^L \exp(-Y)\,\phi^*(Y)\,\mathrm{d}Y}\right) + \frac{1}{h(y)} \left(1 - \exp(+y)\left[1 + \frac{1}{\omega_1}\int_0^{y/\lambda}\Big(1 - h(\lambda Y)\Big)\,\mathrm{d}Y\right]\right)\right\} + 2 - \int_0^1 \exp(-2Y)\,(1 + h(Y\lambda))\,\mathrm{d}Y\right]\lambda + O(\lambda^2)\right), \tag{3.144}$$

$$\hat{V}_{PKW}(y) = -\alpha_0 \frac{i\,k\,\lambda}{h(y)} \left\{\omega_1\Big(\exp(-y) - 1\Big) - \int_0^{y/\lambda} (1 - h(\lambda Y))\,\mathrm{d}Y\right\}\left(1 + O(\lambda)\right), \tag{3.145}$$

$$\hat{P}_{PKW}(y) = \alpha_0 \exp(-y)\left(1+ \left[\omega_1 \left\{1 + k^2 \left(y - 1 + \frac{\int_0^L Y \exp(-Y)\,\phi^*(Y)\,\mathrm{d}Y}{\int_0^L \exp(-Y)\,\phi^*(Y)\,\mathrm{d}Y}\right)\right\} + 2 - \int_0^1 \exp(-2Y)\,(1 + h(Y\lambda))\,\mathrm{d}Y\right]\lambda + O(\lambda^2)\right). \tag{3.146}$$

In Figure 3.13, we show a comparison between the analytical potentially forced Kelvin wave given by equations (3.144) –(3.146), and the numerically determined solution while increasing the topographic length scales (and therefore coastal length scale). The solutions obtained numerically were found using second-order finite differences on a staggered Arakawa C-Grid. Here, we consider the forcing scenario using non-dimensional parameters

$$\omega/f = 1.4, \qquad k\,L_R \approx 1.39 \qquad r/f = 5 \times 10^{-2}, \tag{3.147}$$

with dimensional potential forcing

$$\phi(x, y, t) = g\,\eta_0 \exp(-y/L_R)\,\exp\{i\,(k\,x - \omega\,t)\}, \qquad \eta_0 = 0.3125\,\mathrm{m} \tag{3.148}$$

and shelf-slope topography using $\varphi(Y) = \sin^2(\pi\,Y/2)$ in (3.72).

Figure 3.13, which shows the cross-shore structures of cross-shore velocity and surface displacement (analogous to pressure) consistently shows reasonable representation between the analytical solutions and the numerically determined ones while varying coastal length scales. Note that we show only the cross-shore velocity and pressure as the along-shore velocity is not required for forcing an internal-tide response along a one-dimensional slope with $\partial_x h = 0$.

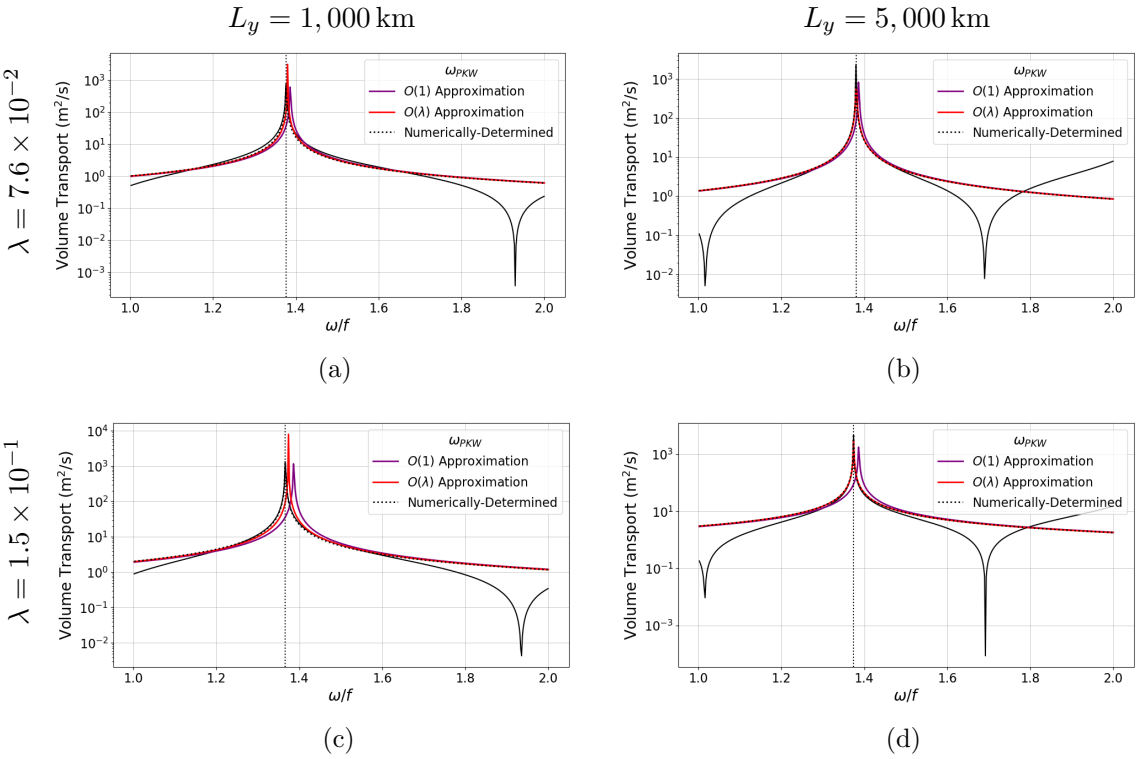

Figure 3.14: Effects of modal frequency accuracy on potentially forced cross-shore volume transport of the perturbed Kelvin wave mode without damping in a domain of width: $L_y = 1,000\,\text{km}$ (left); $L_y = 5,000\,\text{km}$ (right); and with non-dimensional coastal length scale: $\lambda = 7.6 \times 10^{-2}$ (top); $\lambda = 1.5 \times 10^{-1}$ (bottom). Solid black line hand indicates the full spectrum of forced barotropic modes.

We now have an analytical expression for the cross-shore volume transport associated with a potentially forced Kelvin wave along an arbitrary margin of the form (3.72):

$$\hat{Q}_{PKW}(y) = \alpha_0\, Q_{PKW}(y)\Big(1 + O(\lambda)\Big) \tag{3.149}$$

with α_0 as in (3.142) and $Q_{PKW}(y)$, to leading order in λ, as in (3.127), is

$$\begin{aligned} Q_{PKW}(y) &= -i\,k\,\lambda\left\{\omega_1\Big(\exp(-y) - 1\Big) - \int_0^{y/\lambda}(1 - h(\lambda\,Y))\;\mathrm{d}Y\right\} \\ &\approx -i\,k\,(1-\delta)\,y \end{aligned} \tag{3.150}$$

along the continental margin, denoting $\delta = H_C/H_D \ll 1$ as the ratio between shelf depth and deep-ocean depth (as per equation (3.128)).

In Figures 3.14–3.15, we investigate how the accuracy of the perturbed Kelvin wave's modal frequency, ω_{PKW}, impacts the characterisation of resonance in (3.149), both with and without damping. The accuracy of the analytical expression for volume transport at the shelf break, equation (3.149), is also evaluated against the barotropic response of all modes (solid black line) in a channel of width: $L_y = 1,000\,\text{km} \approx 0.5\,L_R$ and $L_y = 5,000\,\text{km} \approx 2.5\,L_R$. For shelf-slope topography shown in Figures 3.10b and 3.11b,

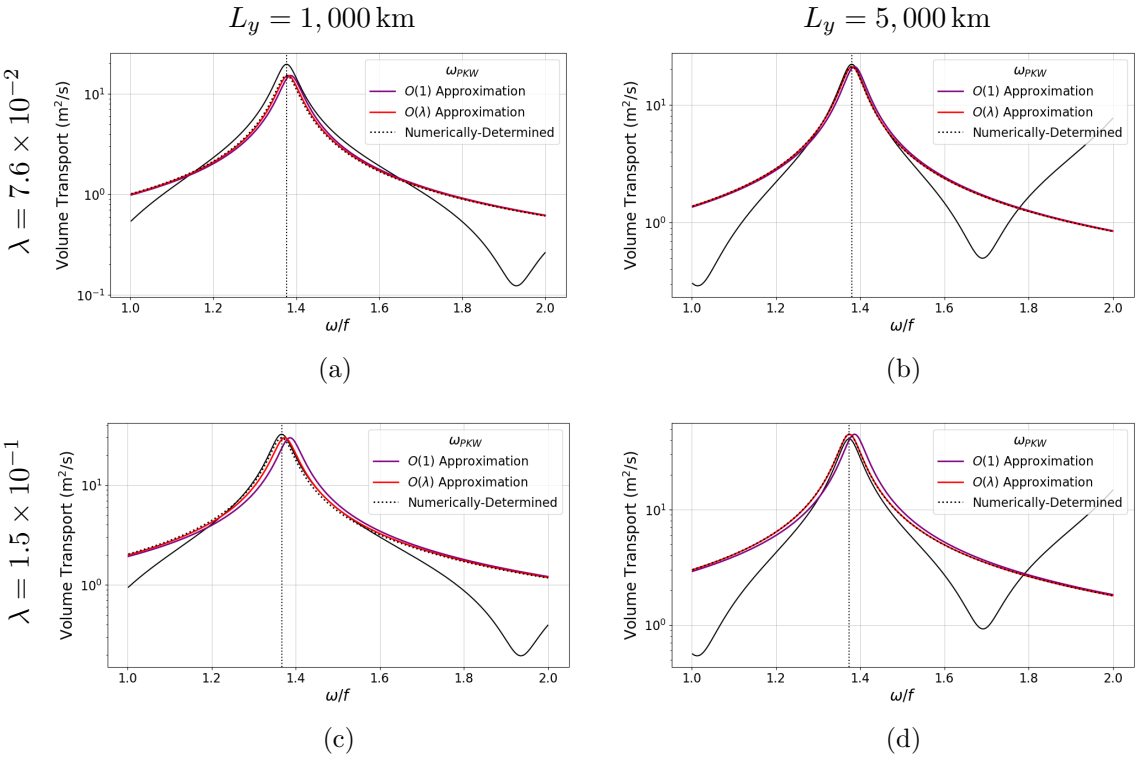

Figure 3.15: Effects of modal frequency accuracy on potentially forced cross-shore volume transport of the perturbed Kelvin wave mode with non-dimensional Rayleigh friction coefficient $r/f = 5 \times 10^{-2}$ in a domain of width: $L_y = 1,000\,\mathrm{km}$ (left); $L_y = 5,000\,\mathrm{km}$ (right); and with non-dimensional coastal length scale: $\lambda = 7.6 \times 10^{-2}$ (top); $\lambda = 1.5 \times 10^{-1}$ (bottom). Solid black line hand indicates the full spectrum of forced barotropic modes.

we also consider two shelf-slope width configurations: $L_C = 100\,\mathrm{km}$ and $L_S = 50\,\mathrm{km}$ ($\lambda = 7.6 \times 10^{-2}$), as well as $L_C = 200\,\mathrm{km}$ and $L_S = 100\,\mathrm{km}$ ($\lambda = 1.5 \times 10^{-1}$). Here, the dimensional potential forcing is

$$\phi(x, y, t) = g\,\eta_0 \exp\left(-y/L_R\right) \exp\left\{i\left(k\,x - \omega\,t\right)\right\} \tag{3.151}$$

with

$$k\,L_R \approx 1.39 \qquad \text{and} \qquad \eta_0 = 0.3125\,\mathrm{m}, \tag{3.152}$$

and is identical to that used in Figure 3.6. The pre-factor is not all-too important because the linear nature of our problem means the response is proportional (so long as flow speed $|U_0| \ll c = \sqrt{g\,h}$). In Section 3.3, it was concluded that this choice of potential forcing had a large shape factor with the unperturbed Kelvin wave and led to strong excitation of the Kelvin mode for typical tidal frequencies. Strong excitation of the Kelvin mode occurs with other choices of potential forcing, as with other modes, so long as the forcing frequency is close to the Kelvin wave's fundamental frequency.

The first remark to be made of Figures 3.14–3.15, is that while the leading-order wave frequency leads to poor characterisation of resonance, the first-order correction to wave frequency (see equation (3.122)) appears almost as good as the numerically determined modal frequency (using the shooting method).

Secondly, Figures 3.14–3.15 show that the wider the channel, the more accurate the volume transport appears to be around the modal frequency. It was deduced that the channel solution approaches the decaying modal solution in the limit of large channel width, and that the error is proportional to $\exp(-L_y/L_R)$, where L_y and L_R denote respectively the channel width and the Rossby radius of deformation in the deep ocean. Furthermore, Figures 3.14–3.15 show that the smaller the coastal length scale, the more accurate the characterisation of resonance, indicated by the peaks around the numerically determined modal frequency (dashed vertical line).

We conclude from Figures 3.14–3.15 that the analytical expression for cross-shore volume transport, equation (3.149), characterises well the forced response of the surface tide around tidal frequencies. The latter is encouraging, as this result can be used to force a baroclinic response along arbitrary coastal topographies of a three-dimensional surface tide (provided that the coastal length scale is small compared to the Rossby radius of deformation), from which baroclinic energy fluxes can be implied over arbitrary coastal topography.

3.5 Summary

We began this chapter, in Section 3.2, by stating the governing equations used to model decoupled barotropic motion. We explain here that baroclinic drag of the barotropic tide can be neglected for internal-tide generation problems along continental margins, although a full scaling argument is presented in Section 4.3. In Section 3.3, the equations of motion presented in Section 3.2 are modified to account for potential forcing and Rayleigh friction. Following the pedagogical structure of Boyce et al. (2017), we present the theory of two-dimensional oscillations in an arbitrary ocean basin as in Platzman (1972).

For some prescribed forcing, we show that for the strong excitation of a mode, either the frequency factor, characterising resonance, or the shape factor, characterising shape correlation, must be strong. In Section 3.3.2, the theory is applied to a crude model of an ocean basin (such as the Atlantic); we consider forced waves in a channel of uniform depth. There are two types of modes which arise: inertia-gravity modes and Kelvin modes. For any wave frequency, whether sub-inertial or super-inertial, there exists a free Kelvin wave with corresponding along-shore wavenumber. On the other hand, the frequencies of inertia-gravity waves are bounded below by the Coriolis parameter, making them super-inertial. From the corresponding dispersion relation, it is observed that for tidal ranges, whether diurnal or semi-diurnal, the Kelvin wave frequency is likely to be excited. Even with small perturbations to uniform topography through the presence of a continental margin, the dispersion relations appear largely unaffected. However, it is not just the frequency factor; there is also the shape factor. Different choices in the form of the equilibrium tide will generate varying responses. Ultimately, a mode will dominate if one forces close to a mode's fundamental frequency, even with damping. This is the case for the Kelvin wave. We argue therefore that a surface tide around continental margin can be modelled as a Kelvin wave.

The focus of the thesis is on internal-tide generation along continental margins. This does not occur without variations in topography since the barotropic and baroclinic modes are decoupled. Furthermore, the introduction of coastal topography over some small length scale leads to a perturbation of the mode. We explore this problem analytically in Section 3.4. By exploiting the small coastal length scale (relative to the Rossby radius of deformation), we reproduce analytical results of the perturbed Kelvin wave (PKW) as in Miles (1972) and Smith (1972). For typical coastal length scales, it was observed that at the shelf break, cross-shore flows can become comparable to along-shore flows along the shoreline. Using the analytical solutions of the perturbed Kelvin wave, the strength of the flow across the shelf was estimated asymptotically.

In Section 3.4.3, we extended the free-wave solutions of the Kelvin wave to consider potential forcing. Derived expressions for the forced Kelvin response are shown to agree with the response of all modes calculated numerically across a range of parameter space encompassing forcing frequency and coastal topography.

Chapter 4

Internal-Tide Generation along Continental Slopes

4.1 Introduction

Surface tides are the periodic motions of the terrestrial ocean basins due to the gravitational and rotational effects induced on the Earth by bodies in our solar system: most notably, the Sun and the Moon. When these deep tidal flows encounter variable bottom topography, the stratified ocean interior is forced to react periodically, leading to the generation of internal waves of tidal frequency—the so-called internal tide (see Wunsch, 1975; Garrett & Kunze, 2007). It is well-understood that internal-tide generation occurs on timescales predominantly determined by the Earth's planetary-rotation rate, where resonant barotropic modes are excited by periodic tidal forcing (Platzman, 1984; Wilkin & Chapman, 1987). Since variable topography is an essential element of the generation of internal waves, internal-tide generation is often observed along continental margins (e.g. R. Pingree & New, 1989; Holloway et al., 2001; Lien & Gregg, 2001) and mid-ocean ridges (e.g. Ray & Mitchum, 1997) where large variations in topography exist.

The focus of this thesis is on the generation of internal tides along continental margins, which is less frequently studied than open-ocean topographic features since its role on abyssal mixing is far less significant. More specifically, our goal is to estimate radiating internal tide energy fluxes for various non-trivial coastal geometries where, as concluded in Chapter 3, coastal Kelvin waves are the principal barotropic motion excited by tidal forcing. It is well-understood that a Kelvin wave in a horizontally bounded domain of uniform fluid depth has zero cross-shore volume flux (see Thomson, 1879; Lamb, 1895; Pond & Pickard, 1983). Sea floor topography, particularly along continental margins at which bathymetric gradients are greatest, means that the barotropic flow field includes a cross-shore component, which, when flowing up and down a continental margin, provides a stable source of tidal dissipation. This source of energy typically radiates away from the generation source in the form of internal waves at tidal frequency, thereby contributing to the open question of how and where internal tides eventually dissipate in ocean basins

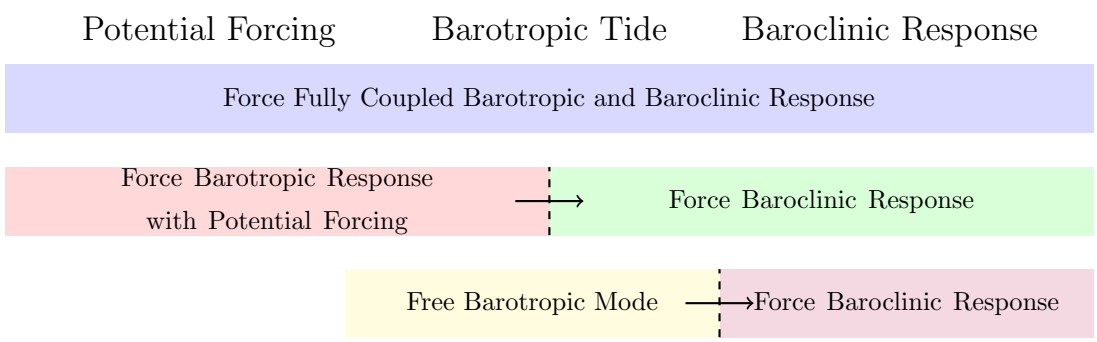

Figure 4.1: Different scenarios by which one can consider the baroclinic response of a prescribed barotropic tide.

(Rudnick et al., 2003; Alford & Zhao, 2007a; Zhao et al., 2016).

The research of internal-tide generation has long been limited by the complex nature of the topography involved. For example, the use of an ocean general circulation model (OGCM) (e.g. Egbert & Ray, 2001; Arbic et al., 2004) is limited through numerical dissipation and the inability to resolve the fine-scale internal-wave beams by which the ocean interior is mixed. In particular, OGCMs offer poor resolution along continental margins, leading to the introduction of potentially inaccurate parameterisations. Alternatively, idealised models may be used to consider internal-tide generation but lack many of the physical complexities that OGCMs incorporate. In addition, it is often assumed that the flow field is two-dimensional; that is, that the topography, and therefore the internal tides, are independent of one horizontal direction (Griffiths & Grimshaw, 2007a). In both cases, however, the general approach is to prescribe some time-periodic barotropic forcing and then model the internal-tide response. However, the means by which the latter is analysed varies in complexity and is the subject of a discussion whose substance is summarised schematically in Figure 4.1.

The first approach to modelling the internal-tide response of a prescribed barotropic potential forcing typically involves solving the shallow-water equations (SWEs) with either primitive or modal variables. Of the three approaches, this method is the most complex, both numerically and analytically. For our purposes, it is comparatively much cleaner to solve the system with modal variables introduced in 2.4.5 for a variety of reasons. The modal decomposition allows a complete separation of the barotropic and baroclinic motions where tidal forcing is uniquely barotropic. It also allows us to prescribe different boundary conditions to the modes. For example, in our work it is most convenient to prescribe radiating boundary conditions on the baroclinic modes (since we anticipate the waves to dampen before reaching the boundaries of our domain), while impermeability on the barotropic. Most importantly, modal decomposition facilitates the calculation of the baroclinic tidal energy fluxes, which is a central element to our research.

The second approach is simpler to the previous and involves decoupling the barotropic and baroclinic motions through the omission of internal wave drag on the barotropic motion. This admits calculation of the barotropic response of a potential forcing without having

simultaneously to calculate that of the baroclinic. Subsequently, the resultant barotropic motion is then used to force a spectrum of baroclinic modes according to the stratification profile of the fluid medium and, while approximate, usually returns similar results to the previous approach. We are able to omit the baroclinic wave drag on the barotropic motion because the term is negligible compared to the tidal forcing, and its effects are felt only when forcing close to resonant frequency acts to dampen the system.

The last approach, the simplest of all, is to use the form of the potentially forced Kelvin wave. Despite the wide array of simplifications in the latter approach, it is often the case that the resulting baroclinic response makes a reasonable approximation to the fully coupled approach.

In this chapter, we shall consider and compare all three approaches of varying complexity. Our ambition is to show that the most direct and simplest approach—the third in Figure 4.1—is comparable to the other more complex approaches.

We begin in Section 4.2 by considering the fully coupled system between a potentially forced three-dimensional surface tide and its internal-tide response. To motivate, solutions of the baroclinic tide are shown, along with the implied baroclinic energy fluxes. Parameter sweeps are conducted on coastal topography. This work is similar to §4 of Griffiths and Grimshaw (2007a), but Griffiths and Grimshaw (2007a) considers a free two-dimensional barotropic tide with cross-shore flow

$$V_0\left(y,t\right)=\frac{Q}{h\left(y\right)}\left[\frac{1+\left(y-L_C\right)/L_S}{1+L_S/L_C}\right]\cos\left(\omega\,t\right) \tag{4.1}$$

along the slope (this is identical to the model used by Craig, 1987). Here Q is some prescribed cross-shore volume flux at the foot of the slope. In our work, we shall consider a potentially forced three-dimensional barotropic tide, as in Chapter 3, in the form of a Kelvin wave.

In Section 4.3, we consider the decoupling of the barotropic and baroclinic modes. This section encompasses the second and third approaches and begins with a scaling analysis to show baroclinic drag on the barotropic equations can be neglected. Section 4.3.1 considers the decoupled internal-tide response to the superposition of potentially forced barotropic modes, while Section 4.3.2 focuses on the use of the analytical form of the potentially forced Kelvin wave derived in Section 3.4.3. Lastly, Section 4.3.3 re-derives the analytical solution presented in §4b of Griffiths and Grimshaw (2007a). This is used to construct analytical expressions for baroclinic energy fluxes radiating shoreward and oceanward for a surface tide as a free Kelvin wave in the limit of shelf topography. The chapter concludes in Section 4.4 by summarising our results, followed by a discussion on the potential impact of our findings.

4.2 Coupled Modal Equations

The modal equations for a two-layer system are those presented in equations (2.205)–(2.208) of Section 2.4.8. Using the anti-symmetric normalisation with modal-interaction coefficients given by equation (2.169), these equations are

$$\partial_t \mathbf{U}_0 + f\,\hat{\mathbf{e}}_z \times \mathbf{U}_0 + \boldsymbol{\nabla} P_0 = +\mathcal{T}_{10}\,\boldsymbol{\nabla} h\, P_1 + \boldsymbol{F}_0, \tag{4.2}$$

$$\partial_t P_0 + \boldsymbol{\nabla}\cdot\left(c_0^2\left(\mathbf{x}\right)\,\mathbf{U}_0\right) = +\mathcal{T}_{10}\,\boldsymbol{\nabla} h\cdot\left(c_1^2\left(\mathbf{x}\right)\,\mathbf{U}_1\right), \tag{4.3}$$

and

$$\partial_t \mathbf{U}_1 + f\,\hat{\mathbf{e}}_z \times \mathbf{U}_1 + \boldsymbol{\nabla} P_1 = -\mathcal{T}_{10}\,\boldsymbol{\nabla} h\, P_0 + \boldsymbol{F}_1, \tag{4.4}$$

$$\partial_t P_1 + \boldsymbol{\nabla}\cdot\left(c_1^2\left(\mathbf{x}\right)\,\mathbf{U}_1\right) = -\mathcal{T}_{10}\,\boldsymbol{\nabla} h\cdot\left(c_0^2\left(\mathbf{x}\right)\,\mathbf{U}_0\right), \tag{4.5}$$

with the former governing barotropic flow, and the latter governing baroclinic flow. These equations include external modal forces $\boldsymbol{F}_0$ and $\boldsymbol{F}_1$. Moreover, the two sets of equations are coupled through variable topography comprising the product of bathymetric gradient and modal-interaction coefficient

$$\mathcal{T}_{10} = \frac{\sqrt{\partial_h\left(c_0^2\right)\,\partial_h\left(c_1^2\right)}}{c_0^2 - c_1^2} = \frac{h_1}{h^2}\sqrt{\varepsilon}\left(1 + O\left(\sqrt{\varepsilon}\right)\right), \qquad \varepsilon \equiv \left(\rho_2 - \rho_1\right)/\rho_2 \ll 1. \tag{4.6}$$

If fluid depth $h\left(x,y\right)$ depends only on cross-shore spatial dimension, we may assume plane-wave solutions of the form

$$A\left(x,y,t\right) = \mathrm{Re}\left[\tilde{A}\left(y\right)\exp\left\{i\left(k\,x - \omega\,t\right)\right\}\right], \tag{4.7}$$

and system (4.2)–(4.5) can be discretised and solved numerically as a boundary-value problem of the form

$$\begin{pmatrix} \mathsf{A}_0 & \mathsf{C}_{01} \\ \mathsf{C}_{10} & \mathsf{A}_1 \end{pmatrix}\begin{pmatrix} \mathbf{q}_0 \\ \mathbf{q}_1 \end{pmatrix} = \begin{pmatrix} \mathbf{F}_0 \\ \mathbf{F}_1 \end{pmatrix}. \tag{4.8}$$

Here, state vector and forcing vector are respectively

$$\mathbf{q}_m = \begin{pmatrix} U_m \\ V_m \\ P_m \end{pmatrix} \qquad \text{and} \qquad \mathbf{F}_m = \begin{pmatrix} F_{x,m} \\ F_{y,m} \\ 0 \end{pmatrix}, \tag{4.9}$$

while system matrices

$$\mathsf{A}_m = \begin{pmatrix} -i\,\omega & -f & i\,k \\ f & -i\,\omega & \partial_y \\ i\,k\,c_m^2 & \partial_y c_m^2 & -i\,\omega \end{pmatrix}, \qquad \mathsf{C}_{mn} = \begin{pmatrix} 0 & 0 & 0 \\ 0 & 0 & \mathcal{T}_{mn}\,h' \\ 0 & \mathcal{T}_{mn}\,h'\,c_n^2 & 0 \end{pmatrix}. \tag{4.10}$$

4.2.1 Idealised Shelf-Slope Topography

Throughout the remainder of this chapter, we shall consider shelf slope topography as in (3.72), where fluid depth

$$h(y) = \begin{cases} H_C, & 0 \le y \le L_C, \\ H_C + (H_D - H_C)\,\varphi\left(\dfrac{y - L_C}{L_S}\right), & L_C \le y \le L_C + L_S, \\ H_D, & y > L_C + L_S. \end{cases} \tag{4.11}$$

We recall that, $H_C = O(200\,\mathrm{m})$, $H_D = O(4,000\,\mathrm{m})$, $L_C = O(100\,\mathrm{km})$ and $L_S = O(50\,\mathrm{km})$ represent the coastal shelf depth, the deep-ocean depth, the shelf width, and the slope width, while the shoreline is positioned at $y = 0$. The function $\varphi : [0,1] \to [0,1]$ is any monotonically increasing function such that $\varphi(0) = 0$ and $\varphi(1) = 1$. Example functions include $\varphi(Y) = Y$ (linear) or $\varphi(Y) = \sin^2(\pi Y/2)$ (differentiable). To clarify, we use the term "differentiable" to label the profile $\varphi(Y) = \sin^2(\pi Y/2)$ since the resulting shelf-slope profile is differentiable at the head and foot of the slope, unlike the profile $\varphi(Y) = Y$.

4.2.2 Parameter Settings

To understand the magnitudes of quantities to be discussed later, we note here the typical quantities one might expect for typical continental shelf settings at mid-latitude. While many key parameters will remain largely fixed regardless of coastal topography, further investigations onto shelf-slope parameter dependence are carried out later on.

We consider by default reduced gravity $g' = 0.1\,\mathrm{m/s^2}$, fixed upper-layer depth $h_1 = 150\,\mathrm{m}$, semi-diurnal tidal frequency $\omega = 1.4 \times 10^{-4}\,\mathrm{s^{-1}}$, Coriolis parameter $f = 10^{-4}\,\mathrm{s^{-1}}$, barotropic Rayleigh coefficient $r = 5 \times 10^{-6}\,\mathrm{s^{-1}}$, along-shore wavenumber $k = 7.07 \times 10^{-7}\,\mathrm{m^{-1}}$, shelf width $L_C = 100\,\mathrm{km}$, slope width $L_S = 50\,\mathrm{km}$, shelf depth $H_C = 200\,\mathrm{m}$, and deep-ocean depth $H_D = 4,000\,\mathrm{m}$.

4.2.3 Boundary Conditions

For boundary conditions, we consider impermeability at the boundaries of the channel of fixed width $L_y = O(L_R)$, where Rossby radius of deformation $L_R = \sqrt{g\,H_D}/|f| \approx 2,000\,\mathrm{km}$ in the case of a deep-ocean depth $H_D = 4,000\,\mathrm{m}$ and Coriolis parameter $f = 10^{-4}\,\mathrm{s^{-1}}$. We impose therefore

$$V_0(x, y = 0, t) = V_0(x, y = L_y, t) = 0. \tag{4.12}$$

For the baroclinic boundary conditions, we seek radiating energy fluxes. The assumption for radiating boundary conditions is that the internal tide dissipates and breaks before reaching the shoreline or any mid-ocean topographic features which reflect propagating waves back over the generation source. In Prinsenberg and Rattray (1975), it was found

that reflected waves generated at a steep slope were damped almost entirely before returning to the shelf break. Examination of the energy flux and energy density of current meter readings off the coast of northwest Africa by Gordon (1978) also suggest that most of the energy flux is dissipated rather than reflected back out to the deep sea. It is for this reason that we consider inviscid flow with the imposition of radiation conditions along the shoreline. Similar arguments can also be constructed to motivate radiating conditions oceanward. If instead an impermeable boundary condition along the shoreline is considered, the time-averaged energy flux shoreward would be zero.

Over uniform topography, we have that the baroclinic equations (4.4)–(4.5) reduce to the linear constant-coefficient ordinary differential equation

$$\left(\frac{\mathrm{d}^2}{\mathrm{d}y^2} + l^2\right) \tilde{V}_1\,(y)\,, \qquad \text{with} \qquad l = +\sqrt{\frac{\omega_f^2}{c_1^2\,(h\,(y))} - k^2} \tag{4.13}$$

typically real if $\omega_f^2 = \omega^2 - f^2 > 0$ (super-inertial tides) and $k^2 \ll 1$, and imply a solution of the form

$$\tilde{V}_1\,(y) = \tilde{C}\,\exp\left(-i\,l\,y\right) + \tilde{D}\,\exp\left(+i\,l\,y\right) \tag{4.14}$$

for $\tilde{C}, \tilde{D} \in \mathbb{C}$ unknown. Since $\tilde{V}$ and $\tilde{P}$ are related by linear constant-coefficient equations over uniform topography, we have also that

$$\tilde{P}_1\,(y) = \frac{-i\,c_1^2\left(\omega\,\dfrac{\mathrm{d}}{\mathrm{d}y} - f\,k\right)}{\omega^2 - c_1^2\,k^2}\,\tilde{V}_1\,(y) \tag{4.15}$$

$$= \frac{c_1^2}{\omega^2 - c_1^2\,k^2}\left[\tilde{D}\,(\omega\,l - i\,f\,k)\exp\left(+i\,l\,y\right) - \tilde{C}\,(i\,f\,k + \omega\,l)\exp\left(-i\,l\,y\right)\right]. \tag{4.16}$$

If we want radiating boundary conditions, we require that the time-averaged cross-shore energy flux, as implied from equation (2.175) of Section 2.4.5,

$$\begin{aligned}\langle J_y\rangle &= \frac{1}{2}\,c_1^2\,\rho^*\,\mathrm{Re}\left\{\tilde{V}_1^*\,(y)\;\tilde{P}_1\,(y)\right\}\\ &= \frac{1}{2}\,\frac{\rho^*\,c_1^4}{\omega^2 - c_1^2\,k^2}\,\mathrm{Re}\left\{-|\tilde{C}|^2\,(\omega\,l - i\,f\,k) + |\tilde{D}|^2\,(\omega\,l + i\,f\,k)\right.\\ &\qquad \left.-\tilde{C}^*\,\tilde{D}\,(\omega\,l - i\,f\,k)\exp\left(+2i\,l\,y\right) + \tilde{C}\,\tilde{D}^*\,(\omega\,l + i\,f\,k)\exp\left(-2i\,l\,y\right)\right\},\end{aligned} \tag{4.17}$$

is negative and constant between $y = 0$ and $y = L_C$, as well as positive and constant between $y = L_C + L_S$ and $y = L_y$. Here, $\langle\cdot\rangle$ denotes the time-averaging operator.

If (4.17) is going to be constant and negative along the continental shelf, it follows that $\tilde{D} = 0$, and that for baroclinic cross-shore wavenumber and wave speed

$$l_C = +\sqrt{\frac{\omega_f^2}{c_C^2} - k^2} \qquad \text{and} \qquad c_C = c_1\,(H_C) = \sqrt{g'\,h_1\,(H_C - h_1)\,/H_C}. \tag{4.18}$$

In addition, cross-shore velocity over the continental shelf

$$\tilde{V}_{1,C}(y) = \tilde{C}\,\exp(-i\,l_C\,y) \qquad \Longrightarrow \qquad |\tilde{C}|^2 = |\tilde{V}_1(y_C)|^2 \tag{4.19}$$

for $y_C \in [0, L_C]$, implying the boundary condition

$$\left(\frac{\mathrm{d}}{\mathrm{d}y} + i\,l_C\right)\tilde{V}_1(y_C) = 0, \tag{4.20}$$

along with, using (4.17), a time-averaged energy flux

$$\langle J_C\rangle = -\frac{1}{2}\,\frac{\rho^*\,c_C^4}{\omega^2 - c_C^2\,k^2}\,|\tilde{V}_1(y_C)|^2\,\omega\,l_C = -\frac{1}{2}\,\frac{\rho^*\,c_C^4}{\omega^2 - c_C^2\,k^2}\,|\tilde{C}|^2\,\omega\,l_C. \tag{4.21}$$

We remark that the radiating condition (4.20) applies also to the cross-shore velocity.

By the same argument, it follows that in the deep ocean, $\tilde{C} = 0$ and that the imposition of a radiating boundary condition requires

$$\left(\frac{\mathrm{d}}{\mathrm{d}y} - i\,l_D\right)\tilde{V}_1(y_D) = 0 \qquad \text{for} \qquad y_D \in [L_C + L_S, L_y], \tag{4.22}$$

and, from (4.17) once more, implies a time-averaged energy flux

$$\langle J_D\rangle = \frac{1}{2}\,\frac{\rho^*\,c_D^4}{\omega^2 - c_D^2\,k^2}\,|\tilde{V}_1(y_D)|^2\,\omega\,l_D = \frac{1}{2}\,\frac{\rho^*\,c_D^4}{\omega^2 - c_D^2\,k^2}\,|\tilde{D}|^2\,\omega\,l_D \tag{4.23}$$

with $|\tilde{D}| = |\tilde{V}_1(y_D)|$, and where the baroclinic phase speed and cross-shore wavenumber are respectively

$$c_D = c_1(H_D) = \sqrt{g'\,h_1\,(H_D - h_1)/H_D} \qquad \text{and} \qquad l_D = +\sqrt{\frac{\omega_f^2}{c_D^2} - k^2}. \tag{4.24}$$

It follows from equations (4.21) and (4.23) that the total time-averaged radiating energy flux is

$$\langle J\rangle = |\langle J_C\rangle| + |\langle J_D\rangle| = \frac{1}{2}\,\omega\,\rho^*\left[\frac{l_C\,c_C^4}{\omega^2 - c_C^2\,k^2}\,|\tilde{C}|^2 + \frac{l_D\,c_D^4}{\omega^2 - c_D^2\,k^2}\,|\tilde{D}|^2\right], \tag{4.25}$$

where baroclinic cross-shore velocity $\tilde{V}_1$ (and thus $\tilde{C}$ and $\tilde{D}$) in remains to be determined. The total radiating energy flux in (4.25) is equivalent (2.186) since the solution is periodic in the along-shore and $\hat{\mathbf{n}}\cdot\langle J\rangle = \langle J_D\rangle - \langle J_C\rangle$ for $\langle J_C\rangle \le 0$ and $\langle J_D\rangle \ge 0$.

We remark that (4.25) may be simplified since $c_1^2\,k^2/\omega^2 = O(\varepsilon)$. In this case, equation (4.25) becomes

$$\langle J\rangle = |\langle J_C\rangle| + |\langle J_D\rangle| = \frac{1}{2}\,\frac{\rho^*}{\omega}\left[l_C\,c_C^4\,|\tilde{C}|^2 + l_D\,c_D^4\,|\tilde{D}|^2\right]. \tag{4.26}$$

For the parameters given in Section 4.2.2, equation (4.18) implies a baroclinic phase speed and cross-shore wavelength of $\sim 1.9\,\mathrm{m/s}$ and $\sim 124\,\mathrm{km}$ over the continental shelf. Similarly, equation (4.24) implies a baroclinic phase speed and cross-shore wavelength of $\sim 3.8\,\mathrm{m/s}$ and $\sim 243\,\mathrm{km}$ in the deep ocean.

4.2.4 Solutions

In this section, we briefly show some solutions of the fully coupled equations ((4.2)–(4.5) subject to (4.12), (4.20) and (4.22)) for the parameter values given Section 4.2.2 using second-order finite-differences on a staggered Arakawa C-grid (see Arakawa & Lamb, 1980) over a channel of width $L_y = 4,000\,\mathrm{km} \approx 2L_R$ with grid spacing $h = 0.5\,\mathrm{km}$. Here, we consider potential forcing

$$\phi\,(\mathbf{x}, t) = g\,\eta_0\,\exp\,(-y/L_R)\,\exp\,\{i\,(k\,x - \omega\,t)\}, \tag{4.27}$$

where equilibrium tidal amplitude at the shoreline $\eta_0 = 0.3125\,\mathrm{m}$, recalling that the Rossby radius of deformation $L_R = \sqrt{g\,H_D}/|f|$. Including Rayleigh friction, the barotropic forcing in (4.8), having divided (4.27) by normalisation coefficient $\hat{Z}_0 = \sqrt{\partial_h c_0^2} = \sqrt{g}$, is

$$\mathbf{F}_0 = \sqrt{g}\begin{pmatrix} i\,k \\ \dfrac{\mathrm{d}}{\mathrm{d}y} \\ 0 \end{pmatrix}\hat{\eta}_{eq}\,(y) - r\begin{pmatrix} 1 & 0 & 0 \\ 0 & 1 & 0 \\ 0 & 0 & 0 \end{pmatrix}\mathbf{q}_0, \tag{4.28}$$

where for our choice of equilibrium tide $\hat{\eta}_{eq} = \eta_0\,\exp\,(-y/L_R)$.

Our goal is to identify the form of the barotropic and baroclinic solutions for semi-diurnal tidal frequency in the case of a linear and differentiable slope function, and how the implied radiating energy fluxes appear to differ.

Figure 4.2 shows the barotropic and baroclinic response to tidal forcing over a linear slope, whereby $\varphi\,(Y) = Y$ in (4.11) (see Figure 4.2c). In the top, Figure 4.2a shows the barotropic (surface) tidal response to tidal forcing. The solution corresponds to a surface displacement of $\sim 2.05\,\mathrm{m}$ at the shoreline which decays in amplitude oceanward much like the Kelvin wave and shows a uniform vertical structure. I.e. the solution in the upper and lower layers are identical (to leading order in $\varepsilon = (\rho_2 - \rho_1)\,/\rho_2 \ll 1$). In the middle, Figure 4.2b shows the baroclinic (internal) tidal response. The figure also shows that the baroclinic solution observes a net depth-integrated volume transport of zero. As for the baroclinic pressure, the pressure field is maximal in the lower layer along the continental shelf at a constant amplitude of $\sim 192\,\mathrm{Pa}$ but is maximal in the upper layer in the deep ocean at a constant amplitude of $\sim 227\,\mathrm{Pa}$.

Similarly, Figure 4.3 shows the barotropic and baroclinic response to tidal forcing over a differentiable slope, whereby $\varphi\,(Y) = \sin^2\,(\pi\,Y/2)$ in (4.11) (see Figure 4.3c). In the top, Figure 4.3a shows the barotropic (surface) tidal response to tidal forcing. The solution corresponds to a surface displacement of $\sim 2.00\,\mathrm{m}$ at the shoreline which decays in ampli-

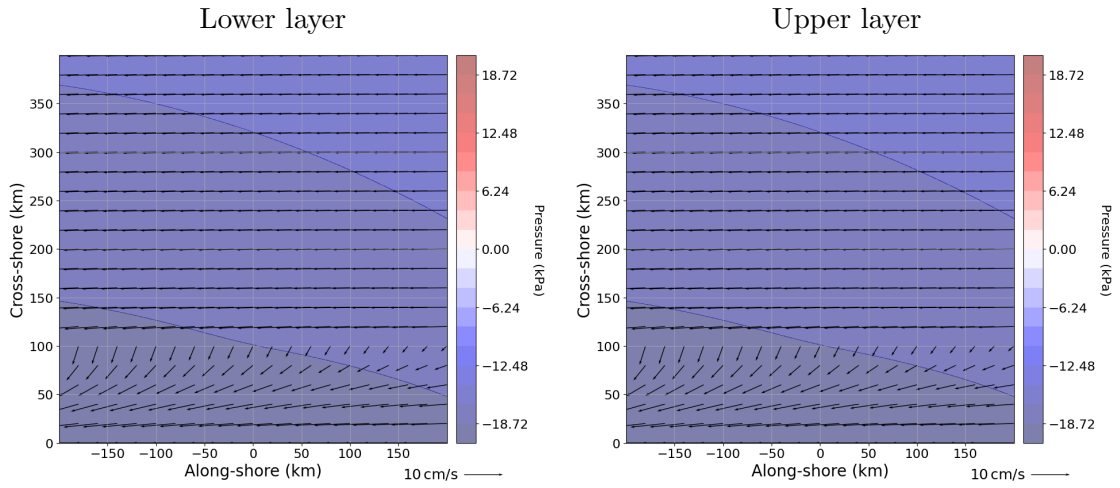

(a) Barotropic

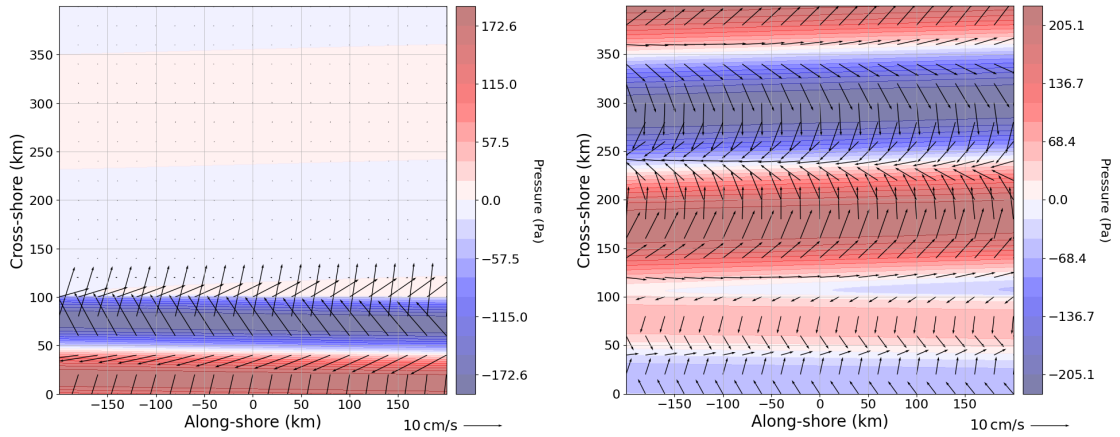

(b) Baroclinic

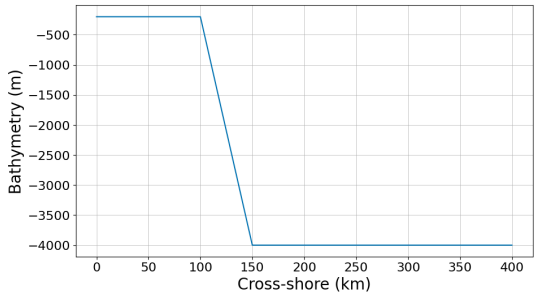

(c) Coastal Topography

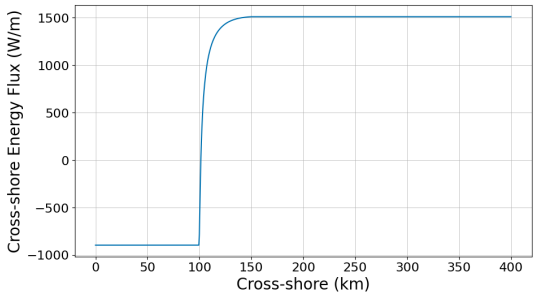

(d) Cross-shore Energy Flux

Figure 4.2: Modal solutions for both the barotropic (top) mode and the baroclinic (middle) mode in the case of a linear slope (bottom), with lower-layer solutions on the left, and upper-layer solutions on the right. The contour plots show the pressure perturbation, with units (kPa) in (a) and (Pa) in (b), while the quiver plots show the horizontal velocity field (see 10 cm/s key). The coastal bathymetry profile $-h(y)$ is shown in (c), and the implied time-averaged cross-shore energy flux of the baroclinic mode is shown in (d).

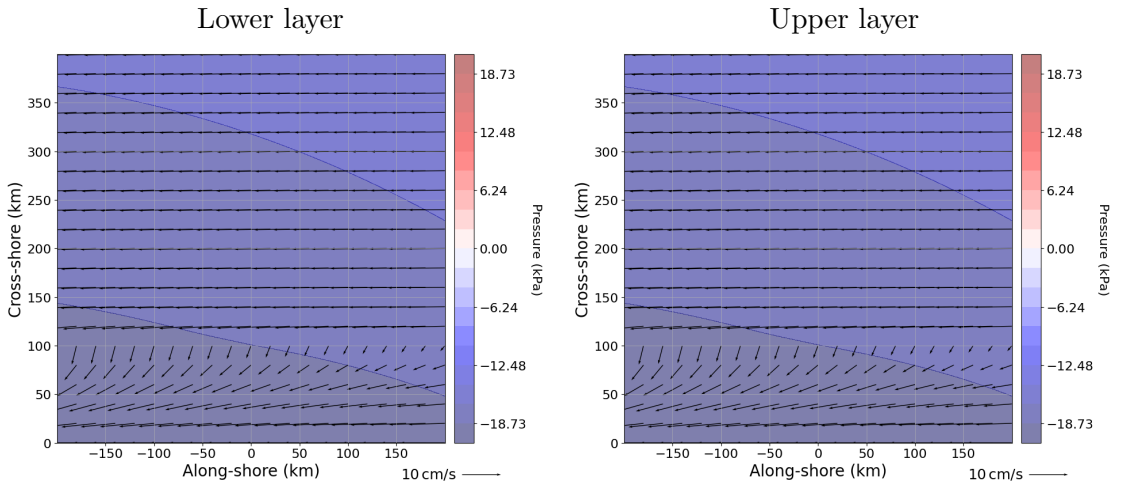

(a) Barotropic

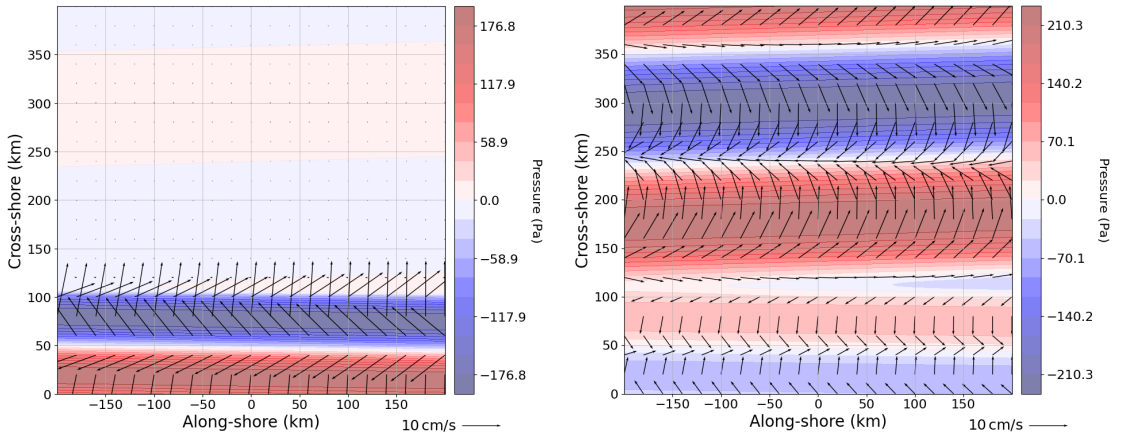

(b) Baroclinic

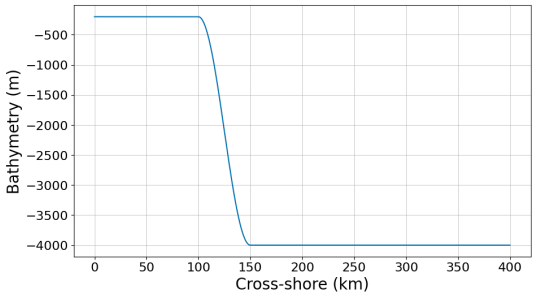

(c) Coastal Topography

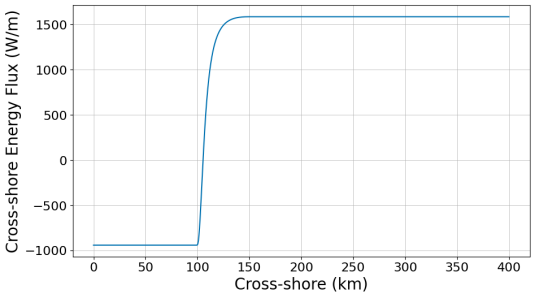

(d) Cross-shore Energy Flux

Figure 4.3: Modal solutions for both the barotropic (top) mode and the baroclinic (middle) mode in the case of a differentiable slope (bottom), with lower-layer solutions on the left, and upper-layer solutions on the right. The contour plots show the pressure perturbation, with units (kPa) in (a) and (Pa) in (b), while the quiver plots show the horizontal velocity field (see 10 cm/s key). The coastal bathymetry profile $-h(y)$ is shown in (c), and the implied time-averaged cross-shore energy flux of the baroclinic mode is shown in (d).

tude oceanward much like the Kelvin wave and shows a uniform vertical structure. In the middle, Figure 4.2b shows the baroclinic (internal) tidal response. Despite a reduction in barotropic tidal amplitudes, the baroclinic response is greater than that of the response over linear topography. This is because the pressure field is maximal in the lower layer along the continental shelf at an increased constant amplitude of $\sim 196\,\mathrm{Pa}$ and is also maximal in the upper layer with an increased constant amplitude of $\sim 234\,\mathrm{Pa}$ in the deep ocean.

Figures 4.2d and 4.3d shows the corresponding time-averaged baroclinic cross-shore energy fluxes of the solutions presented in Figure 4.2 (linear slope) and Figure 4.3 (differentiable slope). More precisely, the linear slope leads to a shoreward energy flux of $\sim 897\,\mathrm{W/m}$ and an oceanward energy flux of $\sim 1,508\,\mathrm{W/m}$, while a differentiable slope leads to a shoreward energy flux of $\sim 941\,\mathrm{W/m}$ and an oceanward energy flux of $\sim 1,586\,\mathrm{W/m}$. The total radiating time-averaged energy flux is $\sim 2.41\,\mathrm{kW/m}$ in the case of a linear slope profile, and $\sim 2.53\,\mathrm{kW/m}$ when the slope profile is differentiable.

4.2.5 Parameter Sweep

In this section, we conduct a series of parameter sweeps to gain a greater understanding of the dependence of the internal-tide response on the continental margin. In the previous section, it was seen that a greater barotropic tidal response of potential forcing does not imply a greater energy transfer from the surface tide to the internal tide. A possible reason for this is the role of wave trapping along the shelf and/or slope, particularly in the case of a linear slope whose gradient is discontinuous at both the shelf break and the foot of the slope. One possible implication of baroclinic wave trapping is the constructive and destructive interference of the waves as the shelf and/or slope width approaches half-integer wavelengths. With radiating boundary conditions, wave trapping is more likely to correlate with slope width than shelf width as the internal waves are not reflected at the shoreline back across the shelf. Another, perhaps more important reason for conducting the following parameter sweeps is to gain a greater understanding of the role coastal geometry plays on the direction and magnitude of internal-tide generation along continental margins. These results will also allow us to compare future analytical scaling laws between coastal topography and internal-tide generation.

In Figures 4.4 and 4.5, we investigate the magnitude and direction of internal-tide generation while varying shelf depth and slope width in the case of a slope profile which is: (a) linear; (b) differentiable. The blue crosses on each contour plot correspond to the default-parameter configuration used in Figures 4.2 and 4.3 and established in Section 4.2.2.

The parameters considered,

$$\frac{c_C^2}{c_D^2} = \frac{H_D\,(H_C - h_1)}{H_C\,(H_D - h_1)} \qquad \text{and} \qquad \frac{c_D - c_C}{\omega_f\,L_S}, \tag{4.29}$$

represent respectively non-dimensional measures of baroclinic squared wave speed on the

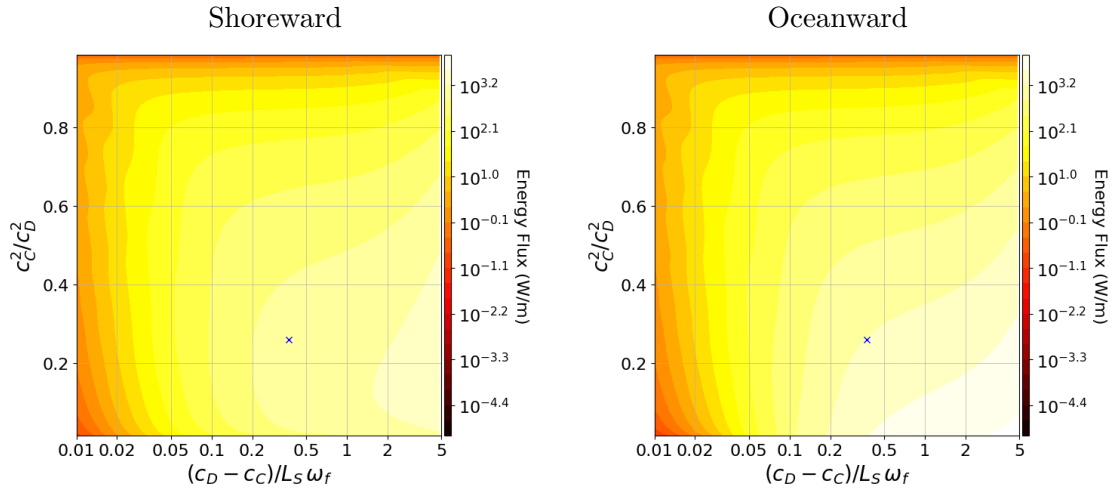

(a) Linear slope

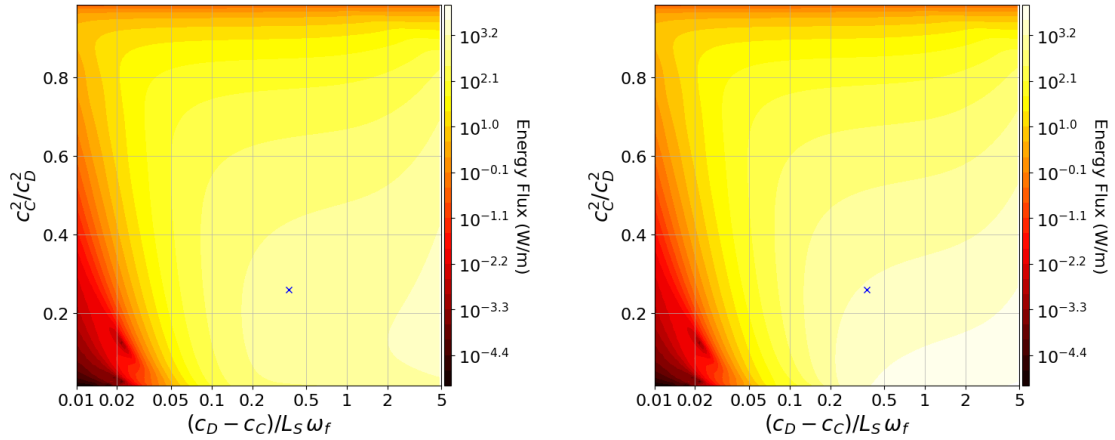

(b) Differentiable slope

Figure 4.4: Contour plot ($\log_{10}$ scale) of time-averaged cross-shore energy fluxes (W/m) of the baroclinic mode in the case of a: (a) linear slope; (b) differentiable slope. The energy flux shoreward is shown on the left, while the energy flux oceanward is shown on the right. On the horizontal axis of each figure, we consider a non-dimensional measure of slope width, while on the vertical a non-dimensional measure of shelf depth. The blue cross indicates the default-parameter case shown in Figures 4.2 and 4.3.

shelf (to that in the deep ocean) and change in baroclinic wavelength (to slope width). The parameter c_C^2/c_D^2 approaches zero in the limit whereby the coastal shelf depth approaches the pycnocline depth, and approaches unity as the shelf depth approaches the deep-ocean depth. The parameter $(c_D - c_C)/\omega_f L_S$ approaches zero in two limits: the shelf depth approaching the deep-ocean depth, and large slope width. The same parameter then approaches infinity in the small slope-width limit ($L_S \to 0\,\text{km}$) or the inertial limit whereby $\omega_f = \sqrt{\omega^2 - f^2} \to 0 \implies \omega^2/f^2 \to 1$.

Figures 4.4 and 4.5 show a wide range of interesting phenomena. In both slope profiles, we see that the energy fluxes, both shoreward and oceanward, of the baroclinic mode tend to zero in the limits of large slope width and shelf depth approaching deep-ocean depth. This is because both limits lead to a cross-shore bathymetric gradient approaching zero,

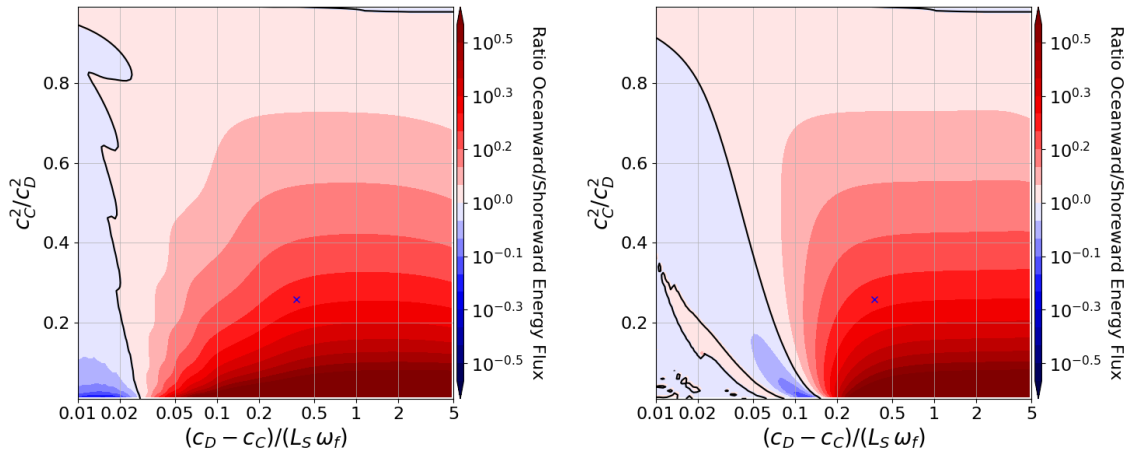

(a) Linear slope

(b) Differentiable slope

Figure 4.5: Ratio between oceanward and shoreward time-averaged cross-shore energy fluxes of the baroclinic mode in the case of a: (a) linear slope; (b) differentiable slope. A value greater than unity suggests there is more energy radiating oceanward than shoreward, and vice-versa. On the horizontal axis of both figures, we consider a non-dimensional measure of slope width, while on the vertical a non-dimensional measure of shelf depth. The black contour shows the region of parameter space where the energy flux shoreward is equal in magnitude to the energy flux oceanward. The blue cross indicates the default-parameter case shown in Figures 4.2 and 4.3.

such that the barotropic and baroclinic modes become increasingly decoupled. However, as the ratio between baroclinic squared wave speeds along the shelf and in the deep ocean approaches unity ($c_C^2/c_D^2 \to 1$ limit), the energy fluxes become independent of slope width. Moreover, the ratio between the magnitude of the energy fluxes oceanward and shoreward approach unity.

The undulations which occur in the large slope-width limit, particularly in the case of a linear slope profile shown in Figure 4.4a, are most likely a result of wave trapping across the slope as the shelf depth varies. This phenomenon appears almost non-existent in the case of a differentiable slope profile. In addition, the linear profile which leads to greater internal-tide generation as slope width is increased.

In the limit of small slope width, we see that the energy fluxes of both slope profiles converge as the two profiles approach that of a step profile. Here, baroclinic energy fluxes are maximal as the shelf depth approaches the pycnocline depth (upper-layer depth h_1). In this same regime for both slope profiles, Figure 4.5 shows that the energy flux oceanward can reach almost ten times greater than the energy flux radiating shoreward.

In Figures 4.6 and 4.7, we investigate the magnitude and direction of internal-tide generation while varying shelf width and slope width in the case of a slope profile which is: (a) linear; (b) differentiable. The variation of shelf width is more interesting than the ratio between shelf depth and deep-ocean depth since it is able to characterise a greater number of continental margins; The depth along continental shelves is typically much smaller than the deep-ocean depth ($H_C/H_D \ll 1$), but continental shelf widths can vary across several

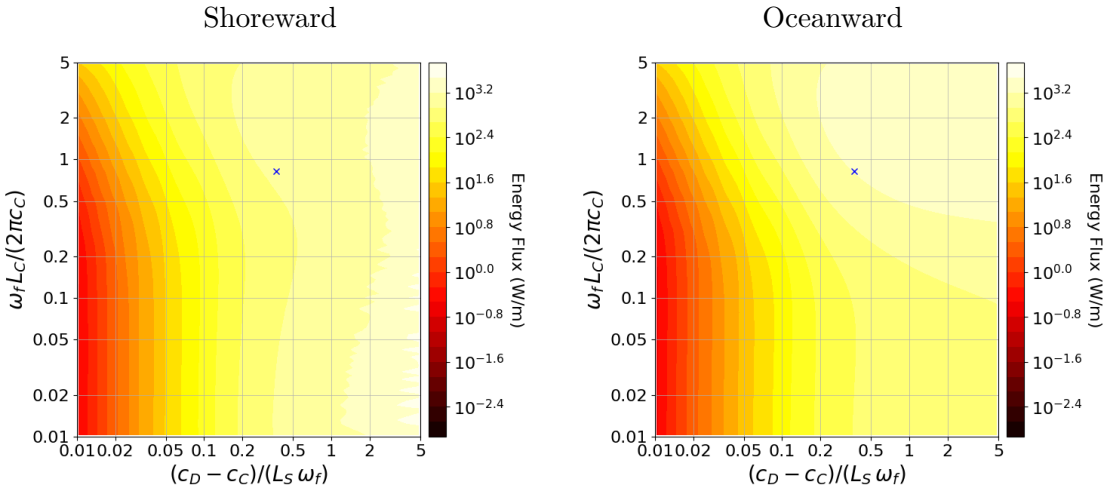

(a) Linear slope

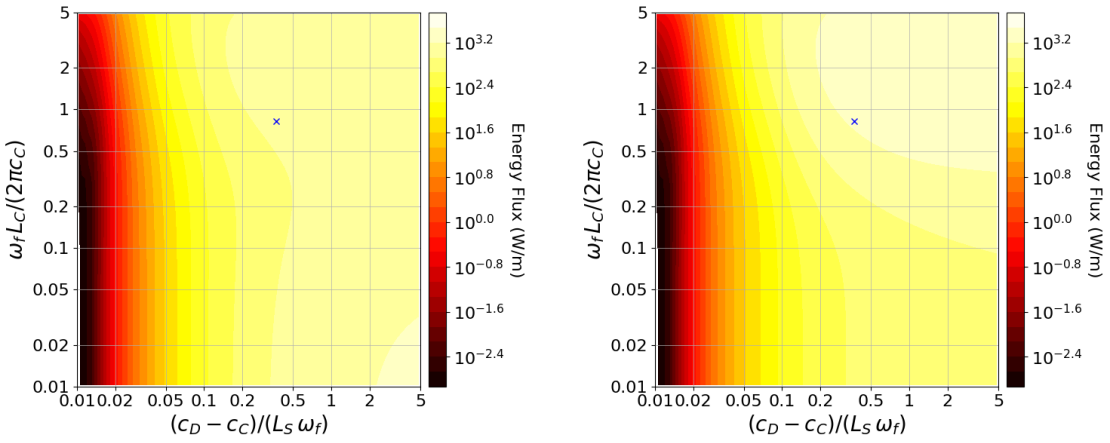

(b) Differentiable slope

Figure 4.6: Contour plot ($\log_{10}$ scale) of time-averaged cross-shore energy fluxes (W/m) of baroclinic response to a fully coupled potentially forced barotropic tide in the case of a: (a) linear slope; (b) differentiable slope. The energy flux shoreward is shown on the left, while the energy flux oceanward is shown on the right. On the horizontal axis of each figure, we consider a non-dimensional measure of slope width, while on the vertical a non-dimensional measure of shelf width. The blue cross indicates the default-parameter case shown in Figures 4.2 and 4.3.

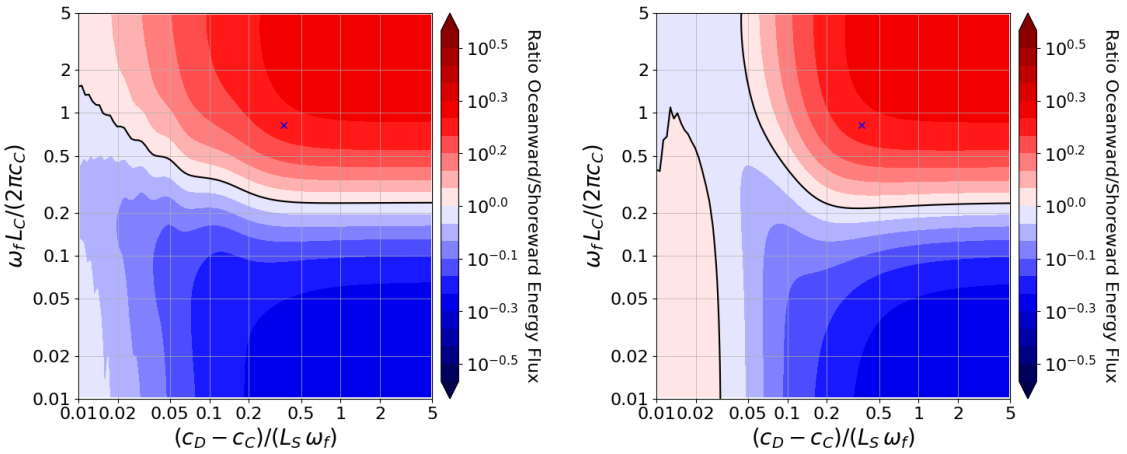

(a) Linear slope

(b) Differentiable slope

Figure 4.7: Ratio between oceanward and shoreward time-averaged cross-shore energy fluxes of the baroclinic mode in the case of a: (a) linear slope; (b) differentiable slope. A value greater than unity suggests there is more energy radiating oceanward than shoreward, and vice-versa. On the horizontal axis of both figures, we consider a non-dimensional measure of slope width, while on the vertical a non-dimensional measure of shelf width. The black contour shows the region of parameter space where the energy flux shoreward is equal in magnitude to the energy flux oceanward. The blue cross indicates the default-parameter case shown in Figures 4.2 and 4.3.

orders of magnitude (see Figure 1.5). We also show the default-parameter configuration established in Section 4.2.2 and used in Figures 4.2 and 4.3 and is indicated by the blue cross on each of the contour plots.

The parameters considered,

$$\frac{\omega_f\, L_C}{2\pi\, c_C} \qquad \text{and} \qquad \frac{c_D - c_C}{\omega_f\, L_S}, \tag{4.30}$$

represent respectively non-dimensional measures of the shelf width (to approximate baroclinic cross-shore wavelength along the continental shelf) and slope width (to the change in cross-shore wavelength across the slope). The parameter $\omega_f\, L_C/2\pi\, c_C$ approaches zero as shelf width approaches zero ($L_C \to 0$) and increases proportionally with shelf width. We recall that the parameter $(c_D - c_C)/\omega_f\, L_S$ approaches zero in two limits: the shelf depth approaching the deep-ocean depth, and large slope width. The same parameter then approaches infinity in the small slope-width limit ($L_S \to 0\,\text{km}$) or the inertial limit whereby $\omega_f = \sqrt{\omega^2 - f^2} \to 0 \implies \omega^2/f^2 \to 1$.

Figures 4.6 and 4.7 also show a wide range of interesting phenomena. In both slope profiles, we see that the energy fluxes, both shoreward and oceanward, of the baroclinic mode tend to zero in the limit of large slope width. Most critically, for fixed shelf width, increasing slope width will reduce energy fluxes shoreward and oceanward. I.e. energy fluxes are maximised in the absence of a slope. However, it is the differentiable slope which leads to a weaker baroclinic energy flux in the limit of large slope width. Furthermore, the

aforementioned behaviour for large slope width appears independent on shelf width in the regime of small shelf width. As shelf width increases, the implied energy fluxes increase, and are maximal in the limit of step topography whereby slope width approaches zero ($L_S \to 0\,\mathrm{km}$). In this regime, Figure 4.7 shows that energy flux oceanward is greater than the energy flux shoreward. It is in the aforementioned parameter regime where the ratio between the two energy fluxes is greatest. Conversely, the energy flux shoreward is greater than the energy flux oceanward in the regime of small shelf width and large slope width.

Having observed a wide range of phenomena while spanning parameter space of coastal topography, the next task is developing an analytical result which helps us understand observations. The preceding results were, relatively speaking, rather costly as each parameter configuration required a system of $\sim 600,000$ unknowns ($\sim 2 \times 3 \times 100,000$).[1] In what follows, we ask ourselves whether simplifications are possible? If so, we seek to develop an analytical means to reveal the non-trivial dependence of coastal and tidal parameters on the rate of barotropic tidal dissipation along continental margins by internal-tide generation.

4.3 Baroclinic Response of Decoupled Barotropic Motion

Significant simplifications arise, facilitating computational and analytical processes, by neglecting the baroclinic dissipation term in the barotropic modal equations in (4.2)–(4.3). To understand why the baroclinic drag term can be neglected, we consider the barotropic momentum equations given by (4.2). By scaling arguments, we require

$$1 \gg \varepsilon^{3/2}\,(h_1/H_D)\,(L_S/L_R)^{-1}\,, \tag{4.31}$$

where the left-hand side of (4.2) scales to $c_0\,|f| \sim L_R\,f^2$. Here, we assume that the baroclinic pressure scales to $c_0^2\,\varepsilon \sim L_R^2\,f^2\,\varepsilon$, and that the bathymetric gradient scales to $(H_D - H_C)\,/L_S \sim H_D/L_S$ given that $H_C/H_D \ll 1$, recalling that L_S, H_C, and H_D denote respectively slope width, shelf depth, and deep-ocean depth. Along the continental margin whereby relative density difference $\varepsilon = O\left(10^{-2}\right)$, pycnocline depth $h_1 = O\left(10^2\,\mathrm{m}\right)$, deep-ocean depth $H_D = O\left(10^3\,\mathrm{m}\right)$, and Rossby radius of deformation $L_R = O\left(10^6\,\mathrm{m}\right)$, we require from (4.31) that

$$L_S \gg L_R\,\varepsilon^{3/2}\,(h_1/H_D) = O\left(0.1\,\mathrm{km}\right). \tag{4.32}$$

For typical coastal topographies, the slope width $L_S = O\left(10\,\mathrm{km}\right)$, which means that the baroclinic drag on the barotropic mode can be neglected when modelling internal-tide generation along continental margins.

The scaling analysis of (4.31) can also be carried out on the barotropic forcing term of baroclinic equations (4.4)–(4.5) for arbitrary coastal shelf depth. Scaling arguments show

[1] Each contour plot required $100 \times 100 = 10,000$ simulations. When solved in series, these contour plots are computationally expensive, despite having sparse matrices.

that

$$\mathcal{T}_{10}\,\boldsymbol{\nabla} h\,P_0 \sim \varepsilon^{1/2}\,h_1\,(1-H_C/H_D)\,(L_S/L_R)^{-1}\,. \tag{4.33}$$

Equation (4.33) quite clearly explains some of the phenomena seen in Section 4.2.5, because the strength of the barotropic forcing tends to zero in the limits of a small pycnocline depth ($h_1 \to 0$), a deep coastal shelf ($H_C \to H_D$), and a large slope width $L_S/L_R \gg 1$. Equation (4.33) also shows that the barotropic forcing is greatest for a large pycnocline depth, a small shelf depth ($H_C/H_D \ll 1$), and a small slope width ($L_S/L_R \ll 1$).

Having neglected the baroclinic drag in equations (4.2)–(4.3), the full system expressed in (4.8) becomes

$$\begin{pmatrix} \mathsf{A}_0 & 0 \\ \mathsf{C}_{10} & \mathsf{A}_1 \end{pmatrix} \begin{pmatrix} \mathbf{q}_0 \\ \mathbf{q}_1 \end{pmatrix} = \begin{pmatrix} \mathbf{F}_0 \\ \mathbf{F}_1 \end{pmatrix}. \tag{4.34}$$

A consequence of (4.34) is that for known barotropic flow denoted by state vector $\mathbf{q}_0$, the baroclinic response is found by solving

$$\mathsf{A}_1\,\mathbf{q}_1 = \mathbf{F}_1 - \mathsf{C}_{10}\,\mathbf{q}_0. \tag{4.35}$$

However, since we know the form of the baroclinic solution along the continental shelf and in the deep-ocean, we need only solve (4.35) along the slope, applying the radiating boundary conditions given by (4.20) and (4.22) at the shelf break and the foot of the slope. Knowing the baroclinic cross-shore velocity at either end of the slope, equations (4.21) and (4.23) can be used to calculate the implied time-averaged radiating energy fluxes shoreward and oceanward.

To find baroclinic state vector $\mathbf{q}_1$, we have two choices for barotropic flow. The first is to consider the same potentially forced problem as in Section 4.2, solving

$$\mathsf{A}_0\,\mathbf{q}_0 = \mathbf{F}_0. \tag{4.36}$$

This problem is explored in Section 4.3.1.

The second involves using the analytical expressions for the potentially forced Kelvin wave that were developed in the previous chapter. It was found in Section 3.4.3 that the potentially forced surface tide for typical tidal parameters resembles that of the Kelvin mode, particularly along the continental margin. Consequently, we need not solve a matrix system, but use the analytical results of equations (3.144)–(3.146). This problem is carried out in Section 4.3.2.

4.3.1 Potentially Forced Barotropic Tide

In what follows, we will briefly compare the fully coupled results presented in Section 4.2 with the baroclinic response of the decoupled potentially forced barotropic motion. By conducting the same parameter sweep involving slope width and shelf width, we are able to observe where implied baroclinic energy fluxes diverge.

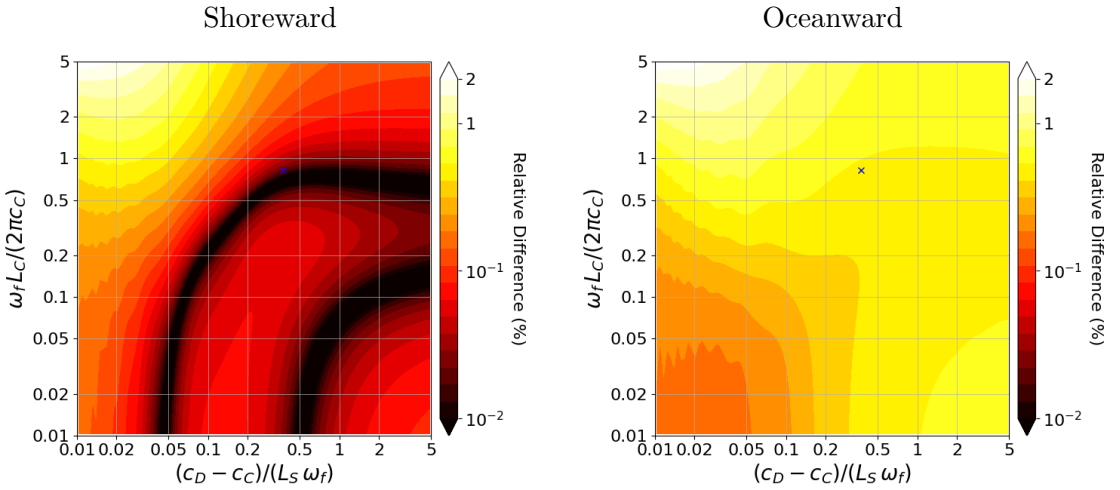

(a) Linear slope

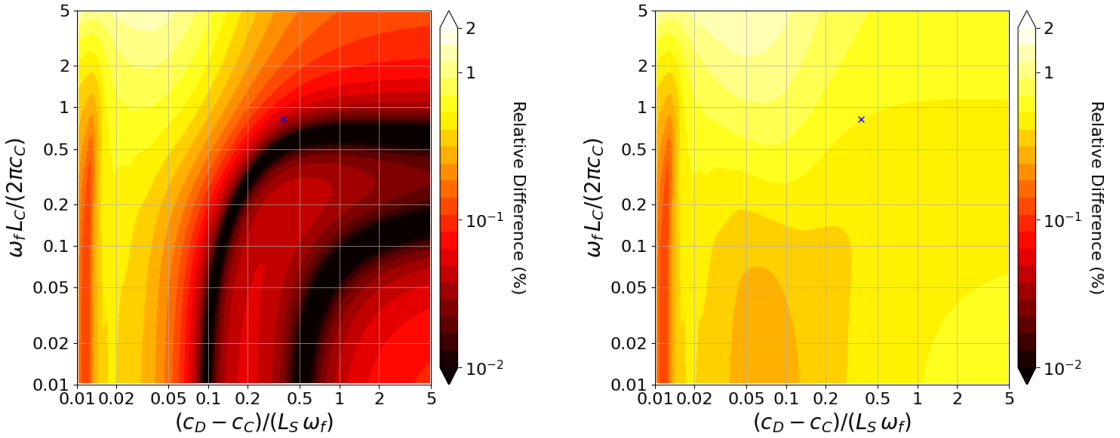

(b) Differentiable slope

Figure 4.8: Contour plot ($\log_{10}$ scale) of relative difference in baroclinic energy fluxes (%) solved using the fully coupled system and the decoupled system in the case of a: (a) linear slope; (b) differentiable slope. The figures on the left concern energy fluxes shoreward, while those on the right concern energy fluxes oceanward. On the horizontal axis of each figure, we consider a non-dimensional measure of slope width, while on the vertical a non-dimensional measure of shelf width.

In Figure 4.8, we conduct the same analysis as in Figure 4.6 for the case of the decoupled system given by (4.34). The relative difference (%) between the two implied energy fluxes, both shoreward and oceanward, are then plotted for the case of a slope which is: (a) linear; (b) differentiable. We recall that varying shelf width and slope width through parameters

$$\frac{\omega_f\, L_C}{2\pi\, c_C} \qquad \text{and} \qquad \frac{c_D - c_C}{\omega_f\, L_S}, \tag{4.37}$$

is more interesting than varying the shelf depth and slope width through parameters

$$\frac{c_C^2}{c_D^2} = \frac{H_D\,(H_C - h_1)}{H_C\,(H_D - h_1)} \qquad \text{and} \qquad \frac{c_D - c_C}{\omega_f\, L_S}, \tag{4.38}$$

as the analysis is able to parameterise a greater variety of typical coastal topographies.

Figure 4.8 shows that for the same parameter regimes considered in Figure 4.6, the relative difference of the implied energy fluxes for either slope, whether shoreward or oceanward, never exceeds $\sim 1.8\%$. This is in part because the smallest value of slope width considered was $L_S = (c_D - c_C)/(5 \times \omega_f) \approx 3.9\,\text{km}$ (see Section 4.2.2 for parameter values used). From equation (4.32), we remain within the regime whereby the baroclinic drag of the barotropic equations can be neglected. In fact, Figure 4.8 shows that the implied radiating energy flux oceanward is more sensitive to decoupling, and that the implied energy fluxes of the two approaches diverge as slope width L_S approaches 0 km (as shown), and rather unexpectedly, in the regime of large shelf width and slope width.

4.3.2 Potentially Forced Barotropic Kelvin Wave

Instead of solving for the full barotropic response of potential forcing, let us consider the barotropic pressure and cross-shore velocity in the analytical form of a potentially forced Kelvin wave, as in equations (3.145) and (3.146). Here, we need only solve for the baroclinic response over the slope to the known form of the surface tide and apply radiating conditions at the head and foot of the slope.

Figure 4.9 shows the resulting cross-shore energy fluxes when using the analytical form of the potentially forced Kelvin wave while varying non-dimensional parameters characterising shelf and slope widths:

$$\frac{\omega_f L_C}{2\pi c_C} \qquad \text{and} \qquad \frac{c_D - c_C}{L_S \omega_f}. \tag{4.39}$$

The two figures on the left show the shoreward energy fluxes, while those on the right show the oceanward energy fluxes. Additionally, the top two figures show the case of a linear slope, while those on the bottom show a differentiable slope.

Comparing Figure 4.9 to Figure 4.6 of the fully coupled potentially forced problem, we see excellent qualitative agreement on the whole between the two scenarios. Where the implied energy fluxes of the analytical decoupled Kelvin wave do visibly appear to differ is in the region of large shelf and slope width, such that the non-dimensional coastal length scale parameter $\lambda \not\ll 1$. Nevertheless, Figure 4.9 continues to show that barotropic dissipation due to internal-tide generation is greatest in the regime of large shelf width but small slope width and is weakest as slope width increases.

To assess the quantitative likeness of the decoupled barotropic tide in the form of an analytical potentially forced Kelvin wave, Figure 4.10 shows the corresponding relative difference between the energy fluxes implied from the fully coupled potentially forced barotropic tide and those implied from the decoupled analytical form of the potentially forced Kelvin wave. A hatched white contour fill is used to show the regime whereby $\lambda = (L_C + L_S)/L_R > 0.2$. In this regime, we expect the accuracy of the forced Kelvin wave to deteriorate. Indeed, Figure 4.10 shows good agreement of the implied energy

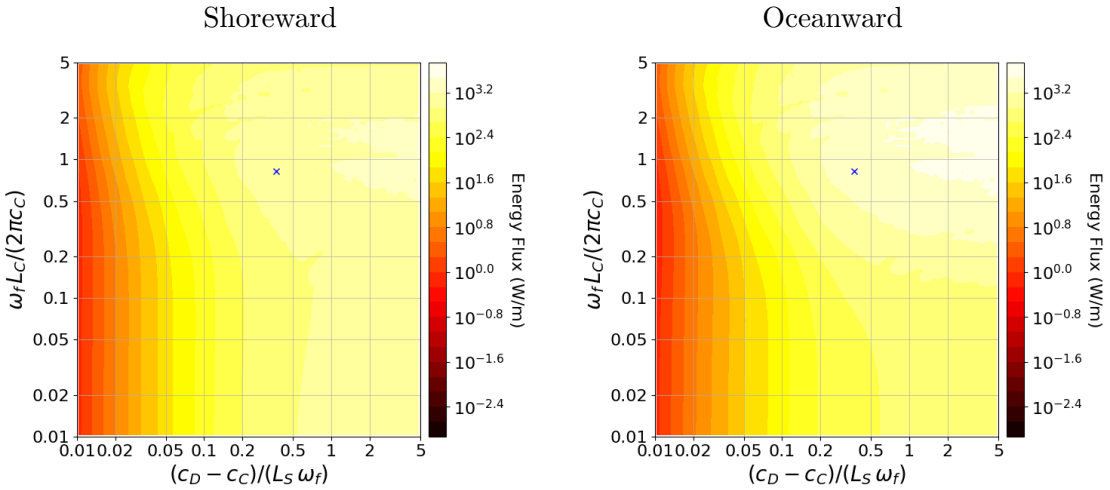

(a) Linear slope

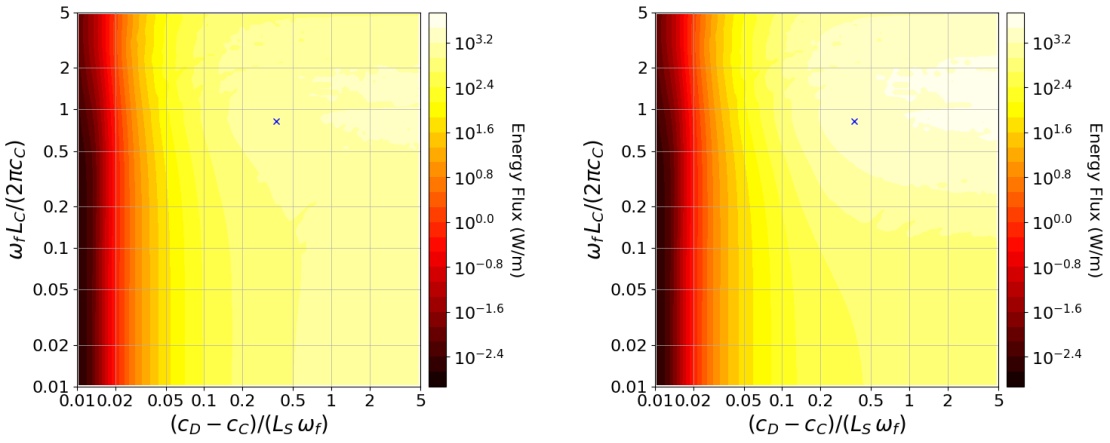

(b) Differentiable slope

Figure 4.9: Contour plot ($\log_{10}$ scale) of time-averaged cross-shore energy fluxes (W/m) of baroclinic response to a decoupled surface tide in the form of an analytical potentially forced Kelvin wave in the case of a: (a) linear slope; (b) differentiable slope. The energy flux shoreward is shown on the left, while the energy flux oceanward is shown on the right. On the horizontal axis of each figure, we consider a non-dimensional measure of slope width, while on the vertical a non-dimensional measure of shelf width. The blue cross indicates the default-parameter case shown in Figures 4.2 and 4.3.

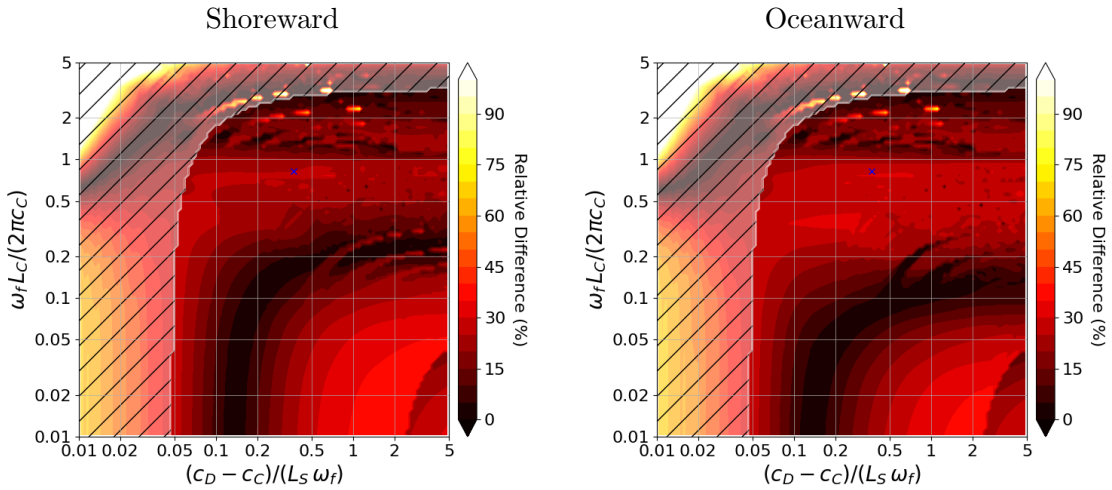

(a) Linear slope

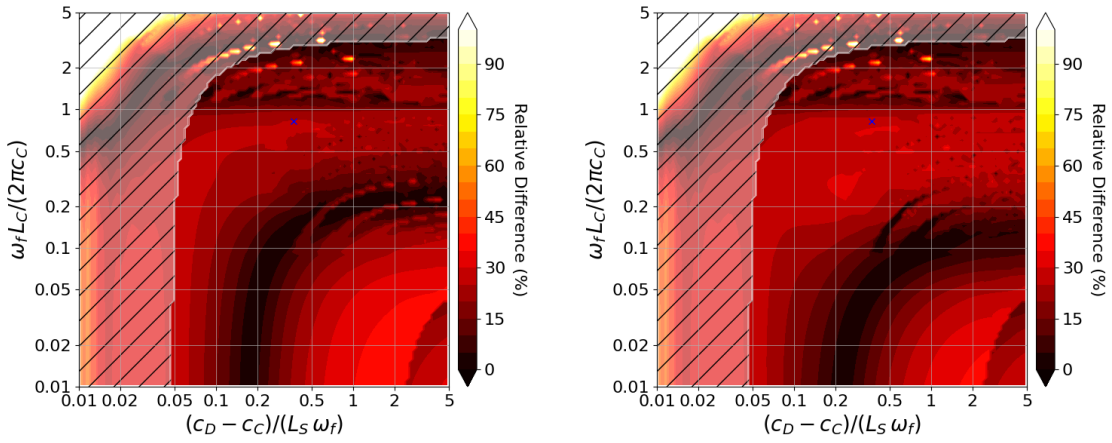

(b) Differentiable slope

Figure 4.10: Contour plot ($\log_{10}$ scale) of relative difference in baroclinic energy fluxes (%) solved using the fully coupled system and the decoupled system in the case of a: (a) linear slope; (b) differentiable slope. Energy fluxes shoreward are shown on the left, while those oceanward are shown on the right. A non-dimensional measure of slope width is used on the horizontal axis, and a non-dimensional measure of shelf width on the vertical. A hatched white contour fill is used to highlight the regime whereby $\lambda \geq 0.2$. In this regime, the accuracy of the analytical form of the surface tide breaks down.

fluxes so long as $\lambda \lesssim 0.2$. Moreover, our idealised form of the barotropic tide is able to approximate the magnitude and direction of energy fluxes largely to within $\sim 30\%$ across a range of shelf-slope profiles provided that $\lambda \ll 1$.

4.3.3 Analytical Result for Internal-Tide Response of Free Kelvin Wave

As shown in Griffiths and Grimshaw (2007a), an exact solution arises by considering a continental margin implied by a piece-wise linear baroclinic wave speed over the slope. That is to say,

$$c_1(y) = \begin{cases} c_C & 0 < y < L_C, \\ c_1(y) = c_C + \omega_f \, \sigma \, (y - L_C) & L_C < y < L_C + L_S, \\ c_D & L_C + L_S < y, \end{cases} \tag{4.40}$$

where $\sigma = (c_D - c_C)/\omega_f \, L_S$. The variable σ is the same non-dimensional parameter considered previously for slope width L_S. This exact solution becomes analytical in the limit $L_S \to 0$, where the continental margin is modelled as a step. We combine the resulting analytical solution with the analytical form for cross-shore volume transport, as in (3.150). This permits an analytical expression for tidal dissipation due to internal-tide generation by a three-dimensional surface tide in the form of a free Kelvin wave of amplitude η_F along the coast.

To begin, we obtain a single equation for cross-shore baroclinic velocity from equations (4.4)–(4.5). Assuming fluid depth of the form (4.11) with slope function $\varphi(y)$ inferred from (4.40), equations (4.4)–(4.5) admit plane-wave solutions of the form given in (4.7). Eliminating the along-shore baroclinic modal velocity, we obtain the two ordinary differential equations

$$i \left(\omega \frac{\mathrm{d}}{\mathrm{d}y} + f \, k \right) P_1(y) + \omega_f^2 \, V_1(y) = -i \, \omega \, \mathcal{T}_{10}(y) \; h'(y) \; P_0(y) \tag{4.41}$$

and

$$\left(\omega^2 - c_1^2 \, k^2 \right) P_1(y) + i \left(\omega \frac{\mathrm{d}}{\mathrm{d}y} - f \, k \right) c_1^2(y) \; V_1(y) = \\ - i \, \omega \, \mathcal{T}_{10}(y) \; h'(y) \; c_0^2(y) \; V_0(y), \tag{4.42}$$

where $\omega_f = \sqrt{\omega^2 - f^2}$. In a bid to remove the baroclinic pressure term, we take the sum of $\left(\omega^2 - c_1^2 \, k^2 \right) \cdot$(4.41) and $-i \left(\omega \frac{\mathrm{d}}{\mathrm{d}y} + f \, k \right) \cdot$(4.42), denoting $\tilde{V}_m(y) = c_m^2 \, V_m(y)$, to arrive at

$$i \, \omega \, k^2 \frac{\mathrm{d}}{\mathrm{d}y} \left(c_1^2(y) \right) \; P_1(y) + \omega^2 \left(\frac{\omega_f^2}{c_1^2(y)} + \frac{\mathrm{d}^2}{\mathrm{d}y^2} - k^2 \right) \tilde{V}_1(y) = \\ - \omega \left[\mathcal{T}_{10}(y) \; h'(y) \left\{ i \left(\omega^2 - c_1^2(y) \; k^2 \right) P_0(y) + \left(\omega \frac{\mathrm{d}}{\mathrm{d}y} + f \, k \right) \tilde{V}_0(y) \right\} + \right. \\ \left. \omega \frac{\mathrm{d}}{\mathrm{d}y} \left(\mathcal{T}_{10}(y) \; h'(y) \right) \tilde{V}_0(y) \right]. \tag{4.43}$$

To aid our ability to write a tractable solution and re-derive the analytical solution presented in §4b of Griffiths and Grimshaw (2007a), we take $k = 0$ in (4.43). This results in the inhomogeneous variable-coefficient ordinary differential equation

$$\left(\frac{\omega_f^2}{c_1^2(y)} + \frac{\mathrm{d}^2}{\mathrm{d}y^2}\right)\tilde{V}_1(y) = -\left[2\mathcal{T}_{10}(y)\, h'(y)\frac{\mathrm{d}}{\mathrm{d}y} + \frac{\mathrm{d}}{\mathrm{d}y}\left(\mathcal{T}_{10}(y)\, h'(y)\right)\right]\tilde{V}_0(y). \tag{4.44}$$

Defining $c_\infty = \sqrt{g' h_1} = \sqrt{g\, h_1\, \varepsilon}$ as in Griffiths and Grimshaw (2007a), it is observed that modal-interaction coefficient

$$\mathcal{T}_{10}(y) = \frac{\sqrt{\varepsilon}}{c_\infty^2}\,\partial_h\left(c_1^2\right) = \frac{\sqrt{\varepsilon}}{c_\infty^2}\frac{\mathrm{d}c_1^2(y)}{\mathrm{d}y}\left(\frac{\mathrm{d}h(y)}{\mathrm{d}y}\right)^{-1}, \tag{4.45}$$

implying that

$$\mathcal{T}_{10}(y)\, h'(y) = \frac{\sqrt{\varepsilon}}{c_\infty^2}\frac{\mathrm{d}c_1^2(y)}{\mathrm{d}y}. \tag{4.46}$$

Upon substitution of the latter, we write (4.44) in the form

$$\begin{aligned}\left(\frac{\omega_f^2}{c_1^2(y)} + \frac{\mathrm{d}^2}{\mathrm{d}y^2}\right)\tilde{V}_1(y) &= -\frac{\sqrt{\varepsilon}}{c_\infty^2}\left[2\frac{\mathrm{d}c_1^2(y)}{\mathrm{d}y}\frac{\mathrm{d}}{\mathrm{d}y} + \frac{\mathrm{d}}{\mathrm{d}y}\left(\frac{\mathrm{d}c_1^2(y)}{\mathrm{d}y}\right)\right]\tilde{V}_0(y)\\ &= -\frac{\sqrt{g\,\varepsilon}}{c_\infty^2}\left[2\frac{\mathrm{d}c_1^2(y)}{\mathrm{d}y}\frac{\mathrm{d}}{\mathrm{d}y} + \frac{\mathrm{d}}{\mathrm{d}y}\left(\frac{\mathrm{d}c_1^2(y)}{\mathrm{d}y}\right)\right]\hat{Q}_{PKW}(y),\end{aligned} \tag{4.47}$$

substituting in for the dimensional form of the barotropic volume transport along the continental margin associated with the free Kelvin wave as in (3.150),

$$\hat{Q}_{PKW}(y) \approx -i\,\eta_F\sqrt{g\,H_D}\,k\,(1 - H_C/H_D)\,y, \tag{4.48}$$

where $|\eta_F|$ is the surface amplitude at the shoreline. Indeed, since $Q'' = 0$, equation (4.47) can be written in the form

$$\begin{aligned}\left(\frac{\omega_f^2}{c_1^2(y)} + \frac{\mathrm{d}^2}{\mathrm{d}y^2}\right)\tilde{V}_1(y) &= -\frac{\sqrt{g\,\varepsilon}}{c_\infty^2}\left(c_1^2(y)\,\cancel{\frac{\mathrm{d}^2}{\mathrm{d}y^2}} + 2\frac{\mathrm{d}c_1^2(y)}{\mathrm{d}y}\frac{\mathrm{d}}{\mathrm{d}y} + \right.\\ &\qquad\left.\frac{\mathrm{d}^2c_1^2(y)}{\mathrm{d}y^2}\right)\hat{Q}_{PKW}(y)\\ &= -\frac{\sqrt{g\,\varepsilon}\,\tilde{Q}}{L_C + L_S}\frac{\mathrm{d}^2}{\mathrm{d}y^2}\left(\frac{c_1^2(y)}{c_\infty^2}\,y\right),\end{aligned} \tag{4.49}$$

where

$$\tilde{Q} = \hat{Q}_{PKW}(L_C + L_S) = -i\,\eta_F\sqrt{g\,H_D}\,k\,(L_C + L_S)\,(1 - H_C/H_D). \tag{4.50}$$

is the volume transport at the foot of the continental slope. Equation (4.49) is equivalent to equations to (37a) of Griffiths and Grimshaw (2007a) and (45) of Shimizu (2011). The derivation of these solutions is provided in Appendix D by Griffiths and Grimshaw (2007a). However, for completeness, we provide the derivation following the methodology

of Griffiths and Grimshaw (2007a) in Appendix A, but with supplementary details.

Most importantly, solutions to (4.49), taking the limit $L_S \to 0$ (corresponding to step topography), take the analytical form

$$\tilde{V}_1(y) = \sqrt{g\,\varepsilon}\,\tilde{Q}\,\frac{c_1^2(y)}{c_\infty^2}\left[\frac{c_D\,c_C}{c_1^2(y)}\left(1+\frac{i\,(c_D-c_C)}{\omega_f\,L_C}\right)-1\right] \tag{4.51}$$

across the slope; this is equivalent to equation (D6) of Griffiths and Grimshaw (2007a). It follows therefore that at either side of the shelf break,

$$\tilde{V}_1\left(L_C^-\right) = c_C^2\,\tilde{C} = \sqrt{g\,\varepsilon}\,\tilde{Q}\,\frac{c_C\,c_D}{c_\infty^2}\left(1-\frac{c_C}{c_D}\right)\left(\frac{i\,c_D}{\omega_f\,L_C}+1\right) \tag{4.52}$$

and

$$\tilde{V}_1\left(L_C^+\right) = c_D^2\,\tilde{D} = \sqrt{g\,\varepsilon}\,\tilde{Q}\,\frac{c_D^2}{c_\infty^2}\left(1-\frac{c_C}{c_D}\right)\left(\frac{i\,c_C}{\omega_f\,L_C}-1\right). \tag{4.53}$$

for $\tilde{C},\tilde{D}$ in (4.21), (4.23) and (4.26). Using $c_1^2\,k^2/\omega^2 \ll 1$, it follows from (4.21) that the energy flux shoreward

$$\langle J_C\rangle = -\frac{\rho^*\,l_C}{2\omega}\,g\,\epsilon\,|\tilde{Q}|^2\,\frac{c_C^2\,c_D^2}{c_\infty^4}\left(1-\frac{c_C}{c_D}\right)^2\left(1+\frac{c_C^2}{\omega_f^2\,L_C^2}\right), \tag{4.54}$$

and from (4.23) that the energy flux oceanward

$$\langle J_D\rangle = +\frac{\rho^*\,l_D}{2\omega}\,g\,\epsilon\,|\tilde{Q}|^2\,\frac{c_D^4}{c_\infty^4}\left(1-\frac{c_C}{c_D}\right)^2\left(1+\frac{c_D^2}{\omega_f^2\,L_C^2}\right). \tag{4.55}$$

Equations (4.54)–(4.55) are equivalent to the fluxes presented in §4b. As a means of verifying the dimensions, we remark that energy flux should have dimensions corresponding to W/m: $\mathrm{M\,L\,T^{-2}}$, where M is mass, L is length and T is time. In SI base units, this is $\mathrm{kg\cdot m\cdot s^{-2}}$. Since $[\rho^*] = \mathrm{M\,L^{-3}}$ (density), $[l] = \mathrm{L^{-1}}$ (baroclinic cross-shore wavenumber), $[\omega] = \mathrm{T^{-1}}$ (forcing frequency), $[g] = \mathrm{L\,T^{-2}}$ (gravity), $\left[\tilde{Q}\right] = \mathrm{L^2\,T^{-1}}$ (volume flux at the shelf break), indeed our expressions for energy flux have the correct dimensions.

Moreover, the ratio of energy flux oceanward to shoreward is given by

$$|\langle J_D\rangle/\langle J_C\rangle| = \frac{c_D}{c_C}\,\frac{\omega_f^2\,L_C^2+c_D^2}{\omega_f^2\,L_C^2+c_C^2}. \tag{4.56}$$

Equation (4.56) indicates that the energy flux shoreward should always be less than the energy flux oceanward. However, this was not that the case in the fully coupled numerics (see Figure 4.7 in the limit $L_S \to 0$ - towards the right in each of the contour plots). For small L_C (bottom right), there is a greater flux shoreward where contours are blue. This may be a result of the two-way coupling between barotropic and baroclinic motions, along with the strong excitation of the Kelvin wave in the limit $L_C \to 0$. Equation (4.56) also suggests that the energy flux shoreward should approach the energy flux oceanward as

$c_C \to c_D$. The latter corresponds to top-right regime in the contour plots of Figure 4.5, and explains why a subtle black contour line—corresponding to unity of (4.56)—is observed.

Combining time-averaged energy fluxes (4.54) and(4.55), the total radiating energy flux is

$$\langle J \rangle = \frac{\rho^* \, g \, \varepsilon \, |\tilde{Q}|^2 \, l_D}{2\omega} \frac{c_D^4}{c_\infty^4} \left(1 - \frac{c_C}{c_D}\right)^2 \left[\frac{c_C}{c_D}\left(1 + \frac{c_C^2}{\omega_f^2 \, L_C^2}\right) + \left(1 + \frac{c_D^2}{\omega_f^2 \, L_C^2}\right)\right], \tag{4.57}$$

where, for completeness,

$$|\tilde{Q}|^2 = |\eta_F|^2 \, g \, H_D \, k^2 \, (1 - H_C/H_D)^2 \; L_C^2, \tag{4.58}$$

recalling that $|\eta_F|$ is the prescribed free-surface amplitude at the shoreline. Moreover, along-shore wavenumber

$$k = \frac{\omega}{\sqrt{g \, H_D}} \left(1 + [1 - H_C/H_D] \, \lambda + O\left(\lambda^2\right)\right), \qquad \lambda = L_C/L_R \ll 1 \tag{4.59}$$

for prescribed wave frequency ω.

The tidal dissipation due to internal-tide generation at a shelf break implied from energy flux in (4.57) approaches zero in several cases. The first is $\varepsilon \to 0$, such that fluid stratification becomes homogeneous. The second is in the limit of no shelf, and is obtained in the limits $L_C \to 0$ or $H_C \to H_D$. If along-shore periodicity with $k = 0$, volume transport at the shelf break $\tilde{Q}$ is also zero. That is to say, we require along-shore periodicity for internal-tide generation by a Kelvin wave. Lastly, the limit $c_C \to c_D$ gives yields no energy fluxes when, excluding the limits already mentioned, upper-layer depth $h_1 \to H_C$.

As for when tidal dissipation is maximised, equations (4.57)–(4.58) suggest this is the case when the shelf depth is really small compared to the deep ocean depth, when along-shore wavenumber is large (corresponding to a small along-shore wavelength), or when the shelf is really long.

4.4 Summary

In this chapter, we have considered three different approaches to modelling internal-tide generation by a forced three-dimensional tide in the form of a Kelvin wave along an idealised two-dimensional continental margin. This is a three-dimensional internal-tide generation problem. For realistic slope widths, solutions are found numerically using a second-order finite differences scheme with a staggered C-grid.

We began, in Section 4.2, we solve the coupled modal equations as in (2.205)–(2.208) for a two-layer fluid using second-order finite-differences with a staggered grid across a wide channel; this is used as a crude model for an ocean basin. To achieve this, idealised topography and default parameter settings are stated in Sections 4.2.1 and Section 4.2.2 respectively. In Section 4.2.3, boundary conditions are provided for the barotropic mode,

and derived for the baroclinic, such that radiating energy fluxes are enforced. In Section 4.2.4, solutions of the coupled barotropic and baroclinic modes are shown to motivate exploration of parameter space further; this is carried out in Section 4.2.5. Here, we discuss regimes in which baroclinic energy fluxes appear maximised or minimised based on idealised shelf-slope topography. For example, increasing slope width appears to always reduce the magnitude of radiating energy fluxes over the continental margin.

In Section 4.3, the dynamics between the barotropic and baroclinic motion are decoupled. A scaling analysis is used to argue that this assumption is valid. In which case, the matrix system of (4.8) can be separated into two, shown in (4.34). While barotropic motion requires still to be solved over the entire width of the channel, the baroclinic motion needs only to be solved over the slope. Not only is the resultant system much faster to compute, but the relative errors of the implied energy fluxes also never exceed 2% when corresponding to the first approach as in Section 4.2.

In Section 4.3.2, we consider the surface tide as in Section 3.4.3; this is a surface tide corresponding to the forced Kelvin wave. This problem was the fastest to compute. Moreover, the implied energy fluxes showed excellent qualitative agreement across parameter space. Moreover, in large parts of parameter space, provided that the coastal length scale is sufficiently small, the magnitude of the implied energy fluxes was within 30% of those corresponding to the fully coupled approach.

Lastly, we consider in Section 4.3.3, an analytical solution to the internal-tide generation problem for a tide in the form of a free Kelvin wave. This follows the methodology of §4b Griffiths and Grimshaw (2007a) in the case of step topography. Our work is in contrast to the two-dimensional free wave used by Griffiths and Grimshaw (2007a). The internal-tide generation problem using step-topography was originally explored as a scattering problem by Rattray (1960). We then exploit this analytical solution to develop an expression for the implied energy fluxes from a three-dimensional surface tide. The expressions are then used to explain previous observations made in Section 4.2.5, as well as to illuminate the non-trivial dependencies of stratification, forcing and topographic parameters on internal-tide generation along a two-dimensional continental margin.

Chapter 5

Discontinuous Galerkin Finite Element Method

5.1 Introduction

In this chapter, we introduce the discontinuous Galerkin finite element method (DG-FEM) and explain how it can be applied to resolve linearised shallow-water tidal dynamics. For those familiar with (continuous) finite element methodology on unstructured grids, the primary difference is that the nodal information is not shared across element boundaries. In other words, there may be more than one nodal value at a given spatial co-ordinate, as shown in Figure 5.1. This discretisation allows for discontinuities in solutions and can be great at modelling shocks and the propagation of waves over discontinuous topography such as steps.

The very first use of DG-FEM appears in Reed and Hill (1973), where the authors proposed solving an equation for steady-state neutron transport by "differencing the discrete ordinates equations on a triangular x–y grid ... based on piece-wise polynomial representations of [an] angular flux". A year later, LeSaint and Raviart (1974) conducted an error analysis on the method. The analysis showed that the method on a triangulated grid of cell size h and polynomial order p has a general convergence rate of $O\left(h^{p}\right)$. When optimised, the method can reach a convergence rate of $O\left(h^{p+1}\right)$. Further analysis conducted by Johnson and Pitkaranta (1986) refined previous analysis by considering general $L^{\mathcal{P}}$-norms and concluded that for $\mathcal{P} = 2$, the method yields a convergence rate of $O\left(h^{p+1/2}\right)$ when the angles of all triangular elements are bounded from below, independent of cell size h.

The numerical method has been applied to model a range of physical phenomena, both linear and non-linear, governed by hyperbolic systems of equations. This includes the Maxwell equations (e.g. Remaki & Fézoui, 1998; Warburton, 1999), the acoustic equations (e.g. Atkins & Shu, 1998; Toulopoulos & Ekaterinaris, 2006), and of course, the shallow-water equations (e.g. Giraldo et al., 2002; Eskilsson & Sherwin, 2004, 2005; Levin et al.,

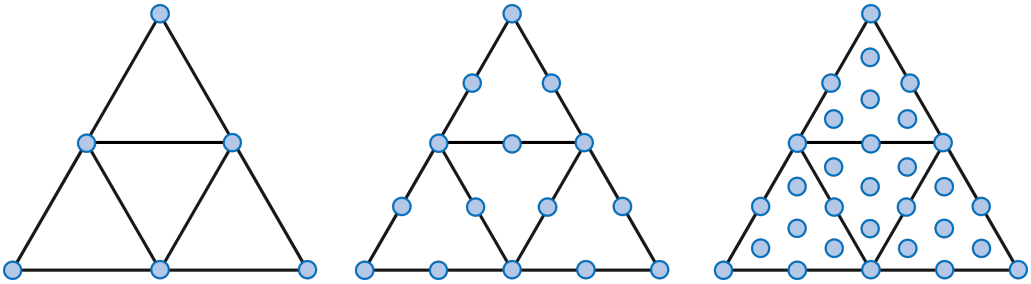

(a) Nodes in a continuous Galerkin discretisation.

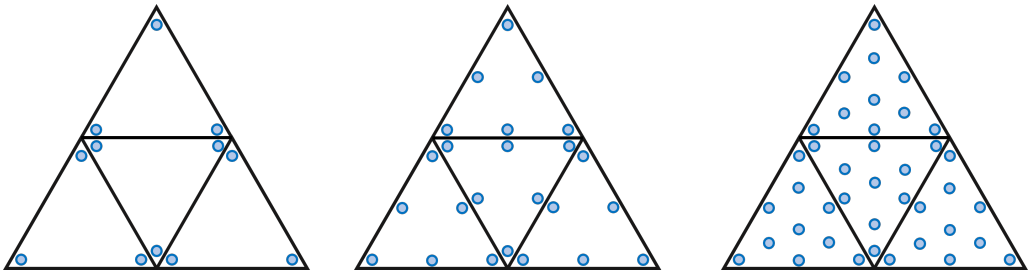

(b) Nodes in a discontinuous Galerkin discretisation.

Figure 5.1: Comparison of continuous and discontinuous Galerkin nodal discretisations of a triangulated domain, where the blue circles and black lines represent respectively nodal points and element boundaries. On the top, we show the nodal points in the case of (continuous) finite elements which are shared across the element boundaries over which continuity is enforced. On the bottom, we show the nodal points for discontinuous finite elements, where nodes are placed either side of a boundary, allowing discontinuities over element boundaries and an explicit local formulation. Figures on the left represent the nodal points for a first-order interpolation across a triangular element, those in the middle for a second-order interpolation, while those on the right for a third-order interpolation.

2006; Ambati & Bokhove, 2007; Salehipour et al., 2013; Khan & Lai, 2014; Steinmoeller et al., 2016).

More sophisticated finite element schemes applied to shallow-water equations do exist. By combining different finite element pairs, the velocity and pressure variables may exhibit ideal mathematical properties (e.g. Le Roux et al., 1998; Walters & Casulli, 1998). One example which uses a discontinuous element function in an element pair is one proposed by Cotter et al. (2009). Here, the velocity field is represented by discontinuous linear element functions, while the pressure field—the paper uses perturbation layer thickness denoted h—is represented by continuous quadratic element functions. Denoted $\mathrm{P1_{DG}}$–P2, the authors show that the element pair has excellent geostrophic-balance properties since the impermeability boundary condition is strongly satisfied. In the non-rotating case, the authors even show that the linearised equations have no small spurious modes. More general information on mixed finite element methods can be found in Boffi et al. (2013).

When compared to more familiar grid-based computational methods, there are many properties of DG-FEM which render the method ideal for shallow-water dynamics around continental margins. In particular, DG-FEM allows one to resolve shallow-water dynamics over discontinuous topographies in complex geometries with high-order adaptive accuracy,

	Complex geometries	High-order accuracy and *hp*-adaptivity	Explicit semi-discrete form	Conservation laws	Elliptic problems
FDM	×	✓	✓	✓	✓
FVM	✓	×	✓	✓	(✓)
FEM	✓	✓	×	(✓)	✓
DG-FEM	✓	✓	✓	✓	(✓)

Figure 5.2: Properties of common grid-based computational methods used for solving partial differential equations, taken from Hesthaven and Warburton (2008). These common grid-based computational methods are finite difference (FDM), finite volume (FVM), finite element (FEM) and discontinuous Galerkin finite element (DG-FEM). Here, a tick is used to indicate the method's success, a cross to indicate a method's shortcoming, while a tick in parenthesis is used to indicate that the method can be adapted to address a typical shortcoming.

all while satisfying energy and mass conservation laws. Furthermore, the localised nature of DG-FEM means that linear discrete operators are often incredibly sparse, making the method much more efficient than regular finite element methods. A succinct summary is provided by Hesthaven and Warburton (2008) and is shown in Figure 5.2. Here, the authors summarise the principal advantages and disadvantages of popular grid-based computational methods. The methods compared are finite difference (FDM), finite volume (FVM), finite element (FEM) and discontinuous Galerkin finite elements (DG-FEM).

We begin, in Section 5.2, by constructing the mathematical formulation of the computational method applied to the governing equations derived in Section 2.4.8. In Section 5.3, we assess the stability of solutions. However, this depends on the choice of numerical flux and boundary conditions. A numerical flux, as explored in Section 5.4, approximates the true flux across an element boundary using a combination of nodal information from adjacent elements (see LeVeque, 2002; Bertoluzza et al., 2009; Toro, 2009). In Section 5.5, the imposition of boundary conditions via ghost nodes are considered. We verify the numerical implementation of the method in Section 5.6 by ensuring convergence of solutions through both *h*- and *p*-refinement.[1] Here, we also provide a brief assessment on the impact of numerical flux on the form of numerical solutions, as well as on convergence rate and time-complexity. We conclude our findings in Section 5.7.

The code used for this chapter requires Python packages:

- `ppp` - see Appendix B.1.
- `DGFEM` - see Appendix Appendix B.2.
- `barotropicSWEs` - see Appendix B.3

Further package dependencies and file structure of aforementioned Python packages are discussed in Appendix B.

[1] There is a third kind of refinement known as *r*-refinement. This method employs an adaptive mesh to move element nodes to increase accuracy of solutions (see Oliveira, 1971; Miller & Miller, 1981; Min et al., 1994).

5.2 DG-FEM Formulation

In the following section, we shall consider the mathematical formulation of the DG-FEM method when modelling barotropic dissipation due to the generation of internal waves along a pycnocline within a basin of domain Ω with boundary $\partial\Omega$ under the influence of planetary rotation. Since our primary aim is to model internal-tide generation at a pycnocline, we concern ourselves with a sole baroclinic mode. Moreover, we shall also be neglecting the baroclinic drag on the barotropic mode, allowing us to solve first of all the barotropic motion in our basin, followed by any baroclinic response which will appear as a forcing term. We consider therefore the barotropic-to-baroclinic coupling of the 2D modal shallow-water equations on an f-plane given by equation (4.34). These are

$$\partial_t \mathbf{U}_0 + \boldsymbol{\nabla} P_0 = -f\,\hat{\mathbf{e}}_z \times \mathbf{U}_0 + \boldsymbol{F}_0, \tag{5.1}$$

$$\partial_t P_0 + \boldsymbol{\nabla}\cdot\left(c_0^2(\mathbf{x})\;\mathbf{U}_0\right) = 0, \tag{5.2}$$

$$\partial_t \mathbf{U}_1 + \boldsymbol{\nabla} P_1 = -\mathcal{T}_{10}\,\boldsymbol{\nabla} h\, P_0 - f\,\hat{\mathbf{e}}_z \times \mathbf{U}_1, \tag{5.3}$$

$$\partial_t P_1 + \boldsymbol{\nabla}\cdot\left(c_1^2(\mathbf{x})\;\mathbf{U}_1\right) = -\mathcal{T}_{10}\,\boldsymbol{\nabla} h\cdot\left(c_0^2(\mathbf{x})\;\mathbf{U}_0\right). \tag{5.4}$$

We recall that for upper- and lower-layer depths h_1 and $h-h_1$, the barotropic and baroclinic modal wave speeds are

$$c_0^2 \approx g\,h \qquad \text{and} \qquad c_1^2 \approx \frac{g'\,h_1\,(h-h_1)}{h}, \tag{5.5}$$

with total fluid depth h, h_1 constant and gravitational acceleration $g = 9.81\,\mathrm{m/s^2}$. Our choice of normalisation in our modal decomposition is such that any self-interaction term, $\mathcal{T}_{mm}$, is zero, and that the modal-interaction coefficient is anti-symmetric. I.e. we have that $\mathcal{T}_{mn} = -\mathcal{T}_{nm}$. In our decoupled two-layer model, we consider uniquely the modal interaction term

$$\mathcal{T}_{10} = \frac{\sqrt{\partial_h\left(c_0^2\right)\;\partial_h\left(c_1^2\right)}}{c_1^2 - c_0^2} = \frac{h_1}{h^2}\sqrt{\varepsilon}\left(1 + O\left(\sqrt{\varepsilon}\right)\right), \tag{5.6}$$

recalling that $\varepsilon = (\rho_2 - \rho_1)/\rho_2$ represents the relative density difference at the interface, and h_1 the fixed upper-layer depth.

In (5.1) we also include the external forcing of the barotropic mode, $\boldsymbol{F}_0$. This term could encompass a range of effects including, but not limited to, potential forcing, self-attraction and loading, as well as Rayleigh damping.

The form of equations (5.1)–(5.4) lends itself ideal when expressing the equations in conservative form: a crucial step in formulating the numerical scheme. On the right-hand side, we consider terms which are either a source/sink terms, or non-gradient terms.

The linearised mode-n shallow-water equations in conservative form are written as

$$\partial_t \mathbf{q}_n + \partial_x \mathbf{F}_n + \partial_y \mathbf{G}_n = \mathbf{S}_n, \tag{5.7}$$

where

$$\mathbf{q}_n = \begin{pmatrix} U_n & V_n & P_n \end{pmatrix}^\mathsf{T}$$

represents the mode n state vector composed of the along-shore and cross-shore velocities, as well as the corresponding pressure, while

$$\mathbf{F}_n = \begin{pmatrix} 0 & 0 & 1 \\ 0 & 0 & 0 \\ c_n^2 & 0 & 0 \end{pmatrix} \mathbf{q}_n \qquad \text{and} \qquad \mathbf{G}_n = \begin{pmatrix} 0 & 0 & 0 \\ 0 & 0 & 1 \\ 0 & c_n^2 & 0 \end{pmatrix} \mathbf{q}_n \tag{5.8}$$

denote respectively the along-shore and cross-shore flux terms.

The principal difference between the conservative form of the barotropic and baroclinic modes lies in the source term (this term will also include any non-gradient terms, including the Coriolis, which are neither sinks nor sources). For the barotropic mode having neglected baroclinic drag, $n = 0$, the source term

$$\mathbf{S}_0 = \mathbf{C}_0 + \mathbf{E}_0 \tag{5.9}$$

is composed of the non-gradient Coriolis term

$$\mathbf{C}_n = - \begin{pmatrix} 0 & -f & 0 \\ f & 0 & 0 \\ 0 & 0 & 0 \end{pmatrix} \mathbf{q}_n, \tag{5.10}$$

as well as the external force

$$\mathbf{E}_0 = \begin{pmatrix} \hat{\mathbf{e}}_x \cdot \boldsymbol{F}_0 & \hat{\mathbf{e}}_y \cdot \boldsymbol{F}_0 & 0 \end{pmatrix}^\mathsf{T}, \tag{5.11}$$

where $\hat{\mathbf{e}}_x$ and $\hat{\mathbf{e}}_y$ denote respectively the unit normal in the along-shore and cross-shore directions.

On the contrary, the baroclinic mode, $n = 1$, the source term,

$$\mathbf{S}_1 = \mathbf{B}_1 + \mathbf{C}_1 + \mathbf{E}_1, \tag{5.12}$$

is composed respectively of the barotropic-forcing term, the non-gradient Coriolis term, as well as any additional external forces to be exerted on the baroclinic mode.

The barotropic-forcing term,

$$\mathbf{B}_1 = -\mathcal{T}_{10} \begin{pmatrix} 0 & 0 & \partial_x h \\ 0 & 0 & \partial_y h \\ c_0^2\, \partial_x h & c_0^2\, \partial_y h & 0 \end{pmatrix} \mathbf{q}_0, \tag{5.13}$$

is proportional to both bathymetric gradient $\boldsymbol{\nabla} h$ and modal-interaction coefficient $\mathcal{T}_{10}$ defined in (5.6).

5.2.1 Localised Weak Form

Now that we have our governing equations in some generalised conservative form, our aim now is to obtain the localised weak form. It should be highlighted that there are two approaches in finite element methods: the variational approach (also known as the energy approach), and the method of weighted residuals. It is the latter approach that we shall be taking. Here, one aims to minimise the local residual error of an approximation by fitting trial functions (see Finlayson & Scriven, 1966; Finlayson, 2013; Chakraverty et al., 2019). To begin, we multiply the residual

$$\boldsymbol{\mathcal{R}}_n\left(\mathbf{x},t\right)=\partial_t\mathbf{q}_n+\partial_x\mathbf{F}_n+\partial_y\mathbf{G}_n-\mathbf{S}_n \tag{5.14}$$

by some local arbitrary test function, $\psi^k\left(\mathbf{x}\right)$, which satisfies the given boundary conditions of our problem, and require that the integral over element domain D^k be zero, such that

$$\int_{\mathsf{D}^k}\psi^k\left(\mathbf{x}\right)\,\boldsymbol{\mathcal{R}}_m\left(\mathbf{x},t\right)\,\mathrm{d}\mathbf{x}=\mathbf{0}. \tag{5.15}$$

Using the divergence theorem, we obtain the localised weak formulation,

$$\begin{aligned}\int_{\mathsf{D}^k}\Big(\psi^k\left(\mathbf{x}\right)\left(\partial_t\mathbf{q}_n-\mathbf{S}_n\right)-\mathbf{F}_n\,\partial_x\psi^k\left(\mathbf{x}\right)-\mathbf{G}_n\,\partial_y\psi^k\left(\mathbf{x}\right)\Big)\,\mathrm{d}\mathbf{x}=\\ -\int_{\partial\mathsf{D}^k}\left(n_x\,\mathbf{F}_n^*+n_y\,\mathbf{G}_n^*\right)\psi^k\left(\mathbf{x}\right)\mathrm{d}\mathbf{x},\end{aligned} \tag{5.16}$$

where $\hat{\mathbf{n}}=\begin{pmatrix}n_x & n_y\end{pmatrix}^\mathsf{T}$ represents the outward-pointing normal along the element boundary. Numerical fluxes $\mathbf{F}^*$ and $\mathbf{G}^*$ represent the unique values by which we use to approximate the true flux at the element boundary $\partial\mathsf{D}^k$ and is typically a combination of information from the two adjacent elements.

By applying Gauss' theorem once more to (5.16), we obtain the strong formulation

$$\int_{\mathsf{D}^k}\psi^k\left(\mathbf{x}\right)\,\boldsymbol{\mathcal{R}}\left(\mathbf{x}\right)\,\mathrm{d}\mathbf{x}=-\int_{\partial\mathsf{D}^k}\left(n_x\left(\mathbf{F}^*-\mathbf{F}\right)+n_y\left(\mathbf{G}^*-\mathbf{G}\right)\right)\psi^k\left(\mathbf{x}\right)\,\mathrm{d}\mathbf{x}, \tag{5.17}$$

which we find more practical when it comes to enforcing boundary conditions introduced at the end points of each element and is a consequence of the discontinuous representation of the solution (Steinmoeller et al., 2016).

5.2.2 Localised Semi-Discrete Strong Form

Approximating the domain Ω by K non-overlapping elements D^k, we develop the scheme further by seeking an approximation to state variables

$$\mathbf{q}_n=\begin{pmatrix}U_n & V_n & P_n\end{pmatrix}^\mathsf{T}\simeq\mathbf{q}_{nh}=\begin{pmatrix}U_{nh} & V_{nh} & P_{nh}\end{pmatrix}^\mathsf{T}. \tag{5.18}$$

These approximations are composed of the direct sum of K local polynomials $\mathbf{q}_{nh}^k$ over each element, giving

$$\mathbf{x} \in \mathsf{D}^k : \qquad \mathbf{q}_{nh}^k(\mathbf{x},t) = \sum_{i=1}^{N_p} \mathbf{q}_{nh}^k(\mathbf{x}_i,t)\ \ell_i^k(\mathbf{x}) = \sum_{i=1}^{N_p} \hat{\mathbf{q}}_{nh}^k(t)\ \psi_i^k(\mathbf{x}), \tag{5.19}$$

where $\ell_i^k(\mathbf{x})$ is the two-dimensional Lagrange polynomial based on grid points $\mathbf{x}_i \in \mathsf{D}^k$, and $\{\psi_n(\mathbf{x})\}_{n=1}^{N_p}$ is an orthonormal two-dimensional polynomial basis. While in the one-dimensional case, N_p represents the number of polynomials needed to construct a basis of order N, in two dimensions, we require

$$N_p = \frac{(N+1)(N+2)}{2}$$

polynomials for triangular elements. For the remainder of the formulation, we shall neglect the index modal notation.

Following the methodology of Hesthaven and Warburton (2008), we consider the mapping from an arbitrary triangular element to a generalised triangular element with vertices $(-1,-1)$, $(1,-1)$ and $(-1,1)$, denoted T, spanned by local co-ordinate variables $\mathbf{r} = (r,s)$. Let us consider therefore the local polynomial approximation

$$\mathbf{q}(\mathbf{r},t) = \sum_{n=1}^{N_p} \hat{\mathbf{q}}_n(t)\ \psi_n(\mathbf{r}) = \sum_{i=1}^{N_p} \mathbf{q}_i(\mathbf{r}_i,t)\ \ell_i^k(\mathbf{r}). \tag{5.20}$$

Expansion coefficients, $\hat{\mathbf{q}}_n$, are defined by constructing an interpolation, such that for Vandermonde matrix $\mathcal{V}$ with entries

$$\mathcal{V}_{ij} = \psi_j(\mathbf{r}_i), \tag{5.21}$$

we have that

$$\mathcal{V}\,\hat{\mathbf{q}} = \mathbf{q}. \tag{5.22}$$

The latter formulation allows one to define the expansion coefficients (e.g. in the matrix-vector form) in terms of the nodal representation without the need of multi-dimensional integrals which can be computationally expensive.

For choice of local test function, we are required to identify an orthonormal basis $\psi_j(\mathbf{r})$ defined over triangle T. To resolve the latter, we consider the canonical basis

$$\psi_m(\mathbf{r}) = r^i\, s^j, \tag{5.23}$$

where

$$m = j + (N+1)\,i + 1 - \frac{i}{2}(i-1), \qquad \forall\,(i,j) \in \mathbb{N}; \qquad i+j \leq N. \tag{5.24}$$

This polynomial basis can then be orthonormalised through the Gram–Schmidt process,

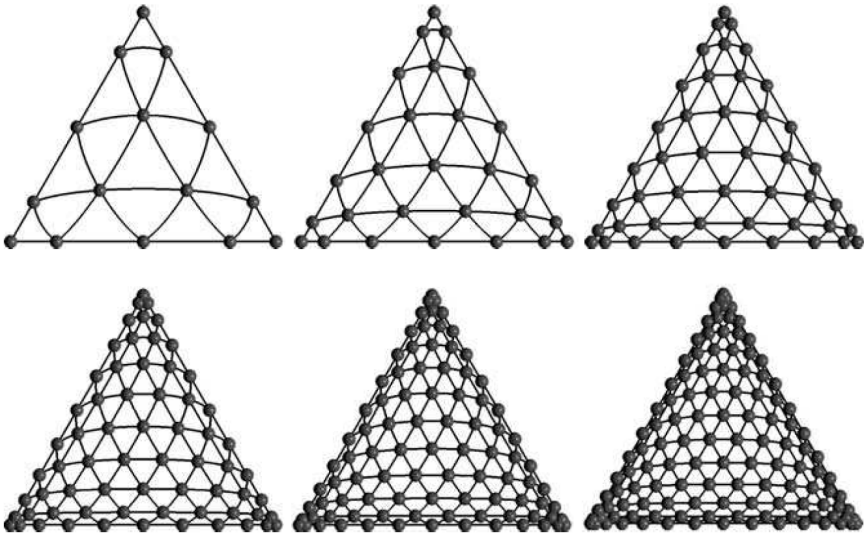

Figure 5.3: Figure 6.6 of Hesthaven and Warburton (2008), examples of α-optimised nodal sets on the equilateral triangle are shown. From left to right, the top row depicts orders 4, 6 and 8, while the bottom depicts orders 10, 12 and 14.

resulting in the basis

$$\psi_m(r,s) = \sqrt{2}\, P_i(a)\; P_j^{(2i+1,0)}(b)\,(a-b)^i; \qquad a = 2\frac{1+r}{1-s} - 1, \qquad b = s, \tag{5.25}$$

where $P_n^{(\alpha,\beta)}(x)$ represents the n-th order Jacobi polynomial.

Having identified a suitable choice of orthonormal polynomials which span triangle T, what remains is to find a suitable choice of N_p grid points over which we construct our Lagrange interpolating polynomials. We remind the reader of Runge's phenomenon which arises when constructing an interpolation polynomial using equi-distant nodes (see Epperson, 1987). Instead, we use the set of α-optimised nodes which minimise the Lebesgue constant

$$\Lambda = \max_{r,s} \sum_{i=1}^{N_p} |\ell_i(r,s)|, \tag{5.26}$$

used to measure the quality of the interpolant (see Table 6.1 of Hesthaven & Warburton, 2008). Examples of these nodal sets constructed over an equilateral triangle are shown in Figure 5.3. Much like with Chebyshev nodes, oscillations of the interpolating polynomial are reduced by considering nodes which are distributed more densely along the edges of the domain, which is what we also see in Figure 5.3.

To summarise, we consider the Lagrange interpolating polynomials constructed using Jacobi polynomials over α-optimised nodes which minimise the Lebesgue constant. As a result, we obtain a means of evaluating a genuinely two-dimensional Lagrange polynomials, $\ell_i(\mathbf{x})$, for which no explicit expression is known (Hesthaven & Warburton, 2008). Of course, this choice of local test function is not a limitation of the theory, but a choice made out of convenience upon numerical implementation.

If we then choose the space of test functions to be the same as the solution space, V_h, we recover the semi-discrete weak statement by substituting (5.19) into (5.16), giving

$$\mathcal{M}^k \left(\frac{\mathrm{d}}{\mathrm{d}t} \mathbf{q}_h^k - \mathbf{S}_h^k \right) - \mathbf{F}_h^k \left(\mathcal{S}_x^k \right)^{\mathsf{T}} - \mathbf{G}_h^k \left(\mathcal{S}_y^k \right)^{\mathsf{T}} = - \int_{\partial \mathsf{D}^k} \left(n_x \, \mathbf{F}^* + n_y \, \mathbf{G}^* \right) \psi^k \left(\mathbf{x} \right) \, \mathrm{d}\mathbf{x}, \tag{5.27}$$

where

$$\mathcal{M}_{lm}^k = \int_{\mathsf{D}^k} \psi_l \left(\mathbf{x} \right) \, \psi_m \left(\mathbf{x} \right) \, \mathrm{d}\mathbf{x} \qquad \text{and} \qquad \left(\mathcal{S}_i^k \right)_{lm} = \int_{\mathsf{D}^k} \psi_l \left(\mathbf{x} \right) \, \partial_{\mathbf{x}_i} \psi_m \left(\mathbf{x} \right) \, \mathrm{d}\mathbf{x} \tag{5.28}$$

are the local mass and stiffness matrices respectively. We may similarly obtain the localised semi-discrete statement in strong form by substituting (5.19) into (5.17), giving

$$\mathcal{M}^k \left(\frac{\mathrm{d}}{\mathrm{d}t} \mathbf{q}_h^k - \mathbf{S}_h^k \right) + \mathbf{F}_h^k \, \mathcal{S}_x^k + \mathbf{G}_h^k \, \mathcal{S}_y^k = - \int_{\partial \mathsf{D}^k} \left(n_x \left(\mathbf{F}^* - \mathbf{F}_h^k \right) + n_y \left(\mathbf{G}^* - \mathbf{G}_h^k \right) \right) \psi^k \left(\mathbf{x} \right) \, \mathrm{d}\mathbf{x}. \tag{5.29}$$

5.3 Boundedness of Solutions

To show boundedness in our solution, particularly in the absence of source terms, we first remark that

$$\begin{aligned} {\mathbf{q}_i}_h^{k\,\mathsf{T}} \, \mathcal{M}^k \, {\mathbf{q}_i}_h^k &= ||{\mathbf{q}_i}_h^k||_{\mathsf{D}^k}^2 \\ &= \int_{\mathsf{D}^k} \left(\sum_{i=1}^{N_p} {\mathbf{q}_i}_h^k \left(x_i^k \right) \, \psi_i^k \left(x \right) \right) \left(\sum_{i=1}^{N_p} {\mathbf{q}_i}_h^k \left(x_i^k \right) \, \psi_i^k \left(x \right) \right) \mathrm{d}x, \end{aligned} \tag{5.30}$$

having dropped the modal index. Consequently, the rate of local modal energy growth in a given element k is

$$\begin{aligned} \frac{\mathrm{d}}{\mathrm{d}t} \mathcal{E}^k &= \left(c^k \right)^2 \left(\mathbf{U}_h^{k\,\mathsf{T}} \, \mathcal{M}^k \, \frac{\mathrm{d}}{\mathrm{d}t} \mathbf{U}_h^k \right) + P_h^{k\,\mathsf{T}} \, \mathcal{M}^k \, \frac{\mathrm{d}}{\mathrm{d}t} P_h^k \\ &= \frac{1}{2} \frac{\mathrm{d}}{\mathrm{d}t} \left(\left(c^k \right)^2 \, || \, \mathbf{U}_h^k \, ||_{\mathsf{D}_k}^2 + || \, P_h^k \, ||_{\mathsf{D}_k}^2 \right), \end{aligned} \tag{5.31}$$

where c^k is the modal wave speed in element k. In addition, we may remark that

$$\begin{aligned} \left(\left(c^k \right)^2 \, \mathbf{U}_{ih}^k \right)^{\mathsf{T}} \, \mathcal{S}_i^k \left(P_h^k \right) + \left(P_h^k \right)^{\mathsf{T}} \, \mathcal{S}_i^k \left(\left(c^k \right)^2 \, \mathbf{U}_{ih}^k \right) &= \\ \int_{\mathsf{D}^k} \left(c^k \right)^2 \, \mathbf{U}_{ih}^k \, \partial_{\mathbf{x}_i} \left(P_h^k \right) \, \mathrm{d}\mathbf{x} + \int_{\mathsf{D}^k} P_h^k \, \partial_{\mathbf{x}_i} \left(\left(c^k \right)^2 \, \mathbf{U}_{ih}^k \right) \, \mathrm{d}\mathbf{x}, & \\ = \int_{\mathsf{D}^k} \partial_{\mathbf{x}_i} \left(\left(c^k \right)^2 \, \mathbf{U}_{ih}^k \, P_h^k \right) \, \mathrm{d}\mathbf{x} = \int_{\partial \mathsf{D}^k} n_i \left(\left(c^k \right)^2 \, \mathbf{U}_{ih}^k \, P_h^k \right) \, \mathrm{d}\mathbf{x}. & \end{aligned} \tag{5.32}$$

Motivated by the form of the depth-integrated modal energy density in (2.175) for our

particular choice of normalisation, we consider the sum of the product of $\left(\left(c^k\right)^2 \mathbf{U}_h^k\right)^\mathsf{T}$ and the discretised form of (5.1), and the product of $\left(P_h^k\right)^\mathsf{T}$ and the discretised form of (5.2). It follows that the energy growth for an individual element is

$$\begin{aligned}
&\frac{1}{2}\frac{\mathrm{d}}{\mathrm{d}t}\left(\left(c^k\right)^2 ||\mathbf{U}_h^k||^2_{\mathsf{D}^k} + ||P_h^k||^2_{\mathsf{D}^k}\right) = -\int_{\partial\mathsf{D}^k} \hat{\mathbf{n}}\cdot\left(\left(c^k\right)^2 \mathbf{U}_h^k(x)\, P_h^k(x)\right)\mathrm{d}\mathbf{x} + \\
&\int_{\partial\mathsf{D}^k} \hat{\mathbf{n}}\cdot\left(\left(c^k\right)^2 \mathbf{U}_h^k\right)\left(P_h^k - (P)^*\right)\mathrm{d}\mathbf{x} + \int_{\partial\mathsf{D}^k} P_h^k\,\hat{\mathbf{n}}\cdot\left(\left(c^k\right)^2 \mathbf{U}_h^k - \left(c^2\,\mathbf{U}\right)^*\right)\mathrm{d}\mathbf{x} \\
&= \int_{\partial\mathsf{D}^k} \hat{\mathbf{n}}\cdot\left(\left(c^k\right)^2 \mathbf{U}_h^k P_h^k - \left(c^k\right)^2 \mathbf{U}_h^k (P)^* - P_h^k\left(c^2\,\mathbf{U}\right)^*\right)\mathrm{d}\mathbf{x}. \qquad (5.33)
\end{aligned}$$

For stability, we must require that

$$\sum_{k=1}^{K}\frac{\mathrm{d}}{\mathrm{d}t}\left(\left(c^k\right)^2 ||\mathbf{U}_h^k||^2_{\mathsf{D}^k} + ||P_h^k||^2_{\mathsf{D}^k}\right) = \frac{\mathrm{d}}{\mathrm{d}t}\left(c^2\,||\mathbf{U}_h||^2_\Omega + ||P_h||^2_\Omega\right) \leq 0, \qquad (5.34)$$

and that being a strict equality in the case of energy preservation. It follows therefore that while not strictly necessary for stability, since $\Omega = \bigcup_{k=1}^K \mathsf{D}^k$, our choice of numerical fluxes $(P)^*$ and $\left(c^2\,\mathbf{u}\right)^*$ guarantees stability if at each interface

$$\int_{\partial\mathsf{D}^k} \hat{\mathbf{n}}\cdot\left(\left(c^k\right)^2 \mathbf{U}_h^k P_h^k - \left(c^k\right)^2 \mathbf{U}_h^k\,(P)^* - P_h^k\,\left(c^2\,\mathbf{U}\right)^*\right)\mathrm{d}\mathbf{x} \leq 0. \qquad (5.35)$$

We shall see further on how our choice of numerical fluxes $\mathbf{F}^*$ and $\mathbf{G}^*$, coupled with the manner in which we apply boundary conditions, affects the stability of our solutions.

5.4 Numerical Fluxes

Numerical fluxes approximate the true flux passing from one element to another across the shared interface using a combination of information from both elements. There are many different types of numerical fluxes, and the choice of which is dependent on the dynamics of the partial differential equation being solved (see Hesthaven & Warburton, 2008). For example, whether the problem is linear, or whether our solutions are smooth: in our case, the smoothness of solutions will depend on the bathymetry. Our choice in numerical flux, as seen in Section 5.3, may also determine the stability of our solutions, as well as the conditioning and sparsity of linear discrete operators.

5.4.1 Riemann Problem

One choice of numerical flux is one which solves exactly the Riemann problem; an application of the Rankine–Hugoniot conditions along a normal, $\hat{\mathbf{n}}$. The work here follows the methodology presented in §6.6 of Hesthaven and Warburton (2008) but applied to the mode m shallow-water equations. We begin by recalling that our flux terms, given in

(5.8), can be written in the linear form

$$\mathbf{F} = \mathcal{A}_x \, \mathbf{q} \qquad \text{and} \qquad \mathbf{G} = \mathcal{A}_y \, \mathbf{q}, \tag{5.36}$$

for matrices

$$\mathcal{A}_x \left(\mathbf{x} \right) = \begin{pmatrix} 0 & 0 & 1 \\ 0 & 0 & 0 \\ c^2 \left(\mathbf{x} \right) & 0 & 0 \end{pmatrix} \qquad \text{and} \qquad \mathcal{A}_y \left(\mathbf{x} \right) = \begin{pmatrix} 0 & 0 & 0 \\ 0 & 0 & 1 \\ 0 & c^2 \left(\mathbf{x} \right) & 0 \end{pmatrix}. \tag{5.37}$$

Assuming that $\mathcal{A}_x$ and $\mathcal{A}_y$ vary smoothly across our domain, Ω, equation (5.7) may be posed in the form

$$\partial_t \mathbf{q} + \mathcal{A}_x \left(\mathbf{x} \right) \, \partial_x \mathbf{q} + \mathcal{A}_y \left(\mathbf{x} \right) \, \partial_y \mathbf{q} + \mathcal{B} \left(\mathbf{x} \right) \, \mathbf{q} = \mathbf{0}, \tag{5.38}$$

where $\mathcal{B} \left(\mathbf{x} \right) = \partial_x \mathcal{A}_x \left(\mathbf{x} \right) + \partial_y \mathcal{A}_y \left(\mathbf{x} \right)$. In the case where $c^2 \left(\mathbf{x} \right)$ is constant, then $\mathcal{B}$ simply disappears. Since we concern ourselves with the formulation of the flux along normal $\hat{\mathbf{n}}$, consider the operator

$$\Pi = n_x \, \mathcal{A}_x \left(\mathbf{x} \right) + n_y \, \mathcal{A}_y \left(\mathbf{x} \right), \tag{5.39}$$

which has eigenvalues $\pm c, 0$ and corresponding eigenvectors

$$\begin{pmatrix} \pm n_x / c & \pm n_y / c & 1 \end{pmatrix}^{\mathsf{T}} \qquad \text{and} \qquad \begin{pmatrix} -n_y & n_x & 0 \end{pmatrix}^{\mathsf{T}}, \tag{5.40}$$

recalling that c is the modal wave speed, having dropped the modal index.

We then assume that matrix Π is diagonalisable, such that

$$\Pi = \mathcal{S} \, \Lambda \, \mathcal{S}^{-1}, \tag{5.41}$$

where diagonal entries of Λ are purely real such that our system is said to be strongly hyperbolic (Gustafsson et al., 2001). The matrix Λ can then be decomposed further in the form

$$\Lambda = \Lambda^+ + \Lambda^- \tag{5.42}$$

with the sign of the superscript notation corresponding to the sign of the entry, such that we decompose the wave speeds into the direction of propagation along said normal. That is to say, the elements of Λ^- correspond to elements of the characteristic vector $\mathcal{S}^{-1} \, \mathbf{q}$ which propagate against the normal. In the case whereby a diagonal entry of Λ is zero, this corresponds to a stationary mode.

It follows therefore that if

$$\hat{\mathbf{n}} \cdot \boldsymbol{\mathcal{F}} = \Pi \, \mathbf{q} = \left(\mathcal{S} \left(\Lambda_+ + \Lambda_- \right) \mathcal{S}^{-1} \right) \mathbf{q}, \tag{5.43}$$

we may re-write our hyperbolic system of equations locally on D^k over which $\mathcal{A}$ is assumed

to be spatially invariant, such that

$$\partial_t \mathbf{r} + (\Lambda_+ + \Lambda_-)\,(\hat{\mathbf{n}} \cdot \boldsymbol{\nabla})\,\mathbf{r} = \mathbf{0}. \tag{5.44}$$

Here, we use

$$\mathbf{r} = \mathcal{S}^{-1}\,\mathbf{q} \tag{5.45}$$

to denote the Riemann invariant on which $\mathrm{d}\mathbf{r}_\pm/\mathrm{d}t = \mathbf{0}$ along characteristic $\mathrm{d}\,(\hat{\mathbf{n}} \cdot \mathbf{x})\,/\mathrm{d}t = c_\pm$. This transforms our original system of equations into two locally uncoupled linear-advection equations,

$$\partial_t \mathbf{r}_\pm + c_\pm\,(\hat{\mathbf{n}} \cdot \boldsymbol{\nabla})\,\mathbf{r}_\pm = \mathbf{0}, \qquad\qquad \mathbf{x} \in \mathsf{D}^k. \tag{5.46}$$

Dropping the "$\pm$" subscript notation indicating direction of wave propagation and integrating over local domain, D^k, we have

$$\frac{\mathrm{d}}{\mathrm{d}t}\int_{\mathsf{D}^k} \mathbf{r}\,(\mathbf{x},t)\;\mathrm{d}\mathbf{x} = -c\int_{\mathsf{D}^k} (\hat{\mathbf{n}} \cdot \boldsymbol{\nabla})\,\mathbf{r}\,(\mathbf{x},t)\;\mathrm{d}\mathbf{x} = -\oint_{\partial\mathsf{D}^k} \boldsymbol{\mathcal{F}}\,(\mathbf{x},t)\;\mathrm{d}\mathbf{x}. \tag{5.47}$$

since flux $\mathcal{F}\,(x,t) = c\,\mathbf{r}\,(x,t)$. On the other hand, since the wave is propagating at constant speed c, we have also that

$$\frac{\mathrm{d}}{\mathrm{d}t}\int_{\mathsf{D}^k} \mathbf{r}\,(\mathbf{x},t)\;\mathrm{d}\mathbf{x} = \frac{\mathrm{d}}{\mathrm{d}t}\oint_{\partial\mathsf{D}^k} (\hat{\mathbf{n}} \cdot \mathbf{x} - c\,t)\,\mathbf{r}\,(\mathbf{x})\;\mathrm{d}\mathbf{x} = -c\oint_{\partial\mathsf{D}^k} \mathbf{r}\,(\mathbf{x})\;\mathrm{d}\mathbf{x}. \tag{5.48}$$

Combining both (5.47) and (5.48), we recover the jump condition (which may also be applied across each local boundary),

$$\forall i: \qquad c_i\left(\mathbf{r}_i^- - \mathbf{r}_i^+\right) = \boldsymbol{\mathcal{F}}^- - \boldsymbol{\mathcal{F}}^+. \tag{5.49}$$

It is this condition which must hold across each wave and is more commonly referred to as the Rankine–Hugoniot conditions. However, for linear-advection equations, these also give the propagation of an initial jump. These conditions result from the conservation of mass and momentum across the boundary of each element, particularly in the case of DG-FEM where continuity of state variables is not strictly enforced.

Using the jump conditions expressed in (5.49) to solve for the Riemann fluxes, we have that across two sides of an interface

$$c^-\left(\mathbf{q}^* - \mathbf{q}^-\right) + \left(\boldsymbol{\mathcal{F}}^* - \boldsymbol{\mathcal{F}}^-\right) = \mathbf{0} \qquad \text{and} \qquad c^+\left(\mathbf{q}^+ - \mathbf{q}^*\right) + \left(\boldsymbol{\mathcal{F}}^+ - \boldsymbol{\mathcal{F}}^*\right) = \mathbf{0}, \tag{5.50}$$

where here we denote the intermediate state as $\mathbf{q}^*$, while

$$\boldsymbol{\mathcal{F}}^* = n_x\,\mathbf{F}^* + n_y\,\mathbf{G}^* \tag{5.51}$$

is the numerical flux along normal $\hat{\mathbf{n}} = (n_x, n_y)$, and

$$\boldsymbol{\mathcal{F}}^{\pm} = n_x \, \mathbf{F}^{\pm} + n_y \, \mathbf{G}^{\pm} \tag{5.52}$$

is simply the flux evaluated on either side of an element boundary.

Eliminating $\mathbf{q}^*$ from equation (5.50) alone, we have that the numerical flux is given by

$$\boldsymbol{\mathcal{F}}^{*} = \frac{2c^{+}\,c^{-}}{c^{+}+c^{-}} \left(\frac{1}{2} \left[\frac{\boldsymbol{\mathcal{F}}^{+}}{c^{+}} + \frac{\boldsymbol{\mathcal{F}}^{-}}{c^{-}} \right] + \frac{1}{2} \left[\mathbf{q}^{-} - \mathbf{q}^{+} \right] \right), \tag{5.53}$$

which in our case, yields

$$\hat{\mathbf{n}} \cdot \boldsymbol{\mathcal{F}}^{*} = c^{*} \begin{cases} \hat{\mathbf{n}} \left(\left\{ \left\{ \dfrac{P}{c} \right\} \right\} + \dfrac{1}{2} \hat{\mathbf{n}} \cdot [[\mathbf{U}]] \right), \\ \hat{\mathbf{n}} \cdot \{\{ c\,\mathbf{U} \}\} + \dfrac{1}{2} \left[[P] \right]. \end{cases} \tag{5.54}$$

Here, we use $c^{*} = 2c^{+}\,c^{-}/(c^{+}+c^{-})$ to denote the harmonic average of wave speed, c, along with the notation

$$\{\{u\}\} = \frac{1}{2}\left(u^{-} + u^{+}\right) \qquad \text{and} \qquad [[u]] = u^{-} - u^{+} \tag{5.55}$$

to indicate respectively an average or jump in quantity u across an element boundary.

In the case where fluid depth h is continuous—and therefore modal wave speed c—equation (5.54) reads

$$\hat{\mathbf{n}} \cdot \boldsymbol{\mathcal{F}}^{*} = \begin{cases} \hat{\mathbf{n}} \left(\{\{P\}\} + \dfrac{1}{2c} \hat{\mathbf{n}} \cdot \left[\left[c^2\,\mathbf{U} \right] \right] \right), \\ \hat{\mathbf{n}} \cdot \left\{ \left\{ c^2\,\mathbf{U} \right\} \right\} + \dfrac{c}{2} \left[[P] \right], \end{cases} \tag{5.56}$$

which we identify as the 2D Lax–Friedrichs numerical flux for the linearised shallow-water equations.

5.4.2 Generalised Numerical Flux Scheme

In what follows, we formulate a general numerical flux scheme which, for various parameter choices, yields well-known flux schemes which one may choose to solve the linearised SWEs, such as the Lax–Friedrichs or the central numerical fluxes. The advantage of such a scheme facilitates both our numerical implementation and our numerical analysis further on, where we need only substitute the relevant parameters associated to a given numerical flux.

Let us consider therefore the general flux scheme whereby

$$\hat{\mathbf{n}} \cdot \boldsymbol{\mathcal{F}}^{*} = \begin{cases} \hat{\mathbf{n}} \left(\{\{P\}\} + \left(\dfrac{1}{2} - \theta \right) [[P]] \right) + \\ \qquad \dfrac{1}{2c} \left(\alpha\, \hat{\mathbf{n}} \left(\hat{\mathbf{n}} \cdot \left[\left[c^2\,\mathbf{U} \right] \right] \right) + \beta\, \hat{\mathbf{t}} \left(\hat{\mathbf{t}} \cdot \left[\left[c^2\,\mathbf{U} \right] \right] \right) \right), \\ \hat{\mathbf{n}} \cdot \left(\left\{ \left\{ c^2\,\mathbf{U} \right\} \right\} - \left(\dfrac{1}{2} - \theta \right) \left[\left[c^2\,\mathbf{U} \right] \right] \right) + \gamma\, \dfrac{c}{2} \left[[P] \right]. \end{cases} \tag{5.57}$$

Scheme	θ	α	β	γ
Alternating	$0 \leq \theta \leq 1$	0	0	0
Central	1/2	0	0	0
Upwind	1/2	0	1	1
Penalty	1/2	1	0	1
Lax–Friedrichs	1/2	1	1	1

Table 5.1: Penalty parameters for specific numerical flux schemes and is adapted from Table 8.5 of Hesthaven and Warburton (2008) to recover also the alternating numerical flux scheme (also known as symmetric local discontinuous Galerkin flux).

The first term corresponds to the alternating flux scheme, and uses an upwind means to approximate the fluxes, and is done such that both P and $c^2\,\mathbf{U}$ are upwinded in opposite directions. The parameter α takes into consideration the normal component of modal velocity in the approximation of $\hat{\mathbf{n}}\,(P)^*$, while parameter β considers the tangential component, and enforces continuity in the respective components. Similarly, γ has a similar effect for eigenfunctions with bounded real part in enforcing continuity of pressure. Table 5.1 displays the choice of parameter values associated with each numerical flux scheme, considering the respective elements as discussed. For example, the choice of $\theta = 1/2$ and $\alpha = \beta = \gamma = 1$ yields the Lax–Friedrichs numerical flux scheme which we saw in equation (5.56) and ensures continuity in the modal velocity $c^2\,\mathbf{U}$ and pressure P for bounded real eigenfunctions.

To determine the stability of our numerical flux scheme, we consider the global flux contribution across each element boundary, as discussed in Section 5.3. Substitution of flux (5.57) into (5.33) yields

$$\begin{aligned}\mathcal{E}^{-1}\,\frac{\mathrm{d}}{\mathrm{d}t}\mathcal{E} &= \mathrm{Im}\,\{\omega\} \\ &= \frac{-\frac{1}{c}\sum_k \int_{\partial \mathsf{D}_k}\left(\gamma\,c^2\,\left[[P]\right]^2 + \alpha\,\left[\left[\hat{\mathbf{n}}\cdot\left(c^2\,\mathbf{U}\right)\right]\right]^2 + \beta\,\left[\left[\hat{\mathbf{t}}\cdot\left(c^2\,\mathbf{U}\right)\right]\right]^2\right)\,\mathrm{d}\mathbf{x}}{c^2\,||\mathbf{U}_h||^2_\Omega + ||P_h||^2_\Omega} \\ &\leq 0,\end{aligned} \tag{5.58}$$

which suggests that there is no flux contribution from the internal boundary elements from both the central and alternating schemes. Equation (5.58) excludes the flux contribution across the boundary domain, which yields an additional term

$$\frac{-\int_{\partial\Omega}\hat{\mathbf{n}}\cdot\left(c^2\,\mathbf{U}_h\,P_h - c^2\,\mathbf{U}_h\,\left(P\right)^* - P_h\,\left(c^2\,\mathbf{U}\right)^*\right)\,\mathrm{d}\mathbf{x}}{c^2\,||\mathbf{U}_h||^2_\Omega + ||P_h||^2_\Omega}. \tag{5.59}$$

Since we shall primarily be considering the homogeneous problem corresponding to an impermeability condition along $\partial\Omega$, it follows that $\hat{\mathbf{n}}\cdot\left(c^2\,\mathbf{U}\right) = \hat{\mathbf{n}}\cdot\left\{\left\{c^2\,\mathbf{U}\right\}\right\} = 0$, giving

instead

$$\frac{\int_{\partial\Omega} \hat{\mathbf{n}} \cdot P_h \left(c^2\,\mathbf{U}\right)^* \,\mathrm{d}\mathbf{x}}{c^2\,||\mathbf{U}_h||^2_\Omega + ||P_h||^2_\Omega} = \frac{\int_{\partial\Omega} P_h\,\hat{\mathbf{n}} \cdot \left(\left(\left\{\left\{c^2\,\mathbf{U}\right\}\right\} - \left(\frac{1}{2} - \theta\right)\left[\left[c^2\,\mathbf{U}\right]\right]\right) + \gamma\,\frac{c}{2}\left[[P]\right]\right)\mathrm{d}\mathbf{x}}{c^2\,||\mathbf{U}_h||^2_\Omega + ||P_h||^2_\Omega}. \tag{5.60}$$

If $\gamma = 0$ and $\theta = 0.5$ at the boundary, the contribution along the boundary reduces to zero. In other words, energy conservation should be obtained for impermeability boundary conditions when using the central flux or the alternating flux with $\theta = 0.5$ along the domain boundary, such that there is no contribution to the global energy across internal boundary elements (equation (5.58) is zero) or along the external boundary (equation (5.59) is zero).

5.5 Boundary Conditions

For the boundary conditions (with and without rotation), we shall consider the generic kinematic boundary condition

$$\hat{\mathbf{n}} \cdot \left(c^2\,\mathbf{U}\right) = \hat{\mathbf{n}} \cdot \left(c^2\,\tilde{\mathbf{U}}\right) \qquad \text{on} \qquad \partial\Omega, \tag{5.61}$$

where $\hat{\mathbf{n}} = \begin{pmatrix} n_x & n_y \end{pmatrix}^\mathsf{T}$ represents the outward-pointing unit normal vector to the domain boundary $\partial\Omega$ and $\tilde{\mathbf{U}}$ denotes the imposed velocity along the boundary. Note that equation (5.61) corresponds to an impermeability boundary condition (no-normal flow) when $\tilde{\mathbf{U}} = \mathbf{0}$.

As Steinmoeller et al. (2016) highlight, the freedom in our choice of numerical flux allows us to conveniently impose the boundary conditions through an appropriate choice of imaginary ghost states, i.e. the exterior traces along the edges of the domain boundaries. Since the boundary operator concerns U, V and c^2, we require three boundary conditions.

Following Ambati and Bokhove (2007), we begin by decomposing the horizontal velocity vector into a normal and tangential component,

$$\mathbf{U} = \hat{\mathbf{n}}\left(\hat{\mathbf{n}} \cdot \mathbf{U}\right) + \hat{\mathbf{t}}\left(\hat{\mathbf{t}} \cdot \mathbf{U}\right), \tag{5.62}$$

where tangential unit vector $\hat{\mathbf{t}} = \begin{pmatrix} -n_y & n_x \end{pmatrix}^\mathsf{T}$. By assuming the fluid depth is continuous either side of the boundary, i.e.

$$\hat{\mathbf{n}} \cdot \boldsymbol{\nabla} c^2 = 0 \qquad \text{on } \partial\Omega, \tag{5.63}$$

we apply the no-slip boundary condition on both components of the velocity:

$$\begin{cases} \hat{\mathbf{n}} \cdot \mathbf{U} = \hat{\mathbf{n}} \cdot \tilde{\mathbf{U}}, & \text{(Normal)} \\ \hat{\mathbf{n}} \cdot \left[\boldsymbol{\nabla} \left(\hat{\mathbf{t}} \cdot \mathbf{U} \right) \right] = 0, & \text{(Tangential)} \end{cases} \qquad \text{on } \partial\Omega. \tag{5.64}$$

The first of these prescribes the background flow along the boundary. The second says that the tangential component of the velocity is identical across the boundary. We have in total three boundary conditions, all without imposing any restrictions on pressure, P.

In weak form, equations (5.63)–(5.64) correspond to the imposition of

$$\{\{\hat{\mathbf{n}} \cdot \mathbf{U}\}\} = \hat{\mathbf{n}} \cdot \tilde{\mathbf{U}}, \qquad \left[\left[\hat{\mathbf{t}} \cdot \mathbf{U}\right]\right] = 0 \qquad \text{and} \qquad \left[\left[c^2\right]\right] = 0, \tag{5.65}$$

such that

$$\begin{cases} \frac{1}{2} \left(\hat{\mathbf{n}} \cdot \mathbf{U}^+ + \hat{\mathbf{n}} \cdot \mathbf{U}^- \right) = \hat{\mathbf{n}} \cdot \tilde{\mathbf{U}}, \\ \hat{\mathbf{t}} \cdot \mathbf{U}^+ - \hat{\mathbf{t}} \cdot \mathbf{U}^- = 0, \\ \left(c^+\right)^2 - \left(c^-\right)^2 = 0, \end{cases} \implies \begin{cases} U^+ = U^- - 2 n_x \, \hat{\mathbf{n}} \cdot \left(\mathbf{U}^- - \tilde{\mathbf{U}} \right), \\ V^+ = V^- - 2 n_y \, \hat{\mathbf{n}} \cdot \left(\mathbf{U}^- - \tilde{\mathbf{U}} \right), \\ \left(c^+\right)^2 = \left(c^-\right)^2. \end{cases} \tag{5.66}$$

There boundary conditions are a slight extension of those used by Ambati and Bokhove (2007) and Steinmoeller et al. (2016), where we have prescribed a non-zero background flow at the boundaries. Here, the interior nodal information along the boundary interface is denoted with a superscript "−", while a superscript "+" is used to represent the exterior nodal information (see Hesthaven & Warburton, 2008).

5.6 Numerical Validation

In this section, we seek to validate our numerical implementation of DG-FEM applied to the decoupled barotropic equations, verifying both convergence and stability for a range of numerical fluxes when refining the element size or adjusting the order of local test function. The latter will give some assurance behind the validity of the proceeding results. The validation of numerical implementation is approached from two fronts: an eigenvalue problem and a boundary-value problem.

For the eigenvalue problem, we consider cases for which results are well-known, e.g. non-rotating uniform depth in a rectangular basin, and rotating uniform-depth in a circular basin. For the boundary-value problem, we look at resolving the spatial structure of the barotropic Kelvin wave explored in Chapter 3.

5.6.1 Domain Discretisation

In what follows, we shall be considering two examples of domain discretisations: a square domain of length 2,000 km, as well as a circular domain of radius 3,000 km. The discretised meshes of the aforementioned domains are shown in Figure 5.4, where a target edge size of 500 km is used. For the square domain, the Python package `OceanMesh` was used (see

MatLab citations Roberts, Pringle, & Westerink, 2019a, 2019b). Remark that the elements in Figure 5.4a are not simply right-angled isosceles. As part of the mesh generation, the goal is to produce elements which are as close to being equilaterals as possible. As for the circular domain, we employ instead the Python package `dmsh` (see Schlömer, 2020).

In the case of the circular domain, we could have considered isoparametric curvilinear elements to increase accuracy and reduce computational effort when resolving elements whose boundaries are not piece-wise linear (see Bond et al., 1973; Bernsen et al., 2005; van der Vegt et al., 2007; Hesthaven & Warburton, 2008; Moxey et al., 2015). However, this would have required additional non-trivial implementations which would have been superfluous within the remits of our studies since our primary focus is on idealised rectangular domains.

5.6.2 Eigenvalue Problem

One of the easiest means of verifying the numerical implementation is to validate the solutions of a corresponding eigenvalue problem to which the wave frequency and modal solution is known. Here, we shall be considering the most physical system which involves the implementation of homogeneous impermeability conditions along the boundaries of a basin. In terms of implementing these boundary conditions in our numerical scheme, as mentioned previously, we will require the use of (5.66) with background flow $\tilde{\mathbf{U}} = \mathbf{0}$.

Assuming time-periodic solutions of the decoupled barotropic shallow-water equations, the rest of the subsection will concern the eigenvalue problem which can be succinctly stated as finding the eigenpair $((\mathbf{U}, P), \omega)$ for which

$$\partial_t \mathbf{U} = -\mathbf{f} \times \mathbf{U} - \boldsymbol{\nabla} P = -i\,\omega\,\mathbf{U}, \tag{5.67}$$

$$\partial_t P = -c^2\,\boldsymbol{\nabla} \cdot \mathbf{U} = -i\,\omega\,P, \tag{5.68}$$

for $\mathbf{x} \in \Omega$, and subject to impermeability boundary conditions

$$\hat{\mathbf{n}} \cdot \mathbf{U} = 0, \qquad \mathbf{x} \in \partial\Omega, \tag{5.69}$$

where $\hat{\mathbf{n}}$ denotes the outward-pointing unit normal along domain boundary $\partial\Omega$, and barotropic wave speed squared $c^2 = g\,H$ is taken constant since both gravitational acceleration g and fluid depth H are taken constant. The index notation indicating the barotropic mode has been dropped since only a single mode is considered.

We know from Section 3.3.1 that the linear operator is self-adjoint, and so therefore we should expect all wave frequencies ω to be real. However, as we indicated in Section 5.4.2, this property will depend greatly on our choice of numerical scheme. We concluded that out of the numerical flux schemes we consider (see Table 5.1), the only two which are (or at least should be) energy-preserving are the central flux and the alternating flux (with parameter $\theta = 0.5$ along the domain boundaries) since there is no growth rate in energy. However, we also concluded that for the penalty parameters considered in each scheme,

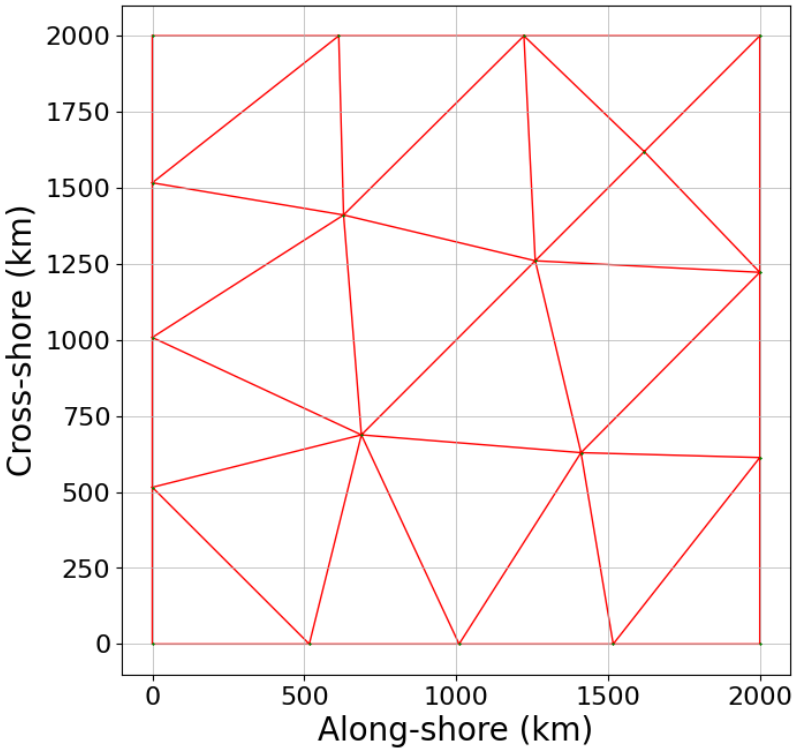

(a) Uniform square mesh with domain $\Omega = [0\,\text{km}, 2,000\,\text{km}]^2$ and a target edge length of 500 km.

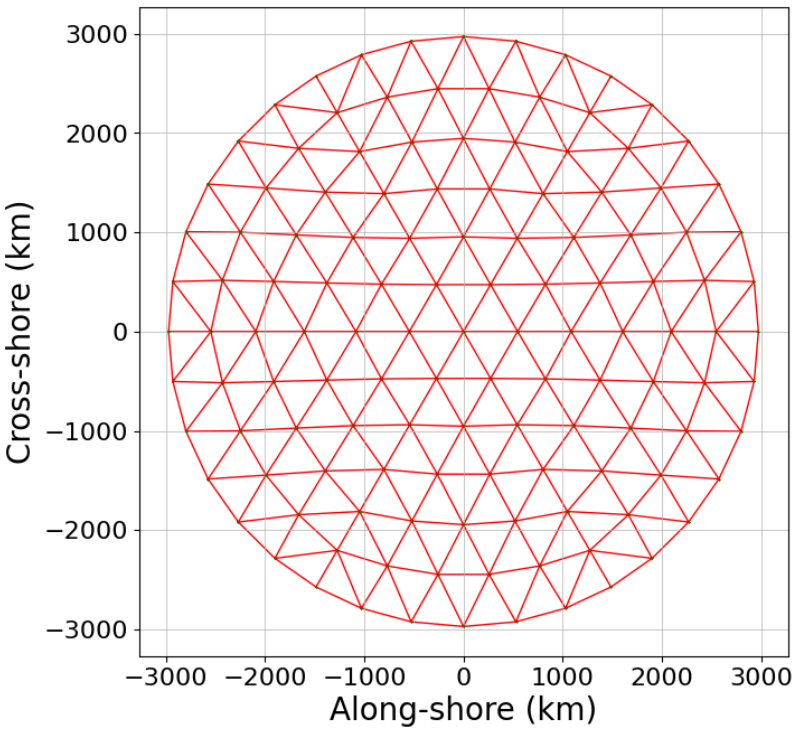

(b) Uniform circular mesh with domain $\Omega = \left\{(x, y) \in \mathbb{R}^2 \mid x^2 + y^2 \leq 3,000\,\text{km}\right\}$ and a target edge length of 500 km.

Figure 5.4: Examples of domain discretisations using piece-wise linear boundaries used in eigenvalue problem test cases for p-refinement. In both cases, there is a target element edge length of $h = 500\,\text{km}$.

the solutions should be bounded, such that the imaginary part of any wave frequency is less than or equal to zero corresponding to a decay in energy.

Non-Rotating Square Basin

In the non-rotating cases whereby Coriolis parameter $f = 0$, we consider a square domain $\Omega = [0,\, L]^2$ for $L = 2,000\,\mathrm{km}$. In this case, for arbitrary amplitude A, equations (5.67)–(5.69) yield a pressure solution with associated wave frequency of the form

$$P\,(x, y, t) = A\,\cos\,(m\,\pi\,x)\,\cos\,(n\,\pi\,y)\,\cos\,(\omega_{mn}\,t), \qquad \omega_{mn} = \frac{c\,\pi}{L}\,\sqrt{m^2 + n^2} \tag{5.70}$$

for uniform fluid depth H, barotropic wave speed $c = \sqrt{g\,H}$ and horizontal wavenumbers $m\,\pi$ and $n\,\pi$ for $m, n \in \mathbb{N}_0$.

In Figure 5.5 we show the full spectrum of non-dimensional eigenvalues for the aforementioned square basin, as illustrated in Figure 5.4a, with uniform fluid depth $H = 4,000\,\mathrm{m}$. The wave frequencies shown have been non-dimensionalised with respect to $c/L = 10^{-4}\,\mathrm{s}^{-1}$. The goal of this figure is to show convergence under p-refinement. Consequently, we increase the order of the Lagrange interpolant polynomial that is our local test function from piece-wise linear ($p = 1$) to piece-wise quintic ($p = 5$). In this figure, it is clear that while the alternating flux and the central flux, when sufficiently resolved, produce energy-conserving modes (imaginary part zero). For the central flux, the wave frequencies will always be purely real, at least to machine precision. Indeed, there are imaginary parts to eigenvalues of the alternating flux for when $\theta = 0.75$, but only when insufficiently resolved. It is not immediately obvious where these imaginary contributions originate. One possibility is that the rate of convergence for eigenmodes using the alternating flux is different to that of the other flux choices based on the weak imposition of the boundary condition. We can also see the effects of the different penalty schemes and how they affect the conditioning of the eigenvalues, and ensure bounded solutions whereby insufficiently resolved eigenvalues have some negative imaginary part which corresponds to rate of energy decay in time.

With analytical solutions shown by the black circle symbols, it is hard to deduce in Figure 5.5 alone how p-refinement leads to convergence towards known analytical wave frequencies. It is for this reason that we also illustrate the wave frequencies of the lowest modes ($|\mathrm{Re}\,(\omega)| \leq 10$) in Figure 5.6. Here, we see that an increase in polynomial order corresponds to greater accuracy, and indeed convergence towards the analytical wave frequency.

To quantify the latter, we shall now consider the asymptotic convergence of the eigenvalues under p-refinement. For this reason, we show in Figure 5.7 the absolute error between known analytical wave frequencies and the corresponding wave frequencies for each of the numerical fluxes under consideration.

It is clear here that the absolute errors corresponding to each flux scheme, apart from the

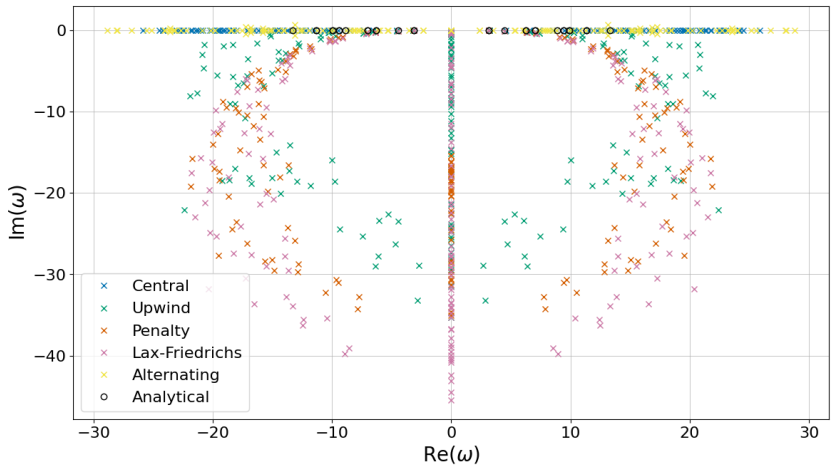

(a) $p = 1$

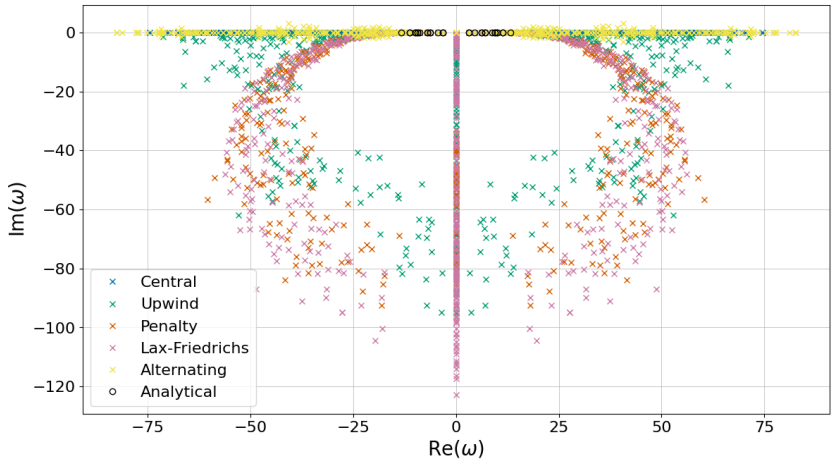

(b) $p = 3$

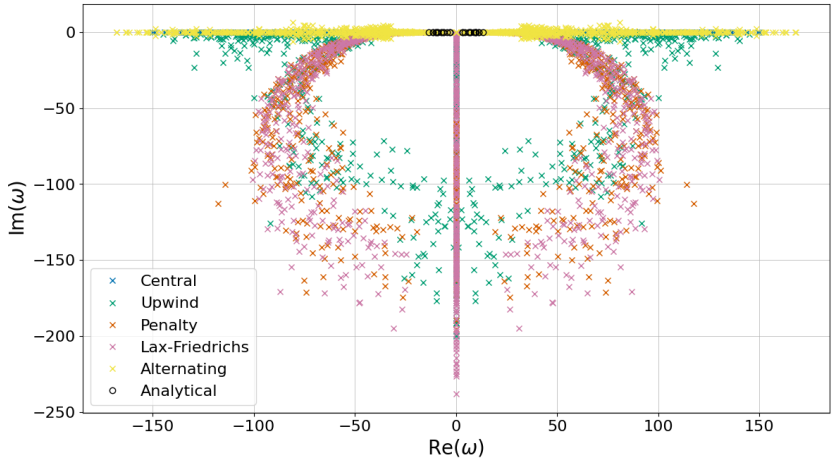

(c) $p = 5$

Figure 5.5: p-refinement, $h = 500\,\mathrm{km}$: Full spectrum of DG-FEM eigenvalues for non-rotating barotropic shallow-water equations in a square domain $\Omega = [0, L]^2$ for $L = 2,000\,\mathrm{km}$ of uniform depth $H = 4,000\,\mathrm{m}$. Here, a target element-edge size of $h = 500\,\mathrm{km}$ is used, along with a θ-value of 0.25 for the alternating flux.

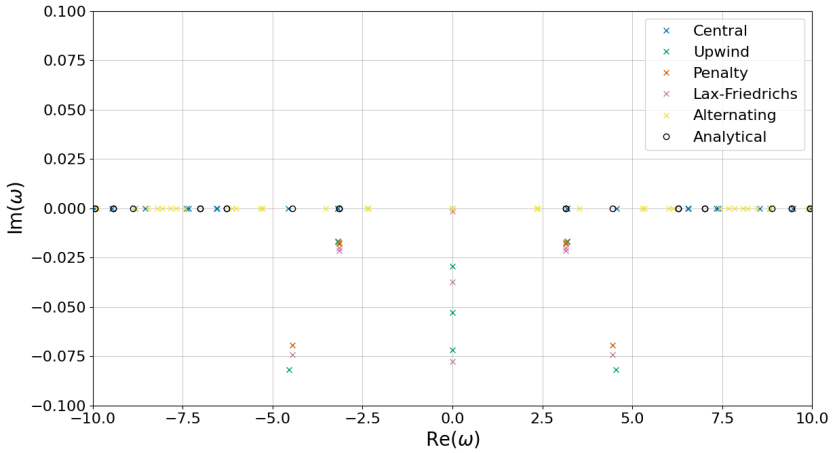

(a) $p = 1$

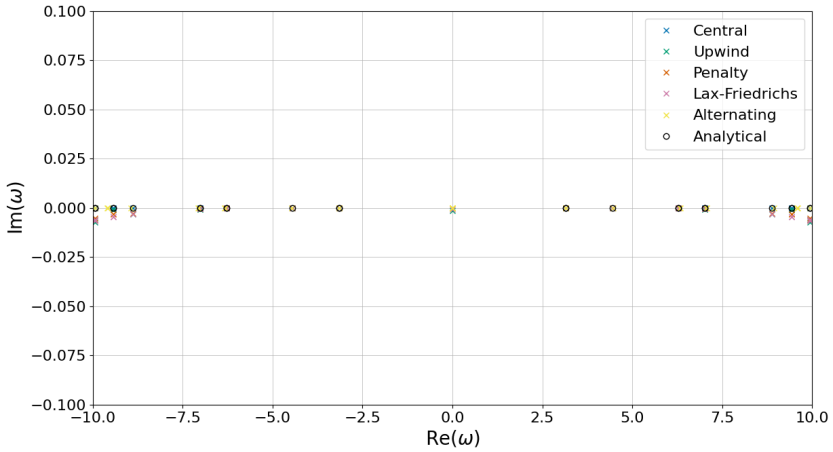

(b) $p = 3$

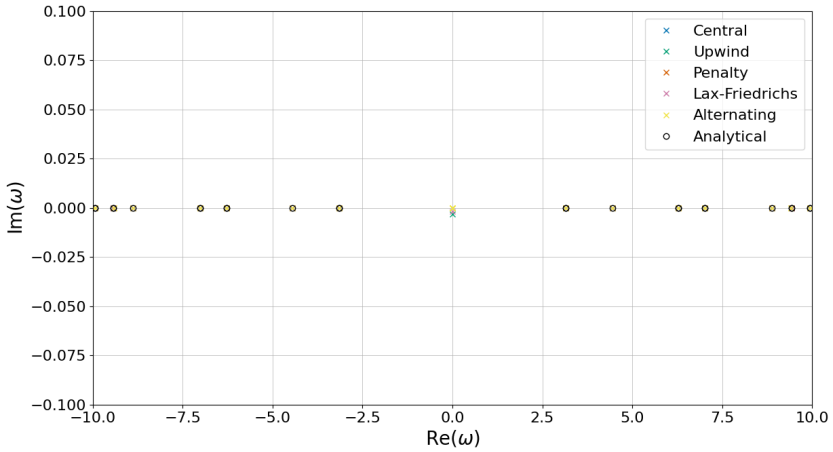

(c) $p = 5$

Figure 5.6: p-refinement, $h = 500\,\mathrm{km}$: Close-up of DG-FEM eigenvalues for non-rotating barotropic shallow-water equations in a square domain $\Omega = [0, L]^2$ for $L = 2,000\,\mathrm{km}$ of uniform depth $H = 4,000\,\mathrm{m}$. Here, a target element-edge size of $h = 500\,\mathrm{km}$ is used, along with a θ-value of 0.25 for the alternating flux.

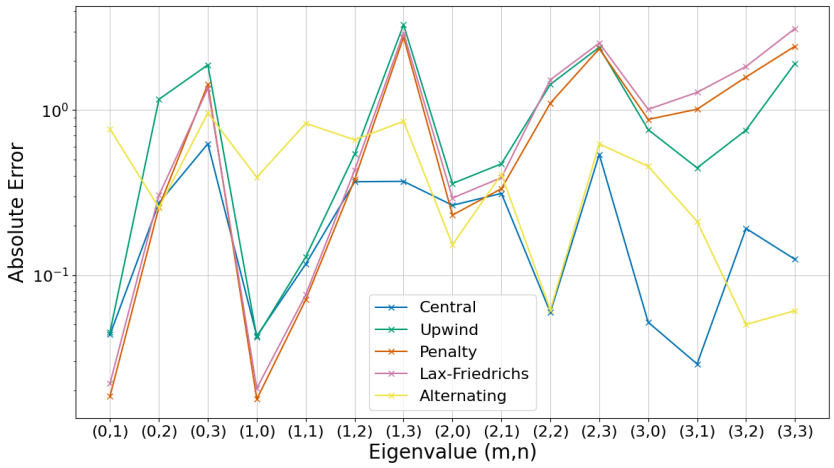

(a) $p = 1$

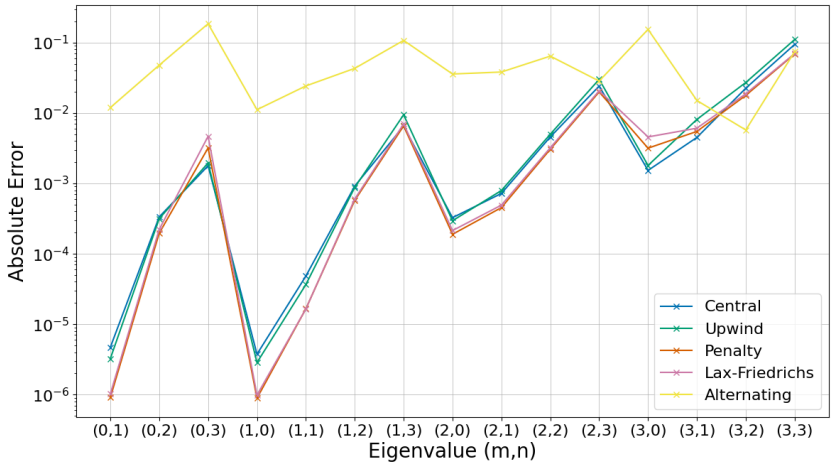

(b) $p = 3$

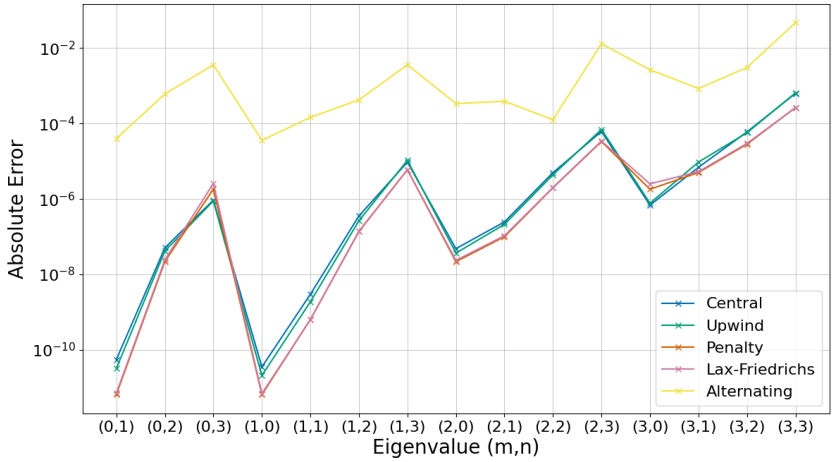

(c) $p = 5$

Figure 5.7: p-refinement, $h = 500\,\mathrm{km}$: Absolute error of DG-FEM eigenvalues for non-rotating barotropic shallow-water equations in a square domain $\Omega = [0, L]^2$ for $L = 2,000\,\mathrm{km}$ of uniform depth $H = 4,000\,\mathrm{m}$. Here, a target element-edge size of $h = 500\,\mathrm{km}$ is used, along with a θ-value of 0.25 for the alternating flux.

alternating flux, are strongly associated with one another, i.e. they observe similar rates of convergence under h- and p-refinement. Furthermore, for all numerical flux schemes, an increase in the order of local test function corresponds to a reduction in the absolute error of eigenvalues. Denoting element-edge size as h, without conducting a detailed analysis, it appears that for all schemes apart from the alternating flux, the absolute error observes a convergence rate of $O\left(h^{2p}\right)$ since an increase of the polynomial order by two corresponds to a reduction of the eigenvalue error by a factor of $\sim 10^4 \approx h^4$. In addition, the Lax–Friedrichs and Penalty flux schemes achieve the best results. On the other hand, it would appear that the alternating flux scheme ($\theta = 0.25$) yields a convergence rate of $O\left(h^p\right)$ since an increase of the polynomial order by two corresponds to a reduction in the error by a factor of $10^2 \approx h^2$. While the latter observation may be cause for further investigation, for the purpose of this thesis it is not of significance since we still have a choice of four other numerical flux schemes which converge optimally. Furthermore, the purpose of this thesis is not one of numerical analysis. However, it is reassuring nonetheless that all numerical flux schemes converge as the order of the local test function, p, is increased.

To finish the validation of our numerical scheme in the case of non-rotating shallow-water equations in a square domain of uniform fluid depth, we shall consider fixed polynomial orders $p = 2$ and $p = 3$, while varying the target size of the edges of each element, h. The latter is commonly referred to as h-refinement. That is to say, we are refining not the polynomial order, but the size of our elements which constitute the computational domain. Our aim here is to consider the asymptotic convergence of the lowest positive wave frequencies under h-refinement.

Figures 5.8 and 5.9 show the process of refining the size of the elements for fixed polynomial orders of 2 and 3 respectively. The associated meshes for these eigenvalue problems are shown in Figure 5.10, where element-edge size is: (a) $h = h_0 = 500\,\text{km}$; (b) $h = h_0/2 = 250\,\text{km}$; (c) $h = h_0/4 = 125\,\text{km}$. First and foremost, we are assured in our implementation of DG-FEM by the fact that all numerical flux schemes see a reduction in absolute error of eigenvalue wave frequencies when undergoing h-refinement. The rate at which the asymptotic convergence occurs depends once more on the choice of numerical flux. For all apart from the alternating flux, halving the target element edge length corresponds to a reduction of the absolute error by a factor of $2^{-6} = (1/2)^{2(p+1)}$. I.e. we appear to observe a convergence rate of $O\left(h^{2(p+1)}\right)$. As for the alternating flux, by halving the target element-edge size, the error now appears to scale by a factor $2^{-3} = (1/2)^{p+1}$, i.e. a convergence rate of $O\left(h^{p+1}\right)$.

Rotating Circular Basin

Here, we consider validating our numerical fluxes in the case of a rotating circular basin of uniform depth and radius a (see Article 203 of Lamb, 1895). The aforementioned problem admits eigenvalues which satisfy the implicit dispersion relation

$$\frac{\omega}{f}\,\kappa\left(a,\omega\right)\,J_n'\left(\kappa\left(a,\omega\right)\right) - n\,J_n\left(\kappa\left(a,\omega\right)\right) = 0, \tag{5.71}$$

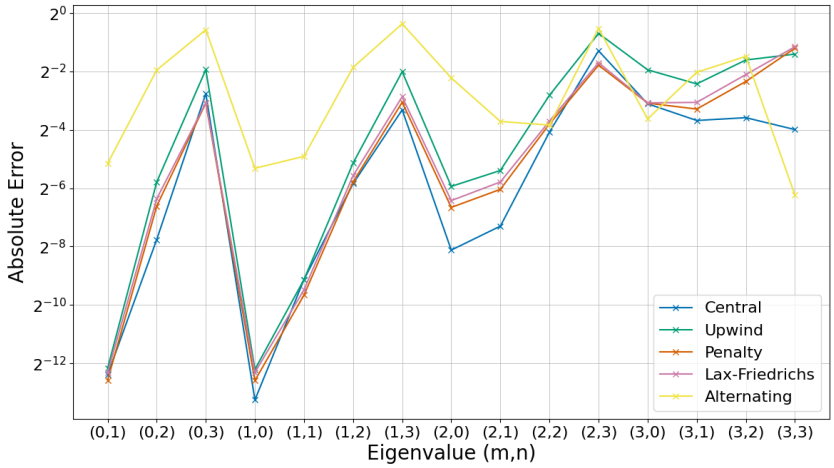

(a) $h = h_0$

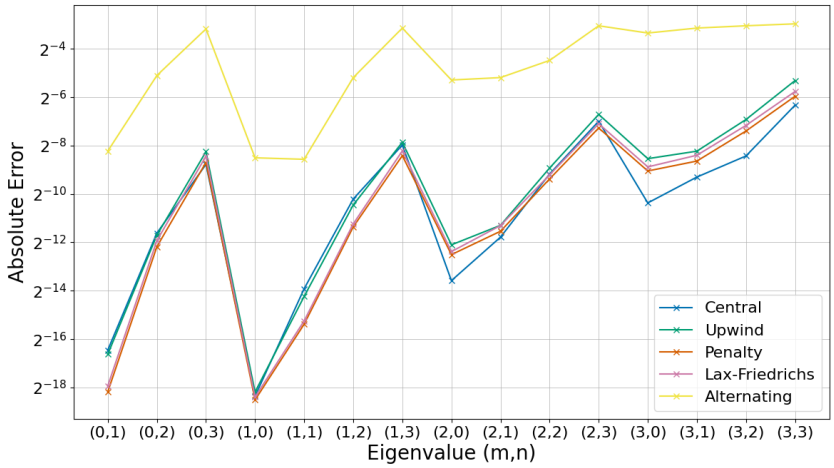

(b) $h = h_0/2$

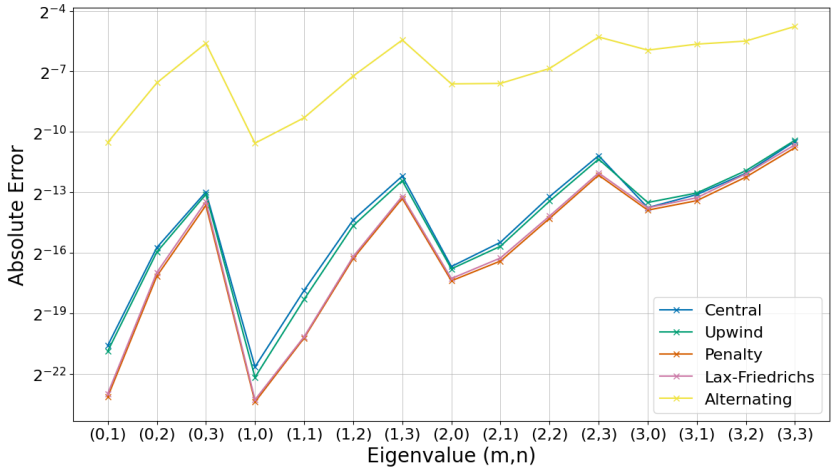

(c) $h = h_0/4$

Figure 5.8: h-refinement, $p = 2$: Absolute error of DG-FEM eigenvalues for non-rotating barotropic shallow-water equations in a square domain $\Omega = [0, L]^2$ for $L = 2,000\,\mathrm{km}$ of uniform depth $H = 4,000\,\mathrm{m}$. Here, a polynomial order of 2 is used, along with an initial target element-edge size of $h_0 = 500\,\mathrm{km}$ and a θ-value of 0.25 for the alternating flux.

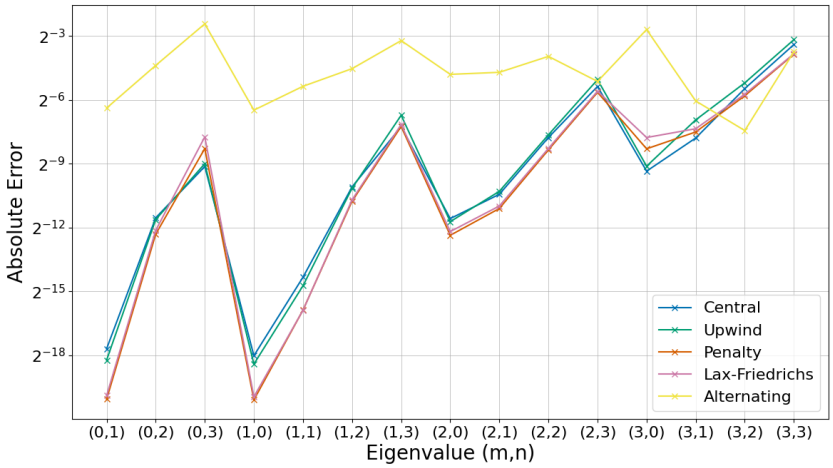

(a) $h = h_0$

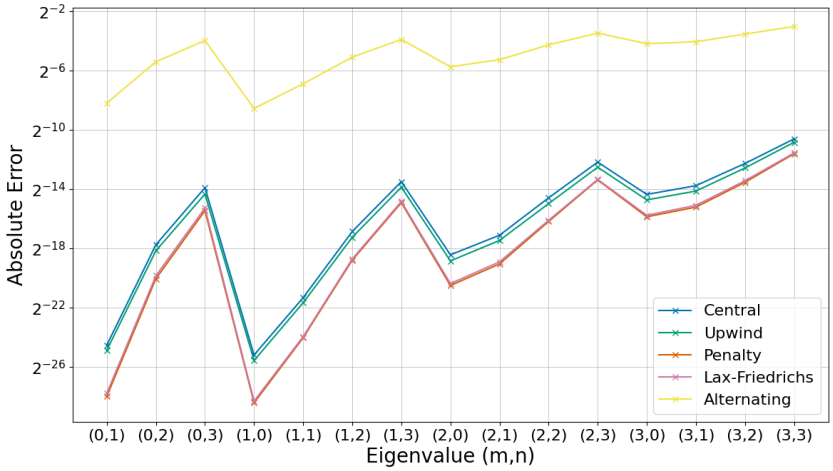

(b) $h = h_0/2$

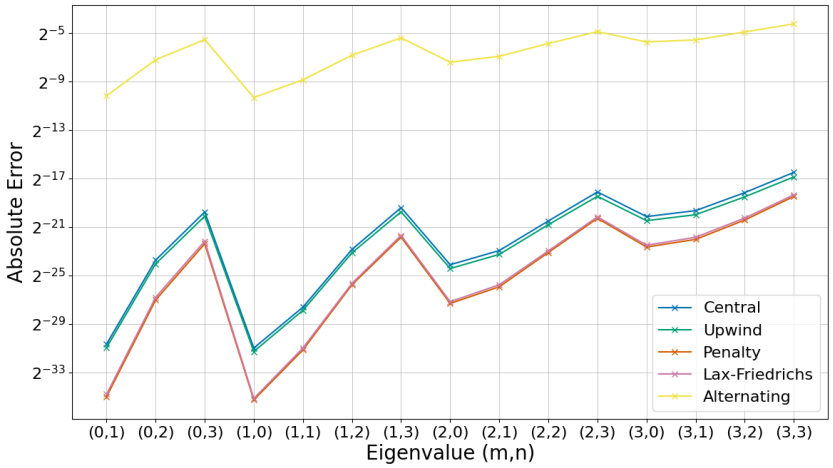

(c) $h = h_0/4$

Figure 5.9: h-refinement, $p = 3$: Absolute error of DG-FEM eigenvalues for non-rotating barotropic shallow-water equations in a square domain $\Omega = [0, L]^2$ for $L = 2,000\,\text{km}$ of uniform depth $H = 4,000\,\text{m}$. Here, a polynomial order of 3 is used, along with an initial target element-edge size of $h_0 = 500\,\text{km}$ and a θ-value of 0.25 for the alternating flux.

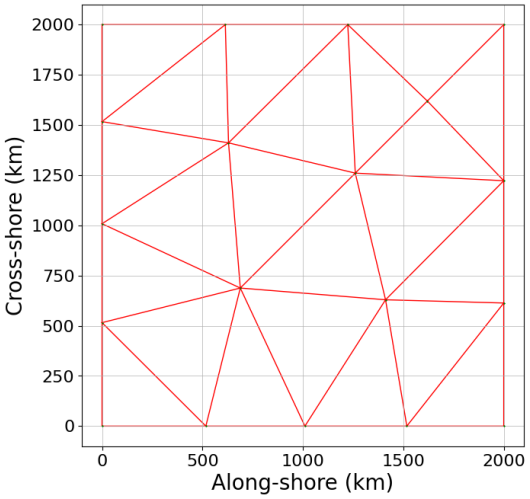

(a) $h = h_0$

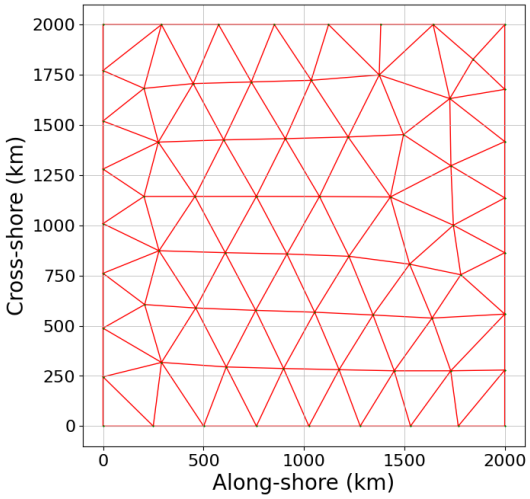

(b) $h = h_0/2$

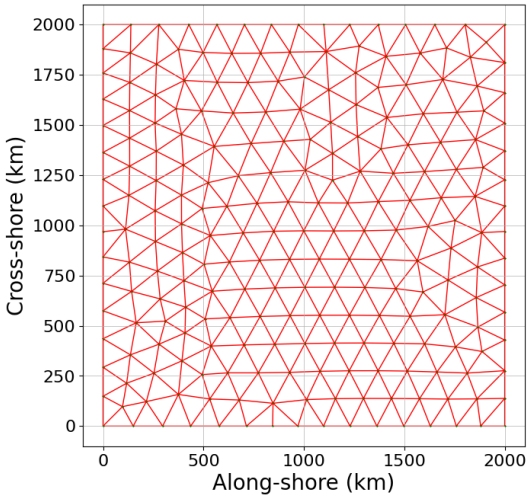

(c) $h = h_0/4$

Figure 5.10: Uniform mesh refinement associated with the results of the eigenvalue problems shown in Figures 5.8–5.9. The target element-edge length h is halved each time, giving: (a) $h = h_0 = 500\,\text{km}$; (b) $h = h_0/2 = 250\,\text{km}$; (c) $h = h_0/4 = 125\,\text{km}$.

where for Rossby radius of deformation $L_R = c/|f|$ and radius a,

$$\kappa\,(a, \omega) = \frac{a\,\sqrt{(\omega/f)^2 - 1}}{L_R}, \tag{5.72}$$

n is the azimuthal wavenumber (which ensures periodicity of our solutions), and J_n denotes the Bessel function of the first kind of real order n. Furthermore, for arbitrary wave amplitude A, the barotropic pressure takes the form

$$P\,(r, \theta, t) = A\,J_n\,(\kappa\,(\omega)\;r)\,\cos\,(n\,\theta - \omega\,t), \qquad\qquad n \in \mathbb{N}. \tag{5.73}$$

In Figure 5.11, we illustrate the full spectrum of eigenvalues for the rotating barotropic

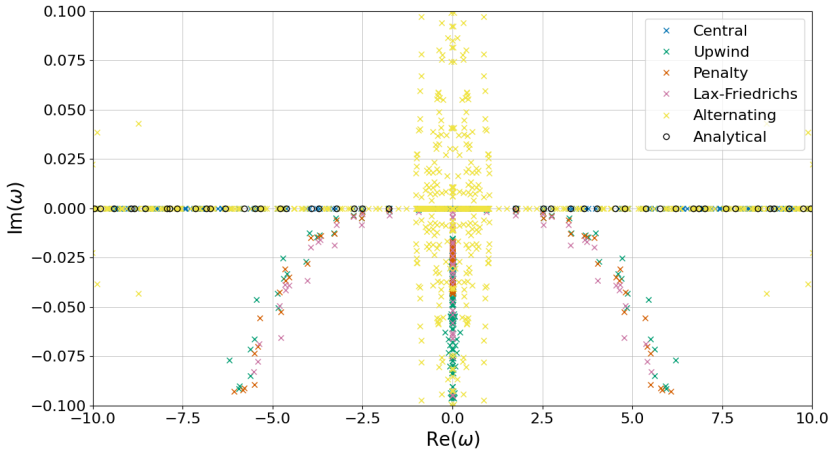

(a) $p = 1$

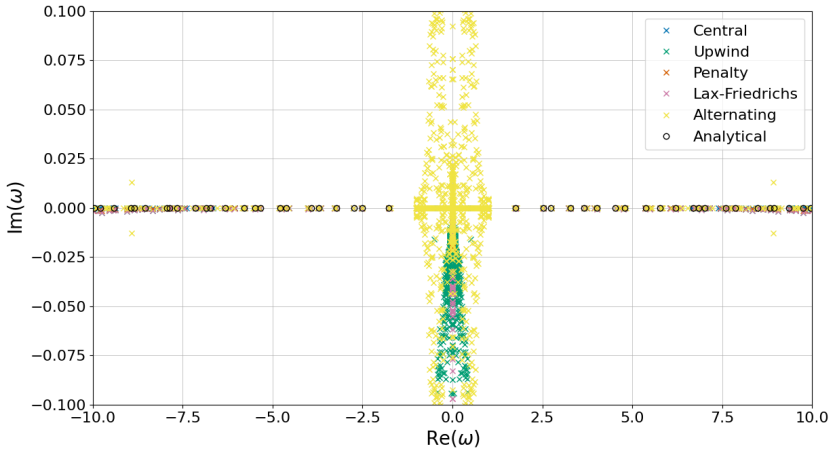

(b) $p = 3$

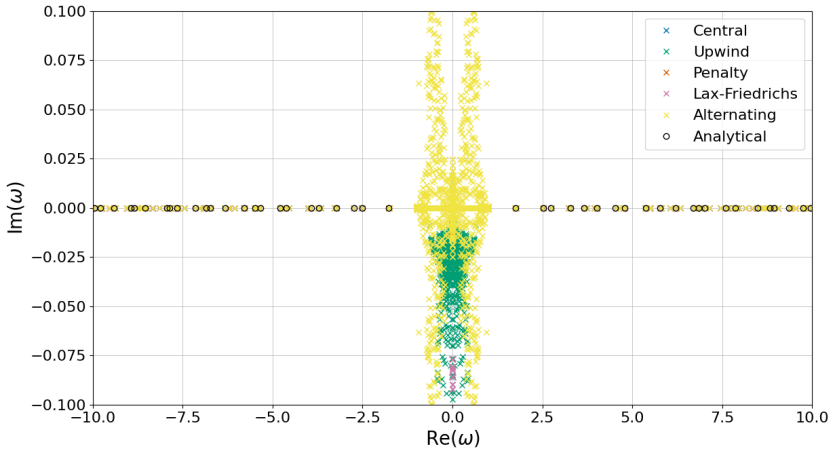

(c) $p = 5$

Figure 5.11: p-refinement, $h = 500\,\mathrm{km}$: Close-up of full spectrum of DG-FEM eigenvalues for rotating barotropic motion in a circular basin of radius $3,000\,\mathrm{km}$ with uniform depth $4,000\,\mathrm{m}$ at mid-latitude with Coriolis parameter $f = 10^{-4}\,\mathrm{s}^{-1}$. Here, a target element-edge size $h = 500\,\mathrm{km}$ is used, along with a θ-value of 0.25 for the alternating flux.

shallow-water equations in a circular basin of radius $3,000\,\mathrm{km}$ and depth $4,000\,\mathrm{m}$ under p-refinement. Here, the wave frequencies have been non-dimensionalised with respect to the Coriolis parameter $f = 10^{-4}\,\mathrm{s}^{-1}$. The different coloured lines represent the numerical flux schemes, as indicated by each plot's legend.

The first remark to be made is that the central and alternating numerical fluxes lead to a vast amount of sub-inertial ($\mathrm{Re}\,(\omega) < f$) spurious modes (there are further wave frequencies corresponding to the central flux underneath those corresponding to the alternating flux). The latter is a result of the geostrophic balance along the boundary not being treated. As a result, there is an increase in the kernel operator since the boundary conditions used do not sufficiently constrain the discrete operator. The latter is likely to be overcome when using a skew-symmetric/Hamiltonian approach (e.g. Ambati & Bokhove, 2007). When dealing with spurious modes, Hesthaven and Warburton (2008) raises the following issues which should be examined:

- Completeness of spectrum, such to guarantee that all eigenvalues of the continuous operator can be represented by the discontinuous approximation for sufficiently small elements.
- Isolation of the discrete kernel modes, such to prevent overlap between the eigenvalues of the discrete operator and the physical eigenvalues.
- Non-pollution of the spectrum, such to disallow discrete eigenvalues which appear to converge under refinement.

However, spurious modes are a much greater problem when considering initial-value problems which affect the stability of the solution in time. For boundary-value problems, these spurious modes would become problematic when seeking the barotropic response of some forcing whose frequency was sub-inertial, e.g. a diurnal potential forcing at mid-latitude. However, the latter can be overcome by using any of the three alternative numerical flux choices which sufficiently constrain the form of the solution.

It should also be noted that Figure 5.12 shows no convergence under p-refinement for any of the numerical fluxes apart from the alternating flux whose convergence rate, as already observed, is sub-optimal. That is because for all numerical fluxes apart from the alternating, there is no change in the error of the eigenvalues when the polynomial order is increased. The reason for this is that the boundary of the circular domain is approximated using piece-wise linear elements. Consequently, all boundary elements will carry an error $O\left(h^2\right)$, regardless of polynomial order. As a result, this error term dominates, and therefore no convergent behaviour is observed under p-refinement.

In Figure 5.13, however, h-refinement is successfully carried out by halving the target element-edge size. The associated meshes for these eigenvalue problems are shown in Figure 5.14, where element-edge size is: (a) $h = h_0 = 1,000\,\mathrm{km}$; (b) $h = h_0/2 = 500\,\mathrm{km}$; (c) $h = h_0/4 = 250\,\mathrm{km}$. Conceptually, being limited to second-order accuracy because of the piece-wise linear approximation of the domain boundary, halving the element-edge

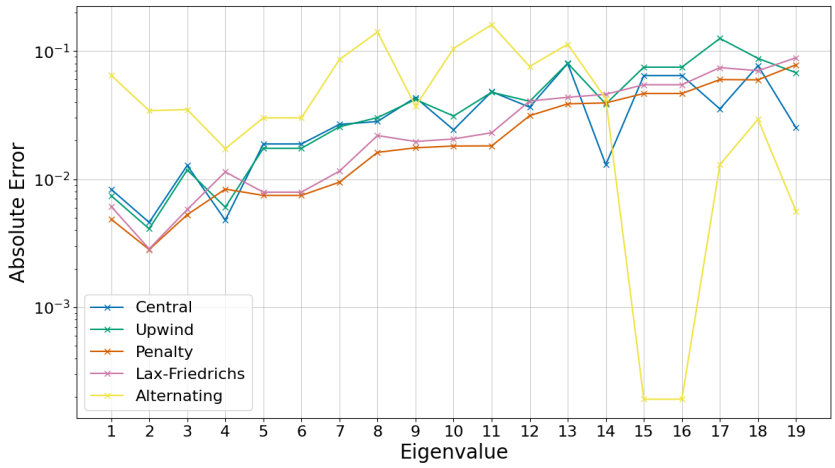

(a) $p = 1$

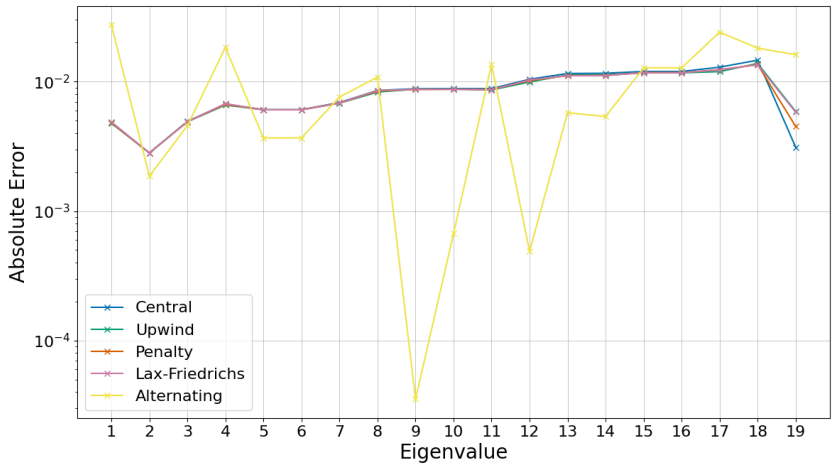

(b) $p = 2$

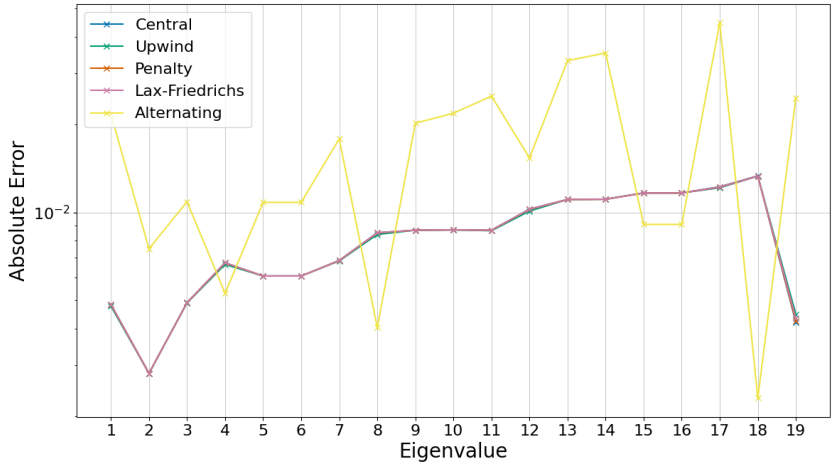

(c) $p = 3$

Figure 5.12: p-refinement, $h = 500\,\mathrm{km}$: Absolute error of DG-FEM eigenvalues for rotating barotropic motion in a circular basin of radius $3,000\,\mathrm{km}$ with uniform depth $4,000\,\mathrm{m}$ at mid-latitude with Coriolis parameter $f = 10^{-4}\,\mathrm{s}^{-1}$. Here, a target element-edge size $h = 500\,\mathrm{km}$ is used, along with a θ-value of 0.25 for the alternating flux.

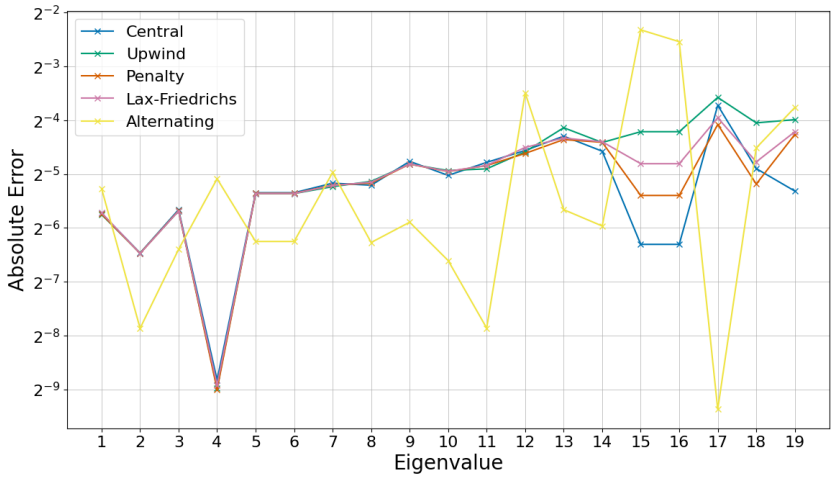

(a) $h = h_0$

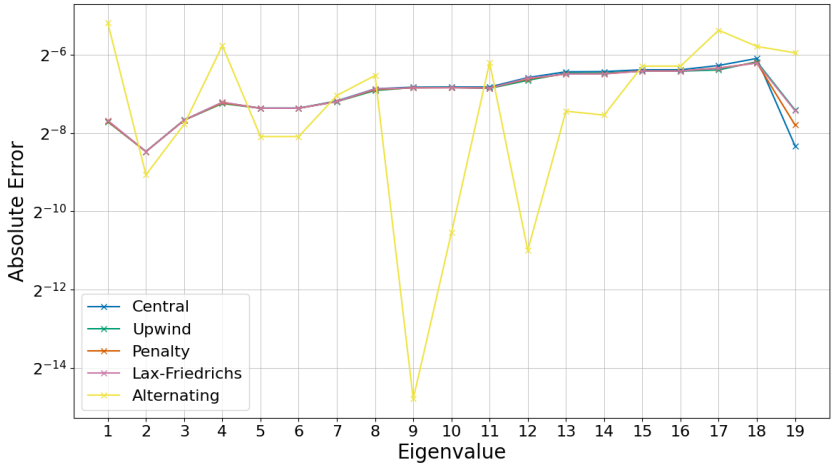

(b) $h = h_0/2$

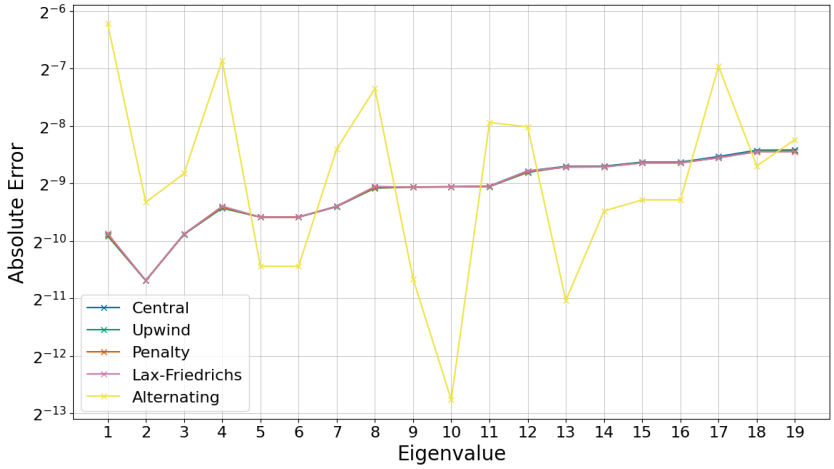

(c) $h = h_0/4$

Figure 5.13: h-refinement, $p = 2$: Absolute error of DG-FEM eigenvalues for rotating barotropic motion in a circular basin of radius $3,000\,\mathrm{km}$ with uniform depth $4,000\,\mathrm{m}$ at mid-latitude with Coriolis parameter $f = 10^{-4}\,\mathrm{s}^{-1}$. Here, a polynomial order of $p = 2$ is used, along with an initial target element edge-size of $h = 1,000\,\mathrm{km}$ and a θ-value of 0.25 for the alternating flux.

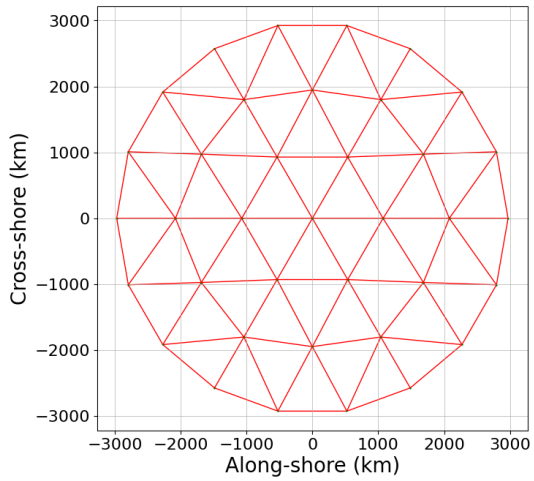

(a) $h = h_0$

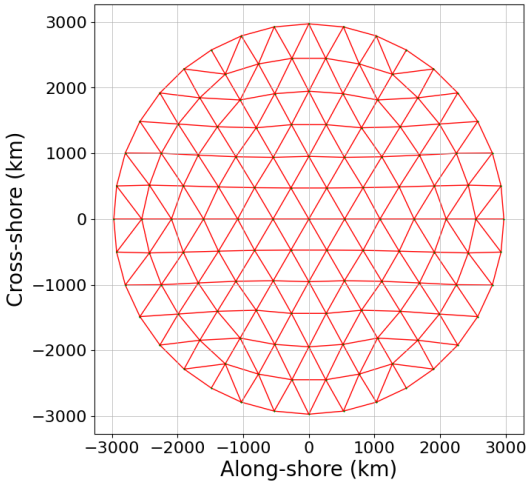

(b) $h = h_0/2$

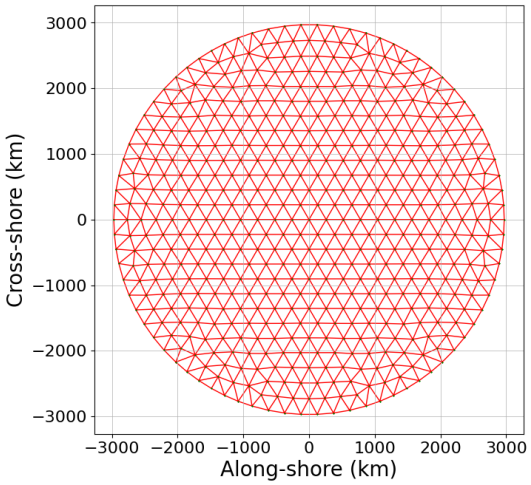

(c) $h = h_0/4$

Figure 5.14: Uniform mesh refinement associated with Figure 5.13. The target element-edge length h is halved each time, giving: (a) $h = h_0 = 1,000\,\text{km}$; (b) $h = h_0/2 = 500\,\text{km}$; (c) $h = h_0/4 = 250\,\text{km}$.

size should mean reducing the error by a factor of four each time. Indeed, the latter is corroborated by Figure 5.13 where an initial element-edge size of $h_0 = 1,000\,\text{km}$ is halved twice. We see that each time the element-edge size h is halved, the error is indeed reduced by a factor of $2^2 = 4$. Again, we see that the alternating flux scheme does not achieve the same convergence rates as the other four. Nonetheless, there is still a general reduction in absolute error of wave frequencies as the element size is reduced.

5.6.3 Boundary-Value Problem for Non-Trivial Coastal Kelvin Wave

In the following subsection, we consider validating the numerical scheme by considering a background flow corresponding to a perturbed Kelvin wave. This mode will be found using the shooting method for a two-point boundary-value problem (see Keller, 1992; Press et al., 2007) with an adaptive step-size (to be precise, the Cash–Karp method - again, see Press et al. (2007)). Having prescribed some forcing frequency and an initial guess for

Parameter	Definition/Use	Dimensional Value	Non-Dimensional Value
H_D	Deep-ocean fluid depth	$4,000\,\mathrm{m}$	1
f	Coriolis parameter	$10^{-4}\,\mathrm{s}^{-1}$	1
L_D	Rossby radius of deformation	$2,000\,\mathrm{km}$	1
H_C	Coastal-shelf fluid depth	$200\,\mathrm{m}$	5×10^{-2}
ω	Forcing tidal frequency	$1.4 \times 10^{-4}\,\mathrm{s}^{-1}$	1.4
L_C	Shelf width	$100\,\mathrm{km}$	5×10^{-2}
L_S	Slope width of continental margin	$50\,\mathrm{km}$	2.5×10^{-2}
$\lambda = L_C + L_S$	Characteristic coastal length scale	$150\,\mathrm{km}$	7.5×10^{-2}

Table 5.2: Table of coastal topography parameters and their definition, along with default values both dimensionally and non-dimensionally.

the associated along-shore wavenumber, a corrected wavenumber is obtained, along with the mode's associated cross-shore structure. The goal here is to verify convergence under both h- and p-refinement for the various numerical flux schemes in a bid to select the most optimal configuration. As for the domain, we will consider two domains corresponding to $300\,\mathrm{km} \times 300\,\mathrm{km}$ and $600\,\mathrm{km} \times 600\,\mathrm{km}$ square patches of coastal flow with a lateral boundary at $0\,\mathrm{km}$ in the cross-shore spatial co-ordinate. The mesh discretisations considered for these domains are shown in Figure 5.15 with target element edge sizes $h = 100\,\mathrm{km}$ (top) and $h = 50\,\mathrm{km}$ (bottom). To emphasise, the goal in the mesh generation is to produce near-equilateral triangular elements, so we are not simply producing meshes composed of right-angled isosceles.

To begin, we define our choice of cross-shore topography using $\varphi(Y) = \sin^2(\pi Y/2)$ in (3.72). The default parameters associated with this slope are shown in Table 5.2, while the slope profile itself is plotted in Figure 5.16. Moreover, we shall be concerning ourselves with the free Kelvin wave of semi-diurnal tidal frequency $\omega = 1.4 \times 10^{-4}\,\mathrm{s}^{-1}$ under the influence of rotation at mid-latitude, such that Coriolis parameter $f = 10^{-4}\,\mathrm{s}^{-1}$ and therefore $\omega/f = 1.4$. As we saw in Section 3.4.2, the Kelvin mode's corresponding along-shore wavenumber will depend on the form of the coastal topographic profile. In particular, we saw that the first-order correction with respect to the non-dimensional parameter characterising the coastal length scale's ratio to the Rossby radius of deformation involved an integral of depth perturbation over the margin (see equation (3.122)).

As for the spatial structure of the Kelvin mode associated with Figure 5.16, it is shown in Figure 5.17. From the shooting method, the associated along-shore wavelength is found to be $\sim 8,300\,\mathrm{km}$. The horizontal velocity profiles and the surface displacement profiles in Figure 5.17 correspond to a $1\,\mathrm{m}$ surface amplitude at the coastal boundary. On the left of Figure 5.17, the form of the mode is shown over a $2,000\,\mathrm{km} \times 2,000\,\mathrm{km}$ domain, while on the right, over a $200\,\mathrm{km} \times 200\,\mathrm{km}$ domain. The former is to highlight the decaying nature of the Kelvin mode away from the coastal boundary, while the latter illustrates the form of the modal solution along the continental margin itself.

In our analysis, we conducted a series of boundary-value problems varying the choice of numerical flux under both p- and h-refinement, recording both the computation time and

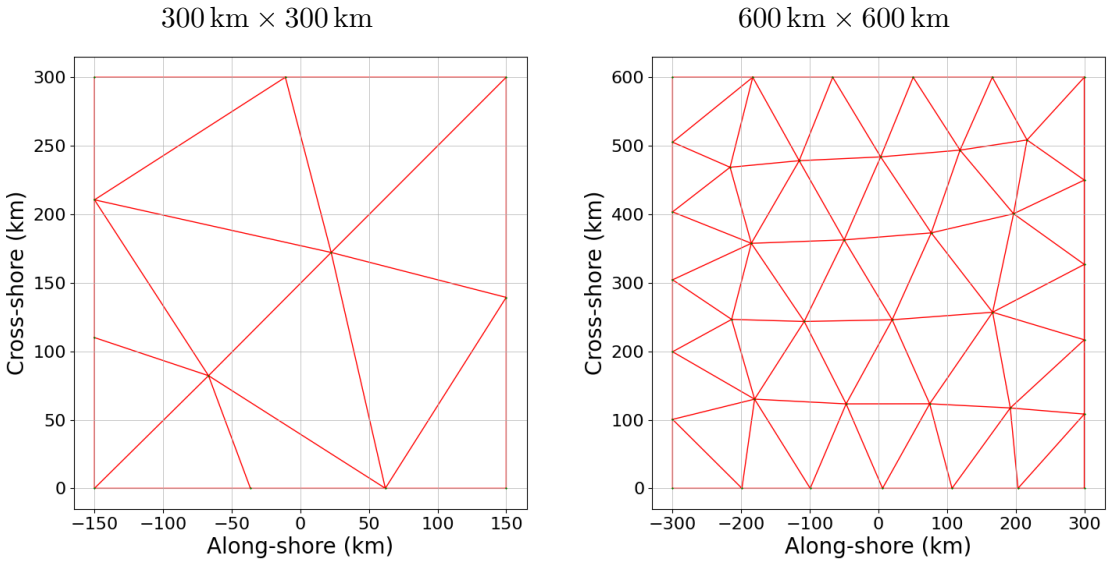

(a) Target edge size $h = 100\,\text{km}$

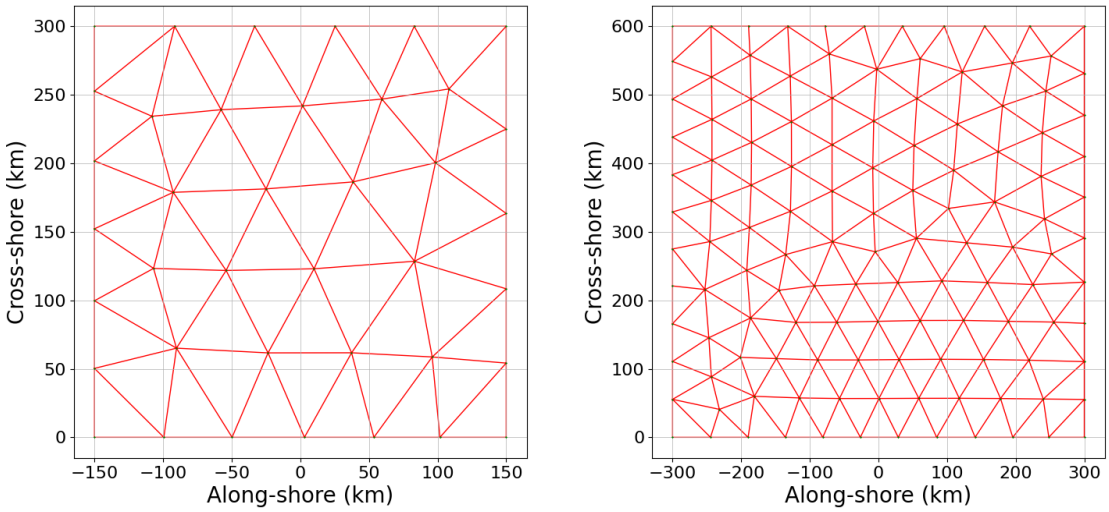

(b) Target edge size $h = 50\,\text{km}$

Figure 5.15: Mesh discretisations used for Kelvin boundary-value problem with target element-edge sizes $h = 100\,\text{km}$ (top) and $h = 50\,\text{km}$ (bottom). Moreover, we consider square domains of length 300 km, while on the right domains of length 600 km.

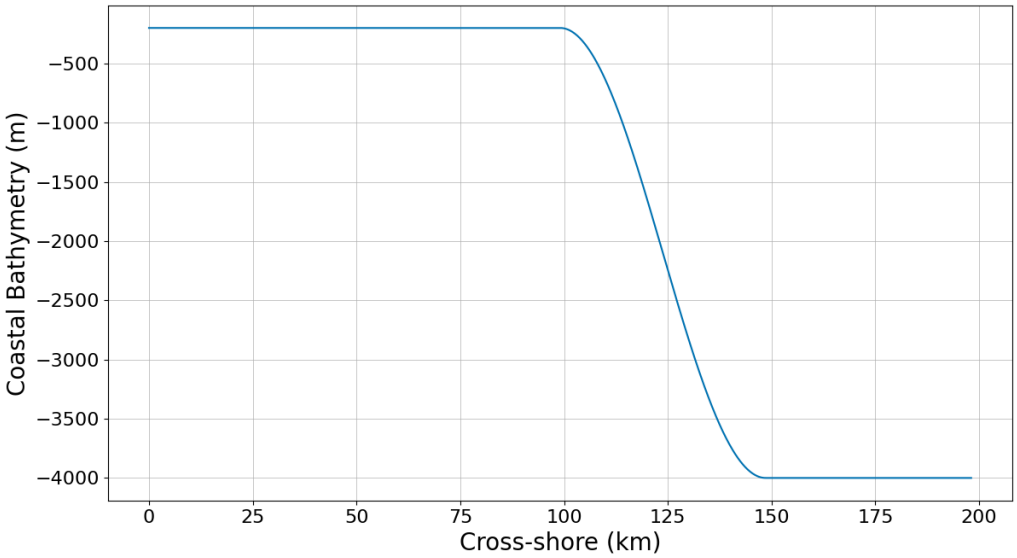

Figure 5.16: Differentiable slope profile used for testing convergence of boundary-value problem associated to non-trivial barotropic coastal Kelvin wave of semi-diurnal frequency at mid-latitude.

a series of norms of the error vector

$$\boldsymbol{E} = \mathbf{v}_{Shooting} - \mathbf{v}_{DGFEM}, \qquad \mathbf{v} = \begin{pmatrix} U/\sqrt{g\,H_D} \\ V/\sqrt{g\,H_D} \\ P/(g\,H_D) \end{pmatrix} \tag{5.74}$$

where $\mathbf{v}_{Shooting}$ and $\mathbf{v}_{DGFEM}$ represent respectively the numerical modal solution found using the shooting method and the DG-FEM solution. The idea here is to optimise our choice of numerical flux for the boundary-value problem while also showing convergence for some non-trivial problem to which the solution is known. As for the norms, we will be considering the $L^{\mathcal{P}}$-norm

$$L^{\mathcal{P}}\left(\boldsymbol{E}\right) = \sqrt[\mathcal{P}]{\sum_{i}^{n} |\boldsymbol{E}_i|^{\mathcal{P}}} \Big/ \sqrt[\mathcal{P}]{\sum_{i}^{n} 1}, \tag{5.75}$$

in the case of $\mathcal{P} = 1$ (average absolute error), $\mathcal{P} = 2$ (Euclidean norm) and $\mathcal{P} = \infty$ (residual norm).

In Figure 5.18, we show the L^1- (top), L^2- (middle) and L^∞-norms (bottom) of the DG-FEM Kelvin mode. With the mesh fixed (target element edge size of $h = 50\,\text{km}$), the polynomial order is varied from $p = 1$ (piece-wise linear) to $p = 9$ (piece-wise nonic) along the horizontal axis. In addition to the latter, the different lines represent the choice of numerical flux and is indicated by the legend. From this figure, it is evident that as one increases the polynomial order, the error norms reduce. The latter means that the solution converges under p-refinement, as one would expect.

As for the asymptotic behaviour, the different norms appear to show slightly different

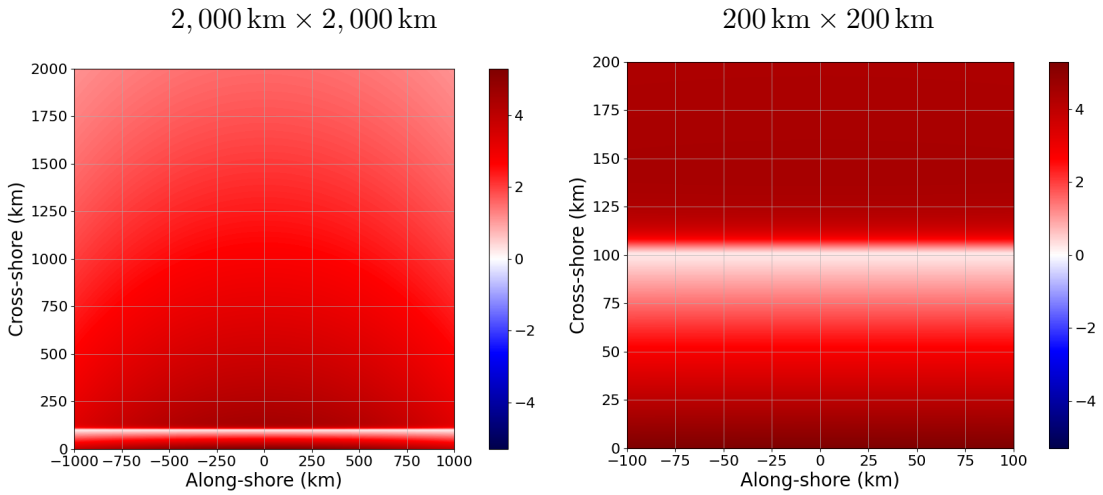

(a) Along-shore velocity profile (cm/s)

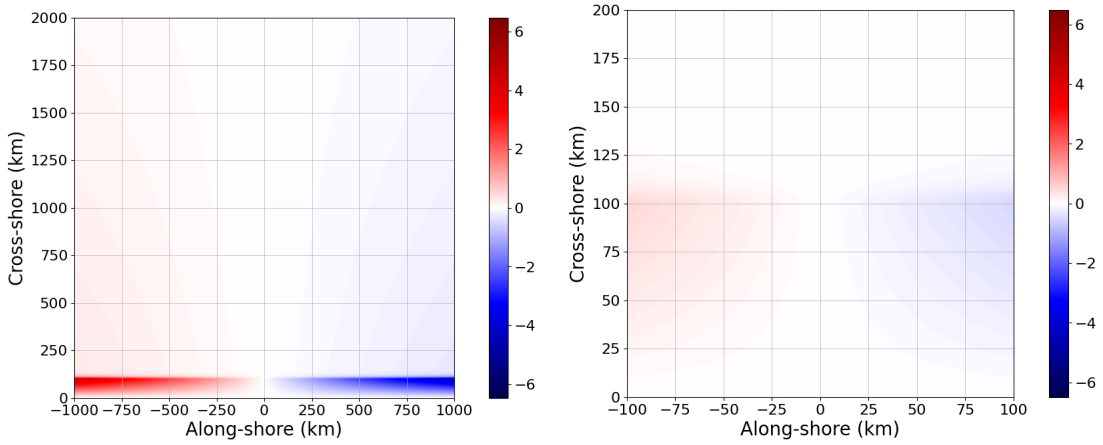

(b) Cross-shore velocity profile (cm/s)

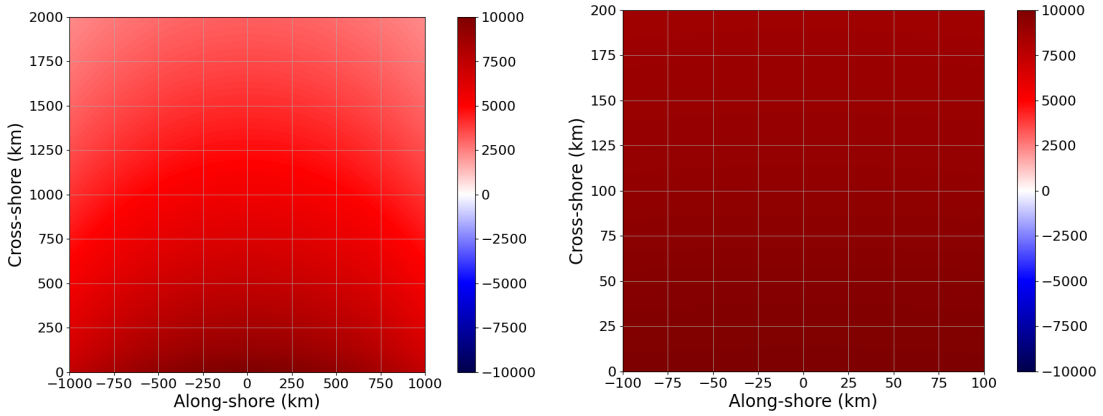

(c) Surface pressure (Pa)

Figure 5.17: Numerical solution (using the shooting method) of non-trivial barotropic coastal Kelvin wave associated with coastal topography profile shown in Figure 5.16 used for testing convergence of boundary-value problem associated to free perturbed barotropic Kelvin mode of semi-diurnal frequency at mid-latitude and surface amplitude $\sim 1\,\mathrm{m}$. The corresponding along-shore wavelength is $\sim 8,300\,\mathrm{km}$. On the left, the solution is shown over a $2,000\,\mathrm{km} \times 2,000\,\mathrm{km}$ square domain, while on the right a $200\,\mathrm{km} \times 200\,\mathrm{km}$.

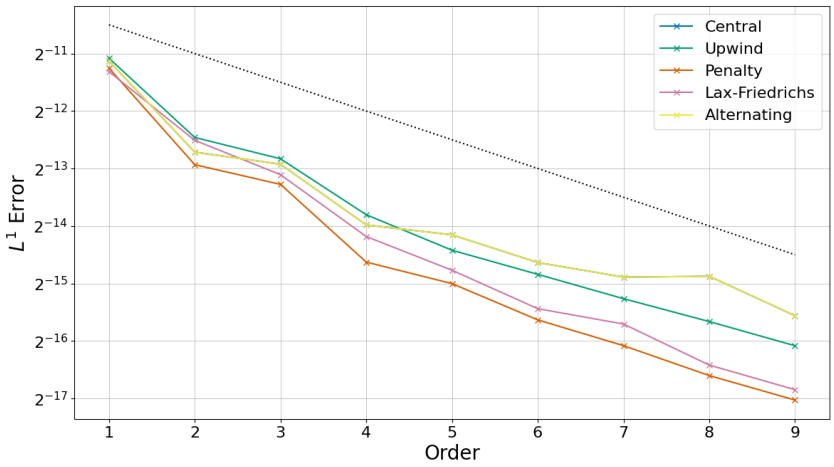

(a) L^1

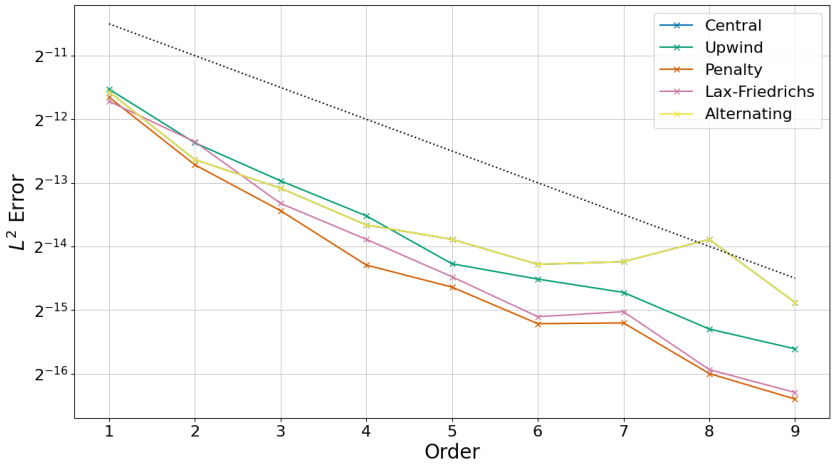

(b) L^2

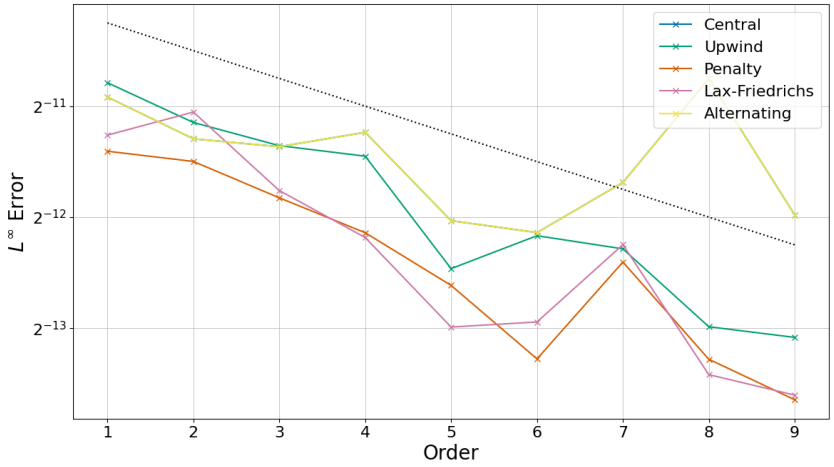

(c) L^∞

Figure 5.18: Error norms of a free Kelvin wave of semi-diurnal frequency over a 300 km × 300 km domain corresponding to the topographic profile shown in Figure 5.16, and solved as a boundary-value problem using DG-FEM. In these Figures, we vary both polynomial order (horizontal axis) and numerical flux (legend), while fixing the uniform element-edge size at $h = 100$ km. The black dotted lines show linear scaling laws.

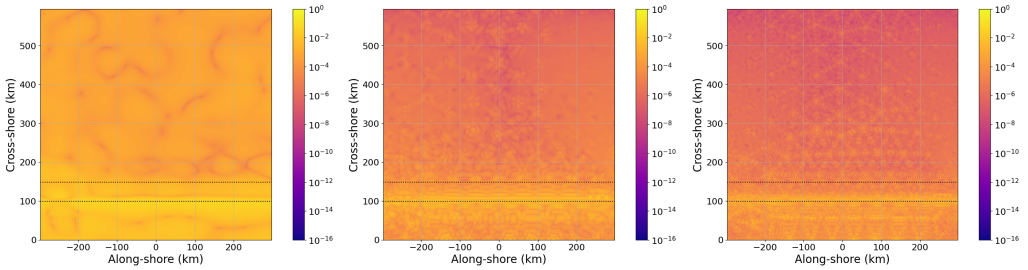

(a) Central

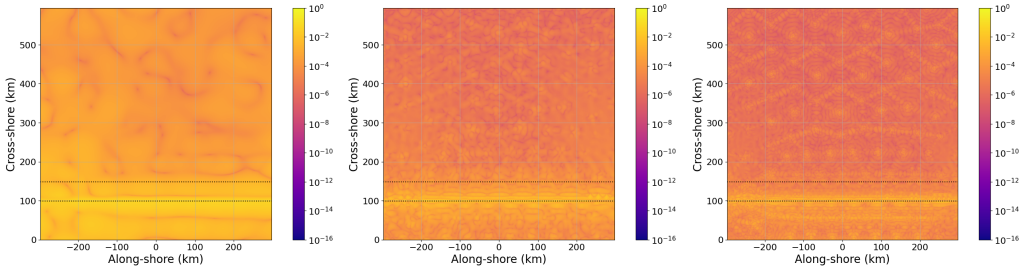

(b) Upwind

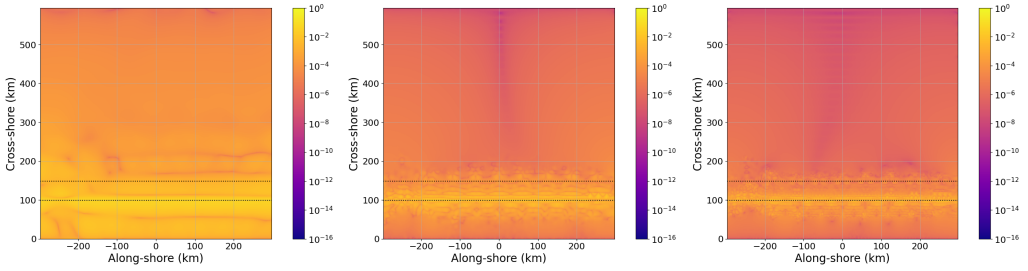

(c) Penalty

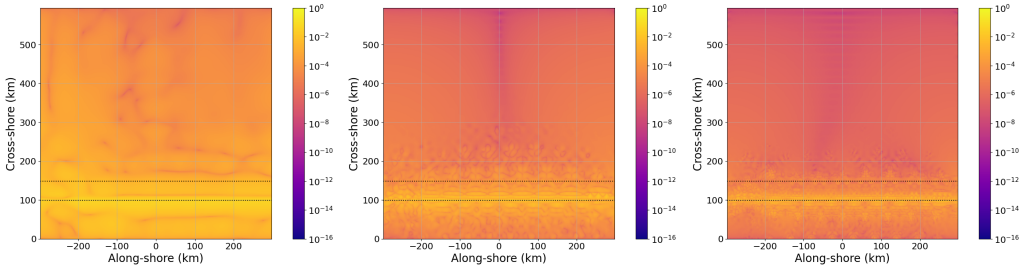

(d) Lax–Friedrichs

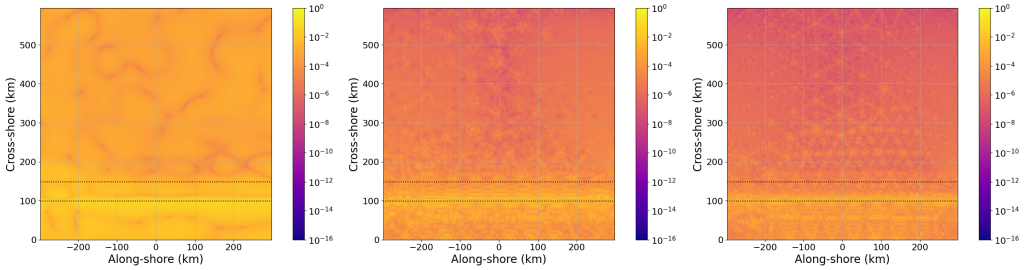

(e) Alternating ($\theta = 0.75$)

Figure 5.19: p-refinement, $h = 50\,\text{km}$: Log of absolute error of Kelvin mode's cross-shore velocity profile (m/s) over $600\,\text{km} \times 600\,\text{km}$ square domain while varying numerical flux scheme and polynomial order. For polynomial order, we show $p = 1$ (left), $p = 5$ (middle) and $p = 9$ (right), while the target element-edge size is fixed at $h = 50\,\text{km}$. The black dashed lines show the head and the foot of the continental slope.

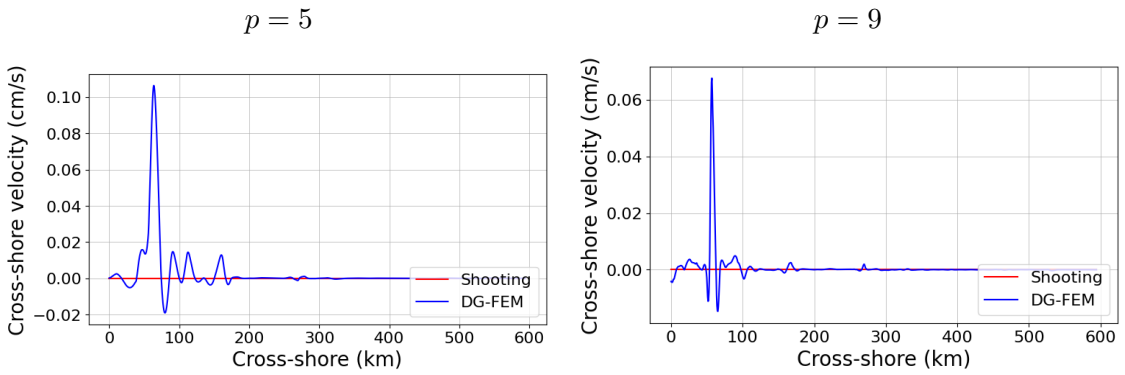

(a) Central

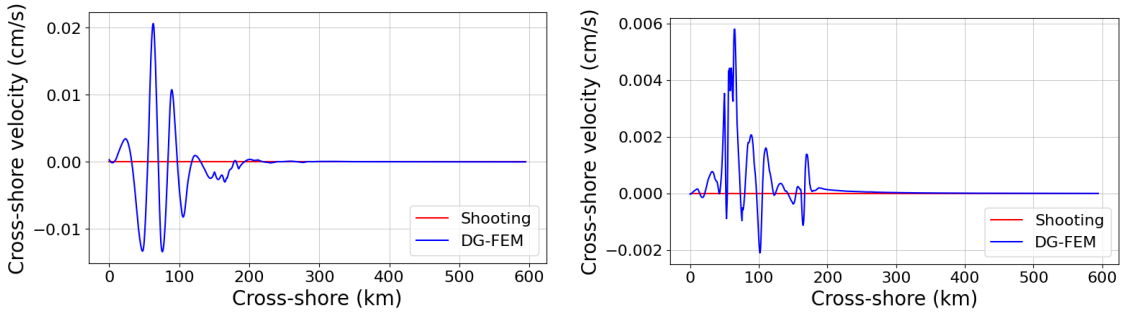

(b) Lax–Friedrichs

Figure 5.20: p-refinement, $h = 50\,\text{km}$: Comparison of velocity profiles computed on a $600\,\text{km} \times 600\,\text{km}$ domain at along-shore position $x = 0\,\text{km}$ for the central (top) and Lax–Friedrichs (bottom) numerical fluxes, as well as local test functions $p = 5$ (left) and $p = 9$ (right). Red line indicates the exact solution obtained by the shooting method, while the blue represents the DG-FEM solution.

convergence rates, which is to be unexpected. However, as shown by the black dotted lines in each of the error norms presented in Figure 5.18, $\log\left(L^{\mathcal{P}}\left(\boldsymbol{E}\right)\right) = \alpha_{\mathcal{P}} + \beta_{\mathcal{P}}\, p$ for real constants $\alpha_{\mathcal{P}}$ and $\beta_{\mathcal{P}}$. Such a variable scaling law, although linear in nature, could be in part due to the variable topography which induces variable length scales over which the tidal dynamics occur. For example, over the coastal shelf where fluid depth is minimal, the cross-shore length scale would be smaller than that of the deep ocean by around a factor of $\sqrt{4000\,\text{m}}/\sqrt{200\,\text{m}} = 2\sqrt{5} \approx 4.5$. Another possible reason is the lack of numerical resolution over the slope: are there enough grid points, especially for the low-order test function cases?

To investigate possible lack of resolution over the shelf and continental slope, a log-error plot of the Kelvin mode's cross-shore velocity is shown in Figure 5.19. In this Figure, we show the error's spatial structure and how it varies for numerical flux under p-refinement. Here, it becomes apparent that the greatest error occurs at the shelf break and along the shelf. The latter is irrespective of the numerical flux scheme. On the other hand, the errors do appear more uniform for the penalty and Lax–Friedrichs numerical flux schemes. One means by which one could overcome the lack of resolution over the shelf is by employing r-refinement.

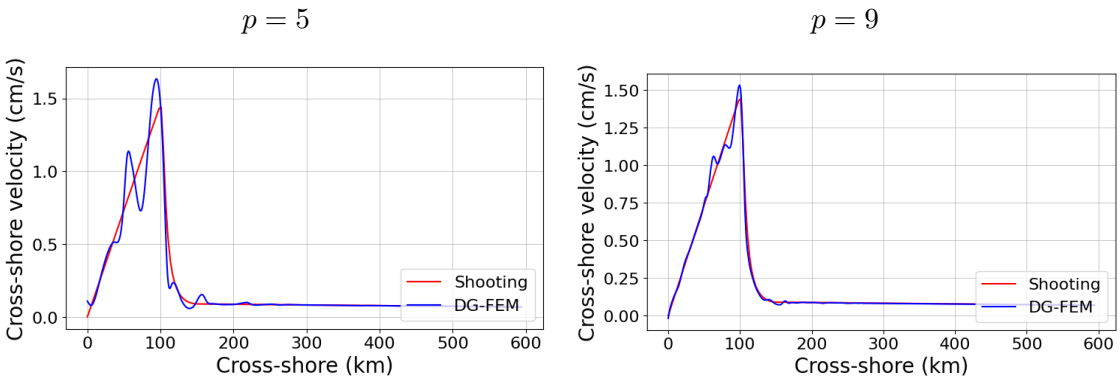

(a) Central

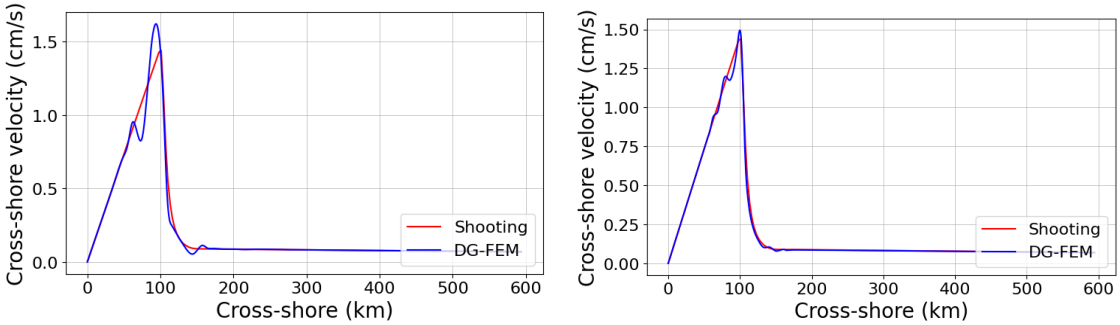

(b) Lax–Friedrichs

Figure 5.21: p-refinement, $h = 50\,\text{km}$: Comparison of velocity profiles computed on a $600\,\text{km} \times 600\,\text{km}$ domain at along-shore position $x = 300\,\text{km}$ for the central (top) and Lax–Friedrichs (bottom) numerical fluxes, as well as local test functions $p = 5$ (left) and $p = 9$ (right). Red line indicates the exact solution obtained by the shooting method, while the blue represents the DG-FEM solution.

Another means by which one could overcome the lack of resolution is by employing non-uniform element-edge size functions. These are functions used to determine the target size of our element edges in space. In the uniform case, considered in this chapter, the edge-size functions are all constant. That is to say, the target length of all triangular elements is the same in space. In Section 6.3, edge-size functions depending on horizontal length scales and bathymetric gradients are discussed, and even shown to be effective. Local mesh refinement will be of paramount importance when seeking to optimally resolve the barotropic and baroclinic tidal dynamics around a submarine canyon which involve much smaller length scales. We could also align the mesh at both the head and foot of the slope.

In Figures 5.20–5.21, we compare at different along-shore positions the cross-shore velocity obtained via the shooting method with the profile obtained using DG-FEM. For each figure, we compare the central numerical flux (top) with the Lax–Friedrichs numerical flux (bottom), as well as with local test functions $p = 5$ (left) with $p = 9$ (right).

In Figure 5.20, we consider the cross-shore structure at the along-shore position $x = 0\,\text{km}$. Here, the cross-shore velocity should be zero for all cross-shore coordinates. While there are oscillations around zero in this case, it is evident from the figure that the amplitude is

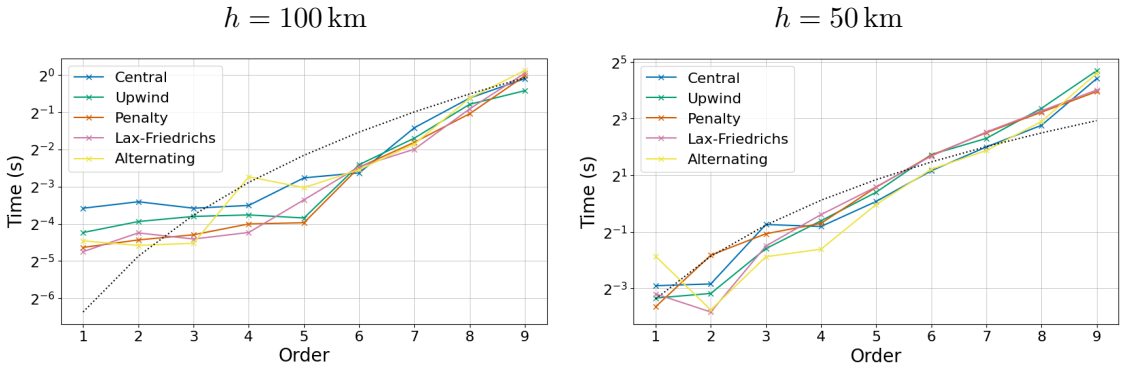

(a) $300\,\mathrm{km} \times 300\,\mathrm{km}$

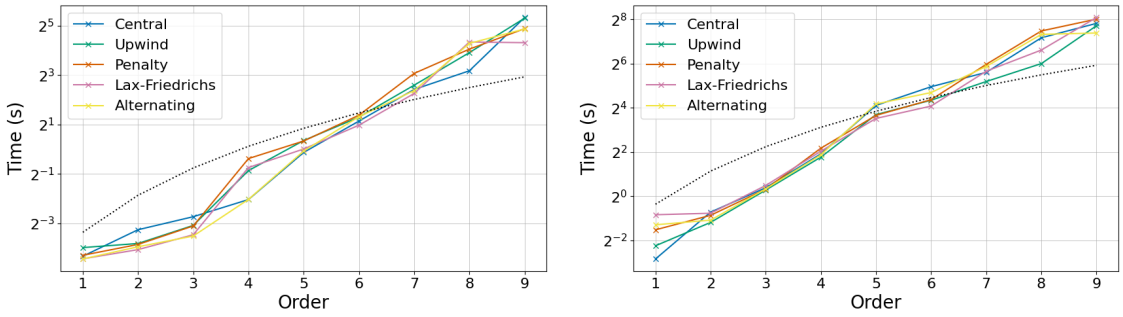

(b) $600\,\mathrm{km} \times 600\,\mathrm{km}$

Figure 5.22: Time taken in seconds to construct matrices and solve the elliptic problem associated with the barotropic coastal Kelvin wave of semi-diurnal frequency. The computation used Python's `scipy.sparse.linalg.spsolve` in series on an 8th Generation Intel® Core™ i7 laptop. On the top, a $300\,\mathrm{km} \times 300\,\mathrm{km}$ coastal domain is considered, while in the bottom $600\,\mathrm{km} \times 600\,\mathrm{km}$. For element-edge size, we show results for $h = 100\,\mathrm{km}$ (left) and $h = 50\,\mathrm{km}$ (right). On the horizontal axis, we indicate the polynomial order, while the different solid lines represent the choice of numerical flux ($\theta = 0.75$ for alternating). The dashed black line represents the time complexity $O\left(n^{3/2}\right)$, where n is the size of the square-matrix system.

reduced when increasing the polynomial order for either flux scheme. However, the error is greater in the case the central numerical flux, by a factor of ten. In Figure 5.20, we consider at the along-shore position $x = 300\,\text{km}$, at the boundary of the computational domain. The same remarks can be made about the accuracy increasing as the local test function is increased for both numerical fluxes. However, two interesting remarks can be made. First of all, the Lax–Friedrichs flux appears to impose the impermeability condition better at cross-shore position $y = 0\,\text{km}$ than the central flux scheme. Secondly, the Lax–Friedrichs solutions appear smoother than those of the central flux. This is to be expected since the Lax–Friedrichs scheme penalises all discontinuities.

In Figure 5.22, we investigate the effects of element size, polynomial order and numerical flux scheme on the time taken to construct the discrete linear operators and solve the aforementioned elliptic problem using Python's `scipy.sparse.linalg.spsolve`. The computations were carried out in series on an 8th Generation Intel® Core™ i7 laptop (Dell XPS 13). In Figure 5.22a, we consider results for $300\,\text{km} \times 300\,\text{km}$ coastal domain, while Figure 5.22b considers results for a $600\,\text{km} \times 600\,\text{km}$ coastal domain. On the left of each sub-figure a target element-edge size of $h = 100\,\text{km}$ is used to generate the mesh, while on the right of each sub-figure a target element-edge size of $h = 50\,\text{km}$.

In general, there appears to be very little difference between the numerical flux schemes in time taken to construct and solve the matrix systems. Halving the element-edge size or doubling the domain corresponds to quadrupling the number of elements. This appears to correlate with the time taken to solve the linear system, since doubling the domain or halving the element-edge size corresponds to an increase in computational time by a factor just over $2^2 = 4$. I.e. there appears to be a near-linear relationship between the number of elements, K, and the computational time. The left sub-figure of 5.22a suggests there is some bottleneck of ~ 0.03 seconds in the process, but that can be mostly neglected, particularly for larger systems which we shall be considering.

To quantify the effects of polynomial order on time taken to construct and solve matrix systems, a line of best fit is constructed, and is indicated by the black dashed line in each plot of Figure 5.22. Here, we considered the number of unknowns, $n = K \times N_p$, where K is the number of elements and $N_p = (p+1)(p+2)/2$ is the number of nodes required per element for an order p local test function. Inspired by the result of Lipton et al. (1979) describing the time complexity of performing Gaussian elimination—a common method of solving sparse linear systems—on planar graphs, we find that the time complexity is approximately $O\left(n^{3/2}\right)$. Bondy and Murty (2008) define planar graphs as "a graph which can be drawn in the plane in such a way that edges meet only at points corresponding to their common ends". Such planar systems do indeed arise in regular two-dimensional FEM (see Lipton et al., 1979). Given the localised nature of DG-FEM, and therefore increased sparsity and reduced bandwidth, it would seem only logical that the time-complexity of solving the matrix system is more efficient.

5.7 Summary

In this chapter, we have introduced core concepts around solving the linearised decoupled two-layer modal shallow water equations using cutting-edge numerics in the form of discontinuous Galerkin finite element methodology (DG-FEM). This method allows multiple means of optimising our problem to increase the accuracy, stability and computational time taken to resolve the dynamics of oceanic tides.

Having introduced the key concepts of DG-FEM and how the method compares to other grid-based computational methods in the introductory section, the mathematical formulation was constructed for linearised two-layer decoupled modal shallow-water equations in Section 5.2. This required posing the modal equations of motion in conservative form and obtaining the localised semi-discrete strong form. In Section 5.3, we discussed boundedness of solutions by considering the rate of change of local modal energy in an arbitrary element. However, this introduced the notion of a numerical flux, as discussed in Section 5.4.

To motivate the concept of a numerical flux, the Riemann problem for our problem was solved exactly in Section 5.4.1. A generalised numerical flux motivated by Hesthaven and Warburton (2008) was then proposed in Section 5.4.2 which incorporated five different numerical fluxes, each with their own unique set of advantages and disadvantages. These included, for example, the continuity of the solution, the conditioning of the discrete linear operators, as well as the discrete operator's sparsity. Such properties of the numerical flux render each one more suitable to different problems. For example, the central numerical flux, in theory, should yield energy-conserving modes through a relatively sparse discrete operator. As such, these methods are exceptionally fast when tackling initial-value problems using explicit time-stepping schemes, or when energy conservation is of utmost importance in a boundary-value problem. To this effect, we discussed boundary conditions and their weak formulation in Section 5.5.

To verify our numerical implementation of DG-FEM, we considered two associated problems of the linearised barotropic shallow-water equations (SWEs) in Section 5.6. Having discussed uniform mesh discretisation of the computational domain in Section 5.6.1, Section 5.6.2 tackles two known eigenvalue problems: non-rotating in a square domain, as well as rotating in a circular basin. In the former, it was shown that all methods converge under both h- and p-refinement, but the rate at which depends on the choice of numerical flux. More specifically, it was concluded that the alternating flux was the least efficient. In the latter, we concluded that for a uniform element edge-size function, p-refinement was futile since the piece-wise approximation of the circular boundary would inherit errors of order $O\left(h^2\right)$. It was also discussed that to overcome this problem, one could consider using isoparametric curvilinear elements along the boundary. It was remarked however that the use of curvilinear elements was not required since our work considers rectangular domains only. We did show however that all numerical fluxes converge under h-refinement. Moreover, it was noted that the issue of geostrophic balance would need to be addressed in the rotating case: the current boundary conditions do not sufficiently constrain the prob-

lem when using a central or alternating numerical flux, and results in spurious sub-inertial eigenmodes. Along with further constraining the boundary conditions, it was highlighted that a possible Hamiltonian/skew-symmetric approach could overcome the latter issue (e.g. Ambati & Bokhove, 2007).

The second problem, discussed in Section 5.6.3, considered the non-trivial boundary-value problem to which the form of the solution was known: the perturbed Kelvin wave (see Section 3.4.2). Since we know the form of the perturbed Kelvin wave for a given cross-shore topographic profile, we could apply a corresponding background free-wave solution and see how the solution vector compares to the numerical (as opposed to the analytical which we showed agreed with the numerical). We also found that using a uniform element-edge size function—the target edge size for all elements discretising the domain is taken constant—leads to the greatest errors at the shelf break. So while we were able to conclude that the solution converges under both h- and p-refinement, localised mesh refinement will be needed to ensure the localised dynamics along the shelf break are sufficiently resolved. We also confirmed here that the Lax–Friedrichs and penalty flux schemes lead to error distributions which are near-spatially uniform.

As for the time complexity, we found that by doubling the domain or halving the element-edge size leads to roughly quadrupling the computational time. The latter suggests an almost-linear relationship between the number of nodes in the system and the time complexity of the sparse system matrix solver. We also compared the time complexity to the result of Lipton et al. (1979) which suggests a Gaussian elimination on planar or near-planar graphs has time complexity $O\left(n^{3/2}\right)$, where n is the number of unknowns.

In conclusion, we have constructed the mathematical formulation of the DG-FEM method applied to the decoupled modal shallow-water equations of a two-layer system with fixed upper-layer depth. The methodology and its implementation are crucial to the work presented in the following two chapters. Our numerical implementation includes a wide range of options regarding polynomial order, size of elements, and choice of numerical flux. We have also successfully shown convergence under h- and p-refinement for associated barotropic eigenvalue and boundary-value problems. However, the need for localised mesh refinement around the shelf break has been emphasised in order to resolve the local dynamics occurring over smaller length scales successfully and optimally. Since there is little difference between numerical fluxes in time taken to construct and solve matrix systems of boundary-value problems, the deciding factor would lie more in the choice of the topography; a central flux would be well-suited towards discontinuous topography so long as the mesh was aligned, while a Lax–Friedrichs flux would be well-suited towards smooth topography. In addition, a central numerical flux is sparse and preserves energy, while the Lax–Friedrichs is well-conditioned and enforces continuity. The alternating flux would be less ideal for discontinuous topography given the scheme's sub-optimal rate of convergence.

Chapter 6

Impact of Canyons on Barotropic Tidal Flow

6.1 Introduction

As established in Section 1.2.2, oceanic submarine canyons are ubiquitous topographical features which incise continental margins. Figure 6.1 shows two well-studied examples: Monterey canyon and Astoria canyon. What makes canyons particularly interesting for the generation of internal tides, is that canyons are able to disrupt along-shelf flow (see Hickey, 1995). Moreover, for continuous stratification canyons offer the potential for strong internal-tide generation through critical or supercritical wave generation.

Research into the mathematical modelling of internal-tide generation by canyons appears to have originated in Huthnance and Baines (1982), wherein mooring data from northwest Africa was analysed. The results of Huthnance and Baines (1982) suggest that Kelvin waves across canyons lead to considerably greater bottom-intensified flow along continental shelves. In this analysis, Kelvin waves were fitted to mooring data to construct the form of the surface tide, and then used to force a baroclinic response. The study concluded that the strong along-shore barotropic flow of the Kelvin wave interacting with along-shore topographic irregularities were responsible. This analysis was similar in methodology to the numerical components of Chapters 3 and 4, but inferred over 2D transects of a canyon.

Later analytical and experimental work by Baines (1983) explored large-amplitude tidal motion observed in oceanic submarine canyons within a controlled laboratory setting. The experiment involved a circular tank with stratified fluid and attached to a rotation table to force "tidal" motion along idealised slit-like canyons. While observations were strongly dependent on the ratio of the bottom slope and the ray characteristic, results showed, corroborated by scaling arguments, that for a sufficiently narrow canyon, the flow appeared driven by the pressure field external to the canyon. This pressure gradient across the canyon resulted in the generation of internal waves almost double in amplitude (and therefore an increase in energy flux by a factor of four).

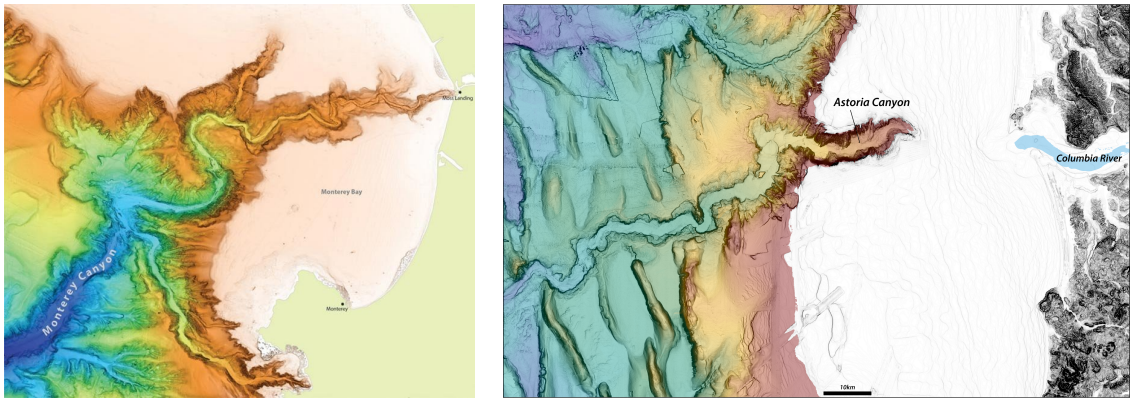

(a) Monterey canyon, California

(b) Astoria canyon, Oregon

Figure 6.1: Bathymetry of the Monterey canyon system (from Merritt, 2019), situated 150 km south of San Francisco in northern California, and of Astoria canyon (from Hill, 2019), located 225 km south west of Seattle.

In this chapter, we investigate the effects of submarine canyons on the form of the surface tide, modelled as a free Kelvin wave of semi-diurnal frequency at mid-latitude (with $\omega/f = 1.4$). Having solved for the form of the surface tide using DG-FEM numerics coupled with locally refined high-quality meshes, we seek to gain a greater understanding of how canyon topography affects the form of the Kelvin wave. More importantly, the form of the tide can then be used to force a baroclinic response.

The chapter begins, in Section 6.2, by discussing idealised models of canyon-slope topography. Previous models (e.g. Baines, 1983; Zhang et al., 2014; Nazarian & Legg, 2017a, 2017b), however, are sub-optimal. We propose instead a novel means of modelling continuous shelf-incising canyons. Satisfied with the choice of idealised canyon-slope topography, Section 6.3 considers the means of mesh discretisation and localised refinement using the Python package OceanMesh; this is core to the effectiveness of discontinuous Galerkin finite element methodology (DG-FM), as in Chapter 5. The effect of canyon topography on the form of a free Kelvin wave is investigated in Section 6.4. By investigating how canyon geometry affects the barotropic pressure, horizontal velocity field, and vertical velocity in and around the canyon, we ask ourselves what the ramifications could be for the baroclinic response and the implied radiating energy fluxes. The chapter concludes with a summary in Section 6.5.

The code used for this chapter requires Python packages:

- `ppp` - see Appendix B.1.
- `DGFEM` - see Appendix B.2.
- `barotropicSWEs` - see Appendix B.3.

Further package dependencies and file structure of aforementioned Python packages are discussed in Appendix B.

6.2 Modelling of Submarine Canyons

A wide variety of idealised canyon models exist in the literature, as illustrated in Figure 6.2. The piece-wise linear approximations of Baines (1983) are shown in Figures 6.2a and 6.2b; the latter differs from the former since the canyon is "widened near the foot so that it [narrows] in both the horizontal and vertical as one [moves] inwards from the foot toward the head". Nazarian and Legg (2017a, 2017b) employ the models shown in Figures 6.2c and 6.2d to model V-shaped canyons. More precisely, Figure 6.2c is used to construct canyons that are near-critical at the head of the slope, having joined two symmetrically inclined planes at the canyon head. However, the notion of criticality only lends itself to continuous stratification and is therefore irrelevant in the context of our two-layer model. Figure 6.2d on the other hand, has a flat bottom, and is used to model a canyon which has the potential to trap incident internal waves. The last model which we shall discuss is that used by Zhang et al. (2014). This model is significantly more complex than the aforementioned models and has the advantage of being smooth everywhere. The caveat for this model, however, is that the canyon lacks compact support. The canyon is constructed using a Gaussian to generate an incision of the slope, and then a tanh function is used to generate the slope. As a consequence, the width and length of the idealised canyon are not well-defined.

Each of these models is deficient in some way for our present purposes. Those shown in Figures 6.2a, 6.2b and 6.2d have discontinuous fluid depth, which is awkward for mesh alignment and the follow-on task of modelling internal-tide generation. Further, data from Harris et al. (2014) gives an average canyon depth of $1,830\,\mathrm{m}$ - this corresponds to an incision around halfway up the slope. This is in contrast to the models shown in Figures 6.2a–6.2e, where the foot of the canyon lies at the foot of the slope.

We thus develop a model for shelf-incising canyons with continuous fluid depth. We define the shelf-slope topography as in equation (3.72) of Section 3.4. Here, we take

$$\varphi(Y) = \sin^2\left(\frac{\pi Y}{2}\right) \tag{6.1}$$

to model the continental slope, although, as discussed in Chapter 3, alternatives do exist, e.g. the linear profile $\varphi(Y) = Y$. An appropriate model would be any function such that $\varphi(0) = 0$ and $\varphi(1) = 1$ with $\varphi'(Y) \geq 0\ \forall Y \in [0,1]$, i.e. the function is monotonically increasing. The slope-shelf profile is then given by

$$h_{slope}(x,y) = \begin{cases} H_C, & 0 \leq y \leq L_C, \\ H_C + (H_D - H_C)\,\varphi\left(\dfrac{y - L_C}{L_S}\right), & L_C < y < L_C + L_S, \\ H_D, & L_C + L_S \leq y. \end{cases} \tag{6.2}$$

Here, (Cartesian) x measures the along-shore position and y measures the off-shore position. By default, the shelf width $L_C = 100\,\mathrm{km}$, the slope width $L_S = 50\,\mathrm{km}$, the shelf

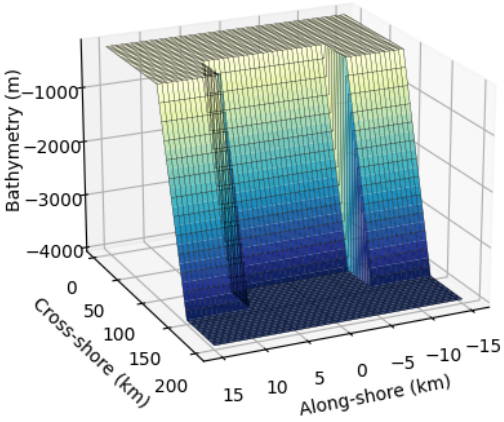

(a) Piece-wise linear canyon

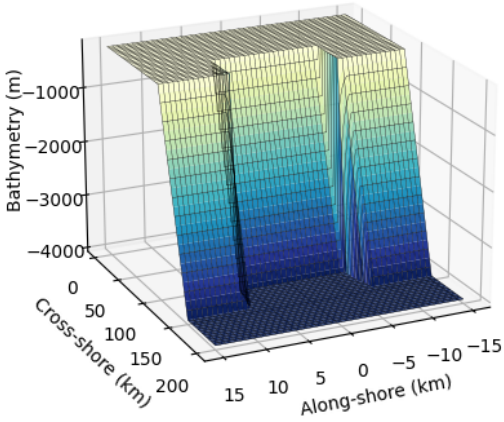

(b) Piece-wise linear V-shaped canyon

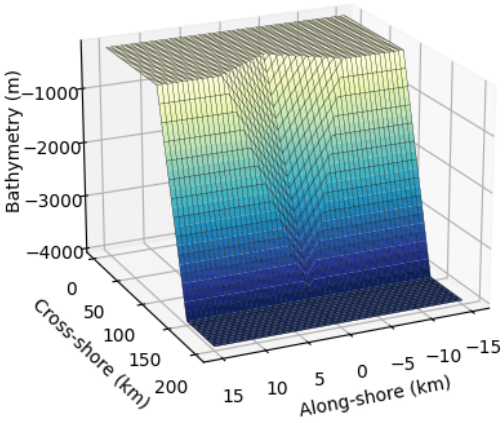

(c) Near-critical V-shaped canyon

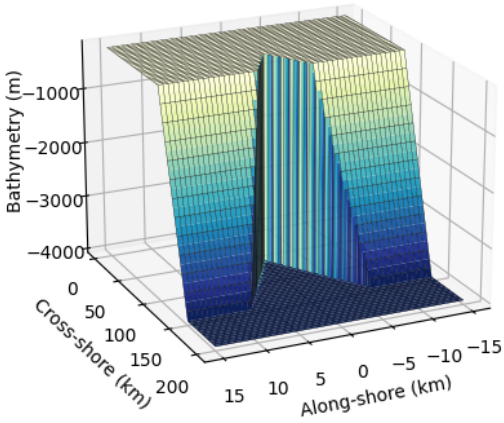

(d) Flat-bottom V-shaped canyon

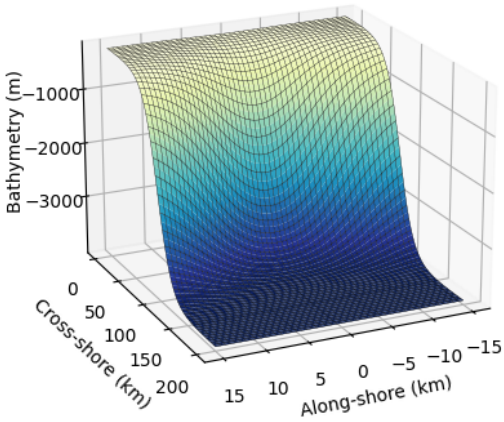

(e) Gaussian-tanh canyon

Figure 6.2: Previous idealised models of canyon-slope topography: (a) and (b) are used by Baines (1983); (c) and (d) are used by Nazarian and Legg (2017a, 2017b); (e) is used by Zhang et al. (2014). Note that (b) differs from (a) in that there is a slight widening of the canyon near the foot.

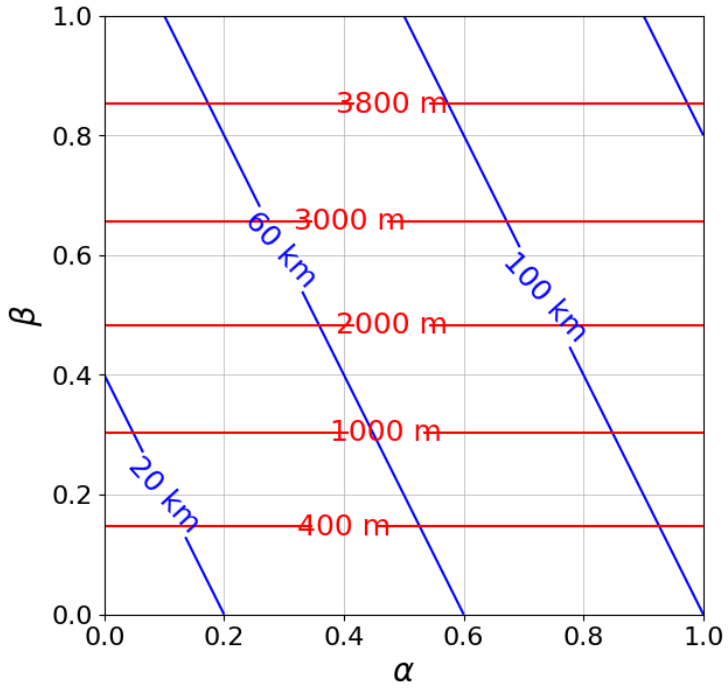

Figure 6.3: Contours of canyon termination depth (red) and canyon length (blue) in α–β parameter space for shelf width $L_C = 100\,\text{km}$ and slope width $L_S = 50\,\text{km}$.

depth $H_C = 200\,\text{m}$ and the deep-ocean depth $H_D = 4,000\,\text{m}$.

To parameterise canyon termination depth (the vertical length scale of the canyon) and length (the cross-shore length scale of the canyon), we introduce two non-dimensional parameters: α is the maximum proportion of the shelf occupied by the canyon, whilst β is the maximum proportion of the slope occupied by the canyon. So both α and β lie between 0 and 1. The total canyon length is

$$L_{canyon}\,(\alpha, \beta) = \alpha\, L_C + \beta\, L_S, \tag{6.3}$$

while the termination depth is

$$D_{canyon}\,(\beta) = H_C + (H_D - H_C)\;\varphi\,(\beta)\,. \tag{6.4}$$

The case $\beta = 0$ corresponds to no canyon topography as the canyon depth $H_C - D_{canyon} = 0$. Shown in Figure 6.3 is a contour plot of canyon termination depth (red) and canyon length (blue) in α–β parameter space for shelf width $L_C = 100\,\text{km}$ and slope width $L_S = 50\,\text{km}$. We recall that Harris and Whiteway (2011) categorises canyons into three types (see Figure 1.7): those which incise the shelf and connect to rivers (type one); those which incise the shelf (type two); those which are confined to the continental slope (type three). With our model, we are able to model canyon types one and two. Assuming sufficiently large β, type one canyons can be considered the regime of large α, while type two canyons can be considered the regime of small α.

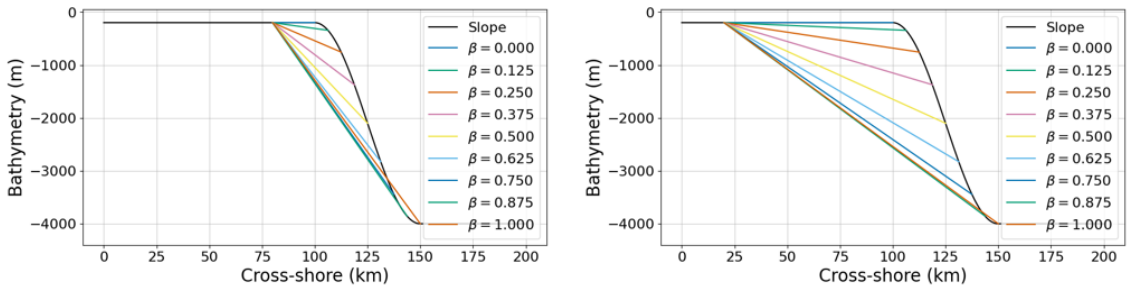

(a) $\alpha = 0.2$ (b) $\alpha = 0.8$

Figure 6.4: Idealised canyon: Valley profiles with shelf width $L_C = 100\,\text{km}$ and slope width $L_S = 50\,\text{km}$, while varying the proportion of the shelf occupied by the canyon α, and the proportion of the slope occupied by the canyon β.

Having prescribed parameters for the canyon length and canyon depth, all that remains is some parameterisation of the canyon width (the along-shore length scale of the canyon). Here we consider a maximum canyon width W located at the shelf break. With all three length scales of the canyon defined, a valley profile along the centre of the canyon is then chosen. Here, a linear profile for the valley is considered:

$$h_{valley}(y) = H_C + \varphi(\beta)\,(H_D - H_C)\,\psi\left(\frac{y - (1-\alpha)\,L_C}{L_{canyon}(\alpha,\beta)}\right), \qquad \psi(Y) = Y. \tag{6.5}$$

More complex models of the valley profile defined by ψ could be considered, so long as $\psi(0) = 0$ and $\psi(1) = 1$ with $\psi'(Y) \geq 0\ \forall Y \in [0,1]$ (monotonically increasing).

Examples of the valley profile given in (6.5) are shown against the slope profile in Figure 6.4. Here, the proportion of the slope occupied by the canyon is varied while fixing the proportion of the shelf occupied by the canyon at: (a) $\alpha = 0.2$ (a canyon confined to the shelf break); (b) $\alpha = 0.8$ (a canyon which extends deep onto the shelf). In both cases, shelf width $L_C = 100\,\text{km}$ and slope width $L_S = 50\,\text{km}$. Figure 6.4 not only shows the effect of varying parameters α and β, but that it is the limit of $\beta \to 0$ that leads to an absence of a canyon valley.

It remains to define the along-shore (or cross-canyon) shape depth profile. We take this to be quadratic, leading to

$$h_{canyon}(x,y) = h_{valley}(y)\left(1 - \left(\frac{x}{L_W}\right)^2\right). \tag{6.6}$$

For a canyon of maximum width W at the shelf break, the value of L_W follows from (α,β) by demanding that $h_{canyon}(W/2, L_C) = H_C$, which implies

$$L_W = \frac{W}{2}\sqrt{1 + \frac{H_C}{(H_D - H_C)\,\varphi(\beta)}\,\frac{L_{canyon}(\alpha,\beta)}{\alpha\,L_C}}. \tag{6.7}$$

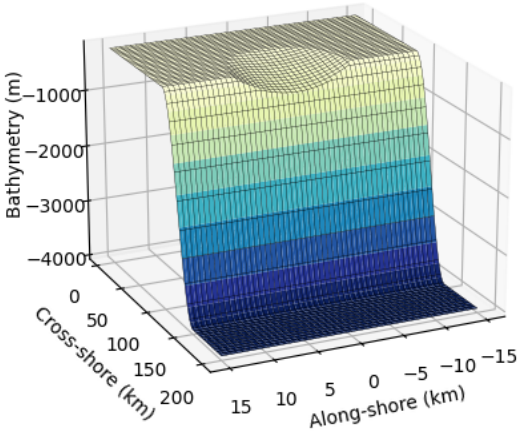

(a) $\alpha = 0.5$, $\beta = 0.2$

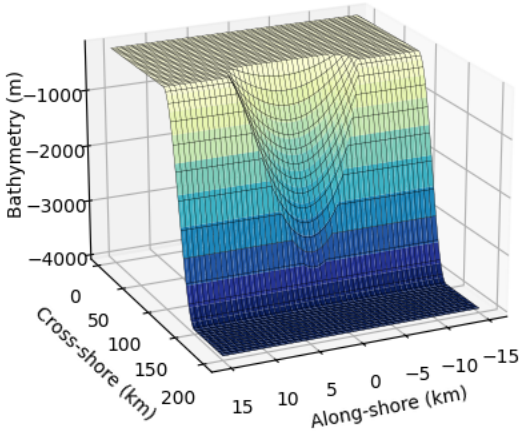

(b) $\alpha = 0.2$, $\beta = 0.8$

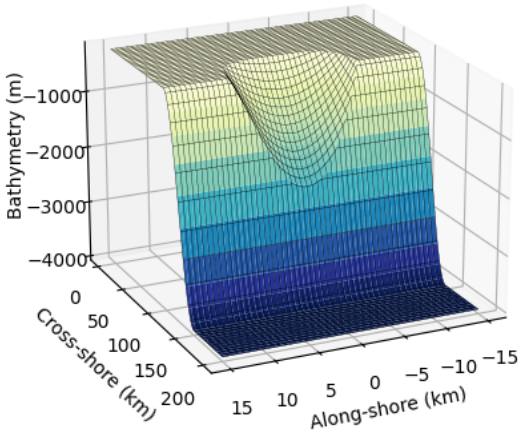

(c) $\alpha = 0.35$, $\beta = 0.5$

Figure 6.5: Idealised canyon-slope topographies with shelf width $L_C = 100\,\text{km}$, slope width $L_S = 50\,\text{km}$ and canyon width $W = 15\,\text{km}$. The canyon-slope topography is shown for three parameter configurations: (a) $\alpha = 0.5$ and $\beta = 0.2$; (b) $\alpha = 0.2$ and $\beta = 0.8$; (c) $\alpha = 0.35$ and $\beta = 0.5$.

Finally, the canyon-slope topography can be expressed in the form

$$h(x,y) = \begin{cases} \max\left\{h_{slope}(x,y), h_{canyon}(x,y)\right\}, & 0 \leq y \leq L_C + L_S, \\ H_D & y > L_C + L_S, \end{cases} \tag{6.8}$$

where canyon topography h_{canyon} and slope topography h_{slope} are given respectively by equations (6.2) and (6.6). For shelf width $L_C = 100\,\text{km}$ and slope width $L_S = 50\,\text{km}$, examples of canyon-slope topography are shown in Figure 6.5 for three parameter configurations of fixed canyon length $L_{canyon} = 60\,\text{km}$: (a) $\alpha = 0.5$ and $\beta = 0.2$; (b) $\alpha = 0.2$ and $\beta = 0.8$; (c) $\alpha = 0.35$ and $\beta = 0.5$.

6.3 Mesh Generation

Having developed an idealised canyon-slope topography, we are now able to consider the mesh discretisation required for the DG-FEM numerics. Not only are we required to define the computational domain, but to also discretise the domain into a series of conforming triangular elements of varying sizes to efficiently resolve both small- and large-scale processes of the tide. These include the mode's wavelength, the coastal boundaries, as well as the bathymetric gradients of the slope and canyon.

In our numerics, we use `OceanMesh` (Roberts, 2019; Roberts, Pringle, & Westerink, 2019a, 2019b; Roberts, Pringle, Westerink, et al., 2019; Pringle et al., 2021): a Python package based on a set of user-friendly Python functions, originally developed in MATLAB, to generate two-dimensional unstructured meshes for coastal ocean circulation problems. Alternative means were considered, such as `dmsh` (see Schlömer, 2020) and `PyMesh`, but were deemed either too complex or unable to effectively produce refined meshes across multiple length scales.

`OceanMesh` integrates mesh generation directly with geophysical datasets such as topo-bathymetric rasters/digital elevation models (DEMs) and shapefiles representing coastal features. The software also provides some necessary pre- and post-processing tools to perform successful numerical simulations and enables the generation of high-quality meshes based on a variety of feature-driven geometric and bathymetric mesh size functions. Mesh generation is achieved through a force-balance algorithm combined with a number of topological improvement strategies aimed at improving the worst-case triangle quality, such as mesh-gradation enforcement and smoothing.

A collaboration was initiated with the code developers to modify the existing Python package for idealised mathematical modelling. The developments include creating fixed points in the mesh generation necessary for maintaining positions of vertices along the boundary (e.g. rectangles), the implementation of a signed-distance function for a rectangular domain, the MATLAB-to-Python translation of a slope-limiting edge function which in itself required the implementation of bathymetric filters, as well as the ability to pass through user-defined functions of fluid depth in lieu of digital elevation models (DEMs).

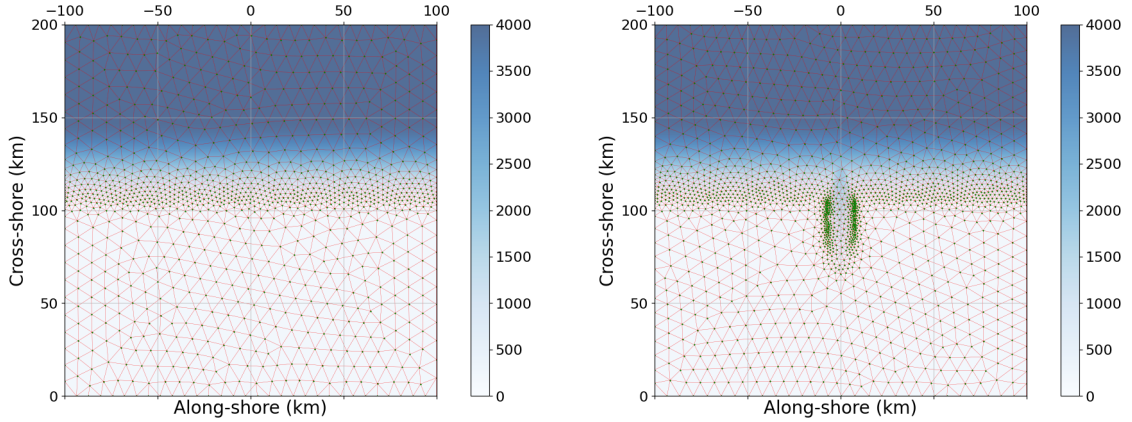

(a) Slope

(b) 15 km wide canyon

Figure 6.6: Examples of meshes used in the mathematical modelling of tidal flow in and around submarine canyons situated along continental margins. These meshes were generated using the Python package `OceanMesh`, and allow enhanced resolution along regions of great bathymetric variation. Contour plot shows a plan view of the fluid depth in metres.

These developments to the `OceanMesh` package were fundamental in our generation of robust and high-quality meshes needed to resolve the small-scale features in the mathematical modelling carried out in this thesis. The primary edge function that is used to produce the meshes required for the work which follows, is the bathymetric gradient function given by equation (9) of Roberts, Pringle, and Westerink (2019a):

$$h_{slp} = \frac{2\pi}{\alpha_{slp}} \frac{h}{|\boldsymbol{\nabla} h|}, \tag{6.9}$$

where $2\pi/\alpha_{slp}$ is the number of elements that resolve the topographic slope, h is fluid depth and $\boldsymbol{\nabla} h$ is the bathymetric gradient evaluated on a structured grid of horizontal resolution $h_0 = O(100\,\mathrm{m})$. The parameter α_{slp} is prescribed by the user and is typically valued between 10 and 30. Over the shelf break, we may expect a resolution $h_{slp} = O(100\,\mathrm{m})$, as seen in Figure 6.6.

Unlike equation (6.9), edge-size functions based on distance (to shoreline), feature size, and/or wavelength can lead to insufficient resolution along continental margins. Consequently, resulting meshes are unable to capture the large gradients which characterise the shelf break. Meshes generated using the slope parameter $h/|\boldsymbol{\nabla} h|$ are much more capable of capturing the dissipative effects as a result of internal tides (Roberts, Pringle, & Westerink, 2019a).

Figure 6.6 shows examples of the meshes we are able to generate using equation (6.9), where enhanced resolution is given to resolve the changes in bathymetry along the continental margin and the flanks of the canyon. In the case of no canyon (Figure 6.6a), the edge size of the mesh varies between 1 km and 10 km, while for the 15 km wide canyon (Figure 6.6b), the edge size varies between 0.5 km and 10 km.

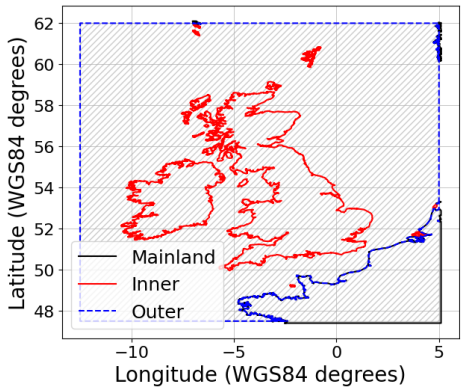

(a) Shape file and boundary box

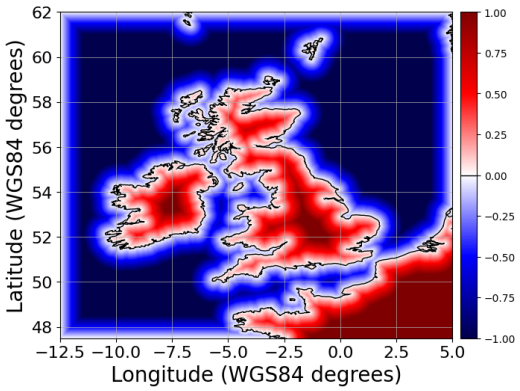

(b) Signed-distance function

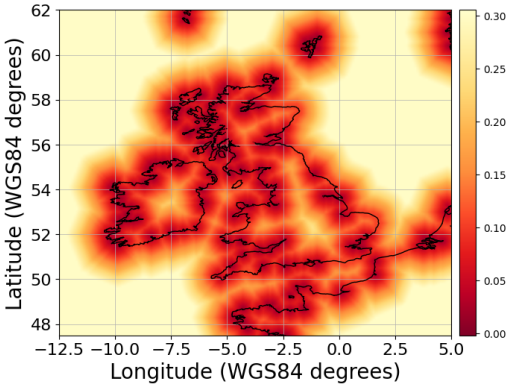

(c) Edge-size function

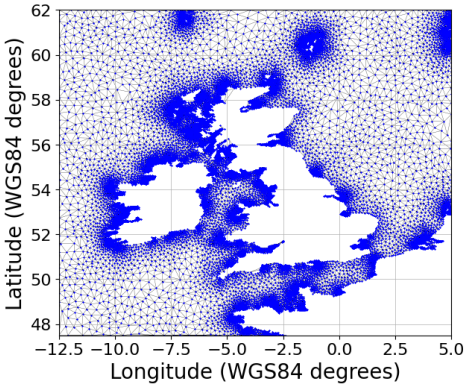

(d) Initial generated mesh

Figure 6.7: Principal steps in generating a mesh using `OceanMesh`: (a) provide a shape file and a boundary box to define domain; (b) produce a signed-distance function to define the domain using shape file and boundary box; (c) produce an edge-size function for cells in generated mesh; (d) generate the mesh through a series of iterations according to signed-distance and edge-size functions.

Of course, `OceanMesh` is not limited to idealised models. As shown in Figures 6.7–6.8, where we have considered the coast of South New England, USA, there are five essential steps to `OceanMesh` in generating a high-quality triangular mesh:

1. Create or load a shape file and specify a boundary box detailing your computational domain. An example of a shape file detailing the coast of New South England, USA, is shown in Figure 6.7a. Any shape object intersecting the boundary box is considered "mainland", while any others are regarded as "inner", or coastlines of islands.

2. Create a signed-distance function of the domain using the shape file. A negative value indicates the interior of the computational domain, while a positive value indicates the exterior.

3. Pass an edge-size function for mesh generation. If passing multiple edge-size functions, one is required to take the minimum output at each location. The new edge-size function is then smoothed, enforcing a mesh gradation by solving a Hamilton–

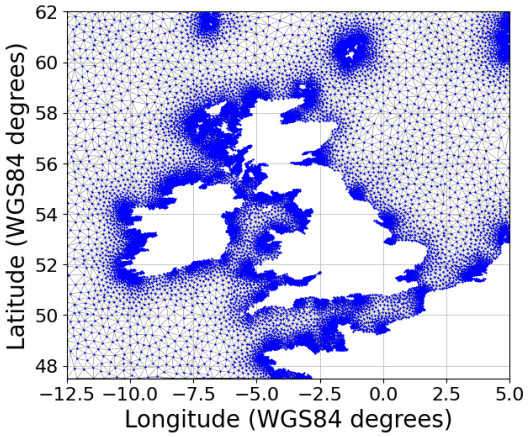

(a) Removing degenerate cells

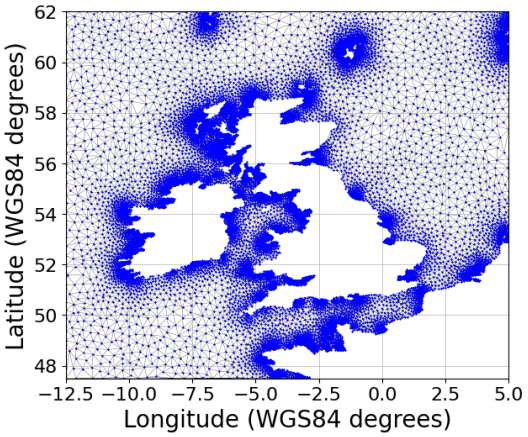

(b) Removing cells connected by single face

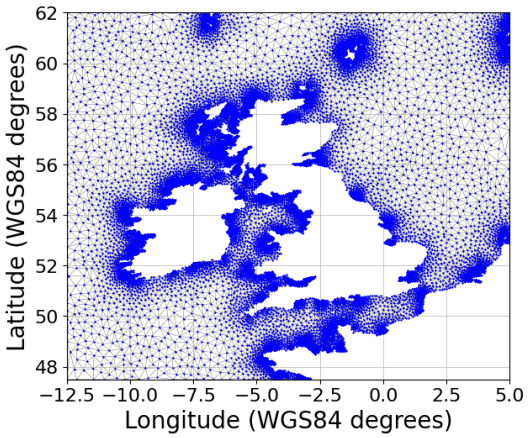

(c) Removing low-quality cells

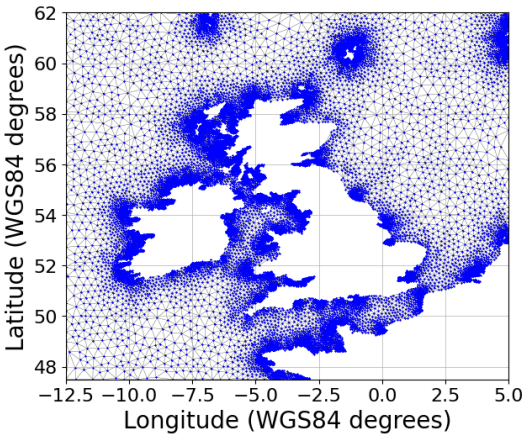

(d) Laplacian smoothing operator

Figure 6.8: Post-processing algorithms provided by `OceanMesh` to improve quality of generated mesh: (a) removing degenerate cells; (b) removing cells which are connected by a single face; (c) removing low-quality cells; (d) apply a Laplacian smoothing operator to nodes.

Jacobi equation (see Persson, 2006).

4. Generate the mesh over a series of iterations according to the signed-distance function and edge-size function.

5. Post-process mesh, as required. This process may include, for example, removing degenerate elements (elements whose nodes all lie on a line), removing low-quality elements (ideally, we want elements with equal angles) and smooth the position of nodes by applying a Laplacian filter.

Steps 1–5 were also required to generate the meshes shown in Figure 6.7. For step one, we were required to pass a shape file consisting of the four vertices which define the rectangular domain. For step three, we use equation (6.9) with $\alpha_{slp} = 28$. For step four, we limit the number of iterations as part of the force-balance process to 50 and prescribe a mesh gradation of 20%. For step five, we need only to ensure that the vertices of each triangle are arranged in a counter-clockwise order, that degenerate mesh faces are removed, and

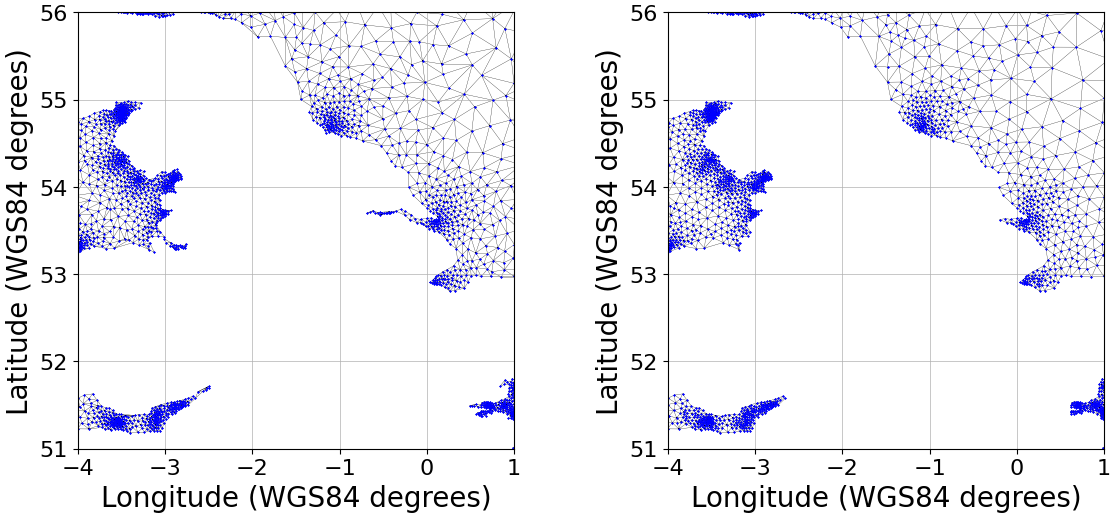

(a) Before

(b) After

Figure 6.9: Zoom-in of meshes before (left) and after (right) post-processing to improve mesh quality.

that all boundary nodes lie on the prescribed rectangular domain. The comparison of the mesh before and after post-processing is made clearer in Figure 6.9 with a zoom-in around central England.

In conclusion, we are able to produce high-quality triangular meshes for the modelling of tidal flows along continental margins using DG-FEM. These meshes offer consistency, as well as localised refinement for resolving the small horizontal length scales in an optimal manner.

6.4 Barotropic Flow around Submarine Canyons

In this section, we extend the problem given in Section 5.6.3 by including along-shore variations in topography. In other words, we are interested in the elliptic problem of time-periodic barotropic flow of semi-diurnal frequency around an idealised canyon. Here, we prescribe the tidal flow in the form of a Kelvin wave with surface amplitude $\sim 1\,\mathrm{m}$ along the entire coastal boundary and observe how the barotropic flow is impacted by a canyon. We are not, for example, considering the scattering problem of an incident Kelvin wave prescribed upstream.

Neglecting all external forces, the linearised motion of the decoupled barotropic tide of frequency ω is governed by

$$-i\,\omega\,\mathbf{U}_0 + f\,\hat{\mathbf{e}}_z \times \mathbf{U}_0 + \boldsymbol{\nabla} P_0 = \mathbf{0}, \tag{6.10}$$

$$-i\,\omega\,P_0 + \boldsymbol{\nabla}\cdot\left(c_0^2\,\mathbf{U}_0\right) = 0, \tag{6.11}$$

recalling that $\mathbf{U}_0$ denotes the barotropic horizontal velocity, while P_0 the barotropic pressure. Moreover, f and $c_0^2\,(\mathbf{x}) \approx g\,h\,(\mathbf{x})$ denote the Coriolis parameter and the barotropic

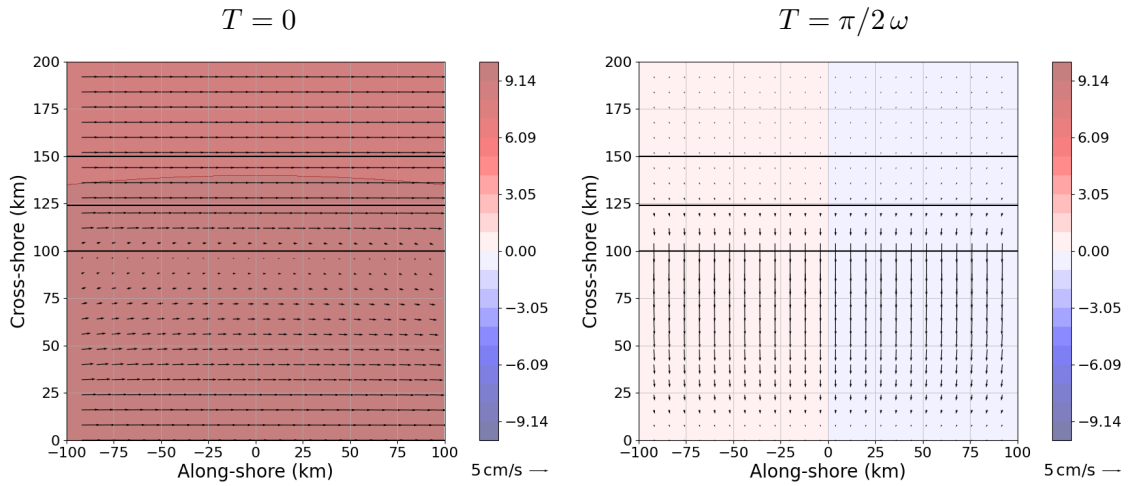

(a) No Canyon

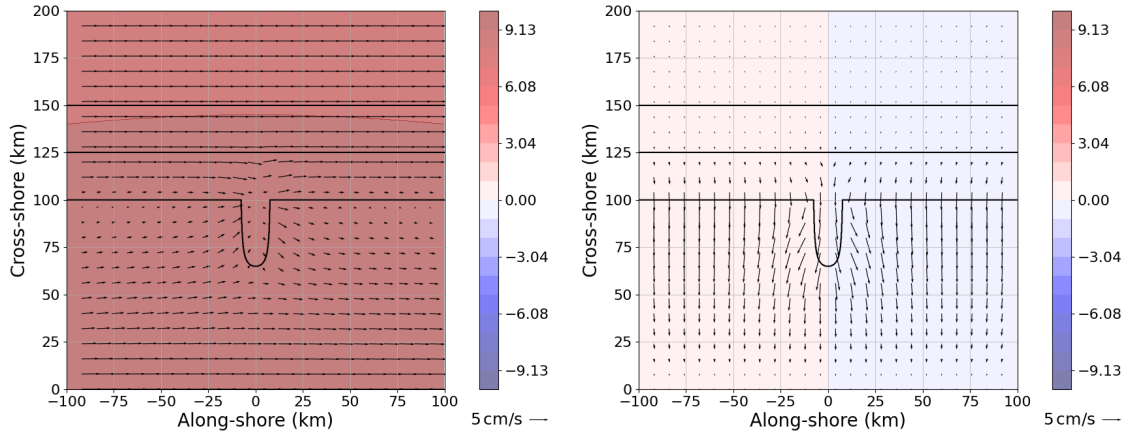

(b) Canyon

Figure 6.10: Solution comparison: velocity vector field (cm/s) with pressure contours (kPa) of barotropic semi-diurnal tide at mid-latitude in the form of a perturbed Kelvin wave of surface amplitude $\sim 1\,\mathrm{m}$. Top row: no canyon. Bottom row: canyon of width 15 km. The solutions on the right are a quarter of a period after those on the left. The black contours show the bathymetric contours of the shelf, the foot of the canyon and the deep ocean (200 m, 2,100 m and 4,000 m respectively).

wave speed squared for gravitational acceleration $g = 9.81\,\mathrm{m/s^2}$ and fluid depth $h(\mathbf{x})$, as determined by the coastal topography. Throughout, we consider $\omega/f = 1.4$. This corresponds to a semi-diurnal tidal frequency and a Coriolis parameter at mid-latitude.

To motivate the effects of the canyon topography on the barotropic tidal motion, we show the spatial solution in Figure 6.10 at two quarterly phases. Here, a canyon width of 15 km was used, along with parameter values $\alpha = 0.35$ and $\beta = 0.5$ corresponding to a canyon termination depth of 2,100 m and a canyon length of 60 km. The solution here was produced using the mesh shown in Figure 6.6b with polynomial order $p = 3$ and a central numerical flux. The quiver plots indicate the horizontal velocity fields of the barotropic tide (see quiver key corresponding to 5 cm/s), while the contour plots illustrate the barotropic pressure field in kPa (see colour bar).

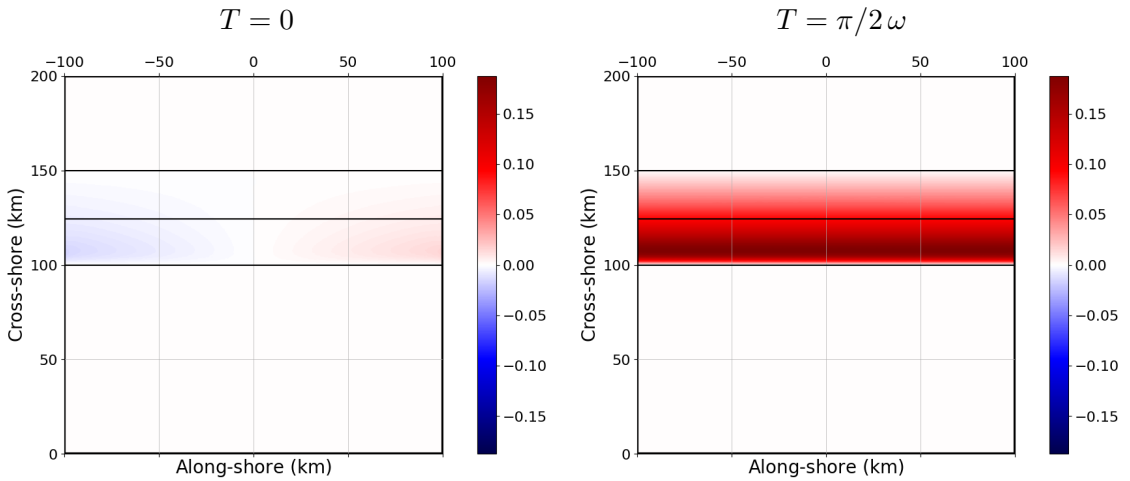

(a) No Canyon

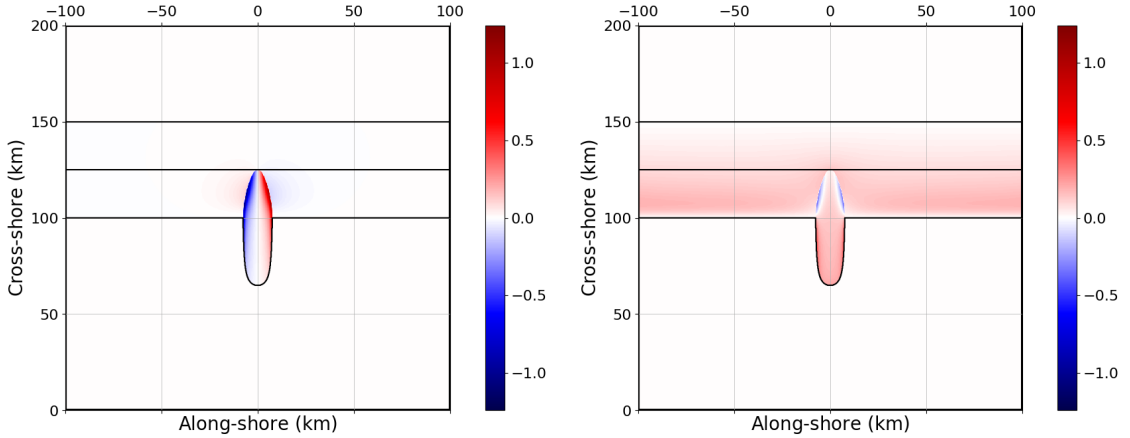

(b) Canyon

Figure 6.11: Solution comparison: contour plot of vertical velocity at the sea floor (cm/s) of a barotropic semi-diurnal tide at mid-latitude in the form of a perturbed Kelvin wave of surface amplitude $\sim 1\,\mathrm{m}$. Top row: no canyon. Bottom row: canyon of width 15 km. The solutions on the right are a quarter of a period after those on the left. The black contours show the bathymetric contours of the shelf, the foot of the canyon, and the deep ocean (200 m, 2,100 m and 4,000 m respectively).

Figure 6.10 shows that the pressure field (contoured) is largely unaffected by the canyon, and that the barotropic motions flows up and down the canyon (at the phase of the tide when there is flow up and down the slope), with some weak flow across the canyon sides. However, the velocity field, particularly along the side walls of the canyon, sees greater horizontal velocities steered by the canyon. One would therefore expect greater vertical motion in and around a canyon since the vertical velocity at the sea floor

$$\hat{W}_0\left(\mathbf{x},t\right) = -\boldsymbol{\nabla} h\left(\mathbf{x}\right) \cdot \hat{\mathbf{U}}_0\left(\mathbf{x},t\right), \tag{6.12}$$

seen previously in equation (2.181), is proportional to both bathymetric gradient and horizontal velocity in the bottom layer (hence the hats). In addition, the horizontal velocity field follows the topographic contours of the canyon.

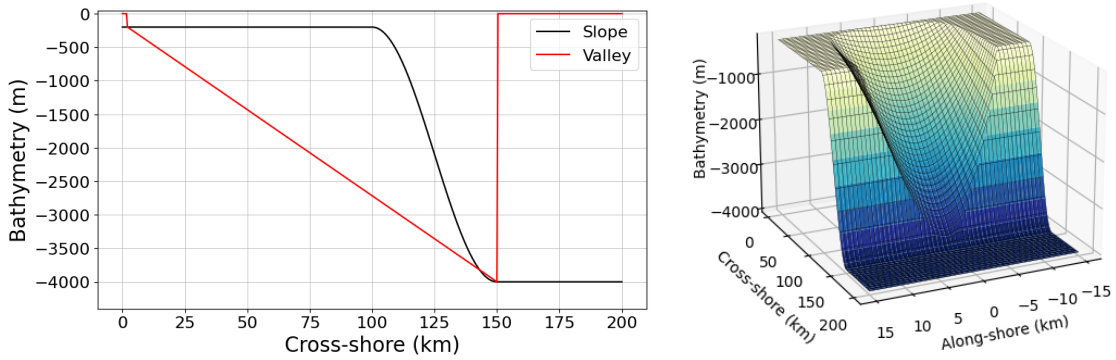

(a) Valley profile

(b) Canyon profile

Figure 6.12: Profiles associated with large canyon topography of width 20 km, length $\sim$ 150 km and termination depth 4,000 m. On the left, the slope and valley profile are shown (see legend), while on the right the full canyon profile as it intersects the continental margin.

Figure 6.11 shows the vertical velocity along the sea floor for the solutions of 6.10. Indeed, the presence of a canyon, as shown in Figure 6.11, sees localised vertical velocities increase from a magnitude of 0.2 cm/s to over 1 cm/s.

In this section, we explore the effects of canyon geometry on the barotropic pressure field, the horizontal velocity field, and the vertical velocity field. The latter quantity is of particular interest, since the barotropic dissipation

$$D\left(\mathbf{x},t\right) \approx \hat{W}_0\left(\mathbf{x},t\right)\, \hat{P}_1\left(\mathbf{x},t\right), \tag{6.13}$$

is proportional to the vertical velocity at the sea floor. Baroclinic pressure in the bottom layer, $\hat{P}_1$, is not considered in this chapter. Ultimately, the barotropic vertical velocity along the sea floor may allow us to quantify the effects of canyon geometry on internal-tide generation and the implied radiating energy flux.

6.4.1 Effects of Domain Size and Polynomial Order

The solutions of Figures 6.10 and 6.11 were just for motivation. Before further analysis, we must configure both the computational domain and the polynomial order. It is important that a sufficiently large domain is chosen such that the choice of boundary along which the background flow is imposed has no effect on the flow in and around the canyon. To reduce computational cost, we wish to have as few degrees of freedom as possible by minimising the computational domain and the polynomial order.

To test the effects of both domain width and polynomial order, we shall consider the largest possible canyon under investigation. The canyon will have a maximum width of 20 km at the shelf break, and span almost the entirety of shelf and slope. This corresponds to model parameters $\alpha = 0.98$ and $\beta = 1$ ($\alpha = 1$ is not recommended since the imposition of no-normal flow along the coastline assumes that the bathymetric gradient is zero along

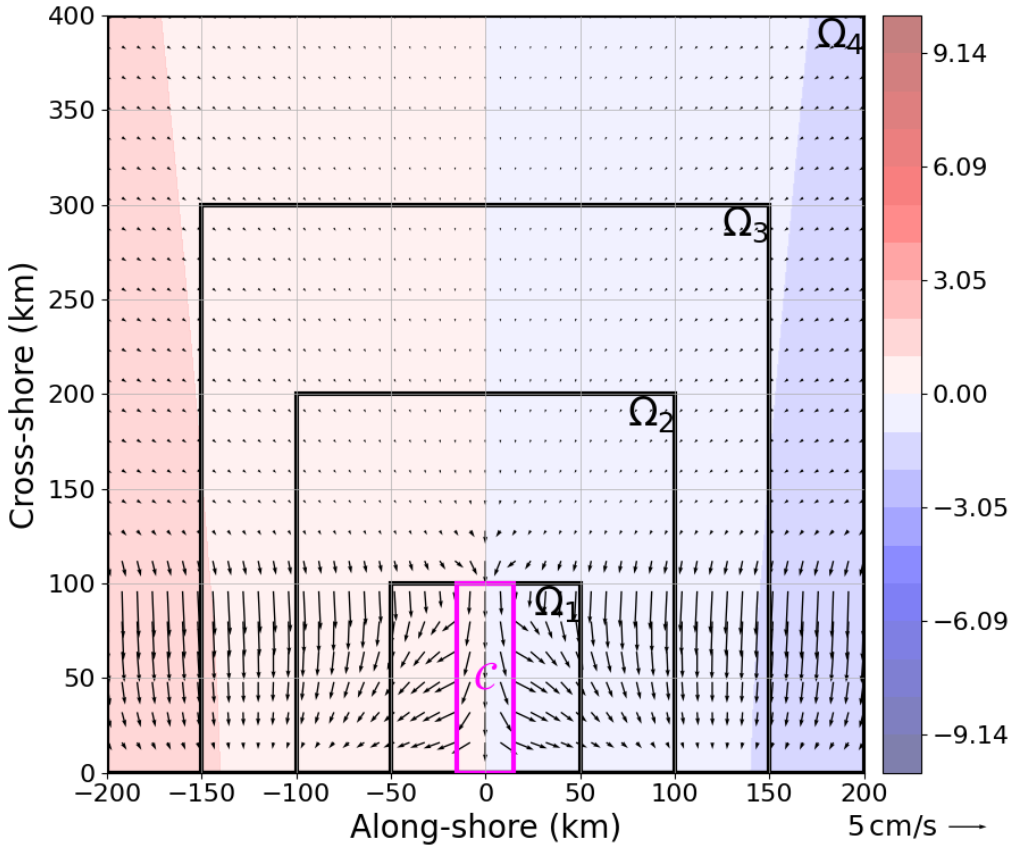

Figure 6.13: DG-FEM vector velocity field (cm/s) and pressure contours (kPa) for barotropic tide of semi-diurnal frequency around a large canyon at mid-latitude using a central numerical flux and polynomial order $p = 4$. Overlaid is a schematic showing computational domains Ω_1, Ω_2, Ω_3 and Ω_4, and curve $\mathcal{C}$ used for understanding convergence under domain size and polynomial order.

the boundary). For a shelf width of 100 km, a slope width of 50 km, a shelf depth of 200 m and a deep ocean depth of 4,000 m, the chosen canyon parameters imply a canyon length of ~ 150 km and a canyon termination depth of $\sim 4,000$ m, and is shown in Figure 6.12.

We argue that this largest possible canyon has the largest remote effect. If a sufficiently large domain is chosen under which the barotropic solution in and around the canyon has sufficiently converged, then it should be the case, assuming meshes of the same quality are used, for all canyon geometries.

To show the convergence under both computational domain and polynomial order, we consider the barotropic horizontal velocity profile along some curve $\mathcal{C}$. This curve $\mathcal{C}$ should be defined along aspects most crucial to internal-tide generation: the solution across the shelf beyond the side walls of the canyon, and along the shelf break itself. For computational domain, we will consider four possible domains $\Omega_i = [-L_i/2, L_i/2] \times [0, L_i]$ for domain length scales $L = \{100\,\text{km}, 200\,\text{km}, 300\,\text{km}, 400\,\text{km}\}$ with index notation i and canyon centred at $x = 0$ km. Both the computational domains and curve $\mathcal{C}$ can be seen in Figure 6.13, along with the DG-FEM numerical solution (central numerical flux and polynomial order $p = 4$) for a barotropic tide of semi-diurnal frequency around a large canyon at mid-latitude in

the form of a perturbed Kelvin wave.

In Figure 6.14, we show the horizontal velocity profiles for increasing domain size and polynomial order along curve $\mathcal{C}$. The distance along curve $\mathcal{C}$ begins at shore on the left-hand side and moves off-shore beyond the shelf break. The curve then moves rightwards, and travels back to the shoreline on the right-hand side. It is immediately obvious from the analysis that domain Ω_1 is not suitable since the domain size does not capture the sloping topography (hence the near horizontal lines as curve $\mathcal{C}$ moves along the shelf break). Moreover, for the meshes we are using, a local test function below order $p = 3$ is insufficient as kinks are clearly visible along $\mathcal{C}$ as it approaches the shelf break.

In terms of domain size, a suitable choice would quite clearly be domain Ω_3. However, if our goal is to sweep parameter space, such a large computational domain would be expensive. Indeed, a more convenient choice would be domain Ω_2. The domain choice would see a maximum relative error along C of around 10%. However, it is a small price to pay to efficiently investigate the impact of canyon topography on barotropic tidal flow. As for polynomial order, there is no visible difference between solutions at $p = 3$ and $p = 4$. Given additional computational time required by the latter, we take $p = 3$.

We conclude therefore that the domain $\Omega_2 = [-100\,\text{km}, 100\,\text{km}] \times [0\,\text{km}, 200\,\text{km}]$ with a polynomial order $p = 3$ is sufficient for understanding the local effects of canyon geometry on tidal flows along continental margins. By optimising both the computational domain and polynomial order, assuming meshes of equal quality, we are able to investigate a large number of the many possible canyon geometries our canyon-slope model permits at a fraction of the time it would take using more primitive computational methods, such as the finite-differences method.

6.4.2 Effects of Canyon Geometry on Pressure Field

The first quantity of interest that we will investigate is the pressure field. In terms of prescribing the background tidal motion, the boundary conditions are applied solely on the normal and tangential components of the horizontal velocity. So while the effects of the velocity field will be largely unchanged towards the boundary, the same cannot immediately be said for the pressure field.

To understand the effects of the canyon topography, we will be interested in the barotropic pressure field of the semi-diurnal tide in the form of a Kelvin wave. To measure the effect, we will consider the L^1- and L^∞-norms, defined in (5.75), of the pressure perturbation P_0 in the domain $[-15\,\text{km}, 15\,\text{km}] \times [0\,\text{km}, 160\,\text{km}]$ around the canyon, all while varying the parameters α, β and canyon width W which define the geometric properties of the shelf-incising canyon. In this case, the L^1-norm can be considered the mean absolute value of the pressure perturbation, and the L^∞-norm is the maximum absolute value. We use the L^1-norm as a measure of the global measure around the canyon, and the L^∞-norm as a measure of localised effects. To clarify, taking the norm of the pressure perturbation eliminates the effect of canyon geometry on tidal phase.

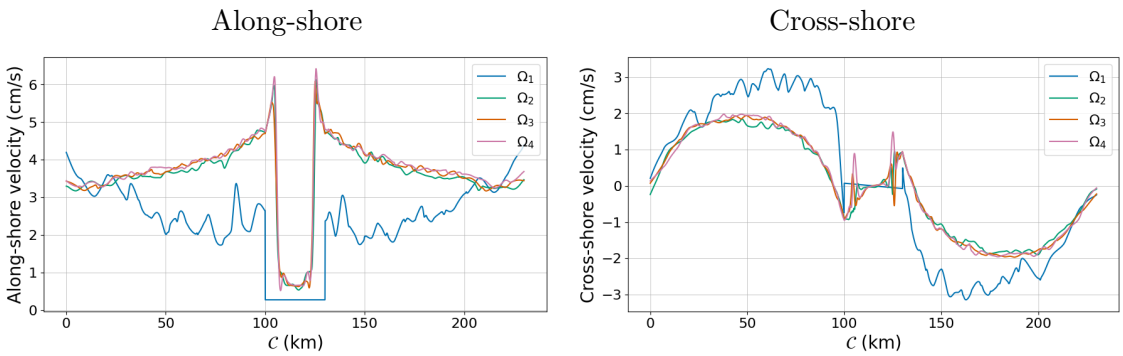

(a) $p = 1$

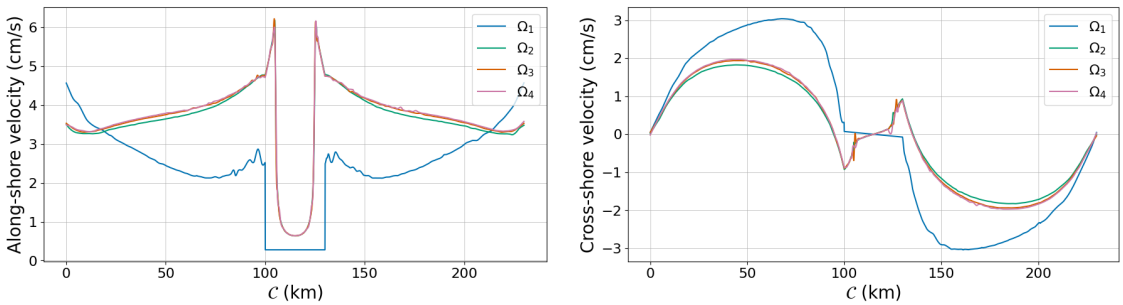

(b) $p = 2$

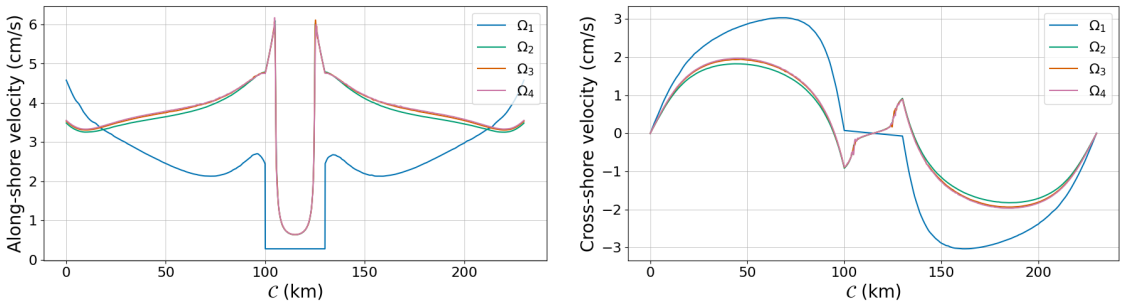

(c) $p = 3$

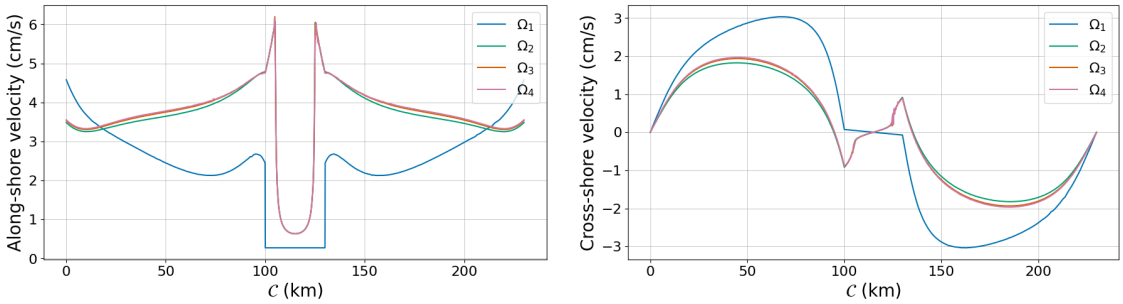

(d) $p = 4$

Figure 6.14: Along-shore (left) and cross-shore (right) velocity profiles (cm/s) along curve $\mathcal{C}$ while varying the computational domain over which the barotropic flow is solved (see Figure 6.13 for curve $\mathcal{C}$, along with domains Ω_1, Ω_2, Ω_3 and Ω_4). At the same time, polynomial order is increased: (a) $p = 1$; (b) $p = 2$; (c) $p = 3$; (d) $p = 4$.

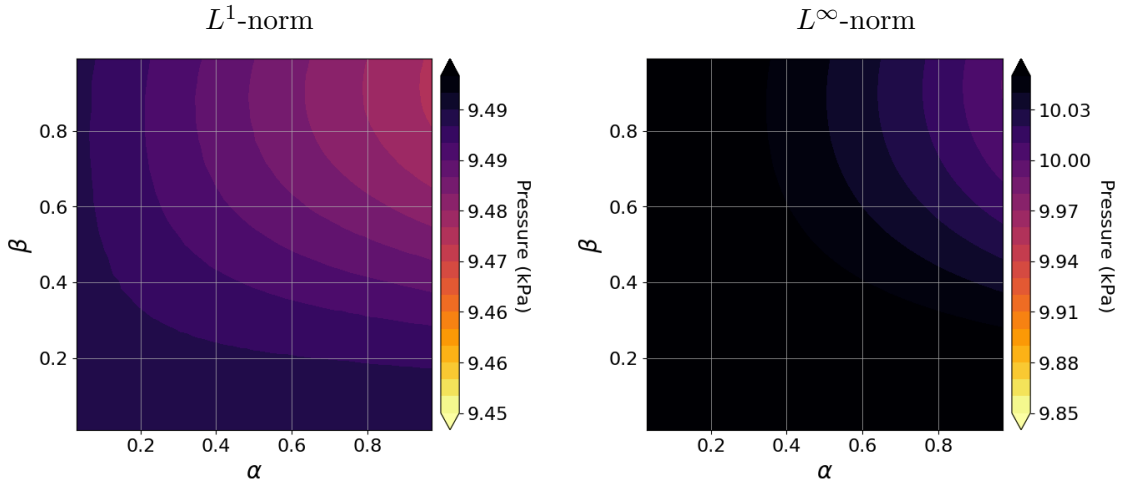

(a) 5 km

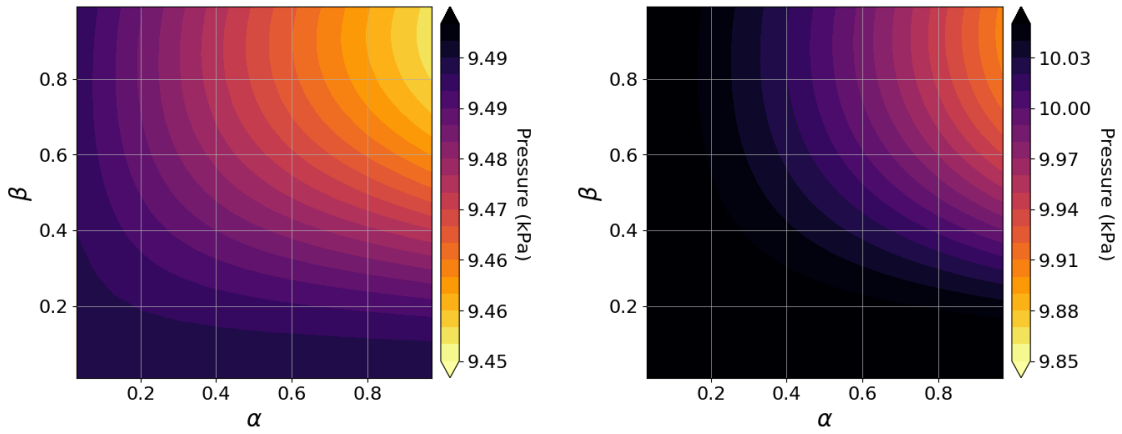

(b) 15 km

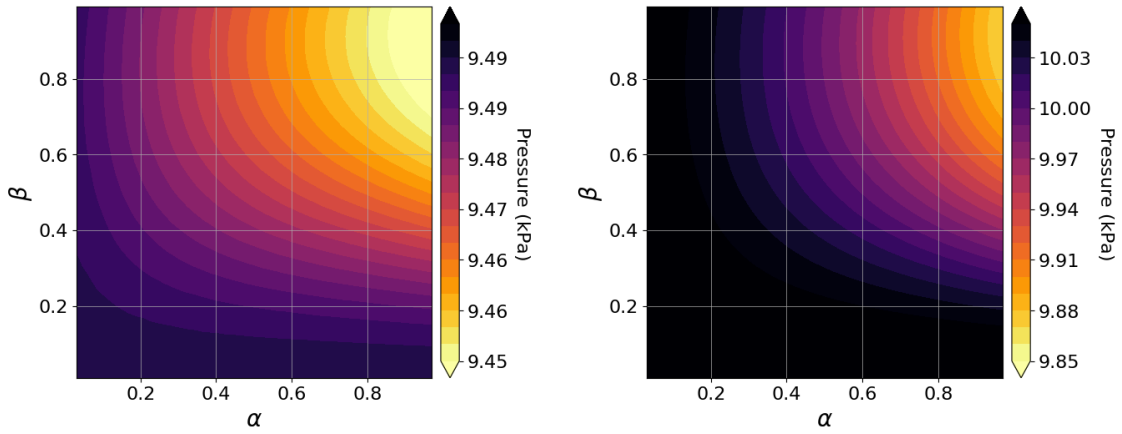

(c) 20 km

Figure 6.15: L^1- (left) and L^∞- (right) norms of barotropic pressure (kPa) in the domain $[-15\,\text{km}, 15\,\text{km}]\times[0\,\text{km}, 160\,\text{km}]$ while varying canyon parameters with fixed canyon width: (a) 5 km; (b) 15 km; (c) 20 km.

The parameter sweep of the pressure field is shown in Figure 6.15. Here, the L^1- (left) and L^∞- (right) norms are shown in α–β parameter space while varying canyon width: (a) 5 km; (b) 15 km; (c) 20 km. There are two key conclusions from this analysis. The first is that the effect of a canyon, both local and global, increases as canyon incision of the margin increases. This effect corresponds to a decrease in the pressure field. However, the second key conclusion is that the relative changes are at most 0.5% for the parameter space under investigation.

Some theoretical justification for this effect was given by Baines (1983). For a crude canyon model of width W in a channel of length L_x and a shelf of depth H_C, he showed that the presence of the canyon has very little effect on the pressure field of wave frequency ω in the parameter regimes whereby

$$\frac{W}{L_x} \ll 1 \qquad \text{and} \qquad \frac{\omega^2 W^2}{g H_C} \ll 1. \tag{6.14}$$

Since the domain size is somewhat arbitrary, the principal restriction lies with the fact that $W^2 \ll g H_C/\omega^2$. For semi-diurnal tidal frequency $\omega = 1.4 \times 10^{-4}\,\mathrm{s}^{-1}$ and a coastal shelf depth of 200 m, we require a canyon shelf width $W \ll 316$ km. In our numerical experiments where canyon width, W, is at most 20 km for $L_x = 200$ km, $\omega = 1.4 \times 10^{-4}\,\mathrm{s}^{-1}$ and $H_C = 200$ m, we have that

$$\frac{W}{L_x} \leq 0.1 \qquad \text{and} \qquad \frac{\omega^2 W^2}{g H_C} \leq 4 \times 10^{-3}. \tag{6.15}$$

Since the presence of a canyon has little effect on the pressure field, any resulting flow will be induced by the background pressure field, which will then be topographically steered. That is to say, one could consider to leading order a pressure field unchanged and solve for a solution of the horizontal velocity in and around the canyon which approaches the solution of the perturbed Kelvin wave away in the far field.

6.4.3 Effects of Canyon Geometry on Horizontal Velocity Field

Having determined that the pressure field remains largely unchanged for the canyon configurations considered, we now consider the effects of canyon geometry on the horizontal velocity field $\mathbf{U}_0(\mathbf{x}, t)$. Since $\mathbf{U}_0$ is prescribed along the domain boundaries, we expect the greatest differences in $\mathbf{U}_0$ to lie away from the domain boundaries, where the solution in the far field is assumed to be the same.

To understand the effects of canyon topography, we consider once again the L^1- and L^∞-norms of the horizontal velocities in the domain $[-15\,\mathrm{km}, 15\,\mathrm{km}] \times [0\,\mathrm{km}, 160\,\mathrm{km}]$ around the canyon. The latter is carried out while varying the parameters α, β and canyon width W which define the geometric properties of the shelf-incising canyon. To motivate this study, we show in Figure 6.16 the horizontal flow of the barotropic solution with and without a shelf-incising submarine canyon, and at two different phases. Here, the canyon has $\alpha = 0.35$, $\beta = 0.5$ and $W = 15$ km. Physically, the canyon has a termination depth of

2,100 m and a length of 60 km.

It appears that the greatest effect of a canyon on the horizontal velocity field is best observed at a phase of $\pi/2$ in our study (see Figure 6.16b). Instead of the flow going up the slope and onto the shelf, the flow is steered by the canyon geometry, and enters the shelf over the side walls of the canyon. Since we have shown that the presence of a canyon has very little effect on the pressure field (at most 0.5%), it can be assumed that any variations of the horizontal velocity field inside and around the canyon is driven by the external pressure field. As a result, the along-shore and cross-shore flows along the side walls of the canyon are now in phase, which will almost certainly lead to greater vertical velocities in and around the canyon.

Shown in Figures 6.17–6.18 are the L^1- and L^∞-norms of the modulus of complex horizontal velocity fields $|U_0|$ (along-shore) and $|V_0|$ (cross-shore) in the domain $[-15\,\text{km}, 15\,\text{km}] \times [0\,\text{km}, 160\,\text{km}]$ around the canyon. Here, we again show α–β parameter space with fixed canyon widths: (a) 5 km; (b) 15 km; (c) 20 km. We recall that the L^1-norm represents the average magnitude and can therefore be considered a global representation of the flow speeds. On the other hand, the L^∞-norm is the global maximum magnitude and is not at all representative of the flow speeds throughout the entire domain over which the norm is taken. In addition, the greater the disparity between these two norms, the more localised the L^∞-norm actually is at characterising the flow speeds.

Recall that the case of no canyon is retrieved in the limits $\beta \to 0$ and $W \to 0\,\text{km}$. Indeed, for $\beta \ll 1$, the norms are independent of α for all values of canyon width W shown. The latter is more evident for the cross-shore flow, shown in Figure 6.18. In which case, the L^1-norm of the along-shore velocity is $\sim 3.15\,\text{cm/s}$ and L^∞-norm is $\sim 5.25\,\text{cm/s}$. On the other hand, the L^1-norm of the cross-shore velocity is $\sim 2.6\,\text{cm/s}$ and L^∞-norm is $\sim 6\,\text{cm/s}$.

The effects of canyon geometry on the along-shore flow, shown in Figure 6.17, are quite complex. For small canyon widths (e.g. Figure 6.17a for canyon width $W = 5\,\text{km}$), the presence of a canyon leads to an increase in the average along-shore speed, while the maximum speed observed decreases. From the latter, it can be deduced that the along-shore speeds become more uniform. However, increasing the canyon width to $W = 15\,\text{km}$ (Figure 6.17b) results in a slightly different behaviour which can be characterised by two regimes in α. In essence, the presence of a canyon ($\beta \not\ll 1$) whose head is positioned in close proximity to the shelf break ($0 < \alpha \ll 1$) leads to an increase in the average along-shore speed. Conversely, if the canyon head moves sufficiently beyond the shelf break with $\alpha, \beta \not\ll 1$, then the average along-shore speed will decrease. As for the maximum speed in the domain of interest, the presence of a canyon ($\alpha, \beta \not\ll 1$) initially leads to a decrease in the maximum along-shore speed. However, as the canyon foot moves beyond the mid-slope ($\beta > 0.5$), the maximum speed increases. As a result, the structure of the along-shore velocity becomes much more localised. The aforementioned effects of canyon depth and length are amplified when the canyon width is increased to $W = 20\,\text{km}$ (Figure 6.17c).

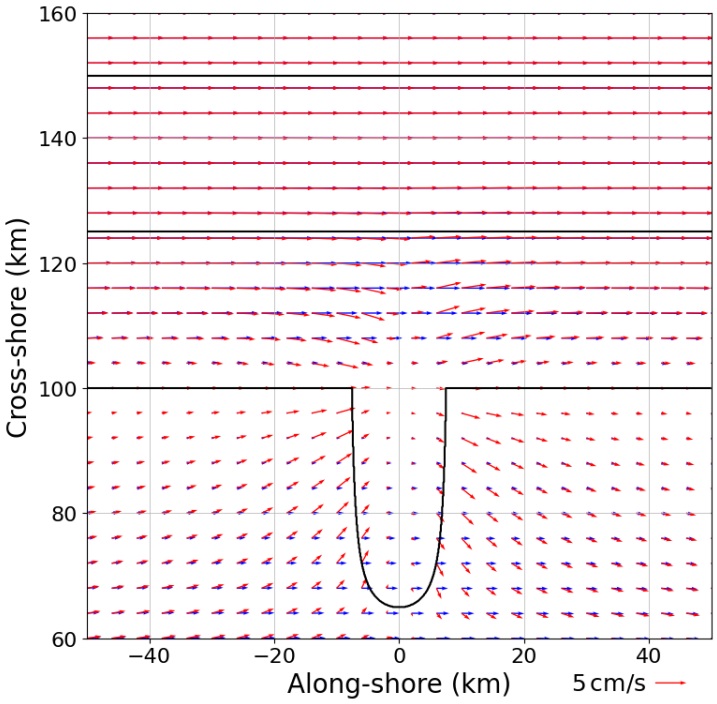

(a) $T = 0$

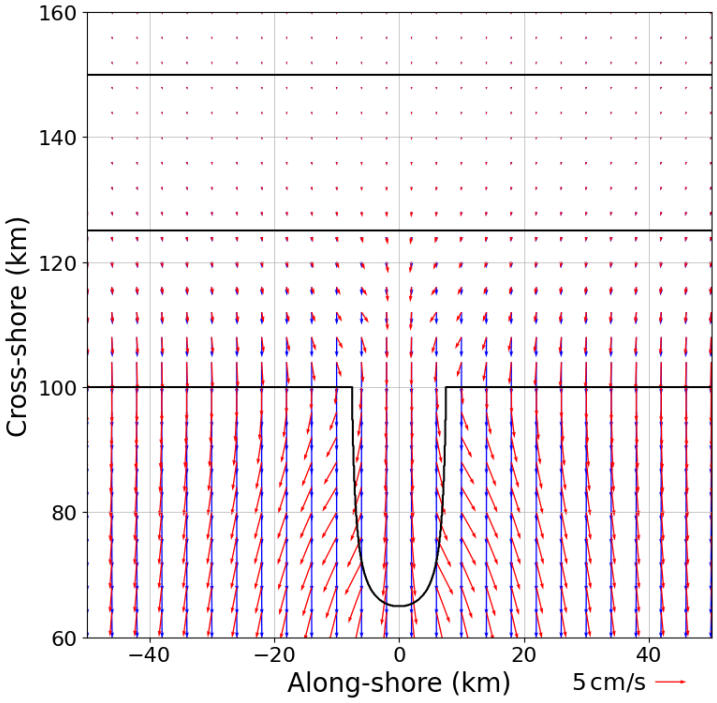

(b) $T = \pi/2\omega$

Figure 6.16: 15 km wide canyon: Velocity field comparison at different phases of the barotropic semi-diurnal tide at mid-latitude in the form of a perturbed Kelvin wave of surface amplitude ~ 1 m. The blue vector field shows the velocity field in the absence of the canyon, while the red vector field shows the velocity field in the presence of the canyon. The black contours show the bathymetric contours of the shelf, the canyon foot and the deep ocean (200 m, 2,000 m and 4,000 m respectively).

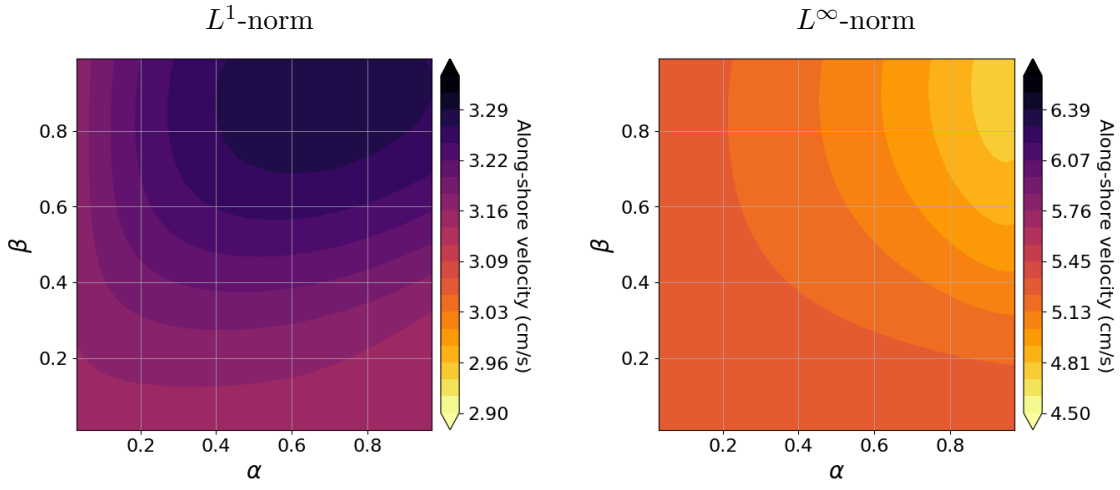

(a) 5 km

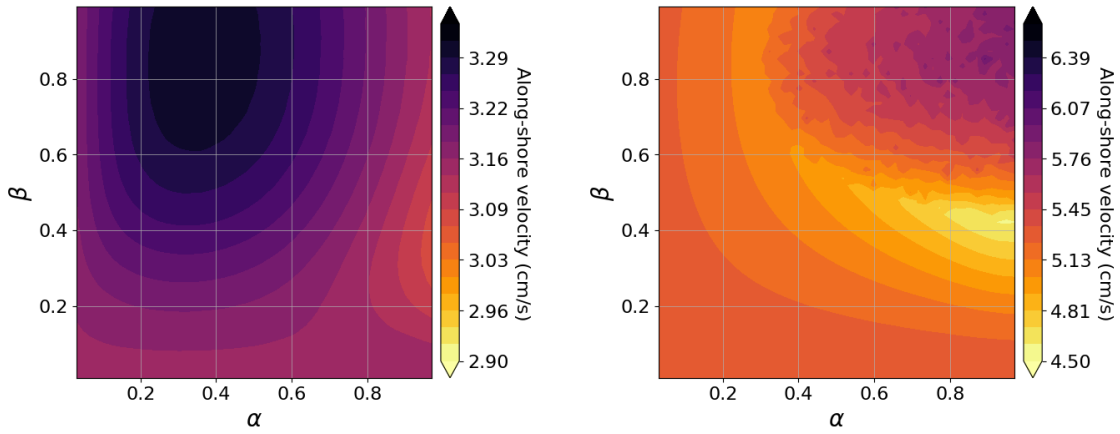

(b) 15 km

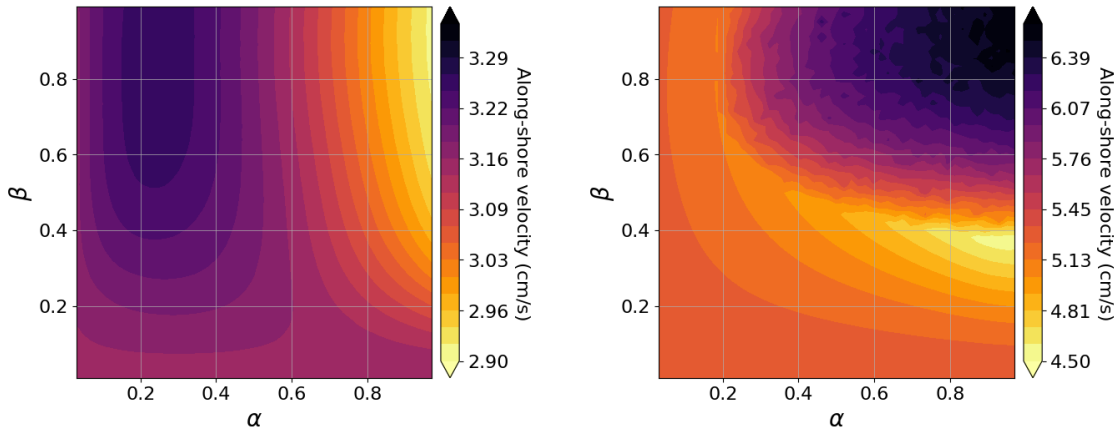

(c) 20 km

Figure 6.17: L^1- (left) and L^∞- (right) norms of along-shore velocity (cm/s) in the domain $[-15\,\text{km}, 15\,\text{km}]\times[0\,\text{km}, 160\,\text{km}]$ while varying canyon parameters with fixed canyon width: (a) 5 km; (b) 15 km; (c) 20 km.

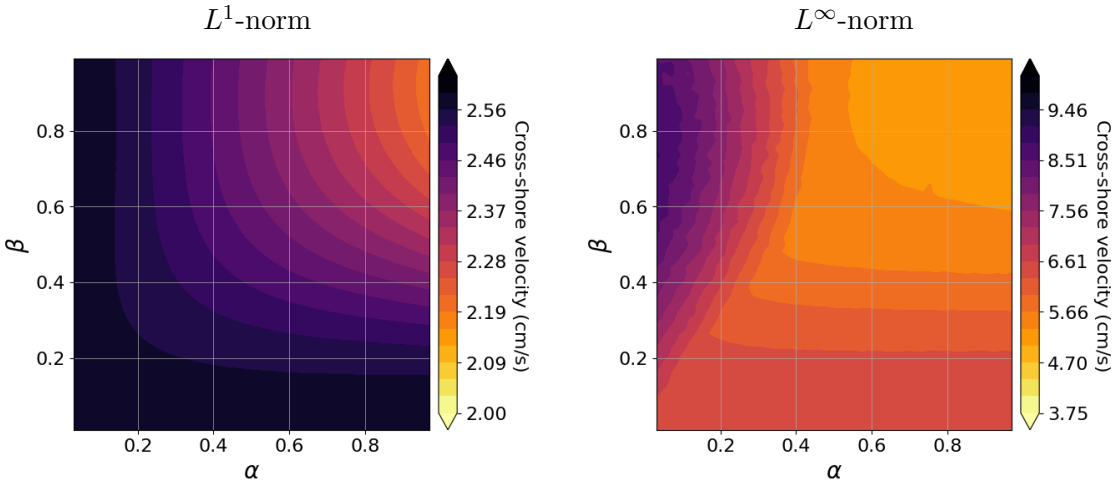

(a) 5 km

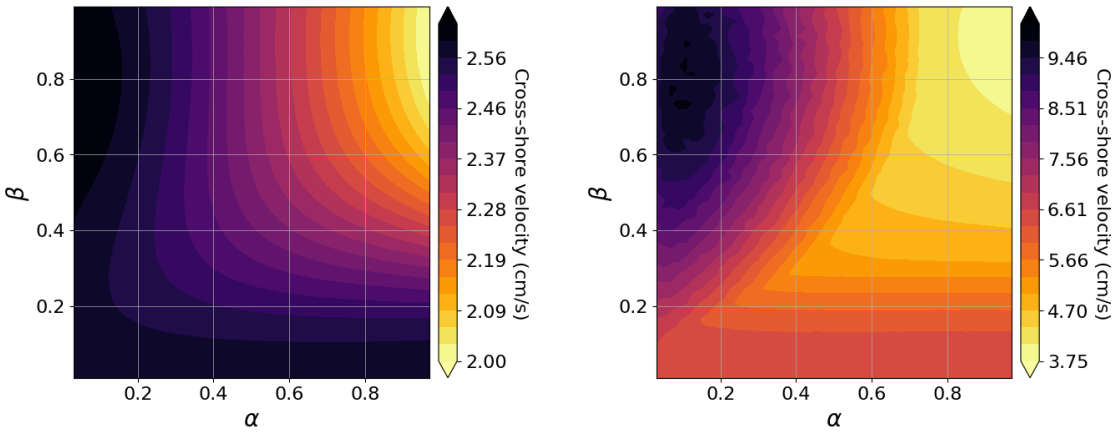

(b) 15 km

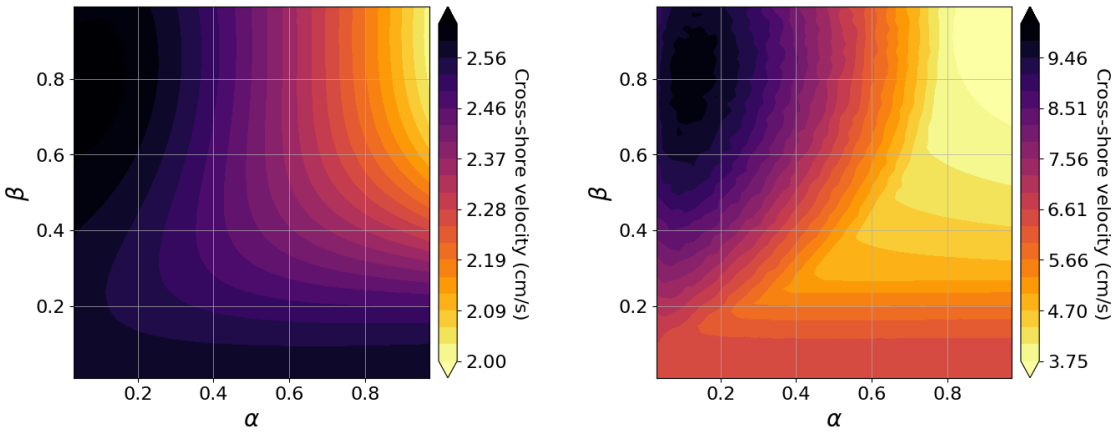

(c) 20 km

Figure 6.18: L^1- (left) and L^∞- (right) norms of barotropic cross-shore velocity (cm/s) in the domain $[-15\,\text{km}, 15\,\text{km}]\times[0\,\text{km}, 160\,\text{km}]$ while varying canyon parameters with fixed canyon width: (a) 5 km; (b) 15 km; (c) 20 km.

As for the cross-shore flow, shown in Figure 6.18, the behaviour is a little more straightforward, and can again be characterised by two regimes in α. For non-negligible canyon termination depths ($\beta \not\ll 1$) which are confined to the shelf break ($\alpha \ll 1$), the presence of a canyon leads to small increases in the average cross-shore speeds, and relative increases of two thirds for the maximum cross-shore speeds. For canyons which extend sufficiently far onto the shelf ($\alpha \not\ll 1$), a canyon reduces the average and maximum cross-shore speeds in and around the canyon. In other words, the presence of a canyon will only lead to significant cross-shore speeds when the canyon is confined to the shelf break, and that greater canyon incision of the margin does not immediately imply greater cross-shore speeds. By increasing canyon width, the effects of canyon depth and length are amplified, with the small-α regime extending further into α–β parameter space.

To summarise, the effect of canyon geometry on horizontal velocity is complex but can be simplified by considering two regimes for canyons of sufficient depth ($\beta \not\ll 1$): those confined to the shelf break and those which extend deep onto the shelf. For canyons which extend deep onto the shelf ($\alpha \not\ll 1$), the effect of parameter β on along-shore velocity depends greatly on canyon width. For small canyon widths, the average along-shore speed is increased, while the average along-shore speed is decreased for larger canyon widths. On the whole, the effect of a canyon for sufficiently large canyon widths sees enhanced localisation since there is a greater difference between the L^1- and L^∞-norms. However, the effect on cross-shore velocity appears considerably less dependent on canyon width. The presence of a canyon which extends deep onto the shelf leads to reduced cross-shore flows throughout the domain of interest. For canyons which are confined to the shelf break, the average cross-shore speed remains largely unchanged, but the maximum cross-shore speed significantly increases. As a consequence, the effect of a canyon confined to the shelf break, for non-zero canyon width, leads to local enhancements of cross-shore speeds. The latter is most likely a consequence of greater bathymetric gradients at the shelf break where the cross-shore velocity—corresponding to a $\sim 1\,\mathrm{m}$ amplitude semi-diurnal tide in the form of a Kelvin wave at mid-latitude—is greatest. From the analysis conducted, it can be expected that for canyons of sufficient depth ($\beta \not\ll 1$), any increase in vertical velocity along the sea floor is likely to be attributed to the cross-shore flow for canyons confined to the shelf break ($\alpha \ll 1 \neq 0$) and the along-shore flow for canyons which extend deep onto the shelf ($\alpha \not\ll 1$).

6.4.4 Effects of Canyon Geometry on Vertical Velocity Field

We also wish to understand the dependence of canyon geometry on the vertical velocity along the sea floor, as given by (6.12). As shown in equation (6.13), the barotropic dissipation rate is proportional to the vertical velocity. As a result, any increase, however localised around the canyon, could be of significance in the generation of internal tides.

From Section 6.4.3, any increase in vertical velocity is likely to be a result of the along-shore velocity for canyons extending deep onto the shelf (large α), and of the cross-shore velocity for canyons confined to the shelf break (small α). Of course, another important

factor is how the horizontal velocity components align with the topographic gradients. Nevertheless, the previous analysis on horizontal velocities was useful since it provided an early indication of the effects of canyon geometry on vertical velocity. Here, we plan to carry out the investigation on vertical velocity.

To conduct our investigation, we show in Figure 6.19 the L^1- and L^∞-norms of the vertical velocity field over the domain $[-15\,\text{km}, 15\,\text{km}] \times [0\,\text{km}, 160\,\text{km}]$ around the canyon. The norms of the vertical velocity are shown in α–β parameter space for canyon widths: (a) 5 km; (b) 15 km; (c) 20 km. Most importantly, Figure 6.19 verifies that the presence of a canyon, particularly for those extending deep onto the shelf, leads to greater vertical velocities. In the absence of a canyon, vertical flows of a Kelvin wave of amplitude 1 m along the shoreline do not exceed 0.2 cm/s along the slope. However, the presence of a 5 km wide canyon leads to vertical flows in excess of 6.5 cm/s along its side walls.

Unquestionably, the effect of canyon geometry on vertical velocity is most prominent in the regime $\alpha, \beta \ll 1$. Such canyons are greatest in length and could reasonably be used to model canyons which connect to river systems (type one canyons), e.g. Monterey canyon. In Figure 6.19, a maximum vertical flow speed of ~ 6.6 cm/s occurs for a canyon width of 5 km; as canyon width increases, the maximum vertical flow speed reduces to ~ 2.8 cm/s for a 20 km wide canyon. Conversely, the average vertical flow speed along the sea floor increases from 0.03 cm/s in the absence of a canyon and reaches around 0.17 cm/s for a 20 km wide canyon.

To summarise, the effect of canyon geometry on vertical flow speed along the sea floor is greatest for narrow, deep canyons which extend far onto the shelf. In particular, the presence of a narrow canyon leads to strong, localised vertical flow speeds. As canyon width increases, the maximum vertical flow speed decreases due to weaker bathymetric gradients in the cross-canyon direction. Conversely, the average vertical flow speed increases as the canyon incision of the margin increases due to strong along-shore flows on the shelf intercepted by the canyon topography.

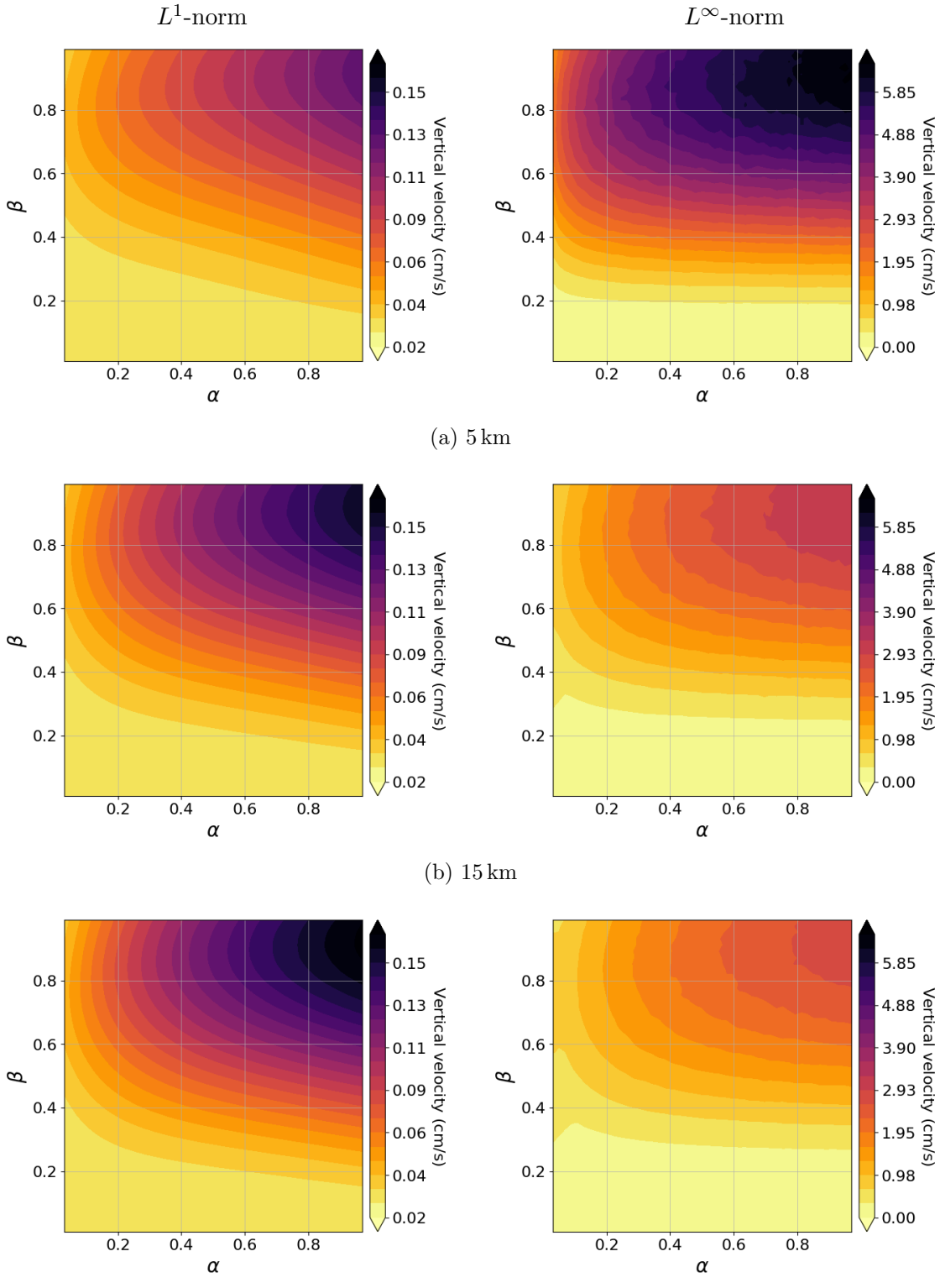

(a) 5 km

(b) 15 km

(c) 20 km

Figure 6.19: L^1- (left) and L^∞- (right) norms of vertical velocity at the sea floor (cm/s) in the domain $[-15\,\text{km}, 15\,\text{km}]\times[0\,\text{km}, 160\,\text{km}]$ while varying canyon parameters with fixed canyon width: (a) 5 km; (b) 15 km; (c) 20 km.

6.5 Summary

In this chapter, the effects of canyon geometry on the form of a surface tide were investigated, particularly with respect to the flow up and down the canyon and the implied vertical flow, because of the internal-tide generation problem. To simplify our work, we considered a surface tide in the form of a free Kelvin wave of semi-diurnal frequency at mid-latitude. We concluded in Chapter 3 that the existence of a Kelvin wave at all frequencies and the strong excitation of the mode for tidal ranges means that the surface tide can be modelled as a Kelvin wave. To resolve the barotropic flow in and around the canyon, an elliptic boundary-value problem of time-periodic flow is solved using discontinuous Galerkin finite element methodology (DG-FEM).

In Section 6.2, we developed a new simple model of an idealised canyon. In contrast to models used in previous studies (see Figure 6.2), this new model has both continuous fluid depth h and is localised. The canyon is defined by the three parameters α (proportion of shelf incised by canyon), β (proportion of slope incised by canyon) and W (maximum canyon width at shelf break); these will be central to the results presented in Chapter 7.

In Section 6.3, we look at the generation of high-quality triangular meshes using the Python package `OceanMesh`. In the previous chapter, it became apparent that uniform resolution would be inefficient to resolve the small-scale length scales introduced by canyons. By collaborating with the code developers, we were able to facilitate idealised mathematical modelling. This included the implementation of fixed points for maintaining vertex positions during the process of mesh generation (useful for rectangular domains), the MATLAB-to-Python translation of a slope-limiting edge function based on slope parameter $h/|\boldsymbol{\nabla} h|$, and the enabling of user-defined functions of fluid depth in lieu of digital elevation models (DEMs).

In Section 6.4, the localised effects of canyon geometry on the surface tide were investigated. Having configured the domain size and choice of polynomial order in Section 6.4.1, it was found in Section 6.4.2 that the presence of a shelf-incising canyon has very little effect on the pressure field, consistent with the theory of Baines (1983). As such, the flow in and around a canyon is topographically steered by the external pressure field. For horizontal and vertical flow fields in and around a canyon, discussed respectively in Sections 6.4.3 and 6.4.4, non-negligible effects of canyon geometry could be characterised by two regimes in α–β parameter space, consistent with type one and type two canyons of Harris and Whiteway (2011) (see Section 1.2.2 or 6.2).

For type one canyons (those connected to river systems which typically extend much further on the shelf), the introduction of a canyon leads to an increase in the average speed in the cross-shore direction for small canyon widths, but a decrease for larger canyon widths. However, for larger canyon widths, the maximum along-shore speed sees an increase of up to $\sim 30\,\%$. Consequently, the greater disparity between the L^1- and L^∞-norms suggests that the along-shore velocity field becomes increasingly localised around the canyon. Conversely, the introduction of a long shelf-incising canyon leads to a reduction in both the L^1-

and L^∞-norms of cross-shore velocity. For the average cross-shore speed, this reduction is around 20%, while around 33% for the maximum. Moreover, type one canyons seem to be much more efficient at producing increased vertical velocities along the sea floor. This is because the long canyons, whose side walls introduce significant along-shore variation in topography, extend further onto the shelf and are able to intercept the strong along-shore flows in the shoreline.

For type two canyons (those confined to the shelf break), the introduction of a canyon sees an increase of $\sim 4.8\%$ in average along-shore flow speeds in and around the canyon, while the maximum flow speed only changes once canyon width exceeds 10 km. On the other hand, the effect on cross-shore velocity is more striking. The average cross-shore flow speed sees a modest increase of at most 2.4%, but the maximum almost doubles from $\sim 6.5\,\mathrm{cm/s}$ in the absence of a canyon to $\sim 10.0\,\mathrm{cm/s}$ for a 20 km wide canyon. Consequently, the effect of a canyon sees localised regions of intense cross-shore velocity where the side walls of the canyon intercept the shelf break. For vertical velocity, it was found that the effect of type two canyons is so localised that the effects appear negligible.

In conclusion, it is hypothesised that the increased strength in vertical velocity which type one canyons produce should be more efficient generators of internal tides. In a similar fashion to step-like shelves leading to greater barotropic dissipation, it is reasonable to believe that the L^∞-norm of vertical velocity will be more indicative of barotropic dissipation. It is this hypothesis that we shall test in the next chapter.

Chapter 7

Internal-Tide Generation by Submarine Canyons

7.1 Introduction

The steep continental slopes that surround oceanic basins are natural sites for strong internal-tide generation; indeed, amongst all submarine topography, these are of the greatest vertical extent, rising from the deep ocean (of depth $\sim 4,000\,\mathrm{m}$) to the shallow continental shelves (of depth $\sim 200\,\mathrm{m}$). Numerous studies have built up a consistent picture of strong internal-tide generation at these slopes, both in the continuously stratified interior and at the sharp density jump of the pycnocline, with energy propagation both off-shore and on-shore, with the latter often in the form of internal solitary waves (e.g. Baines, 1973; R. Pingree & New, 1989; Holloway et al., 2001; Lien & Gregg, 2001; Griffiths & Grimshaw, 2007a).

Although the coastal surface tides that force these internal tides are energetic, the strongest barotropic flows are typically along-shore, with just a weaker barotropic flow cross-shore. We quantified this in Chapter 3, for the case when the surface tide is dominated by a Kelvin wave and estimated the implied internal tide energy fluxes generated by the cross-shore flow in Chapter 4. However, submarine canyons are ubiquitous along continental margins (see Harris & Whiteway, 2011; Harris et al., 2014), and one might expect these to give yet greater internal-tide generation (at least locally), as the (strong) barotropic along-shore flow must cut across these canyons, as modelled in Chapter 6. The aim of this chapter is to study the magnitude of this internal-tide generation in a two-layer fluid, when forced by an idealised surface tide of Kelvin-wave form moving across an idealised canyon.

In the oceanographic literature, many studies, both observational (e.g. Petruncio et al., 1998; Kunze et al., 2002; Johnston et al., 2011; Kunze et al., 2012) and numerical (e.g. Petruncio et al., 2002; Jachec et al., 2006; Wang et al., 2009; Kang & Fringer, 2012; Hall et al., 2014), have been conducted on internal-tide generation in the Monterey canyon

system (see Figure 6.1a). The Monterey canyon system is of particular scientific interest as it is one of the largest canyon systems off the west coast of the United States and is home to an abundance of marine life.

The first quantitative measurements of internal tides in the Monterey canyon system were made in 1994 during two "Internal Tide Experiments" (see Petruncio et al., 1998), and focused on the region between Gooseneck Meander and the canyon head. These experiments found that the nature of the internal tide would vary depending on the stratification brought about by seasonal variability. During Spring the internal tide was found to be progressive in nature, while in Autumn the internal tide became horizontally standing. These observations also revealed strong near-bottom tidal currents in excess of 20 cm/s and isopycnal displacements of ~ 50 m in the upper canyon. In addition, these tidal motions are largely attributed to the M2 tide. Many of these observations were later explored by numerical experiments in Rosenfeld et al. (1999), Petruncio et al. (2002) and Hall et al. (2014), amongst others.

Petruncio et al. (2002) conducted one of the very first idealised three-dimensional numerical studies of internal-tide generation and propagation by a straight canyon system. A total of six experiments (see Table 1 of the paper) were conducted using uniform stratification in a linear, hydrostatic, primitive equation Princeton Ocean Model (POM) (see Blumberg & Mellor, 1987). The study, which used a grid resolution of 1 km in the horizontal and 30 sigma layers in the vertical,[1] was instrumental in showing that internal tides are generated at critical topography, and that most of the energy generated propagates into the canyon itself. Interestingly, Petruncio et al. (2002) were unable to reproduce the same magnitude of flow speeds observed in the field experiments of Petruncio et al. (1998). Petruncio et al. (2002) suggests that this may be due to a number of reasons, including the idealised canyon-slope topography, the use of a single tidal constituent (M2), as well as the lack of along-shore flow used to model the barotropic flow.

In a bid to improve the numerical findings of Rosenfeld et al. (1999) and Petruncio et al. (2002), Jachec et al. (2006) employed the Stanford Unstructured Nonhydrostatic Terrain-following Adaptive Navier–Stokes Simulator (SUNTANS) (see Fringer et al., 2006) to show that higher spatial resolution is required to capture the energy fluxes within a complex canyon system. Indeed, Jachec et al. (2006) successfully reproduced observations of Petruncio et al. (1998). Furthermore, Jachec et al. (2006) were able to locate the main semi-diurnal source of internal-tide generation towards the south of the bay, in the Sur Platform region. Hall and Carter (2011) and Kang and Fringer (2012) obtained similar results. However, results of Jachec et al. (2006) show an energy surplus of 52 MW across the domain of interest, but particular bathymetric features including the Sur Platform region are net dissipative.

More recent work by Zhang et al. (2014) considered the influence of idealised canyon-shelf geometry (see Figure 6.2e) on supercritical internal-tide generation along the Mid-Atlantic

[1] Sigma layers are used in a sigma-coordinate model, where the vertical coordinate follows the terrain and fixes the number of vertical grid points everywhere in space.

Bight (off the coast of New York). They studied the dynamics of asymmetrical internal-tide generation in shelf-break canyons and the resultant on-shore beam radiation seen in observations (e.g. Jackson, 2004; Duda et al., 2013) and numerical experiments (e.g. Carter, 2010; Rainville et al., 2010). Zhang et al. (2014) conducts a series of 13 non-linear simulations (as shown in Table 1 of the paper) using the hydrostatic Regional Ocean Modelling System (ROMS) (see Shchepetkin & McWilliams, 2005) by means of an initial-value problem. An observed stratification profile (according to a summertime climate) is used, along with periodic boundary conditions in the along-shore spatial direction, a 600 km wide sponge layer off-shore, a 10 m high coastal boundary, and a quadratic bottom drag with drag coefficient $C_d = 3\times10^{-3}$. To identify the source of the on-shore asymmetric horizontal beams, the results of the ROMS simulations are compared to a semi-analytical linear model forced with the barotropic source obtained from the ROMS simulations. Zhang et al. (2014) concludes that the localised enhancement upwave (upstream is the term used in the paper) is linked to the phase of the source term, predominantly determined by the "local steepest bathymetric ascent", matching the spatial phase gradient of the freely propagating internal wave. As a result, propagating waves reinforce the generation process (a variation on this for shoaling internal waves is investigated in Kelly & Nash, 2010).

Whilst these previous studies have illuminated the nature of internal-tide generation at shelf-incising canyons to some extent, the 13 simulations of Zhang et al. (2014) are the closest we have to a systematic study. However, given that they consider seven different canyon widths (5 km–70 km) and five different canyon lengths (5 km–20 km) in various combinations, it is clear that even their 13 simulations are only a beginning, from which it would be hard to draw robust conclusions about the dependence of baroclinic energy fluxes, say, upon canyon geometry.

In contrast, in this chapter we will present the results of $\sim 10,000$ linear simulations of internal-tide generation above idealised canyons by an idealised barotropic tide (which takes the form of a Kelvin wave perturbed by the canyon, as developed in Chapter 6). Our simulations will consider variations in canyon length (0 km–150 km), canyon width (5 km–20 km), and the extent to which the canyon sits upon both the shelf and slope (as measured by the parameters α and β of Chapter 6). We then ask

1. How do the amplitude and direction of radiating energy fluxes depend upon canyon geometry?

2. By how much do canyons enhance the tidal dissipation (or, equivalently, the radiating baroclinic energy fluxes), if at all?

To achieve a parameter sweep of such a large extent, some compromises must be made in the modelling. We compromise by assuming (i) linear internal-tide dynamics, (ii) a two-layer fluid (rather than a continuously stratified fluid, as in Zhang et al. (2014), say). This leads us to the two-layer model derived in Section 2.4.8. Even with such a simplified system, the parameter sweep will only be possible with high-efficiency numerics. The small

length scales of the canyon are accurately and efficiently resolved using the discontinuous Galerkin finite element methodology (DG-FEM) explored in Chapter 5 on high-quality triangular meshes generated using `OceanMesh`. The use of our idealised model, unlike typical ocean models, permits the exploration of parameter space from which more robust conclusions may be drawn.

We start, in Section 7.2, by giving further details of the numerical model, focusing on the issue of how radiating internal waves are permitted via sponge layers. In Section 7.3, we give a first look at internal-tide generation in our model at some typical canyon parameters, showing baroclinic pressure, baroclinic energy flux, and tidal dissipation. We present results of the main parameter sweep in Section 7.4, focusing on the magnitude and direction of the baroclinic energy fluxes. In Section 7.5, we consider to what extent these energy fluxes are dependent upon the modification of the barotropic Kelvin wave by the canyon, before concluding in Section 7.6.

The code used for this chapter requires Python packages:

- `ppp` - see Appendix B.1.
- `DGFEM` - see Appendix B.2.
- `barotropicSWEs` - see Appendix B.3.
- `baroclinicSWEs` - see Appendix B.4.

Further package dependencies and file structure of aforementioned Python packages are discussed in Appendix B.

7.2 Numerical Model

7.2.1 Equations of Motion

Using the form of the surface tide found in Chapter 6, we force a radiating baroclinic response of semi-diurnal tidal frequency, ω. The equations of motion for the baroclinic mode, given by (2.207)–(2.208), are

$$-i\,\omega\,\mathbf{U}_1 + f\,\hat{\mathbf{e}}_z \times \mathbf{U}_1 + \boldsymbol{\nabla} P_1 = -\mathcal{T}_{10}\,\boldsymbol{\nabla} h\,(\mathbf{x})\; P_0, \tag{7.1}$$

$$-i\,\omega\,P_1 + \boldsymbol{\nabla}\cdot\left(c_1^2\,(\mathbf{x})\;\mathbf{U}_1\right) = -\mathcal{T}_{10}\,\boldsymbol{\nabla} h\,(\mathbf{x})\cdot\left(c_0^2\,\mathbf{U}_0\,(\mathbf{x})\right), \tag{7.2}$$

where $\mathbf{U}_1$ and P_1 denote the baroclinic horizontal velocity and pressure. The barotropic and baroclinic modal wave speeds are

$$c_0^2 \approx g\,h \qquad \text{and} \qquad c_1^2 \approx \frac{g'\,h_1\,(h-h_1)}{h}, \tag{7.3}$$

with total fluid depth h, upper-layer depth h_1 taken constant and gravitational acceleration $g = 9.81\,\mathrm{m/s^2}$. Furthermore, modal variables are normalised such that modal-interaction

coefficients $\mathcal{T}_{mn} = -\mathcal{T}_{nm}$ and $\mathcal{T}_{mm} = 0$. In our two-layer model, we consider only

$$\mathcal{T}_{10} = \frac{\sqrt{\partial_h \left(c_0^2\right) \, \partial_h \left(c_1^2\right)}}{c_1^2 - c_0^2} \frac{h_1}{h^2} \sqrt{\varepsilon} \left(1 + O\left(\sqrt{\varepsilon}\right)\right), \tag{7.4}$$

where stratification parameter $\varepsilon \equiv (\rho_2 - \rho_1)/\rho_2$ denotes the relative density difference at the interface of the two layers.

In addition, we have using equation (2.186) that for time-periodic flows, the barotropic dissipation due to the generation of internal waves along the pycnocline over some region Ω with boundary $\partial\Omega$ is approximately

$$\int_{\partial\Omega} \frac{h\,(h - h_1)}{h_1} \langle \hat{P}_1 \, \hat{\mathbf{U}}_1 \rangle \, \mathrm{d}\partial\Omega = -\int_{\Omega} \langle \hat{W}_0 \, \hat{P}_1 \rangle \, \mathrm{d}\Omega. \tag{7.5}$$

We recall that $\hat{W}_0$, $\hat{\mathbf{U}}_1$, $\hat{P}_1$ denote respectively the bottom-layer variables of barotropic vertical velocity, baroclinic horizontal velocity and baroclinic pressure.

7.2.2 Open Boundary Conditions

Internal tides typically propagate away from their generation site, and do not return to it following reflection from a remote feature. A prime example is wave breaking due to shoaling as the internal tide approaches the shoreline. At the same time, we want to calculate the energy transfer from the surface tide to the generated internal waves. In two spatial dimensions, the calculation of the latter requires greater attention than that which was given in Chapter 4. For example, we are required to extend the domain to negative cross-shore coordinates to account for sufficient damping without reflection along the coast, as shown in Figure 7.1.

There are two principal means of imposing an open-ocean boundary conditions: (a) the use of radiation/characteristic boundary conditions; (b) the use of an absorbing/sponge layer. The method of characteristics, similar to the approach considered in Chapter 4, was first considered by Flather (1976). This method seeks to prevent outgoing waves from reflecting off the computational boundary by imposing a travelling-wave solution with known characteristics. However, as Lavelle and Thacker (2008) remarks, "dispersive waves approaching the boundary from a non-normal direction can be a problem." In essence, the second method involving the use of a sponge layer allows perturbations to propagate out of a region of interest into an exterior zone. In this exterior zone, it is then allowed to dissipate before reflecting off the boundaries of the computational domain. This method is generally much easier to implement since, as Bodony (2006) explains, it typically requires the addition of a term

$$-\sigma \left(q - q_{ref}\right), \tag{7.6}$$

where σ is the absorption coefficient and q_{ref} is the exterior solution to state variable q.

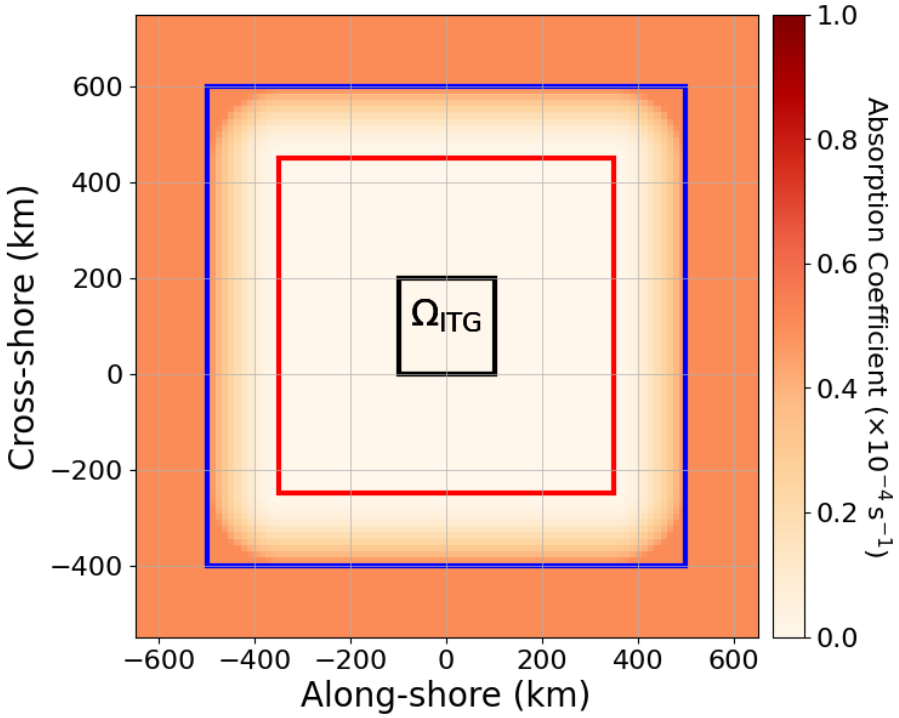

Figure 7.1: Simple sponge layer typically used to impose radiating open boundary conditions. Domain of interest is contained within the black box, while the undamped region is contained within the red box. The undamped region which excludes the region of interest is the domain padding. Between the red and the blue boxes is the transition region, where the sponge layer transitions from zero to a maximum absorption coefficient value of $5 \times 10^{-5}\,\mathrm{s}^{-1}$. Beyond the blue box, the damping is maximal over some sponge-layer thickness. Here, solutions are damped before being able to reflect off the computational boundary and re-enter the undamped region.

Our governing equations (7.1)–(7.2) would thus be adapted to the governing equations

$$-i\,\omega\,\mathbf{U}_1 + f\,\hat{\mathbf{e}}_z \times \mathbf{U}_1 + \boldsymbol{\nabla} P_1 = -\mathcal{T}_{10}\,\boldsymbol{\nabla} h\,(\mathbf{x})\; P_0 - \sigma\,(\mathbf{x})\;\mathbf{U}_1, \tag{7.7}$$

$$-i\,\omega\,P_1 + \boldsymbol{\nabla}\cdot\left(c_1^2\,(\mathbf{x})\;\mathbf{U}_1\right) = -\mathcal{T}_{10}\,\boldsymbol{\nabla} h\,(\mathbf{x})\cdot\left(c_0^2\,\mathbf{U}_0\,(\mathbf{x})\right) - \sigma\,(\mathbf{x})\;P_1, \tag{7.8}$$

where the absorption coefficient $\sigma\,(\mathbf{x})$ is applied to all baroclinic variables (see Martinsen & Engedahl, 1987).

To estimate the magnitude of the absorbing coefficient within the sponge layer, σ_{max}, we note that the disturbance will be damped like $\exp\left(-\sigma_{max}\,t\right)$. The time it takes for the wave to travel through the sponge layer, reflect off the boundary of the computational domain and propagate back out, assuming a layer size of L, will be $\tau = 2 \times L/c_1$ for baroclinic wave speed c_1. For example, if the baroclinic wave speed is $\sim 3\,\mathrm{m/s}$ and the sponge layer is of thickness 100 km, in order to dampen by a factor of 100, we seek σ_{max} such that $0.01 = \exp\left(-\sigma_{max}\,\tau\right)$. The latter implies an absorption coefficient of $\sigma_{max} \approx 7 \times 10^{-5}\,\mathrm{s}^{-1}$. Typically however, there is a transition layer of thickness d over which the amplitude of the wave begins to decay anyway, so it is possible to use a slightly lower coefficient, e.g. $\sigma_{max} \approx 5 \times 10^{-5}\,\mathrm{s}^{-1}$. An example of this simple sponge layer is shown in Figure 7.1,

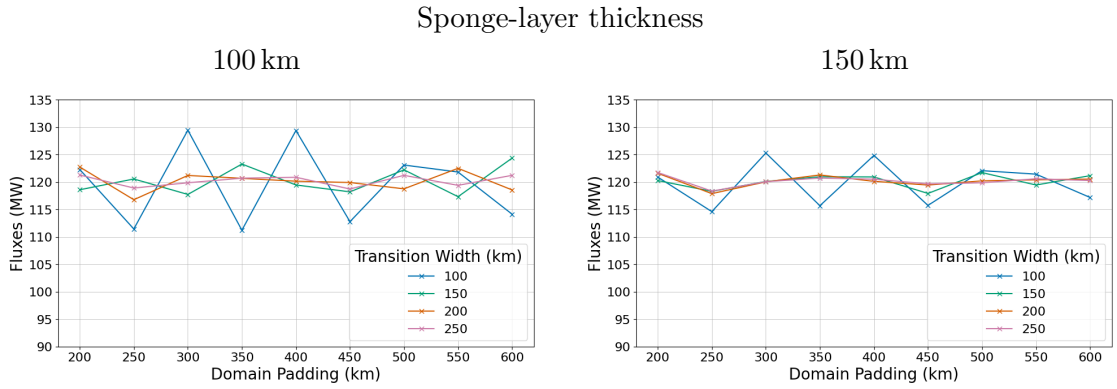

(a) Slope topography

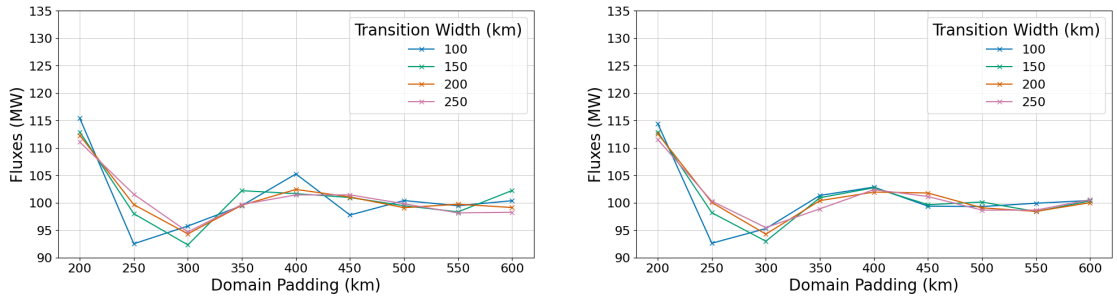

(b) Canyon-slope topography

Figure 7.2: Total energy flux integrated along the boundary of a 200 km × 200 km coastal domain for polynomial order $p = 3$ and a central numerical flux while varying the width of domain padding and the width of the sponge in the case of: (a) slope topography; (b) canyon-slope topography. On the left, a sponge-layer thickness of 100 km is used, while 150 km is used on the right.

where domain of interest is $\Omega_1 = [-100\,\text{km}, 100\,\text{km}] \times [0\,\text{km}, 200\,\text{km}]$, padded domain width $L_{ext} = 300\,\text{km}$, transition layer width $D = 200\,\text{km}$ over which absorption coefficient transitions from zero to $\sigma_{max} = 5 \times 10^{-5}\,\text{s}^{-1}$, and sponge-layer thickness $L = 100\,\text{km}$ is the minimum distance a wave travels through maximum absorption before encountering the boundary of the computational domain.

A more sophisticated approach, is the imposition of a perfectly matched sponge layer, as seen in Hu (2008). The imposition of a perfectly matched layer requires an auxiliary field to prevent outgoing waves from reflecting at the computational boundary. A much simpler approach proposed by Lavelle and Thacker (2008) builds on Hu (2008), but sets the auxiliary fields to zero. The resulting equations lead to a "pretty good" sponge:

$$-i\,\omega\,U_1 - f\,V_1 + \partial_x P_1 = -\mathcal{T}_{10}\,\partial_x h\,(\mathbf{x})\;P_0 - \sigma_x\,(\mathbf{x})\;U_1, \tag{7.9}$$

$$f\,U_1 - i\,\omega\,V_1 + \partial_y P_1 = -\mathcal{T}_{10}\,\partial_y h\,(\mathbf{x})\;P_0 - \sigma_y\,(\mathbf{x})\;V_1, \tag{7.10}$$

$$-i\,\omega\,P_1 + \boldsymbol{\nabla}\cdot\left(c_1^2\,(\mathbf{x})\;\mathbf{U}_1\right) = -\mathcal{T}_{10}\,\boldsymbol{\nabla} h\,(\mathbf{x})\cdot\left(c_0^2\,\mathbf{U}_0\,(\mathbf{x})\right) - \left(\sigma_x\,(\mathbf{x}) + \sigma_y\,(\mathbf{x})\right) P_1. \tag{7.11}$$

To apply the "pretty good" sponge, we are in need of five elements:

- The size of the undamped domain. We want the undamped domain to be as small as

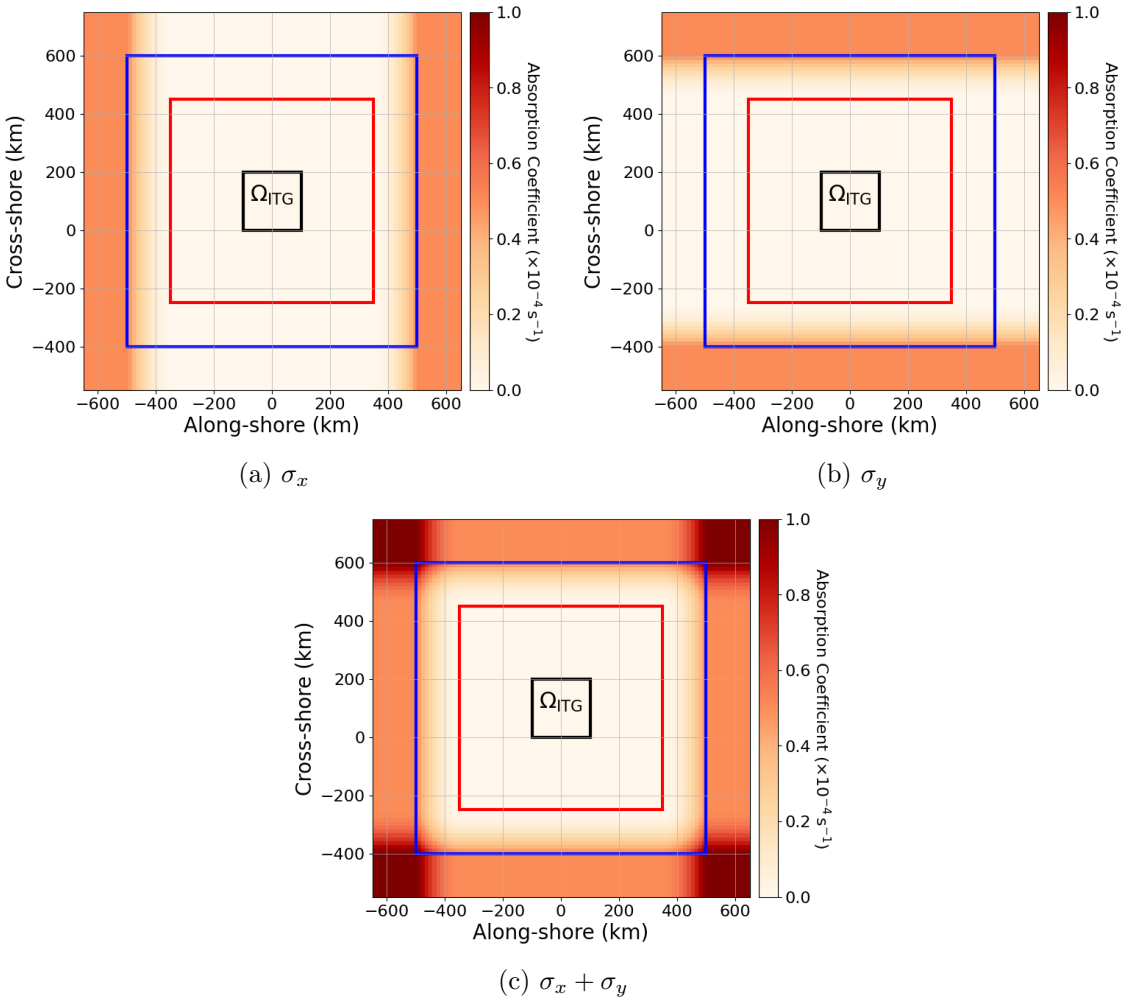

(a) σ_x

(b) σ_y

(c) $\sigma_x + \sigma_y$

Figure 7.3: A "pretty good" sponge layer after configuration according to Figure 7.2. Sponge fields, with a maximum absorption coefficient $\sigma_{max} = 5 \times 10^{-5}\,\mathrm{s}^{-1}$, are applied to time evolution equation of baroclinic: (a) along-shore velocity; (b) cross-shore velocity; (c) pressure. Region enclosed by red box sees no damping.

possible to reduce the number of unknowns for which we solve, but if the undamped region is too small, the effect of the sponge layer will be visible in the smaller computational domain (Ω_{ITG} in Figures 7.1 and 7.3).

- The transition thickness, over which the sponge layer is turned on. We want this as small as possible to reduce the number of unknowns for which we solve, but if the transition layer is too thin, the incident internal waves will reflect and not be absorbed.

- The form of the transition layer. We consider the same function as in Lavelle and Thacker (2008): $\sigma_{max}\,(d/D)^2$, where d is the distance within the sponge transition layer and D is the transition layer thickness.

- The thickness of the sponge layer which lies between the transition layer and the boundary of our computational domain. If the sponge layer thickness is too small, the amplitude of incident internal waves will not have decayed by the time they have

reflected off the computational domain and re-entered the undamped domain.

- The absorption coefficient σ_{max}. If the coefficient is too small, the amplitude of incident internal waves will not have decayed before re-entering the undamped domain, but too large and internal waves will reflect off the sponge layer itself. For our needs as argued above, we chose an absorption coefficient of $\sigma_{max} = 5 \times 10^{-5}\,\mathrm{s}^{-1}$.

In Figure 7.2, the sponge layer used in future simulations is configured using DG-FEM numerics on meshes generated using `OceanMesh` using a central numerical flux and a polynomial order $p = 3$. Here, we measure the total energy flux of the baroclinic response of a $\sim 1\,\mathrm{m}$ semi-diurnal surface tide at mid-latitude in the form of a Kelvin wave while varying sponge layer thickness, undamped domain padding width and the width of the transition layer width for the two extreme cases of: (a) slope topography (without a canyon); (b) a 20 km wide canyon which fills the shelf and slope ($\alpha = 0.98$ and $\beta = 1$). This radiating energy flux is integrated along the boundaries of a 200 km square coastal domain centred around a canyon. Our goal here is to minimise the size of the computational domain, and therefore number of unknowns and size of matrix system, while ensuring that the implied total time-averaged baroclinic energy flux has converged.

From Figure 7.2, we see that a sponge-layer thickness of 150 km leads to less variation between the implied time-averaged tidal dissipation rates in both the slope topography and canyon-slope topography cases. We also conclude that for a sponge-layer thickness of 150 km, the resultant energy fluxes of a sponge layer with a transition width of 150 km performs just as well as one with a transition width of 200 km or 250 km. With respect to domain padding width, we find that beyond 300 km, the implied tidal dissipation varies by no more than 5%. We choose therefore a "pretty good" sponge with a thickness of 150 km, a transition width of 150 km and a domain padding thickness of 350 km. The result is the sponge layer shown in Figure 7.3.

To observe the effect of the configured "pretty good" sponge on the computed baroclinic response of the surface tide, Figure 7.4 shows the near-field and far-field baroclinic response in the upper and lower layers radiating from a 15 km wide canyon which occupies 20% of the shelf and 80% of the slope ($\alpha = 0.2$ and $\beta = 0.8$). To recall, the surface tide takes the form of a free Kelvin wave of semi-diurnal frequency at mid-latitude with an amplitude of $\sim 1\,\mathrm{m}$ at the shoreline. The contour plot, viewed from above with the shoreline at 0 km in the cross-shore spatial coordinate, shows the modal pressure (Pa), while the quiver plot shows the corresponding horizontal velocity field (see 5 cm/s key). The result is the generation of internal waves which radiate away from the canyon-slope topography. The baroclinic flow in the lower layer appears strongest at the head of the canyon at $\sim 15\,\mathrm{cm/s}$. These internal waves are allowed to propagate into the sponge layer, where their amplitude is subsequently damped and not able to re-enter the undamped region. We also highlight that while we are computing the solution over the domain shown in Figure 7.4a, we are only interested in the solution shown in Figure 7.4b to calculate the implied time-averaged radiating energy fluxes.

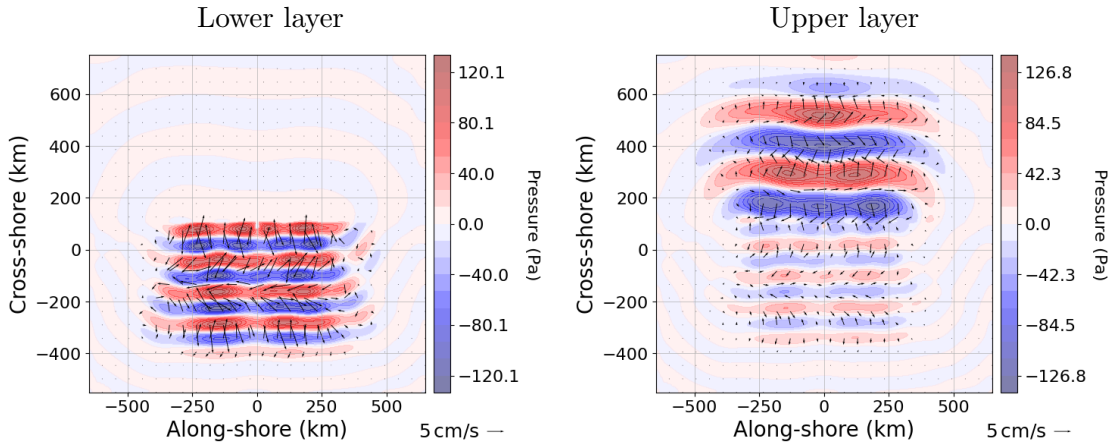

(a) $1,300\,\text{km} \times 1,300\,\text{km}$ computational domain

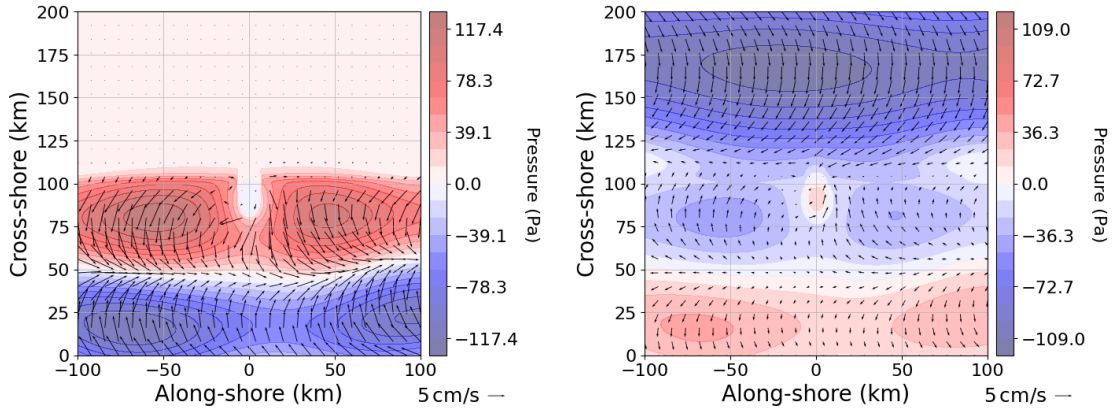

(b) $200\,\text{km} \times 200\,\text{km}$ coastal domain

Figure 7.4: Effect of a configured "pretty good" sponge layer on baroclinic response in and around an idealised shelf-incising canyon of width 15 km (with $\alpha = 0.2$ and $\beta = 0.5$) over the domain: (a) $1,300\,\text{km} \times 1,300\,\text{km}$; (b) $200\,\text{km} \times 200\,\text{km}$. To highlight, (b) is a zoomed-in version of (a). On the right, the internal-tide response of a semi-diurnal Kelvin wave at mid-latitude in the lower layer is shown, while on the left that of the upper layer.

7.3 Solution Structure and On-Shore Beams

Having configured the sponge layer to ensure a radiating baroclinic response, we are now able to investigate the effect of canyon-slope topography on internal-tide generation. The results shown are calculated using DG-FEM numerics with a central numerical flux and a polynomial order $p = 3$. Again, we emphasise that the form of the surface tide resembles a free Kelvin wave of semi-diurnal frequency at mid-latitude with amplitude 1 m at the shoreline. Assuming time-periodic solutions, the far-field solution of the Kelvin wave is known and solved for using the shooting method, and then the flow in and around the canyon is solved for using DG-FEM numerics (see Section 6.4). In this section, we shall keep the canyon width fixed at 15 km (around the mean canyon width) and investigate the effects of canyon occupation of the shelf and slope on the baroclinic response and the implied time-averaged radiating energy fluxes and tidal dissipation (using equation (7.5)).

To qualitatively investigate the effects of canyon geometry on internal-tide generation,

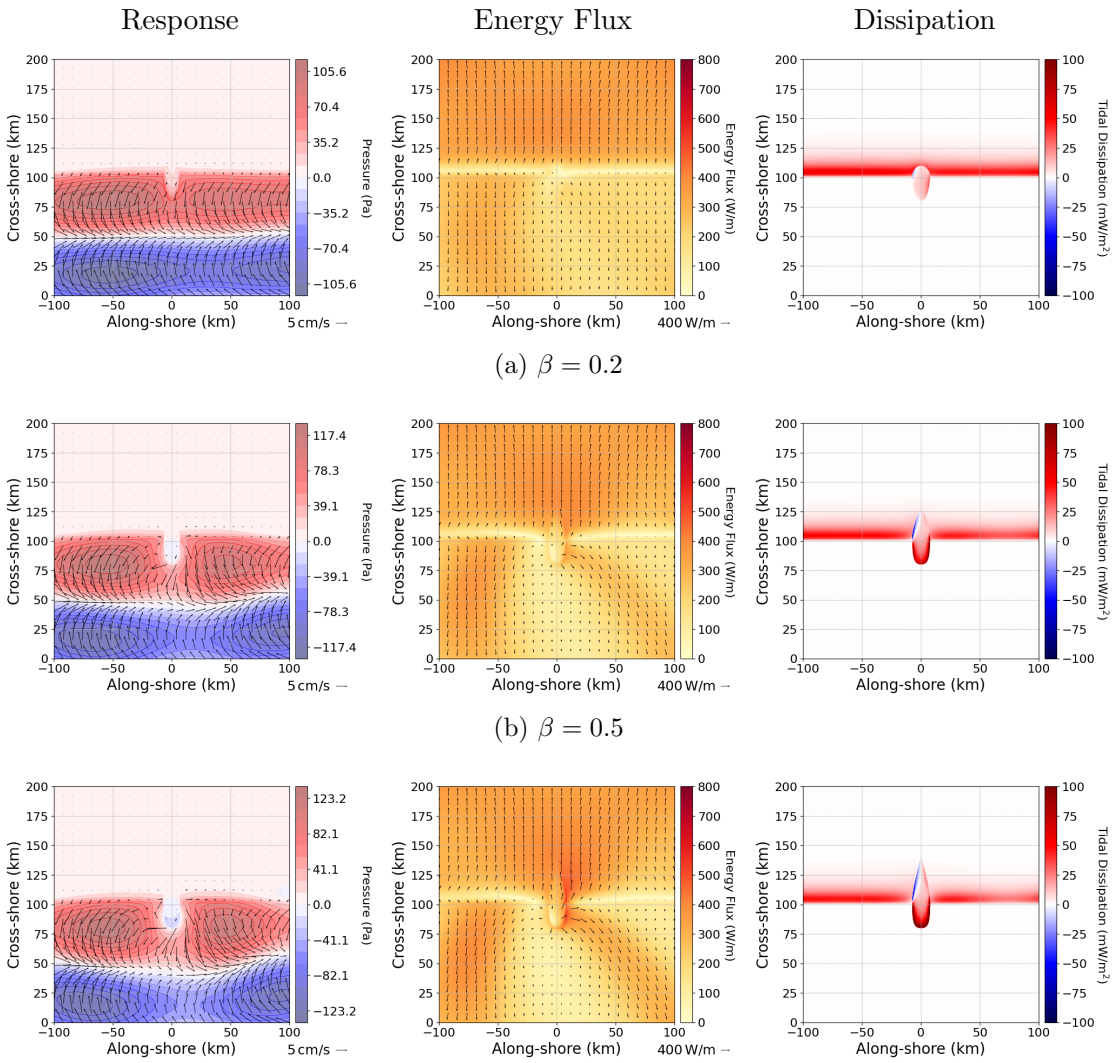

(a) $\beta = 0.2$

(b) $\beta = 0.5$

(c) $\beta = 0.8$

Figure 7.5: Internal-tide generation by canyons confined to the shelf break ($\alpha = 0.2$): bottom-layer baroclinic response in and around a 15 km wide canyon of a semi-diurnal surface tide in the form of a Kelvin wave at mid-latitude, and of amplitude ~ 1 m at the shoreline. Here, we show the effect of canyon depth on the baroclinic response (left), the implied time-averaged energy flux (middle), and the time-averaged barotropic tidal dissipation (right) by varying proportion of canyon on the continental slope with: (a) $\beta = 0.2$; (b) $\beta = 0.5$; (c) $\beta = 0.8$.

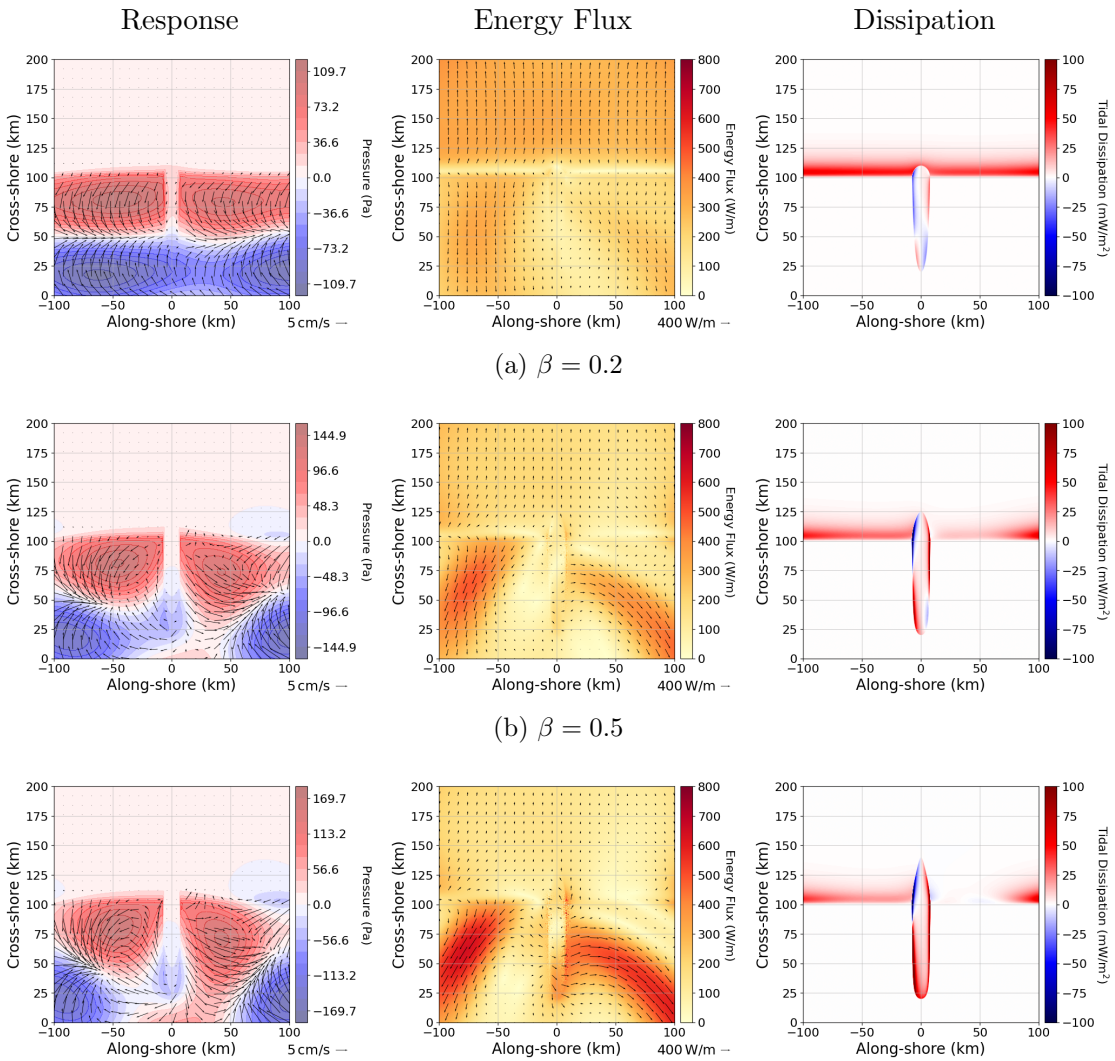

(a) $\beta = 0.2$

(b) $\beta = 0.5$

(c) $\beta = 0.8$

Figure 7.6: Internal-tide generation by canyons which extend far onto the continental shelf ($\alpha = 0.8$): bottom-layer baroclinic response in and around a 15 km wide canyon of a semi-diurnal surface tide in the form of a Kelvin wave at mid-latitude, and of amplitude ~ 1 m at the shoreline. Here, we show the effect of canyon depth on the baroclinic response (left), the implied time-averaged energy flux (middle), and the time-averaged barotropic tidal dissipation (right) by varying proportion of canyon on the continental slope with: (a) $\beta = 0.2$; (b) $\beta = 0.5$; (c) $\beta = 0.8$.

we show in Figures 7.5 (at $\alpha = 0.2$) and 7.6 (at $\alpha = 0.8$) the baroclinic solution in the bottom layer (left), the direction and magnitude of the implied time-averaged energy fluxes (centre), as well as the barotropic tidal dissipation (right). The regions of red on the tidal dissipation figures show the sources of the baroclinic energy flux, while the regions of blue show the sinks of baroclinic energy flux. From the data presented in both figures, as established in equation (2.211) of Section 2.4.8, it is possible to calculate the rate of tidal dissipation due to internal-tide generation. However, it is only from the baroclinic energy flux that the direction of the energy—whether shoreward, oceanward, leftward or rightward—can be deduced. Another benefit of the baroclinic energy flux is that one need only perform a 1D line integral, as opposed to a 2D surface integral, in order to calculate the rate of barotropic tidal dissipation. As previously stated, however, the dissipation figures do indicate the regions of enhanced dissipation, whether positive or negative. For example, we see from Figures 7.5 and 7.6 that the magnitude of the tidal dissipation is considerably higher along the flanks of deep canyons ($\beta \ll 1$) than the continental slope.

To investigate the qualitative effects of canyon geometry on internal-tide generation, we consider two different classifications of canyons: canyons confined to the shelf break (for which $\alpha = 0.2$) in Figure 7.5, and canyons which extend deep onto the continental shelf ($\alpha = 0.8$) in Figure 7.6. In each case, we show the effect on internal-tide generation of increasing the proportion of the slope occupied by the canyon, β.

Starting with Figure 7.5, Figure 7.5a shows that a shallow canyon confined to a shelf break leads to no obvious effect in the baroclinic response apart from the trace of the canyon as fluid depth increases. Indeed, the introduction of a canyon has led to more spatial variation in the baroclinic solution, however, the implied radiating energy fluxes remain, so far at least, largely uniform over the shelf and in the deep ocean. It is also just possible to see the emergence of a baroclinic sink, located on the left flank of the canyon along the continental slope. When considering internal-tide generation along continental slopes, we had only experienced a positive dissipation of the barotropic tide. However, as Figure 4 of Hall and Carter (2011) illustrates, positive and negative tidal dissipation can be observed along canyon side walls. In Hall and Carter (2011), this was said to be due to a phase difference in the internal tides generated remotely and locally. However, our study involves only local generation.

Increasing the proportion of the slope occupied by the canyon to $\beta = 0.5$, Figure 7.5b shows an increase in modal amplitude, particularly in the emergence of packets which emanate from the side walls of the canyon. This leads to the appearance of asymmetric beams of energy flux and are a result of the negative dissipation on the left flank and strong positive dissipation on the right and towards the head of the canyon. This phenomenon is also observed in Petruncio et al. (2002). Of equal significance, Figures 3(b), 4(b), 4(e) and others of Zhang et al. (2014) show almost identical patterns of baroclinic energy flux as in Figure 7.5. So our two-layer model produces results that are consistent with the continuously stratified model of Zhang et al. (2014). It is noted that in Zhang et al. (2014), the first baroclinic mode accounted for $\sim 70\%$ of the total baroclinic energy flux.

Increasing parameter β to 0.8, Figure 7.6c shows that the on-shore beam-like structures are amplified. The result of increasing canyon depth leads to shadowing of baroclinic energy fluxes shoreward of the canyon head. The latter is despite strong amplification of tidal dissipation along the head of the canyon. However this local enhancement is countered by a negative dissipation on the left canyon flank where the canyon incises the slope.

Figure 7.6 concerns canyons which extend far onto the shelf ($\alpha = 0.8$). With a shallow canyon ($\beta = 0.2$), Figure 7.6a shows that negative tidal dissipation within the canyon is greater for a canyon which extends deep onto the shelf than one confined to the shelf break (Figure 7.5a). From the latter, one can expect a greater reduction in tidal dissipation as a result of increasing α. However, tidal dissipation alone cannot tell us where the internal energy fluxes are propagating. In fact, the energy flux field appears largely unchanged for a shallow canyon when increasing the proportion of the shelf occupied by the canyon.

Increasing the canyon depth further by considering $\beta = 0.5$, Figure 7.6b shows that positive tidal dissipation appears more widespread within the canyon. However, there is a visible reduction in tidal dissipation on the slope to the right of the canyon as a result of making the canyon deeper. Near-bottom flow speeds appear strongest on the shelf beyond the walls of the canyon on the shelf at $\sim 10\,\mathrm{cm/s}$. As well as being visibly asymmetric, the observed beams of energy flux are considerably greater in amplitude than those generated by canyons confined to a shelf break (Figure 7.5b with $\alpha = 0.2$ and $\beta = 0.5$). These beams, although localised, are significant as they offer a potential source of instability and mixing. In the most extreme case shown with $\alpha = \beta = 0.8$, a large proportion of the canyon flanks are sites of strong tidal dissipation. However, the presence of a deep canyon appears to reduce tidal dissipation across the slope right of the canyon. What is difficult to say without quantitative measurements, is whether an increase in canyon depth leads to a net increase in tidal dissipation.

7.4 Parameter Sweep

To assess quantitatively how canyon geometry affects the dissipation of a three-dimensional surface tide in the form of a Kelvin wave of semi-diurnal frequency at mid-latitude, we span parameter space while measuring the implied time-averaged energy fluxes of the baroclinic response. Using around 10,000 simulations of different canyon-slope geometries, we show the effect of a shelf-incising canyon on the magnitude and direction of baroclinic energy fluxes using DG-FEM numerics. The numerics used in this section have a local test function order $p = 3$ (piece-wise cubic) with a central numerical flux[1] using high-quality meshes generated using the Python package `OceanMesh` in solving the decoupled barotropic and baroclinic modal equations.

Our results are shown graphically in Figures 7.7–7.11. To perform these parameters sweeps, the HPC facilities at the University of Leeds across ~ 40 cores were used over

[1]The choice of numeric flux, we recall from Section 5.4.2, is not only sparse, but conserves energy and allows discontinuities in topography.

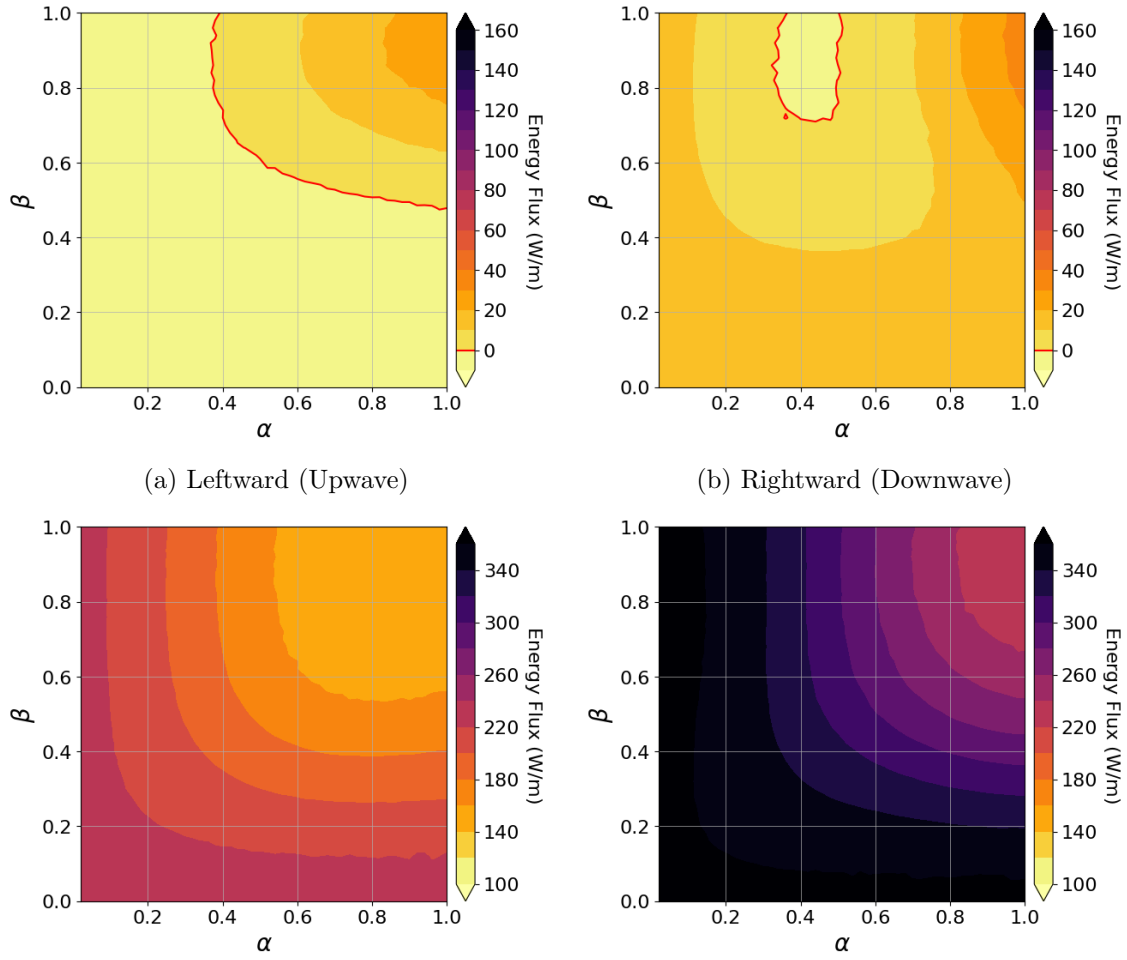

(a) Leftward (Upwave)

(b) Rightward (Downwave)

(c) Shoreward

(d) Oceanward

Figure 7.7: Implied time-averaged energy fluxes of baroclinic response from a 5 km wide canyon. Contours of time-averaged baroclinic energy fluxes radiating from 200 km × 200 km coastal domain around an idealised shelf-incising canyon are shown while varying proportion of canyon on shelf, α, and proportion of canyon on slope, β. From a surface tide in the form of a free Kelvin wave of semi-diurnal frequency at mid-latitude with an amplitude of ~ 1 m at the shoreline, we show the average energy flux radiating: (a) leftward (upwave); (b) rightward (downwave); (c) shoreward; (d) oceanward.

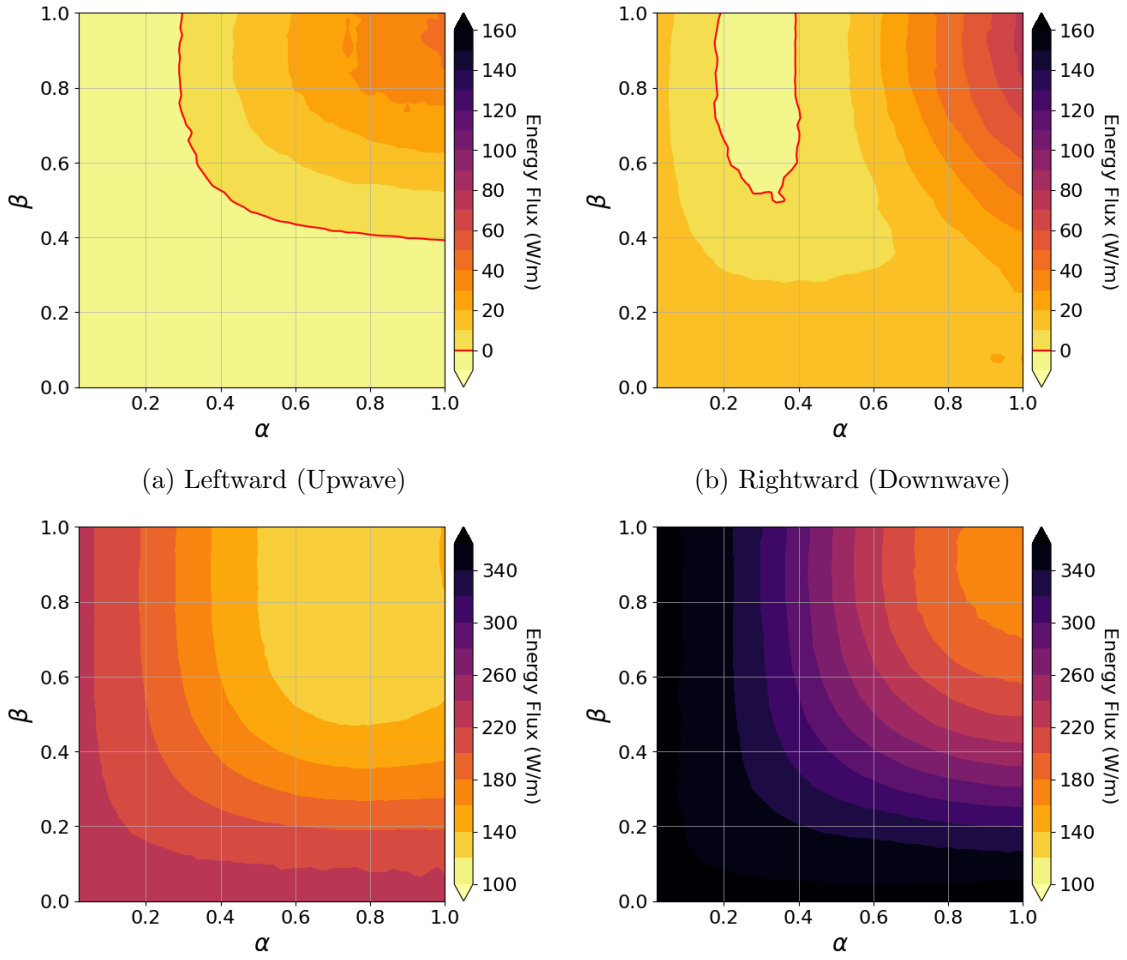

(a) Leftward (Upwave)

(b) Rightward (Downwave)

(c) Shoreward

(d) Oceanward

Figure 7.8: Implied time-averaged energy fluxes of baroclinic response from a 10 km wide canyon. Contours of time-averaged baroclinic energy fluxes radiating from 200 km × 200 km coastal domain around an idealised shelf-incising canyon are shown while varying proportion of canyon on shelf, α, and proportion of canyon on slope, β. From a surface tide in the form of a free Kelvin wave of semi-diurnal frequency at mid-latitude with an amplitude of ~ 1 m at the shoreline, we show the average energy flux radiating: (a) leftward (upwave); (b) rightward (downwave); (c) shoreward; (d) oceanward.

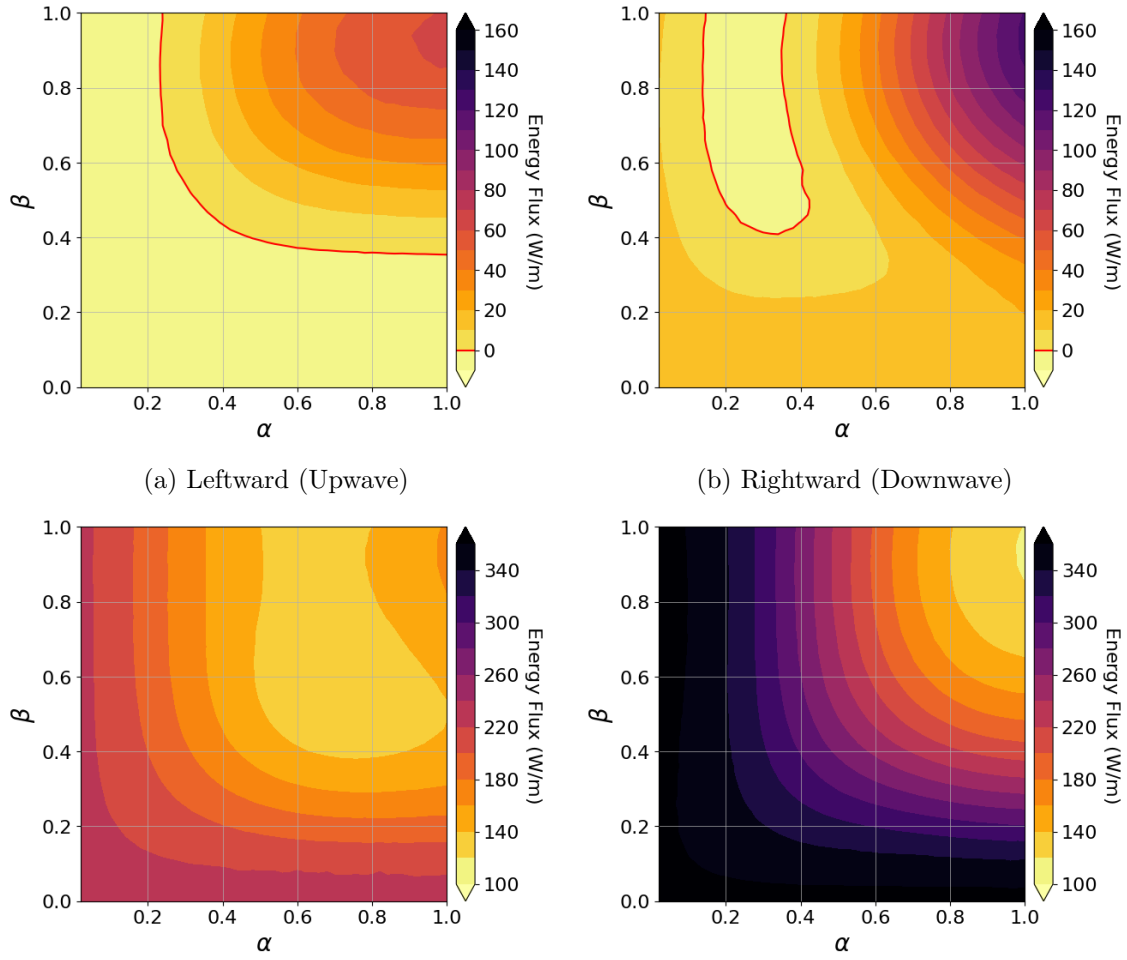

(a) Leftward (Upwave)

(b) Rightward (Downwave)

(c) Shoreward

(d) Oceanward

Figure 7.9: Implied time-averaged energy fluxes of baroclinic response from a 15 km wide canyon. Contours of time-averaged baroclinic energy fluxes radiating from 200 km × 200 km coastal domain around an idealised shelf-incising canyon are shown while varying proportion of canyon on shelf, α, and proportion of canyon on slope, β. From a surface tide in the form of a free Kelvin wave of semi-diurnal frequency at mid-latitude with an amplitude of ~ 1 m at the shoreline, we show the average energy flux radiating: (a) leftward (upwave); (b) rightward (downwave); (c) shoreward; (d) oceanward.

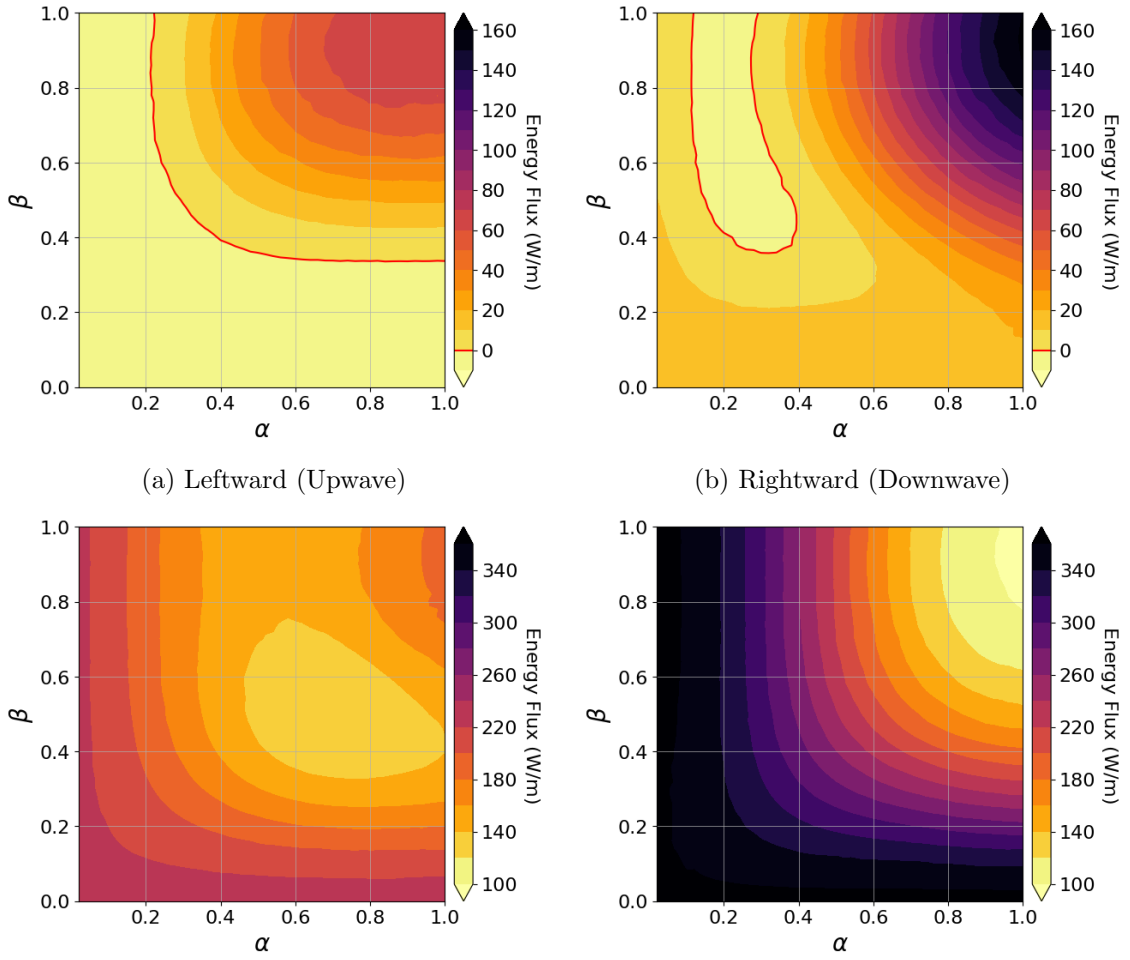

(a) Leftward (Upwave)

(b) Rightward (Downwave)

(c) Shoreward

(d) Oceanward

Figure 7.10: Implied time-averaged energy fluxes of baroclinic response from a 20 km wide canyon. Contours of time-averaged baroclinic energy fluxes radiating from 200 km × 200 km coastal domain around an idealised shelf-incising canyon are shown while varying proportion of canyon on shelf, α, and proportion of canyon on slope, β. From a surface tide in the form of a free Kelvin wave of semi-diurnal frequency at mid-latitude with an amplitude of ~ 1 m at the shoreline, we show the average energy flux radiating: (a) leftward (upwave); (b) rightward (downwave); (c) shoreward; (d) oceanward.

just seven days. The duration it took to sweep parameter space in our idealised model is in stark contrast to the time it might take to perform a similar such study using an ocean circulation model, as in previous studies (e.g. Petruncio et al., 2002; Hall & Carter, 2011; Zhang et al., 2014). An attempt was made at performing the parameter sweeps in parallel. However, this turned out to be less effective, most likely because of the communication overhead as the sparse solvers tried to solve multiple boundary-value problems across the different cores.

Using the same parameter space for canyon geometry as in Chapter 6, we vary canyon width, the proportion of the canyon occupying the shelf α, and the proportion of the canyon occupying the slope β. We recall that the $\beta \to 0$ limit leads to the baroclinic response of slope topography alone (i.e. no canyon). In each figure, the relevant quantity is shown as a contour plot in α–β parameter space for fixed canyon width; we consider canyon widths 5 km, 10 km, 15 km and 20 km. However, it is important to note that a reduction in the minimum resolution for canyons of width 5 km and 10 km was necessary to prevent segmentation faults due to memory thresholds for the Python `scipy.sparse` solvers (the upper limit appeared to be ~ 80 GB). This was despite best efforts to optimise the mesh through variable resolution and increasing virtual memory.

In Figures 7.7–7.10 for fixed canyon width, we show the average energy flux radiating from a 200 km $\times$ 200 km square coastal domain in each of the four directions: (a) leftward (upwave); (b) rightward (downwave); (c) shoreward; (d) oceanward. To be clear, we use upwave to define the direction from which the surface tide propagates before encountering the canyon (left of the canyon), and downwave as the direction towards which the surface tide propagates having encountered the canyon (right of the canyon). In Figure 7.11, the overall tidal dissipation is shown in α–β parameter space while varying canyon width. The overall tidal dissipation is calculated using the sum of the four directional energy fluxes across the four sides of the square coastal domain calculated as a line integral. An alternative measure, as previously discussed, would involve calculating the area integral of the baroclinic drag on the barotropic tide. Through all parameter space considered, the relative error between the two tidal dissipation calculations is always less than 2%.

From Figures 7.7–7.10, we conclude that the rightward (downwave) energy flux is consistently greater than the leftward (upwave) energy flux for all canyon widths and across most of α–β parameter space. The exception is the regime with $\beta \gtrsim 0.4$ and $0.2 \lesssim \alpha \lesssim 0.5$. Canyons described by this regime have a depth greater than 1,300 m and occupy around half of the continental shelf. While for small α and β there is a negative energy flux radiating leftward (corresponding to a net influx of energy across the left boundary), for sufficiently large α and β, the average energy flux can reach ~ 65 W/m with increasing canyon width. For energy fluxes rightward, depending on the proportion of shelf occupied by the canyon α, deep canyons ($\beta > 0.5$) can either lead to a net influx of energy across the boundary, or an increase in outward energy flux by a factor of eight.[1]

[1] See Figure 7.10b, where for large α, energy flux increases from ~ 20 W/m to ~ 160 W/m as β is increased from zero.

As for the energy fluxes in the cross-shore spatial direction, Figures 7.7–7.10 indicate that the oceanward energy flux is consistently greater than the shoreward energy flux irrespective of canyon width. However, for sufficiently large canyon width, Figures 7.9 and 7.10 show that this is not the case in the regime of large α and β. I.e. when both the shelf and slope become dominated by the canyon. The primary reason for this is the rapid reduction in the energy flux oceanward as the volume incision of the continental margin by the canyon increases. We remark that from the parameter space considered, a canyon can reduce the net energy flux oceanward by up to a factor of three (see Figure 7.10d). It appears that the energy flux lost oceanward for large α and β is redirected elsewhere. While some of this is redirected shoreward, a sizeable amount of energy is directed rightward.

In general, an increase in the canyon depth—corresponding to an increase in β—sees the direction of energy flux become more sensitive to the canyon incision of the shelf, α. Moreover, the presence of a canyon leads to a reduction in energy flux both off-shore and on-shore. A sizeable amount of this energy appears to be redirected along-shore, particularly when a sufficiently deep canyon extends far onto the shelf (large α, large β). A possible reason for this is the interception of the along-shore flow which is greatest towards the shoreline. In Figure 6.19 of Section 6.4.4, this region in α–β parameter space corresponded with greater magnitudes of vertical velocity in and around the canyon.

Onto the effects of canyon topography on tidal dissipation due to internal-tide generation, Figure 7.11 shows that the presence of a canyon will always lead to a reduction in tidal dissipation. At least, for a surface tide in the form of a free Kelvin wave of semi-diurnal frequency at mid-latitude for shelf-incising canyons up to 20 km in width. We stress that any relative changes are dependent upon the 200 km $\times$ 200 km domain chosen. If for example we took the limit of an infinitely large domain, the relative difference would approach zero. For canyons of sizeable width, Figures 7.11c and 7.11d show that tidal dissipation along continental margins can even reduce by up to half; from $\sim$ 121 MW in the limit $\beta \to 0$ (no canyon) to $\sim$ 72 MW when $\alpha \approx 0.77$ and $\beta \approx 0.5$. Moreover, the reduction in tidal dissipation does not monotonically decrease for increasing canyon depth (governed by parameter β) or canyon length. For sufficiently wide canyons which extend deep onto the shelf, the strong along-shore flow by the shoreline is able to generate significant internal-tide generation. However, this source of tidal dissipation does not compensate for the reduction observed by the shelf break - this appears to be a result of a reduction in the slope gradient for large canyon lengths and a reduction in cross-shore flow speeds (see Figure 6.18).

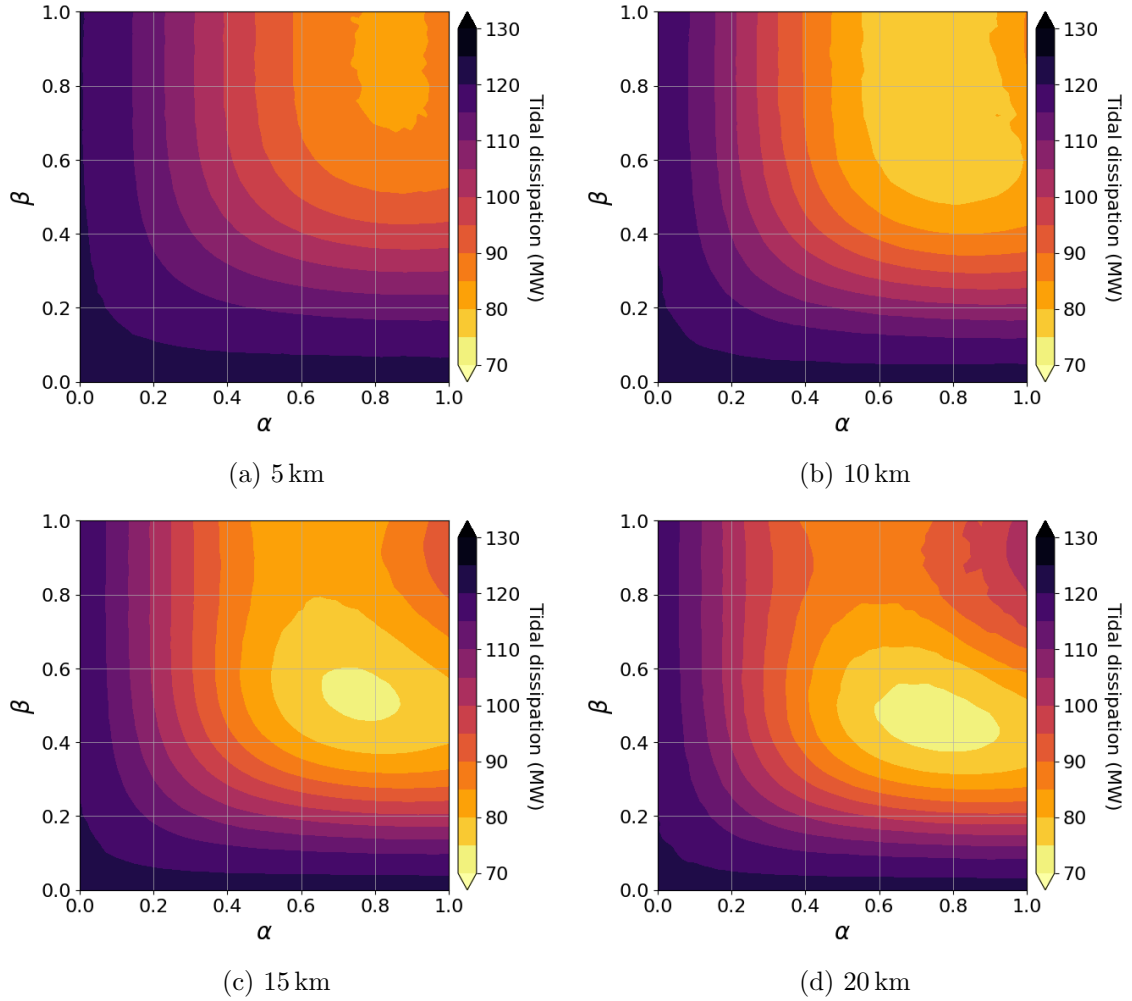

(a) 5 km (b) 10 km

(c) 15 km (d) 20 km

Figure 7.11: Reduction in tidal dissipation due to shelf-incising canyons. Contour plots in α–β parameter space are shown of the barotropic tidal dissipation due to internal-tide generation in a 200 km × 200 km coastal domain around a shelf-incising canyon. From a surface tide in the form of a free Kelvin wave of semi-diurnal frequency at mid-latitude with an amplitude of $\sim$ 1 m at the shoreline, we show net tidal dissipation as a result of a canyon of width: (a) 5 km; (b) 10 km; (c) 15 km; (d) 20 km.

7.5 Dissipation Paradox

The results of Figure 7.11 are significant as they contradict the pre-conceived notion that canyon topography leads to enhanced tidal dissipation along continental margins. The idea being, was that the Kelvin wave's strong along-shore flow, particularly by the shore, would be intercepted by the flanks of the canyon. As a result, strong along-shore bathymetric gradients coincide with strong flow along the shallow depths of the continental shelf. However, our study shows that canyons do not lead to enhanced tidal dissipation due to internal-tide generation.

The idea of a canyon leading to reduced tidal dissipation is also inconsistent with standard theories of internal-tide generation over *small-amplitude* topography, where linearisation around a flat bottom is performed. This is evident in both the studies of Bell (1975a, 1975b), for an ocean of infinite depth, and Llewellyn Smith and Young (2002), for an

ocean of finite depth, in which the tidal dissipation is linked to the Fourier transform of the topography. For example, in the simplest 1D case of Bell (1975a), we have that the dissipation is proportional to

$$\int_0^\infty k\,\tilde{h}(k)\,\tilde{h}^*(k)\,\mathrm{d}k \tag{7.12}$$

where $\tilde{h}(k)$ is the Fourier transform of fluid depth $h(x)$ (see equation (2) of Llewellyn Smith & Young, 2002). So adding more topographic gradients, e.g. in the form of a canyon, should lead to enhanced tidal dissipation.

However, implicit in such small-amplitude theories is that the barotropic tide is prescribed and independent of the topography, i.e. increasing the topography does not change the forcing barotropic flow. As we have already seen in Chapter 6, that is not the case for the large canyons that we consider (which themselves are incising a continental slope that cannot be considered as "small amplitude", in any sense). So is it possible that the canyon itself modifies the local barotropic tide in some non-trivial way, such that the outcome is one of reduced tidal dissipation even though there are greater topographic gradients?

We test this hypothesis by performing an additional set of simulations (for a canyon of width 5 km) in which the forcing barotropic tide is simply prescribed to be that of a Kelvin wave in the absence of a canyon; that is, the canyon is not permitted to modify the barotropic tide in the way already seen in Chapter 6, with strong local flow up and down the canyon valley, for example. The results of this experiment are in Figure 7.12; shown is the difference to the no-canyon case, with red thus denoting an increase in tidal dissipation and blue denoting a reduction.

For the modified surface tide shown in Figure 7.12a, the change in tidal dissipation in the presence of a canyon decreases almost uniformly with increasing parameters α or β and can be as much as ~ 35 MW. Conversely, Figure 7.12b shows that small-amplitude perturbations to the two-dimensional coastal topography (with $\alpha \ll 1$ or $\beta \ll 1$) for an unmodified Kelvin wave lead to an increase in tidal dissipation, as per prior discussion. The difference in the effects of the surface tide on tidal dissipation is shown in Figures 7.12c; i.e. Figure 7.12a−Figure 7.12b. In Figure 7.12a, the relative difference between the changes shown in Figure 7.12d are quantified. Here, it is observed that an unmodified Kelvin wave in the presence of a canyon leads to an increase in tidal dissipation by up to $\sim 34\%$. In addition, the disparity in tidal dissipation between the modified and unmodified surface tide is greatest for the most volume-incised canyons.

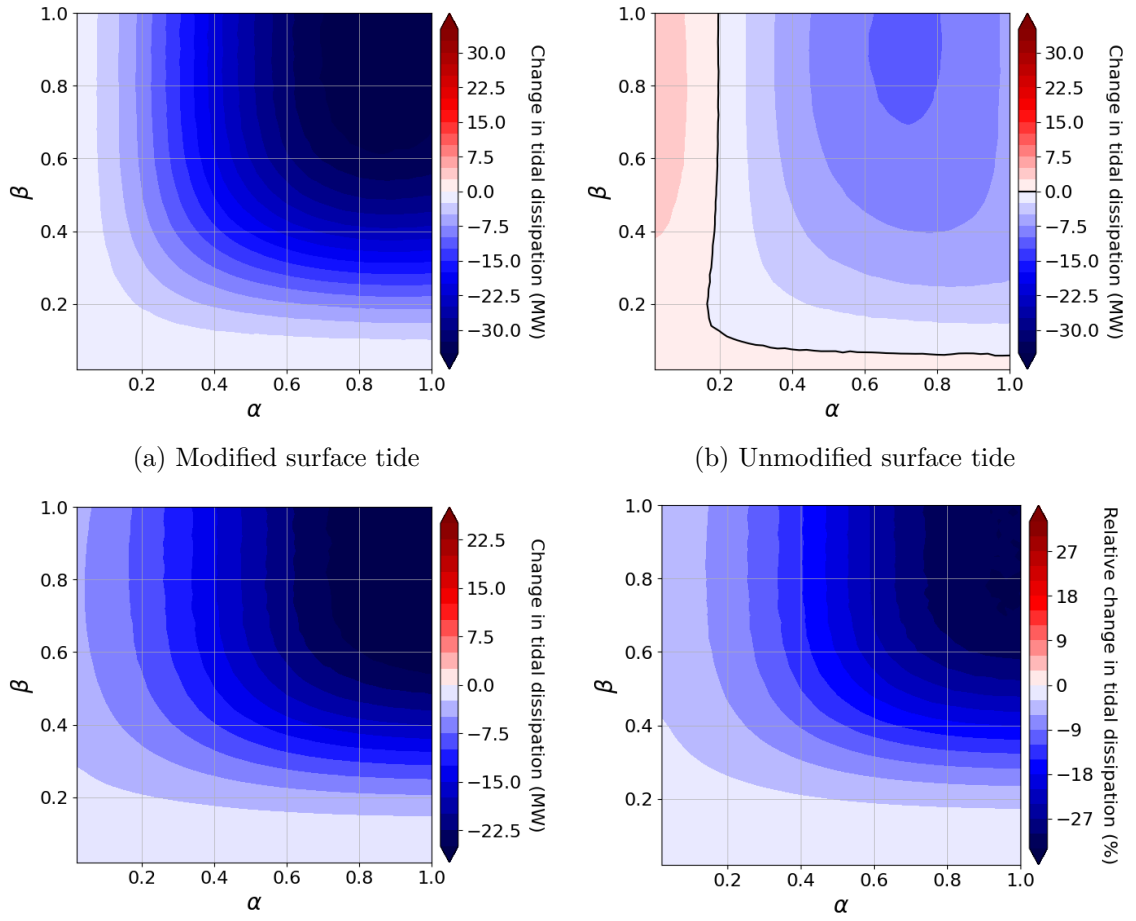

(a) Modified surface tide

(b) Unmodified surface tide

(c) Change due to modified surface tide

(d) Relative change due to modified surface tide

Figure 7.12: Difference in tidal dissipation due to presence of a 5 km wide canyon (relative to the no-canyon case obtained in limit $\beta \to 0$). By solving for the modified surface tide (top left), tidal dissipation is always reduced. However, the tidal dissipation implied from an unmodified surface tide (top right) leads to an increase in tidal dissipation for small canyons ($\alpha \ll 1$ or $\beta \ll 1$). The difference between (a) and (b) is shown in (c), and shows that that tidal dissipation due to the modified surface tide is always less than the tidal dissipation due to the unmodified surface tide. The relative change, shown in (d), suggests that the change in dissipation rate can differ by as much as $\sim 34\%$.

7.6 Summary

In this chapter, we have looked into the effects of canyon topography on the generation of internal tides using the linearised two-layer modal shallow-water equations. Assuming time-periodic motion, a decoupled surface tide in the form of a Kelvin wave of semi-diurnal frequency at mid-latitude was solved in and around a canyon (see Chapter 6). The surface tide was then used to force an internal tide, from which the tidal dissipation can be inferred from the time-averaged baroclinic energy flux radiating outward from a coastal domain around the canyon. Using idealised canyon-shelf topography as proposed in Section 6.2, parameter space defining shelf-incising canyon geometry was spanned by a series of $\sim 10,000$ simulations involving sparse matrices of size $\sim 70,000 \times 70,000$ (with $\sim 23,000$ grid points).

In Section 7.2, we focused on the implementation of sponge layers to promote radiating internal waves. For our study, we considered a sponge layer of the form discussed in Lavelle and Thacker (2008). This sponge layer involved different damping applied to each of the three baroclinic variables. The sponge layer was carefully configured over three relevant parameters which implicitly governed the effectiveness of the sponge layer, ensuring that the tidal dissipation inferred from the radiating energy fluxes along a 200 km × 200 km coastal domain around the largest possible canyon had converged to within 2%. At the same time, minimising the computational domain (and therefore number of unknowns for which we solve) was critical to reduce computational cost.

In Section 7.3, we presented typical results of the internal-tide generation problem. This showed how the baroclinic solution, baroclinic energy flux and tidal dissipation are affected by the presence of canyon topography. One of the major effects of canyon topography on the baroclinic response was the appearance of asymmetric beams of energy flux. These results exhibit the same behaviour as those shown in more complex models of Petruncio et al. (2002) and Zhang et al. (2014) which used well-established ocean circulation models. These concentrated beams of energy flux radiating on-shore, which can be double in magnitude as a result of the canyon topography, are significant since they provide a potential source for instability and enhanced mixing. Zhang et al. (2014) suggests that the radiating beams of energy flux on-shore are a result of resonant internal-tide generation mechanisms.

In Section 7.4, the results of $\sim 10,000$ simulations were analysed, investigating how canyon geometry impacts internal-tide generation along a pycnocline. This involved recording the magnitude and direction of implied time-averaged radiating energy fluxes radiating from a 200 km×200 km domain around the canyon. The results of Section 7.4 show that in general, baroclinic energy fluxes are stronger rightward (downwave) than leftward (upwave), as well as being stronger oceanward than shoreward. However, regions do occur whereby the latter is no longer the case. For deep and moderately incising canyons, energy fluxes leftward become net positive, while those rightward become net negative. For sufficiently wide canyons, greater baroclinic energy fluxes propagate shoreward than oceanward when both the shelf and slope are significantly occupied by the canyon. In this same regime, significant loss of energy flux occurs oceanward, comprising roughly two-thirds. We have shown that the energy oceanward becomes redirected, primarily rightward (upwave).

Finally, our study concludes that tidal dissipation due to internal-tide generation in a two-layer model is not enhanced under any circumstances by the presence of a shelf-incising canyon. For 20 km wide canyons, tidal dissipation due to internal-tide generation can even reduce by a factor of two. However, it is possible that canyons are significantly more efficient at generating internal tides in a continuously stratified fluid, particularly through critical and supercritical topography. Moreover, the reason for the reduction in tidal dissipation appears in part due to the topographic steering of the Kelvin wave around the canyon. For a canyon of width 5 km, the tidal dissipation due to internal-tide generation reduces by up to $\sim 34\%$ by the modification of the surface tide in the presence of a canyon.

Chapter 8

Conclusion

Internal tides are (inertia-)gravity waves which exist within a stratified fluid and are generated as the surface tide interacts with variable bottom topography. Internal tides play a key role in transporting energy in the ocean. The work presented in this thesis considers idealised models for internal-tide generation along continental margins. This process is of scientific interest since internal tides play a significant role in the ocean potential energy budget. Current satellite measurements and ocean general circulation models (OGCMs) are unable to sufficiently resolve all aspects of internal-tide generation and propagation along continental margins. There exists therefore sizeable interest in developing idealised models, both analytical and numerical, which provide greater insight to the wider scientific community into the fundamental aspects of internal-tide generation along continental margins. In particular, this insight could lead to improved parameterisations of tidal dissipation and vertical mixing in atmosphere-ocean models such as the OGCMs used in climate (see Section 1.2).

A summary of the work undertaken as part of the thesis is presented in Section 8.1. The aims of the thesis are then revisited in Section 8.2, highlighting the importance of the work against the scope for research discussed within the introductory chapter, Section 1.2. The thesis concludes in Section 8.3 with suggestions for future research on internal-tide generation along continental margins.

8.1 Summary

In this thesis we have developed idealised models for the generation of internal tides along continental margins. Our model, which focused on the generation of internal waves along the pycnocline, is restricted by three major assumptions: linearisation, hydrostatic balance and layer stratification (with variations in layer thickness restricted to the bottom layer). Our model allows for both analytical and numerical solutions to span relevant parameter regimes characterising representative coastal topographies. By employing cutting-edge numerical modelling, we have been able to apply our model to internal-tide generation by shelf-incising canyons.

In Chapter 2, the linearised hydrostatic equations of motion were derived. The first part of the chapter focused on the theory of normal modes in a continuously stratified fluid. Here, vertical and horizontal motions become entirely decoupled over uniform topography into modes of the same phase speed and vertical structure. A regular Sturm–Liouville eigenvalue problem dependent only on the stratification profile of the fluid medium can be constructed. For Boussinesq uniform stratification, analytical solutions had been found, showing that a barotropic mode exists only with the consideration of a free-surface condition. Numerical solutions were also sought and showed that Chebyshev differential matrices were much easier to implement and required less nodes than its second-order finite differences counterpart.

In the second half of the chapter, the framework for multi-layer stratification profiles was discussed. The formulation of Griffiths, (2020; personal communication) was presented, which expanded on the multi-layer theory of Shimizu (2011) by exploiting the linear algebra of the system. That work made clear that the corresponding eigenvalue problem is a direct analogue of the continuous eigenvalue problem and involves a real-symmetric matrix with orthogonal eigenmodes. This matrix can be concisely constructed in Python. Having derived the multi-layer shallow-water equations, the two-layer equations followed immediately.

In Chapter 3, two-layer modal equations were deconstructed to consider the decoupled surface (barotropic) tide. This involved neglecting the baroclinic dissipation of the surface tide over variable topography. We were principally interested in the form of the surface tide along a continental margin, i.e. potentially forced barotropic motion in a channel of uniform depth. Through well-known analytical dispersion relations, we noted that only Kelvin waves can be strongly excited at all tidal frequencies, unlike shelf waves which are sub-inertial and inertia-gravity waves which are super-inertial. In addition, for tidal alongshore length scales and tidal wave frequencies, the Kelvin wave is the principal component of the surface tide irrespective of the equilibrium tide's cross-shore spatial structure. It is for this reason that the second half of the chapter concerned the analytical form of the Kelvin wave over arbitrary coastal topography. This derivation of the Kelvin mode involved exploiting parameter $\lambda \ll 1$, defined as the ratio of the coastal length scale with the Rossby radius of deformation in the deep ocean.

In Chapter 4, three approaches to the modelling of internal-tide generation by a potentially forced three-dimensional surface tide along two-dimensional coastal topographies were explored: a fully coupled two-layer system; a decoupled potentially forced barotropic system and its baroclinic response; an analytical potentially forced Kevin wave and its baroclinic response. A simple scaling law showed that for sufficiently wide slopes, baroclinic dissipation of the surface tide can be neglected. The latter was corroborated by numerical experiments using finite differences over a staggered grid which showed that the implied energy fluxes of the internal-tide response between coupled and decoupled barotropic motion were almost identical (to within 2%) throughout a wide range of shelf-slope profile configurations. In the last approach, it is observed that the implied baroclinic energy fluxes

of the baroclinic tide are well approximated by using the form of the decoupled potentially forced Kelvin wave over the slope so long as the shelf width and slope width were much smaller than the Rossby radius of deformation ($\lambda \ll 1$). In general, these results showed excellent qualitative agreement with the fully coupled approach. Furthermore, we showed that the same methodology could be used as in Griffiths and Grimshaw (2007a) to develop an analytical solution to the baroclinic response of a free Kelvin wave in the limit of shelf topography. These results gave an analytical expression for the implied baroclinic energy fluxes radiating from the shelf break, allowing direct inference of parameter dependence on, for example, along-shore wavenumber, slope width, shelf depth etc.

In Chapter 5, the application of discontinuous Galerkin finite element methodology (DG-FEM) to the decoupled two-layer modal shallow-water equations is studied in detail. We focused in this chapter on the surface tide. This chapter had two principal aims: to build an understanding of the numerical method so that it may be implemented, and to understand and test the effect of element size, polynomial order, and numerical flux on the accuracy and form of solutions. To test the effect of element size, polynomial order and numerical flux, two approaches were taken. The first approach was an associated eigenvalue problem assuming plane-wave flow in basins for which analytical solutions are known. The second approach was an associated elliptic boundary-value problem, applying the known form of the barotropic Kelvin wave along the boundaries of the domain and resolving the spatial structure therein. These tests verified the implementation of the numerics under both h- (mesh size) and p-refinement (polynomial order). The boundary-value problem also highlighted the need for local mesh refinement along the shelf break. These tests allowed us to optimise our choice of numerical flux; the central numerical flux was the most appropriate choice as it permits energy conservation, allows for discontinuous/non-differentiable topographies, is sparse, and is comparable to the time-complexity and accuracy of the Lax–Friedrichs numerical flux. For smooth topographies, Lax–Friedrichs is optimal for both accuracy and conditioning, and enforces continuity of pressure and volume transport.

In Chapter 6, we investigated the effects of canyon geometry on the form of a surface tide in the form of a free Kelvin wave. Because of the internal-tide generation problem, we were interested in the modification of the barotropic flow in and around the canyon. To resolve the barotropic flow in and around the canyon, an elliptic boundary-value problem of time-periodic flow is solved using DG-FEM. Along the boundaries of the computational domain, a background flow corresponding to the perturbed Kelvin wave is prescribed. To begin, we discussed idealised models of canyons, and how they could be improved to better represent observations. To this effect, a novel means of modelling idealised shelf-incising canyons is proposed, spanned by three parameters: $\alpha \in [0, 1]$ (proportion of shelf occupied by canyon), $\beta \in [0, 1]$ (proportion of slope occupied by canyon), and W (maximum canyon width in km occurring at the shelf break).

To optimise our numerics, the Python package `OceanMesh` is used to generate robust, high-quality triangular meshes. By collaborating with the code developers, we were able to refine mesh size according to slope parameter $h/|\nabla h|$ for fluid depth h. From our

investigation, we found that effect of a canyon on the pressure perturbation field was negligible, consistent with the theory of Baines (1983). Furthermore, the flow became topographically steered by the canyon, driven by the external pressure field. A quantitative analysis looking into L^p-norms of the flow field in the presence of a canyon saw two regimes emerge. These two regimes were consistent with type one and type two canyons of Harris and Whiteway (2011) (see Section 1.2.2 or 6.2).

Depending on the regime, the horizontal velocity field of the surface tide in and around the canyon would become stronger or weaker. For canyons of type one canyon limit, the along-shore flow becomes localised, while in the type two limit, the along-shore flow becomes marginally more uniform than in the case of no canyon (corresponding to the limit $\beta \to 0$). As for the cross-shore flow, the type one limit leads to maximal flows reduced by up to a factor of two, while for a canyon confined to the shelf break, cross-shore flows can increase by up to 50%. In addition, a similar such analysis on the vertical velocity along the sea floor indicated that the flow field in and around the canyon can increase by several factors. By increasing the width of a canyon, the average speed in and around the canyon increases, but the maximum speed decreases. The magnitude of the vertical velocity has a particularly strong along-shore component brought about by the large gradients which exist along the canyon's sidewalls.

In Chapter 7, we investigated the effects of canyon topography on the internal-tide response of the surface tide considered in Chapter 6, along with the implied baroclinic energy flux. The energy flux was used to measure the dissipation rate of the surface tide, as well as the direction of energy propagation. The results of this chapter showed that our idealised model is able to capture the same enhanced asymmetric beams of energy flux radiating shoreward as captured in more complex models used in Petruncio et al. (2002) and Zhang et al. (2014). These enhanced beams provide a potential source for instability and mixing. Moreover, we showed that the presence of a canyon redirects oceanward-propagating energy primarily upwave. In other words, less energy propagates towards the deep ocean where it may break and dissipate energy. This could suggest that canyons lead to less mixing in the deep ocean, and more mixing along the shelf.

Another feature of the work presented in Chapter 7, is that our idealised model has permitted the vast exploration of parameter space defining shelf-incising canyon topography. From our analysis, we were able to conclude that dissipation of the surface tide due to internal-tide generation along a pycnocline is always reduced in the presence of a canyon. This reduction in dissipation, compared with the no-canyon case in the limit $\beta \to 0$, is maximal for wide canyons which incise around halfway up the slope and extend far onto the shelf. Despite an initial hypothesis that canyon topography would enhance tidal dissipation, this is only the case if a small, narrow canyon ($\alpha \ll 1$ or $\beta \ll 1$) incises the slope and the form of the surface tide is unmodified by the canyon topography. In other words, the modification of the surface tide by the canyon cannot be neglected if one wishes to accurately model internal-tide generation and propagation along continental margins.

8.2 Aims Revisited

In the introductory chapter, a set of aims was proposed motivated by current research scope. These aims are revisited here:

- *Understand internal tides generated by a three-dimensional surface tide (in the form of a Kelvin wave) about a two-dimensional topography representing a continental margin.*

  We found that while the Kelvin wave is typically known for its weak cross-shore flow, the magnitude of the cross-shore flow can become comparable to the strong along-shore flows present at the shoreline. Moreover, analytical expressions for a potentially forced Kelvin wave can be used to model internal-tide generation along characteristic slope topographies. These results showed qualitative and quantitative agreement to the full potentially forced problem for a range of shelf and slope widths provided they are sufficiently small relative to the Rossby radius of deformation. An analytical expression for radiating energy fluxes was derived for the free Kelvin wave in the limit of step topography, illuminating the non-trivial dependence on coastal topography and stratification.

- *Understand the role of topographic variations in the along-shore direction, i.e. for a three-dimensional tide above a fully three-dimensional topography in the form of a canyon incising a continental margin.*

  Our results show that tidal dissipation as a result of internal-tide generation in a two-layer model is not enhanced under any circumstances in the presence of shelf-incising canyons. This is in large part because of the non-negligible modification of the surface tide as the barotropic Kelvin wave becomes topographically steered by the canyon topography. For a canyon of width 5 km, tidal dissipation due to internal-tide generation reduces by up to $\sim 34\%$ by the modification of the surface tide in the presence of a canyon. For sufficiently wide canyons, tidal dissipation is reduced by up to a factor of two.

8.3 Future Work

The implementation and configuration of the DG-FEM code to optimise the numerical modelling of linearised modal shallow-water flow was a long and arduous journey. However, the code has enabled the simulation of over 10,000 different canyons covering a wide array of parameter space. These simulations were carried out in a period of a week, running continuously in series over ~ 50 cores on the HPC facilities at the University of Leeds. While this may seem excessive, it is clear that the alternative of using OGCMs, while less idealised, is simply too costly. From this study, were able to conclude that internal-tide generation along the pycnocline at continental margins is not enhanced by the presence of canyon topography.

It is hoped that the work presented in this thesis is only the beginning, and that future individuals may take it upon themselves to develop further understanding around the matter of internal-tide generation along three-dimensional continental margins.

To conclude the thesis, possible avenues for future research are proposed, as follows:

1. *Analytical Solution*
   In the derivation of the analytical solution in Section 4.3.3 of Chapter 4, along-shore wavenumber k had to be omitted, i.e. only $k \to 0$ was considered. Further work would certainly look at developing means of producing a more generalised solution without having to make the assumption on along-shore wavenumber k.

2. *Theoretical modelling of canyon system*
   We have generated in Chapters 6 and 7 lots of interesting results about tidal flow, both surface and internal, in and around submarine canyons. It is natural to try to explore the observed results semi-analytically to understand why a reduction in tidal dissipation is consistently observed. Such a study may require further simplifications around the canyon topography (e.g. boxes) and the surface tide (e.g. non-rotation, constant pressure, constant volume transport).

   We considered in Chapters 6 and 7 an idealised model for a straight shelf-incising canyon. In reality, most canyons are confined to the slope, and meander much like rivers.[1] Moreover, canyons tend not to be isolated. Either other canyons are situated nearby (the average canyon spacing according to Harris and Whiteway (2011) is $\sim 33\,\text{km}$ - see Table 1.3), or a canyon system branches into other tributaries (e.g. Monterey). These observations concerning oceanic canyons along continental margins provide three interesting scopes for further investigation into their effect on internal-tide generation: slope-confined (blind) canyons, canyon systems, and canyon meandering.

   Data from Harris and Whiteway (2011) indicate that only around 30% of canyons are shelf-incising (types one and two), with the remaining typically referred to as blind canyons (type three). Blind canyons are canyons which are confined entirely to the slope. While shelf-incising canyons are, on average, $\sim 25\%$ longer than blind canyons (see Table 1.3), an improved model would consider all possible cases. One could investigate which of the three canyon types leads to the greatest energy fluxes implied from the baroclinic response. This may depend on canyon width, forcing frequency and other system parameters, but such a study would offer a more robust understanding of the role submarine canyons play in the generation of internal tides.

   To consider blind canyons, it is not immediately clear how our idealised canyon model can be extended without a different choice of valley profile ($\psi(y)$ in (6.5)). For parameter space, one could consider negative values of α (proportion of shelf

[1] Hence the sinuosity measurement considering the ratio of canyon length to distance between the head and foot of a canyon in Table 1.3.

occupied by canyon); $\alpha = -1$ could correspond to a canyon head located at the foot of the canyon (and yields the limit of no canyon length).

An investigation into the impact of canyon systems could consider periodic boundary conditions in the along-shore direction while varying the domain size (and therefore canyon spacing). The choice of boundary condition in the along-shore would reduce the size of the computational domain (and therefore number of unknowns). Nevertheless, additional consideration would be required for the surface tide.

Lastly, one could model canyon meandering by using a variable long-canyon axis in the form of a small-amplitude sine-wave (whereby the sinuosity—the ratio between the wavelength and the sinuous arc length—is of order ~ 1.1, as in Table 1.3).

3. *Multi-layer stratification*
   The model used in the thesis supposes a two-layer stratification profile. A more accurate study would consider the use of more layers. Even so, one crucial assumption made when deriving the governing equations was that only the bottom layer could vary. This assumption prevents the intersection of density contours with the bottom topography.

   The current framework without modification could be used to model the generation of internal waves within the deep ocean interior by mid-ocean topographic features. The use of DG-FEM could allow for variable resolution to resolve internal-tide generation at seamounts, ridges and trenches, allowing parameter space to be explored in a similar fashion to the work presented in Chapters 6 and 7. However, the source terms and/or flux terms when posing the governing equations in conservative form may have to be re-formulated to enforce energy conservation between modes.

4. *Continuous stratification*
   A more feasible approach, allowing both critical and super critical wave generation along the slope and canyon, would be the use of continuous stratification. The latter would allow density contours to intersect bottom topography. Solving the system as a boundary-value problem, the major obstacle here would undoubtedly be memory, particularly if as many modes (256 at most) are needed as in §5(c) of Griffiths and Grimshaw (2007a). Nonetheless, the matrix system itself would be hugely sparse, and could be solved as an initial-value problem using explicit integration methods.

   While requiring less memory, the computational time it would take to solve the initial-value problem would render any parameter sweep expensive to conduct. Supposing that we require 64 baroclinic modes and each mode has around $\sim 25,000$ unknowns, that equates to matrices of size 1.6 million. In Zhang et al. (2014), it took a total of six wave periods for the spatial pattern of internal-tide propagation on the continental shelf to reach a steady state. Depending on the damping of transients both on- and off-shore, the time integration may have to be performed over a much longer period. At present, such a study would be hugely expensive. How-

ever, the advance in Graphics Processing Units (GPUs), could render such a study feasible. This advance arises because the architecture of GPUs can be exploited to conduct matrix-vector and vector-vector operations more efficiently.

Another means of reducing computational time is by using instead `Fortran`, `C++` or any other compiled language to construct the matrix system, since Python code is interpreted during run time, rather than being compiled to native code. There are means of reducing computational time for those adamant on using Python, such as `Cython` (ahead-of-time compiler) or `Numba` (just-in-time compiler). Still, these routines will typically not provide the same level of speed-up. As for linear operators, `NumPy` already exploits specialised processor functionality using libraries such as BLAS (Basic Linear Algebra Subprograms) or LAPACK (Linear Algebra PACKage). It is unlikely that the process of solving the matrix systems can be further optimised by using `Fortran` or `C++` alone.

5. *Realistic topography*
   One extension to the work presented in this thesis, readily available thanks to `OceanMesh`, is the use of bathymetric data to solve for the surface tide and calculate the internal-tide response. Here, a likely approach would be to pose impermeability along the shoreline and use a potential forcing to generate a barotropic tidal response. As in Chapter 7, the computational domain of the baroclinic mode needs to be extended to impose open-ocean radiating conditions through a sponge layer. The implied baroclinic energy fluxes generated by observed canyon topography can be compared to those of our idealised canyon-slope model. However, a direct link should be established between the surface tides. For example, for surface tides of the same amplitude along the shoreline. The different topography may require the use of a different surface tide.

6. *Non-linearity*
   An interesting, but less feasible extension could be the use of direct numerical simulation (DNS) to simulate internal-tide generation over 3D coastal topography (e.g. Gayen & Sarkar, 2010). However, it would be computationally expensive to resolve turbulence, shear instabilities and wave-wave interactions in 3D space over many thousand square kilometres. This would, however, provide a better understanding on the local non-linear propagation of the internal waves generated, and the mechanisms by which energy is dissipated locally (as opposed to remotely).

7. *Internal-tide scattering*
   Upon posing the linearised hydrostatic modal equations in conservative form, our canyon topography model and implementation of DG-FEM could be quite easily extended to consider the problem of internal-tide scattering, as in Hall and Carter (2011), Vlasenko et al. (2016), Nazarian and Legg (2017a, 2017b), and Nazarian et al. (2021). This would permit an interesting study on the effects of canyon geometry on the scattering of remotely generated internal waves.

Appendix A

Derivation of Solutions to Internal-Tide Generation Problem

In this appendix, we derive the exact solution as in §4a of Griffiths and Grimshaw (2007a). To begin, the radiating boundary condition (4.20) is obtained from integrating (4.49) between $y = L_C - \epsilon$ and $y = L_C + \epsilon$ and evaluating the limit $\epsilon \to 0$:

$$\lim_{\epsilon\to 0}\int_{L_C-\epsilon}^{L_C+\epsilon}\left(\frac{\mathrm{d}^2}{\mathrm{d}y^2}+\frac{\omega_f^2}{c_1^2\,(y)}\right)\tilde{V}_1\,(y)\;\mathrm{d}y = \\ -\frac{\sqrt{g\,\varepsilon}\,\tilde{Q}}{c_\infty^2\,(L_C+L_S)}\lim_{\epsilon\to 0}\int_{L_C-\epsilon}^{L_C+\epsilon}\frac{\mathrm{d}^2}{\mathrm{d}y^2}\left(c_1^2\,(y)\;y\right)\;\mathrm{d}y, \tag{A.1}$$

which when simplified, yields

$$\left(\frac{\mathrm{d}}{\mathrm{d}y}+i\,l_C\right)\tilde{V}_1\,(y) = -2\sqrt{g\,\varepsilon}\,\frac{c_C}{c_\infty^2}\tilde{Q}\;(1+L_S/L_C)^{-1}\;\frac{\mathrm{d}c_1\,(y)}{\mathrm{d}y} \qquad \text{at} \qquad y = L_C. \tag{A.2}$$

Similarly, integrating at the foot of the slope gives the condition

$$\left(\frac{\mathrm{d}}{\mathrm{d}y}-i\,l_D\right)\tilde{V}_1\,(y) = -2\sqrt{g\,\varepsilon}\,\frac{c_D}{c_\infty^2}\,\tilde{Q}\,\frac{\mathrm{d}c_1\,(y)}{\mathrm{d}y} \qquad \text{at} \qquad y = L_C + L_S. \tag{A.3}$$

To solve (4.49), a change of variable of the form

$$\nu = \frac{c_1\,(y)}{c_\infty} = \frac{c_C+\omega_f\,\sigma\,(y-L_C)}{c_\infty} \qquad \Longrightarrow \qquad \frac{\mathrm{d}^2}{\mathrm{d}y^2} = \frac{\sigma^2\,\omega_f^2}{c_\infty^2}\,\frac{\mathrm{d}^2}{\mathrm{d}\nu^2}$$

is performed, recalling that $\sigma = (c_D - c_C)\,/\omega_f\,L_S$. This gives the inhomogeneous ordinary differential equation

$$\left(\frac{\mathrm{d}^2}{\mathrm{d}\nu^2}+\frac{\sigma^{-2}}{\nu^2}\right)\tilde{V}_1\,(\nu) = \frac{-g\,\sqrt{\varepsilon}\,\tilde{Q}}{1+\Lambda}\,\frac{\mathrm{d}^2}{\mathrm{d}\nu^2}\left(\nu^2\left(\frac{\Lambda\,(\nu\;(c_\infty/c_C)-1)}{(c_D/c_C)-1}+1\right)\right) \tag{A.4}$$

over the continental margin, where $\Lambda \equiv L_S/L_C$ tends to zero in the limits $L_S \to 0$ (step topography) or $L_C \to \infty$ (no coastal boundary).

We observe that the left-hand side of (A.4) is an Euler–Cauchy equation, and therefore admits complementary solutions of the form ν^r. Upon substitution into the left-hand side of (A.4), it follows that

$$r\,(r-1)+\sigma^{-2}=0 \qquad \Longrightarrow \qquad r=\frac{1}{2}\pm i\,\gamma, \qquad \gamma \equiv \sqrt{\sigma^{-2}-\frac{1}{4}}, \tag{A.5}$$

and implies a complementary function

$$\begin{aligned} V_{1,CF}\,(\nu) &= A\,\nu^{1/2+i\,\gamma}+B\,\nu^{1/2-i\,\gamma} \\ &= \nu^{1/2}\left(A\,\exp\left(i\,\gamma\,\ln\left(\nu\right)\right)+B\,\exp\left(-i\,\gamma\,\ln\left(\nu\right)\right)\right). \end{aligned} \tag{A.6}$$

The latter is equivalent to

$$V_{1,CF}\,(\nu)=\nu^{1/2}\left(\tilde{A}\,\cos\left(\gamma\,\ln\left(\nu\right)\right)+\tilde{B}\,\sin\left(\gamma\,\ln\left(\nu\right)\right)\right) \tag{A.7}$$

with

$$\tilde{A}=A+B \qquad \text{and} \qquad \tilde{B}=i\,(A-B)\,. \tag{A.8}$$

To develop the particular solution, we seek solutions of the form

$$V_{1,PS}\,(\nu)=\frac{g\,\sqrt{\varepsilon}\,\tilde{Q}}{1+\Lambda}\,\nu^2\left(a_1+a_2\,\Lambda\,\frac{\nu\,(c_\infty/c_C)-1}{(c_D/c_C)-1}\right), \tag{A.9}$$

which is essentially equivalent to the particular solution in Appendix D of Griffiths and Grimshaw (2007a).

Substituting the particular solution given by (A.9) into (A.4), we find that

$$\begin{aligned} a_1\left(2+\sigma^{-2}\right)-\frac{a_2\,\Lambda}{(c_D/c_C)-1}\left(2+\sigma^{-2}\right)+\frac{a_2\,\Lambda}{(c_D/c_C)-1}\left(6+\sigma^{-2}\right)(c_\infty/c_C)\,\nu = \\ -2\left(1-\frac{\Lambda}{(c_D/c_C)-1}\right)-\frac{6\Lambda}{(c_D/c_C)-1}\,(c_\infty/c_C)\,\nu, \end{aligned} \tag{A.10}$$

from which it is found that

$$a_1=\frac{-2\sigma^2}{2\sigma^2+1}\left(1+\frac{2\Lambda}{(6\sigma^2+1)\,((c_D/c_C)-1)}\right) \qquad \text{and} \qquad a_2=\frac{-6\sigma^2}{6\sigma^2+1}, \tag{A.11}$$

which again, returns identical results as Griffiths and Grimshaw (2007a).

Adding together the complementary function (equation (A.7)) and the particular solution

(equation (A.9)), we obtain the full solution

$$
\begin{aligned}
V_1(\nu) &= V_{1,CF}(\nu) + V_{1,PS}(\nu) \\
&= \frac{g\sqrt{\varepsilon}\,\tilde{Q}}{1+\Lambda}\,\nu^2\left(a_1 + a_2\,\Lambda\,\frac{\nu\,(c_\infty/c_C)-1}{(c_D/c_C)-1} + \right. \qquad \text{(A.12)} \\
&\qquad a_3\left(\frac{c_C}{c_\infty\,\nu}\right)^{3/2}\left[\cos\left(\gamma\,\log\left(\frac{c_\infty\,\nu}{c_D}\right)\right) + \right. \\
&\qquad\qquad \left.\left(i\,\sigma^{-1}-\frac{1}{2}\right)\gamma^{-1}\,\sin\left(\gamma\,\log\left(\frac{c_\infty\,\nu}{c_D}\right)\right)\right] + \\
&\qquad a_4\left(\frac{c_D}{c_\infty\,\nu}\right)^{3/2}\left[\cos\left(\gamma\,\log\left(\frac{c_\infty\,\nu}{c_C}\right)\right) - \right. \\
&\qquad\qquad \left.\left.\left(i\,\sigma^{-1}+\frac{1}{2}\right)\gamma^{-1}\,\sin\left(\gamma\,\log\left(\frac{c_\infty\,\nu}{c_C}\right)\right)\right]\right), \qquad \text{(A.13)}
\end{aligned}
$$

where we have made the following rather complex-looking linear transformations in our complementary solution:

$$
\begin{aligned}
\tilde{A} = \frac{g\sqrt{\varepsilon}\,\tilde{Q}}{1+\Lambda}\left(a_3\left(\frac{c_C}{c_\infty}\right)^{3/2}\left[\cos\left(\gamma\,\log\left(\frac{c_\infty}{c_D}\right)\right) + \right.\right. \\
\left.\left(i\,\sigma^{-1}-\frac{1}{2}\right)\gamma^{-1}\sin\left(\gamma\,\log\left(\frac{c_\infty}{c_D}\right)\right)\right] + \\
a_4\left(\frac{c_D}{c_\infty}\right)^{3/2}\left[\cos\left(\gamma\,\log\left(\frac{c_\infty}{c_C}\right)\right) - \right. \\
\left.\left.\left(i\,\sigma^{-1}+\frac{1}{2}\right)\gamma^{-1}\sin\left(\gamma\,\log\left(\frac{c_\infty}{c_C}\right)\right)\right]\right) \qquad \text{(A.14)}
\end{aligned}
$$

and

$$
\begin{aligned}
\tilde{B} = \frac{-g\sqrt{\varepsilon}\,\tilde{Q}}{1+\Lambda}\left(a_3\left(\frac{c_C}{c_\infty}\right)^{3/2}\left[\sin\left(\gamma\,\log\left(\frac{c_\infty}{c_D}\right)\right) - \right.\right. \\
\left.\left(i\,\sigma^{-1}-\frac{1}{2}\right)\gamma^{-1}\cos\left(\gamma\,\log\left(\frac{c_\infty}{c_D}\right)\right)\right] + \\
a_4\left(\frac{c_D}{c_\infty}\right)^{3/2}\left[\sin\left(\gamma\,\log\left(\frac{c_\infty}{c_C}\right)\right) + \right. \\
\left.\left.\left(i\,\sigma^{-1}+\frac{1}{2}\right)\gamma^{-1}\cos\left(\gamma\,\log\left(\frac{c_\infty}{c_C}\right)\right)\right]\right). \qquad \text{(A.15)}
\end{aligned}
$$

With a_3 and a_4 still unknown, we are able to find coefficients α and β for our radiating solutions (see equations (4.20) and (4.22)) in terms of a_3 and a_4. Evaluating (A.13) at the shelf-break, it follows that

$$
\begin{aligned}
\alpha = \frac{g\,\tilde{Q}\sqrt{\varepsilon}}{1+\Lambda}\left(\frac{c_C}{c_\infty}\right)^2\left\{a_1 + a_3\left[\cos\left(\gamma\,\log\left(\frac{c_C}{C_D}\right)\right) + \right.\right. \\
\left.\left.\left(i\,\sigma^{-1}-\frac{1}{2}\right)\gamma^{-1}\,\sin\left(\gamma\,\log\left(\frac{c_C}{c_D}\right)\right)\right] + a_4\left(\frac{c_D}{c_C}\right)^{3/2}\right\}, \qquad \text{(A.16)}
\end{aligned}
$$

while evaluating at the foot of the slope,

$$\beta = \frac{g\,\tilde{Q}\sqrt{\varepsilon}}{1+\Lambda}\left(\frac{c_D}{c_\infty}\right)^2\left\{a_1 + a_2\,\Lambda + a_3\left(\frac{c_C}{c_D}\right)^{3/2} + a_4\left[\cos\left(\gamma\,\log\left(\frac{c_C}{C_D}\right)\right) + \left(i\,\sigma^{-1}+\frac{1}{2}\right)\gamma^{-1}\,\sin\left(\gamma\,\log\left(\frac{c_C}{c_D}\right)\right)\right]\right\}. \tag{A.17}$$

To find unknown coefficients a_3 and a_4, we may now apply the continuity conditions given in radiating conditions (A.2) and (A.3).

$$\left(\frac{\mathrm{d}}{\mathrm{d}\nu} + i\,\sigma^{-1}\,\frac{c_\infty}{c_C}\right)V_1(\nu) = \frac{-2g\,\sqrt{\varepsilon}\,\tilde{Q}}{1+\Lambda}\,\frac{c_C}{c_\infty}, \qquad \text{at } \nu = c_C/c_\infty \tag{A.18}$$

and

$$\left(\frac{\mathrm{d}}{\mathrm{d}\nu} - i\,\sigma^{-1}\,\frac{c_\infty}{c_D}\right)V_1(\nu) = -2g\,\sqrt{\varepsilon}\,\tilde{Q}\,\frac{c_D}{c_\infty}, \qquad \text{at } \nu = c_D/c_\infty. \tag{A.19}$$

Substitution of (A.13) into equations (A.18)–(A.19) yield

$$\frac{c_C\,g\,\tilde{Q}\,\sqrt{\varepsilon}}{c_\infty\,(1+\Lambda)\,\sigma}\left(a_1\,(2\sigma+i) - \frac{a_2\,c_C\,\Lambda\,\sigma}{c_C-c_D} + 2i\,a_3\,\tilde{D}\right) = \frac{-2g\,\sqrt{\varepsilon}\,\tilde{Q}}{1+\Lambda}\,\frac{c_C}{c_\infty} \tag{A.20}$$

and

$$\frac{c_D\,g\,\tilde{Q}\,\sqrt{\epsilon}}{c_\infty\,(1+\Lambda)\,\sigma}\left((a_1+a_2\,\Lambda)\,(2\,\sigma-i) - \frac{a_2\,c_D\,\Lambda\,\sigma}{c_C-c_D} - 2i\,a_4\,\tilde{D}\right) = -2g\,\sqrt{\varepsilon}\,\tilde{Q}\,\frac{c_D}{c_\infty}, \tag{A.21}$$

where

$$\tilde{D} = \cos\left(\gamma\,\log\left(\frac{c_C}{c_D}\right)\right) + i\,\gamma^{-1}\,\sigma^{-1}\,\sin\left(\gamma\,\log\left(\frac{c_C}{c_D}\right)\right). \tag{A.22}$$

As explained in Griffiths and Grimshaw (2007a), since γ is either real or imaginary, the first term of (A.22) is always real, while the second term is always imaginary. Furthermore, both terms are unable to vanish simultaneously, meaning that $\tilde{D}$ is always non-zero, and our solution across the slope is always well-defined.

Upon rearranging for unknowns a_3 and a_4 through equations (A.20) and (A.21) respectively, we conclude that

$$\begin{aligned} a_3 &= \frac{i\,\sigma}{2\tilde{D}}\left[2 + a_1\left(2 + i\,\sigma^{-1}\right) + a_2\,\Lambda\left(\frac{1}{(c_D/c_C)-1}\right)\right] \\ &= \frac{1}{2\tilde{D}}\left[2i\,\sigma\,(1+a_1) - a_1 + a_2\,\frac{i\,c_C}{\omega_f\,L_C}\right] \end{aligned} \tag{A.23}$$

and

$$\begin{aligned} a_4 &= \frac{-i\,\sigma}{2\tilde{D}}\left[2\,(1+\Lambda) + a_1\left(2 - i\,\sigma^{-1}\right) + a_2\,\Lambda\left(2 - i\,\sigma^{-1} + \frac{1}{1-(c_C/c_D)}\right)\right] \\ &= \frac{-1}{2\tilde{D}}\left[2i\,\sigma\,(1+a_1+\Lambda\,\{1+a_2\}) + a_1 + a_2\,\frac{i\,c_D}{\omega_f\,L_C}\left(1 - i\,\sigma^{-1}\,\frac{c_D-c_C}{c_D}\right)\right], \end{aligned} \tag{A.24}$$

again, agreeing with Griffiths and Grimshaw (2007a) (see equations (D4a) and (D4b)).

To arrive at the step solution, consider the limit $L_S \to 0$ with all other parameters fixed. The latter results in $\Lambda = L_S/L_C \to 0$ and $\sigma = (c_D - c_C)/\omega_f L_S \to \infty$, such that equations (A.11), (A.22), (A.23) and (A.24) simplify to give

$$\begin{pmatrix} a_1 \\ a_2 \end{pmatrix} \to \begin{pmatrix} -1 \\ -1 \end{pmatrix} \qquad \text{and} \qquad \begin{pmatrix} a_3 \\ a_4 \end{pmatrix} \to \frac{1}{2\tilde{D}} \begin{pmatrix} 1 - i\, c_C/\omega_f L_C \\ 1 + i\, c_D/\omega_f L_C \end{pmatrix} \tag{A.25}$$

with

$$\tilde{D} \to \frac{1}{2}\sqrt{c_C\, c_D}\, (c_C + c_D)\,. \tag{A.26}$$

Finally, we substitute equations (A.25) and (A.26) into (A.13) to arrive at the exact solution presented in equation (4.51). The latter is identical to (D6) of Griffiths and Grimshaw (2007a).

Appendix B

Python Code

In this appendix, we attach details regarding the various Python packages which were developed as part of the thesis. The four Python packages were fundamental in the research presented in Chapters 5–7. To allow for reproducibility of the work presented in this thesis, we attach links to the various Python packages stored on `GitHub`.

To install the packages, it is recommended that the repositories are cloned from `GitHub`. The packages are then installed using `pip`. Within a cloned repository, one would execute the following:

```
pip install -U -e .
```

B.1 ppp

The Python package ppp contains a series of general modules which detail general algorithms. These allow, for example, the storage and visualisation of numerical data and the management of file systems. In many cases, but not all, examples of the module's functions are provided at the end of the script, which, when imported, are not called. This is a result of the statement `if __name__ == '__main__'`. There is a requirement that the package ppp is installed before being able to use any of the subsequent packages.

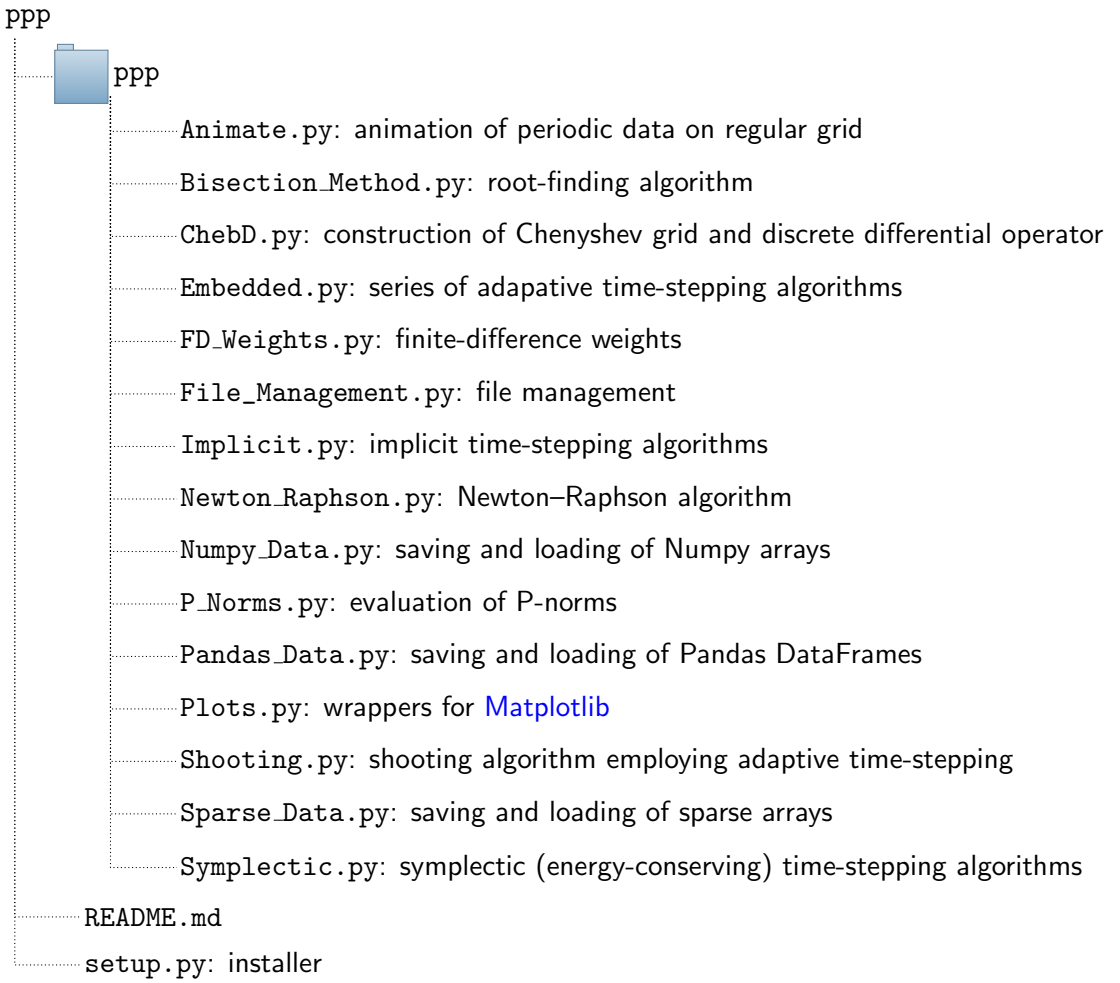

B.2 DGFEM

The Python package `DGFEM` is the module which constructs the finite-element objects using an interpolation polynomial basis of order `N` for any 2D mesh. Based on the MATLAB code presented in Hesthaven and Warburton (2008), the function needs only a set of points `P` and connectivity array `T`. There is also the functionality of applying different boundary conditions, but is often left unprescribed.

In the module `dgfem.py`, there are remnants of code where other features have been partially implemented. For example, initial attempts were made at implementing the use of non-conforming meshes and iso-parametric meshes. However, these were found to be superfluous for the research conducted as part of this thesis.

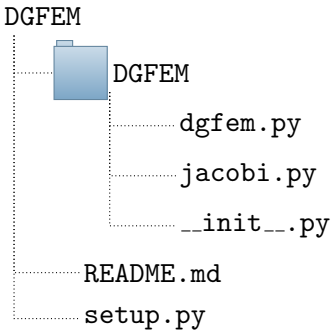

B.3 barotropicSWEs

The purpose of package `barotropicSWEs` is twofold. The package contains the work used to verify the numerical implementation of DG-FEM by solving the barotropic shallow-water equations (see Chapter 5), as well as studying the effect of canyon geometry on the barotropic tide in the form of a Kelvin wave (see Chapter 6).

As shown on the following page, the package is broken down into five directories:

- `Analysis`: Performs the analysis on how idealised canyon geometry modifies the barotropic Kelvin wave.
- `Configuration`: Contains the module `configure.py` which initialises all parameter values. These values are then checked by `namelist.py` against `defaults.json`. This category also contains a series of modules on idealised canyon-slope topographies. In particular, it is the module `topography_sdg_revision.py` which provides the formulation of the idealised shelf-incising canyon model used in Chapters 6 and 7. While `topography_previous_papers.py` contains the formulation of previous idealised canyon models found in literature, the module `topography.py` contains initial attempts at producing novel idealised canyon models. While obsolete for the purposes of this thesis, the module is highlighted for its legacy.
- `Kelvin`: Contains the module which solves numerically for the barotropic Kelvin wave of a prescribed shelf-slope topography and wave frequency.
- `MeshGeneration`: Generates the refined two-dimensional meshes for the barotropic tide by calling `OceanMesh`.
- `Tests`: Validation of numerical implementation of DG-FEM within Python under h- and p-refinement for a series of test cases (see Section 5.6).

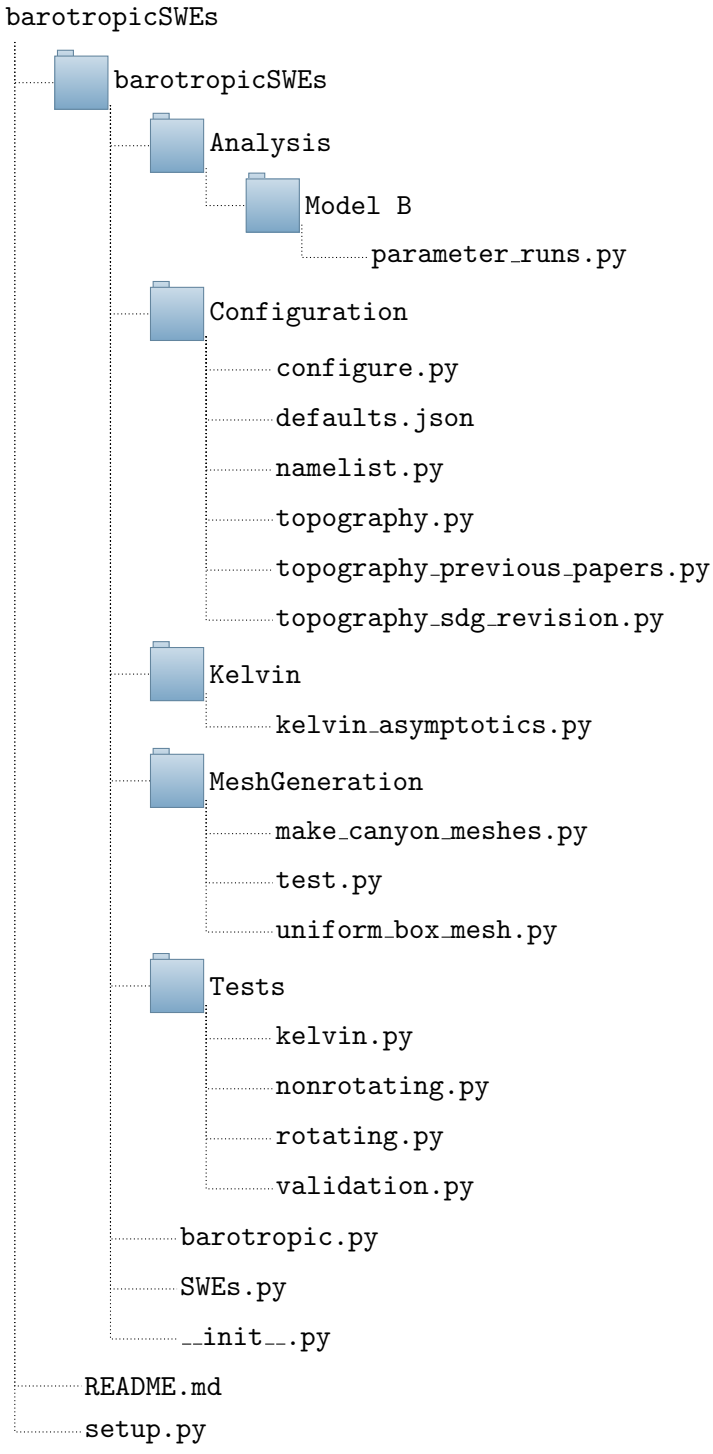

B.4 baroclinicSWEs

Lastly, the package `baroclinicSWEs` contains the code used to study the effect of idealised canyon geometry on internal-tide generation along continental margins, as presented in Chapter 7. The package depends on the preceding three packages, along with `OceanMesh`.

As shown on the following page, the package is divided into three principal directories:

- `Analysis`: Perofrms the analysis on how idealised canyon geometry affects tidal

dissipation along continental margins. In particular, `parameter_runs.py` generates the data presented in Sections 7.3 and 7.4, while `unmodified_flow_analysis.py` generates the data presented in Section 7.5.

- `Configuration`: Provides a series of numerical experiments to configure the analyses on the barotropic and baroclinic tides. In particular, `experiments.py` conducts the experiments to configure both the barotropic domain size and local test function order (see Section 6.4.1), along with the parameters for the"pretty good" sponge (see Section 7.2.2).
- `MeshGeneration`: Generates the refined two-dimensional meshes for the baroclinic tide by calling `OceanMesh`.

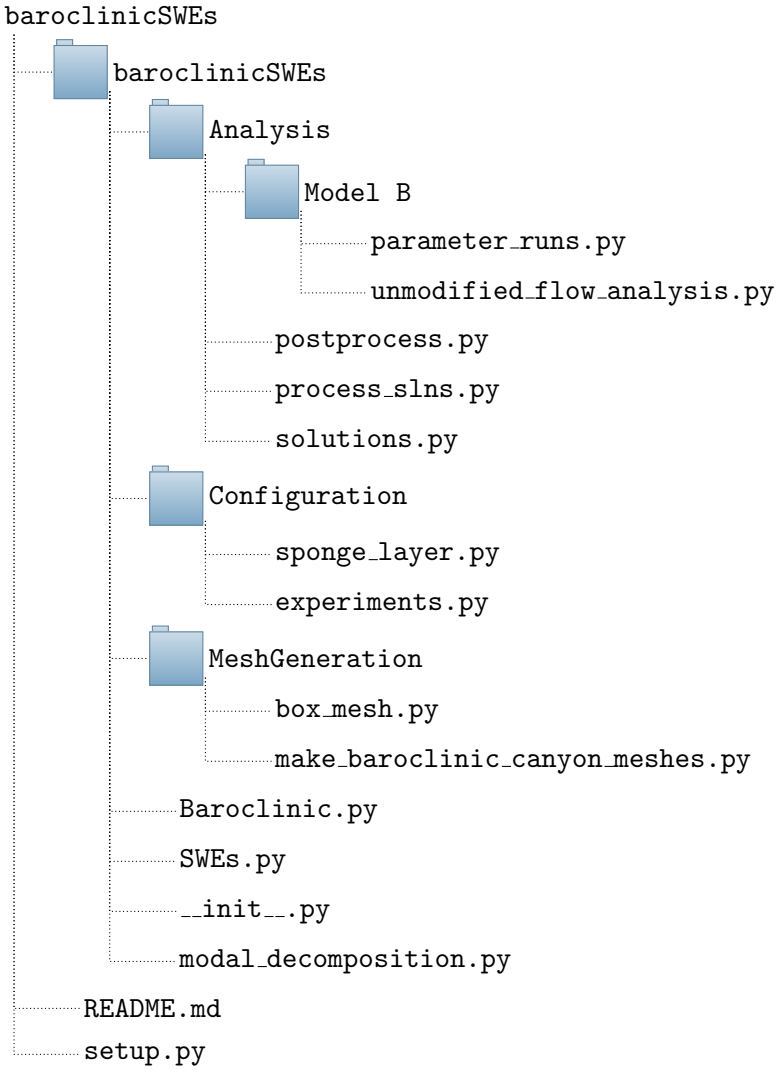

References

Abramowitz, M., & Stegun, I. A. (1964). *Handbook of mathematical functions with formulas, graphs, and mathematical tables* (9th ed.). Dover.

Alford, M. H., & Zhao, Z. (2007a). Global Patterns of Low-Mode Internal-Wave Propagation. Part I: Energy and Energy Flux. *Journal of Physical Oceanography*, *37*(7), 1829–1848. https://doi.org/10.1175/jpo3085.1

Alford, M. H., & Zhao, Z. (2007b). Global Patterns of Low-Mode Internal-Wave Propagation. Part II: Group Velocity. *Journal of Physical Oceanography*, *37*(7), 1849–1858. https://doi.org/10.1175/jpo3086.1

Ambati, V. R., & Bokhove, O. (2007). Space–time discontinuous Galerkin discretization of rotating shallow water equations. *Journal of Computational Physics*, *225*(2), 1233–1261. https://doi.org/10.1016/j.jcp.2007.01.036

Amblas, D., Ceramicola, S., Gerber, T. P., Canals, M., Chiocci, F. L., Dowdeswell, J. A., Harris, P. T., Huvenne, V. A., Lai, S. Y., Lastras, G., Iacono, C. L., Micallef, A., Mountjoy, J. J., Paull, C. K., Puig, P., & Sanchez-Vidal, A. (2018). Submarine Canyons and Gullies. In A. Micallef, S. Krastel, & A. Savini (Eds.), *Submarine geomorphology* (pp. 251–272). Springer International Publishing. https://doi.org/10.1007/978-3-319-57852-1

Arakawa, A., & Lamb, V. R. (1980). A Potential Enstrophy and Energy Conserving Scheme for the Shallow Water Equations. *Monthly Weather Review*, *109*, 18–36. https://doi.org/10.1175/1520-0493(1981)109⟨0018:APEAEC⟩2.0.CO;2

Arbic, B. K., Garner, S. T., Hallberg, R. W., & Simmons, H. L. (2004). The accuracy of surface elevations in forward global barotropic and baroclinic tide models. *Deep Sea Research Part II: Topical Studies in Oceanography*, *51*(25–26), 3069–3101. https://doi.org/10.1016/j.dsr2.2004.09.014

Arbic, B. K., St-Laurent, P., Sutherland, G., & Garrett, C. (2007). On the resonance and influence of the tides in Ungava Bay and Hudson Strait. *Geophysical Research Letters*, *34*(17). https://doi.org/10.1029/2007GL030845

Atkins, H. L., & Shu, C.-W. (1998). Quadrature-Free Implementation of Discontinuous Galerkin Method for Hyperbolic Equations. *AIAA Journal*, *36*(5), 775–782. https://doi.org/10.2514/2.436

Baines, P. G. (1973). The generation of internal tides by flat-bump topography. *Deep Sea Research and Oceanographic Abstracts*, *20*(2), 179–205. https://doi.org/10.1016/0011-7471(73)90050-8

Baines, P. G. (1974). The Generation of Internal Tides over Steep Continental Slopes. *Philosophical Transactions of the Royal Society A: Mathematical, Physical and Engineering Sciences*, *277*(1263), 27–58. https://doi.org/10.1098/rsta.1974.0045

Baines, P. G. (1982). On internal tide generation models. *Deep Sea Research Part A. Oceanographic Research Papers*, *29*(3), 307–338. https://doi.org/10.1016/0198-0149(82)90098-x

Baines, P. G. (1983). Tidal Motion in Submarine Canyons - A Laboratory Experiment. *Journal of Physical Oceanography*, *13*(2), 310–328. https://doi.org/10.1175/1520-0485(1983)013⟨0310:TMISCL⟩2.0.CO;2

Barthélemy, E., Kabbaj, A., & Germain, J. P. (2000). Long surface wave scattered by a step in a two-layer fluid. *Fluid Dynamics Research*, *26*, 235–255. https://doi.org/10.1016/s0169-5983(99)00025-8

Bell, T. H. (1975a). Lee waves in stratified flows with simple harmonic time dependence. *Journal of Fluid Mechanics*, *67*(4), 705–722. https://doi.org/10.1017/s0022112075000560

Bell, T. H. (1975b). Topographically generated internal waves in the open ocean. *Journal of Geophysical Research*, *80*(3), 320–327. https://doi.org/10.1029/jc080i003p00320

Bernsen, E., Bokhove, O., & van der Vegt, J. J. W. (2005). *A (dis)continuous finite element model for generalized 2d vorticity dynamics*. Universiteit Twente, Faculteit Toegepaste Wiskunde. https://research.utwente.nl/en/publications/a-discontinuous-finite-element-model-for-generalized-2d-vorticity-2

Bertoluzza, S., Russo, G., Falletta, S., & Shu, C.-W. (2009). The numerical flux function. *Numerical solutions of partial differential equations* (pp. 89–95). Birkhäuser Basel. https://doi.org/10.1007/978-3-7643-8940-6_7

Blumberg, A. F., & Mellor, G. L. (1987). A description of a three-dimensional coastal ocean circulation model. *Three-dimensional coastal ocean models* (pp. 1–16). American Geophysical Union (AGU). https://doi.org/10.1029/CO004p000

Bodony, D. J. (2006). Analysis of sponge zones for computational fluid mechanics. *Journal of Computational Physics*, *212*(2), 681–702. https://doi.org/10.1016/j.jcp.2005.07.014

Boffi, D., Brezzi, F., & Fortin, M. (2013). *Mixed finite element methods and applications*. Springer. https://doi.org/10.1007/978-3-642-36519-5

Bokhove, O., & Pegler, S. (2018). Lecture notes in MATH 3458/5458: Geophysical Fluid Dynamics.

Bond, T. J., Swannell, J. H., Henshell, R. D., & Warburton, G. B. (1973). A comparison of some curved two-dimensional finite elements. *Journal of Strain Analysis*, *8*(3), 182–190. https://doi.org/10.1243/03093247V083182

Bondy, J. A., & Murty, U. S. R. (2008). *Graph theory*. Springer. https://link.springer.com/gp/book/9781846289699

Bourgault, D., Galbraith, P. S., & Chavanne, C. (2016). Generation of internal solitary waves by frontally forced intrusions in geophysical flows. *Nature Communications*, *9*(1). https://doi.org/10.1038/ncomms13606

Boussinesq, J. (1901). *Théorie analytique de la chaleur mise en harmonie avec la thermodynamique et avec la théorie mécanique de la lumière*. Gauthier-Villars.

Boyce, W. E., DiPrima, R. C., & Meade, D. B. (2017). *Elementary differential equations and boundary value problems*. Wiley. https://books.google.co.uk/books?id=SyaVDwAAQBAJ

Bretherton, C. (2014). Lecture notes in ATMS 509/OCEAN 512 Geophysical Fluid Dynamics I [Accessed: 27/09/2022]. https://atmos.uw.edu/~breth/classes/AS509/lect/lect4.pdf

Buijsman, M. C., McWilliams, J. C., & Jackson, C. R. (2010). East-west asymmetry in nonlinear internal waves from Luzon Strait. *Journal of Geophysical Research*, *115*(C10), C10057. https://eprints.soton.ac.uk/340318/

Carter, G. S. (2010). Barotropic and Baroclinic M2 Tides in the Monterey Bay Region. *Journal of Physical Oceanography*, *40*(8), 1766–1783. https://doi.org/10.1175/2010JPO4274.1

Cartwright, D. E. (1999). *Tides: A scientic history*. Cambridge University Press.

Cartwright, D. E., Edden, A. C., Spencer, R., & Vassie, J. M. (1980). The tides of the northeast Atlantic Ocean. *Philosophical Transactions of the Royal Society of London. Series A, Mathematical and Physical Sciences*, *298*, 87–139.

Chakraverty, S., Mahato, N. R., Karunakar, P., & Rao, T. D. (2019). Weighted residual methods. *Advanced numerical and semi-analytical methods for differential equations* (pp. 31–43). John Wiley & Sons, Ltd. https://doi.org/10.1002/9781119423461.ch3

Chandler, D. L. (2014). The ocean's hidden waves show their power [Accessed: 04/05/2022]. https://news.mit.edu/2013/the-oceans-hidden-waves-show-their-power-0108

Chapront, J., Chapront-Touzé, M., & Francou, G. (2002). A new determination of lunar orbital parameters, precession constant and tidal acceleration from LLR measurements. *Astronomy & Astrophysics*, *387*(2), 700–709. https://doi.org/10.1051/0004-6361:20020420

Charney, J. G. (1955). The Generation of Oceanic Currents by Wind. *Journal of Marine Research*, *14*, 477–498.

Chomaz, J.-M. (2019). Lecture notes in Foundation: Waves & rotation, FDSE Summer School.

Clarke, A. J. (1991). The dynamics of barotropic tides over the continental shelf and slope (review). In B. B. Parker (Ed.), *Tidal hydrodynamics* (pp. 79–108). John Wiley & Sons.

Cotter, C. J., Ham, D. A., & Pain, C. C. (2009). A mixed discontinuous/continuous finite element pair for shallow-water ocean modelling. *Ocean Modelling*, *26*(1), 86–90. https://doi.org/10.1016/j.ocemod.2008.09.002

Cox, C., & Sandstrom, H. (1962). Coupling of internal and surface waves in water of variable depth. *Journal of the Oceanographic Society of Japan*, *20*(18), 499–513.

Craig, P. D. (1987). Solutions for internal tidal generation over coastal topography. *Journal of Marine Research*, *45*(1), 83–105. https://doi.org/10.1357/002224087788400954

Dellar, P. J. (2010). Variations on a beta-plane: derivation of non-traditional beta-plane equations from Hamilton's principle on a sphere. *Journal of Fluid Mechanics*, *674*, 174–195. https://doi.org/10.1017/S0022112010006464

Dodd, R. K., Eilbeck, J. D., & Morris, H. C. (1982). *Solitons and nonlinear wave equations*. Academic Press.

Drazin, P. G. (1988). *Solitons: An introduction*. Cambridge University Press.

Duda, T. F., Newhall, A. E., Gawarkiewicz, G., Caruso, M. J., Graber, H. C., Yang, Y. J., & Jan, S. (2013). Significant internal waves and internal tides measured northeast of Taiwan. *Journal of Marine Research*, *71*(1–2), 47–81. https://doi.org/10.1357/002224013807343416

Egbert, G. D., & Erofeeva, S. Y. (2002). Efficient Inverse Modeling of Barotropic Ocean Tides. *Journal of Atmosphere and Oceanic Technology*, *19*(2), 183–204. https://doi.org/10.1175/1520-0426(2002)019⟨0183:EIMOBO⟩2.0.CO;2

Egbert, G. D., & Ray, R. D. (2000). Significant dissipation of tidal energy in the deep ocean inferred from satellite altimeter data. *Nature*, *405*(6788), 775–778. https://doi.org/10.1038/35015531

Egbert, G. D., & Ray, R. D. (2001). Estimates of M2 tidal energy dissipation from TOPEX/Poseidon altimeter data. *Journal of Geophysical Research: Oceans*, *106*(C10), 22475–22502. https://doi.org/10.1029/2000jc000699

Egbert, G. D., & Ray, R. D. (2003). Semi-diurnal and diurnal tidal dissipation from TOPEX/Poseidon altimetry. *Geophysical Research Letters*, *30*(17). https://doi.org/10.1029/2003gl017676

Ekman, V. W. (1904). On dead water. *Norwegian north polar expedition, 1893–1896* (pp. 83–278). Longmans, Green; co. https://doi.org/10.5962/bhl.title.6514

Epperson, J. F. (1987). On the Runge Example. *The American Mathematical Monthly*, *94*(4), 329–341. Retrieved April 12, 2022, from http://www.jstor.org/stable/2323093

Eskilsson, C., & Sherwin, S. J. (2004). A triangular spectral/hp discontinuous Galerkin method for modelling 2d shallow water equations. *International Journal for Numerical Methods in Fluids*, *45*(6), 605–623. https://doi.org/10.1002/fld.709

Eskilsson, C., & Sherwin, S. J. (2005). Discontinuous Galerkin Spectral/hp Element Modelling of Dispersive Shallow Water Systems. *Journal of Scientific Computing*, *22*(1), 269–288. https://doi.org/10.1007/s10915-004-4140-x

Finlayson, B. A. (2013). *The method of weighted residuals and variational principles*. Society for Industrial; Applied Mathematics. https://doi.org/10.1137/1.9781611973242

Finlayson, B. A., & Scriven, L. E. (1966). The method of weighted residuals - a review. *Applied Mechanics Reviews*, *19*(9), 735–748.

Flather, R. A. (1976). A tidal model of the northwest European continental shelf. *Mémoires de la Société Royale des Sciences de Liège*, *10*(6), 141–164.

Fornberg, B. (1996). *A practical guide to pseudospectral methods*. Cambridge University Press. https://doi.org/10.1017/CBO9780511626357

Fringer, O. B., Gerritsen, M., & Street, R. L. (2006). An unstructured-grid, finite-volume, nonhydrostatic, parallel coastal ocean simulator. *Ocean Modelling*, *14*(3), 139–173. https://doi.org/10.1016/j.ocemod.2006.03.006

Garrett, C. (1972). Tidal Resonance in the Bay of Fundy and Gulf of Maine. *Nature*, *238*, 441–443.

Garrett, C. (1979). Mixing in the ocean interior. *Dynamics of Atmospheres and Oceans*, *3*(2-4), 239–265. https://doi.org/10.1016/0377-0265(79)90011-3

Garrett, C. (2001). Internal waves. In J. H. Steele (Ed.), *Encyclopedia of ocean sciences* (Second, pp. 266–273). Academic Press. https://doi.org/10.1016/B978-012374473-9.00126-0

Garrett, C., & Kunze, E. (2007). Internal Tide Generation in the Deep Ocean. *Annual Review of Fluid Mechanics*, *39*(1), 57–87. https://doi.org/10.1146/annurev.fluid.39.050905.110227

Garrett, C., & Munk, W. (1979). Internal Waves in the Ocean. *Annual Review of Fluid Mechanics*, *11*(1), 339–369. https://doi.org/10.1146/annurev.fl.11.010179.002011

Gayen, B., & Sarkar, S. (2010). Turbulence During the Generation of Internal Tide on a Critical Slope. *Physical review letters*, *104*, 218502. https://doi.org/10.1103/PhysRevLett.104.218502

Gerkema, T. (2019). *An introduction to tides*. Cambridge University Press. https://doi.org/10.1017/9781316998793

Gill, A. E. (1982). *Atmosphere-ocean dynamics*. Academic.

Giraldo, F. X., Hesthaven, J. S., & Warburton, T. (2002). Nodal high-order discontinuous Galerkin methods for the spherical shallow water equations. *Journal of Computational Physics*, *181*(2), 499–525. https://doi.org/10.1006/jcph.2002.7139

Godin, G. (1972). *The analysis of tides*. University of Toronto Press.

Goldstein, H., Poole, C. P., & Safko, J. L. (2001). *Classical mechanics* (3rd ed.). Addison Wesley.

Gordon, R. L. (1978). Internal wave climate near the coast of northwest Africa during JOINT-I. *Deep Sea Research*, *25*(7), 625–643. https://doi.org/10.1016/0146-6291(78)90617-3

Gordon, R. L., & Marshall, N. F. (1976). Submarine canyons: Internal wave traps? *Geophysical Research Letters*, *3*(10), 622–624. https://doi.org/10.1029/GL003i010p00622

Griffiths, S. D. (2010). Global modelling of internal tides. *Second Scotland-Norway Internal Waves Symposium*.

Griffiths, S. D. (2012). THE LONG AND SHORT OF GLOBAL MODELLING OF OCEAN TIDES. *Isaac Newton Institute for Mathematical Sciences*.

Griffiths, S. D., & Grimshaw, R. H. J. (2007a). Internal Tide Generation at the Continental Shelf Modeled Using a Modal Decomposition: Two-Dimensional Results. *Journal of Physical Oceanography*, *37*(3), 428–451. https://doi.org/10.1175/jpo3068.1

Griffiths, S. D., & Grimshaw, R. H. J. (2007b). Modelling internal tide generation using a modal decomposition. *AMS 16th Conference on Atmospheric and Oceanic Fluid Dynamics*. https://doi.org/10.13140/2.1.3705.8563

Grimshaw, R. H. J. (2007). Internal solitary waves in a variable medium. *GAMM-Mitteilungen*, *30*(1), 96–109. https://doi.org/10.1002/gamm.200790014

Gurvan, M., Bourdallé-Badie, R., Chanut, J., Clementi, E., Coward, A., Ethé, C., Iovino, D., Lea, D., Lévy, C., Lovato, T., Martin, N., Masson, S., Mocavero, S., Rousset, C., Storkey, D., Müeller, S., Nurser, G., Bell, M., Samson, G., ... Moulin, A. (2022). NEMO ocean engine. https://doi.org/10.5281/zenodo.6334656

Gustafsson, B., Kreiss, H. O., & Oliger, J. (2001). *Partial differential equations and difference approximations*. John Wiley & Sons.

Hall, R. A., Alford, M. H., Carter, G. S., Gregg, M. C., Lien, R.-C., Wain, D. J., & Zhao, Z. (2014). Transition from partly standing to progressive internal tides in monterey submarine canyon [Submarine Canyons: Complex Deep-Sea Environments Unravelled by Multidisciplinary Research]. *Deep Sea Research Part II: Topical Studies in Oceanography*, *104*, 164–173. https://doi.org/10.1016/j.dsr2.2013.05.039

Hall, R. A., & Carter, G. S. (2011). Internal Tides in Monterey Submarine Canyon. *Journal of Physical Oceanography*, *41*(1), 186–204. https://doi.org/10.1175/2010jpo4471.1

Hallock, Z. R., & Field, R. L. (2005). Internal-Wave Energy Fluxes on the New Jersey Shelf. *Journal of Physical Oceanography*, *35*(1), 3–12. https://doi.org/10.1175/JPO-2662.1

Harris, P. T., Macmillan-Lawler, M., Rupp, J., & Baker, E. K. (2014). Geomorphology of the oceans. *Marine Geology*, *352*, 4–24. https://doi.org/10.1016/j.margeo.2014.01.011

Harris, P. T., & Whiteway, T. (2011). Global distribution of large submarine canyons: Geomorphic differences between active and passive continental margins. *Marine Geology*, *285*(1–4), 69–86. https://doi.org/10.1016/j.margeo.2011.05.008

Hazewinkel, J., & Winters, K. B. (2011). PSI of the Internal Tide on a β Plane: Flux Divergence and Near-Inertial Wave Propagation. *Journal of Physical Oceanography*, *41*(9), 1673–1682. https://doi.org/10.1175/2011JPO4605.1

Heath, R. A. (1981). Estimates of the resonant period and Q in the semi-diurnal tidal band in the North Atlantic and Pacific Oceans. *Deep Sea Research Part A. Oceanographic Research Papers*, *28*(5), 481–493. https://doi.org/10.1016/0198-0149(81)90139-4

Helland-Hansen, B., & Nansen, F. (1909). The Norwegian sea—its physical oceanography based upon the Norwegian researches 1900—1904. *Report on norwegian fishery and marine investigations* (pp. 390–). Kristiania, Det Mallingske bogtrykkeri.

Hendershott, M. C. (1981). Long waves and ocean tides. In B. A. Warren & C. Wunsch (Eds.), *Evolution of physical oceanography* (pp. 292–341). MIT Press.

Hesthaven, J. S., & Warburton, T. (2008). *Nodal discontinuous Galerkin methods : Algorithms, analysis, and applications* (Vol. 54). Springer. https://doi.org/10.1007/978-0-387-72067-8

Hickey, B. M. (1995). Coastal submarine canyons. In P. Muller & D. Henderson (Eds.), *'aha huliko' a workshop on flow topography interactions* (pp. 95–110). SOEST Special Publications.

Hill, J. (2019). Astoria Canyon multibeam bathymetry [Accessed: 04/07/2023]. https://www.usgs.gov/media/images/astoria-canyon-multibeam-bathymetry

Holloway, P. E., Chatwin, P. G., & Craig, P. (2001). Internal Tide Observations from the Australian North West Shelf in Summer 1995. *Journal of Physical Oceanography*, *31*(5), 1182–1199. https://doi.org/10.1175/1520-0485(2001)031⟨1182:ITOFTA⟩2.0.CO;2

Holloway, P. E., & Merrifield, M. A. (1999). Internal tide generation by seamounts, ridges, and islands. *Journal of Geophysical Research: Oceans*, *104*(C11), 25937–25951. https://doi.org/10.1029/1999jc900207

Hotchkiss, F. S., & Wunsch, C. (1982). Internal waves in Hudson Canyon with possible geological implications. *Deep Sea Research Part A. Oceanographic Research Papers*, *29*(4), 415–442. https://doi.org/10.1016/0198-0149(82)90068-1

Hough, S. S. (1898). On the Application of Harmonic Analysis to the Dynamical Theory of the Tides. Part II: On the General Integration of Laplace's Dynamical Equations. *Philosophical Transactions of the Royal Society A*, *191*, 139–185.

Hu, F. Q. (2008). Development of PML absorbing boundary conditions for computational aeroacoustics: A progress review [Turbulent Flow and Noise Generation]. *Computers & Fluids*, *37*(4), 336–348. https://doi.org/10.1016/j.compfluid.2007.02.012

Huthnance, J. M. (1975). On trapped waves over a continental shelf. *Journal of Fluid Mechanics*, *69*(4), 689–704.

Huthnance, J. M. (1981). Waves and currents near the continental shelf edge. *Progress in Oceanography*, *10*(4), 193–226. https://doi.org/10.1016/0079-6611(81)90004-5

Huthnance, J. M. (1989). Internal tides and waves near the continental shelf edge. *Geophysical & Astrophysical Fluid Dynamics*, *48*(1–3), 81–106. https://doi.org/10.1080/03091928908219527

Huthnance, J. M., & Baines, P. G. (1982). Tidal currents in the northwest African upwelling region. *Deep Sea Research Part A. Oceanographic Research Papers*, *29*(3), 285–306. https://doi.org/10.1016/0198-0149(82)90097-8

Intergovernmental Panel on Climate Change (IPCC). (2022). Changing Ocean, Marine Ecosystems, and Dependent Communities. *The ocean and cryosphere in a changing climate: Special report of the intergovernmental panel on climate change* (pp. 447–588). Cambridge University Press. https://doi.org/10.1017/9781009157964.007

Jachec, S. M. (2012). Power Estimates Associated With Internal Tides From the Monterey Bay Area. *Oceanography*, *25*(2), 52–55. 10.5670/oceanog.2012.41

Jachec, S. M., Fringer, O. B., Gerritsen, M. G., & Street, R. L. (2006). Numerical simulation of internal tides and the resulting energetics within Monterey Bay and the surrounding area. *Geophysical Research Letters*, *33*(12). https://doi.org/10.1029/2006GL026314

Jackson, C. R. (2004). *An atlas of internal solitary-like waves and their properties* (2nd ed.). Global Ocean Associates.

Jeffreys, H. (1921). Tidal Friction in Shallow Seas. *Philosophical Transactions of the Royal Society A: Mathematical, Physical and Engineering Sciences*, *221*(582–593), 239–264. https://doi.org/10.1098/rsta.1921.0008

Johnson, C., & Pitkaranta, J. (1986). An Analysis of the discontinuous Galerkin method for a scalar hyperbolic equation. *Mathematics of Computation*, *46*.

Johnston, T. M. S., Rudnick, D. L., Carter, G. S., Todd, R. E., & Cole, S. T. (2011). Internal tidal beams and mixing near Monterey Bay. *Journal of Geophysical Research: Oceans*, *116*(C3). https://doi.org/10.1029/2010JC006592

Kang, D., & Fringer, O. (2012). Energetics of Barotropic and Baroclinic Tides in the Monterey Bay Area. *Journal of Physical Oceanography*, *42*(2), 272–290. https://doi.org/10.1175/JPO-D-11-039.1

Kantha, L. H., & Tierney, C. C. (1997). Global baroclinic tides. *Progress in Oceanography*, *40*(1-4), 163–178. https://doi.org/10.1016/s0079-6611(97)00028-1

Keller, H. B. (1992). *Numerical Methods for Two-point Boundary-value Problems*. Dover Publications. https://books.google.co.uk/books?id=mkPvAAAAMAAJ

Kelly, S. M. (2016). The Vertical Mode Decomposition of Surface and Internal Tides in the Presence of a Free Surface and Arbitrary Topography. *Journal of Physical Oceanography*, *46*(12), 3777–3788. https://doi.org/10.1175/JPO-D-16-0131.1

Kelly, S. M., & Nash, J. D. (2010). Internal-tide generation and destruction by shoaling internal tides. *Geophysical Research Letters*, *37*(23). https://doi.org/10.1029/2010GL045598

Khan, A. A., & Lai, W. (2014). *Modeling shallow water flows using the discontinuous Galerkin method* (1st ed.). CRC Press. https://doi.org/10.1201/b16579

Korteweg, D. J., & de Vries, G. (1895). XLI. On the change of form of long waves advancing in a rectangular canal, and on a new type of long stationary waves. *The London, Edinburgh, and Dublin Philosophical Magazine and Journal of Science*, *39*(240), 422–443. https://doi.org/10.1080/14786449508620739

Kunze, E., MacKay, C., McPhee-Shaw, E. E., Morrice, K., Girton, J. B., & Terker, S. R. (2012). Turbulent mixing and exchange with interior waters on sloping boundaries. *Journal of Physical Oceanography*, *42*(6), 910–927. https://doi.org/10.1175/JPO-D-11-075.1

Kunze, E., Rosenfeld, L. K., Carter, G. S., & Gregg, M. C. (2002). Internal Waves in Monterey Submarine Canyon. *Journal of Physical Oceanography*, *32*(6), 1890–1913. https://doi.org/10.1175/1520-0485(2002)032⟨1890:iwimsc⟩2.0.co;2

Lahaye, N., & Llewellyn Smith, S. G. (2020). Modal Analysis of Internal Wave Propagation and Scattering over Large-Amplitude Topography. *Journal of Physical Oceanography*, *50*(2), 305–321. https://doi.org/10.1175/JPO-D-19-0005.1

Lamb, H. (1895). *Hydrodynamics*. University Press. https://www.biodiversitylibrary.org/item/70745

Lambeck, K. (1980). *The Earth's Variable Rotation: Geophysical Causes and Consequences*. Cambridge University Press. https://doi.org/10.1017/CBO9780511569579

Laplace, P. S. (1775). Recherches sur plusieurs points du système du monde. *Mémoires de l'Académie royale des sciences de Paris*, 71–183.

Lavelle, J. W., & Thacker, W. C. (2008). A pretty good sponge: Dealing with open boundaries in limited-area ocean models. *Ocean Modelling*, *20*(3), 270–292. https://doi.org/10.1016/j.ocemod.2007.10.002

Le Roux, D. Y., Staniforth, A., & Lin, C. A. (1998). Finite Elements for Shallow-Water Equation Ocean Models. *Monthly Weather Review*, *126*(7), 1931–1951. https://doi.org/10.1175/1520-0493(1998)126⟨1931:FEFSWE⟩2.0.CO;2

LeBlond, P. H., & Mysak, L. A. (1978). *Waves in the Ocean*. Elsevier.

Legg, S., & Klymak, J. M. (2008). Internal Hydraulic Jumps and Overturning Generated by Tidal Flow over a Tall Steep Ridge. *Journal of Physical Oceanography*, *38*, 1949–1964. https://doi.org/10.1175/2008JPO3777.1

LeSaint, P., & Raviart, P. A. (1974). On a finite element method for solving the neutron transport equation. In C. de Boor (Ed.), *Mathematical aspects of finite elements in partial differential equations* (pp. 89–123). Academic Press. https://doi.org/10.1016/B978-0-12-208350-1.50008-X

LeVeque, R. J. (2002). *Finite volume methods for hyperbolic problems*. Cambridge University Press. https://doi.org/10.1017/CBO9780511791253

Levin, J. C., Iskandarani, M., & Haidvogel, D. B. (2006). To continue or discontinue: Comparisons of continuous and discontinuous Galerkin formulations in a spectral element ocean model [The Third International Workshop on Unstructured Mesh Numerical Modelling of Coastal, Shelf and Ocean Flows]. *Ocean Modelling*, *15*(1), 56–70. https://doi.org/10.1016/j.ocemod.2005.10.001

Lien, R.-C., & Gregg, M. (2001). Observations of turbulence in a tidal beam and across a coastal ridge. *Journal of Geophysical Research*, *106*, 4575–4592. https://doi.org/10.1029/2000JC000351

Lighthill, M. J. (1969). Dynamic Response of the Indian Ocean to Onset of the Southwest Monsoon. *Philosophical Transactions of the Royal Society of London. Series A, Mathematical and Physical Sciences*, *265*(1159), 45–92. https://doi.org/10.1098/rsta.1969.0040

Lipton, R. J., Rose, D. J., & Tarjan, E. T. (1979). Generalized nested dissection. *SIAM Journal on Numerical Analysis*, *16*(2), 346–358. http://www.jstor.org/stable/2156840

Llewellyn Smith, S. G., & Young, W. R. (2002). Conversion of the Barotropic Tide. *Journal of Physical Oceanography*, *32*(5), 1554–1566. https://doi.org/10.1175/1520-0485(2002)032⟨1554:cotbt⟩2.0.co;2

Longuet-Higgins, M. S. (1952). Water Movements in lakes during Summer Stratification; Evidence from the Distribution of Temperature in Windermere: Appendix: Oscillations in a Three-Layered Stratified Basin. *Philosophical Transactions of the Royal Society of London. Series B, Biological Sciences*, *236*(635), 399–404. Retrieved April 20, 2022, from http://www.jstor.org/stable/92424

Longuet–Higgins, M. S. (1968). The eigenfunctions of Laplace's tidal equation over a sphere. *Philosophical Transactions of the Royal Society of London. Series A, Mathematical and Physical Sciences*, *262*, 511–607. https://doi.org/10.1098/rsta.1968.0003

MacKinnon, J. A., & Winters, K. B. (2005). Subtropical catastrophe: Significant loss of low-mode tidal energy at 28.9°. *Geophysical Research Letters*, *32*(15). https://doi.org/10.1029/2005GL023376

Martinsen, E. A., & Engedahl, H. (1987). Implementation and testing of a lateral boundary scheme as an open boundary condition in a barotropic ocean model. *Coastal Engineering*, *11*, 603–627.

Maugé, R., & Gerkema, T. (2008). Generation of weakly nonlinear nonhydrostatic internal tides over large topography: A multi-modal approach. *Nonlinear Processes in Geophysics*, *15*, 233–244. https://doi.org/10.5194/npg-15-233-2008

Meckes, E. S., & Meckes, M. W. (2018). *Linear algebra*. Cambridge University Press. https://doi.org/10.1017/9781316823200

Melet, A. V., Hallberg, R., & Marshall, D. P. (2022). The role of ocean mixing in the climate system. In M. Meredith & A. Naveira Garabato (Eds.), *Ocean mixing* (pp. 5–34). Elsevier. https://doi.org/10.1016/B978-0-12-821512-8.00009-8

Mercier, M. J., Gostiaux, L., Helfrich, K., Sommeria, J., Viboud, S., Didelle, H., Ghaemsaidi, S. J., Dauxois, T., & Peacock, T. (2013). Large-scale, realistic laboratory modeling of M2 internal tide generation at the Luzon Strait. *Geophysical Research Letters*, *40*(21), 5704–5709. https://doi.org/10.1002/2013GL058064

Merritt, Y. (2019). Offshore deep sea canyon fascinates Monterey Peninsula [Accessed: 04/07/2023]. https://thelutrinae.com/2019/02/offshore-deep-sea-canyon-fascinates-monterey-peninsula/

Miles, J. (1972). Kelvin waves on oceanic boundaries. *Journal of Fluid Mechanics*, *55*, 113–127. https://doi.org/10.1017/S0022112072001685

Miller, K., & Miller, R. N. (1981). Moving Finite Elements. I. *SIAM Journal on Numerical Analysis*, *18*(6), 1019–1032. https://doi.org/10.1137/0718070

Min, J. B., Bass, J. M., & Spradley, L. W. (1994). Solution-adaptive finite element method in computational fracture mechanics. *34th Structures, Structural Dynamics and Materials Conference*, 433–445. https://doi.org/10.2514/6.1993-1449

Morozov, E. G. (1995). Semidiurnal internal wave global field. *Deep Sea Research Part I: Oceanographic Research Papers*, *42*(1), 135–148. https://doi.org/10.1016/0967-0637(95)92886-c

Mortimer, C. H. (1952). Water movements in lakes during summer stratification; evidence from the distribution of temperature in Windermere. *Philosophical Transactions of the Royal Society of London. Series B, Biological Sciences*, *236*(635), 355–398. Retrieved April 22, 2022, from http://www.jstor.org/stable/92423

Moxey, D., Green, M. D., Sherwin, S. J., & Peiró, J. (2015). On the generation of curvilinear meshes through subdivision of isoparametric elements. *New challenges in grid*

generation and adaptivity for scientific computing (pp. 203–215). Springer, Cham. https://doi.org/10.1007/978-3-319-06053-8_10

Müller, P. (2006). *The Equations of Oceanic Motions*. Cambridge University Press. https://doi.org/10.1017/CBO9780511617843

Müller, P., Holloway, G., Henyey, F., & Pomphrey, N. (1986). Nonlinear interactions among internal gravity waves. *Review of Geophysics*, *24*, 493–536. https://doi.org/10.1029/RG024i003p00493

Munk, W. (1981). Internal waves and small-scale processes. In B. A. Warren & C. Wunsch (Eds.), *Evolution of physical oceanography* (pp. 264–291). MIT Press.

Munk, W., Snodgrass, F., & Wimbush, M. (1970). Tides off-shore: Transition from California coastal to deep-sea waters. *Geophysical and Astrophysical Fluid Dynamics*, *1*, 161–235. https://doi.org/10.1080/03091927009365772

Munk, W., & Wunsch, C. (1998). Abyssal recipes II: energetics of tidal and wind mixing. *Deep Sea Research Part I: Oceanographic Research Papers*, *45*(12), 1977–2010. https://doi.org/10.1016/s0967-0637(98)00070-3

Munroe, J. R., & Lamb, K. G. (2005). Topographic amplitude dependence of internal wave generation by tidal forcing over idealized three-dimensional topography. *Journal of Geophysical Research*, *110*(C2), CO2011. https://doi.org/10.1029/2004jc002537

Nansen, F. (1902). Oceanography of the North Pole Basin: Norwegian North Polar Expeditian, 1893–1896. *Scientific Results*, *3*(9), 1–427.

Nash, J. D., Kunze, E., Toole, J. M., & Schmitt, R. W. (2004). Internal Tide Reflection and Turbulent Mixing on the Continental Slope. *Journal of Physical Oceanography*, *34*(5), 1117–1134. https://doi.org/10.1175/1520-0485(2004)034⟨1117:ITRATM⟩2.0.CO;2

National Oceanographic Data Center (U.S.), O. C. L. (2013). *World Ocean Database 2013*. NOAA Printing Office. https://data.nodc.noaa.gov/woa/WOD13/DOC/wod13_intro.pdf

Nazarian, R. H., Burns, C. M., Legg, S., Buijsman, M. C., Kaur, H., & Arbic, B. K. (2021). On the Magnitude of Canyon-Induced Mixing. *Journal of Geophysical Research: Oceans*, *126*(11), e2021JC017671. https://doi.org/10.1029/2021JC017671

Nazarian, R. H., & Legg, S. (2017a). Internal wave scattering in continental slope canyons, part 1: Theory and development of a ray tracing algorithm. *Ocean Modelling*, *118*, 1–15. https://doi.org/10.1016/j.ocemod.2017.07.002

Nazarian, R. H., & Legg, S. (2017b). Internal wave scattering in continental slope canyons, Part 2: A comparison of ray tracing and numerical simulations. *Ocean Modelling*, *118*, 16–30. https://doi.org/10.1016/j.ocemod.2017.07.005

New, A. L., & Pingree, R. (1992). Local generation of internal soliton packets in the central bay of Biscay. *Deep Sea Research Part A. Oceanographic Research Papers*, *39*(9), 1521–1534. https://doi.org/10.1016/0198-0149(92)90045-U

NOAA. (2017). https://oceanservice.noaa.gov/facts/upwelling.html

NOAA National Geophysical Data Center. (2006). 2-minute Gridded Global Relief Data (ETOPO2) v2 [Accessed: 27/11/2018]. https://doi.org/doi:10.7289/V5J1012Q

Oliveira, E. R. A. (1971). *Optimization of Finite Element Solutions* (tech. rep. AFFDL TR 71-160). Technical University of Lisbon. http://contrails.iit.edu/reports/10700

Pedlosky, J. (1987). *Geophysical fluid dynamics* (2nd ed.). Springer.

Pedlosky, J. (2003). *Waves in the Ocean and Atmosphere: Introduction to Wave Dynamics* (1st ed.). Springer. https://doi.org/10.1007/978-3-662-05131-3

Pelinovsky, E., Kurkina, O., Slunyaev, A., & Talipova, T. (2007). Internal solitary waves. WIT Press. https://doi.org/10.2495/978-1-84564-157-3/04

Persson, P.-O. (2006). Mesh size functions for implicit geometries and PDE-based gradient limiting. *Engineering with Computers*, *22*(2), 95–109. https://doi.org/10.1007/s00366-006-0014-1

Pétrélis, F., Llewellyn Smith, S. G., & Young, W. R. (2006). Tidal Conversion at a Submarine Ridge. *Journal of Physical Oceanography*, *36*(6), 1053–1071. https://doi.org/10.1175/jpo2879.1

Petruncio, E. T., Paduan, J. D., & Rosenfeld, L. K. (2002). Numerical simulations of the internal tide in a submarine canyon. *Ocean Modelling*, *4*, 221–248. https://doi.org/10.1016/S1463-5003(02)00002-1

Petruncio, E. T., Rosenfeld, L. K., & Paduan, J. D. (1998). Observations of the Internal Tide in Monterey Canyon. *Journal of Physical Oceanography*, *28*(10), 1873–1903. https://doi.org/10.1175/1520-0485(1998)028⟨1873:OOTITI⟩2.0.CO;2

Petterson, O. (1908). Strömstudier vid Östersjönsportar. *Svenska Hydrogr. Biol. Komm. Skrifter*, *3*, 13–37.

Pingree, R., & New, A. (1989). Downward propagation of internal tidal energy in the Bay of Biscay. *Deep Sea Research Part A. Oceanographic Research Papers*, *36*, 735–758. https://doi.org/10.1016/0198-0149(89)90148-9

Pingree, R. D., Mardell, G. T., & New, A. L. (1986). Propagation of internal tides from the upper slopes of the Bay of Biscay. *Nature*, *321*(6066), 154–158. https://doi.org/10.1038/321154a0

Platzman, G. W. (1972). Two-Dimensional Free Oscillations in Natural Basins. *Journal of Physical Oceanography*, *2*(2), 117–138. https://doi.org/10.1175/1520-0485(1972)002⟨0117:TDFOIN⟩2.0.CO;2

Platzman, G. W. (1984). Normal Modes of the World Ocean. Part IV: Synthesis of Diurnal and Semidiurnal Tides. *Journal of Physical Oceanography*, *14*(10), 1532–1550. https://doi.org/10.1175/1520-0485(1984)014⟨1532:NMOTWO⟩2.0.CO;2

Platzman, G. W. (1991). Tidal evidence for ocean normal modes. In B. B. Parker (Ed.), *Tidal hydrodynamics* (pp. 79–108). John Wiley & Sons.

Polzin, K. L., Toole, J. M., Ledwell, J. R., & Schmitt, R. W. (1997). Spatial Variability of Turbulent Mixing in the Abyssal Ocean. *Science*, *276*(5309), 93–96. https://doi.org/10.1126/science.276.5309.93

Pond, S., & Pickard, G. L. (1983). *Introductory dynamical oceanography* (2nd ed.). Pergamon Press.

Press, W. H., Teukolsky, S. A., Vetterling, W. T., & Flannery, B. P. (2007). *Numerical recipes* (3rd ed.). Cambridge University Press.

Pringle, W. J., Wirasaet, D., Roberts, K. J., & Westerink, J. J. (2021). Global storm tide modeling with ADCIRC v55: unstructured mesh design and performance. *Geoscientific Model Development*, *14*(2), 1125–1145. https://doi.org/10.5194/gmd-14-1125-2021

Prinsenberg, S., & Rattray, M. (1975). Effects of continental slope and variable brunt-väisälä frequency on the coastal generation of internal tides. *Deep Sea Research and Oceanographic Abstracts*, *22*(4), 251–265. https://doi.org/10.1016/0011-7471(75)90030-3

Rainville, L., Shaun Johnston, T. M., Carter, G. S., Merrifield, M. A., Pinkel, R., Worcester, P. F., & Dushaw, B. D. (2010). Interference Pattern and Propagation of the M2 Internal Tide South of the Hawaiian Ridge. *Journal of Physical Oceanography*, *40*(2), 311–325. https://doi.org/10.1175/2009JPO4256.1

Rattray, M. (1960). On the coastal generation of internal tides. *Tellus*, *12*(1), 54–62. https://doi.org/10.1111/j.2153-3490.1960.tb01283.x

Rattray, M., Dworski, J. G., & Kovala, P. E. (1969). Generation of long internal waves at the continental slope. *Deep Sea Research Part I: Oceanographic Research Papers*, *16*(Supplement), 179–195.

Ray, R. D., & Mitchum, G. T. (1997). Surface manifestation of internal tides in the deep ocean: Observations from altimetry and island gauges. *Progress in Oceanography*, *40*(1-4), 135–162. https://doi.org/10.1016/s0079-6611(97)00025-6

Reed, W. H., & Hill, T. R. (1973). *Triangular mesh methods for the neutron transport equation* (tech. rep. LA-UR-73-479). Los Alamos Scientific Laboratory Report. https://digital.library.unt.edu/ark:/67531/metadc1036080/

Remaki, M., & Fézoui, L. (1998). *Une méthode de Galerkin discontinu pour la résolution des équations de maxwell en milieu hétérogéne* (tech. rep. No. 3501). INRIA.

Roberts, K. J. (2019). *Unstructured mesh generation and dynamic load balancing for coastal ocean hydrodynamic simulation* (Doctoral dissertation). University of Notre Dame.

Roberts, K. J., Pringle, W. J., & Westerink, J. J. (2019a). Oceanmesh2d 1.0: Matlab-based software for two-dimensional unstructured mesh generation in coastal ocean modeling. *Geoscientific Model Development*, *12*(5), 1847–1868. https://doi.org/10.5194/gmd-12-1847-2019

Roberts, K. J., Pringle, W. J., & Westerink, J. J. (2019b). Oceanmesh2d: User guide - precise distance-based two-dimensional automated mesh generation toolbox intended for coastal ocean/shallow water. https://doi.org/10.13140/RG.2.2.21840.61446/2

Roberts, K. J., Pringle, W. J., Westerink, J. J., Contreras, M. T., & Wirasaet, D. (2019). On the automatic and a priori design of unstructured mesh resolution for coastal ocean circulation models. *Ocean Modelling*, *144*, 101509. https://doi.org/10.1016/j.ocemod.2019.101509

Rosenfeld, L. K., Paduan, J. D., Petruncio, E. T., & Goncalves, J. E. (1999). Numerical simulations and observations of the internal tide in a submarine canyon. *Proceedings of the 11th 'Aha Huliko'a Hawaiian Winter Workshop*, 63–71.

Rossby, C.-G. et al. (1939). Relation between variations in the intensity of the zonal circulation of the atmosphere and the displacements of the semi-permanent centers of action. *Journal of Marine Research*, *2*(1), 38–55.

Rudnick, D. L., Boyd, T. J., Brainard, R. E., Carter, G. S., & Egbert, G. D. (2003). From Tides to Mixing Along the Hawaiian Ridge. *Science*, *301*(5631), 355–357. https://doi.org/10.1126/science.1085837

Salehipour, H., Stuhne, G. R., & Peltier, W. R. (2013). A higher order discontinuous Galerkin, global shallow water model: Global ocean tides and aquaplanet benchmarks. *Ocean Modelling*, *69*, 93–107. https://doi.org/10.1016/j.ocemod.2013.06.001

Schlömer, N. (2020). Dmsh. https://github.com/nschloe/dmsh

Schmaltz, J. (2016). NASA Image of the Day for February 17, 2016: Atmospheric waves and internal waves make an appearance on the same day off the western coast of Australia. [Accessed: 12/05/2020]. https://eoimages.gsfc.nasa.gov/images/imagerecords/87000/87519/indianocean_tmo_2016041_lrg.jpg

Schott, F. (1977). On the energetics of baroclinic tides in the North Atlantic. *Annales de Géophysique*, *33*, 41–62.

Shchepetkin, A. F., & McWilliams, J. C. (2005). The Regional Oceanic Modeling System (ROMS): A split-explicit, free-surface, topography-following-coordinate oceanic model. *Ocean Modelling*, *9*, 347–404. https://doi.org/10.1016/j.ocemod.2004.08.002

Shepard, F. P. (1963). *Submarine geology* (2nd ed.). Harper & Row.

Shimizu, K. (2011). A Theory of Vertical Modes in Multilayer Stratified Fluids. *Journal of Physical Oceanography*, *41*(9), 1694–1707. https://doi.org/10.1175/2011jpo4546.1

Small, J., Hallock, Z. R., Pavey, G., & Scott, J. C. (1999). Observations of large amplitude internal waves at the Malin Shelf edge during SESAME 1995. *Continental Shelf Research*, *19*, 1389–1436. https://doi.org/10.1016/S0278-4343(99)00023-0

Smith, R. (1972). Nonlinear Kelvin and continental-shelf waves. *Journal of Fluid Mechanics*, *52*(2), 379–391. https://doi.org/10.1017/S002211207200148X

St. Laurent, L., & Garrett, C. (2002). The Role of Internal Tides in Mixing the Deep Ocean. *Journal of Physical Oceanography*, *32*(10), 2882–2899. https://doi.org/10.1175/1520-0485(2002)032⟨2882:troiti⟩2.0.co;2

Steinmoeller, D. T., Stastna, M., & Lamb, K. G. (2016). Discontinuous Galerkin methods for dispersive shallow water models in closed basins: Spurious eddies and their removal using curved boundary methods. *Ocean Modelling*, *107*, 112–124. https://doi.org/10.1016/j.ocemod.2016.10.007

Stokes, G. G. (1847). *On the theory of oscillatory waves*. Printed at the Pitt Press by John W. Parker. https://books.google.co.uk/books?id=cUPhvQEACAAJ

Subeesh, M. P., Unnikrishnan, A. S., & Francis, P. A. (2021). Generation, propagation and dissipation of internal tides on the continental shelf and slope off the west coast of India. *Continental Shelf Research*, *214*, 104321. https://doi.org/10.1016/j.csr.2020.104321

Sutherland, B. R. (2010). *Internal gravity waves*. Cambridge University Press. https://doi.org/10.1017/CBO9780511780318

Taylor, G. I. (1936). The Oscillations of the Atmosphere. *Proceedings of the Royal Society of London. Series A - Mathematical and Physical Sciences*, *156*(888), 318–326. https://doi.org/10.1098/rspa.1936.0150

Teeluck, V. (2013). *Surface and internal tides above sea-floor topography* (Doctoral dissertation). University of Leeds. https://etheses.whiterose.ac.uk/6351/

Thomson, W. (1879). On Gravitational Oscillations of Rotating Water. *Proceedings of the Royal Society of Edinburgh*, *10*, 92–100. https://doi.org/10.1017/S0370164600043467

Thorpe, S. A. (1975). The excitation, dissipation, and interaction of internal waves in the deep ocean. *Journal of Geophysical Research*, *80*(3), 328–338. https://doi.org/10.1029/jc080i003p00328

Toro, E. F. (2009). *Riemann Solvers and Numerical Methods for Fluid Dynamics: A Practical Introduction* (3rd ed.). Springer. https://doi.org/10.1007/b79761

Toulopoulos, I., & Ekaterinaris, J. A. (2006). High-order discontinuous Galerkin discretizations for computational aeroacoustics in complex domains. *AIAA Journal*, *44*(3), 502–511. https://doi.org/10.2514/1.11422

Vallis, G. K. (2006). *Atmospheric and oceanic fluid dynamics*. Cambridge University Press.

van der Vegt, J. J. W., Izsak, F., & Bokhove, O. (2007). Error analysis of a continuous-discontinous Galerkin finite element model for generalized 2d vorticity dynamics. *SIAM journal on numerical analysis*, *45*(1/4), 1349–1369. https://doi.org/10.1137/050633202

Veronis, G., & Stommel, H. (1956). The Action of Variable Wind Stress on a Stratified Ocean. *Journal of Marine Research*, *15*, 43–75.

Vic, C., Naveira Garabato, A. C., Mattias Green, J. A., Waterhouse, A. F., Zhao, Z.-K., Melet, A., de Lavergne, C., Buijsman, M. C., & Stephenson, G. R. (2019). Deep-ocean mixing driven by small-scale internal tides. *Nature Communications*, *10*. https://doi.org/10.1038/s41467-019-10149-5

Vlasenko, V., Stashchuk, N., & Hutter, K. (2005). *Baroclinic tides: Theoretical Modeling and Observational Evidence*. Cambridge University Press. https://doi.org/10.5670/oceanog.2006.107

Vlasenko, V., Stashchuk, N., Inall, M. E., Porter, M., & Aleynik, D. (2016). Focusing of baroclinic tidal energy in a canyon. *Journal of Geophysical Research*, *121*, 2824–2840. https://doi.org/10.1002/2015JC011314

Walters, R. A., & Casulli, V. (1998). A robust, finite element model for hydrostatic surface water flows. *Communications in Numerical Methods in Engineering*, *14*(10), 931–940. https://doi.org/10.1002/(SICI)1099-0887(1998100)14:10⟨931::AID-CNM199⟩3.0.CO;2-X

Wang, X., Chao, Y., Dong, C., Farrara, J., Li, Z., McWilliams, J. C., Paduan, J. D., & Rosenfeld, L. K. (2009). Modeling tides in Monterey Bay, California [AOSN II: The Science and Technology of an Autonomous Ocean Sampling Network]. *Deep*

Sea Research Part II: Topical Studies in Oceanography, *56*(3), 219–231. https://doi.org/10.1016/j.dsr2.2008.08.012

Warburton, T. (1999). Application of the discontinuous Galerkin method to Maxwell's equations using unstructured polymorphic hp-finite elements. In B. Cockburn, G. E. Karniadakis, & C. W. Shu (Eds.), *Discontinuous Galerkin Methods: Theory, Computation and Applications* (pp. 451–458). Springer-Verlag. https://doi.org/10.1007/978-3-642-59721-3_47

Wilkin, J. L., & Chapman, D. C. (1987). Scattering of Continental Shelf Waves at a Discontinuity in Shelf Width. *Journal of Physical Oceanography*, *17*(6), 713–724. https://doi.org/10.1175/1520-0485(1987)017⟨0713:SOCSWA⟩2.0.CO;2

Wunsch, C. (1975). Internal tides in the ocean. *Reviews of Geophysics*, *13*(1), 167–182. https://doi.org/10.1029/rg013i001p00167

Wunsch, C. (2000). Moon, tides and climate. *Nature*, *405*, 743–744. https://doi.org/10.1038/35015639

Wunsch, C., & Ferrari, R. (2004). Vertical mixing, energy, and the general circulation of the oceans. *Annual Review of Fluid Mechanics*, *36*(1), 281–314. https://doi.org/10.1146/annurev.fluid.36.050802.122121

Yankovsky, A. E., & Zhang, T. (2017). Scattering of a Semidiurnal Barotropic Kelvin Wave into Internal Waves over Wide Continental Shelves. *Journal of Physical Oceanography*, *47*(10), 2545–2562. https://doi.org/10.1175/jpo-d-16-0284.1

Yuan, C., Grimshaw, R. H. J., & Johnson, E. (2018). The evolution of second mode internal solitary waves over variable topography. *Journal of Fluid Mechanics*, *836*, 238–259. https://doi.org/10.1017/jfm.2017.812

Yuan, C., Grimshaw, R. H. J., Johnson, E., & Chen, X. (2018). The Propagation of Internal Solitary Waves over Variable Topography in a Horizontally Two-Dimensional Framework. *Journal of Physical Oceanography*, *48*(2), 283–300. https://doi.org/10.1175/JPO-D-17-0154.1

Yuan, C., Grimshaw, R. H. J., Johnson, E. R., & Whitfield, A. J. (2020). Generation of nonlinear internal waves by flow over topography: Rotational effects. *Physical review. E*, *101 3-1*, 33104. https://doi.org/10.1103/PhysRevE.101.033104

Zeilon, N. O. (1912). On Tidal Boundary-waves and Related Hydrodynamical Problems. *Kungliga Sven. Vetensk. Handl. Ny Följden*, *47*(4), 1–46.

Zeilon, N. O. (1934). Experiments on boundary tides: A preliminary report. *Göteborgs Kungiga. Vetenskaps-och vitterhets-samhälles handlingar*, *B3*(10), 1–8.

Zhang, W. G., Duda, T. F., & Udovydchenkov, I. A. (2014). Modeling and Analysis of Internal-Tide Generation and Beamlike Onshore Propagation in the Vicinity of Shelfbreak Canyons. *Journal of Physical Oceanography*, *44*(3), 834–849. https://doi.org/10.1175/JPO-D-13-0179.1

Zhao, Z., Alford, M. H., Girton, J. B., Rainville, L., & Simmons, H. L. (2016). Global Observations of Open-Ocean Mode-1 M2 Internal Tides. *Journal of Physical Oceanography*, *46*(6), 1657–1684. https://doi.org/10.1175/JPO-D-15-0105.1